UNIVERSITEIT VAN PRETORIA
UNIVERSITY OF PRETORIA
YUNIBESITHI YA PRETORIA

Electrochemical and Electrocatalytic Properties of Carbon Nanotubes Integrated with Selected Metal and Metal Oxide Nanoparticles

by

Abolanle Saheed Adekunle

A dissertation submitted in fulfillment of the requirements for the degree of

DOCTOR OF PHILOSOPHY

in the Faculty of Natural and Agricultural Science

University of Pretoria

Supervisor: Dr. K. I. Ozoemena

October 2010

© University of Pretoria

UNIVERSITEIT VAN PRETORIA
UNIVERSITY OF PRETORIA
YUNIBESITHI YA PRETORIA

DECLARATION

I declare that the dissertation which is hereby submitted to the Department of Chemistry, Faculty of Natural and Agricultural Sciences, University of Pretoria, is my work and has not been submitted by me for a degree at any other University, and that all material contained therein has been duly acknowledged.

DEDICATION

This dissertation is dedicated first to the glory of the Almighty Allah for giving me the strength to see the end of the programme despite all odds. And my parents, Engineer Alabi Saubana Adekunle, Mr Tajudeen Ayinla Adekunle and Mrs Agbeke Temilola Adekunle for their unquantified support.

ACKNOWLEDGEMENTS

Firstly, I wish to express my unending appreciation to Almighty Allah for giving me the strength and the health to completing this programme. My gratitude's to my able supervisor, Dr. K. I. Ozoemena for his patience and guidance in making this dream a reality. Thank you Doc.! My appreciations also go to my wife, Mrs Rukoyat Adekunle; my daughter, Firdaus Adekunle; my parents, Engineer Alabi Saubana Adekunle, Mr Tajudeen Ayinla Adekunle and Mrs Agbeke Temilola Adekunle; Dr. B.O. Agboola, Dr Jamiu Abdulazeez, Mr Winston Doherty, friends and my family at large for their love, prayers and support. My sincere gratitude to the authority of Obafemi Awolowo University for enabling me to proceed on the study leave, Prof M.S. Akanni, my HOD, Prof. I.A.O. Ojo and other staff and colleagues of the Department of Chemistry, OAU, Ile-Ife, Nigeria. Finally, I thank the National Research Foundation (NRF, South Africa), DST/NRF Nanotechnology Innovation Centre (NIC)-Sensors, South Africa, and the University of Pretoria, for their financial and facilities assistance. Thanks to Andrew Botha, Chris Merwe, Helena Steyn and Wiebke Grote for acquiring the HRSEM, TEM, EDX and XRD spectra. My colleagues in the same group for their love and support, and every other person that made this work a success. Thank you all!

ABSTRACT

This work describes metal (M) and metal oxides (MO) films (where M = Ni, Co and Fe) obtained by electrosynthesis and chemical synthesis, and modified with carbon nanotubes (CNTs) on edged plane pyrolytic graphite electrode (EPPGE). The MO nanoparticles investigated are nickel oxide (NiO), cobalt oxide (Co_3O_4) and iron oxide (Fe_2O_3). Successful modification of the electrodes with the M or MO/CNT nanocomposite was confirmed by field emission scanning electron microscopy (FESEM), high resolution scanning electron microscopy (HRSEM), high resolution transmission electron microscopy (HRTEM), atomic force microscopy (AFM), x-ray diffraction spectroscopy (XRD), x-ray photoelectron spectroscopy (XPS), electron dispersive x-ray spectroscopy (EDX), fourier transformed infra-red spectroscopy (FTIR) and ultraviolet-visible (UV-vis) spectroscopy. Electron transport (ET) properties of the modified electrodes was explored using cyclic voltammetry (CV) and electrochemical impedance spectroscopic techniques (EIS) with ferricyanide/ferrocyanide ($[Fe(CN)_6]^{3-/4-}$) as the redox probe. The electron transfer constant (k^0) differs in terms of materials, method of synthesis and electrical equivalent circuits used in the fitting or modelling process. Generally, the k^0 values are in the 10^{-3} – 10^{-2} cms^{-1} with Ni nanoparticles having the highest k^0 or fastest electron transport. The presence of CNTs also enhances the ET compared

with electrodes without CNTs. The electrocatalytic properties of the modified electrodes were explored using the following analytical probes: diethylaminoethanethiol (DEAET), hydrazine, nitrite and dopamine. The study showed that the electrocatalytic oxidation of DEAET and hydrazine was favoured on electrode modified with Ni nanoparticles; nitrite and dopamine were best catalysed by the Co and Fe_2O_3 nanoparticles, respectively. Electroanalysis results (using chronoamperometry, square wave voltammetry and linear sweep voltammetry) indicated some level of adsorption of DEAET, hydrazine and nitrite on the modified electrode, while dopamine electrocatalytic oxidation and detection followed a simple diffusion-controlled process. The adsorption process was found to be physically induced and could be eliminated by repetitive cycling of the electrode in the aqueous electrolyte solution. Electrodes modified with chemically-synthesised material (particularly nickel) were less adsorptive towards DEAET and hydrazine detection, and gave sensitivity and limit of detection values that compared with data obtained using electrochemical deposition / synthesis. The chemical stability and reproducibility of the modified electrodes were determined and discussed. Finally, electrochemical properties were studied to help screen these electrode materials in supercapacitors. CNT-NiO nanocomposites exhibit remarkable supercapacitive behaviour in neutral and acidic media compared to the other CNT-MO nanocomposites investigated. Interestingly, the

capacitive behaviour of the CNT-NiO was more enhanced in H_2SO_4 solution than in Na_2SO_4, possibly due to the high conductivity of the former. The CNT-NiO electrode maintained good stability with only about 5% loss of its specific capacitance after 1000 cycle life.

TABLE OF CONTENTS

DECLARATION i
DEDICATION ii
ACKNOWLEDGEMENTs iii
ABSTRACT iv
TABLE OF CONTENTS vii
LIST OF ABBREVIATIONS xvi
LIST OF SYMBOLS xviii
LIST OF FIGURES xx
LIST OF SCHEMES xxxiv
LIST OF TABLES xxxv

SECTION A

CHAPTER ONE

Introduction

1.1 General Overview of Thesis: Problem Statement 2
1.1.1 Carbon nanotube-metal and metal oxide nanocomposite in electrochemistry 3
1.1.1.1 Carbon nanotubes as electrical conducting nanowires.....3
1.1.1.2 Metal (M) and metal oxide (MO) nanoparticles as electrocatalyst 4
1.1.1.3 Carbon nanotube-metal and metal oxide modified electrode as sensor for the hydrazine, diethylaminoethanethiol, dopamine and nitrite. 5
1.1.1.4 Electron transport behaviour of CNT-M/MO modified electrodes. 5
1.1.2 Aim of thesis. 8

1.2 Overview of Electrochemistry 9
1.2.1 Basics of electrochemistry 9
1.2.1.1 Electrochemical equilibrium: Introduction 9
1.2.1.2 Electrochemical equilibrium: Electron transfer at the electrode-solution interface 11
1.2.1.3 Classification of electrochemical techniques 12
1.2.1.4 Faradaic and non-Faradaic processes 13
1.2.1.5 The electrochemical cell 13
1.2.1.6 Mass transport processes 14
1.3 Voltammetric Techniques 18
1.3.1 Types of voltammetry 19
1.3.1.1 Cyclic voltammetry 19
1.3.1.2 Square wave voltammetry 24
1.3.1.3 Linear sweep voltammetry (LSV) 25
1.3.1.4 Rotating disk electrode 26
1.3.1.5 Chronoamperometry 26
1.3.1.6 Galvanostatic charge discharge technique 28
1.3.1.7 Electrocatalysis using voltammetry 29
1.4 Electrochemical Impedance Spectroscopy (EIS) 31
1.4.1 Basics of impedance spectroscopy 31
1.4.2 Application and data presentation 33
1.5 Chemically Modified Electrodes 38
1.5.1 Carbon Electrodes 39
1.5.2 Carbon nanotubes modified electrodes 41
1.5.3 Metal and metal oxides nanoparticles (NPS) 43
1.5.4 Electrocatalytic behaviour of carbon nanotubes-metal nanocomposite modified electrodes 43
1.5.4.1 Nickel and nickel oxide carbon nanotubes modified electrodes 45
1.5.4.2 Iron and iron oxide carbon nanotubes modified electrodes 50

1.5.4.3 Cobalt and cobalt oxide carbon nanotubes modified electrodes 54
1.5.5 Supercapacitive behaviour of carbon nanotubes metal oxides 57
1.5.6 Electrode modification techniques 62
1.5.6.1 Electrodeposition 62
1.5.6.2 Electropolymerisation 63
1.5.6.3 Dip-dry 64
1.5.6.4 Drop-dry 64
1.5.6.5 Spin-coating 64
1.5.6.6 Composite technique: 64
1.5.6.7 Sol-gel method 65
1.5.6.8 Self-assmbled-monolayers 65
1.5.6.9 Langmuir- Blodgett technique 65
1.5.6.10 Chemical vapour deposition 66
1.6 Nanoscience in Electrochemistry 67
1.7 Langmuir Isotherm Adsorption Theory. 69
1.8 Microscopy and Spectroscopy Techniques 73
1.8.1 Microscopy 73
1.8.1.1 Scanning electron microscope (SEM) 73
1.8.1.2 Transmission electron microscope (TEM) 74
1.8.1.3 Atomic force microscope 75
1.8.2 Spectroscopy 76
1.8.2.1 Energy dispersive X-ray spectroscopy (EDS) 76
1.8.2.2 X-ray photoelectron spectroscopy 77
1.8.2.3 X-ray diffraction spectroscopy 78
1.8.2.4 Infrared spectroscopy 79
1.8.2.5 Ultraviolet-visible spectroscopy 80
1.9 Overview of Analytes Used As Analytical Probe 81
1.9.1 Hydrazine 81
1.9.2 Diethylaminoethanethiol 82
1.9.3 Nitrite 84

1.9.4 Dopamine 85
REFERENCES 87

CHAPTER TWO

Experimental

2.1 Materials and Reagents 112
2.1.1 Synthesis of funtionalised CNTs 113
2.1.2 Synthesis of nickel and nickel oxide nanoparticles 114
2.1.3 Synthesis of cobalt and cobalt oxide nanoparticles 115
2.1.4 Synthesis of iron and iron oxide nanoparticles 115
2.2 Equipment and Procedure 117
2.2.1 Assay of dopamine hydrochloride injection 119
2.3 Electrode Modification and Pretreatments 120
2.3.1 Electrode cleaning 120
2.3.2 Electrode modification 120
2.3.2.1 Drop-dry / electrodeposition techniques 120
2.3.1.2 Modification with Prussian blue (PB) nanoparticles 122
2.3.1.3 Electrode modification with synthesised M and MO nanoparticles. 123
2.4 Electron Transport Experimental Procedure.....124
2.5 Electrocatalytic and Electroanalysis Experiment Procedure**.**..125
2.5.1 Electrocatalytic procedure 125
2.5.2 Electroanalysis procedure 127
2.6 Electrochemical supercapacitive procedure 128
REFERENCES 131

SECTION B

RESULT AND DISCUSSION

CHAPTER THREE

Insights Into the Electro-oxidation of Hydrazine at Single-Walled Carbon Nanotube – Modified Edge-Plane Pyrolytic Graphite Electrode Electrodecorated with Metal and Metal Oxide Films

3.1 Comparative FESEM images and Electron-Dispersive X-rays. 135
3.2 Comparative Redox Chemistry of modified EPPGEs in Aqueous Solution 137
3.3 Comparative electrocatalytic oxidation of hydrazine 139
3.4 Electrochemical impedimetric studies 142
3.5 Effect of varying scan rates.....150
3.6 Chronoamperometric investigations 152
REFERENCES 157

CHAPTER FOUR

Electron Transfer Behaviour of Single-Walled Carbon Nanotubes Electro-Decorated with Nickel and Nickel Oxide Layers and Its Electrocatalysis Towards Diethylaminoethanethiol (DEAET): An Adsorption-Controlled Electrode Process

4.1 FTIR, SEM images and EDX characterisation 161
4.2 Comparative redox chemistry in aqueous solution 165
4.3 Comparative Electron Transport Properties 171
4.4 Electrochemical response of the Ni-modified electrodes 179
towards DEAET oxidation. 179
4.5 Comparative electrochemical response to DEAET at different Ni deposition time 181
4.6 Electroanalysis of DEAET 182
4.6.1 Scan rate study 182
REFERENCES 190

CHAPTER FIVE

Electron Tranport and Electrocatalytic Properties of MWCNT/Nickel Nanocomposite: Hydrazine and Diethylaminoethanethiol as Analytical Probes

5.1 Comparative TEM, XRD and EDX spectra 193
5.2 Comparative Electrochemical characterization.....196
5.3 Comparative electrocatalytic properties: DEAET and Hydrazine as analytical probe. 200
5.4 Effect of varying scan rates.....206
5.6 Electroanalysis of DEAET and Hydrazine 209
REFERENCES 217

CHAPTER SIX

Probing the Electrochemical Behaviour of SWCNT-Cobalt Nanoparticles and Their Electrocatalytic

Activities Towards the Detection of Nitrite in Acidic and Physiological pH Conditions

6.1 Comparative FESEM, AFM images EDX spectra 220
6.2 Comparative Electrochemical characterization 223
6.3 Comparative electron transport properties 224
6.4 Electrocatalytic oxidation of Nitrite in neutral and acidic pH. 229
6.5 Electrochemical impedance studies 231
6.6 Effect of varying scan rate 234
6.7 Electroanalysis of nitrite at neutral and acidic pH 236
REFERENCES 253

CHAPTER SEVEN

Electrocatalytic Detection of Dopamine at Single-Walled Carbon Nanotubes-Iron (iii) Oxide Nanoparticles Platform

7.1 Characterisation with FESEM, AFM, EDX and XPS 257
7.2 Electrocatalytic detection of dopamine: Voltammetric and Impedimetric properties.....262
7.3 Effect of varying potential scan rates.....268
7.4 Analytical Application.....270
7.5 Interference study.....274
7.6 Real sample analysis: Dopamine drug.....276
REFERENCES 295

CHAPTER EIGHT

Electrocatalytic Properties of Prussian Blue Nanoparticles Supported on Poly(m-Aminobenzenesulfonic Acid) – Funtionalized Single-Walled Carbon Nanotubes Toward the Detection of Dopamine

8.1 Comparative TEM and AFM images and UV-vis spectra 299
8.1.1. UV-vis-absorption spectroscopy characterization of the SWCNT-PABS, PB and the SWCNT-PB nanoparticles. 300
8.2 Cyclic voltammetric characterisation of the electrodes. 302
8.3 Electrocatalytic oxidation of dopamine.....305
8.4 Effect of varying scan rate 310
8.5 Electroanalysis using square wave voltammetry (SWV), chronoamperometric (CA) and Linear Sweep Voltammetry (LSV) 313
8.6 Detection of DA in the presence of AA (Interference study). 317
8.7 Real sample analysis: Dopamine drug 318
REFERENCES 320

CHAPTER NINE

Electrocatalytic Oxidation of Diethylaminoethanethiol, Hydrazine and Nitrite at Single-Walled Carbon Nanotubes Modified with Prussian Blue Nanoparticles

9.1 Microscopic and spectroscopic characterisation 323
9.2 Electrochemical characterization 327

9.3 Electrocatalytic oxidation properties 329
9.4 Concentration studies and proposed mechanism..... 338
REFERENCES 341

CHAPTER TEN

Supercapacitive Behaviour of Single-Walled/Multi-Walled Carbon Nanotubes-Metal (Ni, Fe, Co) Oxide Nanocomposites in Acidic and Neutral pH Conditions

10.1 Comparative EDX, XPS and FESEM 344
10.2 Comparative cyclic voltammetric experiments 348
10.3 Comparative galvanostatic charge / discharge experiments 349
10.4 Electrochemical impedance studies 355
References 371

CONCLUSIONS AND RECOMMENDATIONS 374

CONCLUSIONS 375

RECOMMENDATIONS 380

APPENDIX A List of publications in peer-reviewed journals from this thesis 381

APPENDIX B List of conference presentation from this thesis 383

LIST OF ABBREVIATIONS

A	Electrode surface area (cm^{-2})
AFM	Atomic force microscopy
Ag	Silver wire pseudo-reference electrode
Ag/AgCl	Silver/silver chloride reference electrode
BPPGE	Basal plane pyrolytic graphite electrode
CA	Chronoamperometric
CME	Chemically modified electrode
CNT	Carbon nanotubes
CV	Cyclic voltammetry
CV	Cyclic voltammogram
DMF	Dimethylformamide
EIS	Electrochemical impedance spectroscopy
EPPGE	Edge plane pyrolytic graphite electrode
EPPGE-SWCNT	Edge plane pyrolytic graphite electrode decorated single-walled carbon nanotubes
$Fe_4(III)[Fe(II)(CN)_6]^3$	Divalent iron (II)/(III) cyanide complex
FTIR	Fourier transform infrared
GCE	Glassy carbon electrode
LCR	Linear concentration range
LoD	Limit of detection
LSV	Linear sweep voltammetry
MMPs	Magnetic nanoparticles
MWCNT	Multi-walled carbon nanotubes
NPs	Nanoparticles
OSWV	Osteryoung square wave voltammogram
PBS	Phosphate buffer solution
R.E.	Reference electrode
R_{ad}	Resistance due to adsorption
SAM	Self-assembled monolayer
SCE	Standard calomel electrode

SDS	Sodium dodecyl sulphate
SEM	Scanning electron microscopy
SWCNT	Single-walled carbon nanotubes.
SWCNT-PABS	Poly(m-aminobenzenesulphonated) single-walled carbon nanotubes
SWV	Square wave voltammetry
W.E.	Working electrode
XPS	X-ray photoelectron spectroscopy

LIST OF SYMBOLS

A	Rate of electron transfer
Γ	Surface coverage or concentration
π	Pi bonding
λ	Wavelength
A	Absorbance
C	Molar concentration of analyte
C	Capacitance
C_{dl}	Double-layer capacitance
CPE	Constant phase electrode
C_{Ox}	Concentration of the oxidized form of an analyte
C_{Red}	Concentration of the reduced form of an analyte
C_s	Specific interfacial capacitance
d	Diameter
D	Diffusion coefficient
E_f	Final potential
E_i	Starting potential
E_{pa}	Anodic peak potential
E_{pc}	Cathodic peak potential
E	Potential
E^o	Standard potential
$E_{1/2}$	Half-wave potential
ΔE_p	Anodic-to-cathodic peak potential separation
f	Frequency
F	Faraday constant

h	Plank's constant
Hz	Hertz
I_{abs}	Absorbed light
i_{pa}	Anodic peak current
i_{pc}	Cathodic peak current
k	Heterogeneous electron transfer coefficient
K	Equilibrium constant
K_a	Dissociation constant
K	Kelvin
N	Number of electron
N_A	Avogadro's constant
q	Electrical charge
Q	Electrical charge (C)
R	Universal gas constant
R_{ct}	Charge transfer resistance
R_s	Resistance of electrolyte
ν	Scan rate
V	Volts
Z_{im}	Imaginary impedance
Z_{re}	Real impedance
Z_w	Warburg impedance

LIST OF FIGURES

Figure 1.1: A platinum wire immersed into an aqueous solution containing both ferrocyanide and ferricyanide 10

Figure 1.2: The energy of electrons in the ions in solution and in the metal wire 12

Figure 1.3: (a) Galvanic and (b) electrolytic cells 14

Figure 1.4: The three modes of mass transport process: (a) Diffusion, (b) Migration and (c) Convection 16

Figure 1.5: Three electrode set-up: (1) working electrode (2) auxillary electrode (3) reference electrode 19

Figure 1.6: Typical cyclic voltammogram for a reversible process.21

Figure 1.7: Typical Cyclic voltammogram for an irreversible process. 23

Figure 1.8: Waveform and measurement scheme for square wave voltammetry. Shown in bold is the actual potential waveform applied to the working electrode. The light intervening lines indicate the underlying staircase onto which the square wave can be regarded as having been superimposed. In each cycle, a forward current sample is taken at the time indicated by the solid dot, and a reverse current sample is taken at the time marked by the shaded dot 25

Figure 1.9: Linear potential sweep.....25

Figure 1.10: Typical waveform for a double potential step chronoamperometry.....27

Figure 1.11: Typical galvanostatic charge-discharge curve.....29

Figure 1.12: (a) Applied sinusoidal voltage and resulting sinusoidal current response. (b) Vector representation of real Z' and imaginary Z'' of impedance Z 32

Figure 1.13: (a) Typical Randles equivalent circuit for an ideal electrochemical system. (b) Modified Randles equivalent circuit for real, practical situation.....34

Figure 1.14: Typical Nyquist plot for (a) bare and (b) modified electrode. (c) is the corresponding Bode plots. 36

Figure 1.15: Pyrolytic graphite plate showing the basal and the edge plane sites 40

Figure 1.16: Structure of (a) SWCNT and (b) MWCNT. 41

Figure 1.17: Cyclic voltammogram showing electrocatalytic process of an analyte on the bare and modified electrode.....44

Figure 1.18: Principle of single-cell double-layer capacitor showing charge separation and storage at current collectors. ..58

Figure 1.19: Repetitive cyclic voltammograms of an electrode modified with metal oxides film. 63

Figure 1.20: Typical SAM modified electrode showing formation of monolayer. 65

Figure 1.21: A Typical SEM Image showing formation of metal oxide nanoparticles film on modified electrode. 74

Figure 1.22: A Typical TEM Image of CNT decorated with metal nanoparticles. 74

Figure 1.23: (a) Atomic force microscope block diagram. (b) AFM three dimentional (3D) image of a nanomaterial growth on a modified electrode. 76

Figure 1.24: EDX profile of a material showing the possible elemental composition.....77

Figure 1.25: Wide scan XPS spectrum showing the present elements. 78

Figure 1.26: (a) X-ray diffraction pattern formed when X-rays are focused on a crystalline material (b) XRD spectrum of synthesised metal nanoparticles showing identified peaks of the metal at different 2θ position 79

Figure 1.27: IR spectroscopy apparatus 80

Figure 3.1: Typical FESEM images of the (a) bare EPPGE, (b) EPPGE- SWCNT, (c) EPPGE-SWCNT-Ni, (d) EPPGE-SWCNT-Fe, (e) EPPGE-SWCNT-NiO and (f) EPPGE-SWCNT-FeO. 135

Figure 3.2: Typical EDX plots of the (a) bare EPPGE, (b) EPPGE-SWCNT, (c) EPPGE-SWCNT-Ni, and (d) EPPGE-SWCNT-NiO. 136

Figure 3.3: Examples of voltammetric evolutions of the bare-EPPGE and modified EPPGEs in 0.1 M pH 7.0 PBS. Scan rate = 50 mV/s. The voltammograms of the modified EPPGEs were obtained after 20 continuous scans. Other scans have been omitted for clarity. 138

Figure 3.4: (a) Examples of cyclic voltammograms recorded at the various electrodes in 0.1 M Na_2SO_4 solution containing 1 mM hydrazine, and (b) comparative cyclic voltammograms recorded at the EPPGE-SWCNT-Ni in 0.1 M Na_2SO_4 with and without hydrazine. Inset of (b) is the background substracted hydrazine response of the EPPGE-SWCNT-Ni. Scan rate = 25 mVs^{-1}.....140

Figure 3.5a: Examples of typical Nyquist plots of modified EPPGEs obtained in 0.1 M Na_2SO_4 containing 1 mM hydrazine, between 10 kHz and 0.1 Hz. Inset are similar plots obtained 100 kHz and 0.1 Hz. The data points are experimental while the solid lines represent fitted (theoretical) spectra obtained from the proposed equivalent circuit model shown in figure 5b.....142

Figure 3.5b: Equivalent circuit model used in fitting the spectra obtained in Figure 3.5a.....142

Figure 3.6: Examples of typical Bode plots of modified EPPGEs obtained in 0.1 M Na_2SO_4 containing 1 mM hydrazine, between 10 kHz and 0.1 Hz. 146

Figure 3.7: Typical comparative cyclic voltammetric evolutions of the electrodes (EPPGE-SWCNT and EPPGE-SWCNT-Ni) in 5 mM $[Fe(CN)_6]^{4-}$ / $[Fe(CN)_6]^{3-}$ solution (PBS pH 7.0). Scan rate = CVs (50mV/s).....147

Figure 3.8a: Typical Nyquist plots of the of the electrodes obtained in 5 mM $[Fe(CN)_6]^{4-}$ /$[Fe(CN)_6]^{3-}$ solution (PBS pH 7.0) at fixed potential of 0.30 V and 0.45 V vs Ag|AgCl sat'd KCl. 149

Figure 3.8b: Equivalent circuit model used in fitting the spectra obtained in Figure 3.8a.....149

Figure 3.9: (a) Examples of cyclc voltammetric evolutions of EPPGE-SWCNT-Ni obtained in 0.1 M Na_2SO_4 containing

1 mM hydrazine at scan rates 10, 25 and 50 mVs^{-1}(inner to outer). Inset compares voltammograms obtained at 50 and 140 mVs^{-1} (inner to outer). (b) Current function plot, $I_p/\nu^{1/2}$ vs ν. 151

Figure 3.10: Chronoamperometric evolutions of the EPPGE-SWCNT-Ni in 0.1 M Na_2SO_4 solution containing different concentrations of hydrazines (0.0, 33.3, 47.4, 50.5 and 54.5 μM (from (i) to (v)) at fixed potential of 0.6V. Inset is plot of slope vs square root of the concentration of hydrazine. 154

Figure 4.1: Comparative FTIR of pristine SWCNTs (a) and acid-treated SWCNTs (b). 161

Figure 4.2: FESEM images of bare EPPGE (a), EPPGE-SWCNT (b), EPPGE-SWCNT-Ni (c) and EPPGE-SWCNT-NiO (d). The size bars are 50 μm for (a) and 5 μm for (b)–(d). 163

Figure 4.3: EDX spectra of (a) EPPGE-SWCNT, (b) EPPGE-SWCNT-Ni, and (c) EPPGE-SWCNT-NiO. 164

Figure 4.4: Comparative current response of the bare-EPPGE, EPPGE-SWCNT, EPPGE-NiO and EPPGE-SWCNT-NiO in pH 7.0 PBS. Scan rate = $50mVs^{-1}$. 166

Figure 4.5: (a) Repetitive cyclic voltammetric evolution (20 scans) of EPPGE-SWCNT-Ni in 0.1M NaOH solution. (b) Comparative cyclic voltammetric evolution (1st scan) of the EPPGE-SWCNT-Ni in 0.1M NaOH at different nickel deposition time (5–40 min). Scan rate = $100mVs^{-1}$. 167

Figure 4.6: Voltammetric evolutions of EPPGE-SWCNT-Ni in 0.1MNaOHsolution at varying scan rates of 25, 50, 75, 100, 150, 200, 250 and $300mVs^{-1}$ (inner to outer). The electrode was obtained at 5 min deposition and used for the study after 2nd scan. 170

Figure 4.7: Typical examples of cyclic voltammetric evolutions of the electrodes in 5mM $[Fe(CN)_6]^{4-}/[Fe(CN)_6]^{3-}$ solution (PBS pH 7.0). Scan rate = $50mVs^{-1}$. 171

Figure 4.8: Typical Nyquist plots of the of the electrodes obtained in 5mM $[Fe(CN)_6]^{4-}/[Fe(CN)_6]^{3-}$ solution (PBS pH 7.0) at fixed potential of 0.30V vs. Ag|AgCl sat'd KCl. 173

Figure 4.9: Equivalent circuit diagrams used for fitting the impedance data obtained in this work. Circuit (a) was

used to fit the bare EPPGE, EPPGE-SWCNT and nickel disk hydroxide electrodes; (b) was used to fit the EPPGE-Ni, EPPGE-SWCNT-Ni, EPPGESWCNT-NiO and EPPGE-NiO; (c) was used for EPPGE-SWCNT-Ni$(OH)_2$. 175

Figure 4.10: Bode plots obtained for the electrodes obtained at 0.30V vs. Ag|AgCl sat'd KCl. 178

Figure 4.11: (a) Examples of comparative cyclic voltammograms recorded at the various electrodes in 0.1 M PBS (pH 9.4) containing 0.1 mM DEAET. (b) Plot of charge transfer resistance (R_{ct}) against deposition time of nickel (biased at 0.6 V vs Ag|AgCl, sat'd KCl) obtained at EPPGE-SWCNT-Ni. (c) Circuit diagram used in the fitting of impedance data in (b). 180

Figure 4.12: (a) Typical examples of linear sweep voltammetric evolutions of EPPGE-SWCNT-Ni in phosphate buffer solution (pH 9.4) containing different concentrations of DEAET (0.0, 28.6, 33.3, 37.5, 41.2 and 44.5 μM (i to vi)). Inset is plot of log current response (background-subtracted) vs log DEAET concentrations. (b) Typical examples of chronoamprometric evolutions of EPPGE-SWCNT-Ni in phosphate buffer solution (pH 9.4) containing different concentrations of DEAET (0.0, 20, 40, 60, 80 100 nM (i to vi)) at fixed potential 0.6V vs Ag|AgCl, sat'd KCl. Inset is plot of log current response (background-subtracted) vs log DEAET concentrations. 184

Figure 5.1: TEM images of (a) Pristine MWCNT (b) MWCNT-COOH (c) MWCNT-Ni and (d) MWCNT-NiO.....193

Figure 5.2: (a) XRD spectrum of NiO. Inset in (a) is the XRD spectrum of Ni. (b) and (c) represent the EDX spectra of MWCNT-Ni and MWCNT-NiO, respectively.....195

Figure 5.3: Comparative cyclic voltammetric evolutions of the electrodes in (a) 0.1 M PBS (pH 7.0), scan rate = 100 mVs^{-1}. (b) 5 mM $[Fe(CN)_6]^{4-}$ / $[Fe(CN)_6]^{3-}$ solution (in PBS pH 7.0). Scan rate = 50 mVs^{-1}.....197

Figure 5.4: Typical Nyquist plots obtained for the electrodes in 5 mM $[Fe(CN)_6]^{4-}$ / $[Fe(CN)_6]^{3-}$ solution (PBS pH 7.0) at a fixed potential of 0.2 V (vs Ag|AgCl, sat'd KCl). Inset represents the circuit used in the fitting of the EIS data. 199

Figure 5.5: Comparative current response (after background current subtraction) of the electrodes in (a) 0.1 mM DEAET solution in pH 9.4 PBS and (b) 1.0 mM hydrazine solution in 0.1 M Na_2SO_4, scan rate = 25 mVs^{-1}.....202

Figure 5.6: Comparative current response (after background current subtraction) for different Ni loading at the EPPGE-MWCNT-Ni electrode in (a) 0.1 mM DEAET solution in pH 9.4 PBS and (b)1.0 mM hydrazine solution in 0.1 M Na_2SO_4, scan rate = 25 mVs^{-1}.....203

Figure 5.7: (a) Typical Nyquist plots obtained for EPPGE-MWCNT-Ni in 0.1 mM DEAET solution in PBS 9.4 and 1.0 mM hydrazine in 0.1 M Na_2SO_4 solution respectively (at fixed potential 0.6 V vs Ag|AgCl, sat'd KCl). Inset represents the circuit used in fitting the EIS data. (b) represents the Bode plots obtained for the EPPGE-MWCNT-Ni, showing the plots of -phase angle / deg. vs log (f / Hz)) and the plot of log |Z/Ω| vs log (f/Hz) for both DEAET and hydrazine.....205

Figure 5.8: Cyclic voltammetric evolutions at the EPPGE-MWCNT-Ni for (a) 0.1 mM DEAET in 0.1 M pH 9.4 PBS (at 25, 75, 400, 600, 950, 1200 and 1400 mVs^{-1}, inner to outer), and (b) 1.0 mM Hydrazine in 0.1 M Na_2SO_4 solution after background subtraction (at 25, 75, 150 and 200 mVs^{-1}, inner to outer) 207

Figure 5.9: (a) Typical chronoamperograms obtained for the EPPGE-MWCNT-Ni in 0.1 M Na_2SO_4 solution containing different concentrations of hydrazine (0.0, 91, 167, 231, 286, and 333 μM, (i to vi)). Inset represents the plot of current response vs hydrazine concentration. (b) Typical linear sweep voltammograms obtained for the EPPGE-MWCNT-Ni in 0.1 M Na_2SO_4 solution containing different concentrations of hydrazine (0.0, 91, 130, 167, 231, 286, 333, 355, and 375 μM (i to ix)). 211

Figure 6.1: FESEM of (a) EPPGE, (b) EPPGE-SWCNT, (c) EPPGE-SWCNT-Co, (d) EPPGE-SWCNT-CoO. (e) and (f) are the AFM topography images for the EPPGE-SWCNT-Co and the EPPGE-SWCNT-CoO while (g) and (h) are their respective cross-sections. 221

Figure 6.2: EDX spectra of (a) EPPGE (b) EPPGE-SWCNT, and (c) EPPGE-SWCNT-CoO. 222

Figure 6.3: Typical examples of some cyclic voltammetric evolutions of the electrodes in 5 mM $[Fe(CN)_6]^{4-}$ / $[Fe(CN)_6]^{3-}$ solution (PBS pH 7.0). Scan rate = 50 mV/s. 225

Figure 6.4: (a) Typical Nyquist plots of some of the electrodes obtained in 5 mM $[Fe(CN)_6]^{4-}$ / $[Fe(CN)_6]^{3-}$ solution (PBS pH 7.0) at fixed potential of 0.30 V vs Ag|AgCl sat'd KCl. (b) Represents the circuit used in the fitting of the EIS data. (c) and (d) are the Bode plots obtained for the electrodes, showing the plots of (-phase angle deg. vs log (f/Hz)) and log |Z / Ω| vs log (f/Hz). 226

Figure 6.5: Comparative current response (after background current subtraction) of the EPPGE, EPPGE- SWCNT, EPPGE-SWCNT-Co and EPPGE-SWCNT-CoO in (a) 1 mM nitrite solution in pH 7.4 PBS and (b) 1 mM nitrite solution in pH 3.0 PBS, scan rate = 25 mV/s. 230

Figure 6.6: (a) Typical Nyquist plots of some electrodes in 1 mM nitrite solution (PBS pH 7.4) at fixed potential of 0.80 V vs Ag|AgCl sat'd KCl. Inset is the enlarged portion of the high frequency region (b) Represents the circuit used in the fitting of the EIS data in 6a (c) Bode plot obtained for EPPGE-SWCNT-Co showing the plot of -phase angle (deg.) vs log (f/Hz). 232

Figure 6.7: Plot of peak current (I_p) versus square root of scan rate ($v^{1/2}$) for EPPGE-SWCNT-Co in 0.1M pH 7.4 PBS containing 10^{-3} M nitrite. 235

Figure 6.8: Typical examples of chronoamperogram obtained for EPPGE-SWCNT-Co in phosphate buffer solution (pH 7.4) containing different concentrations of nitrite (0.0, 32.3, 62.5, 118.0, 143.0, and 189.0 μM (i to vi)). Inset is typical plot of current response vs nitrite concentration. 237

Figure 6.9: TEM images of (a) Co and (b) Co_3O_4 nanoparticles. c and d are the FESEM micrographs of Co and Co_3O_4 nanoparticles, respectively.....241

Figure 6.10: XRD spectra of Co (a) and Co_3O_4 (b) nanoparticles. 242

Figure 6.11: Comparative cyclic voltammetric evolutions of the EPPGE, EPPGE-Co and EPPGE-Co_3O_4 electrodes in (a) 0.1 M PBS (scan rate = 100 mVs^{-1}), and (b) 5 mM

$[Fe(CN)_6]^{4-}/[Fe(CN)_6]^{3-}$ solution in pH 7.0 PBS (scan rate = 50 mVs^{-1}). 243

Figure 6.12: Typical Nyquist plots obtained for the electrodes in 5 mM $[Fe(CN)_6]^{4-}$ / $[Fe(CN)_6]^{3-}$ solution at a fixed potential of 0.2 V (vs Ag|AgCl, sat'd KCl). Inset in Figure 6.12 is the circuit used in the fitting of the EIS data. 245

Figure 6.13: Comparative current response of (a) EPPGE, EPPGE-Co and EPPGE-Co_3O_4 (after background current subtraction) in pH 7.4 PBS containing 1.0 mM NO_2^- solution (scan rate = 25 mVs^{-1}). EPPGE-Co-b represents 7.5 mg/mL Co loading in pH 7.4 PBS containing 1.0 mM NO_2^- solution. 247

Figure 6.14: Typical Nyquist plots obtained for EPPGE, EPPGE-Co and EPPGE-Co_3O_4 in 1.0 mM NO_2^- solution at a fixed potential of 0.8 V (vs Ag|AgCl, sat'd KCl).....248

Figure 6.15: Typical chronoamperogram of EPPGE-Co in (a) 0.1 M PBS pH 7.4 containing different concentration of NO_2^- (0.0, 11.1, 20.0, 27.3, 31.0 and 33.3 μM (i to vi)). Inset is the plot of peak current (I_p) versus NO_2^- concentrations.....251

Figure 7.1: Typical AFM images of (a) bare glassy carbon (GC) plate, (b) GC-SWCNT, (c) SWCNT-SWCNT-Fe and (d) GCE-SWCNT-Fe_2O_3. 259

Figure 7.2: Typical EDX profile of the (a) bare EPPGE, (b) EPPGE-SWCNT, (c) EPPGE-SWCNT-Fe and (d) EPPGE-SWCNT-Fe_2O_3. 260

Figure 7.3: Typical XPS of EPPGE-SWCNT-Fe_2O_3 modified electrode. Inset shows the enlarged portion showing the peak corresponding to the Fe $2p_{3/2}$ and Fe $2p_{1/2}$ bands. 261

Figure 7.4: Typical cyclic voltammograms, original (a) and background- subtracted (b) of bare EPPGE (i), EPPGE-SWCNT (ii), EPPGE-SWCNT-Fe (iii), and EPPGE-SWCNT-Fe_2O_3 (iv) in 0.1 M PBS (pH 7.0) containing 2 x 10^{-4} M DA (Scan rate = 25 mV s^{-1}). 263

Figure 7.5: (a) Typical Nyquist plot of the bare EPPGE (i), EPPGE-SWCNT (ii), EPPGE-SWCNT-Fe (iii), and EPPGE-SWCNT-Fe_2O_3 (iv) obtained in 0.1 M PBS containing 2 x 10^{-4} M DA (biased at 0.2 V), between 10 KHz and 0.1 Hz, and

(b) Equivalent circuit model used in fitting the spectra obtained in Figure 7.5 (a). 264

Figure 7.6: (a) Cyclic voltammetric evolutions of EPPGE-SWCNT-Fe_2O_3 obtained in 0.1 M PBS containing 2 x 10^{-4} M DA at scan rates 25 to 1000 mV s^{-1} (inner to outer). (b) Plot of I_p vs. $\nu^{1/2}$ for both anodic and cathodic process. ...269

Figure 7.7: Square wave voltammetric evolutions of the EPPGE-SWCNT-Fe_2O_3 in 0.1 M PBS solution containing different concentrations of DA (i–viii represent 0.00, 3.23, 6.25, 9.09, 11.76, 14.30, 18.92, and 31.82 μM, respectively). Inset is the plot of current vs. concentration of DA...270

Figure 7.8: Typical square wave voltammograms responses of EPPGE-SWCNT-Fe_2O_3 in (i) 1 mM AA alone, and mixture of (ii) 33.3 μM DA / 0.83 mM AA, (iii) 46.2 μM DA / 0.77 mM AA, and (iv) 88.9 μM DA / 0.56 mM AA in PBS pH 7.0. 275

Figure 7.9: TEM images of (a) MWCNT-Fe (b) MWCNT-Fe_2O_3. (c) and (d) HRSEM picture of MWCNT-Fe and MWCNT-Fe_2O_3 respectively. 277

Figure 7.10: XRD spectrum of Fe_2O_3 nanoparticles. Inset is the XRD spectrum of Fe nanoparticles.....278

Figure 7.11: EDX profiles of MWCNT-Fe and MWCNT-Fe_2O_3 respectively. 279

Figure 7.12: Comparative cyclic voltammetric evolutions of the bare and Fe/Fe_2O_3 modified electrodes in (a) 5 mM $[Fe(CN)_6]^{4-}$/$[Fe(CN)_6]^{3-}$ in pH 7.0 PBS and (b) 0.1 M pH 7.0 PBS (scan rate = 50 mVs^{-1}). 281

Figure 7.13: (a) Typical Nyquist plots obtained for some of the MWCNT modified electrodes in 5 mM $[Fe(CN)_6]^{4-}$ / $[Fe(CN)_6]^{3-}$ solution at a fixed potential of 0.2 V (vs Ag|AgCl, sat'd KCl). (b) is the circuit used in the fitting of the EIS data in (a). 282

Figure 7.14: Comparative current response (after background current subtraction) of the electrodes: (i) EPPGE, (ii) EPPGE-MWCNT, (iii) EPPGE-Fe, (iv) EPPGE-Fe_2O_3, (v) EPPGE-MWCNT-Fe, and (vi) EPPGE-MWCNT-Fe_2O_3 in 2x10^{-4} M DA solution in pH 7.0 PBS (scan rate = 25 mVs^{-1}).....285

Figure 7.15: Cyclic voltammetric evolutions of EPPGE-MWCNT-Fe_2O_3 obtained in 0.1 M PBS containing 2 x 10^{-4} M DA (scan rate range 25 – 1000 mVs^{-1}; inner to outer). 286

Figure 7.16: Typical Nyquist plots obtained for some of the MWCNT modified electrodes in 2 x 10^{-4} M DA solution at a fixed potential of 0.2 V. Inset is the Randles circuit model used in fitting the data. 287

Figure 7.17: Square wave voltammetric evolutions of the EPPGE-MWCNT-Fe_2O_3 in 0.1 M PBS pH 7.0 containing different concentration of DA (6.25, 11.8, 14.7, 21.1, 23.1 and 27.0 μM). 290

Figure 7.18: Typical square wave voltammograms responses of EPPGE-MWCNT-Fe_2O_3 in (i) 1 mM AA alone, and mixture of (ii) 4.76 μM DA and 0.95 mM AA, (iii) 9.09 μM DA and 0.91 mM AA, (iv) 13.04 μM DA and 0.87 mM AA, (v) 20.0 μM DA and 0.8 mM AA, (vi) 25.93 μM DA and 0.74 mM AA, and (vii) 28.57 μM DA and 0.71 mM AA in PBS pH 7.0. 292

Figure 8.1: Typical TEM images of (a) PB and (b) SWCNT-PB nanoparticles. (c) and (d) are the AFM topography image and the cross section of the SWCNT-PB showing the particle size distribution in nano dimensions. 300

Figure 8.2: UV/VIS spectra of Prussian blue (PB), SWCNT-PABS and SWCNT-PB. 301

Figure 8.3: Typical cyclic voltammograms of (a) EPPGE (i), EPPGE-SWCNT-PABS (ii) and EPPGE-SWCNT-PB (iii) in 0.1 M KCl electrolyte (scan rate: 25 mVs^{-1}). (b) is the cyclic voltammogram showing the electrochemical stability of EPPGE–SWCNT-3PB modified electrode (50 cycles) in pH 7.0 PBS containing 0.1 M KCl electrolytes (scan rate: 100 mVs^{-1}). 304

Figure 8.4: Cyclic voltammograms showing the current responses (background subtracted) of (a) (i) bare EPPGE, (ii) EPPGE-SWCNT-PABS, (iii) EPPGE-PB and (iv) EPPGE-SWCNT-PB in 0.1 M pH 7.0 PBS containing 2 x10^{-4} M DA (scan rate: 25 mVs^{-1}). (b) (i) EPPGE-SWCNT-PB, (ii) EPPGE-SWCNT-2PB and (iii) EPPGE-SWCNT-3PB in 0.1 M pH 7.0 PBS containing 2 x10^{-4} M DA (scan rate: 25 mVs^{-1}).....306

Figure 8.5: (a) Typical Nyquist plots obtained for (i) EPPGE-SWCNT-PB, (ii) EPPGE-SWCNT-2PB and (iii) EPPGE-SWCNT-3PB in 0.1 M pH 7.0 PBS containing 2 x10^{-4} M DA. (b) is the Bodes plot of –phase angle versus logf, and log |Z/Ω| versus logf for the electrodes in (a) above. 309

Figure 8.6: (a) Cyclic voltammogram showing the current response of EPPGE-SWCNT-3PB electrodes in 0.1 M PBS solution containing 2x10^{-4} M DA (scan rate: 25 to 1000 mVs^{-1}). (b) plot of I_p vs $\nu^{1/2}$ (c) a RDE voltammograms obtained for the EPPGE-SWCNT-3PB in 0.1 M PBS solution containing 2 x 10^{-4} M DA (rotating disc speed: 100 to 2900 rpm) (d) is the plot of I_p^{-1} vs. $\omega^{-1/2}$. Inset in (d) is the plot of E/V versus log [i x i_L/i_L – i].....311

Figure 8.7: (a) Square wave voltammograms evolution of the EPPGE-SWCNT-3PB in 0.1 M PBS solution containing different concentrations of DA (0.0, 6.5, 12.5, 18.2, 23.5, 28.6, 33.3, 42.1 and 50.0 μM (inner to outer; i – ix). (b) Linear sweep voltammogram responses of the EPPGE-SWCNT-3PB in 0.1 M PBS solution containing different concentrations of DA (0.00, 18.2, 28.6, 37.8, 50, 60.5, 66.7, 72.3 μM (inner to outer; i – viii). 315

Figure 8.8: Typical square wave voltammograms responses of EPPGE-SWCNT-3PB in (i) 0.1 M pH 7.0 PBS, (ii) 10 mM AA alone, and mixture of (iii) 9.1 μM DA / 9.1 mM AA, (iv) 16.7 μM DA / 8.3 mM AA, (v) 23.1 μM DA / 7.7 mM AA, (vi) 28.6 μM DA/7.1 mM AA, (vii) 33.3 μM DA/6.7 mM AA and (viii) 41.2 μM DA/5.9 mM AA in PBS pH 7.0. 318

Figure 9.1: TEM of (a) Prussian blue (PB) nanoparticles (b) SWCNT-PB nanocomposite.....323

Figure 9.2: FTIR spectra of (i) SWCNT-PABS and (ii) SWCNT-PB nanocomposite.....324

Figure 9.3: XPS spectrum of SWCNT-PB showing the presence of Fe^{2+} and Fe^{3+} ions the PB nanoparticles. Inset is the XPS spectrum indicating clearly the Fe peaks and the dominance of Fe^{3+} peak over Fe^{2+} peak.....325

Figure 9.4: EDX spectra of (a) SWCNT-PABS and (b) SWCNT-PB nanocomposites. 326

Figure 9.5: (a) Cyclic voltammograms showing the current responses of the electrodes modified with and without

10^{-4} M PB Prussian blue in 0.1 M KCl within the potential range of -0.4 to 1.2 V. Scan rate: 25 mVs^{-1}. (b) Current response of the EPPGE-SWCNT-PB electrode (30 scans) in (a) 0.1 M KCl electrolyte. 328

Figure 9.6: Comparative current response (after background current subtraction) of the modified electrodes in (a) 10^{-4} M DEAET in pH 9.4 PBS and (b) 0.1 M Na_2SO_4 solution containing 10^{-3} M hydrazine, (c) 10^{-3} M NO_2^- at pH 7.4 and (d) 10^{-3} M NO at pH 3.0 PBS (Scan rate: 25 mVs^{-1}).....330

Figure 9.7: (a) Nyquist plots for the EPPGE-SWCNT-PB electrode in (i) 0.1 M pH 9.4 PBS containing 10^{-4} M DEAET, (ii) 0.1 M pH 3.0 PBS containing 10^{-3} M NO, (iii) 0.1 M pH 7.4 PBS containing 10^{-3} M NO_2-, (iv) 0.1 M Na_2SO_4 solution containing 10^{-3} M hydrazine. (b) is the circuit diagram used in the fitting of the impedance data in (a). 332

Figure 9.8: Current response of the EPPGE-SWCNT-PB electrode in (a) 0.1 M pH 9.4 PBS containing 10^{-4} M DEAET (scan rates between 25 and 1200 mVs^{-1}, from inner to outer). (b) Plots of E_p vs logν for (I) DEAET and (II) Hydrazine. (c) Current function plots (I_p/ν vs ν).....335

Figure 9.9: Typical chronoamperogram of EPPGE-SWCNT-PB in (a) 0.1 M Na_2SO_4 solution containing different concentrations of hydrazine (0.0, 47.6, 90.9, 130.0, 167.0, 231.0, and 286.0 μM (i to vii)). Inset represents the plots of I_{cat} / I_{buff} vs $t^{1/2}$ obtained from the chronoamperometric evolutions (i-vi correspond to 47.6, 90.9, 130.0, 167.0, 231.0 and 286.0 μM, respectively). (b) pH 9.4 PBS containing different concentrations of DEAET (0.0, 16.7, 23.1, 28.6, 31.0 and 33.3 μM (i to vi)). Inset represents the plots of I_{cat} / I_{buff} vs $t^{1/2}$ obtained from the chronoamperometric evolutions (i-v correspond to 16.7, 23.1, 28.6, 31.0 and 33.3 μM respectively).....337

Figure 9.10: Typical linear sweep voltammograms of EPPGE-SWCNT-PB in (a) 0.1 M pH 9.4 PBS containing different concentrations of DEAET (0.0, 20.0, 28.6, 31.0, 33.3, 35.5, 37.5 and 41.2 μM (i) – (viii)). Inset in (a) represents the plot of peak current vs DEAET concentrations. (b) 0.1 M Na_2SO_4 solution containing different concentrations of hydrazine (0.0, 47.6, 90.9, 130.0, 167.0, 200 and 231 mM (i to vii)). Inset in (b) is

the plot of peak current vs hydrazine concentrations. 339

Figure 10.1: EDX spectra of (a) SWCNT-NiO, (b) SWCNT-Co_3O_4 and (c) SWCNT-Fe_2O_3 344

Figure 10.2: XPS spectra of (a) SWCNT-NiO, (b) SWCNT-Co_3O_4 and (c) SWCNT-Fe_2O_3.....346

Figure 10.3: FESEM images of (a) SWCNT-NiO (b) SWCNT-Co_3O_4 and (c) SWCNT-Fe_2O_3.....347

Figure 10.4: Comparative CVs showing the capacitive behaviour of: BPPGE, BPPGE-SWCNT, BPPGE-SWCNT-NiO, BPPGE-SWCNT-Co_3O_4 and BPPGE-SWCNT-Fe_2O_3 in (a) 1 M Na_2SO_4 and (b) 1 M H_2SO_4 aqueous electrolytes. Scan rate = 25 mVs^{-1}.....349

Figure 10.5: Typical examples of comparative galvanostatic charge discharge plot of the metal oxide SWCNTs/nanocomposite modified electrodes at an applied current density of 0.1 $mAcm^{-2}$ in (a) 1 M Na_2SO_4 and (b) 1 M H_2SO_4 aqueous electrolyte.....352

Figure 10.6: shows the effect of cycle number (1000) or cycle life on stability of BPPGE-SWCNT-NiO electrode in 1 M H_2SO_4 aqueous electrolytes. Inset is the typical examples of some of the charge-discharge curve (1000 cycles) for the BPPGE-SWCNT-NiO electrode in 1 M H_2SO_4 aqueous electrolytes.....355

Figure 10.7: Typical Nyquist plots of (i) BPPGE-SWCNT-Fe_2O_3, (ii) BPPGE-SWCNT-NiO and (iii) BPPGE-SWCNT-Co_3O_4 electrodes in (a) 1 M Na_2SO_4 and (b) 1 M H_2SO_4 aqueous solutions at a fixed potential of 0.30 V vs Ag|AgCl sat'd KCl.....356

Figure 10.8: Cyclic voltammograms obtained for symmetry (a) and (b); and asymmetry (c) and (d) MWCNT-NiO based supercapacitor (two-electrode cell) in 1 M H_2SO_4 and 1 M Na_2SO_4 aqueous electrolyte respectively at scan rate 5, 25, 50, 100, 200, 300, 400 and 500 mVs^{-1} (a-h, inner to outer); mass of each electrode, 1.4 mg. 361

Figure 10.9: Typical Nyquist plots obtained for symmetry: (i) MWCNT-NiO|H_2SO_4|MWCNT-NiO, (ii) MWCNT-NiO|Na_2SO_4|MWCNT-NiO; and the asymmetry: (iii) MWCNT-NiO|H_2SO_4|MWCNT,(iv) MWCNT-

NiO|Na_2SO_4|MWCNT supercapacitors at a fixed potential of 0.55 V vs Ag|AgCl sat'd KCl. Figure 10.9b-d is the circuit used for fitting the impedance data in (a). Circuit 10.9b fitted impedance data obtained for the symmetry assembly in 1 M H_2SO_4 and 1 M Na_2SO_4, while circuit 10.9c fitted the impedance data for the asymmetry assembly in 1 M H_2SO_4. Circuit 10.9d fitted impedance data for asymmetry assembly in 1 M Na_2SO_4 365

Figure 10.10: Typical examples of galvanostatic charge discharge profile of the symmetry MWCNT-NiO based supercapacitor (two-electrode cell) in (a) 1 M H_2SO_4 and (b) 1 M Na_2SO_4 aqueous electrolytes, at an applied current density of 0.25 $mAcm^{-2}$. 368

Figure 10.11: Typical examples of galvanostatic charge discharge profile of the asymmetry MWCNT-NiO bases supercapacitor (two-electrode cell) in (a) 1 M H_2SO_4 and (b) 1 M Na_2SO_4 aqueous electrolytes, at an applied current density of 0.25 $mAcm^{-2}$. 369

Figure 10.12: Cyclic life (1000 cycles) of the symmetry MWCNT-NiO|H_2SO_4|MWCNT supercapacitor showing the stability in 1 M H_2SO_4 aqueous electrolytes. Inset is the section of the charge-discharge curves obtained for the cell at applied current density of 2.5 $mAcm^2$.....370

LIST OF SCHEMES

Scheme 1.1: Schematic diagram showing electrocatalytic process at modified electrode. 30

Scheme 2.1: Procedures for the synthesis of NiO nanoparticles. . 115

Scheme 2.2: Procedure for the metal and metal oxide nanoparticles modified electrodes. 121

Scheme 2.3: Procedures for electrode modification with Prussian blue (PB) nanoparticles. 123

Scheme 2.4: Procedure for electrode modification with synthesized metal (M) and metal oxides (MO) nanoparticles. ...124

Scheme 7.1: Schematic of electrode modification process. 257

LIST OF TABLES

Table 1.1: Electrocatalytic oxidation of some analytes on nickel and nickel oxide modified electrode.....48

Table 1.2: Electrocatalytic oxidation of some analytes on iron and iron oxide modified electrode. 52

Table 1.3: Electrocatalytic oxidation of some analytes on cobalt and cobalt oxide modified electrode. 56

Table 3.1: Impedance data ($E_{1/2}$ = 0.6V) for the electrocatalytic oxidation of 10^{-3} M Hydrazine (between 10 kHz and 0.1 Hz) on the modified and unmodified EPPGE-electrodes. All values were obtained from the fitted impedance spectra after several iterations using the circuits. Note that the values in parentheses are errors of data fitting. 144

Table3.2: Comparative analytical data for the detection of hydrazine at chemically modified electrodes.....155

Table 4.1: Impedance data obtained for the modified electrodes in 5mM $[Fe(CN)_6]^{4-}/[Fe(CN)_6]^{3-}$ solution (PBS pH 7.0) at 0.30V vs. Ag|AgCl sat'd KCl. All values were obtained from the fitted impedance spectra after several iterations using the circuits. Note that the values in parentheses are errors of data fitting. 177

Table 4.2: Comparative analytical data for the detection of DEAET at chemically modified electrodes 186

Table 5.1: Impedance data obtained for the bare EPPGE and the modified electrodes in 5 mM $Fe(CN)_6]^{4-}/[Fe(CN)_6]^{3-}$ solution at 0.2 V (vs Ag|AgCl sat'd KCl).....200

Table 5.2: Comparative analytical data for the detection of DEAET and hydrazine at chemically modified electrodes.....214

Table 6.1: Impedance data obtained for the EPPGE modified electrodes in 5 mM $[Fe(CN)_6]^{4-}$ / $[Fe(CN)_6]^{3-}$ solution (PBS pH 7.0) at 0.30 V vs Ag|AgCl sat'd KCl. 228

Table 6.2: Impedance data obtained for the modified EPPGE-SWCNT-Co electrodes in 10^{-3} M NO_2^- (in PBS pH 7.4 and 3.0) at 0.80 V vs Ag|AgCl sat'd KCl.....233

Table 6.3: Impedance data obtained for EPPGE, EPPGE-Co and EPPGE-Co_3O_4 electrodes in 5 mM $Fe(CN)_6]^{4-}$/$[Fe(CN)_6]^{3-}$ solution at 0.2 V (vs Ag|AgCl sat'd KCl). 246

Table 6.4: Impedance data obtained for some of the electrodes in 1.0 mM NO_2^- (in PBS pH 7.4 at 0.80 V vs Ag|AgCl sat'd KCl. 249

Table 7.1: Impedance data obtained for the electrodes in 2 x 10^{-4} M DA solution in pH 7.0 PBS (at 0.2 V vs Ag|AgCl sat'd KCl). 265

Table 7.2: Voltammetric response for dopamine using various modified electrodes. 272

Table 7.3: Determination of dopamine content in dopamine hydrochloride injections (40 mg mL^{-1}), n =5 (at 95% confidence limit). 276

Table 7.4: Impedance data obtained for the bare and the MWCNT modified EPPGE electrodes in 5 mM $Fe(CN)_6]^{4-}$ /$[Fe(CN)_6]^{3-}$ solution at 0.2 V (vs Ag|AgCl sat'd KCl). 283

Table 7.5: Impedance data obtained for the bare and the modified EPPGE electrodes in 2 x 10^{-4} M DA in pH 7.0 PBS at 0.2 V (vs Ag|AgCl sat'd KCl). 288

Table 7.6: Determination of dopamine content in dopamine hydrochloride injections (40 mg mL^{-1}), n =5 (at 95% confidence limit) using EPPGE-MWCNT-Fe_2O_3 electrode. 293

Table 8.1: Impedance data obtained for the EPPGE-SWCNT-PB modified electrodes (at different deposition cycles) in 0.1M pH 7.0 PBS containing 2 x 10^{-4} M DA ($E_{1/2}$ = 0.2 V vs Ag|AgCl sat'd KCl). 308

Table 8.2: Voltammetric response for dopamine using various modified electrodes. 316

Table 8.3: Determination of dopamine content in dopamine hydrochloride injections (40 mg mL^{-1}), n =5 (at 95% confidence limit) using EPPGE-SWCNT-3PB modified electrode. 319

Table 9.1: Electrocatalytic and electroanalytical parameters of the EPPGE-SWCNT-PB towards the detection of DEAET, hydrazine and nitrite. The values in parentheses are values obtained from the linear sweep voltammetry. 331

Table 9.2: Impedance data obtained for the EPPGE-SWCNT-PB modified electrodes in 10^{-4} M DEAET (in PBS 9.4, at 0.60 V) and 10^{-3} M hydrazine in 0.1 M Na_2SO_4 solution at 0.68 V. 334

Table 10.1: Supercapacitive properties of the MO nanoparticles integrated with SWCNTs determined using cyclic voltammetry and galvanostatic discharge methods.....351

Table 10.2: Impedance data obtained for MO nanocomposite modified electrodes in 1 M H_2SO_4 and 1 M Na_2SO_4 electrolytes at a fixed potential of 0.30 V vs Ag|AgCl sat'd KCl. 358

Table 10.3: Specific capacitance ($mFcm^{-2}$) for the symmetric and asymmetric MWCNT-NiO based supercapacitor (two-electrode cell) in 1 M H_2SO_4 and 1 M Na_2SO_4 aqueous electrolyte respectively. Values in parenthesis are the specific capacitance in F/g. 363

Table 10.4: Impedance data obtained for the symmetry and asymmetry MWCNT-NiO nanocomposite based supercapacitor (two-electrode cell) in 1.0 M H_2SO_4 and 1.0 M Na_2SO_4 electrolytes at a fixed potential of 0.55 V vs Ag|AgCl sat'd KCl. 366

CHAPTER ONE

INTRODUCTION

1.1 General Overview of Thesis: Problem Statement

The quick determination of trace quantities of analytes by simple methods is of special interest in analytical chemistry. The construction and application of sensitive electrode as a sensor offers interesting advantages such as simplicity, relatively fast response, low cost, wide linear dynamic range and ease of preparation and procedures. These characteristics have inevitably led to the preparation of numerous sensors for several analytes, and the list of available electrodes has grown substantially over the past years. Despite this, the electrochemical and electrocatalytic behaviour of carbon nanotubes-metal (CNTs-M) or carbon nanotubes-metal oxides (CNTs-MO) nanoparticles (NPs) modified electrode as potential nanocomposite for chemically modified electrodes, especially on a non-convectional electrode platform such as edge plane pyrolytic graphite electrode as a support have not received much attention or hugely explored. It is also anticipated that the supercapacitive properties of such electrode system for potential application in supercacitor still remain a virgin area for prospective research opportunities if explored.

This work describes the electron transport and electrocatalytic properties of single or double-walled carbon nanotubes (SWCNTs/MWCNTs) integrated with metal (M) and metal oxide (MO) nanoparticles supported on edge plane pyrolytic graphite electrode (EPPGE) platform towards the detection of biologically and environmentally important analytes: diethylaminoethanethiol (DEAET), hydrazine, dopamine and nitrite.

1.1.1 Carbon nanotube-metal and metal oxide nanocomposite in electrochemistry

1.1.1.1 Carbon nanotubes as electrical conducting nanowires

Carbon nanotubes (CNTs), discovered in 1978 [1] and rediscovered in 1991 [2] by Ijima, have attracted immense attraction around the world. Carbon nanotubes have found application in plethora of areas such as in nanoscale hydrodynamics [3], field emission devices [4], catalysis of redox reactions [5–7], nanoelectronics [8], hydrogen storage [9], electrochemical capacitors [10,11] and electrochemical sensors [12]. The material receives considerable attention in the area of electrochemistry not only due to their reported structural, mechanical or electronic properties but because they represent the world's smallest electrodes allowing electrochemistry to be performed where other electrode materials cannot penetrate. Its first application in electrochemical sensing was first carried out by Britto and Co-workers [13] but was largely neglected until Joseph Wang and co-workers demonstrated their beneficial use for the electroanalytical detection of nicotinamide adenine dinucleotide (NADH) [14]. Since then CNTs application in electrochemistry has grown profusely, where CNTs-modified electrodes have shown interesting catalytic properties toward electrochemical processes since it acts as electrical conducting nanowires between the base electrode and the electroactive species on the surface. Despite its numerous application, CNTs integration with metal nanoparticles (especially Co, Ni and Fe which are important members of mixed-valence transition metals) to give hybrid systems which form the basis of this project as electroactive material for sensor have not been fully explored.

1.1.1.2 Metal (M) and metal oxide (MO) nanoparticles as electrocatalyst

Metal nanoparticles are potentially useful for sensing, catalysis, transport, and other applications in biological and medical sciences [15, 16]. Transition metals nanoparticles (especially Ni, Fe and Co) are found to demonstrate better sensing and catalytic properties towards detection and determination of both environmental and biological analytes [17-21]. Metal oxide nanoparticles on the other hand are extensively used in a considerable number of applications in food, material, chemical and biological sciences [22]. It is well known that bulk materials based on TiO_2, SiO_2 and aluminium (Al) and iron oxides have been massively produced for many years. Recently, nanoparticulate versions of these metal oxides have been manufactured. They are introduced in commercial products such as cosmetics and sunscreens (TiO_2, Fe_2O_3 and ZnO) [23], fillers in dental fillings (SiO_2) [24], catalysis (TiO_2) [25], and as fuel additives (CeO_2) [26]. In contrast, nickel (Ni), iron (Fe) and Cobalt (Co) are important transition metals which application in catalysis and other industrial applications have been neglected for many years. More importantly, their nanocomposite with CNTs and their redox active behaviour to influence electron transfer kinetics on chemically modified electrode for application in catalysis are hardly reported or not fully explored. Therefore, this thesis dwell deeply into the synthesis, characterization and electrocatalytic behaviour of these important transition metals and their oxides (NiO, Fe_2O_3, Co_3O_4) towards sensing of some important environmental molecules.

1.1.1.3 Carbon nanotube-metal and metal oxide modified electrode as sensor for the hydrazine, diethylaminoethanethiol, dopamine and nitrite.

Recently there has been renewed interests in the preparation and characterization of carbon nanotubes/metal (CNT–M) hybrid systems as electroactive material for sensors [27–32] and catalysts [33,34]. Among these metals, Co, Ni and Fe have proven to have excellent properties in electrocatalysis. The detection of the hydrolysis products of V-type nerve agents is still hugely unexplored. But it was observed previously that surface-confined nickel micropowder (ca. 17 – 60 mm range) immobilized on basal plane pyrolytic graphite electrode showed good electrocatalytic response towards DEAET [35]. Even with that, research report on its detection on CNT/M nanocomposite modified electrode is very scarce or unavailable. On the other hand, there are huge literature on the electro-oxidation of hydrazine on carbon-based electrodes [36–45], but the use of CNTs decorated with metal nanoparticle is limited [46]. Authors have also reported the electrocatalytic properties of other modified electrodes towards the electrocatalytic response of dopamine [47-57], nitite and nitric oxide [58-67] but the detection of these molecules on CNT/M or CNT/MO modified electrodes is rarely established. Thus, this thesis did not only explore catalysis of these analytes on CNT/M modified electrode, but also reported the mechanism behind their electrocatalytic oxidation using different electrochemical techniques.

1.1.1.4 Electron transport behaviour of CNT-M/MO modified electrodes.

Studies have shown that CNTs provided a large surface for metal deposition on electrodes and thus provided a synergistic relationship for an improve electron transfer between the base

electrode and the CNT–M hybrids [16,68-70]. However, the extent and the mechanism for the electron transfer of the CNT–M and carbon nanotubes–metal oxide (CNT–MO) modified electrodes are not clearly understood. Electron transport (ET) process between the surface active material and the underlying electrode is important in achieving a maximal overlap between electrode modifier, the electrolyte or the analyte in solution for enhanced or active electrocatalysis. An effective electron transfer lowers the formal potential of catalysis, reduces the peak to peak separation (ΔE) and ensures that the ratio of the anodic to cathodic peak current is close to unity which in principle indicates a favourable reversible process. This principle is more important in biological system where the orientation of the active biological catalyst to the electrode is of great importance for effective electron transport and catalysis. For example, nickel oxide film has a great effect on the electrode kinetics and provides a suitable environment for the glucose oxidase to transfer electron with underlying GC electrode in blank phosphate buffer solution pH 7.0 [16]. This can be as a result of the strong interaction between GOx molecules and NiOx nanoparticles.

The electron transport (ET) behaviour of iron nanocomposite modified electrodes has been studied in different electrolytes. For example, ET of iron-5,10,15,20-tetrakis[aaaa-2-trismethylammoniomethyl-phenyl]porphyrin,nanocomposite modified gold electrode (MWNTs-FeTMAPP/Au) was determined in 0.1 M KCl containing 1.0 mM $[Fe(CN)_6]^{3-}$ .The redox peak currents of $[Fe(CN)6]^{3-/4-}$ redox couple greatly increased and was attributed to the larger apparent surface of the electrode due to the presence of the nanocomposite [71]. In a related experiment, electron transfer behaviour of nanostructured iron(II)phthalocyanine (nanoFePc) at edge plane pyrolytic graphite electrodes (EPPGEs) was investigated using cyclic voltammetry and electrochemical impedance spectroscopy (EIS). This showed that the nanoFePc-

based electrode exhibits faster heterogeneous electron transfer constant, k_{app} (about a magnitude higher) than the bulk FePc in $[Fe(CN)6]^{3-/4-}$ redox probe [72]. In another study, presence of Fe_3O_4 nanoparticles on chitosan iron oxide indium tin oxide electrode (CH/Fe_3O_4/ITO) results in increased active surface area of chitosan iron oxide nanocomposite and resulted in increased electron transport between $[Fe(CN)_6]^{3-/4-}$ redox species and the electrode [73]. Electrochemical impedance spectroscopy (EIS) studies of chitosan indium tin oxide modified electrode (CH/ITO film) and chitosan magnetic iron oxide nanoparticles indium tin oxide modified electrode (CH–Fe_3O_4/ITO) was investigated in phosphate buffer solution. From the Nyquist plots obtained, the semicircle part, which corresponds to the electron transfer limited process is smaller for the CH–Fe_3O_4 nanocomposite than CH film ITO modified electrode thus suggesting that the electron transfer in the CH–Fe_3O_4 nanocomposite film is easier between the solution and electrode [74]. Zhao et al. [75] reported that multilayer of CH–Fe_3O_4 promotes direct electron transfer of haemoglobin. Other studied on electron transport of iron and iron oxide nanoaparticles have been reported [76].

There are many literatures on the ET of CoOx NPs at electrode surface but in most cases, the CoOx NPs mediates ET between a biomolecule and the underlying electrode. For example, Haemoglobin (Hb) undergoes a quasi-reversible redox process at the glassy carbon electrode modified with cobalt oxide nanoparticles, not observed at the bare GC electrode and was attributed to the cobalt oxide providing a suitable environment for the hemoglobin to transfer electron with underlying GC electrode [77]. In another report, flavine adenine dinucleotide (FAD) undergoes a quasi-reversible redox process at glassy carbon electrode modified with cobalt oxide (CoOx) nanoparticles in pH 7.0 PBS. No peak was observed for GC/CoOx or bare GC electrode in

the same electrolyte [19]. The result suggests that CoOx influence kinetics of electrode reaction and provides a suitable environment for the FAD to transfer electron with underlying GC electrode. Other literatures on the ET behaviour of Co and CoOx NPs on electrode surface have been reported [78,79].

1.1.2 Aim of thesis.

The main objectives of this project are:

i. To characterise redox active metal and metal oxide nanoparticles made by both electrodeposition and simple chemical syntheis, and integrated with single or multi-walled carbon nanotubes using microscopy, spectroscopy and electrochemical techniques.

ii. To modify bare edge plane pyrolytic electrode with the CNT-M or CNT-MO films through a simple drop-dried method and establish their electrochemical properties which are:

(i) Heterogenous electron transfer kinetics and

(ii) Electrocatalysis towards the detection of DEAET, hydrazine dopamine and nitrite.

iii. To investigate the supercapacitive or energy storing properties of the CNT/MO nanocomposite materials in neutral and acidic pH conditions.

This introductory chapter will provide information on the general overview of electrochemistry, electrochemical techniques,electrochemical impedance spectroscopy, chemically modified electrodes, electrode modification process, nanoscience in electrochemistry, microscopy and spectroscopy techniques and the analytes (DEAET, hydrazine, dopamine and nitrite) used in this work as analytical probe. Chapter two provides the experimental procedure adopted. Chapter three to ten discuss the results obtained.

1.2 Overview of Electrochemistry

1.2.1 Basics of electrochemistry

Several analytical techniques have been developed over the years for the detection and quantification of arrays of biological and environmentally important analytes. Among these is titrimetric [80], flourimetry [81], high performance liquid chromatography (HPLC) [82], mass spectroscopy [83] among others. However, these methods require a lot of chemical derivatization procedures and are time consuming. Some are very cumbersome and expensive and not even portable enough for field analysis. Therefore in recent time, the properties and the application of these electrodes for analytical purposes have been investigated using electrochemical technique.

1.2.1.1 Electrochemical equilibrium: Introduction

An electrochemical equilibrium established when two solutions are separated by a membrane that is impermeable to some of the ions in the solution. In more physical terms, it is an equilibrium set up when two coexisting phases are subject to the restriction that one or more of the ionic components cannot pass from one phase into the other; commonly, this restriction is caused by a membrane which is permeable to the solvent and small ions but impermeable to colloidal ions or charged particles of colloidal size [84].

Consider the following process:

$$Fe(CN)_6^{3-}(aq) + e^-(m) \rightleftharpoons Fe(CN)_6^{4-}(aq) \qquad (1.1)$$

Such an equilibrium was established by first preparing a solution containing both potassium hexacyanoferrate (II), $K_4Fe(CN)_6$, and

potassium hexacyanoferrate(III), $K_3Fe(CN)_6$ dissolved in water and then inserting an electrode made of platinum or other inert metal into the solution (Figure 1.1). Equilibrium is established at the surface of the electrode and involves the two dissolved anions and the electrons in the metal electrode.

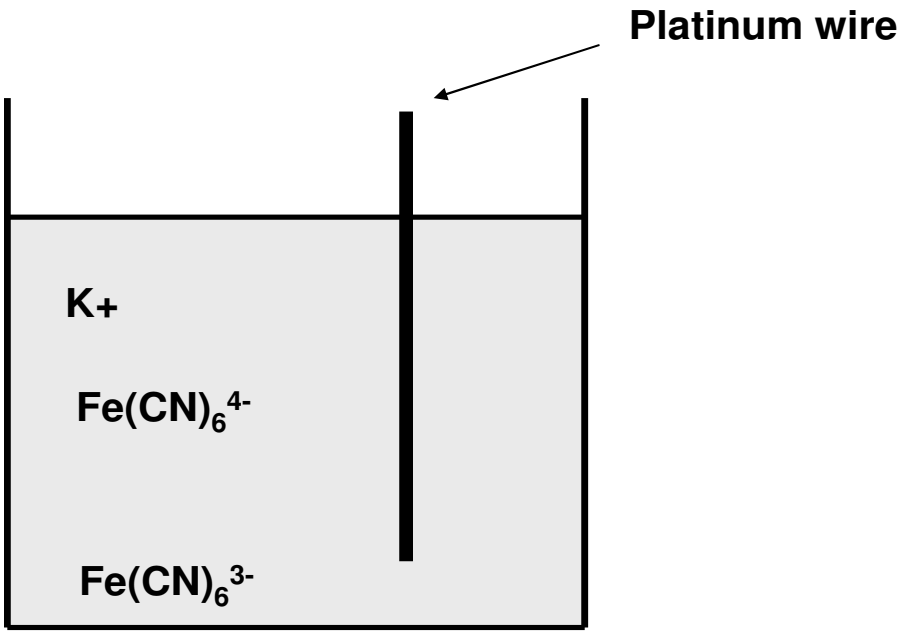

Figure 1.1: A platinum wire immersed into an aqueous solution containing both ferrocyanide and ferricyanide [84].

The establishment of equilibrium implies that the rate of at which $Fe(CN)_6^{4-}$ gives up electrons (become oxidized) to the metal wire or electrode is exactly balanced by the rate at which electrons are released by the wire to the $Fe(CN)_6^{3-}$ anions (become reduced). Once this dynamic equilibrium is established, no further change occurs. Also, the net number of electron that are transferred in one direction or another is infinitesimally small, such that the concentrations of $Fe(CN)_6^{4-}$ and $Fe(CN)_6^{3-}$ are not measurably changed from their values before the electrode is introduced into the solution.

1.2.1.2 Electrochemical equilibrium: Electron transfer at the electrode-solution interface

Considering the equation below:

$$Fe(CN)_6^{3-}(aq) + e^-(m) \rightleftharpoons Fe(CN)_6^{4-}(aq) \qquad (1.2)$$

Transfer of electrons between the metal electrode and the solution phase is a function of the energy levels associated with the species involved in the potential determining equilibrium. For example for the system represented in Equation 1.2 above, the electronic structure of the metal involves electronic conduction 'bands' in which the electrons are free to move throught the solid, binding the (metal) cations rigidly together. The energy levels in these bonds filled up to an energy maximum known as the Fermi level. On the other hand, the energy level associated with the solution phase $Fe(CN)_6^{4-}$ and $Fe(CN)_6^{3-}$ (aq) ions are discrete and relate to an unfilled molecular orbital in $Fe(CN)_6^{3-}$, which gains an electron to form $Fe(CN)_6^{4-}$ [84]. Figure 1.2 shows that before electron transfer takes place between the electrode and the solution, the Fermi level is higher than the vacant orbital in the $Fe(CN)_6^{3-}$ ion thus making it energetically favourable for electrons to leave the Fermi level and join the $Fe(CN)_6^{3-}$ species converting them to $Fe(CN)_6^{4-}$ ions. This energy difference is the driving force of the electron transfer in the system. As this electron transfer proceeds, positive charge builds up on the electrode (metal) and corresponding negative charge in the solution phase therefore creating an electrical double layer. Correspondingly, the electronic energy level in the metal becomes lower while that in the solution phase becomes higher. A situation is reached where the Fermi level lies in between the energy levels of the two ions, so that the rate at which electrons leave the electrode and reduced $Fe(CN)_6^{3-}$ ions equals the rate at which electrons join

the metal from the $Fe(CN)_6^{4-}$ ions which becomes oxidized. At this equilibrium point, there is a charge separation between the electrode and the solution, and this is the origin of the electrode potential established on the metal.

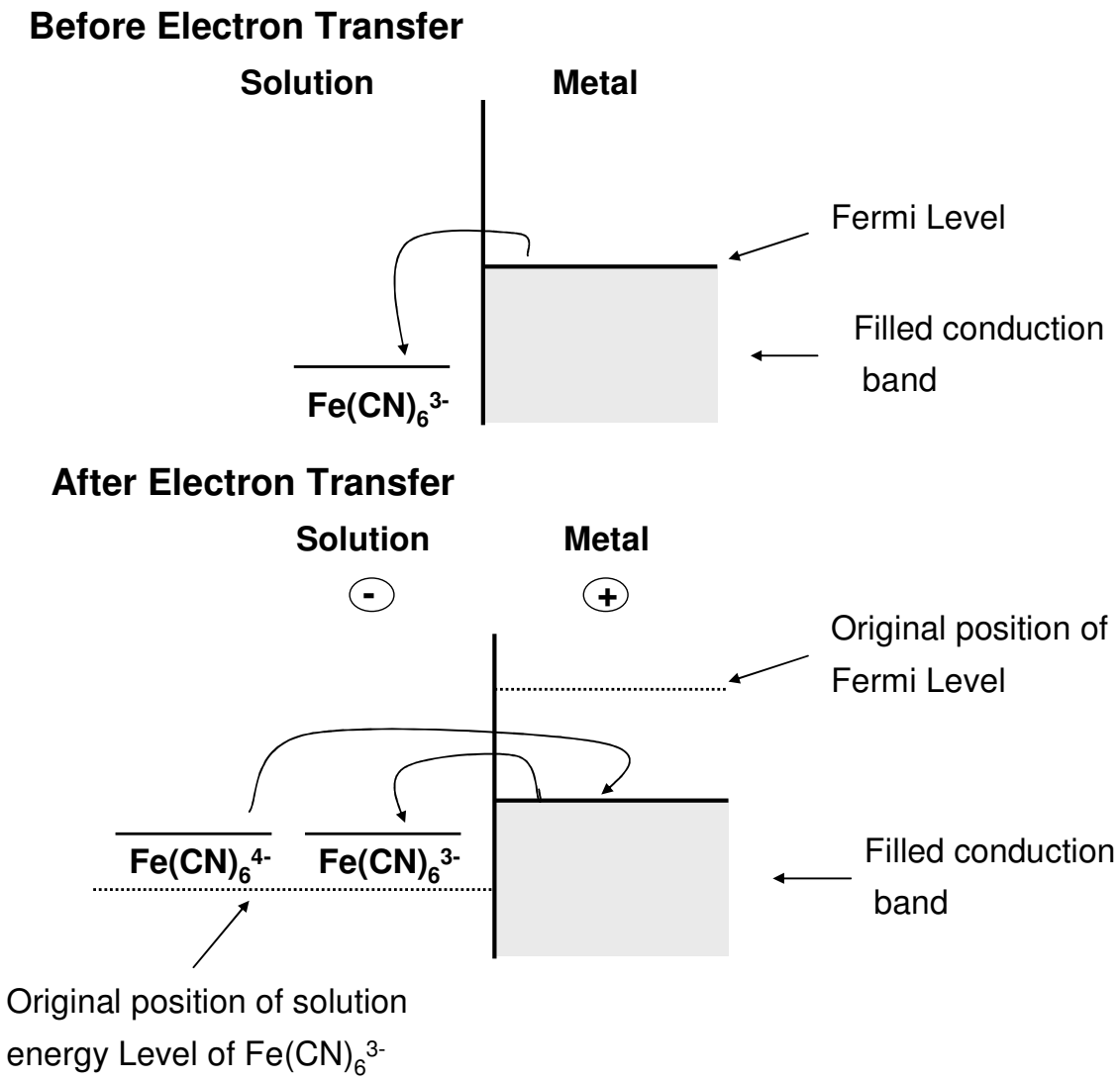

Figure 1.2: The energy of electrons in the ions in solution and in the metal wire [84].

1.2.1.3 Classification of electrochemical techniques

Electrochemical techniques can either be 'bulk' or 'interfacial' technique. Bulk techniques are based on the phenomena that occur in the solution itself while interfacial techniques are based on the events occurring at the electrode-

solution interface. Interfacial technique is sub-divided into potentiometric and voltammetric methods. Voltammetric technique can either be divided into controlled-potential and controlled-current methods. Controlled-potential techniques have advantages such as high sensitivity and selectivity, protable and low cost instrumentation. It allows for potential controlled while the current is measured. Examples include voltammetry and chronoamperometry.

1.2.1.4 Faradaic and non-Faradaic processes

The objective of controlled-potential electroanalytical experiments is to obtain a current response which is related to the concentration of the target analyte. This objective is accomplished by monitoring the transfer of electron(s) during the redox process of the analyte:

$$\mathbf{O} + ne^- \rightleftharpoons \mathbf{R} \qquad (1.3)$$

where O and R are the oxidized and the reduced forms, respectively, of the redox couple. These reactions are called Faradaic process as electrons are transferred across the electrode-solution interface. Non-Faradaic process on the other hand arises where there is no charge transfer across the electrode-solution interface. Processes such as adsorption and desorption can occur, and the structure of the electrode-solution interface can change with changing potential or solution composition. The Non-Faradaic process can be governed by 'transient current' when the potential, electrode area, or solution composition changes.

1.2.1.5 The electrochemical cell

Electrochemical cells in which faradaic currents are flowing are classified as either *galvanic* or *electrolytic* cells. A *galvanic cell* is one in which reactions occur spontaneously at the electrodes

when they are connected externally by a conductor (Figure 1.3a). These cells are often employed in converting chemical energy into electrical energy. Galvanic cells of commercial importance include *primary (nonrechargeable) cells* (e.g., the Leclanche Zn-MnO_2 cell), *secondary (rechargeable) cells* (e.g., a charged Pb-PbO_2 storage battery), and *fuel cells* (e.g., an H_2-O_2 cell). An *electrolytic cell* is one in which reactions are effected by the imposition of an external voltage greater than the open-circuit potential of the cell (Figure 1.3b). These cells are frequently employed to carry out desired chemical reactions by expending electrical energy. Commercial processes involving electrolytic cells include electrolytic syntheses (e.g., the production of chlorine and aluminum), electrorefining (e.g., copper), and electroplating (e.g., silver and gold). The lead-acid storage cell, when it is being "recharged," is an electrolytic cell [85].

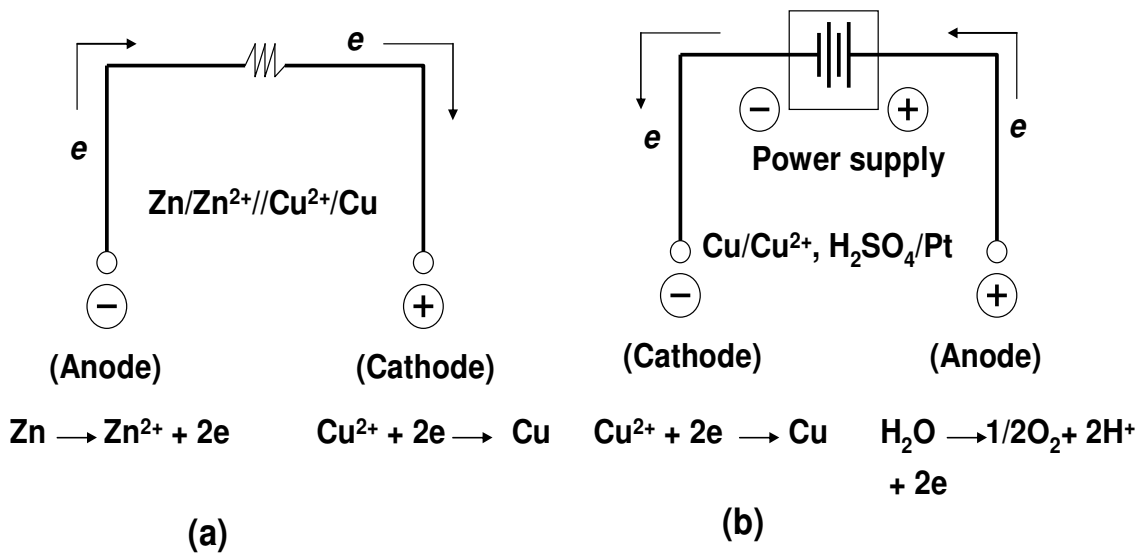

Figure 1.3: (a) Galvanic and (b) electrolytic cells [85].

1.2.1.6 Mass transport processes

In an electrochemical cell, mass transport is a process which governs the net movement of ions, charge or neutral species across the electrode-electrolyte interface. It is considered as mass transfer of an electroactive species in an electrolyte near the electrode. The

mass transport process can be in form of **diffusion, migration** or **convection**. The three mass transport processes are summarised in Figure 1.4.

(a) Diffusion

Diffusion is a spontaneous movement under the influence of concentration gradient, that is, the process in which there is movement of a substance from an area of high concentration of that substance to an area of lower concentration, aimed at minimising concentration differences [86]. If the potential at an electrode oxidizes or reduces an analyte, its concentration at the electrode surface will be lowered, and therefore, more analyte moves to the electrode from the bulk of the solution, which makes it the main current-limiting factor in voltammetric process.

Although migration carries the current in the bulk solution during electrolysis, diffusion should also be considered because, as the reagent is consumed or the product is formed at the electrode, concentration gradient between the vicinity of the electrodes and the electroactive species arise. Under some circumstances, the flux of electroactive species to the electrode is due almost completely to diffusion.

(b) Migration

Migration is the type of charge transport involving movement of charged particles along an electrical field (i.e., the charge is carried through the solution by ions according to their transference number [86]. Controlled-potential experiments require a supporting electrolyte to decrease the resistance of a solution and eliminate electromigration effects to maintain a constant ionic strength. To eleiminate or suppress electromigration, addition of excess or large concentration of inert salt such as KCl is used this work. In analytical applications, the presence of a high concentration of

supporting electrolyte which is hundred times higher than the concentration of electroactive ions means that the contribution of examined ions to the migrational transport is less than one percent.

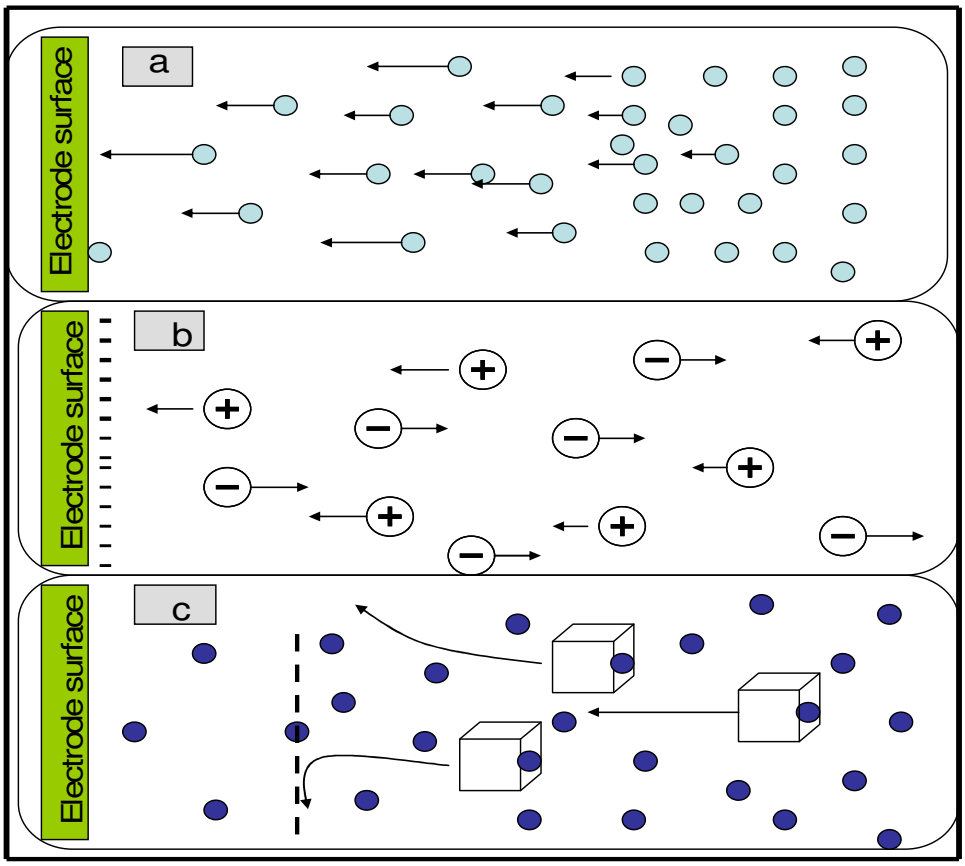

Figure 1.4: The three modes of mass transport process: (a) Diffusion, (b) Migration and (c) Convection [86].

Then it can be assumed that the transport of the examined species towards the working electrode is by diffusion only. Migration of electroactive species can either enhance or diminish the current flowing at the electrode during reduction or oxidation of cations. It helps reduce the electrical field by increasing the solution conductivity, and serves to decrease or eliminate sample matrix effects. The supporting electrolyte ensures that the double layer remains thin with respect to the diffusion layer, and it establishes a uniform ionic strength throughout the solution. However, measuring the current under mixed migration-diffusion conditions may be an

advantage in particular electrochemical and electroanalytical situation.

(c) Convection

It is the transport of charges to the electrode by a gross physical movement; such as fluid flow occurs by stirring or flowing the solution and by rotating or vibrating the electrode (i.e., forced convection) or because of density gradient (i.e., natural convection) [86]. The effect is eliminated during voltammetry experiment by maintaining the cell under quiet and stable condition.

1.3 Voltammetric Techniques

This section gives a brief overview of the electrochemical techniques employed in this study. Electrochemistry involves the measurement of potential (potentiometry) or current response (voltammetry). This study focused on current measurement (voltammetry) and therefore before the different voltammetry techniques used are discussed, it is imperative to understand the concept of the word **voltammetry**.

Voltammetry is a category of electroanalytical methods used in analytical chemistry and various industrial processes. In voltammetry, information about an analyte is obtained by measuring the current as the potential is varied [87,88]. Voltammetry experiments investigate the half cell reactivity of an analyte. Most experiments control the potential (volts) of an electrode in contact with the analyte while measuring the resulting current (amperes) [85]. To conduct such an experiment requires three electrodes (Figure 1.5). The *working* electrode, which makes contact with the analyte, must apply the desired potential in a controlled way and facilitate the transfer of electrons to and from the analyte. A second electrode acts as the other half of the cell. This second electrode must have a known potential with which to gauge the potential of the working electrode, furthermore it must balance the electrons added or removed by the working electrode. While this is a viable setup, it has a number of shortcomings. Most significantly, it is extremely difficult for an electrode to maintain a constant potential while passing current to counter redox events at the working electrode. To solve this problem, the role of supplying electrons and referencing potential has been divided between two separate electrodes. The *reference* electrode is a half cell with a known reduction potential. Its only role is to act as reference in measuring and controlling the working electrodes potential and at

no point does it pass any current. The *auxiliary* electrode passes all the current needed to balance the current observed at the working electrode. To achieve this current, the *auxiliary* will often swing to extreme potentials at the edges of the solvent window, where it oxidizes or reduces the solvent or supporting electrolyte. These electrodes, the *working*, *reference*, and *auxiliary* make up the modern three electrode system.

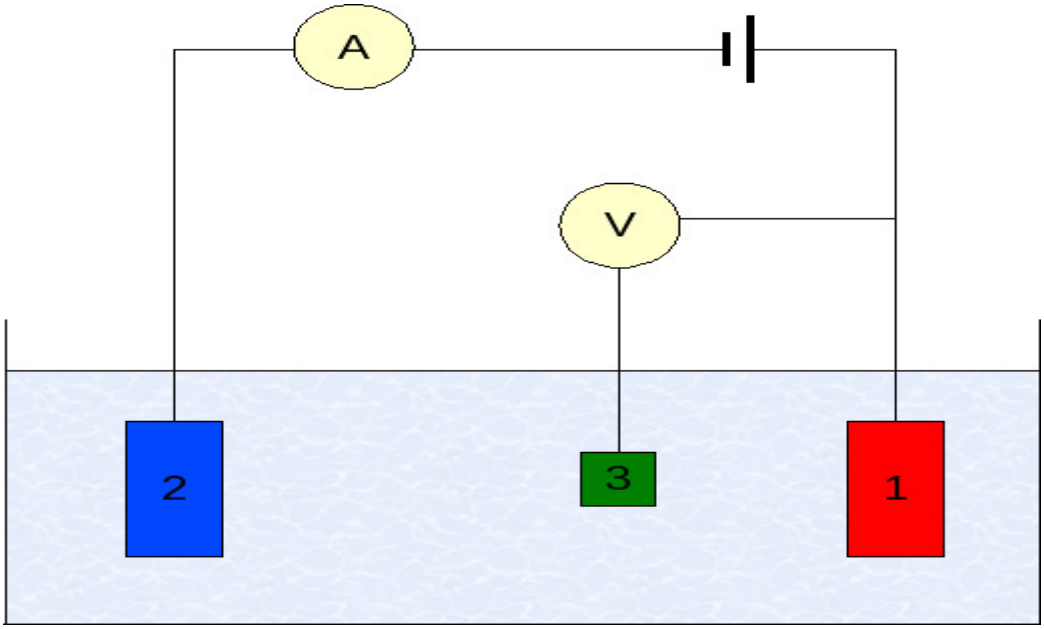

Figure 1.5: Three electrode set-up: (1) working electrode (2) auxillary electrode (3) reference electrode [89].

1.3.1 Types of voltammetry

1.3.1.1 Cyclic voltammetry

Cyclic voltammetry (CV) is the most widely used electrochemical technique. The technique can be used to study electron transfer mechanisms in reactions including providing information on the reversibility, kinetics, and formal reduction and oxidation potentials of a system [85]. The CV experimental set-up consist of a working electrode which can be gold, platinum, glassy carbon etc., a reference electrode against, which the potential is measured against and can be standard calomel electrode (SCE) or

silver|silver chloride (Ag|AgCl) and counter electrodes such as platinum wire can be used. During the CV experiment, the solution is kept stationary and is therefore not stirred in order to avoid movement of ions to the electrode surface by mechanical means.

In a cyclic voltammetry experiment, the potential of an electrode is cycled from a starting potential, E_i to a final potential, E_f (the potential is also called the switching potential) and then back to E_i, (Figure 1.6). The potential at which the peak current occurs is known as the peak potential, E_p. At this potential, the redox species has been depleted at the electrode surface and the current is diffusion limited. The magnitude of the Faradaic current, I_{pa} (anodic peak current) or I_{pc} (cathodic peak current), is an indication of the rate at which electrons are being transferred between the redox species and the electrode. The electron transfer process during cyclic voltammetry experiment can be classified as follows: (i) reversible process (ii) irreversible process and (iii) quasi-reversible process.

A **reversible process** obeys the Nernst reaction in which the electron transfer is rapid, allowing the assumption that the concentration of both the oxidized (O) and the reduced species (R) are in a state of equilibrium (Equation 1.4). Figure 1.6 shows a typical CV for a reversible process. The electroactive species are stable and so the magnitudes of I_{pc} and I_{pa} are equal and they are proportional to the concentrations of the active species. ΔE (E_{pa}-E_{pc}) should be independent of the scan rate, ν but in practice ΔE slightly increases with ν, this is due to the solution resistance, R_s between the reference and working electrodes [90].

$$\mathbf{O} + ne^- \rightleftharpoons \mathbf{R} \qquad (1.4)$$

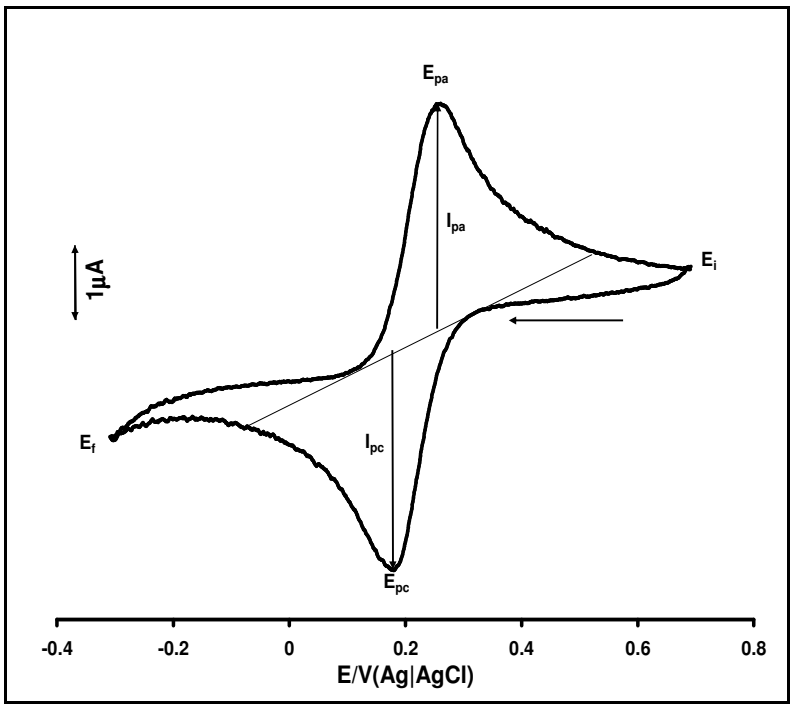

Figure 1.6: Typical cyclic voltammogram for a reversible process.

For a reversible process, the half-wave potential ($E_{1/2}$) equals the formal potential ($E^{o'}$) and are related to the standard potential (E^{o}) as follows (Equation 1.5):

$$E_{1/2} = E^{o'} = E^{o} + \frac{RT}{2F}\ln\frac{[O]}{[R]} \qquad (1.5)$$

where R = gas constant, T = temperature (K), F = Faraday's constant (96485 $Cmol^{-1}$), [**O**] = concentration of oxidized species (mol L^{-1}), [**R**] = concentration of reduced species (mol L^{-1})
The formal redox potential, $E^{o'}$ can be calculated from Equation 1.6:

$$E^{o'} = \frac{E_{pa} + E_{pc}}{2} \qquad (1.6)$$

where E_{pa} = anodic peak potential, E_{pc} = cathodic peak potential

The number of electron transferred in a reversible process can be calculated from Equation 1.7:

$$\Delta E = E_{pc} - E_{pa} = \frac{RT}{nF} \quad (1.7)$$

At 25 °C, $\Delta E = \frac{0.059V}{n}$ (1.8)

where n = number of electrons transferred, other symbols as in Equation 1.5. At 25°C, the peak current of a reversible process is given by the Randles-Sevcik Equation, 1.9

$$I_p = (2.69x10^5)n^{3/2}[O]A(D\nu)^{1/2} \quad (1.9)$$

where I_p = peak current (A), A = electrode area (cm^{-2}), D = diffusion coefficient ($cm^2\ s^{-1}$), ν= scan rate ($V\ s^{-1}$).
Using the Randles-Sevcik Equation (1.9), a linear plot of I_p vs. $\nu^{1/2}$ is obtained for a planar diffusion [91,92] to the electrode surface. Deviation from linearity indicates the presence of chemical reaction involving either the oxidized, reduced or both species.

For an **irreversible process**, only forward oxidation or reduction peak is observed but at times with a weak reverse peak, Figure 1.7. This process is usually due to slow electron exchange or slow chemical reactions at the electrode surface [93]. Nernst equation is not applicable in this case since the rate of electron transfer is insufficient to maintain surface equilibrium and thus the oxidized [O] and reduced [R] species are not at equilibrium. The peak current, I_p for irreversible process is given by Equation 1.10.

$$I_p=(2.99x10^5)n[(1-\alpha)n]^{1/2}AC(D\nu)^{1/2} \quad (1.10)$$

where α is the rate of electron transfer, C is the concentration of the active species in mol cm^{-3} and the other symbols already defined under Equation 1.9. For a totally irreversible system, ΔE_p is calculated from Equation 1.11:

$$\Delta E_p = E^{o'} - RT/\alpha nF[0.78 - In(k^o/D^{1/2})In(\alpha nF\nu/RT)^{1/2}] \quad (1.11)$$

k^o = heterogeneous electron transfer constant (cms^{-1}). The rest of the symbols are as in above and they are listed in the Table of symbols.

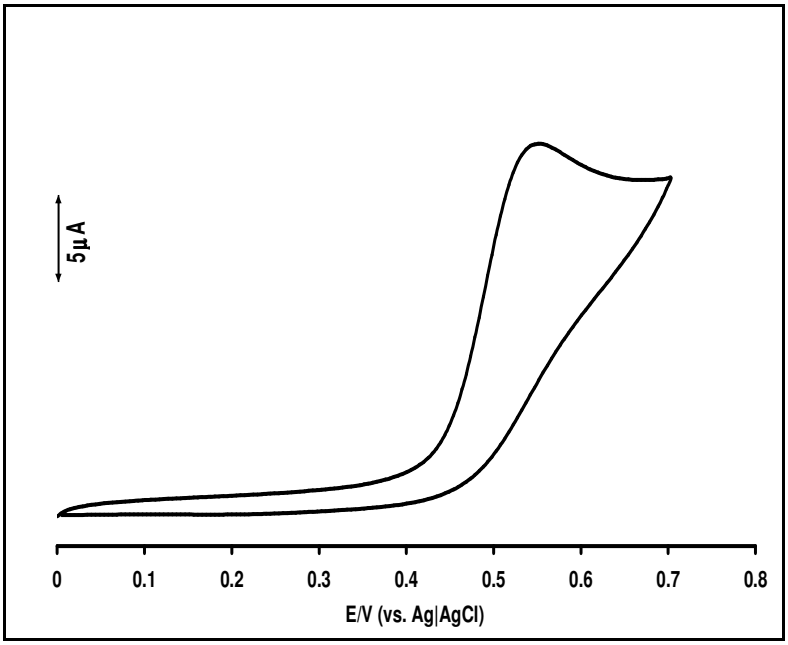

Figure 1.7: Typical Cyclic voltammogram for an irreversible process.

Quasi-reversible process is intermediate between reversible and irreversible systems. The current due to quasi-reversible processes is controlled by both mass transport and charge transfer kinetics [86,94]. The process occurs when the relative rate of electron transfer with respect to that of mass transport is insufficient to maintain Nernst equilibrium at the electrode surface. For quasi-reversible process, I_p increases with

$\upsilon^{1/2}$ but not in a linear relationship and $\Delta E > 59/n$ mV increases with increasing υ.

1.3.1.2 Square wave voltammetry

Exceptional versatility is found in a method called *square wave voltammetry* (SWV), which was invented by Ramaley and Krause [95], but has been developed extensively in recent years by the Osteryoungs and their coworkers [96,97]. This is a differential technique in which potential waveform composed of a symmetrical square wave of constant amplitude superimposed on a base staircase potential (Figure 1.8) [85,86,98]. It is the plot of the difference in the current measured in forward (i_f) and reverse cycle (i_r), plotted against the average potential of each waveform cycle. In this technique, the peak potential occurs at the $E_{1/2}$ of the redox couple because the current function is symmetrical around the potential [96,99].

The scan rate of a square wave voltammetry experiment is given by the Equation 1.12:

$$v = f.\Delta E_s \qquad (1.12)$$

Where f is the frequency (Hz) and ΔE_s is the potential size. The main advantages of SWV are excellent peak separation, high sensitivity and ability to eliminate capacitive charging current compared with cyclic voltammetry or the differential pulse voltammetry.

1.3.1.3 Linear sweep voltammetry (LSV)

Linear sweep voltammetry (LSV) is a voltammetric method where the current at a working electrode is measured while the potential between the working electrode and a reference electrode is swept linearly in time (Figure 1.9). Oxidation or reduction of

species is registered as a peak or trough in the current signal at the potential at which the species begins to be oxidized or reduced [85]

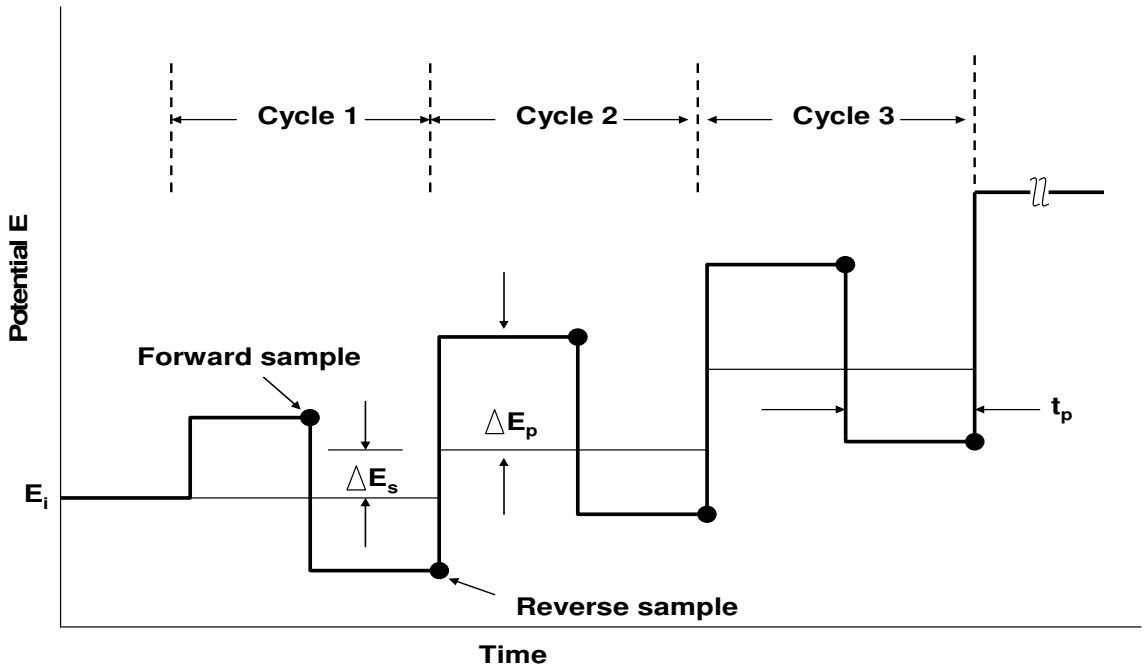

Figure 1.8: Waveform and measurement scheme for square wave voltammetry. Shown in bold is the actual potential waveform applied to the working electrode. The light intervening lines indicate the underlying staircase onto which the square wave can be regarded as having been superimposed. In each cycle, a forward current sample is taken at the time indicated by the solid dot, and a reverse current sample is taken at the time marked by the shaded dot [85].

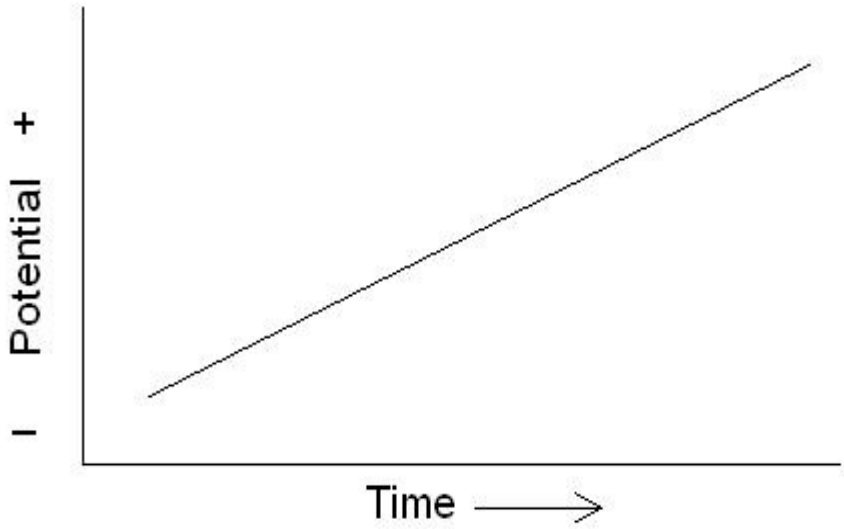

Figure 1.9: Linear potential sweep

1.3.1.4 Rotating disk electrode

The *rotating disk electrode* (RDE) provides an efficient and reproducible mass transport, and hence the analytical measurement can be made with high sensitivity and precision. The convective nature of the electrode results in very short response time [86]. The detection limits of the electrode can be lowered via periodic changes in the rotation speed, and isolation of small mass-transport-dependent currents from simultaneously flowing surface-controlled background currents. The electrode consists of a disk imbedded in a rod of an insulating material. The rod is attached to a motor directly by a chuck or by a flexible rotating shaft or pulley arrangement and is rotated at a certain frequency, / (revolutions per second). The more useful descriptor of rotation rate is the angular velocity, ω (s^{-1}), where $\omega = 2\pi rf$. Electrical connection is made to the electrode by means of a brush contact. During experiment, the current flux of the analyte is induced towards the electrode. The limiting current (for a reversible system) is thus proportional to the square root of the angular velocity by the *Levich equation* (Equation 1.13):

$$i_{l,c} = 0.62nFAD_0^{2/3}\omega^{1/2}\nu^{-1/6}C_0 \qquad (1.13)$$

where $i_{l,c}$ is the diffusion-limited currents, *n* is the number of electrons transferred, and other symbols are defined above and are listed on the list of symbols.

1.3.1.5 Chronoamperometry

It is an electrochemical technique in which the potential of the working electrode is stepped, and the resulting current from faradic processes occurring at the electrode (caused by the potential step) is monitored as a function of time (Figure 1.10). In the waveform

(Figure 1.10), the current response followed the working electrode potential being stepped from an initial potential at which the oxidized (reduced) species is stable in solution, to the first step potential where a redox reactions occurred forming the reduced (oxidized) species and held at this value for the time duration (for a single potential experiment) or stepped to a second potential where it is held for the duration of the second step time.

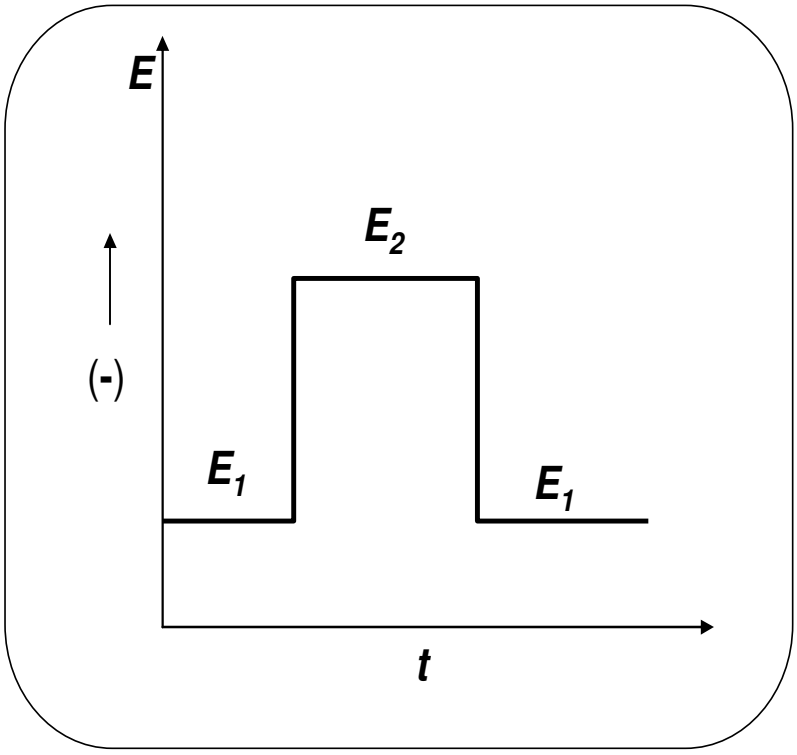

Figure 1.10: Typical waveform for a double potential step chronoamperometry [85].

Limited information about the identity of the electrolyzed species can be obtained from the ratio of the peak oxidation current versus the peak reduction current. However, as with all pulsed techniques, chronoamperometry generates high charging currents, which in this case, decay exponentially with time. To measure the faradic current (the current that is proportional to the concentration of the analyte), current in the last 70-80% of each scan is integrated (when charging current has dissipated). Most commonly

investigated with a three electrode system. Since the current is integrated over relatively longer time intervals, chronoamperometry gives a better signal to noise ratio in comparison to other amperometric technique [85,87]. For a current-time dependent relationship (Cottrell equation; Equation 1.14) for a linear diffusion controlled process [85,86], the diffusion coefficient (D) can be estimated from the slope of the plot of I versus $t^{-1/2}$.

$$I = \frac{nFAD^{1/2}C}{\pi^{1/2}t^{1/2}} \tag{1.14}$$

All symbols are as in above and they are listed in the list of symbols. Also using the relationship in Equation 1.15 [85,86] where I_{cat} and I_{buff} are the currents in the presence and absence of analyte, respectively; C is the analyte bulk concentration, k is the catalytic rate constant ($M^{-1}s^{-1}$) and t is the elapsed time (s), the catalytic rate constant K can be obtained from the plots of I_{cat}/I_{buff} vs. $t^{1/2}$.

$$\frac{I_{cat}}{I_{buff}} = \pi^{1/2}(kCt)^{1/2} \tag{1.15}$$

1.3.1.6 Galvanostatic charge discharge technique

This is an electrochemical measuring technique for electrochemical analysis or for the determination of the kinetics and mechanism of electrode reactions based on the control of the current flowing through the system. The method consists of placing a constant current pulse upon an electrode and measuring the variation of the resulting current through the solution. This is called the galvanostatic method for measuring the rate of an electrochemical reaction. The potentiostatic is constituted by

applying a potential pulse while observing the variation of the rate as a function of time (Figure 1.11). The technique is usually used to investigate the charging and the discharging process of electrochemical capacitors [100,101].

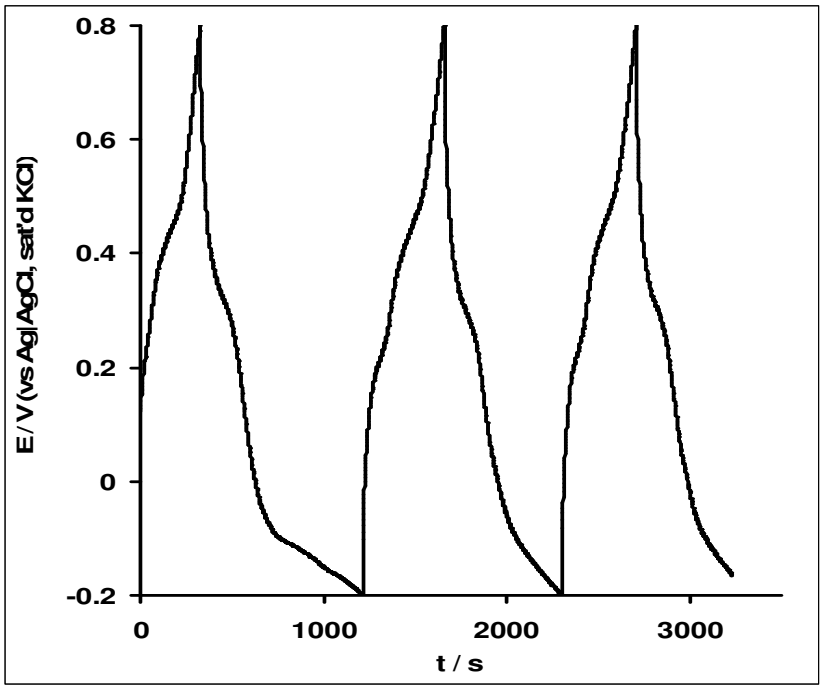

Figure 1.11: Typical galvanostatic charge-discharge curve.

1.3.1.7 Electrocatalysis using voltammetry

The electrocatalysis process studied in this project using the voltammetric techniques already discussed above mainly involves electron transfer between the analyte and the electrode surface. The mechanism involve is briefly described in scheme 1.1. In this work, the catalyst (M or MO) on the CNT platforms become oxidized in the electrolyte. The oxidized catalyst interacts with the analyte which are mostly in their reduced state. Electron transfer process takes place leading to the oxidation of the analyte while at the same tme; the catalyst is simultaneously reduced and regenerated for further catalysis.

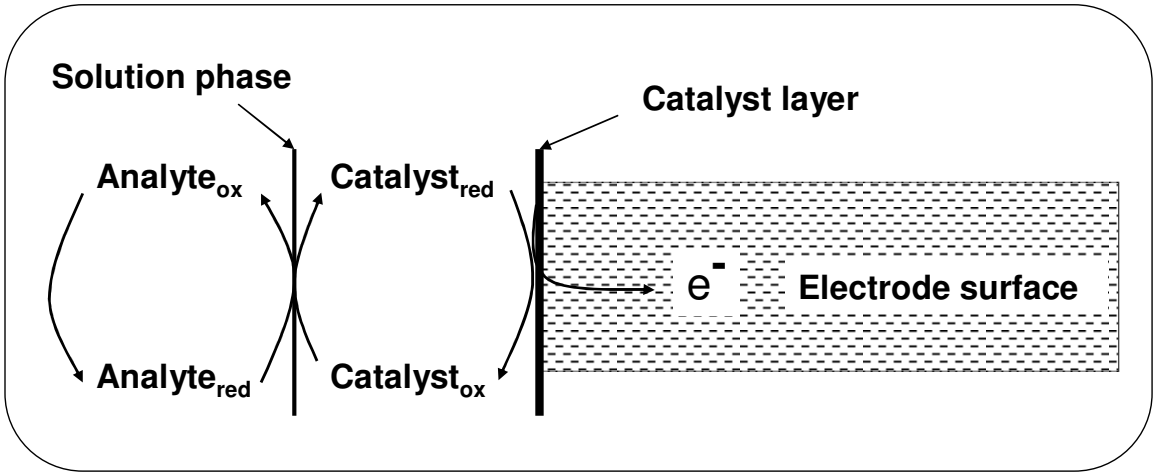

Scheme 1.1: Schematic diagram showing electrocatalytic process at modified electrode [86].

1.4 Electrochemical Impedance Spectroscopy (EIS)

Electrochemical impedance spectroscopy (EIS) is a relatively new and powerful method of characterizing many of the electrical properties of materials and their interfaces with electronically conducting electrodes. It may be used to investigate the dynamics of bound or mobile charge in the bulk or interfacial regions of any kind of solid or liquid material: ionic, semiconducting, mixed electronic–ionic and even insulators (dielectrics) [102]. It is also used to explore the properties of porous electrodes, and for investigating passive surfaces [103]. EIS technique has been shown to be effective for probing the redox and structural features of a surface-confined species [104]. Other advantages include: (i) rapid acquisition of data such as ohmic resistance, capacitance, inductance, film conductivity, as well as charge or electron transfer at the electrode-film interface, (ii) the ability to obtain accurate, reproducible measurement, (iii) the capacity of the system to remain at equilibrium due to use of low amplitude-sinusoidal voltage (~ 5 mV), (iv) capability to adapt for various applications and (v) characterize interfacial properties in the absence of redox reactions.

1.4.1 Basics of impedance spectroscopy

Impedance is measured by applying a sinusoidal potential *V (t)*, of small amplitude to an electrochemical cell and measuring resultant sinusoidal current *I (t)*, through the cell [105-108]. The applied sinuisodal potential and current are represented as a function of time. These measurements are done over a suitable frequency range and the results can be related to the physical and chemical properties of the material [105-108]. The relationship is shown in Equation 1.16:

$$Z = \frac{V(t)}{I(t)} \tag{1.16}$$

where $V(t)$ is the sinusoidal applied voltage at time t, $V(t) = V_o \sin \omega t$ where V_0 is the maximum potential applitude, ω is the radial frequency (in rad.s^{-1}) and can be related to frequency f *(Hz)* as $\omega = 2\pi f$. At the same frequency as the applied sinusoidal potential, the current response $I(t)$ is also sinusoidal but with a shift in phase, $I(t) = I_o \sin(\omega + \theta)$, where I_o is the maximum current applied and θ is the phase shift by which the voltage lags the current (Figure 1.12a) [105]. Therefore, impedance is a vector quantity where the quantity $Z = V/I$ represents the magnitude and θ represent the direction (Figure 1.12b). The complex notation of impedance is shown in Equation 1.17.

$$Z = Z' + jZ'' = Z_{real} + jZ_{imaginary}. \tag{1.17}$$

where Z' and Z'' are the real and imaginary parts of the impedance respectively and j is a complex number [105].

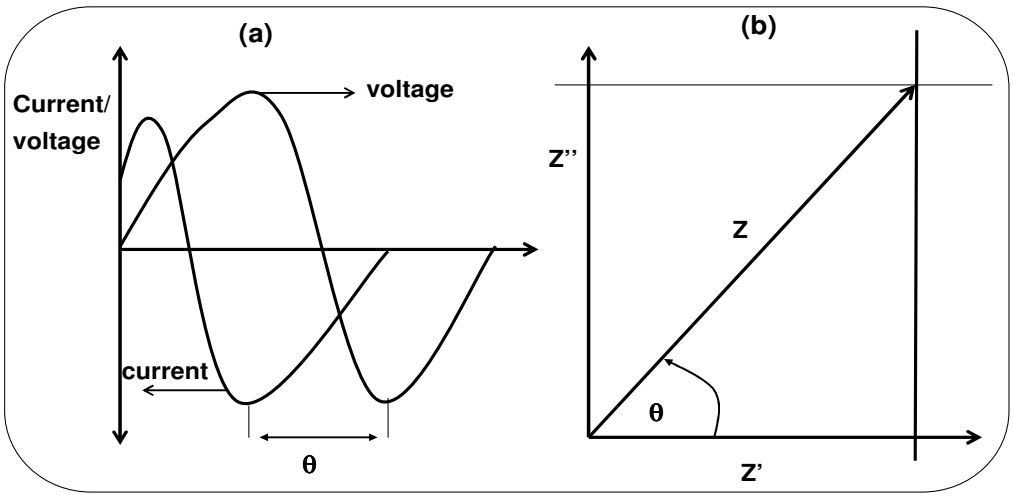

Figure 1.12: (a) Applied sinusoidal voltage and resulting sinusoidal current response. (b) Vector representation of real Z' and imaginary Z'' of impedance Z [105].

1.4.2 Application and data presentation

Impedance measurements include both the electrical resistance and resistance due to morphological state of the materials. EIS has been used to monitor the whole procedure in preparing modified electrodes, which could provide useful information for each step and be used for probing the changes of the surface modification. The impedance data are fitted to an equivalent circuit using the FRA software package for complex non-linear least squares calculations based on the EQUIVCRT programme. Simple electrical elements such as resistors and capacitors in the circuit measure resistance and capacitance respectively during the electrochemical process [102-105,108-111]. The resistance in the circuit is an indication of the electrical conductivity of the electrolyte and the constant phase element (*CPE*) results from the charge which is in excess at the electrode-electrolyte interface. Ideal Randles equivalent circuit involves double layer (C_{dl}) (Figure 1.13a). It incorporates various contributions to the interfacial barrier behaviour; these factors are the resistance of electrolyte (R_s), the charge transfer resistance (R_{ct}), double-layer capacitance (C_{dl}) and Warburg impedance (Z_w). Modified Randles circuit uses *CPE* in place of C_{dl} as illustrated in Figure 1.13b. The impedance of *CPE* is defined as

$$Z_{CPE} = \frac{1}{[Q(j\omega)^n]} \tag{1.18}$$

where Q is the frequency-independent constant relating to the surface electroactive properties, ω is the radial frequency, the exponent n arises from the slope of log Z vs log f (and has values $-1 \leq n \leq 1$). If $n = 0$, the CPE behaves as a pure resistor; $n = 1$, *CPE* behaves as a pure capacitor, $n = -1$, *CPE* behaves as an

inductor; while n = 0.5 corresponds to Warburg impedance (Z_w) which is associated with the domain of mass transport control arising from the diffusion of ions to and from the electrode|solution interface. Generally speaking, *CPE* has been known to occur via several factors notably (i) the nature of the electrode (e.g., roughness and polycrystallinity), (ii) distribution of the relaxation times due to heterogeneities existing at the electrode/electrolyte interface, (iii) porosity and (iv) dynamic disorder associated with diffusion [112]. Most times, *CPE* represents the real and practical situations experienced during electrochemical impedance experiment as compared to C_{dl}.

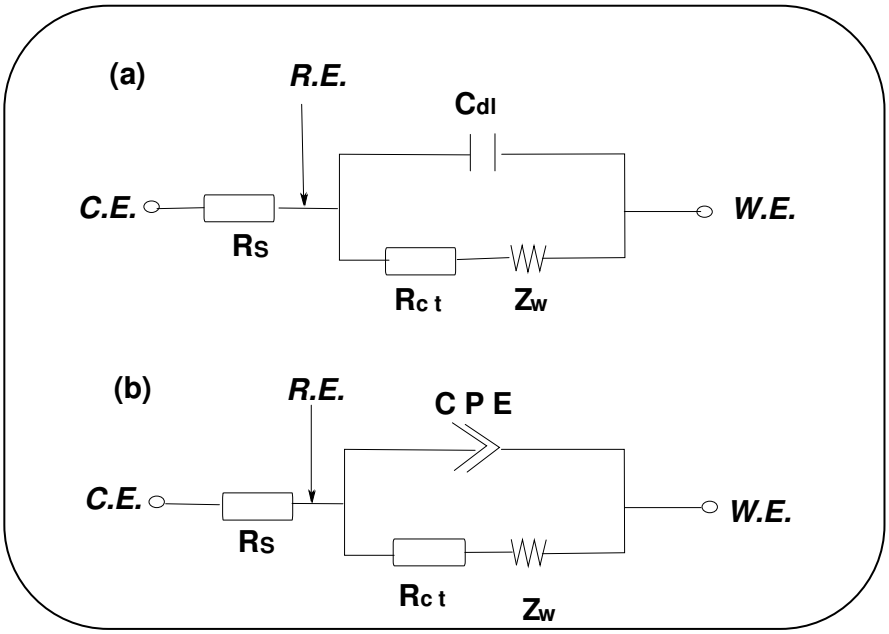

Figure 1.13: (a) Typical Randles equivalent circuit for an ideal electrochemical system. (b) Modified Randles equivalent circuit for real, practical situation.

Apart from the normal and modified Randles circuit, several other circuit models have been used in the fitting of the impedance data in this study. Some include an inductance (L). Inductive behaviour takes place when the Faradaic current is governed by the occupation of an intermediate state [113-115]. The inductive behaviour can be attributed to factors such (1) instrumental

artefacts, or (2) the inductance of the electrode, or (3) the inductance of the connecting wires [116]. The curve obtained from the impedance fitting is called the Nyquist plot, which is imaginary impedance versus the real impedance ($-Z_{imaginary}$ versus Z_{real}) (Figure 1.14a). It includes a semicircular part and a linear part. The semicircular part at higher frequencies corresponds to the electron-transfer-limited process and its diameter is equal to the electron transfer resistance (R_{ct}), which controls the electron transfer kinetics of the redox probe at the electrode interface. Meanwhile, the linear part at lower frequencies corresponds to the diffusion process.

All the obtained spectra were first subjected to the Kramaers-Kronig (K-K) test. The main essence of the K-K test is simply to check whether the measured impedance spectra comply with the assumptions of the well known K-K transformation, viz (i) that the impedimetric response is only related to the excitation signal; (ii) that the impedimetric response is linear (or the perturbation is small, e.g., <10mV, for non-linear systems; (iii) that the system does not change with time, say due to ageing, temperature changes, non-equilibrium conditions, etc; and (iv) that the system is finite for all values of ω, including zero and infinity [117,118]. Failure of the K-K test, signified by a large value of pseudo χ^2 is usually an indication that no good fit can be obtained using the electrical equivalent circuits' methods. It should be noted that aside from visual inspection of goodness of the fitting lines, two accurate ways to establish how well the modeling functions reproduce the experimental data sets are the relative error estimates (in %) and chi-square functions (χ^2) [119], which is the sum of squares of the relative residuals (i.e., sum of the real and imaginary χ^2), easily obtained from the K-K test.

Generally, a bare electrode should exhibit an almost straight line for the Nyquist plot (Figure 1.14a) because electrochemical

reactions at such electrode surfaces are expected to be mass diffusional limiting electron-transfer processes [102-105,117]. For a modified electrode, the Nyquist plot shows characteristic semi-circle pattern due to barrier to the interfacial electron transfer (Figure 1.14b). The interfacial barrier behaviour has been described by Randles equivalent circuit (Figure 1.13a). The R_{ct} value is influenced by the film thickness and the nature of the films on the electrodes. The R_{ct} is the domain of kinetic control and it is proportionally related to the diameter of the semi-circle of the Nyquist plot. In some systems the reaction rate might be controlled by transport phenomenon and this effect needs to be taken into consideration. The measured impedance can be explained based on its relationship with the Warburg impedance (Z_w) as described above.

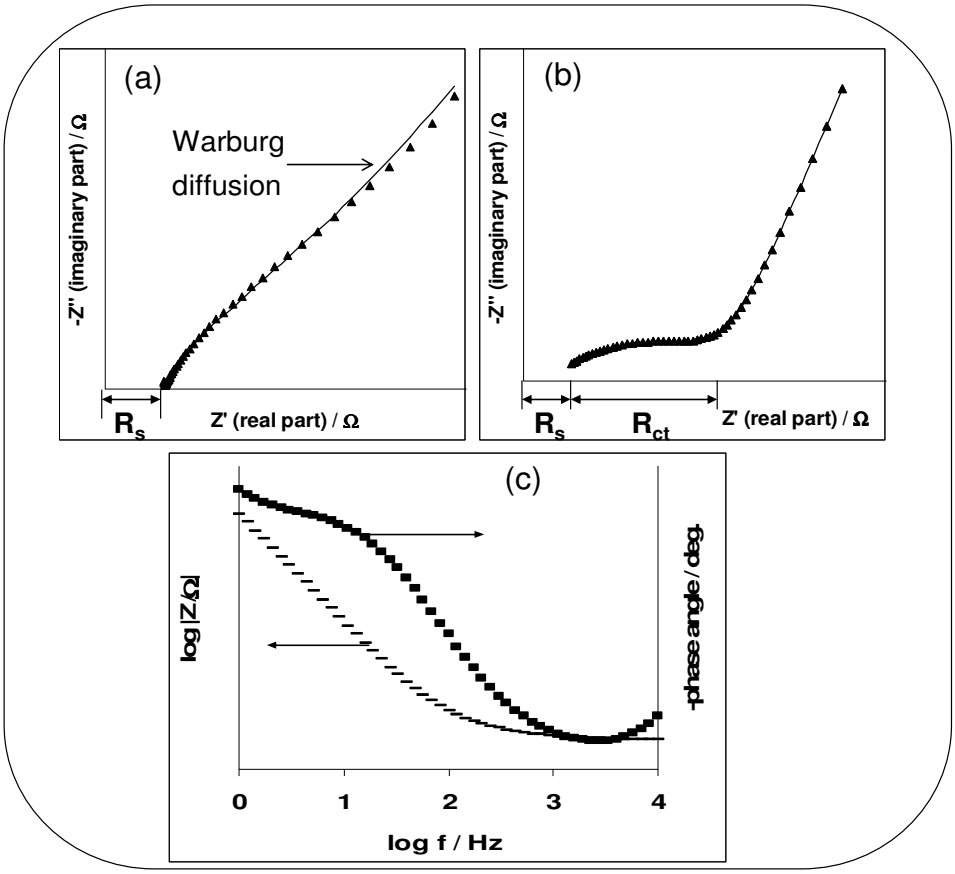

Figure 1.14: Typical Nyquist plot for (a) bare and (b) modified electrode. (c) is the corresponding Bode plots.

Another important plot obtained from the EIS experiment is the Bode plots (Figure 1.14c) [102-105,117]. Bode plots is the plot of phase angle (θ) versus the logarithm of the frequency (log *f*), or the logarithm of impedance magnitude (log *Z*) versus the logarithm of the frequency (log *f*). The plot provides information about the capacitive properties of a modified electrode. From the plot phase angle (θ) versus log *f*, the peak height represented the capacitive nature of the electrode while the phase angle and the frequency values gives an idea of the relaxation process of the electrode|solution interface. Slope obtained from the plot of log *Z* versus log f also described the capacitive behaviour of the system. An ideal capacitive behaviour requires a phase angle of 90^0 and a slope value of – 1.0.

1.5 Chemically Modified Electrodes

A chemically modified electrode (CME) is an electrode surface coated with a thin film of selected conducting materials for the purpose of improving the chemical, electrochemical, optical, electrica, and electron transfer properties of the film in a rational, chemically designed manner [120].

The desired redox reaction at the bare electrode using voltammetric techniques such as CV and SWV often involves slow transfer kinetics and therefore occurs only at an appreciable rate only at potential substantially higher than its thermodynamic redox potential. Such reactions can be catalysed by attaching to the surface a suitable electron-transfer mediator. The function of the mediator is to fascilitate the charge transfer between the analyte and the electrode. In most cases, the mediated reaction sequence (e.g. for a reduction process) can be described by equations below.

$$M_{ox} + ne^- \longrightarrow M_{red} \qquad (1.19)$$

$$M_{red} + A_{ox} \longrightarrow M_{ox} + A_{red} \qquad (1.20)$$

where M represents the mediator and A the analyte. Hence, the electron transfer takes place between the electrode and mediator and not directly between the electrode and analyte. The net results of this electron shuttling are a lowering of the over-voltage to the formal potential of the mediator and an increase in current density. The efficiency of the electrocatalytic process depends also upon the actual distance between the bound redox site and the surface (since electron-transfer rate decreases exponentially when the electron-tunneling distance is increased).

For the determination of surface concentration of the electroactive material, Equation (1.21) or Equation (1.22) for a surface confined species was`employed, where I_p (μA) is directly proportional to the scan rate, ν (Vs^{-1}) [84-86].

$$\Gamma = \frac{Q}{nFA} \tag{1.21}$$

$$I_p = \frac{n^2 F^2 A \Gamma \nu}{4RT} \tag{1.22}$$

where Γ = total surface coverage by electroactive species *Q* = quantity of charge in coulombs, the rest of the symbols have their usual meaning.

1.5.1 Carbon Electrodes

Carbon electrodes (such as the glassy carbon, carbon paste, highly oriented pyrolytic graphites, basal plane pyrolytic graphite and edge plane pyrolytic graphites electrodes) have long been recognised as versatile and supporting platforms for electrocatalysis and electrochemical sensing due to their numerous advantages such as low cost, chemical inertness and wide potential window in most electrolyte solutions over the precious metal electrodes (e.g gold, platinum, aluminium, silver copper). Among this carbon based electrodes, edged plane pyrolytic graphite electrode (EPPGE) have been reported to have a better catalytic and reactivity which is solely due to edge plane sites/defects (Figure 1.15) which are the key to fast heterogeneous charge transfer [121].

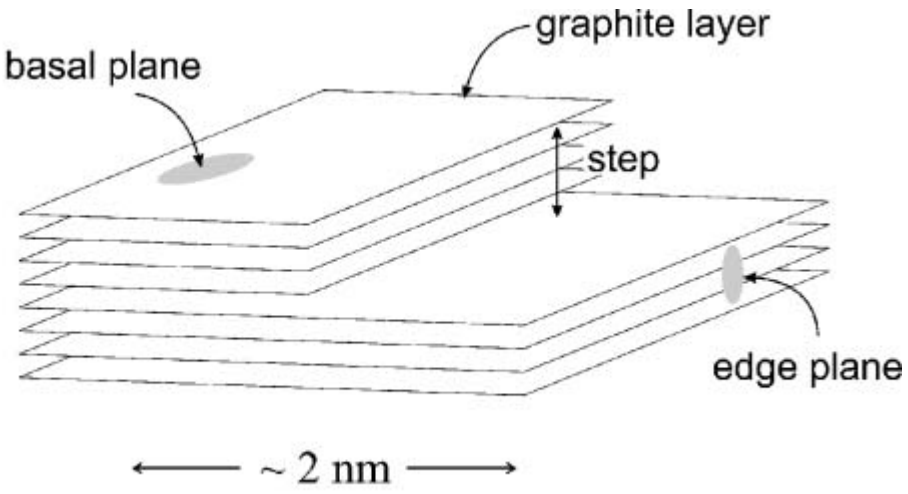

Figure 1.15: Pyrolytic graphite plate showing the basal and the edge plane sites [121].

For example, the electrochemical oxidation of homosteine in 0.1 M phosphate buffer solution was studied at boron-doped diamond (BDD), glassy carbon (GC), EPPG and BPPG electrodes and a CNT film modified BPPG electrode. While no appreciable oxidation waves seen in the potential range studied for the other electrodes, the EPPG electrode exhibited a large and easily quantifiable signature at *ca* + 0.66 V (*vs.* SCE) demonstrating a significant reduction in the overpotential in comparison with the other commonly used electrode substrate while also exhibiting an enhanced signal-to-noise ratio [122]. EPPG electrode has also been explored for the detection of nitrogen dioxide. Its response was compared with that of BDD, BPPG and GC electrodes. For the three later electrodes, no Faradaic waves were observed in contrast to the well-defined signal seen at the EPPG electrode [123]. Other application of EPPG electrode includes the detection of NADH [124], chlorine [125], halides [126], ascorbic acid [127], cathodic stripping voltammetry of manganese [128] and anodic stripping voltammetry of silver [129]. This outstanding property of EPPG electrode over other carbon based electrodes has made it the best choice for the studies reported in this work. It is well known that

the slow electron transfer behaviour at the bare electrode can be improved upon by surface modification with electron transfer mediators such as CNTs and redox active metal catalyst. These surface modifiers substantially enhance the electrochemical response at the bare electrode.

1.5.2 Carbon nanotubes modified electrodes

Carbon nanotubes occur in two main types: single-walled carbon nanotubes (SWCNTs) which consist of single rolled-up graphite sheet or single graphite tube with a diameter of approximately 1 nm and multi-walled carbon nanotubes (MWCNTs), which consist of several sheets of graphites rolled into concentric tubes with various lengths and diameters [130].

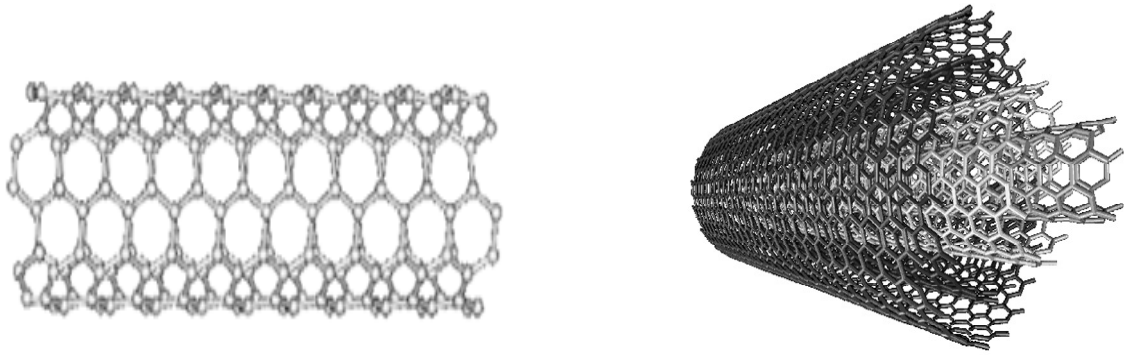

(a) (b)

Figure 1.16: Structure of (a) SWCNT and (b) MWCNT.

Carbon nanotubes are generated by arc evaporation [131], laser ablation [132], pyrolysis [133], and electronic methods [134]. Ijima and co-workers also showed that the synthetic yield of SWCNT preparation can be improved by adding cobalt or other transition metals such as nickel, iron, and molybdenum, with the graphite in the arc vaporisation process [135]. Properties of CNTs

have been widely investigated and SWCNTs possess important mechanical, thermal, photochemical and electrical properties [136] which are industrially useful. MWCNTs contain several SWCNTs in their structure and, therefore, possibly have analogous physicochemical properties to those corresponding to SWCNTs. These nanomaterials are robust and stiff but flexible and they have been reported as the strongest of all the synthetic fibres [136]. Materials containing CNTs may, however, be strong enough to build spacecrafts, space elevators, artificial muscles, and land and sea vehicles [136]. SWCNTs can conduct twice the electricity of copper, making these materials excellent electrical conductors, and may also be used to improve rechargeable batteries and fuel cell production [136]. Its presence on the surface of bare electrodes such as glassy carbon [137], graphite [138], carbon fiber [139], gold [140], and platinum (Pt) electrodes [141] has enhanced their electrical properties tremendously.

Several authors have reported the excellent electrocatalytic properties of nanotubes in the redox behaviour of different molecules and bio-molecules. There are reports on the advantages of CNTs modified electrodes on the electrocatalytic response of hydrazine [142], glucose [143], dihydronicotinamide adenine dinucleotide (NADH) [144], dopamine [145], nitric oxide [146], ascorbic acid [147], hydrogen peroxide [148]. Thus CNTs-modified electrodes have shown interesting catalytic properties toward electrochemical processes. Studies have shown that carbon nanotubes provided a large surface for metal deposition on electrodes and thus provided a synergistic relationship for an improve electron transfer between the base electrode and the CNT-M hybrids [16,69]. However, the extent and the mechanism for the electron transfer of the CNT-M or CNT-MO modified electrodes are not clearly understood. Therefore, this study investigated some of this rection mechanism using different electrochemical techniques

and the information provided is discussed in Chapter 3 to 9. It must be noted that electrodes modified with carbon nanotubes have increased surface areas and adsorption efficiency compared to other common electrodes, and exhibit intriguing ability to enhance the electrochemical responses of several organic molecules [149, 150], thus making them more favourable as electrode materials for the type of investigation reported in this work compared to other common electrodes.

1.5.3 Metal and metal oxides nanoparticles

The use of metal nanoparticles for electrode preparation is no longer news in the field of electro-analytical chemistry. Several methods have been developed for making metal and metal oxides nanoparticles: (1) electrodeposition [151], electropolymerisation [152], self-assembled monolayers (SAM) [153], Sol-gel technique [154], photolytic reduction [155], radiolytic reduction [156], sonochemical method [157], solvent extraction reduction [158], microemulsion technique [159], polyol process [160] and alcohol reduction [161]. Some of these methods are employed for electrode modification with the NPS and are discussed later. The synthesis and electrocatalytic behaviour of these important metals and their oxides towards sensing of biological and environmentally important molecules forms the subject of discussion in this thesis.

1.5.4 Electrocatalytic behaviour of carbon nanotubes-metal nanocomposite modified electrodes

Electrochemical detection of biological and environmental analytes using metal and metal oxide modified electrode was found very cheap and convenient over other methods of determination. Not only that, metal and metal oxides have been used to modify

electrodes for use as electrocatalysts and sensors [65,66,162-166]. These materials act as electron mediators, increasing the rate of electron transfer at the electrode-solution interface and also lowering the over-potentials for redox processes. The modification introduces some chemical and electrochemical properties which the bare electrodes do not posses. Electrocatalysis can be observed by comparing the CV of an analyte on modified electrode with that on bare electrodes; higher catalytic current, I_p and a shift to less positive peak potential in the CV of the former compared to the latter is an indication of electrocatalytic oxidation of the analyte. Typical example of electrocatalysis is shown in Figure 1.17.

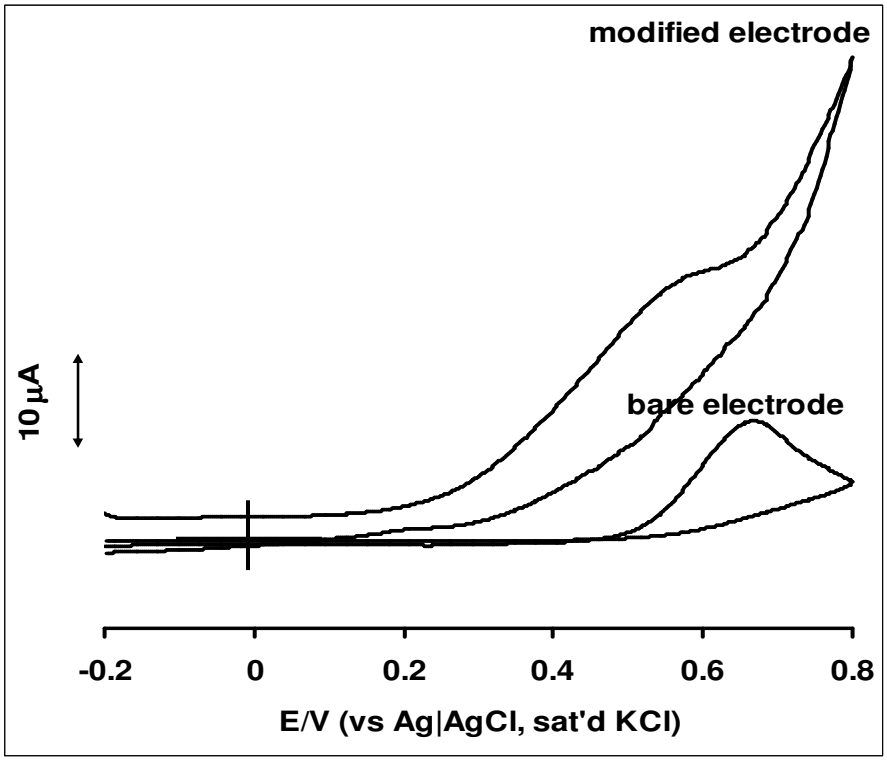

Figure 1.17: Cyclic voltammogram showing electrocatalytic process of an analyte on the bare and modified electrode.

Research on the possible applications of CNTs decorated with metal nanoparticles, particularly nickel, cobalt, and iron is beginning to receive some attention in electrochemistry especially in catalysis, supercapacitor an as an electron transfer mediator on

electrode surface [162-168]. Further to CNT-metal nanoparticles investigated in this work is the decoration of CNT with Prussian blue nanoparticles. Prussian blue (PB) is an iron cyanide complex with the molecular formula $Fe_4(III)[Fe(II)(CN)_6]_3$. It is used as an electron-transfer mediator due to its excellent electrocatalytic properties and has found applications in electrochromic devices [169], nanomagnetic [170], biomedical [171], molecular sieves [172], catalysis [150] and in solid-state batteries [173]. It was reported that electrodes modified with PB nanoparticles demonstrate a significantly decreased background, resulting in improved signal-to-noise ratio [174]. Several methods have been employed for PB preparation [175,176] but PB prepared by chemical deposition was considered to be more stable in a wider pH range [177]. CNT-PB modified electrodes have been used for the detection of many biomolecules including hydrogen peroxide [177], glucose [178], haemoglobin [179], oxygen [180], and NADH [181]. However, to the best of my knowledge, this is the first time the analyte reported in this work will be studied on CNT-PB modified electrode.

1.5.4.1 Nickel and nickel oxide carbon nanotubes modified electrodes

For many decades, nickel was regarded as a potentially toxic element, since its concentration in various foods was higher than that needed for living organisms. More recently, it is now considered a possible essential element for plants, although deficiencies can occur under certain circumstances. Not only that, the element either as pure metal or as nanoparticles has found uses in the area of electrochemistry as sensors for different compounds in food, water and other component of the environment. It is interesting to know that nickel nanoparticles have been used as sensor for both biological and chemical analyte. Pure nickel

electrodes and nickel-coated electrodes find various applications in the field of electroanalytical chemistry. Nickel electrodes can be used for electrochromic devices [182], alkaline batteries [183] and as electrocatalysts [184]. It has been reported that sensor having nickel as its working electrode reduces material cost and affords good long-term stability [185].

There are many literature on the used of nickel modified electrode for the catalysis of many organic and inorganic molecules such as nitrite (NO_2^-) [65,66]; acetaminophen [186]; dopamine [187]; glucose [188]; ethanol [189]; sulphite (SO_3^{2-}) [190]; sulphide (S^{2-}) [191]; chlorate ion (ClO^{4-}) [192]; methanol [193]; insulin [154]; phenol [194]; hydrogen peroxide [195]; ascorbic acid [188]; amino acids [115]; acethycholine [196]; thiocyanate ions [197]; thiosulphite ion [167]; hydrazine [198]; thiols [199] etc. but research reports on the use of nickel or nickel oxide nanoparticles as electrode modifier for the same purpose were very sketchy. However, recently, due to the advent of nanoscience and nanotechnology, some of these molecules are detected using electrode modified with nickel nanoparticles. Applications of nickel and nickel oxide nanoparticles modified electrodes as sensors in electrochemistry include: the electrochemical detection of acetaminophen (ACOP) on the carbon coated nickel magnetic nanoparticles modified glassy carbon electrode (C–Ni/GCE) [186]. The C–Ni/GCE has been applied successfully to the simultaneous determination of ACOP, dopamine (DA) and ascorbic acid (AA) in their mixture [186]. Nanostructured nickel based ethanol sensors have been developed by sputtering technique for ethanol sensing [200] Performance was increased using this technique. Shibli et al. [21] developed electrochemical sensor by electroplating nano nickel oxide reinforced nickel on graphite substrate. The modified electrode showed good sensing performance with a response time as low as 8 s during sensing and estimation of acetylcholine.

Glucose oxidase (GOx) was successfully co-deposited on nickel-oxide (NiO) nanoparticles at a glassy carbon using electrodeposition technique and the biosensor shows excellent electrocatalytical response to the oxidation of glucose with fast amperometric response when ferrocenmethanol was used as an artificial redox mediator [162]. Electrocatalytic oxidation and determination of hydrazine on nickel hexacyanoferrate (NiHCF) nanoparticles-modified carbon ceramic electrode (CCE) have been reported [167]. Electrocatalytic reduction of hydrogen peroxide (H_2O_2) on the self-immobilized cytochrome c on the electrodeposited NiO NPs modified glassy carbon electrode (Cyt c/NiO NPs/GC) has been studied [168].

Catalytic reduction of H_2O_2 on horseradish peroxidase/nickel oxides nanoparticles/glassy carbon (HRP/NiO NPs/GC) electrode had been reported [201]. Other literature reports on the catalytic application of Ni and NiO NPs are summarised in Table 1.1. While most of the modified electrode reported on the Table employed the catalytic activities of Ni and NiO nanopartilces as composite with other materials, the relationship between CNT/M or CNT/MO as simple and cheap electrode materials for catalysis was not given much attention. Thus, this study was basically aim at investigating the effect of the synergistic behaviour of the nanocomposite formed between the M or MO nanoparticles and CNT on the catalysis of some analyte. The effect will be discussed under Chapter 3.

Table 1.1: Electrocatalytic oxidation of some analytes on nickel and nickel oxide modified electrode.

Modified Electrodes	Fabrication method	Analyte	Medium	Ep (Volt)	LOD	Ref
C-Ni/GCE	Drop-dry	ACOP	BR buffer	0.569	0.60 μM	186
C-Ni/GCE	Drop-dry	ACOP/DA/AA	BR buffer	0.52 / 0.348 /0.164	2.3/1.2/4.1μM	200
GOx/NiO/GCE	Electrodeposition	Glucose	PBS/MeOH	0.25	24.0 μM	162
NiHCF/CCE	Electrodep/Dip Dry	Hydrazine	PBS	0.52	8.0 μM	167
Cytc/NiO NPs/GC	Electrodep / SAM	H_2O_2	PBS	- 0.25	-	168
HRP/NiO NPs/GC	Electrodeposition	H_2O_2	PBS	- 0.30	123.0 μM	201
Hb/NiO/GCE	Electrodeposition	H_2O_2	PBS	-0.25	0.63 μM	202
Cat/NiO/GCE	Electrodeposition	H_2O_2 / NO_2^-	PBS	-0.45 /-0.55	0.60 μM	203
$NiCo(OH)_2$/ITO	Electrodeposition	Urea	KOH	0.50	-	22
Ga/NiO/GCE	Electrodeposition	Insulin	PBS	0.65	22.0 pM	204
Co-Ni/C	Electrodeposition	O_2	KOH	0.65	-	205
Ni-P-C	Electrodeposition	H_2	NaOH	-	-	206
Mb/NiO NPs/GC	Electrodeposition	H_2O_2	PBS	- 0.25	75.0 μM	207
GC/NiOx/CB	Electrodep/dip-dry	H_2O_2	PBS	- 0.27	1.67.0 μM	208
GC/NiOx/TH	Electrodep/Dip dry	H_2O_2	PBS	- 0.27	0.36 μM	208
CoNiFe/GCE	Electrodeposition	H_2	NaOH	-	-	209
Pt/NiO composite	Mixing/Drop dry	CH_3OH	H_2SO_4	0.53	-	210
CholOxNiNP/MWCNT/GC	Electrodeposition	Cholesterol	PBS	- 0.20	1.0 μM	211

NCGC	Electrodeposition	Fructose	NaOH	0.35	0.98 μM	151
Ni/Ti	Dip-Dry	Cyclohexanol	NaOH	0.43	-	212
MWCNTs/NMN	Electrodep/Drop Dry	Methane	NaOH	0.4	-	213
PtRuNi/C	Drop dry	CO / CH_3OH	H_2SO_4	0.53 / 0.50	-	214
Ni/Pt/Ti/Al_2O_3	Sputtering	CH_3CH_2OH	KOH	0.61		215

HCF: hexacyanoferrate nanoparticles; **CCE:** carbon ceramic electrode; **Hb:** Hemoglobin **GCE:** glassy carbon electrode;**BR:** mixture of H_3PO_4/boric acid/H2SO4; **ACOP:** Acetaminophen; **FerMeOH:** Ferrocenemethanol; **ITO:** indium tinoxide electrode; **Cyt c:** cytochrome c; **NPs:** nanoparticles; **Mb:** myoglobin; **HRP:** horseradish peroxidase; **CholOx:** Cholesterol oxidase; **NC:** nano-structured Ni(II)–curcumin film; **NMN:** nickel hydroxide nanoparticles modified nickel electrode.

1.5.4.2 Iron and iron oxide carbon nanotubes modified electrodes

Applications of nanosized magnetic particles have received considerable attention in biotechnology and medicine for their novel properties [216,217]. Up to date, the application of magnetic nanoparticles have stretched to various areas including magnetic recording, magnetic fluids [218], immobilization of proteins [219], detection of DNA hybridization [220], drug delivery catalytic reactions [216]. Iron is a versatile element and can form several phases with different oxidation states and structures such as shown below [221].

$$FeO \leftrightarrow FeO \leftrightarrow Fe_3O_4 \leftrightarrow \gamma\text{-}Fe_2O_3 \leftrightarrow \alpha\text{-}Fe_2O_3 \leftrightarrow FeOOH \qquad (1.23)$$

Magnetite (Fe_3O_4), maghemite (γ-Fe_2O_3), and hematite (α-Fe_2O_3) are probably the most common out of the many oxides form in which iron oxides exist in nature [222].

Some of the catalytic works of iron nanocomposite modified electrodes have been reported. For example, Siswana et al. [223] reported that nanoparticles of iron (II) phthalocyanine (nanoFePc) impregnated on a carbon paste electrode (nanoFePc-CPE) revealed interesting electrocatalytic behaviour towards amitrole; pure catalytic diffusion-controlled process, with high Tafel slope suggesting strong binding of amitrole with nanoFePc catalyst. A carbon–iron nanoparticle modified glassy carbon electrode (CIN-GCE) has been developed for the determination of calcium dobesilate (CD) in pharmaceutical formulations with improved sensitivity and better reproducibility [224]. The electrocatalytic behaviour of an iron-cobalt carbon nanocomposite modified GCE electrode (FeCo/CNT/GCE) towards H_2O_2 reduction was studied [225]. Methanol oxidation in aqueous solution using FePt alloy nanoparticles modified glassy carbon electrode have been investigated. The modified electrode has strong catalytic oxidation of methanol in aqueous environment

compared with the bare GCE [226]. Mamuru and Ozoemena [72] reported that the nano iron pthalocyanine (nanoFePc) modified electrode exhibited enhanced electrocatalytic properties towards the detection of thiocyanate and nitrite in aqueous solutions compared to the bulk FePc counterpart. Gangeri et al. [227] compared the electrocatalytic activities of Pt/CNT and Fe/CNT on Nafion membrane electrode for fuel cell oxidation of CO_2. Their study indicated that Fe/CNT shows a better behavior than Pt/CNT (although a faster deactivation) in the conversion of carbon dioxide to liquid fuels, particularly isopropanol. Carbon-coated iron nanoparticles (CIN, a new style fullerence related nanomaterial) modified glassy carbon electrode (CIN/GCE) has been developed for the determination of uric acid (UA) [175]. The highly electrocatalytic activity of CNT/nano-Fe_3O_4 coated electrodes toward not only the reduction but also the oxidation of hydrogen peroxide have been reported [176]. Table 1.2 summarises other related literature reports.

Table 1.2: Electrocatalytic oxidation of some analytes on iron and iron oxide modified electrode.

Modified Electrodes	Fabrication method	Analyte	Medium	Ep (V)	LOD	Ref
nanoFePc-EPPGE	Drop-dry	SCN^- / NO_2^-	PBS	0.96	-	72
nanoFePc-CPE	Chemical Mixing	Amitrole	PBS/Na_2SO_4	0.42	3.62 nM	223
FeCo/CNT/GCE	Drop-dry	H_2O_2	KHphthalate	- 0.69	-	225
FePt/GCE	Drop-dry	CH_3OH	H_2SO_4	0.64	-	226
Fe/CNT/CC/Nafion membrane	Drop-dry/hot-pressing	CO_2	$KHCO_3$	-	-	227
CIN/GCE	Drop-dry	Uric acid	PBS	0.425	0.15 μM	163
Nano-Fe_2O_3/CPE	Chemical mixing	H_2O_2	H_3PO_4/H_3BO_3/ CH_3COOH	-0.56	$2x10^{-5}$ M	164
FeTMAPP/MWCNT/Au	SAM	O_2	PBS	- 0.25	0.38 μM	177
ssCT-DNA/CH-Fe_3O_4/ITO	Drop-dry	Nucleic-Acid	PBS	0.15	2.5ppb	228
Ur-GLDH/CH-Fe_3O_4/ITO	Dip-dry	Urea	PBS	0.18	0.5mg/dL	74
GOx/CH–Fe_3O_4/ITO	Dip-dry	Glucose	PBS	0.25	-	229
Fe_3O_4 MNPs	-	Phenol/ Anniline	PBS	-	-	230
Fe_3O_4@AuNPs/HS$(CH_2)_6$Fc/CPE	SAM	Dopamine	PBS	0.38	0.64 μM	231
IgGs/CH–Fe_3O_4/ITO	Drop-dry	Ochratoxin-A	PBS	0.45	$0.5ngdL^{-1}$	232
CNT/Fe_3O_4/CTS/GOx/PG	Magnetic loading / Drop-dry	Glucose	PBS	-	-	233
CNT/nano-Fe_3O_4/PG	Magnetic loading / Drop-dry	H_2O_2	PBS	- 0.36	-	234
Hb/CIN-CH/GCE	Drop-dry.	H_2O_2	PBS	0.50	1.2 μM	235
Nano-Fe-BDD	Electrodeposition	Trichloroacetate	NH_4F	-1.50	-	236
Nano-Fe-Pd	Chemical mixing	Lindane/ atrazine	CH_3OH	-	$0.1\ \mu gl^{-1}$	237

MMPs: magnetic nanoparticles; **nanoFePc-CPE:** nano iron phthalocyanine carbon paste electrode; **GNP/MWNTs-FeTMAPP-Au:** gold nanoparticles multi wall carbon nanotubes iron-5,10,15,20-tetrakis[aaaa-2-trismethylammoniomethyl-phenyl]porphyrin modified gold electrode; **FeCo/CNT/GCE:** iron –cobalt nanocomposite modified glassy carbon electrode; **ssCT-DNA/CH-Fe_3O_4/ITO :** single standard *calf thymus* deoxyribose nucleic acid (ssCT-DNA) - chitosan (CH)-iron oxide (Fe3O4) nanoparticles based hybrid nanobiocomposite indium tin oxide modified electrode; **CC:** carbon cloth; **Ur-GLDH/CH-Fe_3O_4/ITO:** Urease and glutamate dehydrogenase co-immobilized iron oxide nanoparticles-chitosan (CH) based nanobiocomposite film modified indium-tinoxide (ITO) glass plate; **GOx/CH–Fe3O4/ITO:** glucose oxidase-chitosan-iron oxide nanobiocomposite indium tinoxide electrode; **Fe3O4@AuNPs/HS(CH2)$_6$Fc/CPE:** 6-ferrocenylhexanethiol (HS(CH2)6Fc) functionalized iron oxide at gold nanoparticles films on carbon paste electrode; **IgGs/CH–Fe3O4/ITO:** immunoglobulin antibodies chitosan–iron oxide nanoparticles-indium–tin oxide (ITO) electrode; **CNT/Fe3O4/CTS/GOx/PG:** carbon nanotubes-iron oxide nanocomposite-chiotsan-immobilised glucose oxidase-plexiglas plate; **CIN/GCE:** Carbon-coated iron nanoparticles modified glassy carbon electrode.

1.5.4.3 Cobalt and cobalt oxide carbon nanotubes modified electrodes

Pure cobalt nanoparticles (2–20 nm) are of great research interest due to its unusual phenomena (quantum effects) and industrial applications [238,239]. They are used materials for magnetic, fluids, optoelectronics and in data storage applications [238-240]. Cobalt atoms has been largely employed for preventing the formation of less electroactive β phase of $Ni(OH)_2$ nanoparticles during electrode modification. Furthermore, the inclusion of Co^{3+} also increases the hydroxide conductivity shifting the redox peaks of $Ni(OH)_2$ to less positive potentials [241]. On the other hand, cobalt oxide films are composed of nanosized metal oxide particles, and have been intensively investigated in recent years for their use in processes such as energy storage system [242], electrochromic thin films [243], magnetoresistive devices [244] and heterogeneous catalysis [245].

Studies using Co and cobalt oxides (CoxOy) decorated electrodes for biological and environmental sensing have been reported [165,166,246-248]. Electrodes decorated with cobalt oxide nanoparticles without CNTs for sensing properties have also been studied [19,249]. Few studies using CNT-Co modified electrodes have been carried out [250-254], for example, Yang *et al.* [252] used chemically prepared cobalt hexacyanofferate nanoparticles-CNT-chitosan modified electrode (CoNP-CNT-CHIT) for glucose detection. Recently, Shen *et al.* [253] reported Pt-Co nanoparticles supported on single-walled carbon nanotubes (SWCNTs-Pt-Co) obtained via chemical process for methanol oxidation. Also, Zhao *et al.* [254] made the composite by chemical reduction of cobalt salt in CNT solution and the electrode, containing other metals as composite shows good electrocatalysis towards methanol oxidation. Other literature reports include: glassy carbon and gold electrodes modified cobalt oxide nanoparticles for electrocatalytic processes using

different organic molecules such as glucose [255], cysteine [256], propylamine [257], hydroquinone [258] and methanol [259] as model compounds [217]. Cobalt oxide/FAD composite modified GC electrode shows excellent catalytic activity for nitrite reduction at reduced over potential [19]. Novel cobalt oxide nanoparticles based sensor for the detection of trace amount of As^{3+} ion in aqueous solution has been developed. The modified electrode shows excellent catalytic activity toward arsenic oxidation at wide pH range [217]. Electrocatalytic reduction of hydrogen peroxide and oxygen at GC electrode modified with haemoglobin (Hb) and cobalt oxide nanoparticles have been reported [77]. Other works reported in literature are summarised in Table 1.3.

Table 1.3: Electrocatalytic oxidation of some analytes on cobalt and cobalt oxide modified electrode.

Modified Electrodes	Fabrication	Analyte	Medium	Ep (V)	LOD	Ref
Co-Ni/C	Drop-dry	O_2	KOH	0.65	-	218
FeCo/CNT/GCE	Drop-dry	H_2O_2	KHthalate	- 0.69	-	225
FAD/CoOx/GCE	Electrodeposition	NO_2^-	PBS	-0.45	0.20 μM	19
GC/CoOx	Electrodeposition	As^{3+} ion	PBS	0.80	11.0 nM	217
Hb-CoOx/GCE	Electrodeposition	H_2O_2	PBS	-0.55	0.50 μM	77
SWCNT-Co-EPPGE	Electrodeposition	NO_2^-	PBS	0.88	5.61 μM	79
Pt-Co/C	Drop-dry	CH_3OH	KOH	-0.35	-	260
$NiCo(OH)_2$/ITO	Electrodeposition	Urea	KOH	0.50	-	165
GC/CoOx	Electrodeposition	H_2O_2	PBS	0.85	0.4 nM	261
CHM-GCE	Electrodeposition	Cysteine	NaOH	0.60	85.2 μM	262
CoNP–CNT–CHIT	Drop-dry	H_2O_2	PBS	- 0.20	-	263
CoNP–CNT–CHIT-GOx	Drop-dry	Glucose	PBS	- 0.20	5.0 μM	263
GOD–NanoCoPc/PGE	Drop-dry	Glucose	PBS	0.55	5.0 μM	264
NanoCoPc/PGE	Drop-dry	H_2O_2	PBS	0.58	-	264
CoNP/MWCNT/GCE	Drop-dry	Thioridazine	PBS	0.55	5.0×10^{-8} M	265
Co_3O_4/C	Chemical Mixing	H_2O_2 / O_2	NaOH	- 0.2	-	266
CoHCF nanotubes	Electrodeposition	Ascorbicacid/ Dopamine	PBS	0.04/ 0.22	1.2 μM	267
PtCo/Ebonex	Electrodeposition	O_2	KOH	> 1.50	-	268
LOD–NanoCoPc/GCE	Drop-dry	AscorbicAcid (lactate)	PBS	0.50	-	269

CHM-GC: cobalt hydroxide nanoparticles modified glassy carbon electrode; **GOD–NanoCoPc/PGE:** glucose oxidase nano cobalt phthalocyanine modified pyrolytic graphite electrode; **SSF:** stainless steel foils; **LOD–NanoCoPc/GCE:** lactase oxidase nano cobalt phthalocyanine composite modified glassy carbon electrode.

1.5.5 Supercapacitive behaviour of carbon nanotubes metal oxides

The CNT/MO nanocompoiste investigated in this work are characterised by charging or capacitive current in the electrolytes. Therefore, it becomes imperative to establishing the charge storage properties of these materials as a potential source for energy generation. The study is important especially in response to the increasing demands for clean energy technologies, where supercapacitors are considered to be the most promising energy storage and power output technologies [270] for portable electronics, electric vehicles, and renewable energy systems. Supercapacitors fill the gap between batteries and conventional dielectric capacitors and have considerable potential for use in high power applications [271]. The amount of energy stored is usually small and can be delivered instantaneously, making supercapacitor devices able to provide pulsed high power rather than high amount of energy [272]. Supercapacitors or electrochemical capacitors are basically classified into two types depending on the nature of the charge-storage mechanism [273]: double-layer and pseudocapacitors. Double-layer capacitors stores charges through nonfaradaic processes while the pseudocapacitors are through faradaic process. In the former, charge separation (ions, or ions and electrons) arises at interfaces between solids and ionic solutions, especially at colloids, metal electrodes, and semiconductors, giving rise to the so-called double-layer [101] (Figure 1.18). The charge difference (Δq) gives rise to a corresponding potential build up ΔV across the interface, thus resulting in a capacitance $C = \Delta q/\Delta V$ or $d(\Delta q)/d(\Delta V)$ which is referred to as the 'double-layer' capacitance [101].

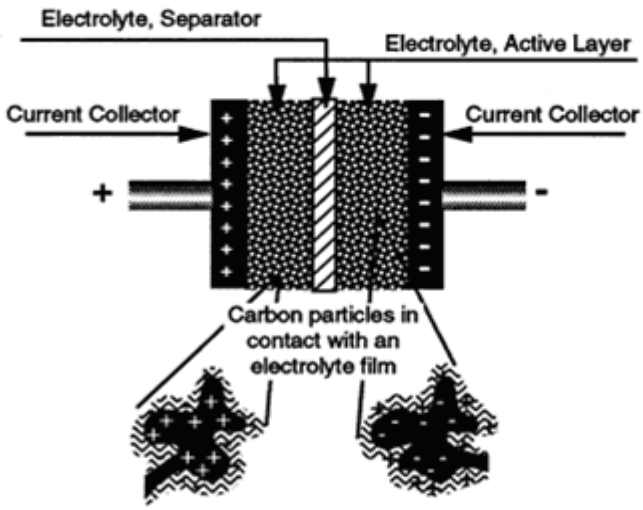

Figure 1.18: Principle of single-cell double-layer capacitor showing charge separation and storage at current collectors.

Electrochemical redox supercapacitors consist of electroactive materials with several oxidation states and their high capacitance and energy characteristics have been investigated [274]. Several materials such as the redox active metals, transition metal oxides [275-277] and conducting polymers [278] with various oxidation states have been used for this supercapacitor type. RuO_2 is well known as a good metal oxide in supercapacitors because of its high specific capacitance values (740 F g^{-1}) [279], from a three electrode system. However, its application is limited because of its disadvantages such as the high cost and toxic nature. In the quest for an alternative sources, researchers have explored the charge storage properties of different materials such as anhydrous cobalt–nickel oxides [280], MnO_2 or MnOx [273,281], NiO [282], Co_3O_4 [283], and Fe_3O_4 [284] as inexpensive alternatives to RuO_2. Thus, the need for other transition metal and metal oxides and their composites which are user- and environmentally friendly, providing a sufficiently high power and energy, and can be made available at a relatively cheap price for commercial application cannot be overemphasised.

NiOx is preferred material for supercapacitor applications [286-287]. Researchers have been actively engaged in the synthesis of NiOx film of high surface area, uniform and ordered meso- or nano-porous network by using available physical and chemical methods to obtain superior capacitive performance [286, 287]. The surface area and morphology which can enhance ion transfer in the pore system and the active material–electrolyte interfacial area, is considered as the boosting factor. Furthermore, nickel oxide is easily available and possesses a high specific capacitance that is comparable with carbon materials [288]. For example, the performances of the electrochemical double layer capacitor from nickel acetate/polyacrylonitrile-based Ni/C nanocomposite fibers with different mass ratios have been evaluated. The results show that the introduction of a proper proportion of nickel into carbon could enhance both specific capacitance and electrochemical stability of the nickel/carbon composite electrodes [289]. In another study, composite electrodes for electrochemical supercapacitors were fabricated by impregnation of slurries of the manganese dioxide nanofibers and multiwalled carbon nanotubes (MWCNTs) into porous nickel foam current collectors. It was demonstrated that MWCNT improved electrochemical performance of the electrodes by forming a secondary conductivity network within the nickel foam cells [290]. Porous nickel oxide/multiwalled carbon nanotubes (NiO/MWNTs) composite material was synthesized and its electrochemical behaviour was studied. The composite shows an excellent cycle performance at a high current and keeps capacitance retention of about 89% over 200 charge/discharge cycles [291]. Recently, nickel oxide ordered mesoporous carbons (NiO-OMC) have drawn great interest due to the application as electrochemical double-layer capacitor. Results showed that NiO nanoparticles embedded inside the mesoporous carbon particles enhances its capacitive behaviour

[292]. Lee et al. [293] reported the synthesis of novel mesostructured of NiO/C composite with NiO nanoparticles studded in the wall of mesoporous carbon. Such novel structure was important for the mass-transfer process in the electrode reaction, consequently, resulting in a large specific capacitance

Other works using the electrochemical properties of Ni and NiO nanocomposite materials as energy storage devices in supercapacitors have been reported [294-297]. Most of the studies reported above were carried out in basic medium probably due to the interaction of the OH^- ions (nucleophile) with the Ni^{2+} ion. Thus, this work focused on establishing the supercapacitive behaviour of the synthesised NiO nanoparticles in acidic and neutral media which could be better or alternative electrolyte to the presently explored alkaline medium.

Fe_3O_4 is another recently discovered inexpensive electrode material, exhibiting pseudocapacitance with alkali sulfites and sulfates electrolytes, but is very sensitive to the electrolyte anion species and the dispersion of the oxide crystallites [298]. These behaviours suggest a different capacitance mechanism from that of either RuO_2 or MnO_2. Wang et al. [299] have investigated the capacitance mechanisms of Fe_3O_4 capacitor in Na_2SO_3, Na_2SO_4, and KOH aqueous solutions by various analysis methods. Kuo's group [300] have studied and reported the supercapacitive behaviour of MFe_2O_4 (M = Mn, Fe, Co, or Ni) and similar crystal structures to Fe_3O_4.The capacitance with $MnFe_2O_4$ as pseudocapacitive electrode materials decreased by ~18% during the first 1000 cycles and then remained unchanged throughout 3000 cycles. They attributed the good cycling stability to the very small volume variation. Chen et al. [296] reported the electrochemical properties of nanosized $Ni_3(Fe(CN)_6)_2(H_2O)$ prepared by simple co-precipitation method, using cyclic voltammetry (CV), constant charge/discharge tests and electrochemical impedance spectroscopy (EIS). Chen et al. [301]

studied the supercapacitive behaviour of Fe_3O_4 film deposited on stainless steel in 1 M Na_2SO_3 solution at different scan rate using cyclic voltammetry experiment. The Fe_3O_4 film demonstrated pseudocapacitive properties. Other reports on the supercapacitive properties of Fe and FexOy nanoparticles materials in different electrolytes have been reported [302,297]. Just like NiO NPs, the integration of Fe_xO_y nanoparticles with CNT and its supercapacitive behaviour (especially in acidic medium) on carbon electrode such as BPPGE have not been given much attention. Therefore, this work provides information on the findings in both acidic and neutral medium using the electrode or cell system described and reported in Chapter 2 and 10.

Chen et al. [297] reported the application of nano-sized insoluble iron, cobalt and nickel hexacyanoferrates (Mhcf) for supercapacive purpose. Cyclic voltammogram and constant charge-discharge in 1 M KNO_3 showed different electrochemical capacitive performance due to the different types of the second metal. In another study, a high specific capacitance (508 Fg^{-1}) was obtained for cobalt sulphide nanowire (CoS) in 3 M KOH which is very competitive with the best supercapacitor material, RuO_2 (720 – 760 Fg^{-1}) but its cost is remarkably lower than RuO_2 [303]. Wang et al. [299] prepared a thin-film electrode with a Co/Al nanocomposite that gave specific capacitance of 2500 F cm^{-3} (833 Fg^{-1}) in 6 M KOH electrolyte and a good high-rate capability to show the best performance when used as an electrode in thin-film supercapacitors (TFSCs). Yu et al. [304] synthessied cuspate deltoid cobaltous oxide (CoO) crystallites and investigated its supercapacitive property in 2 M KOH. The cyclic voltammetry results indicate that the CoO shows acceptable capacitive behavior with specific capacitance of about 88 Fg^{-1}. Zheng et al. [305] reported that the galvanostatic electrochemical results of CoO-doped mesoporous NiO nanoplatelets in 5 M KOH indicated much-improved specific capacity and better

reversible stability than that of the pure NiO porous nanoplatelets and CoO-doped NiO microparticles.

1.5.6 Electrode modification techniques

Various techniques can be used to modify electrodes. These techniques include:

1.5.6.1 Electrodeposition

It is a plating process that uses electrical current to reduce cations of a desired material from a solution and coat a conductive object with a thin layer of the material, such as a metal [201-205]. Both the anode and the cathode components are immersed in a solution called an electrolyte containing one or more dissolved metal salts as well as other ions that permit the flow of electricity. A rectifier supplies a direct current to the anode, oxidizing the metal atoms that comprise it and allowing them to dissolve in the solution.

$$\text{e.g.} \quad NiSO_{4(aq)} \longrightarrow Ni^{2+} + SO_4^{2-} \quad \text{(Anode)} \qquad (1.24)$$

At the cathode, the dissolved metal ions in the electrolyte solution are reduced at the interface between the solution and the cathode, such that they "plate out" onto the cathode.

$$Ni^{2+} + 2e^- \longrightarrow Ni_{(s)} \quad \text{(Cathode)} \qquad (1.25)$$

The rate at which the anode is dissolved is equal to the rate at which the cathode is plated, vis-a-vis the current flowing through the circuit. The metal oxide can also be deposited by repetitive cycling (Figure 1.19) the metal in phosphate buffer solution. Unlike electropolymerisation, a polymer is not formed and the first cycle is almost similar to the subsequent scans.

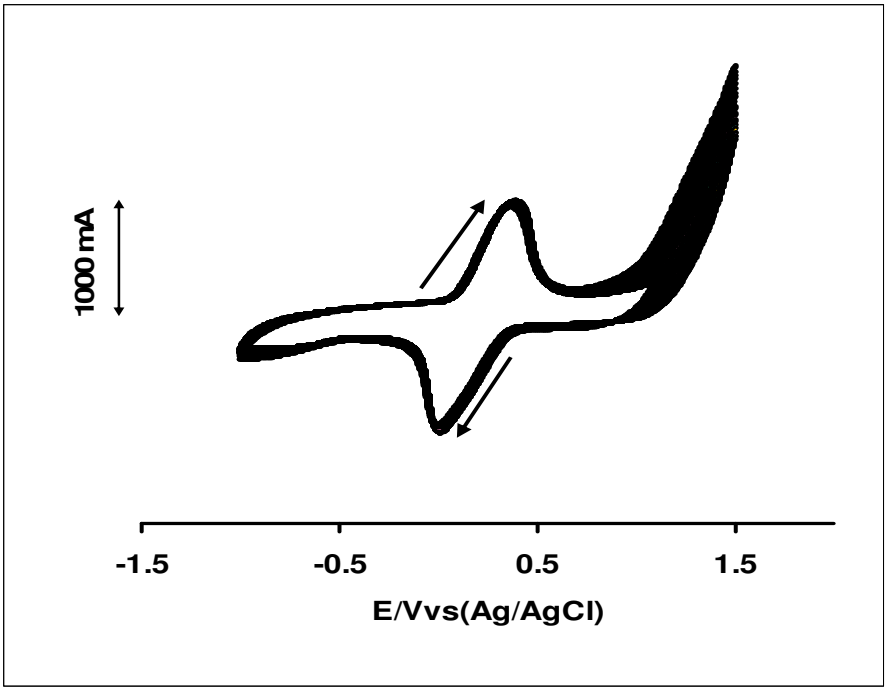

Figure 1.19: Repetitive cyclic voltammograms of an electrode modified with metal oxides film.

This method along side with the drop-dried electrode modification procedures are the major techniques used in this study because of their simplicity, and the advantage of setting a constant deposition potentials which guide against variation in the amount of nanomaterials deposited on the electrode from one experiment to another. The surface concentration of the deposited nanomateria, were obtained using Equations (1.20) or Equation (1.21) above. A well formed M/CNT and MO/CNT have a surface coverage concentration of about approximately 10^{-9} to 10^{-8} mol cm^{-2}.

1.5.6.2 Electropolymerisation

Electropolymerisation is the most efficient method of depositing polymer films on electrodes. Electropolymerisation process involves the repetitive voltammetric scanning of the solution of the modifier monomers at the electrode surface within a specific potential window [203,211]. This can be oxidative or

reductive voltammetric scanning in which the monomer forms radicals which combine to form polymers on electrodes. It is a reproducible process and also it is possible to control the film thickness by varying the conditions for polymerisation process such as time, scan rate, potential range and the type of electrolytes. Various conducting surfaces such as metals, metal oxides and carbon based electrodes can be used as the depositing surface. Many works have been done using electropolymerization for the deposition of thick layer of metal oxides and hydroxides [203,211].

1.5.6.3 Dip-dry

It involves the immersion of an electrode in solution of a catalyst or a modifier for a period of time to allow for surface adsorption of the material. The electrode is later withdrawn and the solvent is allowed to dry [167,208,212].

1.5.6.4 Drop-dry

The electrode is modified by placing few drops of the catalyst or modifier on its surface and allowing the solvent to dry off [114,200,214].

1.5.6.5 Spin-coating

It involves evaporation of solution of a modifier from electrode surface by high speed rotations using centrifugal force. Example is the modification of indium tin oxide substrate with xerogel oxide film by spin-coating a viscous gel [306].

1.5.6.6 Composite technique:

It is a process of impregnating the buck electrode material with a chemical modifier [307].

1.5.6.7 Sol-gel method

The sol-gel process is a wet-chemical technique (a.k.a. chemical solution deposition) widely used recently in the fields of materials science and ceramic engineering. Typical precursors are metal alkoxides and metal chlorides, which undergo various forms of hydrolysis and polycondensation reactions to give metal oxides. Sol-gel derived materials have diverse applications in optics, electronics, energy, space, (bio)sensors, medicine (e.g., controlled drug release), reactive material and separation (e.g., chromatography) technology [308].

1.5.6.8 Self-assmbled-monolayers

It is the formation of highly ordered molecular assemblies formed by the adsorption of molecules from solution directly onto the surface of an appropriate substrate (Figure 1.20). SAM technique has a number of advantages which include simplicity, reproducibility and formation of highly ordered and stable monolayers which are chemically bound onto electrodes [177,231].

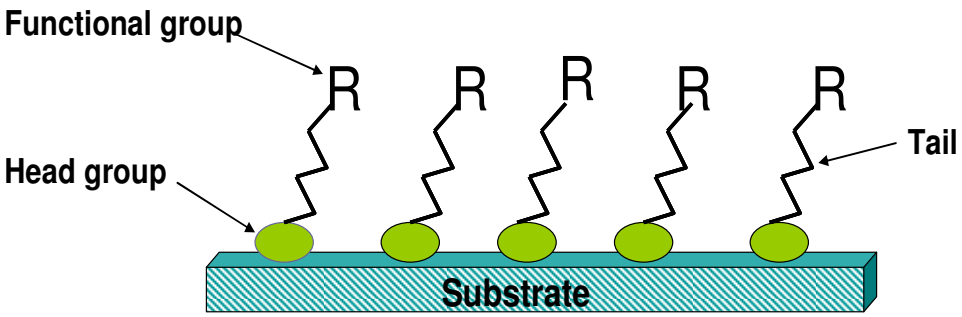

Figure 1.20: Typical SAM modified electrode showing formation of monolayer.

1.5.6.9 Langmuir- Blodgett technique

Langmuir-Blodgett (LB) technique is a method of depositing crystalline films one molecular layer at a time, by dipping the

substrate into water containing a polymer that forms a single layer of molecular chains on the surface. This layer is then transferred from the water to the substrate. The dipping can be repeated to create an ordered multilayer film that does not require poling to orient the molecules. The main advantages of this method are large-scale defect-free areas, very short preparation time, and very neat products [309].

1.5.6.10 Chemical vapour deposition

Chemical vapor deposition (CVD) is a chemical process used to produce high-purity, high-performance solid materials. The process is often used in the semiconductor industry to produce thin films. In a typical CVD process, the water (substrate) is exposed to one or more volatile precursors, which react and/or decompose on the substrate surface to produce the desired deposit. Frequently, volatile by-products are also produced, which are removed by gas flow through the reaction chamber [310].

1.6 Nanoscience in Electrochemistry

In electrochemistry, the use of bare electrodes for electrochemical detection of species has a number of limitations, such as low sensitivity and reproducibility, the slow electron transfer reaction, low stability over a wide range of solution composition and high over-potential at which the electron transfer process occurs. In the face of some of these challenges, the quest for a plausible way of fabricating an efficient sensor of significant advantages and applications in food, industries and environment has lead to the advent of nanoscience and nanotechnology applications. Thus, the chemical modification of inert substrate electrodes with redox active thin film offers significant advantages in the design and development of chemical sensor and biosensors.

The development of nanoscience and nanotechnology has been increasing very fast along the last years and nanostructured materials have raised a remarkable attention due to their unique properties provoked by quantum size effects [311] or due to the great superficial area achieved by nanostructures, largely employed in solar cells [312], electrochromic devices [313], catalysis [314] sensors and biosensors [315,316]. Nanoscience involves the study of materials on the nanoscale level between approximately 1 and 100 nm [317] and involves study of how to control the formation of two- and three-dimensional assemblies of molecular scale building blocks into well-defined nanostructures or nanomaterials [318]. In general, these nanoparticles (NPs) can be categorised into carbon-based materials such as fullerenes and carbon nanotubes and inorganic nanoparticles including the ones based on metal oxides (zinc oxide, iron oxide, titanium dioxide and cerium oxide etc), metals (gold, silver and iron) and quantum dots (cadmium sulfide and cadmium selenide) [319]. Other metals of wide application in the area of electrochemistry and nanoscience include nickel, cobalt, zinc, copper, aluminium, platinum, titanium etc. NPs differ from

larger materials in that the number of atoms at the surface and their physical properties are different from those of bulk materials [320]. Properties associated with the bulk materials are averaged properties, such as density, resistivity and magnetisation and the dielectric constant. Critically, however, many properties of these materials change over at the NP scale [321]. These differences arise from the small size and large number of surface atoms of the particles and related effects.

1.7 Langmuir Isotherm Adsorption Theory

Many electrochemical phenomena and processes are to a great extent influenced by different adsorption processes. Of prime importance is the adsorption on the electrode surface of components of the electrolyte solution, as well of those participating in the electrode reaction, or those "inert" components that do not participate. Depending on the nature of the system, the adsorption process can be either reversible or irreversible. In the first case adsorption equilibrium exists between the particles adsorbed on the adsorbent's surface and the particles in the electrolyte (or in any other phase contacting with the adsorbent). After removing the substance from the electrolyte, adsorbed particles leave the surface and enter into the electrolyte. In the case of an irreversible adsorption, the adsorbed particles remain at the surface even if their concentration in the bulk phase drops to zero. In this case the adsorbed particles can be removed from the surface only by means of a chemical reaction (e.g., their oxidation by oxygen) or by a displacement process during the adsorption of other substances. Processes of physical adsorption are often reversible, wheras processes of chemisorption are mostly irreversible. A convenient parameter for quantitative estimates of adsorption which is of the monolayer type is the degree of surface coverage (θ) defined by the relation [322]:

$$\theta = \frac{A_j}{A_j^o} \quad (1 \geq \theta \geq 0) \qquad (1.26)$$

A_j is the amount of species of the adsorbed substance j (adsorbate) per unit area of the true surface area of the electrode, A_j^o is limiting adsorption value when the surface is covered completely by particles of a given substance (i.e., at full monolayer coverage). By

convention, adsorption is regarded as insignificant when $\theta<0.1$, and as significant when $\theta>0.5$.

The adsorption of a component *j* in a given system depends on temperature *T* and on the component's concentration, $C_{V,j}$, in the bulk phase. The overall adsorption equation can be written as $A_j = f(T, C_{V,j})$ where *f* is the activity coefficient. The relation between adsorption and the adsorbate's bulk concentration (or pressure, in the case of gases) at constant temperature is called the *adsorption isotherm*; the relation between adsorption and temperature at constant concentration is called the *adsorption isobar*. From the shape of the adsorption isotherms, the adsorption behaviour can be interpreted. In the case of monolayer adsorption, the isotherms are usually written in the form $\theta_j = f(C_{V,j})$.

At higher values of θ, when the number of free sites on the surface diminishes, one often observes relations of the form:

$$\theta = BC_V\ (1+ BC_V) \quad \text{or } \theta\,(1-\theta) = BC_V \qquad (1.27)$$

Where *B* is the adsorption coefficient (units: dm^3mol^{-1}). At low values of the bulk concentration ($BC_V<<1$), the degree of surface coverage is proportional to this concentration, but at high values it tends toward a limit of unity. The rate of adsorption is proportional to the bulk concentration and to the fraction $1-\theta$ of vacant sites on the surface: $\nu_a = k_a(1-\theta)$, while the rate of desorption is proportional to the fraction of sites occupied: $\nu_d = k_d\theta$. In the steady state these two rates are equal. With the notation $k_a/k_d = B$, Equation (1.26) was obtained [322]. In 1918, Irving Langmuir derived this equation and based it on four assumptions: (1) The surface of the adsorbent is uniform (homogenous). That is, all the adsorption sites are equivalent and have the same heat of adsorption and hence, the same adsorption coefficient *B*. (2) Adsorbed molecules do not interact. (3) All adsorption occurs

through the same mechanism and adsorption is reversible. (4) At the maximum adsorption, only a monolayer is formed: molecules of adsorbate do not deposit on other, already adsorbed, molecules of adsorbate, only on the free surface of the adsorbent [322]. These four assumptions are seldom all true: there are always imperfections on the surface, adsorbed molecules are not necessarily inert, and the mechanism is clearly not the same for the very first molecules to adsorb to a surface as for the last. The Langmuir isotherm is nonetheless the first choice for most models of adsorption, and has many applications in surface kinetics and thermodynamics.

The Langmuir adsorption equation has also been derived for less ideal situations, involving quasi- and irreversible adsorbing electroactive molecules with different strenghths of adsorption of the reactant and products as [98,323-325]:

$$\theta = \frac{\mathrm{BC}}{(1+\mathrm{BC})} \tag{1.28}$$

Here θ is the ratio of the surface coverage of the analyte Γ of analyte at concentration C to its maximum surface concentration Γ_{max} (i.e, $\theta = \Gamma / \Gamma_{max}$). Therefore,

$$\frac{\mathrm{C}}{\Gamma} = \frac{\mathrm{I}}{\mathrm{B}\Gamma_{max}} + \frac{\mathrm{C}}{\Gamma_{max}} \tag{1.29}$$

Assuming that the stripping peak current is proportional to the surface concentration of the analyte, Equation 1.29 can be re-written as:

$$\frac{C}{I_p} = \frac{I}{BI_{p,max}} + \frac{C}{I_{p,max}} \qquad (1.30)$$

A plot of C/I_p versus C gives a linear relationship. From the slope and the intercept of the line, the adsorption equilibrium constant B is obtained. The standard free energy change due to adsorption of the analyte can be evaluated from the relationship:

$$\Delta G^o = - RT\ln B. \qquad (1.31)$$

This theory and equations are applied in this work for evaluating the extent of adsorption of the analytes investigated, especially DEAET and hydrazine on the modified electrodes.

1.8 Microscopy and Spectroscopy Techniques

1.8.1 Microscopy

Microscopy is the technical field of using microscopes to view samples or objects. There are three well-known branches of microscopy, optical, electron and scanning probe microscopy. Optical and electron microscopy involve the diffraction, reflection, or refraction of electromagnetic radiation/electron beam interacting with the subject of study, and the subsequent collection of this scattered radiation in order to build up an image. This process may be carried out by wide-field irradiation of the sample (e.g transmission electron microscopy) or by scanning of a fine beam over the sample (e.g. scanning electron microscopy). Scanning probe microscopy involves the interaction of a scanning probe with the surface or object of interest [326].

1.8.1.1 Scanning Electron Microscope (SEM)

A scanning electron microscope (SEM) is a powerful microscope that images the sample surface by scanning it with a high-energy beam of electrons in a raster scan pattern. The electrons interact with the atoms that make up the sample producing signals that contain information about the sample's surface topography, composition and other properties such as electrical conductivity [326]. Applications include failure analysis, identification of fracture modes and origins, physical and chemical characterization of surfaces, microstructural analysis, corrosion damage and pitting, nanoscience, particle analysis and foreign materials. Figure 1.21 represents the SEM image of a modified electrode.

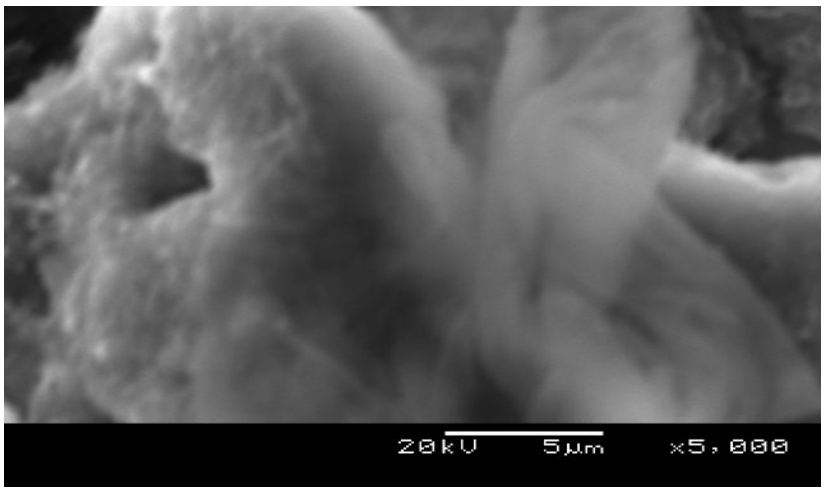

Figure 1.21: A Typical SEM Image showing formation of metal oxide nanoparticles film on modified electrode.

1.8.1.2 Transmission electron microscope (TEM)

Transmission electron microscopy (TEM) is a microscopy technique whereby a beam of electrons is transmitted through an ultra thin specimen, interacting with the specimen as it passes through. An image is formed (e.g., Figure 1.22) from the interaction of the electrons transmitted through the specimen; the image is magnified and focused onto an imaging device, such as a fluorescent screen, on a layer of photographic film, or to be detected by a sensor such as a CCD camera. TEM forms a major analysis method in a range of scientific fields, in both physical and biological sciences. TEMs find application in cancer research, virology, materials science as well as pollution and semiconductor research [327].

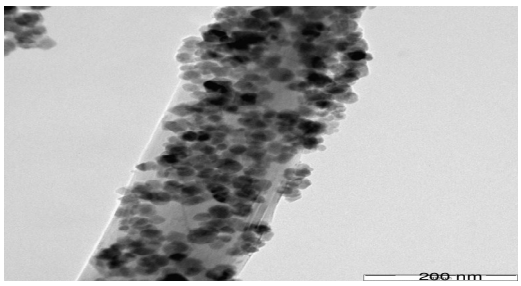

Figure 1.22: A Typical TEM Image of CNT decorated with metal nanoparticles.

1.8.1.3 Atomic force microscope

The atomic force microscope (AFM) or scanning force microscope (SFM) is a very high-resolution type of scanning probe microscope, with demonstrated resolution of fractions of a nanometer, more than 1000 times better than the optical diffraction limit. AFM is one of the foremost tools for imaging, measuring and manipulating matter at the nanoscale. The information is gathered by "feeling" the surface with a mechanical probe. Piezoelectric elements that facilitate tiny but accurate and precise movements on (electronic) command enable the very precise scanning.

The AFM consists of a microscale cantilever with a sharp tip (probe) at its end that is used to scan the specimen surface (Figure 1.23). The cantilever is typically silicon or silicon nitride with a tip radius of curvature on the order of nanometers. When the tip is brought into proximity of a sample surface, forces between the tip and the sample lead to a deflection of the cantilever according to Hooke's law. Typically, the deflection is measured using a laser spot reflected from the top surface of the cantilever into an array of photodiodes. A feedback mechanism is employed to adjust the tip-to-sample distance to maintain a constant force between the tip and the sample. The AFM can be operated in a number of modes, depending on the application. In general, possible imaging modes are divided into static (also called Contact) modes and a variety of dynamic (or non-contact) modes where the cantilever is vibrated [328].

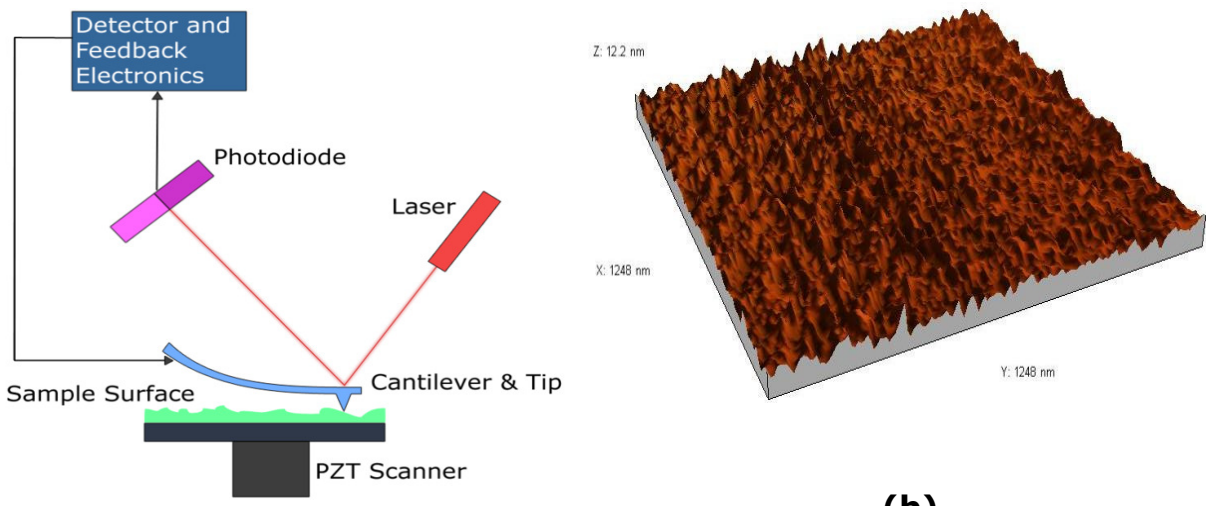

(a) **(b)**

Figure 1.23: (a) Atomic force microscope block diagram. (b) AFM three dimentional (3D) image of a nanomaterial growth on a modified electrode [328].

1.8.2 Spectroscopy

Spectroscopy is the study of the interaction between radiation and matter as a function of wavelength, frequency or energy which is usually in the form of photon of light and represented as $E = hv$ where h is the Planck constant. A plot of the response as a function of wavelength—or more commonly frequency—is referred to as a spectrum.

1.8.2.1 Energy dispersive X-ray spectroscopy (EDS)

Energy dispersive X-ray spectroscopy (EDS) is an analytical technique used for the elemental analysis or chemical characterization of a sample (Figure 1.24). As a type of spectroscopy, it relies on the investigation of a sample through interactions between electromagnetic radiation and matter, analyzing X-rays emitted by the matter in response to being hit with charged particles. The characteristic X-rays of an element's atomic structure to be identified is unique and can be separated from other [329,330].

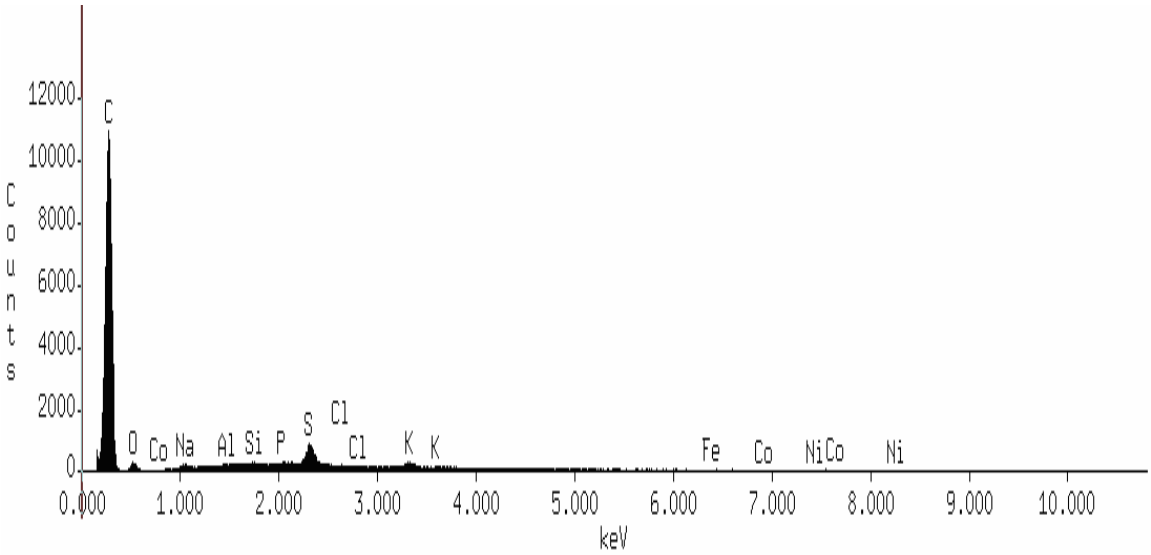

Figure 1.24: EDX profile of a material showing the possible elemental composition.

1.8.2.2 X-ray photoelectron spectroscopy

X-ray photoelectron spectroscopy (XPS) is a quantitative spectroscopic technique that measures the elemental composition, empirical formula, chemical state and electronic state of the elements that exist within a material (Figure 1.25). XPS spectra are obtained by irradiating a material with a beam of aluminium or magnesium X-rays while simultaneously measuring the kinetic energy (KE) and number of electrons that escape from the top 1 to 10 nm of the material being analyzed. XPS is routinely used to analyze inorganic compounds, metal alloys, semiconductors, polymers, elements, catalysts, glasses, ceramics, paints, papers, inks, woods, plant parts, make-up, teeth, bones, medical implants, bio-materials, viscous oils, glues, ion modified materials and many others [331].

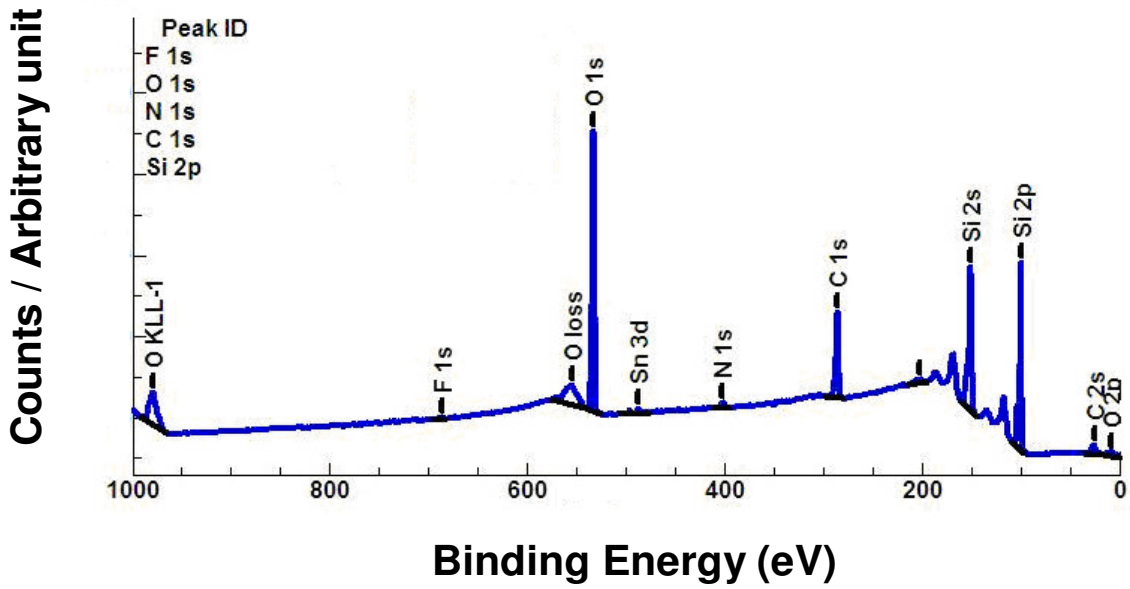

Figure 1.25: Wide scan XPS spectrum showing the present elements.

1.8.2.3 X-ray diffraction spectroscopy

X-ray diffraction finds the geometry or shape of a molecule using X-rays. X-ray diffraction techniques are based on the elastic scattering of X-rays from structures that have long range order. Single-crystal X-ray diffraction is a technique used to solve the complete structure of crystalline materials, ranging from simple inorganic solids to complex macromolecules, such as proteins. Powder diffraction (XRD) is a technique used to characterize the crystallographic structure, crystallite size (grain size), and preferred orientation in polycrystalline or powdered solid samples. Powder diffraction is commonly used to identify unknown substances, by comparing diffraction data against a database maintained by the International Centre for Diffraction Data [332]. Figure 1.26 showed the X-ray diffraction pattern formed when X-rays are focused on a crystalline material and a typical XRD spectrum obtained.

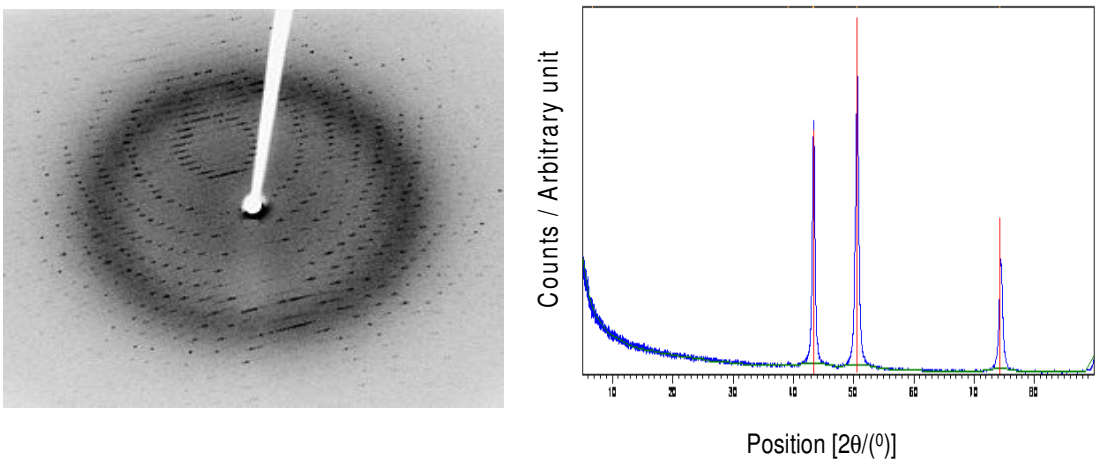

Figure 1.26: (a) X-ray diffraction pattern formed when X-rays are focused on a crystalline material (b) XRD spectrum of synthesised metal nanoparticles showing identified peaks of the metal at different 2θ position [332].

1.8.2.4 Infrared spectroscopy

Infrared (IR) spectroscopy is a well known analytical technique which deals with the infrared region of the electromagnetic spectrum. It can be used to identify compounds or investigate sample composition. Figure 1.27 presents an IR apparatus showing the different components. Infrared spectroscopy exploits the fact that molecules have specific frequencies at which they rotate or vibrate corresponding to discrete energy levels (vibrational modes). These resonant frequencies are determined by the shape of the molecular potential energy surfaces, the masses of the atoms and, by the associated vibronic coupling. Infrared spectroscopy is widely used in both research and industry as a simple and reliable technique for measurement, quality control and dynamic measurement. It is of especial use in forensic analysis in both criminal and civil cases, enabling identification of polymer degradation for example. It is perhaps the most widely used method of applied spectroscopy [346].

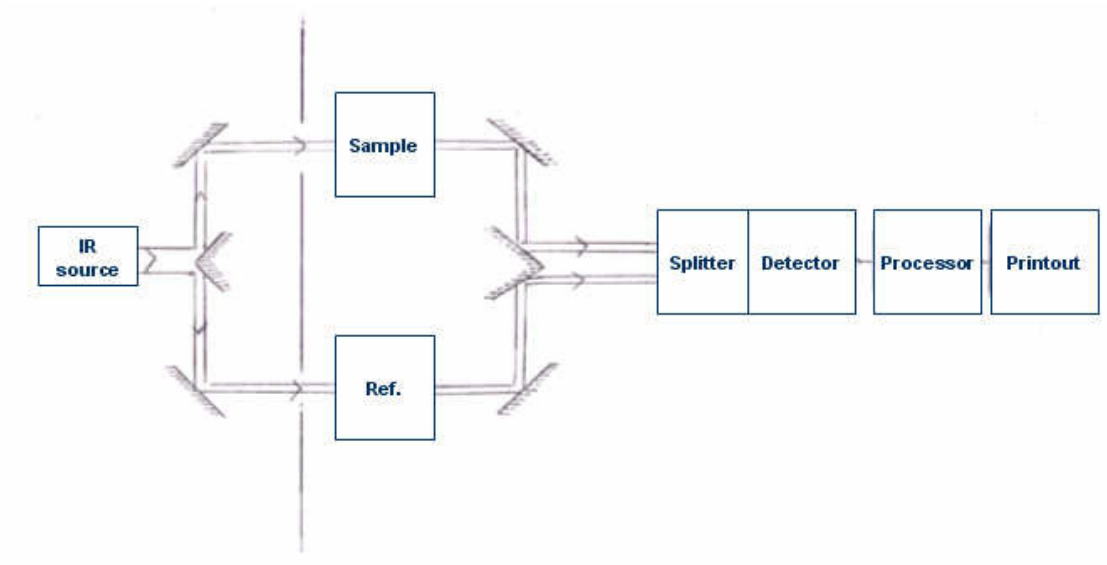

Figure 1.27: IR spectroscopy apparatus [333].

1.8.2.5 Ultraviolet-visible spectroscopy

Ultraviolet-visible spectroscopy (UV-Vis) involves the spectroscopy of photons in the UV-visible region. The absorption in the visible ranges directly affects the color of the chemicals involved. In this region of the electromagnetic spectrum, molecules undergo electronic transitions. Absorption of photons of light measures transitions from the ground state to the excited state. UV/Vis spectroscopy is routinely used in the quantitative determination of solutions of transition metal ions and highly conjugated organic compounds [333, 334].

1.9 Overview of Analytical Probes Used in this Work

1.9.1 Hydrazine

Electro-oxidation of hydrazine (N_2H_4) on carbon surfaces has continued to receive significant research interests [36 - 45] due to the extensive applications of hydrazine and its derivatives in a plethora of areas relating to chemical industry, military, agriculture and pharmaceuticals. Hydrazine is regarded an important anodic material for fuel cell and used for zero-emission fuel cells, it is also used as a fuel in high energy-energy propellant in rockets and spacecrafts by the military and aerospace industries [41,335]. On the negative side, hydrazine and its methyl derivatives have been implicated as potential carcinogens, mutagens and hepatotoxic substances that could cause liver and kidney damages [336]. Also, in 2003, hydrazine was implicated in terrorist incident [337]. It could be said therefore that it is this dual purpose of hydrazine as useful materials in several applications such as fuel cell development and as hazardous substances that underpins the need to investigate its electro-oxidative behaviour at low cost and easily available carbon electrodes.

Despite huge literature on the electro-oxidation of hydrazine on carbon based electrodes [36-45], the use of carbon nanotubes decorated with metal nanoparticle is limited. Hitherto, all attention on CNT-supported metal nanoparticles, as evident in the recent review by Wildgoose *et al*. [338], has been directly only on metals such as Pt, Pd, Ru, Ag and Au. It has also been constantly reported that HiPCo, MWCNTs and SWCNTs are inherently contaminated with iron nanoparticles thus explaining why "electrocatalysis" observed on such CNT-based carbon electrodes [339-342] for certain analytes, including hydrazine [340] are/could be strongly influenced by the iron nanoparticle impurities. More recently, however, Kruusma *et al.* [340] demonstrated that HiPCo SWCNTs contain

residual iron oxide impurities which dominated their electrochemical activity towards the detection of hydrogen peroxide and hydrazine. Given the ability of iron impurities in CNTs to influence electro-oxidation of hydrazine [340], it could be interesting to explore the electrochemical response of metal-decorated SWCNTs ('deliberate metal impurification') towards the electro-oxidation of hydrazine and this form part of the investigation carried out in this study. To the best of my knowledge, no consideration has been given to this type of investigation, especially with nickel and iron nanoparticles which have been established to be the major impurities of SWCNTs.

1.9.2 Diethylaminoethanethiol

Chemical warfare agents are toxic chemical substances used by terrorists with the intention to kill, injure or incapacitate their perceived enemies. Under the provisions of the Chemical Weapons Convection [343], such agents are regarded as the "poor man's atomic bomb because of the low cost and the low technology required to develop them [343]. It is known that about 70 different chemicals have been used or stockpiled as chemical weapon agents during the 20th and 21st century. Notable of these agents are the so-called V-type (i.e., VE, VG, VM and VX) nerve agents [343,344]. The V-type nerve agents are considered more dangerous because they are more persistent, do not easily evaporate into a gas, and therefore present primarily a contact hazard to man. One of the main thiol hydrolysis products (Equation 1.32) of the V-type nerve agents is the 2-diethylaminoethanethiol (DEAET) [344].

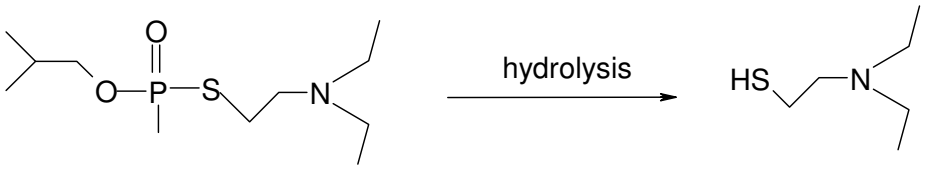

(1.32)

R-VX

Diethylaminoethanethiol(DEAET)

2-diethylaminoethanethiol (DEAET) is a thiol compound, a well known degradation product of the V-type nerve agent [343-345]. Since, DEAET is more stable in the aqueous environment than its parent Russian analogue of the V-type nerve agent, called R-VX (i.e.,*O*-isobutyl-*S*-(2-diethylaminoethyl)methylphosphonothioate), it serves as one of the excellent models for electrochemical detection and interrogation of the behaviour of the R-VX nerve agent or thiol compounds at electrode surface. Although several methods including chromatography, mass spectrometry and electrochemistry are common for the detection of thiols, the use of such analytical methods for the detection of the hydrolysis products of V-type nerve agents is still hugely unexplored. Few reports involving electrophoresis [346,347] and electrochemical techniques [28,106,107,348] have emerged for the detection of DEAET. Some of the reported techniques are fraught with some notable drawbacks such as the employment of unstable enzyme materials, time-consuming electrode preparation involving chemical pre-treatments and derivatizations. Also, electrochemical oxidation of thiols at conventional electrodes occurs at very high potential, thus the need for chemically modified electrodes cannot be overemphasised. Therefore, this study explored the detection of DEAET on CNT-metal nanocomposite platform. The study also represent the first time the catalytic behaviour of this nanocomposite on EPPG electrode will be investigated. To the best of my knowledge, there has been no report on the use of electrodes modified with nickel nanoparticle-decorated carbon nanotubes for the detection of degradation products of V-type nerve agents. Indeed, compared to transition metals, nickel is not a popular redox-mediator in electroanalysis. But it was observed previously that surface-confined nickel micropowder (ca. 17 – 60 mm range) immobilized on basal plane pyrolytic graphite electrode showed good electrocatalytic response towards DEAET

1.9.3 Nitrite

Nitrite ion is important as it is commonly used as an additive in some foods [349]. Other uses include color fixative and preservation in meats, manufacturing diazo dyes, in the textile industry, photography, manufacture of rubber chemicals, fertilizers in agriculture [350] and medicinal agents (used as a vasodilator [351], bronchodilator [352], intestinal relaxant [353]. It can be formed as a result of the degradation of some fertilizers and corrosion inhibitor [354]. Nitrite is one of the major components of waste water from nuclear power production [355] and is involved in the bacterial process known as the nitrogen cycle [356]. It also plays important physiological roles in the form of NO, for example, as an intra- and messenger, a neurotransmitter, and an immune system mediator [349]. Nitrite promotes corrosion when dissolved in water and is also classified as an environmentally hazardous species because of its toxicity [357]. The ions can interact with amines to form carcinogenic nitrosamines [358].

Due to the importance of nitrite in the environmental sciences and in food chemistry, a large number of analytical methods have been used to determine nitrite ions, including spectrophotometry [359-362], chromatography [363] and electrochemical methods [364-366] in recent years but with some shortcomings such as interference by other ions and complicated sample pre-treatment process, unsuitability for on-site monitoring and inability for detoxification. Electrochemical methods offer useful alternative since they allow a faster and precise analysis [59,367,368]. In order to tackle this problems, devices which are simple, inexpensive, stable and having the potential for the detoxification of these molecules are highly in demand. Electrochemical devices fall into this category, therefore electrocatalytic oxidation of nitrite on CNT/M or CNT/MO EPPGE modified electrode is reported in this study for the first time.

1.9.4 Dopamine

Dopamine (DA) is a biological molecule formed as a result of the decarboxylation of 3, 4- dihydroxy phenylalanine. It acts as a neurotransmitter in both the central and peripheral nervous system. Dopamine level can be as high as 50 nmol/g in the mammalian central nervous system in a region of the brain known as the "caudate nucleus" [182]. Low concentration of this compound in the extra cellular fluid of the caudate nucleus or its complete depletion has been associated with a disease called Parkinson's disease in which the patient suffers ability to having control over his movement [183]. Other diseases resulting from the abnormal metabolism of dopamine include epilepsy, senile dementia and HIV infection [185, 369,370]. Thus, it becomes imperative that the fabrication of a sensor that will determine the presence of this molecule in human fluid should be the focus of neuro-scientist. More importantly, because of the interfering effect of this molecule with other biological molecules such as ascorbic acid (AA) and uric acid (UA), fabrication of a very sensitive and selective analytical sensor has been a major challenge in its detection.

Several analytical techniques have been used in the past for DA detection but each with one disadvantage or the other. Electrochemical methods have also been employed with the use of different electrodes as sensors such as nanostructure material in polymer matrix (e.g. gold nanoparticles on polymer matrix) [371,372], GC/ Nafion/ NanoPt [372], carbon nanotube [183,373], ordered mesoporous carbon [183,374], carbon ionic liquid [183,375] and so on are among several carbon based materials that have been used for the electrochemical determination and separation of DA and AA. Generally, the electrochemical techniques have proven to be the more effective analytical method for determination of biological molecules including DA and AA. However, despite the success of the different electrochemical

technique used so far, there is a need for an effective, efficient, simple and low cost sensor that will selectively determine DA in the presence of AA and UA in biological fluid. Therefore, in this study, an iron oxide carbon nanotubes modified electrode (EPPGE) was fabricated. The electrode conveniently detects DA in the presence of 1000 times AA concentration.

References

1. P.G. Wiles, J. Abrahamson, *Carbon* 6 (1978) 341.

2. S. Iijima, *Nature* 354 (1991) 56.

3. M. Majumder, N. Chopra, R. Andrews, B.J. Hinds, *Nature* 438 (2005) 930.

4. R.H. Baughman, A.A. Zakhidov, W.A. de Heer, *Science* 297 (2002) 787.

5. J.J. Davis, R.J. Coles, H. Allen, O. Hill., *J. Electroanal Chem.* 440 (1997) 279.

6. H. Luo, Z. Shi, N. Li, Z. Gu, Q. Zhuang, *Anal Chem*. 73 (2001) 915.

7. J.M. Nugent, K.S.V. Santhanam, A. Rubio, P.M. Ajayan, *Nano Lett.* 1 (2001) 87.

8. S.J. Tans, A.R.M. Verschueren, C. Dekker, *Nature* 393 (1998) 49.

9. C. Liu, Y.Y. Fan, M. Liu, H.T. Cong, H.M. Cheng, M.S. Dresselhaus, *Science* 286 (1999) 1127.

10. C.Y. Liu, A.J. Bard, F. Wudl, I. Weitz, J.R. Heath, *Electrochem. Solid State Lett.* 2 (1999) 577.

11. J.S. Ye, X. Liu, H.F. Cui, W.D. Zhang, F.S. Sheu, T.M. Lim, *Electrochem. Commun.* 7 (2005) 249.

12. J.J. Gooding, *Electrochim. Acta* 50 (2005) 3049.

13. N.L. Pocard, D.C. Alsmeyer, R.L. McCreery, T.X. Neenan, M.R. Callstrom, *J. Mater. Chem.* 2 (1992) 771.

14. M.Musameh, J.Wang, A.Merkoci, Y. Lin, *Electrochem.Commun.* 4 (2002) 743.

15. Y.-C. Weng, J.F. Rick, T.-C. Chou, *Biosens. Bioelectron.* 20 (2004) 41.

16. A. Salimi, E. Sharifi, A. Noorbakhsh, S. Soltanian, *Biosens. Bioelectron.* 22 (2007) 3146.

17. A.R. Tao, S. Habas, P.D. Yang, *Small* 4 (2008) 310.

18. C.J. Murphy, A.M. Gole, S.E. Hunyadi, J.W. Stone, P.N. Sisco, A. Alkilany, B.E. Kinard, P. Hankins, *Chem. Comm.* 5 (2008) 544.

19. A. Salimi, R. Hallaj, H. Mamkhezri, S. Mohamad, T. Hosaini, J. *Electroanal. Chem.* 619 (2008) 31.

20. X. Zhang, K.-Y. Tsang, K.-Y. Chan, *J. Electroanal. Chem.* 573 (2004) 1.

21. S.M.A. Shibli, K.S. Beenakumari, N.D. Suma, *Biosens. Bioelectron.* 22 (2006) 633.

22. M. Vidotti, M.R. Silva, R.P. Salvador, S.I. C´ordoba de Torresi, L.H. Dall'Antonia*, Electrochim. Acta* 53 (2008) 4030.

23. R.J. Aitken, M.Q. Chaudhry, A.B.A. Boxall, M. Hull, *Occup. Med.* 56 (2006) 300.

24. B. Nowack, T.D. Bucheli, *Environ. Pollut.* 150 (2007) 5.

25. A. Balamurugan, G. Sockalingum, J. Michel, J. Faure, V. Banchet, L. Wortham, S. Bouthors, D. Laurent-Maquin, G. Balossier, *Mater. Lett.* 60 (2006) 3752.

26. N. Laosiripojana, W. Sutthisripok, S. Assabumrungrat, *Chem. Eng. J.* 112 (2005) 13.

27. K.I. Ozoemena, J. Pillay, T. Nyokong, *Electrochem. Commun.* 8 (2006) 1391.

28. J. Pillay, K.I. Ozoemena, *Electrochim. Acta* 52 (2007) 3630.

29. B.S. Sherigara, W. Kutner, F. D'Souza, *Electroanalysis* 15 (2003) 753.

30. A. Salimi, C.E. Banks, R.G. Compton, *Analyst* 129 (2004) 225.

31. V. Selvaraj, M. Alagar, K. Sathish Kumar, *Appl. Cat. B: Environm.* 75 (2007) 129.

32. L. Zhang, Z. Fang, G.-C. Zhao, X.-W. Wei, *Int. J. Electrochem. Sci.*, 3 (2008) 746.

33. M. Yang, Y. Yang, Y. Liu, G. Shen, R. Yu*, Biosens. Bioelectron*, 21 (2006) 1125.

34. D.G. Rickerby, M. Morrison, *Sci. Technol. Adv. Mater.* 8 (2007) 19.

35. J. Pillay, K.I. Ozoemena, *Electrochem. Commun.* 9 (2007) 1816.

36. C. Lin, A.B. Bocarsly, *J. Electroanal. Chem. Interfacial Electrochem.* 300 (1991) 325.

37. H. Razmi-Nerbin, M.H. Pournaghi-Azar, *J. Solid State Electrochem.* 6 (2002) 126.

38. Y-D. Zhao, W.-D. Zhang, H. Chen, Q-M. Luo, *Talanta* 58 (2002) 529.

39. D. Geraldo, C. Linares, Y-Y. Chen, S. Ureta-Zanartu, J.H. Zagal, *Electrochem. Commun.* 4 (2002) 182.

40. M.H. Pournaghi-Azar, R. Sabzi *J. Electroanal. Chem.* 543 (2003) 115.

41. K. Yamada, K. Asazawa, K. Yasuda, T. Loroi, H. Tanaka, Y. Miyazaki, T. Kobayashi, *J Power Sources* 115 (2003) 236.

42. C. Linares, D. Geraldo, M. Paez, J.H. Zagal, *J. Solid State Electrochem.* (2003) 7: 626-631.

43. K.I. Ozoemena, *Sensors* 6 (2006) 874.

44. M. Revenga-Parra, E. Lorenzo, F. Pariente, *Sens. Actuators* B 107 (2005) 678.

45. G.I. Cardenas-Jiron, V. Paredes-Garcia, D. Venegas-Yazigi, J.H. Zagal, M. Paez, J. Costamagna, *J. Phys. Chem.* A 110 (2006) 11870.

46. X. Ji, C.E. Banks, A.F. Holloway, K. Jurkschat, C.A. Thorogood, G.G. Wildgoose, R.G. Compton, *Electroanalysis* 18 (2006) 2481.

47. X. Wang, N. Yang, Q. Wan, X. Wang, *Sens. Actuators* B 128 (2007) 83.

48. D.-M. Zhou, H.-X. Ju, H.-Y. Chen, *J. Electroanal. Chem.*, 408 (1996) 219.

49. M.H. Pournaghi-Azar, R. Ojani, *Talanta* 42 (1995) 1839.

50. H. Razmi, M. Agazadeh, B. Habibi-A, *J. Electroanal. Chem.*, 547 (2003) 25.

51. H. Razmi, A. Azadbakht, Electrochim. Acta 50 (2005) 2193.

52. J.-J. Sun, J.-J. Xu, H.-Q. Fang, H.-Y. Chen, *Bioelectrochem. Bioenergetics* 44 (1997) 45.

53. M. Mazloum-Ardakani, H. Beitollahi, B. Ganjipour, H. Naeimi, M. Nejati, *Bioelectrochem.* 75 (2009) 1.

54. R.K. Shervedani, M. Bagherzadeh, S.A. Mozaffari, *Sens. Actuators B* 115 (2006) 614.

55. L.S. Rocha, H.M. Carapuça, *Bioelectrochem.* 69 (2006) 258.

56. M.A. Kamyabi, Z. Asgari, H. Hosseini Monfared, A. Morsali, *J. Electroanal. Chem.* 632 (2009) 170.

57. M.A. Kamyabi, F. Aghajanloo, *J. Electroanal. Chem.* 614 (2008) 157.

58. J. Lei, H. Ju, O. Ikeda, *J. Electroanal. Chem.* 567 (2004) 331.

59. M.H Pournaghi-Azar, H. Dastangoo, *J. Electroanal. Chem.* 567 (2004) 211.

60. J.L. Manzoori, M.H. Sorouraddin, A.M. Haji-Shabani, *Talanta* 46 (1998) 1379.

61. P. Tau, T. Nyokong, *J. Electroanal. Chem.* 611 (2007) 10.

62. W.S. Cardoso, Y. Gushikem, *J. Electroanal. Chem.* 583 (2005) 300.

63. A. Salimi, H. Mamkhezri, S. Mohebbi, *Electrochem. Commun.* 8 (2006) 688.

64. D. Zheng, C. Hu, Y. Peng, S. Hu, *Electrochim. Acta* 54 (2009) 4910.

65. C. Xia, W. Ning, G. Lin, *Sens. Actuators B* 137 (2009) 710.

66. W.J.R. Santos, P.R. Lima, A.A. Tanaka, S.M.C.N. Tanaka, L.T. Kubota, *Food Chemistry* 113 (2009) 1206.

67. Z. Wang, Q. Liang, Y.Wang, G. Luo, *J. Electroanal. Chem.* 540 (2003) 129.

68. F.H. Wu, G.C. Zhou, X.W. Wei, *Electrochem. Commun.* 4 (2002) 690.

69. R.P. Deo, N.S. Lawrence, J.Wang, *Analyst* 129 (2004) 1076.

70. W. Li, C. Liang, W. Zhou, J. Qiu, Z. Zhou, G. Sun, Q. Xin, *J. Phys. Chem. B* 107 (2003) 6292.

71. Y. Liu, Y-L. Yan, J. Lei, F. Wu, H. Ju, *Electrochem. Commun.* 9 (2007) 2564.

72. S. A. Mamuru, K.I. Ozoemena, *Mat. Chem. Phys.* 114 (2009) 113.

73. A. Kaushik, P.R. Solanki, A.A. Ansarib, B.D. Malhotra, S. Ahmad, *Biochem. Eng. J.* 46 (2009) 132.

74. A. Kaushik, P.R. Solanki, A.A. Ansari, G. Sumana, S. Ahmad, B.D. Malhotra, *Sens. Actuators B* 138 (2009) 572.

75. S. Zhang, X. Zhao, H. Niu, Y. Shi, Y. Cai, G. Jiang, *J. Hazardous Mat.* 167 (2009) 560.

76. F. Moura, G.C. Oliveira, M.H. Araujo, J.D. Ardisson, W.A.A. Macedob, R.M. Lago, *Applied Catalysis A: General* 307 (2006) 195.

77. A. Salimi, R. Hallaj, S. Soltanian, *Biophysical Chem.* 130 (2007) 122.

78. M. Khodzitskiya, L. Lutsevb, S. Tarapova, A. Zamkovojc, A. Stognijd, N. Novitskii, *J. Magnetism Magnetic Materials* 320 (2008) L37.

79. W. Tao, D. Pan, Y. Liu, L. Nie, S. Yao, *Anal. Biochem.* 338 (2005) 332.

80. G. Burgot, F. Auffret, J.L. Burgot, *Anal. Chim. Acta* 343 (1997) 125.

81. A.B. Moreira, H.P.M. Oliveira, T.D.Z. Atvars, I.L.T. Dias, G.O. Neto, E.A.G. Zagatto, L.T. Kubota, *Anal. Chim. Acta* 539 (2005) 257.

82. W. Peng, T. Li, H. Li, E. Wang, *Anal. Chim. Acta* 298 (1994) 415.

83. D.A. Kippen, F. Cerini, L. Vadas, R. St¨ocklin, L. Vu, R.E. Offord, K. Rose, *J. Biol. Chem.* 272 (1997) 12513.

84. R.G. Compton, C.E. Bank , *Understanding Voltammetry*, World Scientific Publishing Co. Pte. Ltd. WC2H 9HE UK, 2007.

85. A.J. Bard, L.R. Faulkner, *Electrochemical Methods: Fundamentals and Applications*, 2nd Ed., John Wiley & Sons, Hoboken NJ 2001.

86. J. Wang, *Analytical Electrochemistry*, VCH Publisher Inc., New York (1994).

87. K. Peter; W.R. Heineman, *Laboratory Techniques in Electroanalytical Chemistry,* Second Edition, Revised and Expanded (2 ed.) CRC. (1996).

88. C.G. Zoski. *Handbook of Electrochemistry*. Elsevier Science (2007).

89. http://en.wikipedia.org/wiki/File:Three_electrode_setup.png (Acessible online, April 5, 2009).

90. P.A. Christenson, A. Hamnet, *Techniques and Mechanisms in Electrochemistry*, 1st ed, Blackie Academic and Professional, London, 1994.

91. J.E.B. Randles, *Trans. Faraday Soc*. 44 (1948) 327.

92. R.S. Nicholson, I. Shain, *Anal. Chem.* 36 (1964) 1351.

93. W.R. Heineman, P.T. Kissinger in *Laboratory Techniques in Electroanalytical Chemistry,* 2nd ed., eds. P.T. Kissinger and W.R. Heineman, Marcel Dekker Inc., New York, 1996.

94. M.L. Foresti, R. Guidelli, L. Nyholm *J. Electroanal. Chem.* 269 (1989) 27.

95. L. Ramaley, M. S. Krause, Jr., *Anal. Chem.* 41 (1969) 1362.

96. J. Osteryoung, *Accts. Chem. Res.* 26 (1993) 77.

97. R.A. Osteryoung, J. Osteryoung, *Phil. Trans. Roy. Soc. London, Ser. A* 302 (1981) 315.

98. J. Wang, D.B. Luo, P.A.M. Farias, J.S. Mahmoud, *Anal. Chem.* 57 (1985) 158.

99. J.G. Osteryoung, R.A. Osteryoung, *Anal. Chem*. 57 (1985) 101A.

100. B.E. Conway, *J. Electrochem.* 138 (1991) 1539.

101. B.E. Conway, V. Birss, J. Wojtowicz, J. of Power Sources 66 (1997) 1.

102. E. Barsoukov, J.R. Macdonald, *Impedance Spectroscopy, Theory, Experiment, and Applications*, 2nd Edn. John Wiley and Sons Inc., New Jersey, 2005.

103. J.R. Macdonald, Ed., *Impedance Spectroscopy Emphasizing Solid Materials and Systems*, Wiley/Interscience, New York, 1987.

104. E. Katz and I. Wilner, *in: Ultrathin Electrochemical Chemo- and Biosensors. Technology and Performance*, V.M. Mirsky Ed. Springer- Verlag, New York, 2004, pp. 68–116, Chapter 4.

105. J.R. Macdonald, W.B. Johnson in : E. Barsoukov, J.R. Macdonald (Eds.), *Impedance Spectroscopy*, 2nd ed., John Wiley and Sons Inc., 2005.

106. K.A. Joshi, M. Prouza, M. Kum, J. Wang, J. Tang, R. Haddon, W. Chen, A. Mulchandani, *Anal. Chem.* 78 (2006) 331.

107. O.V. Shoulga, C. Palmer, *Anal. Bioanal. Chem.* 385 (2006) 1116.

108. Q. He, W. Chen, S. Mukerjee, S. Chen, F. Laufek, *J. Power Sources* 187 (2009) 298.

109. J.J. Feng, J.J. Xu, H.Y. Chen, *J. Electroanal. Chem.* 585 (2005) 44.

110. W. Chen, L.-P. Xu, S. Chen, *J. Electroanal. Chem.* 631 (2009) 36.

111. S. Chen, *J. Electroanal. Chem.* 574 (2004) 153.

112. V. Ganesh, S. Pitchumani, V. Lakshminarayanan, *J. Power Sources* 158 (2006) 1523.

113. J. Bisquert, H. Randriamahazaka, G. Garcia-Belmonte, *Electrochim Acta* 51 (2005) 627.

114. M. Jafarian, M.G. Mahjani, H. Heli, F. Gobal, H. Khajehsharifi, M.H. Hamedi, *Electrochim Acta* 48 (2003) 3423.

115. S. Majdi, A. Jabbari, H. Heli, A.A. Moosavi-Movahedi *Electrochim. Acta* 52 (2007) 4622.

116. Research Solutions & Resources available online at: http://www.consultrsr.com/resources/eis/induct2.htm (accessed 0nline, 24 February 2008).

117. User Manual for Frequency Response Analysis (FRA) for Windows version 4.9, Eco Chemie B.V., Utrecht, The Netherlands, 200 and references therein.

118. B.A. Boukamp, *J. Electrochem. Soc.* 142 (1995) 1885.

119. G. Nurk, H. Kasuk, K. Lust, A. Janes, E. Lust, *J. Electroanal. Chem.* 553 (2003) 1.

120. F. Zhi, X. Lu, Y. Jiandong, X. Wang, H. Shang, S. Zhang, X. Zhongua, *J. Phys. Chem. C* 113 (2009) 13166.

121. Craig E. banks, R.G. Compton, *Analyst* 131 (2006) 15.

122. R.R. Moore, C.E. Banks, R.G. Compton, *Analyst* 129 (2004) 755.

123. C.E. Banks, A. Goodwin, C.G.R. Heald, R.G. Compton, *Analyst*, 130 (2005) 280.

124. C.E. Banks, R.G. Compton, *Analyst* 130 (2005) 1232.

125. E.R. Lowe, C.E. Banks, R.G. Compton, *Anal. Bioanal. Chem.*, 382 (2005) 1169.

126. E.R. Lowe, C.E. Banks, R.G. Compton, *Electroanalysis*, 17 (2005) 1627.

127. F. Wantz, C.E. Banks, R.G. Compton, *Electroanalysis*, 17 (2005) 1529.

128. C.M. Welch, C.E. Banks, S. Komorsky-Lovric, *Croat. Chim. Acta* (in press).

129. F. Wantz, C.E. Banks, R.G. Compton, *Electroanalysis* 17 (2005) 655.

130. G. Gao, *Nanostructures and nanomaterials. Synthesis, Properties & Applications.* London: Imperial College Press; 2004.

131. T.W. Ebbesen, *Ann. Rev. Mater. Sci.* 24 (1994) 235.

132. M. Paradise, T. Goswami, Mater. Des. 28 (2007) 1477.

133. M. Endo, K. Takeuchi, S. Igarashi, K. Kobori, M. Shiraishi, H.W. Kroto, J. Phys. Chem. Solids 54 (1993) 1841.

134. W.K. Hsu, J.P. Hare, M. Terrones, H.W. Kroto, D.R.M. Walton, P.J.F. Harris, *Nature* 377 (1995) 687.

135. S. Arepalli, P. Nikolaev, W. Holmes, B.S. Files, *Appl. Phys. Lett.* 78 (2001) 1610.

136. S. Ijima, T. Ichihashi, *Nature* 363 (1993) 603.

137. Rubianes, G.A. Rivas, *Electrochem. Commun.* 9 (2007) 480.

138. F. Valentini, A. Amine, S. Orlanducci, M.L. Terranova, G. Palleschi, *Anal. Chem.* 75 (2003) 5413.

139. N. Maleki, A. Safavi, F. Tajabadi, *Anal. Chem.* 78 (2006) 3820.

140. R.S. Chen, W. Huang, H.Tong, Z. Wang, J. Cheng, *Anal. Chem.* 75 (2003) 6341.

141. A. Abbaspour, A. Izadyar, *Talanta* 71 (2007) 887.

142. H. R. Zare, N. Nasirizadeh, F. Chatraei, S. Makarem, *Electrochim. Acta* 54 (2009) 2828.

143. J. Wang, M. Musameh, *Analyst* 11 (2003) 1382.

144. M. Musameh, J. Wang, A. Merkoci, Y. Lin, *Electrochem. Commun.* 4 (2002) 743.

145. Z. Wang, Q. Liang, Y. Wang, G. Luo, *J. Electroanal. Chem.* 540 (2003) 129.

146. F.H. Wu, G.C. Zhou, X.W. Wei, *Electrochem. Commun.* 4 (2002) 690.

147. H. Luo, Z. Shi, N. Li, Z. Gu, Q. Zhuang, *Anal. Chem.* 73 (2001) 915.

148. J. Wang, M. Mosameh, Y. Lin, *J. Am. Chem. Soc.* 125 (2003) 2408.

149. G. Selvarani, S.K. Prashant, A.K. Sahu, P. Sridhar, S. Pitchumani, A.K. Shukla, *J. Power Sources* 178 (2008) 86.

150. K.C. Pan, C.S. Chuang, S.H. Cheng, Y.O. Su, *J. Electroanal. Chem.* 501 (2001) 160.

151. M.Y. Elahi, M.F. Mousavi, S. Ghasemi, *Electrochim. Acta* 54 (2008) 490.

152. S. Griveau, J. Pavez, J.H. Zagal, F. Bedioui, *J. Electroanal. Chem.* 497 (2001) 75.

153. Y. Liu, Y.-L. Yan, J. Lei, F. Wu, H. Ju, *Electrochem. Commun.* 9 (2007) 2564.

154. A. Salimi, M. Roushani, B. Haghighi, S. Soltanian, Biosens. Bioelectron. 22 (2006) 220.

155. S. Remita, M. Mostafavi, M.O. Delcourt, Radiat. Phys. Chem. 47 (1996) 275.

156. J.H. Hodak, A. Henglein, M. Giersig, G.V. Hartland, *J. Phys. Chem. B* 104 (2000) 11708.

157. Y. Mizukoshi, K. Okitsu, Y. Maeda, T.A. Yamamoto, R. Oshima, Y. Nagata, *J. Phys. Chem. B* 101 (1997) 7033.

158. M. Brust, M.Walker, D. Bethell, D.J. Schiffrin, R.Whyman, *J. Chem. Soc. Chem. Commun.* 7 (1994) 801.

159. K. Osseo-Asare, F.J. Arriagada, *Ceram. Trans.* 12 (1990) 3.

160. L.K. Kurihara, G.M. Chow, P.E. Schoen, *Nanostruct. Mater.* 5 (1995) 607.

161. H.H. Huang, X.P. Ni, G.L. Loy, C.H. Chew, K.L. Tan, F.C. Loh, J.F. Deng, G.Q. Xu, *Langmuir* 12 (1996) 909.

162. M. Yang, J. Jiang, Y. Lu, Y. He, G. Shen, R. Yu, *Biomaterials* 28 (2007) 3408.

163. S. Wang, Q. Xu, G. Liu, *Electroanalysis* 20 (2008) 1116.

164. J. Hrbac, V. Halouzka, R. Zboril, K. Papadopoulos, T. Triantis, *Electroanalysis* 19 (2007) 1850.

165. M. Vidotti, M.R. Silva, R.P. Salvador, S.I. Cordoba de Torresi, L.H. Dall'Antonia, *Electrochim. Acta* 53 (2008) 4030.

166. C. Ding, F. Zhao, M. Zhang, S. Zhang, *Bioelectrochem.* 72 (2008) 28.

167. A. Abbaspour, A. Khajehzadeh, A. Ghaffarinejad, *J. Electroanal. Chem.* 631 (2009) 52.

168. A.B. Moghaddam, M.R. Ganjali, R. Dinarvand, T. Razavi, A. A. Saboury, A.A. Moosavi-Movahedi, Parviz Norouzi, *J. Electroanal. Chem.* 614 (2008) 83.

169. P.R. Somani, S. Radhakrishnan, *Mater. Chem. Phys.* 77 (2003) 117.

170. M. Taguchi, K. Yamada, K. Suzuki, O. Sato, Y. Einaga, *Chem. Mater.* 17 (2005) 4554.

171. D.M. DeLongchamp, P.T. Hammond, *Adv. Funct. Mater.* 14 (2004) 224.

172. M. Pyrasch, A. Toutianoush, W.Q. Jin, J. Schnepf, B. Tieke, *Chem.Mater.* 15 (2003) 245.

173. M. Jayalakshimi, F. Scholz, *J. Power Sources* 87 (2000) 212.

174. F. Qu, A. Shi, M. Yang, J. Jiang, G. Shen, R. Yu, *Anal. Chimic Acta* 605 (2007) 28.

175. S.J. Nakanishi, G.T. Lu, , H.M. Kothari, E.W. Bohannan, J.A. Switzer, *J. AM. Chem. Soc.* 125 (2003) 14998.

176. J.M. Zen, P.Y. Chen, A.S. Kumar, *Anal. Chem.* 75 (2003) 6017.

177. S. Han, Y. Chen, R. Pang, P. Wan, *Ind. Eng. Chem. Res.* 46 (2007) 6847.

178. W. Zhao, J.J. Xu, C.G. Shi, H.Y. Chen. *Langmuir* 21 (2005) 9630.

179. Y. Xian, Y. Zhoua, Y. Xian, L. Zhouc, H. Wang , L. Jin, *Anal. Chimic. Acta* 546 (2005) 139.

180. Y. Miao, J. Chen, X. Wu, J. Miao, *Colloids Surfaces A*: *Physicochem. Eng. Aspects* 295 (2007) 135.

181. A-M Gurban, T. Noguer, C. Bala, L. Rotariu, *Sens. Actuat. B* 128 (2008) 536.

182. S. Thiagarajan, S. Chen, *Talanta* 74 (2007) 212.

183. G. Xu, M. Xu, J. Zhang, S. Kim, Z. Bae, *Bioelectrochem*. 72 (2007) 87.

184. O. Hornykiewicz, S.J. Kish, *Adv. Neurol.* 45 (1986) 19.

185. X. Cao, L. Luo, Y. Ding, X. Zou, R. Bian, *Sens. Actuator* 129 (2007) 941.

186. S. Wang, F. Xie, R.-F. Hu, (2006). *Sens. Actuators* B 123 (2007) 495.

187. G.-R. Xu, M.-L. Xu, J.-M. Zhang, S. Kim, Z.-U. Bae, *Bioelectrochem.* 72 (2008) 87.

188. A. Salimi, M. Roushani, *Electrochem. Commun.* 7 (2005) 879.

189. Y.C. Weng, J.F. Rick, T.C. Chou, *Biosens. Bioelectron.* 20 (2004) 41.

190. A. Salimi, M. Roushani, R. Hallaj, *Electrochim. Acta* 51 (2006) 1952.

191. D. Giovanelli, N.S. Lawrence, S.J. Wilkins, L. Jiang, T.G.J. Jones, R.G. Compton, *Talanta* 61 (2003) 211.

192. M.R. Ganjali, P. Norouzi, F. Faridbod, M. Yousefi, L. Naji, M. Salavati-Niasari, *Sens. Actuators B* 120 (2007) 494.

193. Z.-H. Wang, L.-L. Zhang, K.-Y. Qiu, *J. Power Sources* 161 (2006) 133.

194. J. Obirai, F. Bedioui, T. Nyokong, *J. of Electroanal. Chem.* 576 (2005) 323.

195. Y.Y. Liao, T.C. Chou, *Electroanalysis* 12 (2000) 55.

196. S. Lin, T.-C. Chou, *J. Electrochem. Soc.* 152 (2005) H53.

197. H.A. Zamani, F. Malekzadegan, M.R. Ganjali, *Anal. Chim. Acta* 555 (2006) 336.

198. S.J. Richard, S. Prabakar, S. Narayanan, *J. Electroanal. Chem.* 617 (2008) 111.

199. E.F. Perez, L.T. Kubota, A.A. Tanaka, G. De Oliveira Neto *Electrochim. Acta* 43 (1998) 1665.

200. Y.-C. Weng, J.F. Rick, T.-C. Chou, *Biosens. Bioelectron.* 20 (2004) 41.

201. A. Mohammadi, A.B. Moghaddam, M. Kazemzad, R. Dinarvand, J. Badraghi, *Mat. Sc. Eng. C* 29 (2009) 1752.

202. A. Salimi, E. Sharifi, A. Noorbakhsh, Saied Soltanian, *Electrochem. Commun.* 8 (2006) 1499.

203. A. Salimi, E. Sharifi, A. Noorbakhsh, S. Soltanian, *Biophys. Chem.* 125 (2007) 540.

204. A. Salimi, A. Noorbakhash, E. Sharifi, A. Semnani, *Biosens. Bioelectron.* 24 (2008) 792.

205. J. Ahmed, S. Sharma, K.V. Ramanujachary, S.E. Lofland, A.K. Ganguli, *J. Coll. Interf. Sci.* 336 (2009) 814.

206. R.K. Shervedani, A.R. Madram, *INTERN. J. HYDROGEN ENERGY* 33 (2008) 2468.

207. Abdolmajid Bayandori Moghaddam, Mohammad Reza Ganjali, Rassoul Dinarvand, Sara Ahadi, Ali Akbar Saboury, *Biophys. Chem.* 134 (2008) 25.

208. Abdollah Noorbakhsh, Abdollah Salimi, *Electrochim. Acta* 54 (2009) 6312.

209. M. Jafarian, O. Azizia, F. Gobal, M.G. Mahjani, *International Journal of Hydrogen Energy* 32 (2007) 1686.

210. YuLin Min, YouCun Chen, YingGuo Zhao, Chao Chen, *Mat. Lett.* 62 (2008) 4503.

211. M. Yang, Y. Yang, F. Qu, Y. Lu, G. Shen, R. Yu, *Anal. Chim. Acta* 571 (2006) 211.

212. Q. Yi, W. Huang, J. Zhang, X. Liu, L. Li, *J. Electroanal. Chem.* 610 (2007) 163.

213. J. Qiao, S. Tang, Y. Tian, S. Shuang, C. Dong, M.M.F. Choi *Sens. Actuat. B* 138 (2009) 402.

214. M.V. Martı´nez-Huerta, S. Rojas, J.L. Go´mez de la Fuente, P. Terreros, M.A. Pen, J.L.G. Fierro, *Appl. Cat. B: Environmental* 69 (2006) 75.

215. Y.C. Weng, J.F. Rick, T.C. Chou, *Biosens. Bioelectron.* 20 (2004) 41.

216. S.H. Huang, M.H. Liao, D.H. Chen, *Biotechnol. Prog.* 19 (2003) 1095.

217. L. Josephson, J.M. Perez, R. Weissleder, *Angew. Chem. Int. Ed.* 40 (2001) 3204.

218. Z.H. Wang, C.J. Choi, B.K. Kim, J.C. Kim, Z.D. Zhang, *Carbon* 41 (2003) 1751.

219. L.M. Rossi, A.D. Quach, Z. Rosenzweig, Anal. Bioanal. Chem. 380 (2004) 606.

220. M. Pumera, M.T. Castaneda, M.I. Pividori, R. Eritja, A. Merkoci, S. Alegret, *Langmuir* 21 (2005) 9625.

221. R.W. Cornell e, U. Schwertmann, *The Iron Oxides*, VCH, Weinheim, 1996.

222. R.M. Cornell, U. Schwertmann, *The Iron Oxides: Structure, Properties, Reactions, Occurrences and Uses*, second ed. Wiley-VCH, Weinheim, 2003.

223. M. Siswana, K.I. Ozoemena, T. Nyokong, *Talanta* 69 (2006) 1136.

224. S. Wang, Q. Xu, X. Zhang, G. Liu, *Electrochem. Commun.* 10 (2008) 411.

225. P Yuan, H.-Q. Wu, H.-Y. Xu, D.-M. Xu, Y.-J. Cao, X.-W. Wei, *Mat. Chem. Phys.* 105 (2007) 391.

226. M. Wen, H. Qi, W. Zhao, J. Chen, L. Li, Q. Wu, *Coll. Surf. A: Physicochem. Eng. Aspects* 312 (2008) 73.

227. M. Gangeri, S. Perathoner, S. Caudo, G. Centi, J. Amadou, D. Begin, C. Pham-Huu , M.J. Ledoux , J.-P. Tessonnier, D.S. Su, R. Schlogl, *catalysis Today* 143 (2009) 57.

228. J. Wang, G. Liu, A. Merkoçi, *Anal. Chim. Acta* 482 (2003) 149.

229. A. Kaushika, R. Khana, P.R. Solankia, P. Pandeya, J. Alamb, S. Ahmadb, B.D. Malhotra, *Biosens. Bioelectrtn.* 24 (2008) 676.

230. S. Zhang, X. Zhao, H. Niu, Y. Shi, Y. Cai, G. Jiang, *J. Hazard. Mat.* 168(2009) 1.

231. J.-D. Qiu, M. Xiong, R.-P. Liang, H.-P. Peng, F. Liu, *Biosens. Bioelectron.* 24 (2009) 2649.

232. A. Kaushik, P.R. Solanki, A.A. Ansari, S. Ahmad, B.D. Malhotra, *Electrochem. Commun.* 10 (2008) 1364.

233. S. Qu, J. Wang, J. Kong, P. Yang, G. Chen, *Talanta* 71 (2007) 1096.

234. H.-L. Zhang, X.-Z. Zou, G.-S. Lai, D.-Y. Han, F. Wang, *Electroanalysis* 19 (2007) 1869.

235. H.-L. Zhang, X.-Z. Zou, G.-S. Lai, D.-Y. Han, F. Wang, *Electroanalysis* 19 (2007) 1869.

236. V. Saez, J. Gonzalez-Garcia, M.A. Kulandainatha, F. Marken, *Electrochem. Commun.* 9 (2007) 1127.

237. S.H. Joo, D. Zhao, *Chemosphere* 70 (2008) 418.

238. H. Gleiter, *Prog. Mater. Sci.* 33 (1989) 223.

239. J.P. Chen, C.M. Sorensen, K.J. Klabunde, G.C. Hadjipanayis, *Phys. Rev. B* 51 (1995) 11527.

240. K. Tanabe, *Mater. Lett.* 61 (2007) 4573.

241. S.I.C. deTorresi, K. Provazi, M. Malta, R.M.Torresi, *J. Electrochem. Soc.* 148 (2001) A1179.

242. V. Srinivasan, J.W. Weidner, *J. Power Sources* 108 (2002)15.

243. L.D. Kadam, S.H. Pawar, P.S. Patil, *Mater. Chem. Phys.* 68 (2001) 280.

244. H. Okabe, J. Akimitsu, T. Kubodera, M. Matoba, T. Kyomen, M. Itoh, Phys*. B Condens. Matter*. 378–380 (2006) 863.

245. J. Tyczkowski, R. Kapica, J. Lojewska, *Thin Solid Films* 515 (2007) 6590.

246. E. Villagra, F. Bedioui, T. Nyokong, J.C. Canales, M. Sancy, M.A. Paez, J. Costamagna, J.H. Zagal, *Electrochim. Acta* 53 (2008) 4883.

247. N. Sehlotho, S. Griveau, N. Ruille, M. Boujtita, T. Nyokong, F. Bedioui, *Mater. Sci. Eng.* C, 28 (2008) 606.

248. J. Arguello, H.A. Magosso, R. Landers, Y. Gushikem, *J. Electroanal. Chem.* 617 (2008) 45.

249. A. Salimi, H. Mamkhezri, R. Hallaj, S. Soltanian, *Sens. Actuators*, B 129 (2008) 246.

250. M.D. Abad, J.C. Sánchez-López, A. Berenguer-Murcia, V.B. Golovko, M. Cantoro, A.E.H. Wheatley, A. Fernández, B.F.G. Johnson, J. Robertson, *Diamond Relat. Mater.* 17 (2008) 1853.

251. Z. Dong, K. Ma, J. He, J.Wang, R. Li, J. Ma, *Mater. Lett.* 62 (2008) 4059.

252. M. Yang, J. Jiang, Y. Yang, X. Chen, G. Shen, R. Yu, *Biosens. Bioelectron.* 21 (2006) 1791.

253. J. Shen, Y. Hu, C. Li, C. Qin, M. Ye, *Electrochim. Acta* 53 (2008) 7276.

254. H. Zhao, L. Li, J. Yang, Y. Zhang, *Electrochem. Commun.* 10 (2008) 1527.

255. I.G. Casella, M.R. Guascito, *J. Electroanal. Chem.* 476 (1999) 54.

256. I.G. Casella, M. Gatta, *J. Electroanal. Chem.* 534 (2002) 31.

257. I.G. Casella, *J. Electroanal. Chem.* 520 (2002) 119.

258. L.F. Fan, X.Q. Wu, M.D. Guo, Y.T. Gao, *Electrochim. Acta* 52 (2007) 3654.

259. M. Jafarian, M.G. Mahjani, H. Heli, F. Gobal, H. Khajehsharifi, M.H. Hamedi, *Electrochim. Acta* 48 (2003) 3423.

260. Xin Zhang, Kwok-Ying Tsang, Kwong-Yu Chan, *J. Electroanal. Chem.* 573 (2004) 1.

261. A. Salimi, R. Hallaj, S. Soltanian, H. Mamkhezri, *Anal. Chim. Acta* 594 (2007) 24.

262. M. Hasanzadeh, G. Karim-Nezhad, N. Shadjou, M. Hajjizadeh, B. Khalilzadeh, L. Saghatforoush, M.H. Abnosi, A. Babaei, S. Ershad, *Anal. Biochem.* 389 (2009) 130.

263. M. Yang, J. Jiang, Y. Yang, X. Chen, G. Shen, R. Yu, *Biosens. Bioelectron.* 21 (2006) 1791.

264. K. Wang, J.-J. Xu, H.-Y. Chen, *Biosens. Bioelectron.* 20 (2005) 1388.

265. S. Shahrokhiana, M. Ghalkhania, M. Adeli, M.K. Amini, *Biosens. Bioelectron.* 24 (2009) 3235.

266. D. Cao, J. Chao, L. Sun, G. Wang, *J. Power Sources* 179 (2008) 87.

267. Y. Shi, B. Zhou, P. Wu, K. Wang, C. Cai, *J. Electroanal. Chem.* 611 (2007) 1.

268. E. Slavcheva, V. Nikolova, T. Petkova, E. Lefterova, I. Dragieva, T. Vitanov, E. Budevski, *Electrochim. Acta* 50 (2005) 5444.

269. K. Wang, J.-J. Xu, H.-Y. Chen, *Sens. Actuators* B, 114 (2006) 1052.

270. B.E. Conway, *Electrochemical SuperCapacitors*, Kluwer Academic/Plenum Publishers, New York, 1999.

271. M. Winter, R. J. Brodd, *Chem. Rev*. 104 (2004) 4245.

272. C. Peng, S. Zhang, D. Jewell, G.Z. Chen, *Prog. Nat. Sci.* 18 777 (2008).

273. T. Shinomiya, V. Gupta, N. Miura, *Electrochim. Acta* 51 (2006) 4412.

274. C-M Huang, C-H Hu, K-H Chang, J-M Li, Y-F Li, *J. Electrochem. Soc.* 156 (2009) A667.

275. P. Ghosh, S. Mahanty, R.N. Basu, *J. Electrochem. Soc.* 156 (2009) A681.

276. M. S. Wu, H-H. Hsieh, *Electrochim. Acta* 53 (2008) 3427.

277. V. Srinivasan, J.W. Weidner, *J. Electrochem. Soc.* 147 (2000) 880.

278. M. D. Ingram, H. Staesche, K. S. Ryder, *J. Power Sources* 129 (2004) 107.

279. C-H Hu, K-H Chang, M-C lin, and Y-T Wu, *Nano. Letters* 6 (2006) 2690.

280. Z. Fan, J. Chen, K. Cui, F. Sun, Y. Xu, and Y. Kuang, *Electrochim. Acta* 52 (2007) 2959.

281. S. Devaraj, N. Munichandraiah, *J. Electrochem. Soc.* 154 (2007) A80.

282. K.W. Nam, K.B. Kim, *J. Electrochem. Soc.* 149 (2002) A346.

283. L. Cao, M. Lu, H.L. Li, *J. Electrochem. Soc.* 152 (2005) A871.

284. S.Y. Wang, K.C. Ho, S.L. Kuo, N.L. Wu, *J. Electrochem. Soc.* 153 (2006) A75.

285. Y. Zhang, Y. Gui, X. Wu, H. Feng, A. Zhang, L. Wang, T. Xia, *Intern. J. hydrogen energy* 3 4 (2 0 0 9) 2 4 6 7.

286. M. Wu, J. Gao, S. Zhang, A. Chen, *J. Porous Mater.* 13 (2006) 407.

287. D. Zhao, W. Zhou, H. Li, *Chem. Mater.* 19 (2007) 3882.

288. M.S. Wu, H.-H. Hsieh, *Electrochim. Acta* 53 (2008) 3427.

289. J. Li, E.-H. Liu, W. Li, X.-Y. Meng, S.-T. Tan, *J. Alloys Compds.* 478 (2009) 371.

290. J. Li, Q.M. Yang, I. Zhitomirsky, *J. Power Sources* 185 (2008) 1569.

291. Y. Zheng, M. Zhang, P. Gao, *Mat. Res. Bull.* 42 (2007) 1740.

292. Y. Cao, J. Cao, M. Zheng, J. Liu, G. Ji, *J. Sol. State Chem.* 180 (2007) 792.

293. J.Y. Lee, K. Liang, K.H. Ana, Y.H. Lee, *Synthetic Metals* 150 (2005) 153.

294. F. Miao, B. Tao, P. Ci, J. Shi, L. Wanga, P.K. Chu, *Mat. Res. Bull.* 44 (2009) 1920.

295. H. Li, Y. Li, R. Wang, R. Cao, *J. Alloys Compds* 481 (2009) 100.

296. J. Chen, K. Huang, S. Liu, X. Hu, *J. Power Sources* 186 (2009) 565.

297. J. Chen, K. Huang, S. Liu, *Electrochem. Commun.* 10 (2008) 1851.

298. N. L. Wu, S. Y. Wang, C. Y. Han, D. S. Wu, and L. R. Shiue, *J. Power Sources* 113 (2003) 173.

299. Y. Wang, W. Yang, C. Chen, D.G. Evans, *Journal Power Sources* 184 (2008) 682.

300. S.-L. Kuo, N.-L. Wu, *Electrochem. Solid-State Letters* 8 (2005) A495.

301. J. Chen, K. Huang, S. Liu, *Electrochim. Acta* 55 (2009) 1.

302. M. Mallouki, F. Tran-Van, C. Sarrazina, C. Chevrot, J.F. Fauvarque, *Electrochim. Acta* 54 (2009) 2992.

303. F. Tao, Y.-Q. Zhao, G.-Q. Zhang, H.-L. Li, *Electrochem. Commun.* 9 (2007) 1282.

304. Y. Yu, G. Ji, J. Cao, J. Liu, M. Zheng, *J. Alloys Compd.* 471 (2009) 268.

305. Z. Zheng, L. Huang, Y. Zhou, X. Hu, X. Ni, *Solid State Sciences* 11 (2009) 1439.

306. J. Wang, T. Golden, K. Varughese and I. El-Rayes, *Anal. Chem.* 61 (1989) 509.

307. Z. Chen, Y. Zhou, *Surface and Coating Technology* 201 (2006) 2419.

308. C.J. Brinker, G.W. Scherer, *Sol-Gel Science: The Physics and Chemistry of Sol-Gel Processing*. Academic Press (1990). ISBN 0121349705.

309. K.B. Blodgett, *J. Amer. Chem. Soc.* 56 (1934) 495.

310. http://en.wikipedia.org/wiki/Chemical_vapor_deposition (Accessed online, September 15, 2009).

311. T. Trindade, O. O˘ıBrien, N.L. Pickett, *Chem. Mater.* 13 (2001) 3843.

312. B. Oregan, M. Gratzel, *Nature* 353 (1991) 737.

313. A.P. Baioni Torre, M. Vidotti, P.A. Fiorito, E.A. Ponzio, S.I. C´ordoba de Torresi, *Langmuir* 27 (2007) 6796.

314. M. Haruta, N. Yamada, T. Kobayashi, S. Iijima, *J. Catal.* 115 (1989) 301.

315. J. Wang, M. Musameh, *Anal. Chem.* 75 (2003) 2075.

316. P.A. Fiorito, V.R. Goncales, E.A. Ponzio, S.I. C´ordoba de Torresi, *Chem. Commun.* (2005) 366.

317. V.M. Rotello. *Nanoparticles: Building Blocks for Nanotechnology*. 1st Ed. New York: Springer; 2003.

318. N.L. Rosi, C.A. Mirkin, *Chem. Rev.* 105 (2005) 1547.

319. Y. Ju-Nam, J.R. Lead, *Science of the Total Environment* 400 (2008) 396.

320. C.P. Poole, F.J. Owens, *Introduction to Nanotechnology*. Hoboken: Wiley-Interscience; 2003.

321. M.C. Daniel, D. Astruc, *Chem. Rev.* 104 (2004) 293.

322. V.S. Bagotsky, Fundamental of Electrochemistry, 2nd Edition, John Wiley & Sons, Inc., New Jersey, 2006.

323. P.J. Pearce, A.J. Bard, J. Electroanal. Chem. 114 (1980) 89.

324. R.H. Wopschall, I. Shain, Anal. Chem. 39 (1967) 1514

325. H.X. Ju, L. Donal, *J. Electroanal. Chem.* 484 (2000) 150.

326. C.A. Gervasi, P.E. Alvarez, M.V. Fiori Bimbi, M.E. Foilquer, *J. Electroanal. Chem.* 601 (2007) 194.

327. E. Le Bourhis, G. Patriarche, Micron 38 (2007) 377.

328. The Free Encyclopedia, http://en.wikipedia.org/wiki/Atomic_force_microscope (accessed online 24 August, 2009).

329. J.B. Hudson, *Surface Science: An Introduction*, John Wiley&Sons, New York, 1998.

330. X. Jiang, T. Wang, *Applied Surface Science* 252 (2006) 8029.

331. D. Briggs, M.P. Seah, *Practical Surface Analysis* by Auger and X-Ray Photoelectron Spectroscopy, Eds. New York: Wiley 1983.

332. *The Free Encyclopedia,* http://en.wikipedia.org/wiki/X-ray-diffraction (accessed online 24 August, 2009).

333. H.H. Willard, L.L. Merritt, J.A. Dean, F.A. Settle, Instrumental Methods of Analysis, 7th Edition, Belmont, Calif: Wadsworth, 1988.

334. *The Free Encyclopedia,* http://en.wikipedia.org/wiki/Ultraviolet-visible_spectroscopy (accessed online July, 2009).

335. K. Yamada, K. Yasuda, N. Fujiwara, Z. Siroma, H. Tanaka, Y. Miyazaki, T. Kobayashi, *Electrochem. Commun.* 5 (2003) 892.

336. R.A. Becker, L.R. Barrows, R.C. Shank, *Carcinogenesis* 2 (1981) 1181.

337. *Homeland Security Information Bulletin* US Department of Homeland Security: Washington DC May 2003.

338. G.G. Wildgoose, C.E. Banks, R.G. Compton, *Small* 2(2006) 182.

339. C.E. Banks, A. Crossley, C. Salter, S.J. Wilkins, R.G. Compton, *Angew Chem. Int. Ed.* 45: (2006) 2533.

340. J. Kruusma, N. Mould, K. Jurkschat, A. Crossley, C.E. Banks Electrochem. Commun. 9 (2007) 2330.

341. C.P. Jones, K. Jurkschat, A. Crossley, R.G. Compton, B.L. Riehl, C.E. Banks, *Langmuir* 23 (2007) 9501.

342. K. Jurkschat, X. Ji, A. Crossley, R.G. Compton, C.E. Banks, *Analyst* 132 (2007) 21.

343. Available at http://en.wikipedia.org/wiki/Chemica warfare (Accessed online 15 April, 2009).

344. E. W. Hooijschuur, A. Hulst, A. de Long, L. de Reuver, S. van Krimpen, B. van Baar, E. Wils, C. Kientz, U.A. Brinkman, *Trends Anal. Chem. (TrAC)* 21 (2002) 116.

345. Y.Yang, *Acc. Chem. Res.* 32 (1999) 109.

346. C.L. Copper, G.E. Collins, *Electrophoresis*, 25 (2004) 897.

347. J. Wang, J. Zima, N.S. Lawrence, M.P. Chatrathi, *Anal. Chem.*, 76 (2004) 4721.

348. J. Pillay, K.I. Ozoemena, *Electrochem. Commun.*, 9 (2007) 1816.

349. C.A. Claudia, F. Bedioui, J.H. Zagal, *Electrochim. Acta* 47 (2002) 1489.

350. N.S. Bryan, *Free Radical Biol. Med.*, 41 (2006) 691.

351. E.T. Reichert, S.W. Mitchell, *Am. J. Med. Sci.* 159 (1980) 158.

352. C.J. Hunter, *Nat. Med.* 10 (2004) 1122.

353. A.V. Kozlov, *Shock* 15 (2001) 366.

354. N. Sparatu, T.N. Rao, D.A. Tryk, A. Fujishima, *J. Electrochem. Soc.* 148 (2001) E112.

355. H.J. Choi, G. Kwag, S. Kim, *J. Electroanal Chem.* 508 (2001) 105.

356. A.L. Leninger, D.L. Nelson, M.M. Cox, *Principles of Biochemistry*, 2nd ed., Worth Publishers, New York 1993, p. 689.

357. S.Y. Ha, S. Kim, *J. Electroanal. Chem.* 468 (1999) 131.

358. Z.H. Wen, T.F. Kang, *Talanta* 62 (2004) 351.

359. D. Giustarini, I. Dalle-Donne, R. Colombo, A. Milzani, R. Rossi, *Free Rad. Res.* 38 (2004) 1235.

360. W. Frenzel, J. Schulz-Brussel, B. Zinvirt, *Talanta* 64 (2004) 278.

361. S. Arias-Negrete, L.A. Jimenez-Romero, M.O. Soliis-Martiinez, J. Ramiirez-Emiliano, E.E. Avila, P. Cuella-Mata, *Anal. Biochem.* 328 (2004) 14.

362. A. Aydin, O. Ercan, S. Tascioglu, *Talanta* 66 (2005) 1181.

363. M.I.H. Helaleh, T. Korenaga, *J. Chromatogr. B* 744 (2000) 433.

364. X. Cai, Z. Zhao, *J. Electroanal. Chem.* 252 (1988) 361.

365. J.E. Newbry, M.P.L. de Haddad, *Analyst* 110 (1985) 81.

366. M. Trojanowicz, W. Matuszewski, B. Szostek, *Anal. Chim. Acta* 261 (1992) 391.

367. C.A. Caro, F. Bedioui, J.H. Zagal, *Electrochim. Acta* 47 (2002) 1489.

368. S.Q. Wang, Y.M. Yin, X.Q. Lin, *Electrochem. Commun.* 6 (2004) 259.

369. J.W. Mo, B. Ogorevc, *Anal. Chem.* 73 (2001)1196.

370. R.M. Wightman, L.J. May, A.C. Michael, *Anal. Chem.* 60 (1998) 769A.

371. R.C. Retna, T. Okajima, T. Ohsaka, *J. Electroanal. Chem.* 543 (2003) 127.

372. T. Selvaraju, R. Ramaraj, *J.Electroanal. Chem.* 585 (2005)290.

373. P. Zhang, F.H. Wu, G.C. Zhao, X.W. Wei, *Bioelectrochem.* 67 (2005) 109.

374. N.Q. Jia, Z.Y. Wang, G.F. Yang, H.B. Shen, L.Z. Zhu, *Electrochem. Commun.* 9 (2007)233.

375. Y.F. Zhao, Y.Q. Gao, D.P. Zhan, H. Liu, Q. Zhao, Y. Kou, Y.H. Shao, M.X. Li, Q.K. Zhuang, Z.W. Zhu, *Talanta* 66 (2005) 51.

CHAPTER TWO

EXPERIMENTAL

2.0 EXPERIMENTAL

2.1 Materials and Reagents

The pristine single-walled carbon nanotubes (SWCNTs, 06509HB Aldrich) and multi-walled carbon nanotubes (MWCNTs) were purchased from Aldrich chemicals and digested by subjecting them to harsh acid conditions for -COOH modification following the method already described [1]. Digestion with strong acids serves the purposes of transforming the CNTs into shorter, uncapped nanotubes bearing mainly acidic groups. A single-walled carbon nanotube poly(m-aminobenzene sulphonic acid (SWCNT-PABS) was also purchased from Aldrich chemical and was used directly without further treatment. The nitrate salts of the metals, nickel nitrate hexahydrate ($Ni(NO_3)_2.6H_2O$); iron nitrate nonahydrate ($Fe(NO_3)_2.9H_2O$); cobalt nitrate hexahydrate ($Co(NO_3)_2.6H_2O$) are products of Sigma-Aldrich. Dopamine-hydrochloride ($C_8H_{11}NO_2.HCl$); Hydrazine sulphate ($H_6N_2O_4S$); sodium nitrite ($NaNO_2$); diethylaminoethanethiol (DEAET) are bought from Sigma chemicals. Sodium sulphate (Na_2SO_4); sodium hydroxide (NaOH); ammonium carbonate ($(NH_4)_2CO_3$); ferric chloride ($FeCl_3$); hydrated potassium hexacyano ferrate(II) ($K_4[Fe(CN)_6].6H_20$); potassium hexacyano ferrate(III) ($K_3Fe(CN)_6$); potassiumchloride(KCl); cetyltrimethylammoniumbromide (CTAB); dimethylformamide $(CH_3)_2NC(O)H$); acetone (C_3H_3O); ethanol (C_2H_5OH); isopropyl alcohol (C_3H_7OH); ethylene glycol ($C_3H_8O_3$); sulphuric acid (H_2SO_4); phosphoric acid (H_3PO_4); nitric acid (HNO_3); hydrochloric acids (HCl); hydrazinium hydroxide (N_2H_5OH); ammonia solution ($NH_3.H_2O$); sodium borohydride ($NaBH_4$), and other reagent were of analytical grade and obtained from Sigma-Aldrich and Merck chemicals respectively. Dopamine drug (Dopamine HCl-Fresenius® (200 mg / 5 ml) product of Bodene (pty) Ltd South Africa, was

supplied by a local pharmacy store. Ultra pure water of resistivity 18.2 MΩcm was obtained from a Milli-Q Water System (Millipore Corp., Bedford, MA, USA) and was used throughout for the preparation of solutions. 0.1 M acetate and phosphate buffer solutions of pH 3.0, 4.0, 7.0, 7.4 and 9.4 respectively were prepared using acetic acid (CH_3COOH), sodium acetate (CH_3COONa), sodium hydrogen phosphate di-hydrate ($NaH_2PO_4.2H_2O$) and di-sodium hydrogen phosphate di-hydrate ($Na_2HPO_4.2H_2O$) or their potassium salts. The pH is adjusted with 0.1 M H_3PO_4 or NaOH. All solutions were prepared using double distilled deionised water and purged with pure nitrogen to eliminate oxygen and any form of oxidation during experiment. All other reagents were of analytical grades and were used as received from the suppliers without further purification. All electrochemical experiments were performed with nitrogen-saturated PBS.

2.1.1 Synthesis of funtionalised CNTs

Briefly, the starting material pristine SWCNTs or MWCNTs (Aldrich) was purified and cut into short and uncapped nanotubes bearing acid functional groups (CNT-COOH) according to the multi-step procedures developed [1] (with some little modification) by refluxing a known weight of the SWCNTs in 2.6 M HNO_3 for 48 h. The product was washed with copious amount of water, centrifuged to drive away the water and dried. The residue is ultrasonicated at 40 ^{0}C in a mixture of concentrated H_2SO_4 and HNO_3 (3:1, v/v) for 24 h. The material was filtered again, washed with copious amount of water and dried. Finally, the suspension was stirred at 70 ^{0}C in a mixture of concentrated H_2SO_4 and 30% aqueous H_2O_2 (4:1, v/v) for 4 h. The product was filtered and washed with copious amount of water until the pH of the filtrate is neutral. The black solid

material obtained was dried in an oven over night and characterised using FTIR (to confirm the carbonyl functional group (C=O) of the –COOH), SEM and TEM (to established structural changes after modification). The ash treatment employed cut the nanotubes to smaller sizes that allow for COOH modification.

2.1.2 Synthesis of nickel and nickel oxide nanoparticles

Nickel nanoparticles were synthesised adopting the method described by Wu and Chen, 2003 [2]. An appropriate amount of nickel nitrate (50 mM) was dissolved in ethylene glycol (25 mL). To the solution were added hydrazinium hydroxide (2.0 mL, 1.0 M) and 1.0 M NaOH solution (72 $\mu L mL^{-1}$) in sequence. The reaction was maintained at 60 ^{0}C and nickel nanoparticles were formed after about an hour in a capped volumetric flask under stirring. The reduction reaction is shown below.

$$2Ni^{2+}_{(aq)} + N_2H_{4(aq)} + 4OH^-_{(aq)} \longrightarrow 2Ni_{(s)} + N_{2(g)} + 4H_2O_{(l)} \qquad (2.1)$$

Nickel oxide (NiO) nanoparticles were prepared using the method described by Xiang et al. [3]. 100 mL of precipitation solution (NH_4HCO_3) was dropped at the rate of 5.0 mL min^{-1} into 50 mL of 0.5 M Ni^{2+} solution. During precipitation, the suspension was kept at constant temperature (40 ^{0}C), and constant stirring (800 rpm) for 1 h. The precipitate formed was washed with distilled water and copious amount of ethanol several times to removed possible adsorbed ions such as Ni^{2+}, NH_4^+, Cl^-, NO_3^-, CO_3^{2-}, and OH^-. The precipitate was oven-dried at 105 ^{o}C for 12 h, and later heated in air at 400 ^{o}C for 1 h. The product was pulverised and used for analysis. The procedure is summarised in scheme 2.1 below.

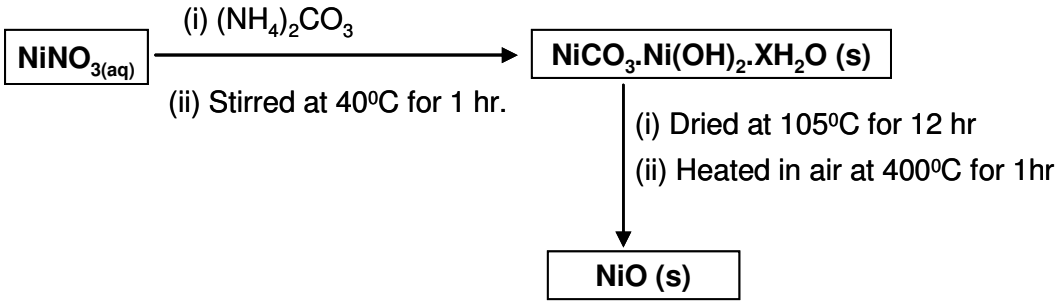

Scheme 2.1: Procedures for the synthesis of NiO nanoparticles.

2.1.3 Synthesis of cobalt and cobalt oxide nanoparticles

Co nanoparticles were synthesized using the method described by Shen et al. [4]. 71.4 mg of $Co(NO_3)_2.6H_2O$ was dissolved in 20 ml ethylene-glycol in 5 mL H_2O. The precursor was reduced by slowly adding solution containing mixture of 0.1 M $NaBH_4$ and 1.0 M NaOH. The mixture was quickly heated to 120 ^{0}C for 2h to reduce the Co completely. Cobalt oxide nanoparticles were prepared using the method described by Yao et al. [5]. A given amount (3.0 g) of $Co(NO_3)_2.6H_2O$ was dissolved into 100 ml of isopropyl alcohol-water (1:1, v/v) solution in a three-necked round-bottom flask. Then appropriate amount (30 - 50 mL) of isopropyl alcohol-ammonia solution was added into the solution and aged for hours to ensure complete precipitation. The precipitate was filtered and dried under vacuum at 70 ^{0}C. The CO_3O_4 was finally obtained by calcining the $Co(OH)_2$ precursor at 500 ^{0}C in Ar for 2h.

2.1.4 Synthesis of iron and iron oxide nanoparticles

Nanoscale zero-valent iron particles were synthesized by the sodium borohydride method [6-8]. The synthesis was conducted in a flask reactor with three open necks. The central neck was housed

with a tunable mechanical stirrer at 400 rpm. Through titration at a rate of 0.625 mL/s, 50 mL (0.2 M) $NaBH_4$ was titrated slowly into 50 mL (0.05 M) $Fe(NO_3).9H_2O$ solution. The borohydride was introduced to reduce ferric ion (Fe^{3+}) to zero-valent iron [Fe^0], according to the following reaction:

$$4Fe^{3+} + 3BH_4^- + 9H_2O \longrightarrow 4Fe^0 + 3H_2BO_3^- + 12H^+ + 6H_2 \qquad (2.2)$$

The mixture was vigorously mixed in the flask reactor for additional 30 min after the titration. The generated iron particles were harvested with vacuum filtration and stabilized with a large volume of deionized water (>100 mL/g) to wash, and at the end, with diluted ethanol (~5%).

The maghemite (Fe_2O_3) nanoparticles were synthesized by the method described by Sun et al. [9]. First, Magnetite (Fe_3O_4) nanoparticles were synthesized according to the method proposed by Qu et al. [10] with some modification. Briefly, 9 mL (2 M) $Fe(NO_3).9H_2O$ (dissolved in 2 M HCl) was added to 300 mL double-distilled water, and 10 mL Na_2SO_3 (1 M) was added to the former solution drop wise in 1 min under magnetic stirring. The colour of the solution changed from light yellow to red, indicating complex ions formed between the Fe^{3+} and SO_3^{2-}. When the color of the solution turned black again, the solution was added to 300 mL $NH_3.H_2O$ solution (0.85 M) under vigorous stirring. A black precipitate is formed and allowed to crystallize completely for about an hour under magnetic stirring. The precipitate was washed with copious amount of water to bring the pH of the suspension to less than 7.5. The suspension was dried into black powder at ambient temperature under vacuum. The black precipitate obtained above was diluted to a volume of 300 mL. The suspension temperature was raised to 90 ^oC in 5 min, and was stirred under aeration for 60

min at about 100 °C. The colour changed from black to reddish-brown slowly while the suspension became clear and transparent. The reddish-brown solution was washed four times with water by magnetic decantation. It was then dried to powder in the oven at 70 °C. The morphology of the synthesised M (Ni, Co, Fe) and MO (NiO, Co_3O_4, Fe_2O_3) nanoparticles was investigated with high resolution scanning electron microscopy (HRSEM), transmission electron microscopy (TEM), electron dispersive spectroscopy (EDX) and X-ray Diffractometry (XRD) using CoKα radiation.

2.2 Equipment and Procedure

The edge plane pyrolytic graphite electrode plate (EPPGE) (3.0 and 5.0 mm diameter) or basal plane pyrolytic graphite electrode plate (BPPGE) (5.0 mm diameter) was purchased from Le Carbone, Sussex, UK and was constructed in-house at the University of Pretoria technical workshop by placing it in a teflon tube, extended outside with a copper wire (held in place with conducting silver varnish L 100 (Kemo Electronic, Germany) to make electrical contact with the electrochemical equipment.

Field emission scanning electron microscope (FESEM) images were obtained from JEOL JSM 6000 LV (Japan), high resolution scanning electron microscope (HRSEM) images were obtained using the Zeiss Ultra Plus 55 HRSEM (Germany), while the energy dispersive x-ray spectra (EDX) were obtained from NORAN VANTAGE (USA) at the Microscopy and Microanalysis Laboratory of the University of Pretoria. TEM experiment was performed using a Model JEOL JEM-2100F field emission transmission electron microscope, Tokyo (Japan). AFM experiments were performed with AFM 5100 System (Agilent Technologies, USA) using a contact mode AFM scanner interfaced with a PicoView 1.4.3 controller (scan range 1.25 μm in x–y and 2.322 μm in z). Silicon type PPP-CONT-20 (Nanosensors®) of thickness 2.0±1.0 μm, length 450±10 μm,

width 50±7.5 μm, spring constants 0.02-0.77 N m^{-1}, resonant frequencies of 6–21 kHz and tip height of 10-15 μm were used. All images (256 samples/line × 256 lines) were taken in air at room temperature and at scan rates 0.5–0.6 lines s^{-1}. The X-ray photoelectron spectra (XPS) were obtained using a Physical Electronics model 5400 spectrometer system with monochromatic Mg Kα radiation at 1253.6 eV at take-off angles of 45°. Infrared spectroscopy data were obtained with PerkinElmer GX 2000 FT-IR Spectrometer attached to a PerkinElmer Auto Image Microscope System equipped with liquid nitrogen cooled MCT detector. The samples were analyzed using KBr in the transmission mode. UV/Vis experiment was performed with a UV-Visible spectrophotometer, 100 Bio Varian Win UV, Australia. The XRD analysis was done using a back loading preparation method. The sample was analysed using a PANalytical X'Pert Pro powder diffractometer with X'Celerator detector and variable divergence- and receiving slits with Fe filtered Co-Kα radiation. The samples are scanned at the required 2θ angle ranges (5° – 90°). The phases were identified using X'Pert Highscore plus software.The voltage and current is 35 kV and 50 mA.

Electrochemical experiments (e.g cyclic voltammetry, square wave voltammetry, Linear sweep voltammetry) were carried out using an Autolab Potentiostat PGSTAT 302 (Eco Chemie, Utrecht, and The Netherlands) driven by the GPES software version 4.9. The RDE experiments were performed using AUTOLAB-RDE, (Eco Chemie, Utrecht, The Netherlands) with a locally fabricated RDE EPPGE electrode (5.0 mm in diameter) as the working electrode. Linear sweep voltammetry (LSV) was performed at potential range of 0.0 to 1.0 V (vs Ag|AgCl, sat'd KCl) after 15 min adsorption (by keeping the electrode in a stirred analyte solution). Electrochemical impedance spectroscopy (EIS) measurements were performed with an Autolab Frequency Response Analyser (FRA) software between 100 mHz and 100 kHz using a 5 mV rms sinusoidal modulation in a

solution of 5 mM of $K_4Fe(CN)_6$ and a 5 mM $K_3Fe(CN)_6$ (1:1) mixture in phosphate buffer solution (PBS) of pH 7.0 and at the $E_{1/2}$ of the $[Fe(CN)_6]^{4-}/[Fe(CN)_6]^{3-}$ vs. Ag|AgCl in sat'd KCl. The FRA software allowed the automatic fitting of the raw EIS data to equivalent circuit models using a *non-linear least squares* (CNLS) method based on the EQUIVCRT programme [11], with *Krammers-Kronig rule check*. EIS experiment was also carried out in buffer solution containing different concentrations of the analytes DEAET, hydrazine, dopamine, nitrite and nitric oxide respectively. Bare EPPGE/BPPGE and modified electrodes are used as working electrode. A Ag|AgCl in saturated KCl and platinum wire were used as reference and counter electrodes, respectively. A bench top pH / ISE ORION meter, model 420A, was used for pH measurements. All solutions were de-aerated by bubbling nitrogen prior to each electrochemical experiment. All experiments were performed at 25 ± 1 °C.

All the procedure involves loading (by drop-dry and electrodeposition method) a thin film of the M or MO/CNT nanocomposite on the base electrode (EPPGE or BPPGE), or a conducting carbon electrode (e.g glass carbon plate in cases where the working electrode did not fit into the machine) in preparation for analysis. The detail of the electrode modification process is discussed below.

2.2.1 Assay of dopamine hydrochloride injection

A 2 mL of the dopamine drug (injection), Dopamine HCl-Fresenius®, sample was diluted to 100 mL with distilled de-ionised water. 2 mL of this diluted solution was pipette into each of 50 mL volumetric flask and all except one were spiked with different concentration of standard dopamine solution (standard addition method), and made to volume with phosphate buffer pH 7.0. The concentration of each test aliquot solution was determined using

square wave voltammetry. Four different injections from the same batch were analysed using the same procedure. The experiment was repeated 5 times for each sample.

2.3 Electrode Modification and Pretreatments

2.3.1 Electrode cleaning

Electrodes were prepared using the following procedures. First, the EPPGE surface was cleaned by gentle polishing in aqueous slurry of alumina oxide nanopowder (Sigma-Aldrich) on a SiC-emery paper and then to a mirror finish on a Buehler felt pad. The electrode was then subjected to ultrasonic vibration in acetone or ethanol to remove residual alumina particles that might be trapped at the surface. On the other hand, BPPGE surface was cleaned by gentle polishing on a carborundum paper and the surface was smoothened by a paper tape. The electrode was then subjected to ultrasonic vibration in absolute ethanol to remove adhesives that might be trapped at the surface.

2.3.2 Electrode modification

2.3.2.1 Drop-dry / electrodeposition techniques

About 20 µL drop of the CNTs/DMF solution (2.5 mg SWCNT-COOH, MWCNT-COOH or SWCNT-PABs in 1 mL DMF) solution was dropped on the bare EPPGE / BPPGE and dried in an oven at 50 ^{o}C for 5 min. The modified electrode obtained is herein denoted as EPPGE-SWCNT, EPPGE-SWCNT-PABs or BPPGE-MWCNT as the case may be. The EPPGE-CNT-M (where M = Fe, Ni or Co) was obtained using similar procedure adopted by others [12-16] for the electrodeposition of metal nanoparticles on carbon electrodes using chronoamperometric strategy. Briefly, EPPGE-CNT was immersed in 5 mM solution of the nitrate salts of the metals ($Ni(NO_3)_2.6H_2O$, $Fe(NO_3)_2.9H_2O$ or $Co(NO_3)_2.6H_2O$, at a fixed potential of -2.0 V (vs

Ag|AgCl, sat'd KCl) for 5 min. A 5 min deposition time as reported by Salimi et al. [12-15] and Giovanelli et al. [16] was chosen for this work. Also the preliminary investigation of the electrochemical response of EPPGE-SWCNT-Ni in 0.1 M NaOH solution obtained at different deposition time's intervals of between 5 - 40 min yielded the highest current response at the lowest deposition time. The resulting electrodes are denoted as, EPPGE-SWCNT-Ni, EPPGE-SWCNT-Co and EPPGE-SWCNT-Fe. EPPGE-Ni, EPPGE-Co and the EPPGE-Fe modified electrodes are obtained through the same procedure but without CNT. The modified electrodes are stored in refrigerator before ready for use. The electrodes, EPPGE-CNT-MO (where M = Fe, Ni or Co) were obtained by immersing the EPPGE-CNT-M in 0.1 M PBS (pH 7.0) and repetitively scanning (20 scans) between 1.5 and -0.8 V potential window at a scan rate of 100 mV/s. The modified electrodes are represented as, EPPGE-SWCNT-NiO, EPPGE-SWCNT-Co_3O_4, EPPGE-SWCNT-Fe_2O_3, EPPGE-NiO, EPPGE-Co_3O_4 EPPGE-Fe_2O_3 respectively. The modification procedure is summarised in scheme 2.2. The electroactive surface coverage area of the electrodes was determined in 5 mM ferri/ferro ($[Fe(CN)_6]^{3-/4-}$) redox probe and estimated by using the relationship; $Q = nFA\Gamma$ [17]).

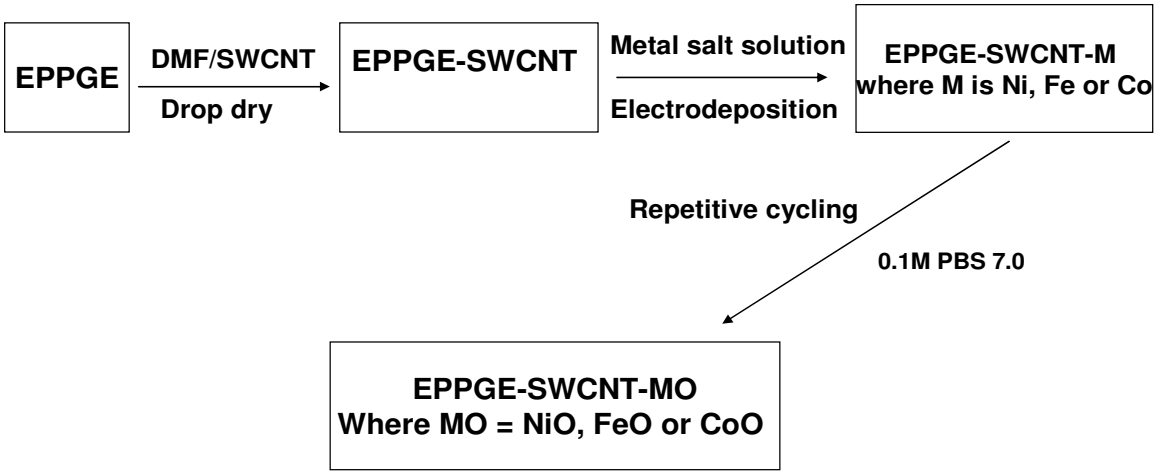

Scheme 2.2: Procedure for the fabrication of metal and metal oxide nanoparticles modified electrodes.

Morphology of the modified electrodes were examined with field emission scanning electron microscopy (FESEM), high resolution scanning electron microscopy (HRSEM), transmission electron microscopy (TEM), atomic force microscopy (AFM), electron dispersive X-ray spectroscopy (EDX) and X-ray photoelectron spectroscopy (XPS).

2.3.1.2 Modification with Prussian blue (PB) nanoparticles

The synthesis of Prussian blue (PB) nanoparticles and its integration with the single-walled carbon nanotubes poly(m-aminobenzene sulphonic acid) (SWCNT-PABS) are described below. EPPGE-SWCNT-PABS was prepared by a drop-dry method. About 20 µL drop of the SWCNT-PABS/H_2O or SWCNT-PABS/CTAB solution (0.1 mg SWCNT-PABS in 1 mL H_2O or 1 mL CTAB solution) was dropped on the bare EPPGE and dried in an oven at 50 ^{0}C for 5 min. The electrodes obtained are herein abbreviated as EPPGE-SWCNT-PABS or EPPGE- CTAB-SWCNT-PABS.

The deposition of PB nanoparticles on the EPPGE-SWCNT-PABS modified electrodes follows the procedure described by Han et al. [18] and summarised in scheme 2.3. $FeCl_3$ and $K_4[Fe(CN)_6]$ of the same concentration (e.g. 10^{-4} M) were used for the deposition experiment. The EPPGE-SWCNT-PABS electrode or the EPPGE-CTAB-SWCNT-PABS electrode was immersed in stirred 10^{-4} M $FeCl_3$ solution for 30min. After 30min, the electrode was rinsed, dried and immersed in 10^{-4} M $K_4[Fe(CN)_6]$ for another 30min. It was then rinse and dry again to give the first layer of PB nanoparticles corresponding to the first deposition cycle. The electrode obtained is herein denoted as EPPGE-SWCNT-PB or EPPGE-CTAB-SWCNT-PB electrode. Second and the third layer of PB nanoparticles were obtained on the electrode by systematically repeating the step described above using solutions of $FeCl_3$ and $K_4[Fe(CN)_6]$.

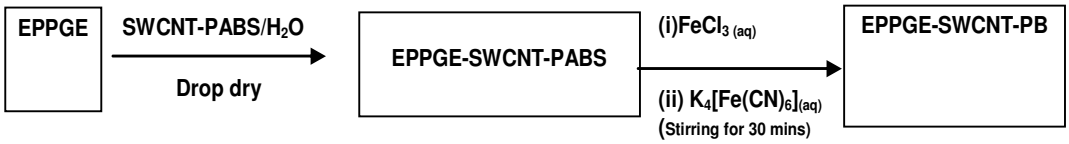

Scheme 2.3: Electrode modification procedure with Prussian blue (PB) nanoparticles.

The modified electrodes morphology were examined with scanning electron microscopy (SEM), transmission electron microscopy (TEM), atomic force microscopy (AFM), electron dispersive x-ray spectroscopy (EDX) and X-ray photoelectron spectroscopy (XPS). The solid SWCNT-PB nanocomposite film formed on the electrode thorugh several layers was scraped and characterized using UV/Vis, infra-red (IR) spectroscopy and X-ray Diffractometry (XRD) using CoKα radiation.

2.3.1.3 Electrode modification with synthesised M and MO nanoparticles.

For the chemical synthesis experiment, acidified MWCNT was used in place of acidified SWCNTs. The motivation for using MWCNT and employing chemical synthesis procedure are: (i) MWCNT was cheaper and commercially available than SWCNT, (ii) chemical synthesis produces M and MO nanoparticles in commercial quantity compared to electrodeposition method, (iii) the synthesised nanoparticles can easily be used on screen printed electrode (SPE) for disposable experiment, (iv) earlier work using SWCNT and electrodeposition method have been associated with adsorption of the analytes due to large surface area of the SWCNT. Electrode modification follows simple drop-dried procedure (Scheme 2.4). Different weight (2.5 to 10 mg) of the synthesised metal (M) and the metal oxides (MO) nanoparticles were weighed and dissolved in dimethylformamide (1 ml DMF) along with and without 2 mg of the

functionalised MWCNT. The mixture was stirred at room temperature for 48 h. About 20 µL of the obtained MWCNT-M was dropped on the EPPGE and left in the oven for 5min. The modified electrode is denoted as EPPGE-MWCNT-M (where M = Ni, Co or Fe). Similar procedure was employed for modifying the EPPG electrode with MO nanoparticles and the resulting electrode is represented as EPPGE-MWCNT-MO (where MO = NiO, Fe_2O_3 or Co_3O_4). Therefore, the modified electrodes obtained are: EPPGE-Ni, EPPGE-Co, EPPGE-Fe, EPPGE-MWCNT, EPPGE-MWCNT-Ni, EPPGE-MWCNT-Co, EPPGE-MWCNT-Fe; EPPGE-NiO, EPPGE-Co_3O_4, EPPGE-Fe_2O_3, EPPGE-MWCNT-NiO, EPPGE-MWCNT-Co_3O_4 and EPPGE-MWCNT-Fe_3O_4.

The electrodes morphology were examined with high resolution scanning electron microscopy (HRSEM), transmission electron microscopy (TEM), atomic force microscopy (AFM), electron dispersive spectroscopy (EDX) and X-ray Diffractometry (XRD) using CoKαradiation.

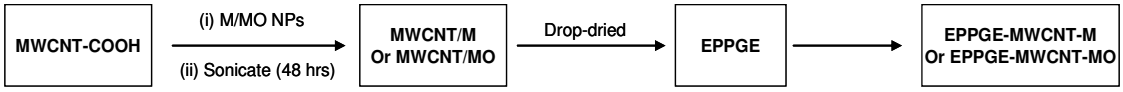

Scheme 2.4: Procedure for electrode modification with synthesized metal (M) and metal oxides (MO) nanoparticles.

2.4 Electron Transport Experimental Procedure

The electron transport (ET) of the redox-active M, MO and PB nanoparticles integrated with or without CNTs were interrogated in a solution containing an outer-sphere redox probe 5 mM $[Fe(CN)_6]^{3-}/[Fe(CN)_6]^{4-}$ using cyclic voltammetry (CV) and electrochemical impedance spectroscopy (EIS). This usually represents a preliminary experiment conducted to establishing the successful modification and the electrical properties of the redox

active nano materials on the modified electrodes. Bare and modified EPPG or BPPG electrodes were used as the working electrode. Ag|AgCl, sat'd KCl and platinum electrodes were employed as reference and counter electrodes respectively. The CV experiment was done by running the bare and the modified electrodes in the $[Fe(CN)_6]^{3-}/[Fe(CN)_6]^{4-}$ redox probe within the potential window of 0.2 to 1.0 V at a scan rate of 50 mVs^{-1}. From the voltammogram obtained, the $E_{1/2}$, ΔE, E_p, I_p, I_c, I_p/I_c for the electrodes were determined and these parameters gave insight into the electron transport properties of the respective electrodes. The EIS experiment is conducted by running the bare and the modified electrodes in $[Fe(CN)_6]^{3-}/[Fe(CN)_6]^{4-}$ solution ($E_{1/2}$ 0.2 or 0.3 V vs. Ag|AgCl in sat'd KCl) between 100 mHz and 10 kHz using a 5 mV rms sinusoidal modulation. The data points generated are fitted with a particular equivalent circuit and the charge transfer resistant (R_{ct}) which controls the electron transfer kinetics of the redox probe at the electrode interface is determined from the EIS fitting.

2.5 Electrocatalytic and Electroanalysis Experiment procedure.

2.5.1 Electrocatalytic procedure

Experiments for electrocatalytic oxidation of the analytes (e.g. DEAET, Hydrazine, Nitrite and Dopamine) were carried out using N_2 purged PBS and Na_2SO_4 solutions at different pH at which the analyte ionizes best unless otherwise stated. For example, 10^{-4} M DEAT was prepared in 0.1 M pH 9.4 PBS, 10^{-3} M nitrite was prepared in 0.1 M pH 7.4 and pH 3.0 PBS, 10^{-3} M hydrazine was prepared in 0.1 M pH 7.0 Na_2SO_4 solution, and 2 x 10^{-4} M dopamine was prepared in 0.1 M pH 7.0 PBS respectively. Generally, the experiment was carried out at scan rate of 25 mVs^{-1} and within the oxidation potential window as wide as -1.3 to 1.3 V. The

electrocatalytic experiment was divided into two parts: (i) catalysis using electrode modified by electrodeposition of metal and metal oxide nanoparticles and (ii) catalysis using electrode modified with chemically synthesised metal and metal oxide nanoparticles. In each case, a comparative study of the electrocatalytic behaviour of the modified electrodes towards the analyte was investigated. Preliminary characterisation study showed that DEAET and hydrazine are better catalysed on Ni modified electrode, nitrite on Co modified electrodes and dopamine on Fe modified electrode. Thus in this study, DEAET and hydrazine electrocatalysis was focused on Ni and NiO modified electrode, nitrite on Co and Co_3O_4 modified electrodes and dopamine on Fe and Fe_2O_3 modified electrodes. The interfering effect of ascorbic acid (AA) in a mixture containing dopamine (9.1 μM DA) and 1000 folds AA concentration (9.1 mM AA) was carried out. Dopamine oxidation on PB modified electrodes (described above) was also investgated. Effect of PB concentration (i.e 10^{-4}, 10^{-3} and 10^{-2} M PB) and deposition cycles or layer of PB that is, EPPGE-SWCNT-PB, EPPGE-SWCNT-2PB and EPPGE-SWCNT-3PB towards electrocatalytic oxidation of $2x10^{-4}$ M DA solution was studied. Other electrodes investigated are EPPGE-PB, EPPGE-SWCNT-PABS, EPPGE-CTAB-SWCNT-PABS, EPPGE-SWCNT-PB, EPPGE-CTAB-SWCNT-PB. The effect of stabilising agent such as cetyltrimethylammonium bromide (CTAB) on PB electrocatalytic activities towards DA was studied and compared with electrode modified without CTAB.

Generally, cyclic voltammetry (CV) and electrochemical impedance (EIS) experiments were conducted to investigating the electrocatalytic behaviour of the electrodes towards the analyte. From CVs experiment, electrochemical parameters such as peak current (I_p), peak potential (E_p), ΔE and formal potential ($E_{1/2}$) were measured and discussed. In addition, square wave voltammetry (SWV) and rotating disc electrode (RDE) experiments were carried

out for DA to monitoring its kinetic at the electrode, and to monitoring the interfering effect of AA on DA at the electrode. In every case of measurement, the bare or modified electrode is the working electrode while Ag|AgCl, sat'd KCl and platinum electrodes are the reference and counter electrodes respectively. EIS experiment was done by fixing the peak potential (E_p) at which the analyte was best catalyzed (vs Ag|AgCl, sat'd KCl) or its half potential ($E_{1/2}$) especially for a reversible electrocatalytic process.

2.5.2 Electroanalysis procedure

The effect of scan rate (25 to 1000 mVs^{-1}) on the electrode kinetics during analyte oxidation was investigated using the best electrode from the electrocatalytic experiment. Several kinetic parameters such as E_p, I_p, the peak-to-peak separation (ΔE_p) were obtained. The plot of the anodic (I_{pa}) peak current against square root of scan rate ($\nu^{1/2}$) which is an indication of diffusion-controlled reaction was investigated.

As part of the analysis experiment, concentration study on each analyte was carried out using chronoamperometric (CA) experiment. Analysis of the analytes was carried out at their respective peak potential of catalysis. For example, a peak potential of 0.6 V was fixed during DEAET and hydrazine, 0.8 V for nitrite and 0.2 V for dopamine analysis respectively. Different aliquot of the stock analyte solution (corresponding to different concentrations) was injected into 25 or 30 mL of buffer solution and the mixture stirred thoroughly for 5 min. The modified electrode is run in both the buffer and the analyte solutions and the chronoamperogram obtained after 40 to 60 min. From the chronoamperogram, the catalytic current I_{cat} and the buffer current I_{buff} were estimated and recorded. The catalytic rate constant K [19,20] and the diffusion coefficient D [21] of the analyte on the electrode were calculated.

From the plot of peak current response I_p versus different analyte concentration *[analyte]*, sensitivity and the limit of detection (LoD =3.3 s/m [22], where *s* is the relative standard deviation of the intercept and *m*, the slope of the linear current versus the concentration of analyte) were estimated.

To evaluate the extent of adsorption of the analyte at the electrode, linear sweep voltammetry experiment was carried out at different concentration of the analyte. Different aliquot of the sample (corresponding to different concentrations) was injected into 25 or 30 mL of buffer solution and the modified electrode was left in the solution while stirring for 15 min. Thereafter, experiments were carried out using the modified electrodes as the working electrodes in the analyte solution at 25 mVs^{-1} with a potential range of 0.0 to 1.0 V. From the linear sweep voltammogram obtained and applying the Langmuir adsorption isotherm theory (Equation 2.3 [23]), the adsorption equilibrium constant (β) and the standard free energy (ΔG^o) due to adsorption were calculated. The symbols are defined in Chapter 1 and represented on the list of symbols.

$$\frac{[\text{Analyte}]}{I_{cat}} = \frac{I}{\beta I_{max}} + \frac{[\text{Analyte}]}{I_{max}} \qquad (2.3)$$

2.6 Electrochemical supercapacitive procedure

The electrochemical supercapacitive behaviour of the MO or CNT/MO modified electrodes in 1 M Na_2SO_4 (neutral) and 1 M H_2SO_4 (acidic) solutions was studied using cyclic voltammetry (CV), charge discharge (CD) and electrochemical impedance spectroscopy (EIS) experiments. In this experiment, BPPGE was used as the base electrode because of his high capacitive current in 5 mM $Fe(CN)_6]^{4-}$ /$[Fe(CN)_6]^{3-}$ redox probe compared with EPPGE. The supercapacitor experiment was mainly focused on the MO modified electrodes for

the following reasons: (i) the CVs for MO or CNT/MO modified electrode gave high charging or capacitive current in most cases in the electrolytes used in this study (see Chapters 3 and 4) (ii) because of the electroactive nature of the material, it is envisaged that the metal nanoparticles (Ni, Fe and Co) will possibly oxidized to their oxide state in the electrolytes used for the supercapacitive study, thus may not give the true picture of their capacitive behaviour.

The supercapacitor experiment is divided into two: (i) using CNT-MO (where M= Ni, Co and Fe) materials made by electrodeposition and (ii) using CNT-MO materials made by chemical synthesis. For the electrodeposition experiment, the electrodes investigated are: BPPGE, BPPGE-NiO, BPPGE-Fe_2O_3, BPPGE-Co_3O_4, BPPGE-SWCNT, BPPGE-SWCNT-NiO, BPPGE-SWCNT-Fe_2O_3, and BPPGE-SWCNT-Co_3O_4. For the chemical synthesis experiment, the electrodes investigated are: BPPGE, BPPGE-NiO, BPPGE-Fe_2O_3, BPPGE-Co_3O_4, BPPGE-MWCNT, BPPGE-MWCNT-NiO, BPPGE-MWCNT-Fe_2O_3, and BPPGE-MWCNT-Co_3O_4. Comparative CV of the electrodes was carried out in 1 M Na_2SO_4 and 1 M H_2SO_4 electrolyte solutions at potential window of 0.2 - 0.8 V (vs Ag|AgCl, sat'd KCl) using three electrode electrochemical system. EIS studies was carried out in 1 M Na_2SO_4 and 1 M H_2SO_4 aqueous electrolytes at a bias potential of 0.3 V (vs Ag|AgCl, sat'd KCl). Charge-discharge (CD) experiment of the electrodes in 1 M Na_2SO_4 and 1 M H_2SO_4 was investigated at different current densities (0.5 to 10 A/g) and potential window of 0.2 - 0.8 V. In the CD experiment, three electrode systems was employed, the modified electrode is the working electrode, Ag|AgCl, sat'd KCl and platinum as the reference and counter electrode respectively. Comparative CD values for the electrodes were estimated at the current density of 0.5 A/g while stability study for the electrode with the highest SC value was carried out at current density of 10 A/g.

The electrochemical performance of the prepared powder of MWCNT-MO nanocomposite made by chemical synthesis was also investigated using two-electrode coin-type cells (CR 2032) with steel foil as reference electrode. The working electrode was assembled by coating the slurry of the MWCNT-MO on an aluminium foil current-collector of 12 mm in diameter. The mixture composed of 71.4 wt. % active material, 14.3 wt. % functionalised MWCNT and 14.3 wt. % binder (polyvinylidene fluoride) in a N-methylpyrrolidione (NMP) solvent. After drying in an oven at 80 ^{0}C for 2 h, the electrodes were pressed under a pressure of 7MPa for 1min. The weight of the active materials was determined by weighing the Al foil before and after pressing the powders. The supercapacitive behaviour was investigated in both acidic (1 M H_2SO_4) and neutral (1 M Na_2SO_4) electrolytes. In each case, both the symmetric (using MWCNT-MO as both anode and cathode material) and asymmetric (using MWCNT-MO as anode and CNT alone as cathode material) assembly are studied. In the asymmetry assembly, the working electrode (MWCNT-MO) was used as the positive electrode while the CNT was used as the negative electrode. The electrodes were soaked in the electrolyte for about 10 min before assembled in the coin cells. A polypropylene (PP) film (Cellgard 2400) was used as the separator.

References

1. J.A. Liu, , G. Rinzler, H. Dai, J.H. Hanfer, R.K Bradley, P.J. Boul, A. Lu, T Iverson, K. Shelimov, C.B. Huffman, F.R. Macias, Y.S. Shon, T.R. Lee, D.T. Colbert, *Science* 280 (1998) 1253.

2. S.H. Wu, D.H. Chen, *J. Colloid Interf. Sci*. 259 (2003) 282.

3. L. Xiang, X.Y. Deng, Y. Jin, *Scripta Mater.* 47 (2002) 219.

4. J. Shen, Y. Hu, C. Li, C. Qin, M. Ye, 53 (2008)7276.

5. W-L. Yao, J-L. Wang, J. Yang, G-D. Du, *J. Power Sources* 176 (2008) 369.

6. Y-P. Sun, X-q. Li, J. Cao, W-x. Zang, H. P. Wang, *Adv. Colloid Interf. Sci.* 120 (2006) 47.

7. W. Zhang, *J. Nanopart. Res.* 5 (2003) 323.

8. C. Wang, W. Zhang, *Environ. Sci. Technol.* 31 (1997) 2154.

9. Y-K. Sun, M. Ma, Y. Zhang, N. Gu, *Colloids and Surfaces A: Physicochem.Eng.Aspects* 245 (2004) 15.

10. S. Qu, H. Yang, D. Ren, S. Kan, G. Zou, D. Li, M. Li, *J. Colloid Interf. Sci.* 215 (1999) 190.

11. B.A. Boukamp, *Solid State Ionics* 20 (1986) 31.

12. A. Salimi, R. Hallaj, S. Soltanian, *Biophys. Chem.* 130 (2007) 122.

13. A. Salimi, E. Sharifi, A. Noorbakhsh, S. Soltanian, *Electrochem. Commun.* 8 (2006) 1499.

14. A. Salimi, E. Sharifi, A. Noorbakhsh, S. Soltanian, *Biophys. Chem.* 125 (2007) 540.

15. A. Salimi, E. Sharifi, A. Noorbakhsh, S. Soltanian, *Biosens. Bioelectron.* 22 (2007) 3146.

16. D. Giovanelli, N.S. Lawrence, S.J. Wilkins, L. Jiang, T.G.J. Jones, R.G. Compton, *Talanta* 61 (2003) 211.

17. J. Wang, *Analytical Electrochemistry*, VCH, New York, 1994, ch. 6, p. 171.

18. S. Han, Y. Chen, R. Pang, P. Wan, M. Fan, *Ind. Eng. Chem. Res.*, 46 (2007) 6847.

19. M.H. Pournaghi-Azar, R. Sabzi, *J. Electroanal. Chem.* 543 (2003) 115.

20. K.M. Manesh, P. Santosh, A.I. Gopalan, K.P. Lee, *Electroanalysis* 18 (2006) 894.

21. A.J. Bard, L.R. Faulkner *Electrochemical Methods: Fundamentals and Applications*, 2nd ed, John Wiley & Sons, Hoboken NJ (2001).

22. G. D. Christian, Analytical Chemistry, 6th ed. John Wiley and Sons New York, 2004, p 113.

23. H.X. Ju, L. Donal, *J. Electroanal. Chem.* 484 (2000) 150.

SECTION B

RESULT AND DISCUSSION

---

*Chapters 3-10 comprise the results and discussion and the publications in peer-reviewed journals that are obtained from this thesis.

CHAPTER THREE

Insights Into the Electro-oxidation of Hydrazine at Single-Walled Carbon-Nanotube-Modified Edge-Plane Pyrolytic Graphite Electrodes Electrodecorated with Metal and Metal Oxide Films*

* The publication below resulted from part of the research work presented in this chapter and it is not referenced further in this thesis:

1. **Abolanle S. Adekunle**, Kenneth I. Ozoemena, *J. Solid State Electrochem*. 12 (2008)1325-1336.

3.1 Comparative FESEM images and Electron-Dispersive X-rays.

Figure 3.1 compares the SEM images of the bare EPPGE, EPPGE-SWCNT and EPPGE-SWCNT-Ni. The edge-plane sites of the EPPGE are evident in its SEM image (a).

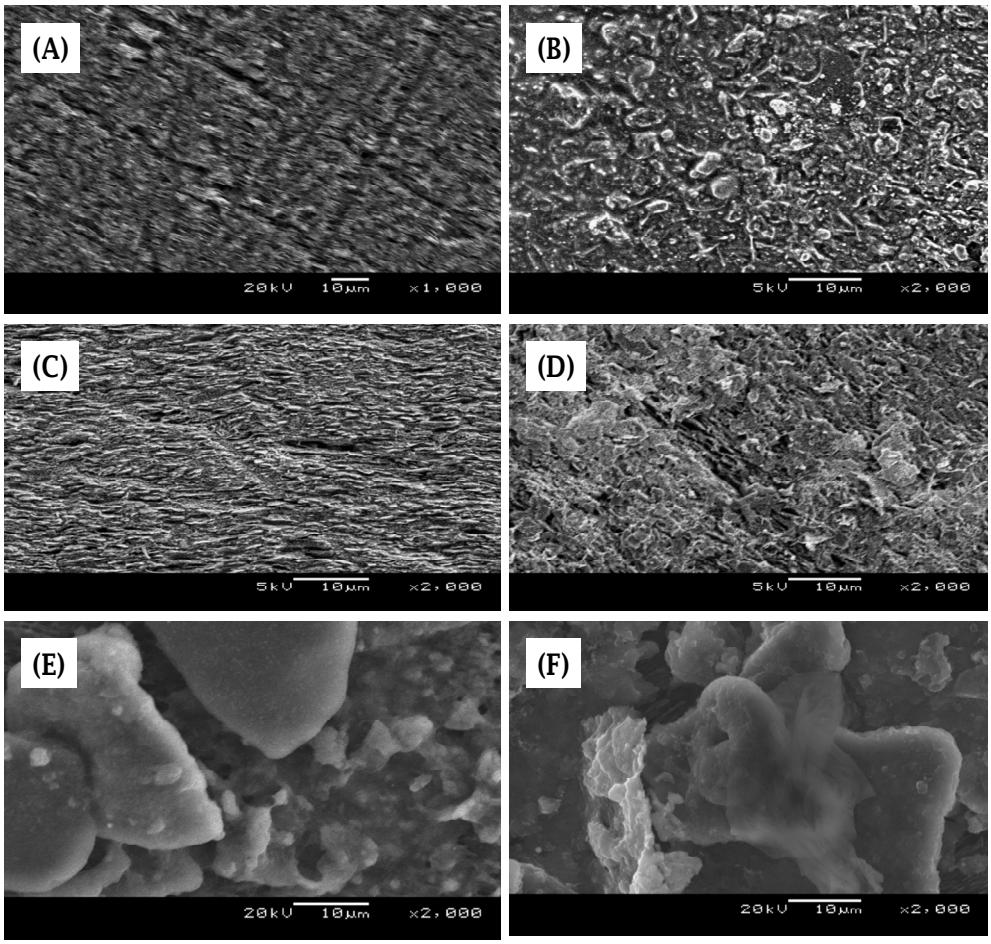

Figure 3.1: Typical FESEM images of the (a) bare EPPGE, (b) EPPGE- SWCNT, (c) EPPGE-SWCNT-Ni, (d) EPPGE-SWCNT-Fe, (e) EPPGE-SWCNT-NiO and (f) EPPGE-SWCNT-FeO.

Upon modification of the EPPGE with the acid-treated and washed SWCNTs, the morphology shows aggregated SWCNTs (b). Upon introduction of the metal particles, an interconnected layer-structured network image of the SWCNT-modified EPPGE (c and d) was observed. However, upon electrochemical treatment in aqueous solution these layer-structured networks become disconnected

transforming into lumps with exposed interiors (e and f), with sizes in the micrometer ranges. As also speculated by other workers [1,2]. It may be reasonable to assume here that these metal particles could either be trapped in the graphite layers and/or located on the outside of the tubes exposed to the solutions, and/or mixed amongst the aggregated bundles of the tubes. To corroborate the SEM results, EDX experiments were run at the various electrodes. The EDX profile (Figure 3.2) gives the analytical details of the elemental composition of the different electrodes. As expected, the unmodified EPPGE (a) predominantly showed carbon. The acid-treated SWCNT (b) confirmed presence of oxo-funtionalities, with sulphur peak which could have arisen from the sulphuric acid solution used in the fuctionalization and washing of the SWCNTs.

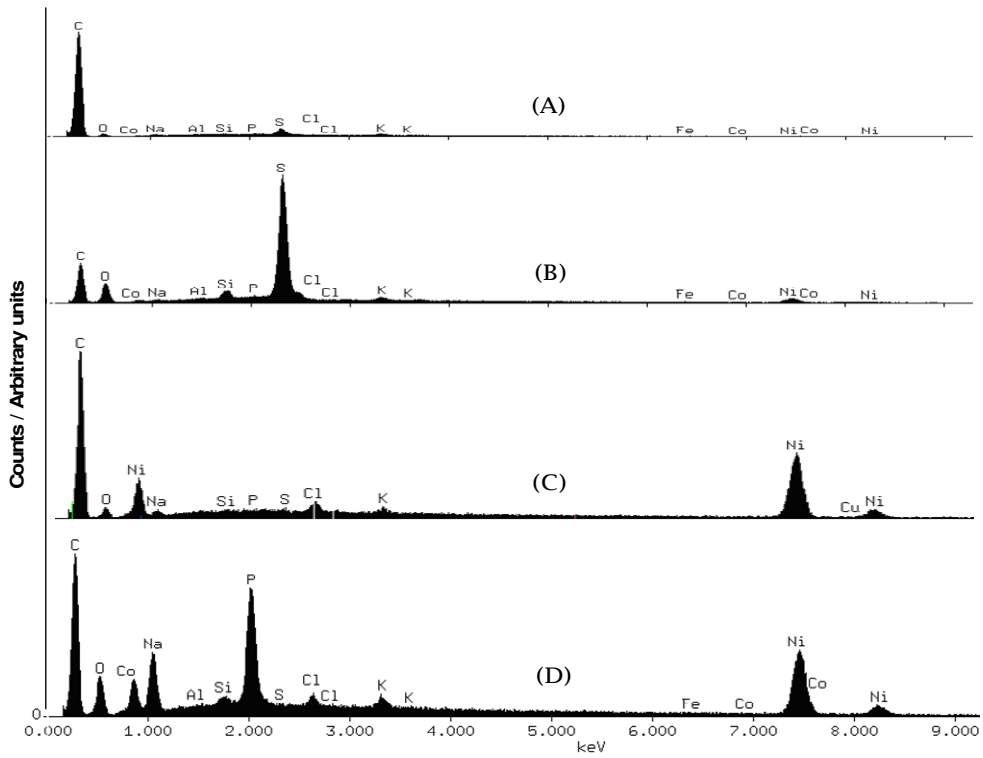

Figure 3.2: Typical EDX plots of the (a) bare EPPGE, (b) EPPGE-SWCNT, (c) EPPGE-SWCNT-Ni, and (d) EPPGE-SWCNT-NiO.

Traces of nickel impurities on the acid-treated and washed SWCNTs indicate these metal impurities are intrinsic to the Aldrich SWCNTs used in this study and cannot be completely removed. A similar result has recently been reported by Jurkschat et al. for HiPCo SWCNTs found to contain iron impurities [3]. The EDX profile of EPPGE-SWCNT-Ni (c) and EPPGE-SWCNT-NiO (d) showed well defined nickel peaks, confirming the successful electrodecoration of the EPPGE-confined SWCNTs. The occurrence of P and Na peaks in the EDX of EPPGE-SWCNT-NiO is ascribed to the treatment of the electrode with sodium phosphate buffer solution while the enhanced oxygen peak confirms the modification of the electrode to its oxide form. Similar trend in the SEM images and EDX profiles were observed for the Fe- and Co-based electrodes (not shown).

3.2 Comparative Redox Chemistry of modified EPPGEs in Aqueous Solution

Figure 3.3 shows examples of the voltammetric responses of the bare and modified EPPGEs (EPPGE-NiO, EPPGE-SWCNT, EPPGE-SWCNT-NiO, EPPGE-SWCNT-FeO and EPPGE-SWCNT-CoO) in 0.1 M phosphate buffered solution (pH 7.0). Successful integration of the metals and metal oxides films with the SWCNTs was observed, confirmed by features such as (i) the presence of the well-defined redox waves of the M(II)/M(III) (M = Ni, Fe and Co; $E_{1/2} \approx 0.45$ V vs Ag|AgCl, sat'd KCl); (ii) the increased current response following the incorporation of the metal particles with the SWCNTs, and (iii) the high background current of the EPPGE-SWCNT-MO compared to other electrodes. These metal oxide nanoparticles exhibit electrochemical stability as the redox peak (II) remained essentially the same even after 50th scan. Some other important features in Figure 3.3 are (i) EPPGE-SWCNT exhibited a pair of weak redox peak ($E_a \approx -0.01$ V and $E_c \approx -0.30$ V), which is typical of immobilized SWCNTs at a carbon electrode. The origins of the broad

cathodic couples (I/I') are the redox processes of the SWCNTs and/or overlapped processes of the M(I)/M(II) and SWCNTs, while the other couple (II/II') are due to the redox processes of the M(II)/M(III). The voltammograms are unsymmetrical with the ratios of the oxidation to reduction charges larger than unity, which are characteristic of quasi-reversible behaviour [4].

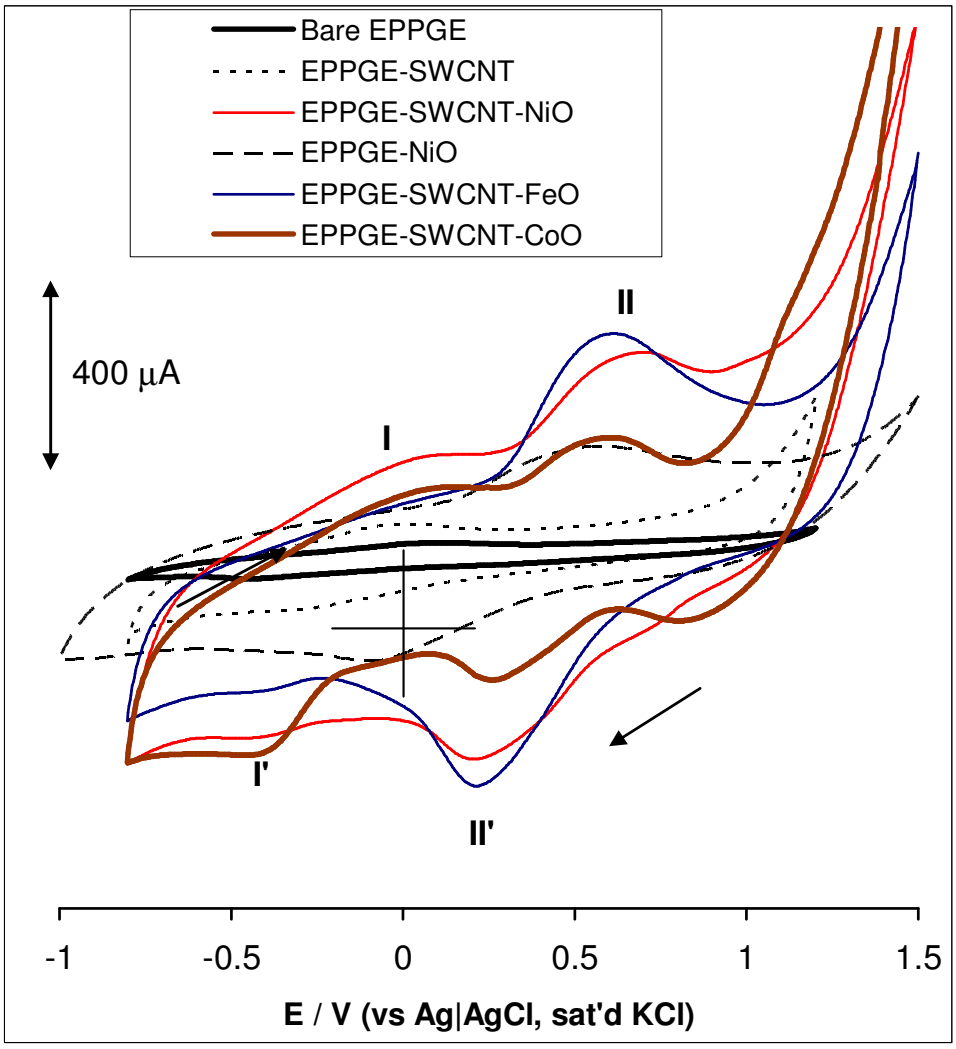

Figure 3.3: Examples of voltammetric evolutions of the bare-EPPGE and modified EPPGEs in 0.1 M pH 7.0 PBS. Scan rate = 50 mV/s. The voltammograms of the modified EPPGEs were obtained after 20 continuous scans. Other scans have been omitted for clarity.

An interesting observation here is the significant decrease in the peak-to-peak separation potential (ΔE) value of the M(II)/M(III)

redox process in the presence of SWCNTs (ΔE = 0.37, 0.42 and 0.50 V for CoO, FeO and NiO, respectively) compared to the absence of SWCNTs (ΔE = 0.70 V). Also, the electrochemical response of the cobalt based electrode is lower than those of the iron and nickel based electrodes. In general, the results suggest the ability of the SWCNTs to serve as efficient conducting carbon materials for electronic communication between the metal nanoparticles and the underlying carbon electrode, EPPGE.

3.3 Comparative electrocatalytic oxidation of hydrazine

Figure 3.4 compares the voltammetric evolutions of the various electrodes in 0.1 M Na_2SO_4 containing 1 mM hydrazine. For a clearer picture of the electro-oxidative responses of the electrodes, the observed voltammograms were subtracted from those generated by their respective electrolytes (as exemplified in Figure 3.4b using the EPPGE-SWCNT-Ni). Peaks (I) (broad at ~ 0.0 V), II ($E_{1/2}$ = 0.35 V) and (III) (E_p = 0.60 V) are due to the redox processes of the SWCNTs, nickel and hydrazine oxidation, respectively. In general, peak current (after background current subtraction) of the hydrazine followed this trend: EPPGE-SWCNT-Ni (~ 44 μA) > EPPGE-SWCNT (~ 37 μA) > EPPGE-SWCNT-Fe (~ 26 μA) > EPPGE-SWCNT-CoO (~23 μA) > EPPGE-SWCNT-NiO (~ 21 μA) > EPPGE-SWCNT-Co (~19 μA) > EPPGE-SWCNT-FeO (~ 18 μA) > EPPGE-FeO (~17 μA) > EPPGE-Fe (~ 16 μA) > EPPGE-Ni (~15 μA) ≈ EPPGE-NiO ≈ Bare EPPGE (~ 15 μA). The oxidation peak of the EPPGE-SWCNT-Ni appeared at about 0.6 V while others occurred at slightly more positive potentials (≥ 0.66 V). The EPPGE modified with metal and metal oxide layers showed weak oxidation peak at more positive potential (*ca.* 0.1 V), suggesting that in the experimental conditions employed in this study, metal and metal oxide layers did not show activity towards hydrazine.

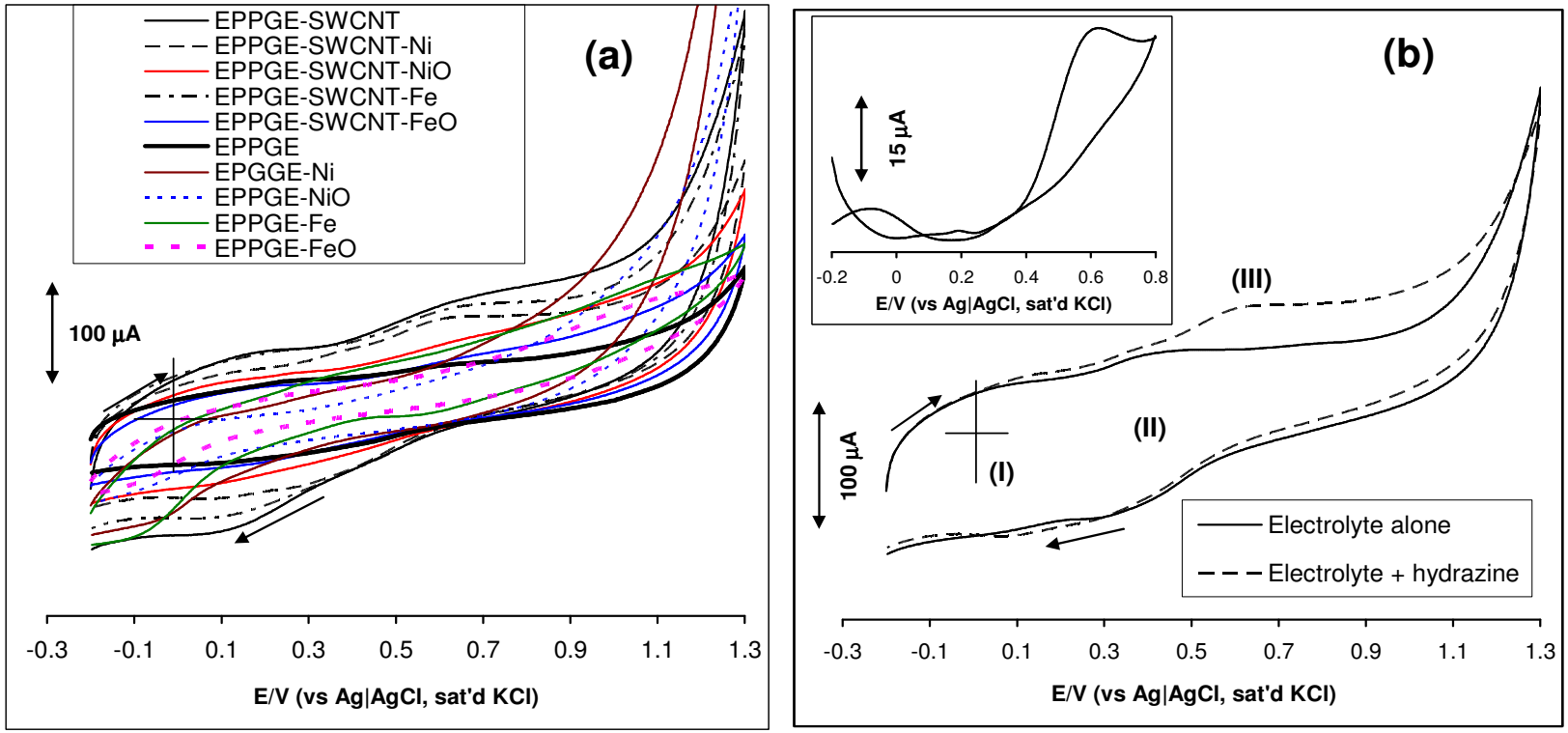

Figure 3.4: (a) Examples of cyclic voltammograms recorded at the various electrodes in 0.1 M Na_2SO_4 solution containing 1 mM hydrazine, and (b) comparative cyclic voltammograms recorded at the EPPGE-SWCNT-Ni in 0.1 M Na_2SO_4 with and without hydrazine. Inset of (b) is the background substracted hydrazine response of the EPPGE-SWCNT-Ni. Scan rate = 25 mVs^{-1}.

The response of the EPPGE-SWCNT is associated with larger background (capacitive) current compared to other electrodes, which is characteristic of acid-treated SWCNTs [5]. The response of SWCNT towards hydrazine oxidation is somewhat controversial. For example, while Guo and Li [6] did not observe any electro-oxidation of hydrazine at SWCNT-paste electrode, Banks and co-workers have consistently observed electro-oxidation of hydrazine at basal plane pyrolytic graphite electrodes modified with either MWCNTs [7,8] or SWCNTs [1,3] which they attributed to the presence of iron oxide impurities. Since the EDX results for the Aldrich SWCNTs (B) did not show iron oxide impurities and no dramatic current responses with both the EPPGE-SWCNT-Fe and EPPGE-SWCNT-FeO was obseved, the influence of iron oxide influencing the electro-oxidation of hydrazine was ruled out; the most likely metal catalyst impurities are the nickel and its oxides. The better electrochemical response exhibited by the EPPGE-SWCNT-Ni compared to other electrodes could be due to the synergistic activities of SWCNTs and Ni particles. The low current response of the metal oxide based electrodes is interesting in that, up to now, for example, only carbon electrodes modified with nickel oxide nanoparticles have been reported for electrocatalytic detection. For example, Salimi *et al.* have used GCEs modified with nickel oxide or cobalt oxide nanoparticles to study the electrochemistry of haemoglobin [9,10], hydrogen peroxide [11], catalase [12] and glucose oxidase [13]. The low response of the nickel oxides modified electrode is attributed to surface layer passivation during electrode modification which results in the layers acting as insulator to charge transfer. Following the better electroactivity of the EPPGE-SWCNT-Ni over the other electrodes, all subsequent studies in this work, unless otherwise stated, were focussed on this electrode.

3.4 Electrochemical impedimetric studies

Insights into the electro-oxidation process of hydrazine at these electrodes were obtained from electrochemical impedance spectroscopy (EIS), at a fixed potential (0.6 V vs Ag/AgCl, sat'd KCl). EIS is a powerful, non-destructive and very informative technique for probing molecules at surfaces. For example, it provides vital information about the charge transfer phenomenon across the electrode|electrolyte interface [14-19]. Figure 3.5 shows examples of the impedance spectra (Nyquist plots) obtained with the electrodes, EPPEGE-SWCNT, EPPGE-SWCNT-Fe, EPPGESWCNT-Ni and EPPGESWCNT-Co at frequencies between 10 kHz and 0.1 Hz.

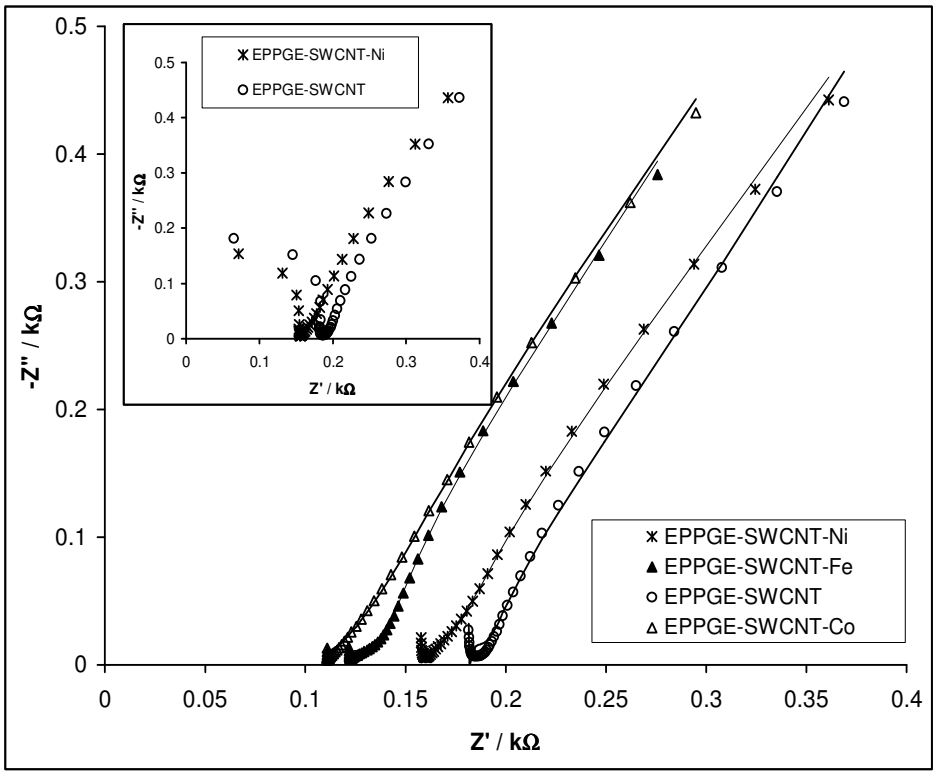

Figure 3.5: Examples of typical Nyquist plots of modified EPPGEs obtained in 0.1 M Na_2SO_4 containing 1 mM hydrazine, between 10 kHz and 0.1 Hz. Inset are similar plots obtained 100 kHz and 0.1 Hz. The data points are experimental while the solid lines represent fitted (theoretical) spectra obtained from the proposed equivalent circuit model shown in figure 5b.

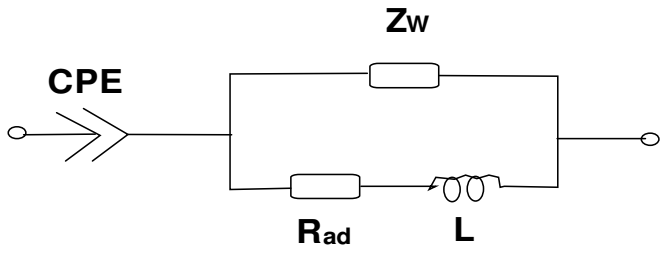

Figure 3.5b: Equivalent circuit model used in fitting the spectra obtained in Figure 3.5a.

The impedance spectra were rather complicated, showing small and distorted semicircle in the high frequency region. Several efforts to obtain a suitable equivalent circuit, including the original Randles model [1] that describes 'true' Faradaic process (i.e., true charge transfer at the electrode|solution interface) were unsuccessful. However, the equivalent circuit model (Figure 3.5b), which incorporates the constant phase element (CPE) and an inductor *L,* yielded satisfactory results as evident from the low percentage error values as evident in Table 3.1. These EIS data were obtained from fitting the equivalent cirquits after several iterations. Presently, the impedance behaviour of the electro-oxidation of hydrazine is virtually non-existent. From the abstract of the only existing report on the electro-oxidation of hydrazine, carried out in alkaline solution on Pd dispersed over graphite cloth, by Duarte *et al*. [20], it is understood that the impedance behavior of the system was also complex. The complexity of the spectra was attributed to several factors including electrode structure, interfacial graphite properties and reaction kinetics. The authors [20] also observed small and distorted semicircle in the high frequency region which they attributed to the porous structure of this carbon-based electrode. The complex impedance behaviour observed in this system may also be associated to the same factors as interpreted by Duarte *et al*. [20].

Table 3.1: Impedance data ($E_{1/2}$ = 0.6V) for the electrocatalytic oxidation of 10^{-3} M Hydrazine (between 10 kHz and 0.1 Hz) on the modified and unmodified EPPGE-electrodes. All values were obtained from the fitted impedance spectra after several iterations using the circuits. Note that the values in parentheses are errors of data fitting.

Electrodes	**Q / mF**	**N**	**Z_w / μΩcm^2**	**L / mHcm^2**	**R_{ad} / μΩcm^2**
EPPGE	0.32 ±0.02	0.62 ±0.02	1.85 ±0.12	0.75 ±0.08	32.60 ±0.98
EPPGE-SWCNT	0.49 ±0.03	0.84 ±0.02	3.92 ±0.21	0.93±0.09	45.16 ±0.71
EPPGE-SWCNT-Ni	0.47 ±0.03	0.81 ±0.02	3.67 ±0.19	0.64 ±0.06	32.94 ±0.47
EPPGE-SWCNT-Fe	0.53 ±0.02	0.84 ±0.01	5.34 ±0.26	0.54 ±0.04	31.39 ±0.34
EPPGE-SWCNT-Co	0.50±0.02	0.80±0.01	5.85±0.28	0.50±0.04	26.23±0.35
EPPGE-SWCNT-NiO	0.37 ±0.02	0.82 ±0.02	2.42 ±0.16	0.39 ±0.04	24.10 ±0.33
EPPGE-SWCNT-FeO	0.28 ±0.01	0.73 ±0.01	8.62 ±0.45	0.41 ±0.04	22.48 ±0.38
EPPGE-SWCNT-CoO	0.35±0.02	0.84±0.02	3.69±0.22	0.36±0.04	19.95±0.29

The absence of the solution resistance in the equivalent circuit model suggests that at high frequency the spectra (semi-circle) could possibly extend to the zero point of the real and imaginary impedance plots. Figure 3.5 (inset) shows Nyquist plots carried out between 100 kHz and 0.1 Hz, indicating the possibility of obtaining such semi-circle loop extending the zero point. In this electrical equivalent circuit (Figure. 3.5b), R_{ad} (resistance to adsorption) and L are well known as electrical elements associated with the adsorption of reaction intermediate(s) [21-23], clearly suggesting the involvement of the hydrazine intermediate products in the overall electrooxidative process. Duarte *et al*. [20] also detected the existence of an adsorbed intermediate in their system. In electrocatalytic reactions, it is known that inductive behaviour takes place when the Faradaic current is governed by the occupation of an intermediate state [21,23]. The R_{ad} value is therefore interpreted here as the consequence of the adsorption of the intermediate(s) on the electrodes. The R_{ad} values of the metal oxide films are slightly less than those of their metal films, suggesting that the adsorption process is less pronounced at the metal oxides films. *CPE* is ascribed to the geometrical or energetic inhomogeneity of the surface and it is related to n. The n is a factor describing the deviation from the ideal capacitive behaviour (i.e., n = 1.0). Thus, the n value of less than the ideal 1.0 is indicative of pseudocapacitaive processes confirming the presence of the CPE in the circuit. The Warburg (Z_w) impedance relates to the semi-infinite linear diffusion. This occurrence of the inductance was attributed to to the electrode, possibly due to the intermediate absorbed species during the electro-oxidative reactions of hydrazine (further discussed below).

More information on the electrical properties of the electrodes during hydrazine oxidation is provided by closer look at the Bode plot (Figure 3.6).

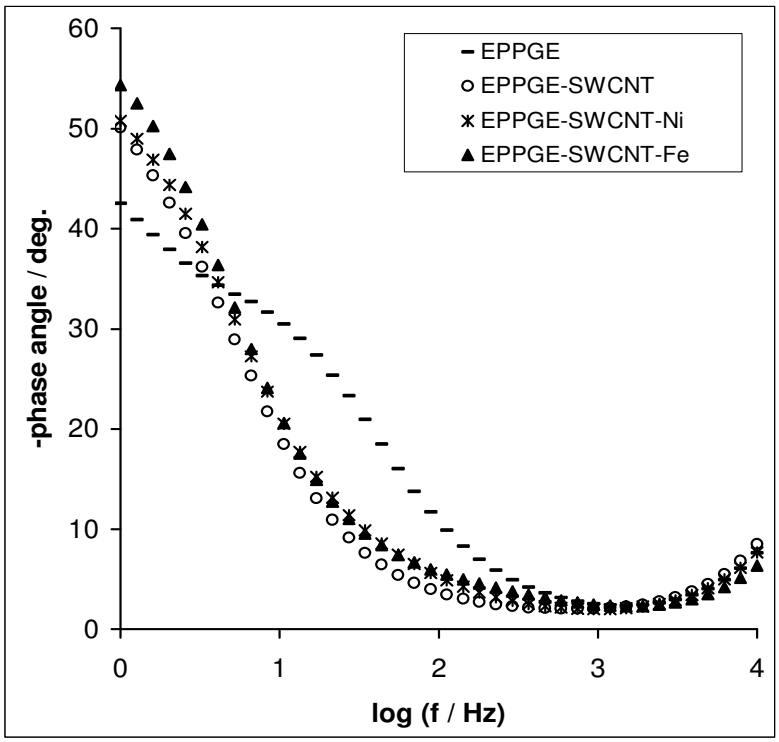

Figure 3.6: Examples of typical Bode plots of modified EPPGEs obtained in 0.1 M Na_2SO_4 containing 1 mM hydrazine, between 10 kHz and 0.1 Hz.

The appearance of a dip or curve in the high frequency region (Figure 3.6) rather than a peak, normally observed for solution resistance (R_s) in the high frequency region, could indicate the dominance of the inductance phenomenon over the solution resistance. The peak at about -35° depicts the relaxation process of the EPPGE|solution interface; the disappearance of this peak confirms the modification of the EPPGE and replacement by the EPPGE-SWCNT-M Film|solution interface.

Inductive behaviour at high frequency range is thought to be due to either the (i) instrumental artifacts, or (ii) the inductance of the electrode, or (iii) the inductance of the connecting wires [24]. To attempt to rule out (i) and (iii), the experiment was repeated for ten times, but same results were obtained. To provide some insights into the possibility of the electrode itself, i.e., possibility (iii), it was thought to be necessary to carry out the experiment in a

simple redox system. The cyclic voltammetric and impedance spectral evolutions of the EPPGE-SWCNT and EPPGE-SWCNT-Ni in the presence of simple redox probe, $[Fe(CN)_6]^{4-}/[Fe(CN)_6]^{3-}$) were examined. As shown in Figure 3.7, the voltammograms showed redox peak at range -0.20 to 0.30 V for the EPPGE-SWCNT and broad redox peak at 0.45 V for the EPPGE-SWCNT-Ni. The broad peak of the EPPGE-SWCNT-Ni was attributed to possible overlap of the $[Fe(CN)_6]^{4-}/[Fe(CN)_6]^{3-}$ and Ni(II)/Ni(III) redox processes.

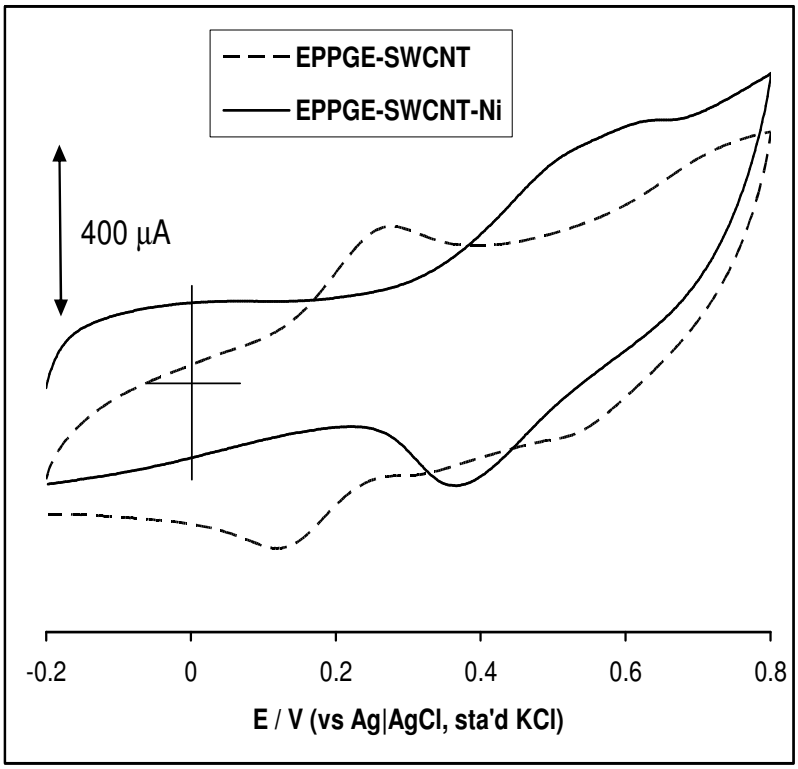

Figure 3.7: Typical comparative cyclic voltammetric evolutions of the electrodes (EPPGE-SWCNT and EPPGE-SWCNT-Ni) in 5 mM $[Fe(CN)_6]^{4-}$ / $[Fe(CN)_6]^{3-}$ solution (PBS pH 7.0). Scan rate = CVs (50mV/s).

Thus, the EIS was perfomed at 0.3 V for both electrodes and also at 0.45 V for the EPPGE-SWCNT-Ni. The Nyquist plots in Figure 3.8 show the experimental data fitted with the equivalent model (Figure 3.8b).

It should be clearly seen that, unlike in hydrazine solution, the equivalent circuit model (Figure 3.8b) incorporates the R_s (the solution/electrolyte resistance) with no inductive behaviour. The excellent fitting of the theoretical model (Figure 3.8b) with the experimental spectra clearly justifies the choice of this circuit model. Interestingly, it was noticed from literature [25] that this equivalent circuit exhibits good resemblance to the equivalent circuit of the so-called "electrolyte-insulator-semiconductor (EIS)" sensors. An electrolyte-insulator-semiconductor device comprises a doped semiconductor acting as substrate for a thin insulating layer, normally an oxide or nitride, which can be immersed in an electrolyte containing a fixed concentration of anionic species to be measured. Indeed, the most important message here is the distinct difference between the EIS data in hydrazine solution and data from solution of simple redox probe, which clearly indicate that these results are not just the consequences of electrode geometry, but electrode mechanisms (notably adsorption phenomena). More detailed study is being undertaken for the EIS evolutions for these electrodes.

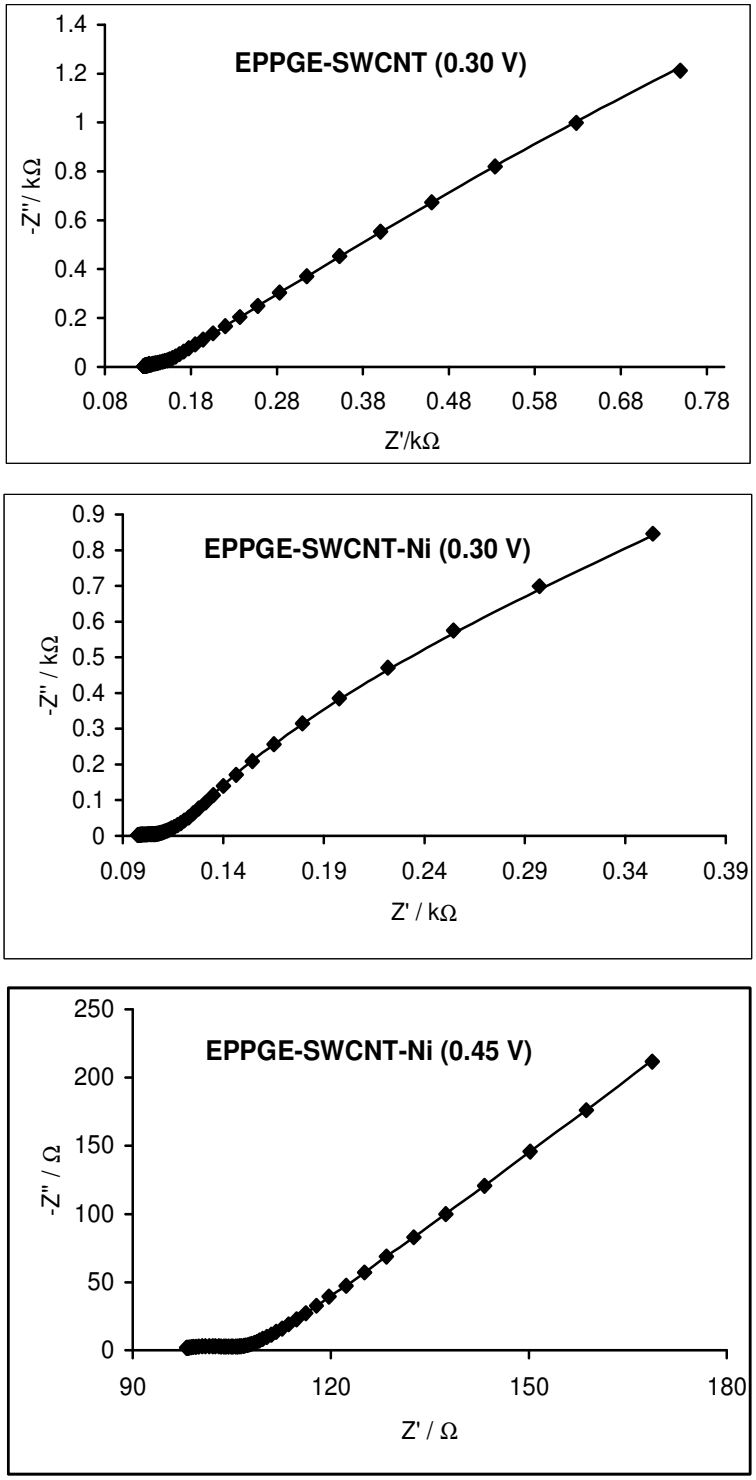

Figure 3.8a: Typical Nyquist plots of the of the electrodes obtained in 5 mM $[Fe(CN)_6]^{4-}$ /$[Fe(CN)_6]^{3-}$ solution (PBS pH 7.0) at fixed potential of 0.30 V and 0.45 V vs Ag|AgCl sat'd KCl.

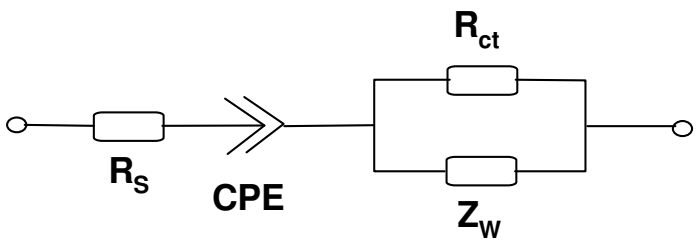

Figure 3.8b: Equivalent circuit model used in fitting the spectra obtained in Figure 3.8a.

3.5 Effect of varying scan rates

Cyclic voltammetric experiments were carried out with a view to establishing the impact of scan rates (ν) at constant concentration (0.01 M) of the hydrazine in 0.1 M Na_2SO_4 solution (Figure 3.9). It was observed that hydrazine peak at 0.6 V and the Ni(II)/Ni(III) redox peak at 0.2 V simultaneously increase with increase in scan rates (scan rates ranging from 10 – 200 mVs^{-1}). At > 100 mVs^{-1} (see inset of Figure 3.6) the Ni(II)/Ni(III) redox process became more pronounced than the hydrazine peak. Their is no firm explanation for this surprising and rare occurrence at this moment, but it may not be unconnected with electrode fouling by intermediate products (radicals) of the hydrazine electro-oxidation (due to adsorption) coupled with the efficient reductive activity of hydrazine solution towards nickel ions as reported by the Bettahar group [26,27]. The plot of peak current versus square root of scan rate ($\nu^{1/2}$) was linear (R^2 = 0.9938), an indication of diffusion-controlled electro-oxidative process. The current function plot (Figure 3.9b) confirms coupled chemical reaction (EC_{cat}) for hydrazine. Recall that the electrooxidation of hydrazine in carbon-based electrodes follows a four-electron process generating nitrogen and water as products.

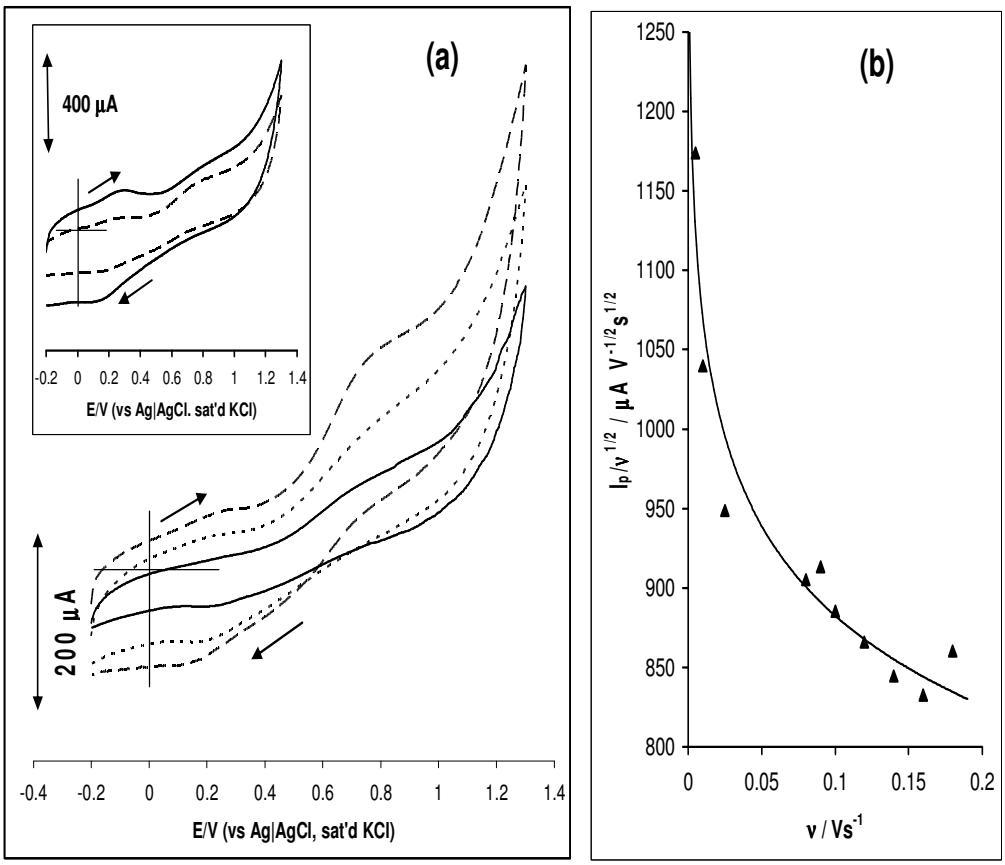

Figure 3.9: (a) Examples of cyclc voltammetric evolutions of EPPGE-SWCNT-Ni obtained in 0.1 M Na_2SO_4 containing 1 mM hydrazine at scan rates 10, 25 and 50 mVs^{-1}(inner to outer). Inset compares voltammograms obtained at 50 and 140 mVs^{-1} (inner to outer). (b) Current function plot, $I_p/v^{1/2}$ vs v.

Lin and Bocarsly [28] had elegantly described the electrooxidation of hydrazine at nickel ferricyanide modified electrode, proposing series of very fast sequential charge transfer processes with intermediates that also adsorb on the electrode. From the results above, it might thus be concluded here that the electrooxidation process of hydrazine on the electrode system does not only occur at the SWCNT-metal film|solution interface, due to its small size [28], hydrazine molecule has the possibility of penetrating the SWCNT-metal film. Three main rate-limiting possibilities could be (i) mass transport of hydrazine in the solution, (ii) diffusion or permeation of the hydrazine and/or its intermediates

through the SWCNT-Metal film, and (iii) charge transport through the film (or rate at which the metal catalyst is regenerated). On the basis of the information, the following general mechanism for the oxidation of hydrazine can be suggested. The redox process of the SWCNT-confined metal (M = Ni or Fe or Co) species is:

$$(M^{3+})\text{film} \rightleftharpoons (M^{2+})\text{film} + e^- \qquad (3.1)$$

The interaction of the M^{3+} with aqueous hydrazine results to the regeneration of the M^{2+} and the formation of hydrazine oxidation intermediates:

$$(M^{3+})\text{film (Hydrazine)} \longrightarrow (M^{2+})\text{film} + \text{Intermediates} + e^- \qquad (3.3)$$

The oxidation intermediate(s) are further oxidized to the final product(s), via similar mediated electro-oxidation process:

$$(M^{3+}) + \text{Hydrazine (aq)} \longrightarrow (M^{3+})\text{film (Hydrazine)} \qquad (3.2)$$

$$(M^{3+})\text{film (Intermediates)} \longrightarrow (M^{2+})\text{film} + \text{Products} \qquad (3.4)$$

The enhanced current response of the Ni^{2+}/Ni^{3+} redox process at high scan rates suggest in Figure 3.6 (inset) may be ascribed to this efficient regeneration of the Ni^{2+} ions on the SWCNTs surface by hydrazine and its oxidation products.

3.6 Chronoamperometric investigations

Further studies on electro-oxidative processes of hydrazine solution at the EPPGE-SWCNT-Ni were investigated using chronoamperometric experiments. Figure 3.10 shows typical results obtained from chronomperometric experiments performed by polarizing the working electrode potentials at 0.60 V. A linear relationship between background-subtracted transient current and hydrazine concentrations was obtained as:

$$I/\mu A = (0.52 \pm 0.02)\ [\text{hydrazine}]/\mu M - (9.92 \pm 0.85) \qquad (3.5)$$

The sensitivity was calculated as 0.52 ± 0.02 AM^{-1} (R^2=0.9954) while the limit of detection (LoD = 3.3 s/m [29], where *s* is the relative standard deviation of the intercept and *m* the slope of the linear current versus the concentration of hydrazine) was 5.3 ± 0.1 μM. Table 3.2 compares the linear concentration range, LoD and sensitivity value obtained in this study with literature values [30-37].

The catalytic rate constants (k) for the oxidation of hydrazine at both EPPGE-SWCNT-Ni and EPPGE-SWCNT-Fe were estimated from the relationship [38,39] (Equation 3.6):

$$\frac{I_{cat}}{I_{buff}} = \pi^{1/2}(kCt)^{1/2} \qquad (3.6)$$

where I_{cat}, I_{buff}, *k* and t are already defined (Chapter 1, section 1.3). From the plots of I_{cat}/I_{buff} vs $t^{1/2}$ at different hydrazine concentrations (not shown), and a plot of the slopes vs square root of the hydrazine concentrations (exemplified with EPPGE-SWCNT-Ni in Figure 3.8 inset), *k* values were approximately the same, (2.2 ± 0.18) x 10^4, (2.0 ± 0.16) x 10^4 and (0.24 ± 0.02) x 10^4 cm^3 $mol^{-1}s^{-1}$ for EPPGE-SWCNT-Ni, EPPGE-SWCNT-Fe and EPPGE-SWCNT-Co respectively, suggesting that the electrocatalytic oxidation of hydrazine was least favoured at the EPPGE-SWCNT-Co but essentially the same for both EPPGE-SWCNT-Ni and EPPGE-SWCNT-Fe.

The diffusion coefficient, *D*, of hydrazine at the EPPGE-SWCNT-Ni was estimated from the Cottrell Equation [40]:

$$I = \frac{nFAD^{1/2}C}{\pi^{1/2}t^{1/2}} \qquad (3.7)$$

where all symbols are already defined (Chapter 1, section 1.3) and included on the list of symbols. Assuming n ≈ 4 [26-28]. From the experimental plots of I versus $t^{-1/2}$ at different concentrations (not shown), the diffusion coefficient D of hydrazine was calculated as (2.5 ± 0.24) x10^{-5} cm^2s^{-1}.

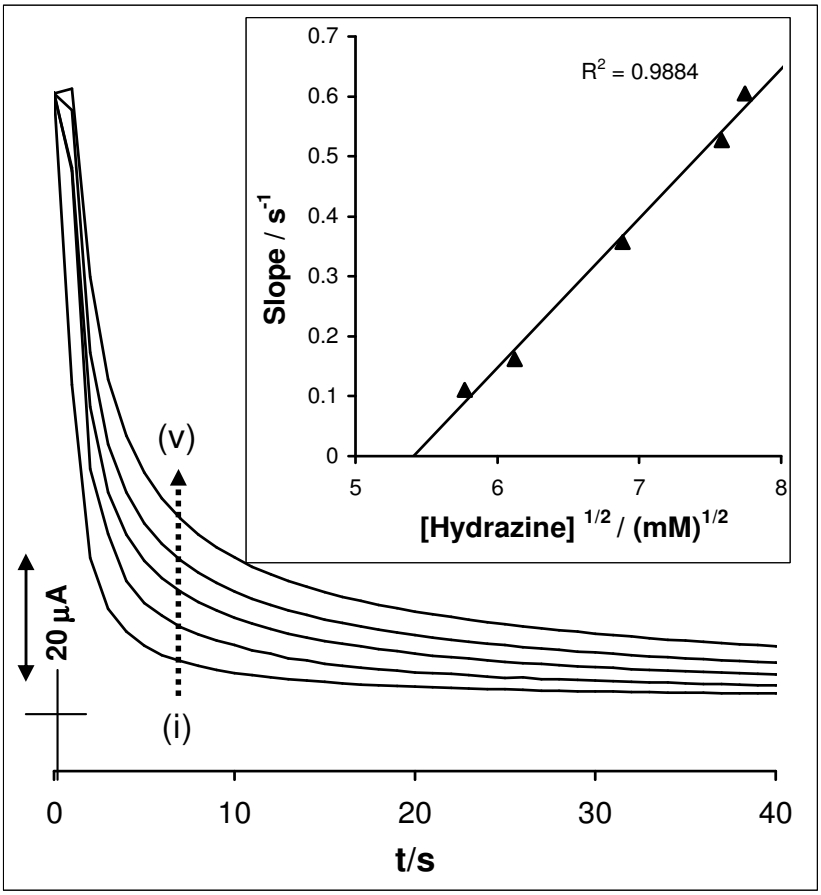

Figure 3.10: Chronoamperometric evolutions of the EPPGE-SWCNT-Ni in 0.1 M Na_2SO_4 solution containing different concentrations of hydrazines (0.0, 33.3, 47.4, 50.5 and 54.5 µM (from (i) to (v)) at fixed potential of 0.6V. Inset is plot of slope vs square root of the concentration of hydrazine.

Table 3.2: Comparative analytical data for the detection of hydrazine at chemically modified electrodes

Electrodes	**Methods**	**Analytical Parameters**			
		LCR / μM	**LoD/ μM**	***Sensitivity* /μAμM^{-1}**	**Ref**
CM-MWCNT-GCE	CA	2.0 – 44	1.4	0.0229	30
CCE-NiHCF	CV	20 - 2000	8.0		31
IMWCNTCPE	DPV	0.6-8.0 8.0-100.0	0.29	0.167 0.014	32
MnHCF-graphite wax	CA	33.3– 8,180,000	6.65	0.0475	33
TCNQ-CPE	CA	2.0–100.0	0.6	0.36	34
MnTPPS-GCE	CA	0.25–250	0.03	-	35
Rutheniumcomplex-GCE	CA	10.0-90.0	8.5	-	36
ST-NiTsPc	CA	100-600	10	–	37
EPPGE-SWCNT-Ni	CA	33.3-54.5	5.3 ± 0.1	0.52 ± 0.02	This work

CA: Chronoamperometry; CV: Cyclic voltammetry; DPV: Differential pulse voltammetry; CM-MWCNT-GCE:Curcumin- multi-walled carbon nanotube modified glassy carbon electrode; CCE-NiHCF: carbon ceramic electrode (CCE) modified with nickel hexacyanoferrate; IMWCNTCCE: indenedione derivatives multi-walled carbon nanotube modified carbon ceramic electrode; MnHCF:Manganese hexacyanoferrate graphite wax modified electrode; TCNQ-CPE: Tetracyanoquinodimethanide-titanium oxide modified carbon paste electrode; MnTPPS-GCE: *meso*-tetra(4-sulphonatephenyl)porphyrinate manganese(III) complex glassy carbon modified electrode; Glassy carbon electrodes modified with (5-amino-1,10-phenanthroline)bis(bipyridine)ruthium(II) chloride hydrate, [(bpy)(2)Ru(5-phenNH(2))]Cl(2).H(2)O; ST-NiTsPc: Nickel tetrasulfonated phthalocyanine (NiTsPc) immobilized onto titanized silica gel.

It has been shown that edge plane pyrolytic graphite electrodes modified with Aldrich SWCNTs electro-decorated with nickel and iron nanoparticles exhibit comparable electrochemical response in buffered aqueous solution (pH 7.0) and towards electro-

oxidation of hydrazine in Na_2SO_4 solution. Also, it was established from electrochemical impedance spectroscopy that these SWCNT-metal hybrids are rather complicated and follow electrical equivalent circuit model typical of adsorption-controlled charge transfer kinetics. EIS data obtained in a simple redox probe, ($[Fe(CN)_6]^{3-}$/($[Fe(CN)_6]^{4-}$), showed that EPPGE-SWCNT and EPPGE-SWCNT-Ni followed electrical equivalent circuit models typical of partial charge transfer or adsorption-controlled kinetics with some resemblance to the behaviour of electrolyte-insulator-semiconductor sensors. These differences in the data clearly, and for the first time, provide some insights into the electrooxidative mechanism of hydrazine at carbon electrodes modified with single-walled carbon nanotubes decorated with metal and metal oxide films.

References

1. J. Kruusma, N. Mould, K. Jurkschat, A. Crossley, C.E. Banks, *Electrochem. Commun.* 9 (2007) 2330.

2. M. Pumera, *Langmuir* 23 (2007) 6453.

3. K. Jurkschat, X. Ji, A. Crossley, R.G. Compton, C.E. Banks, *Analyst* 132 (2007) 21.

4. A.J. Bard, L.R. Faulkner, *Electrochemical Methods: Fundamentals and Applications*, 2nd ed, John Wiley & Sons, Hoboken NJ (2001).

5. C. Peng, J. Jin, G.Z. Chen, *Electrochim. Acta* 53 (2007) 525.

6. D-J. Guo, H-L. Li, *J. Colloid Interf. Sci.*, 286 (2005) 274.

7. C.E. Banks, A. Crossley, C. Salter, S.J. Wilkins, R.G. Compton, *Angew. Chem. Int. Ed.* 45 (2006) 2533.

8. C.P. Jones, K. Jurkschat, A. Crossley, R.G. Compton, B.L. Riehl, C.E. Banks, *Langmuir* 23 (2007) 9501.

9. A. Salimi, R. Hallaj, S. Soltanian, *Biophys. Chem.* 130 (2007) 122.

10. A. Salimi, E. Sharifi, A. Noorbakhsh, S. Soltanian, *Electrochem. Commun.* 8 (2006) 1499.

11. A. Salimi, R. Hallaj, S. Soltanian, H. Mamkhezri, *Anal. Chim. Acta* 594 (2007) 24.

12. A. Salimi, E. Sharifi, A. Noorbakhsh, S. Soltanian, *Biophys. Chem.* 125 (2007) 540.

13. A. Salimi, E. Sharifi, A. Noorbakhsh, S. Soltanian, *Biosens. Bioelectron.* 22 (2007) 3146.

14. E. Barsoukov, J.R. Macdonald (eds.), *Impedance Spectroscopy: Theory, Experiment, and Applications*, 2nd ed. Hoboken NJ Wiley (2005).

15. X. Wu, H. Ma, S. Chen, Z. Xu, A. Sui, *J. Electrochem. Soc.* 146 (1999) 1847.

16. G. Nurk, H. Kasuk, K. Lust, A. Janes, E. Lust, *J. Electroanal. Chem.* 553 (2003) 1.

17. C. Hu, X. Dang, S. Hu, *J. Electroanal. Chem.* 572 (2004) 161.

18. T. Thomberg, J. Nerut, E. Lust, *J. Electroanal. Chem.* 586 (2006) 237.

19. P.M.S. Monk, *Fundamentals of Electroanalytical Chemistry*, John Wiley and Sons, Chichester, 2001, p.172.

20. M.M.E. Duarte, M.M. Stefenel, C.E. Mayer, *J. Arg. Chem. Soc.* 90 (2002) 111.

21. J. Bisquert, H. Randriamahazaka, G. Garcia-Belmonte, *Electrochim. Acta* 51 (2005) 627.

22. M. Jafarian, M.G. Mahjani, H. Heli, F. Gobal, H. Khajehsharifi, M.H. Hamedi, *Electrochim. Acta* 48 (2003) 3423.

23. S. Majdi, A. Jabbari, H. Heli, A.A. Moosavi-Movahedi, *Electrochim. Acta* 52 (2007) 4622.

24. Research Solutions & Resources available online at: http://www.consultrsr.com/resources/eis/induct2.htm (accessed 24 February 2008).

25. E. Bonanos, B.C.H. Steele, E.P. Butler, in: *Impedance Spectroscopy: TheoryExperiment, and Applications*, 2nd ed, E. Barsoukov and J.R. Macdonald eds.), Wiley, Hoboken, New Jersey, 2005, Chap. 4, p 284.

26. A-G. Boudjahem, S. Monteverdi, M. Mercy, M.M. Bettahar *Langmuir* 20 (2004) 208.

27. R. Wojcieszak, M. Zielinski, S. Monteverdi, M.M. Bettahar *J. Colloid Interf. Sci.* 299 (2006) 238.

28. C. Lin, A.B. Bocarsly, *J. Electroanal. Chem. Interf. Electrochem.* 300 (1991) 325.

29. G.D. Christian (2004) Analytical Chemistry, 6th ed. John Wiley and Sons New York, p 113.

30. L. Zheng, J.-f. Song, *Sens. Actuat. B* 135 (2009) 650.

31. A. Abbaspour, A. Khajehzadeh, A. Ghaffarinejad, *J. Electroanal. Chem.* 631 (2009) 52.

32. H.R. Zare, N. Nasirizadeh, F. Chatraei, S. Makarem, *Electrochim. Acta* 54 (2009) 2828.

33. D. Jayasri, S.S. Narayanan, *J. Hazard. Mater.* 144 (2007) 348.

34. J.C. Duarte, R.C.S. Luz, F.S. Damos, A.B. Oliveira, L.T. Kubota, *J. Solid State Electrochem.* 11 (2007) 631.

35. M.S.M. Quintino, K. Araki, H.E. Toma, L. Angnes, *Talanta* 74 (2008) 730.

36. J.S. Pinter, K.L. Brown, P.A. DeYoung, G.F. Peaslee, *Talanta* 71 (2007) 1219.

37. E.F. Perez, G.-O. Neto, A.A. Tanaka, L.T. Kubota, *Electroanalysis* 10 (1998) 111.

38. M.H. Pournaghi-Azar, R. Sabzi, *J. Electroanal. Chem.* 543 (2003) 115.

39. K.M. Manesh, P. Santosh, A.I. Gopalan, K-P. Lee, *Electroanalysis* 18 (2006) 894.

40. D. Giovanelli, N.S. Lawrence, S.J. Wilkins, L. Jiang, T.G.J. Jones, R.G. Compton, *Talanta* 61 (2003) 211.

CHAPTER FOUR

Electron Transfer Behaviour of Single-Walled Carbon Nanotubes Electro-Decorated with Nickel and Nickel Oxide Layers and Its Electrocatalysis Towards Diethylaminoethanethiol (DEAET): An Adsorption-Controlled Electrode Process*

* The following publications resulted from part of the research work presented in this chapter and they are not referenced further in this thesis:

2. **Abolanle S. Adekunle**, Kenneth I. Ozoemena, *Electrochim. Acta* 53 (2008) 5774-5782.
3. **Adekunle A. S.**, Pillay J., Ozoemena K. I., *Electroanalysis* 20 (2008) 2587-2591.

4.1 FTIR, SEM images and EDX characterisation

Figure 4.1 shows the comparative Fourier transformed infra-red (FTIR) spectra of the pristine (a) and acid-treated SWCNTs (b).

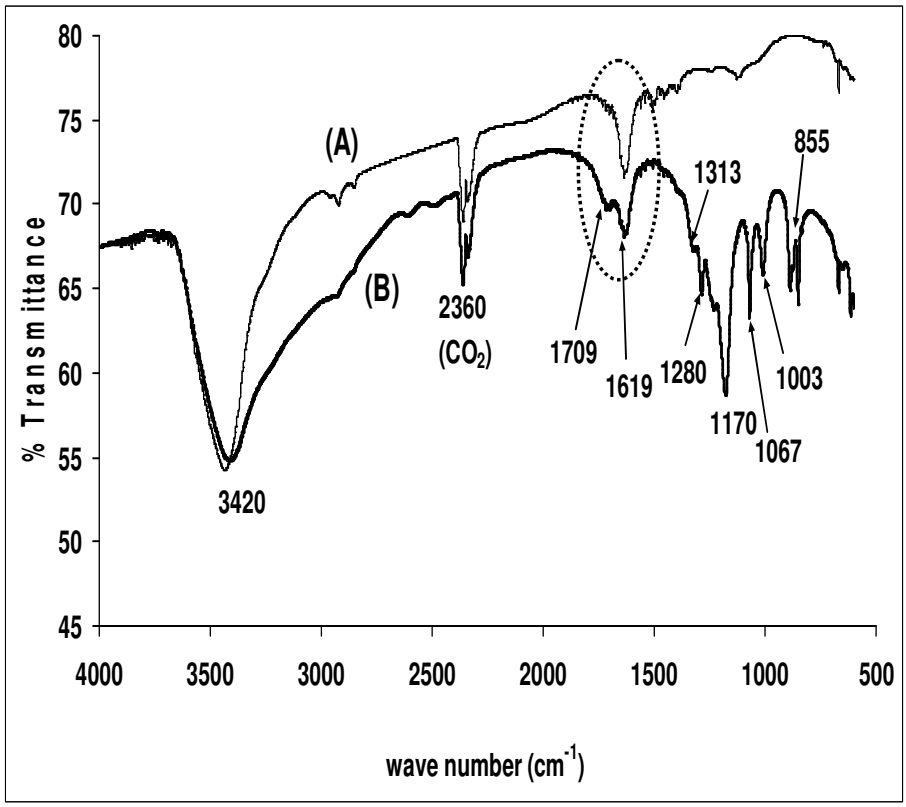

Figure 4.1: Comparative FTIR of pristine SWCNTs (a) and acid-treated SWCNTs (b).

An intense band at 3420 cm^{-1} was obseved for the pristine SWCNT which is attributed to OH group, possibly due to moisture absorption of the pristine. This is in agreement with the observation of Martinez et al. [1] that even the untreated SWCNTs do contain some functional groups. The acid treated species (b) gave a very broad band in the 3420 cm^{-1} region compared to the pristine SWCNTs, clearly indicating the presence of -OH stretching of the COOH group. Both species gave vibrational modes corresponding to C=C bonds at 1619 cm^{-1}, assigned to the nanotube phonon modes. More

importantly, after the acid treatment (b), a new band appeared at 1704 cm^{-1} due to the C=O of the COOH groups. The diminished intensity of the band at 1619 cm^{-1} for the acid-treated compared to that of the pristine SWCNTs is a clear indication that some of the C=C bands have now been functionalized with COOH groups. The sharp band at 1170 cm^{-1} is ascribed to the thiocarbonyl (C-S) [2]. The bands at the 1067 and a shoulder at 1003 cm^{-1} are ascribed to the asymmetric and symmetric stretching modes of SO_3, respectively. These S=O stretching modes resulted from the formation of hydrated sulfonic acid group ($SO_3^-H^+$ H_2O) due to the presence of trace water. The presence of these sulphur groups is clearly visible in the EDX spectra (Figure 4.2). The bands near 855 cm^{-1} regions are due C-H bending, while those at the 1280 and 1313 cm^{-1} are assigned to the O-C. The peak at 3460 cm^{-1}, with similar intensity for both pristine and acid-treated SWCNTs, is ascribed to the interfering CO_2, possibly arising from the nitrogen gas purge boxes of the FTIR experimental setup. No attempt was made to experimentally quantify the extent of carboxylation of the SWCNTs. However, as clearly indicated in the Wang et al. [3], it is known that the procedure employed in the carboxylation process generally give solubility ≤0.08mg of SWCNTs ml^{-1} of solvent. It is reported [3] that the use of microwave strategy that resulted in stable concentrations as high as 10mg SWCNTs ml^{-1} in deionized water, which is approximately two orders of magnitude higher than those obtained using similar strategies. Wang et al. [3] also reported that 33.3% of the carbon atoms on the SWCNTs backbone were carboxylated. From this report, it could be easily be inferred that the extent of carboxylation used in this work could not be more than 0.5%.

Figure 4.2 exemplifies FESEM images of the EPPGE (a), EPPGESWCNT (b), EPPGE-SWCNT-Ni (c) and EPPGE-SWCNT-NiO (d).

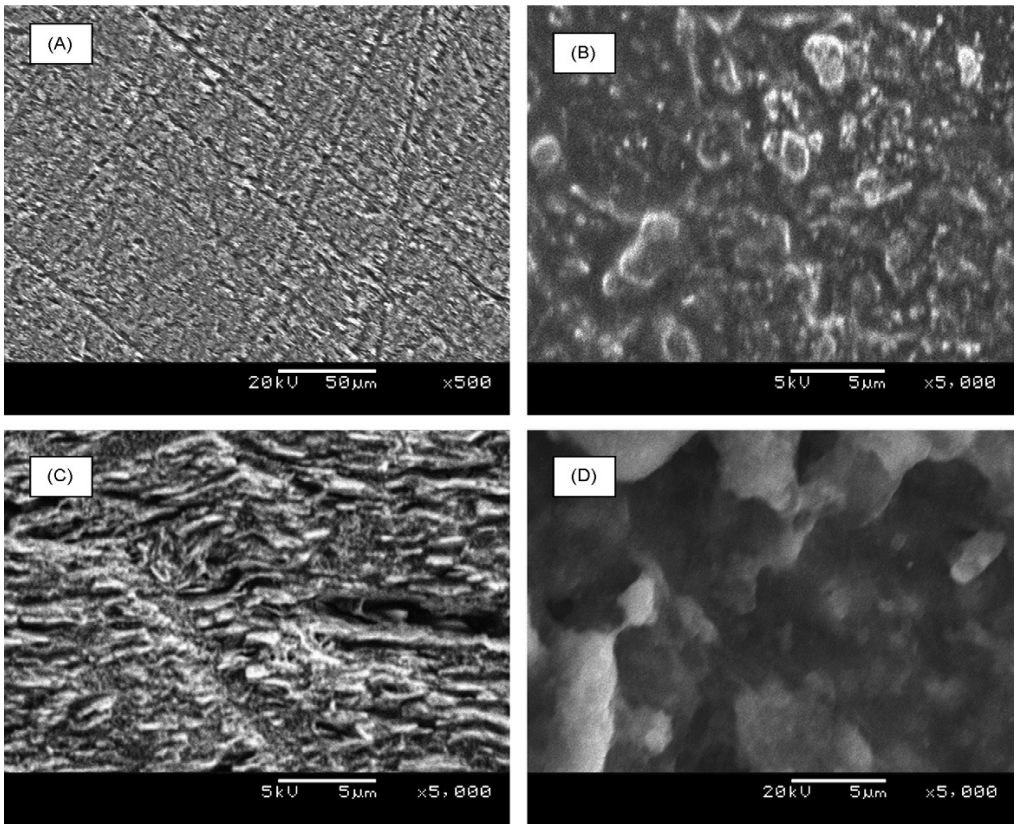

Figure 4.2: FESEM images of bare EPPGE (a), EPPGE-SWCNT (b), EPPGE-SWCNT-Ni (c) and EPPGE-SWCNT-NiO (d). The size bars are 50 µm for (a) and 5 µm for (b)–(d).

The results indicate that the original edge-plane surface of the EPPGE (a) is replaced with aggregated acid-treated SWCNTs (b), and upon introduction of the nickel particles an interconnected layer-structured network image of the SWCNT-modified EPPGE (c) was observed. However, upon electrochemical treatment in aqueous solution these layer-structured networks (c) are disconnected transforming to lumps with exposed interior (d), with sizes in the micrometer ranges. Like other reports on CNTs containing metal or

metal oxide impurities [4], it may be reasonable to speculate here that these nickel particles are either trapped in the graphite layers and/or located on the outside of the tubes exposed to the solutions, and/or mixed amongst the bundles of the SWCNT.

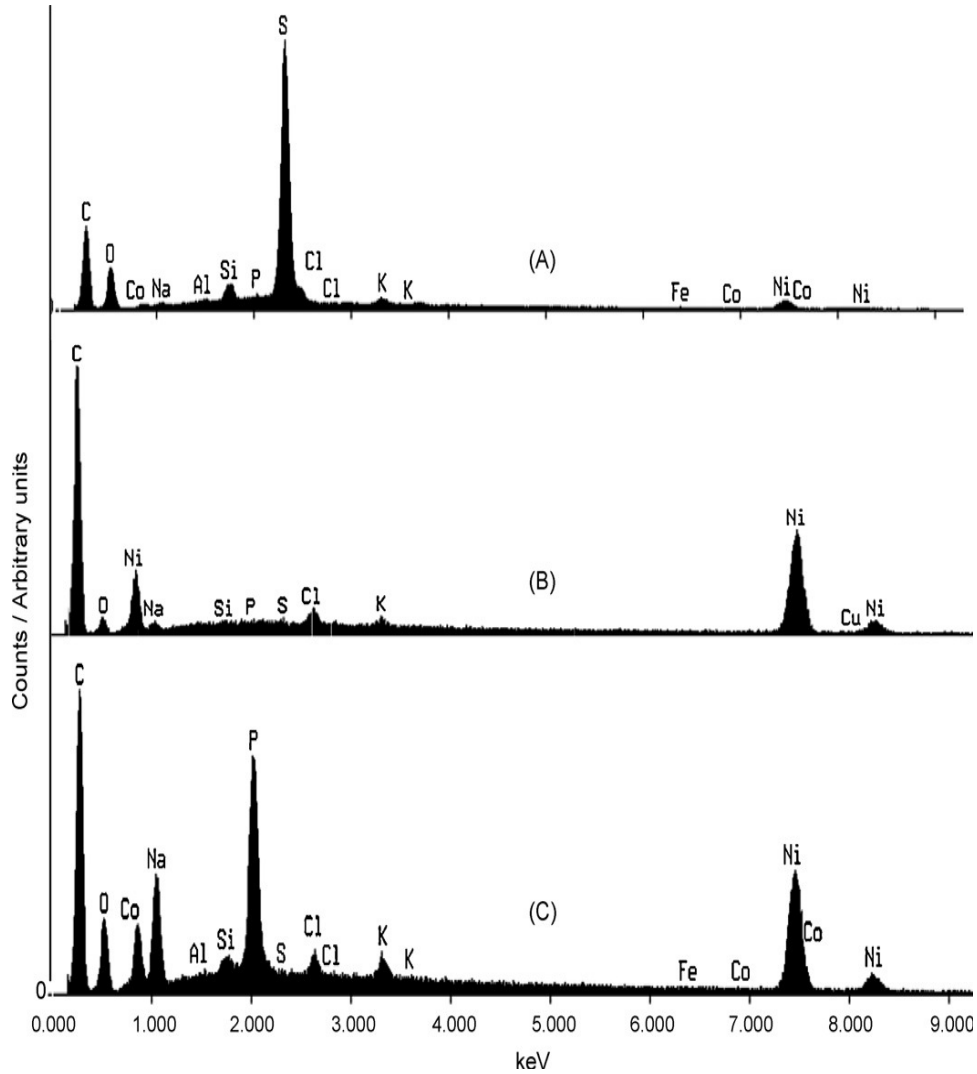

Figure 4.3: EDX spectra of (a) EPPGE-SWCNT, (b) EPPGE-SWCNT-Ni, and (c) EPPGE-SWCNT-NiO.

The EDX profile (Figure 4.3) of the modified electrodes showed well-defined nickel peaks, confirming the successful electrodecoration of the EPPGE-confined SWCNTs. The acid-treated SWCNT (b) showed traces of nickel impurities. The pronounced

sulphur peak could have arisen from the sulphuric acid solution used in the functionalization and washing processes in agreement with the FTIR data. The occurrence of P and Na peaks in the EDX of EPPGESWCNT-NiO (b) is associated with the treatment of the electrode with sodium phosphate buffer solution while the enhanced oxygen peak also confirms the modification of the electrode to its oxide form.

4.2 Comparative redox chemistry in aqueous solution

Figure 4.4 shows examples of voltammetric responses of the electrodes, EPPGE, EPPGE-NiO, EPPGE-SWCNT and EPPGE-SWCNT-NiO, indicating successful integration of the nickel particles with the SWCNTs, confirmed by features such as (i) the presence of the well-defined redox waves of the surface-confined Ni(II)/Ni(III) ($E_{1/2}$ ≈ 0.45V vs. Ag|AgCl, sat'd KCl); (ii) the increased current response following the incorporation of the nickel with the SWCNTs, and (iii) the high charge (capacity) of the EPPGE-SWCNT-NiO compared to other electrodes. EPPGE-SWCNT also exhibited a pair of weak redox peak (E_a ≈ −0.02V and E_c ≈ −0.30 V), which is typical of immobilized SWCNTs at a carbon electrode [5]. The two pairs of redox processes shown by the EPPGE-SWCNT-NiO (E_a ≈ −0.03 V (I) and E_c ≈ −0.44 V (I^I)) and (E_a ≈ 0.67 V (II) and E_c ≈ 0.20V (II^I)) are attributed to the redox processes of the surface-confined SWCNTs and Ni(II)/Ni(III), respectively. An interesting observation here is the significant decrease in the peak-to-peak separation potential (ΔE_p) value of the Ni(II)/Ni(III) redox process in the presence of SWCNTs (ΔE = 0.47 V) compared to the absence of SWCNTs ΔE_p = 0.70 V), indicating a faster electron transport due to the SWCNTs.

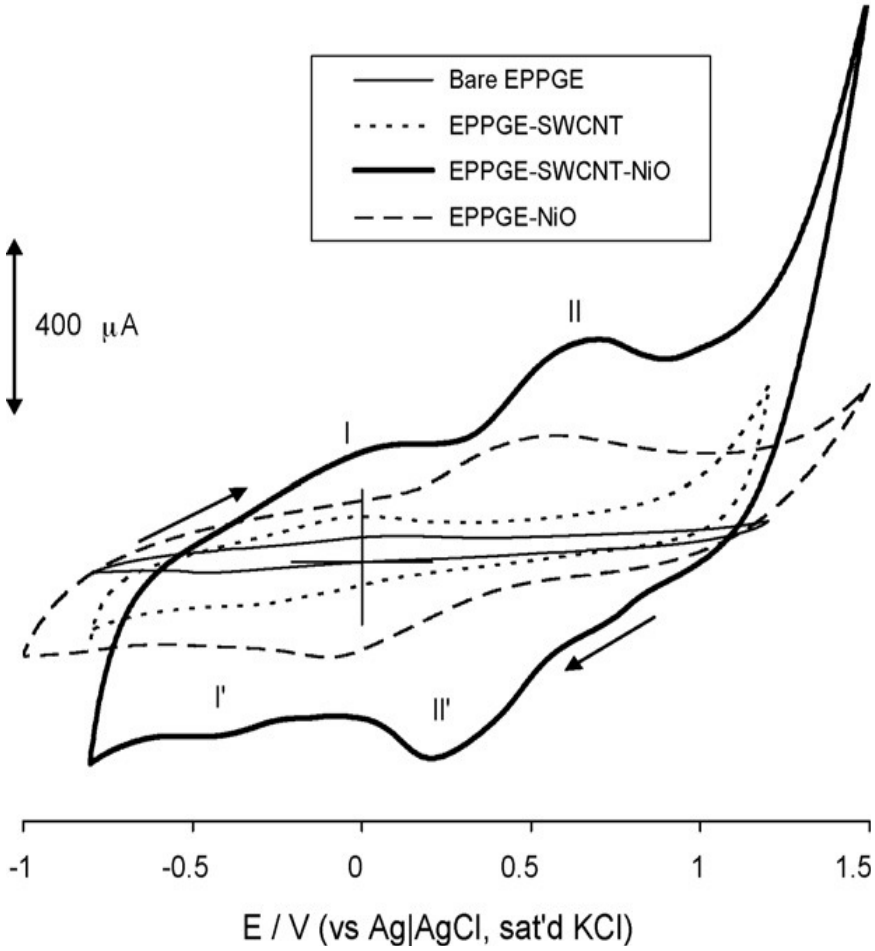

Figure 4.4: Comparative current response of the bare-EPPGE, EPPGE-SWCNT, EPPGE-NiO and EPPGE-SWCNT-NiO in pH 7.0 PBS. Scan rate = 50m Vs^{-1}.

Electrodes modified with nickel hydroxide films are well reported for electrocatalysis and sensing applications. Figure 4.5a shows an example of voltammetric evolutions obtained during continuous scanning (20 scans) of the EPPGE-SWCNT-Ni (obtained at 5 min potentiostatic deposition time) in 0.1M NaOH to form the EPPGE-SWCNT-$Ni(OH)_2$. The first scan appeared with two broad anodic peaks (E_{pa}) at around 0.12 V and 0.73 V with a sharp return cathodic peak at 0.36 V.

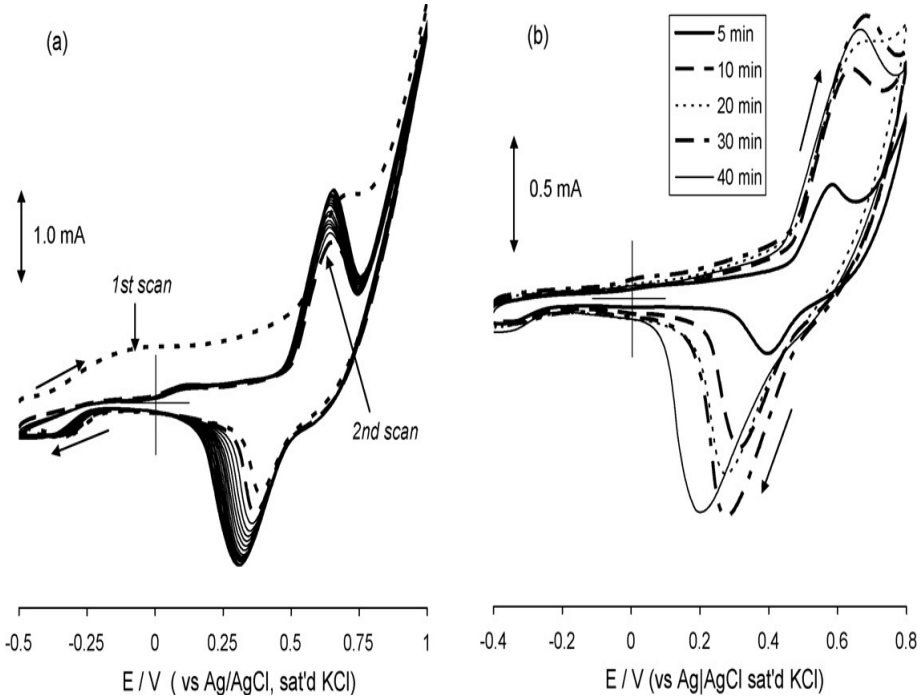

Figure 4.5: (a) Repetitive cyclic voltammetric evolution (20 scans) of EPPGE-SWCNT-Ni in 0.1M NaOH solution. (b) Comparative cyclic voltammetric evolution (1st scan) of the EPPGE-SWCNT-Ni in 0.1M NaOH at different nickel deposition time (5–40 min). Scan rate = 100 mVs^{-1}.

In accordance with literature [6–8], the first anodic peak of this first scan may be ascribed to the oxidation of the Ni(0) to the α-$Ni(OH)_2$ (Equation 4.1), while the anodic peak at the higher potential is due to the conversion of the α-$Ni(OH)_2$ to its β-$Ni(OH)_2$ form (Equation 4.2):

$$Ni + 2OH^- \longrightarrow \alpha\text{-}Ni(OH)_2 + 2e^- \quad (4.1)$$

$$\alpha\text{-}Ni(OH)_2 \longrightarrow \beta\text{-}Ni(OH)_2 \quad (4.2)$$

The weak cathodic peak observed at −0.36 V is attributed to the reduction of unconverted α-$Ni(OH)_2$ to Ni. Salimi et al. [8] indicated they observed such peak at −0.30 V with their nickel powder-doped

carbon composite electrode. The second scan occurred with a sharp peak at E_{pa} = 0.66 V with a decrease in the anodic current (*ca.* 500 μA) compared to that of the first scan, suggesting that β-$Ni(OH)_2$ has been formed on the electrode surface, poisoned it. During this second scan, the β-$Ni(OH)_2$ is first oxidized via proton coupled reaction to the β-NiOOH (and possibly to a very small amount of γ-NiOOH, assume <1% [7]) (Equation 4.3), which is subsequently reduced to the β-$Ni(OH)_2$ species (Equation 4.4).

$$\beta\text{-Ni(OH)}_2 + OH^- \longrightarrow (\beta,\gamma)\text{-NiOOH} + H_2O + e^- \quad (4.3)$$

$$(\beta,\gamma)\text{-NiOOH} + H_2O + e^- \longrightarrow \beta\text{-Ni(OH)}_2 + OH^- \quad (4.4)$$

It should be noted that during the second cycle the peak at 0.12V was no longer observed. According to the interpretation made by a similar observation by Czerwinski and co-workers [6,7], such behaviour of nickel electrode is not unusual and is associated with the inability of the β-$Ni(OH)_2$ formed from the fresh α-$Ni(OH)_2$ in Equation (4.2) to be transformed back to the α-$Ni(OH)_2$. This irreversible transition process is described as the "aging effect" [7]. It is noteworthy that several reports [6-8] acknowledge that *α*-$Ni(OH)_2$ transforms to the *β*-$Ni(OH)_2$ slowly during the potential scans and accumulate on the electrode surface. The results therefore imply that the conversion of the *α*-$Ni(OH)_2$ to the *β*-$Ni(OH)_2$ on the EPPGE-SWCNT surface occurs much faster than on bulk electrode surfaces. The shift of the cathodic peak from about 0.37 V at the onset of the electrochemical process to ≈ 0.30 V at the 20th scan is attributed to the difficulty of reducing the *β*-NiOOH to *β*-$Ni(OH)_2$ as the scan number increases.

To gain some insights into the impact of electrodeposition time of nickel nanoparticles on electron transport in alkaline conditions, the cyclic voltammetric evolutions obtained at different deposition time of nickel nanoparticles on the EPPGE-SWCNT surface was compared. The impact of deposition time was examined because many literature reports on electrodes electrodeposited with metal particles have used deposition time (usually in the ≤5min) but did not provide reasons for such choices. Figure 4.5b compares cyclic voltammograms (using first scans) obtained for the EPPGE-SWCNT-Ni in 0.1 M NaOH at different electrodeposition time (5 – 40 min) of the nickel nanoparticles onto the EPPGE-SWCNT surface. The voltammetric peak heights increased simultaneously with deposition time, stabilizing at 30 min. Also, the surface concentrations of the nickel nanoparticles increased from about 10 nmol cm^{-2} at 5 min to 57 nmol cm^{-2} at 40 min. The ΔE increased from 0.28 V at 5 min to 0.47 V at 40 min. The stabilisation of both the anodic and cathodic peak current heights at 30 min and the increased ΔE values are indicative of some kinetic frustrations possibly due to the increased generation of the inactive β-NiOH from the α-$Ni(OH)_2$ species as more nickel nanoparticles are deposited on the electrode surface. This interpretation is in agreement with previous reports which suggest that α-$Ni(OH)_2$ slowly and steadily transforms to β-NiOH species [6-8].

Preliminary investigation on the impact of scan rate on the EPPGE-SWCNT-Ni in 0.1M NaOH (Figure 4.6) was only possible between 25 and 300mVs^{-1} as very high peak-to-peak separation (ΔEp) values, ranging from 0.5 V at 25 mVs^{-1} to 1.6 V at 300 mVs^{-1} were obtained. This result means that, in this electrolyte conditions, as the scan rate is increased the electrode reactions become irreversible, typical of poor electron transport behaviour. This also reflects a slow diffusion of hydroxide ions into the limited

wetting section of electrode surfaces [8]. It was observed that the ratio of cathodic to anodic peak currents is less than unity, suggesting possible side reactions. Thus, no further investigation on the effect of scan rate was carried out in this initial report. However, it should be stated that in future investigations on the possible applications of this electrode in the alkaline conditions (such as in electrocatalysis and sensing of organic species) more detailed electrochemical studies should be performed on these deposition time especially to establish, for example, the possible impact of deposition time on the electrocatalytic response of the analytes at the different deposition time and scan rates.

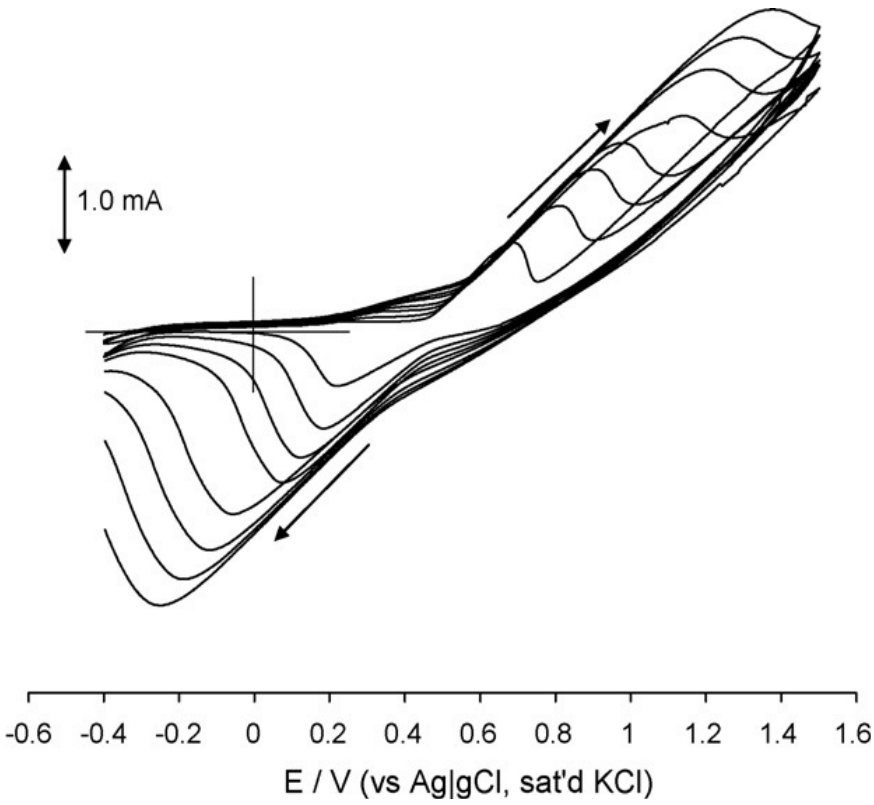

Figure 4.6: Voltammetric evolutions of EPPGE-SWCNT-Ni in 0.1MNaOHsolution at varying scan rates of 25, 50, 75, 100, 150, 200, 250 and 300 mVs^{-1} (inner to outer). The electrode was obtained at 5 min deposition and used for the study after 2nd scan.

4.3 Comparative Electron Transport Properties

The electron transport features of the various Ni and NiO modified electrodes were interrogated using 0.1 M pH 7.0 PBS containing 5 mM $[Fe(CN)_6]^{4-}$ / $[Fe(CN)_6]^{3-}$ as redox probe (Figure 4.7). Some interesting observations are made from the comparative CVs. First, the Faradaic current responses follow the trend: EPPGE-SWCNT-Ni > EPPGE-SWCNT >> EPPGE-Ni > EPPGE-SWCNT-NiO > EPPGE-SWCNT-$Ni(OH)_2$ > EPPGE-NiO > EPPGE-Bare > nickel disk > nickel disk hydroxide.

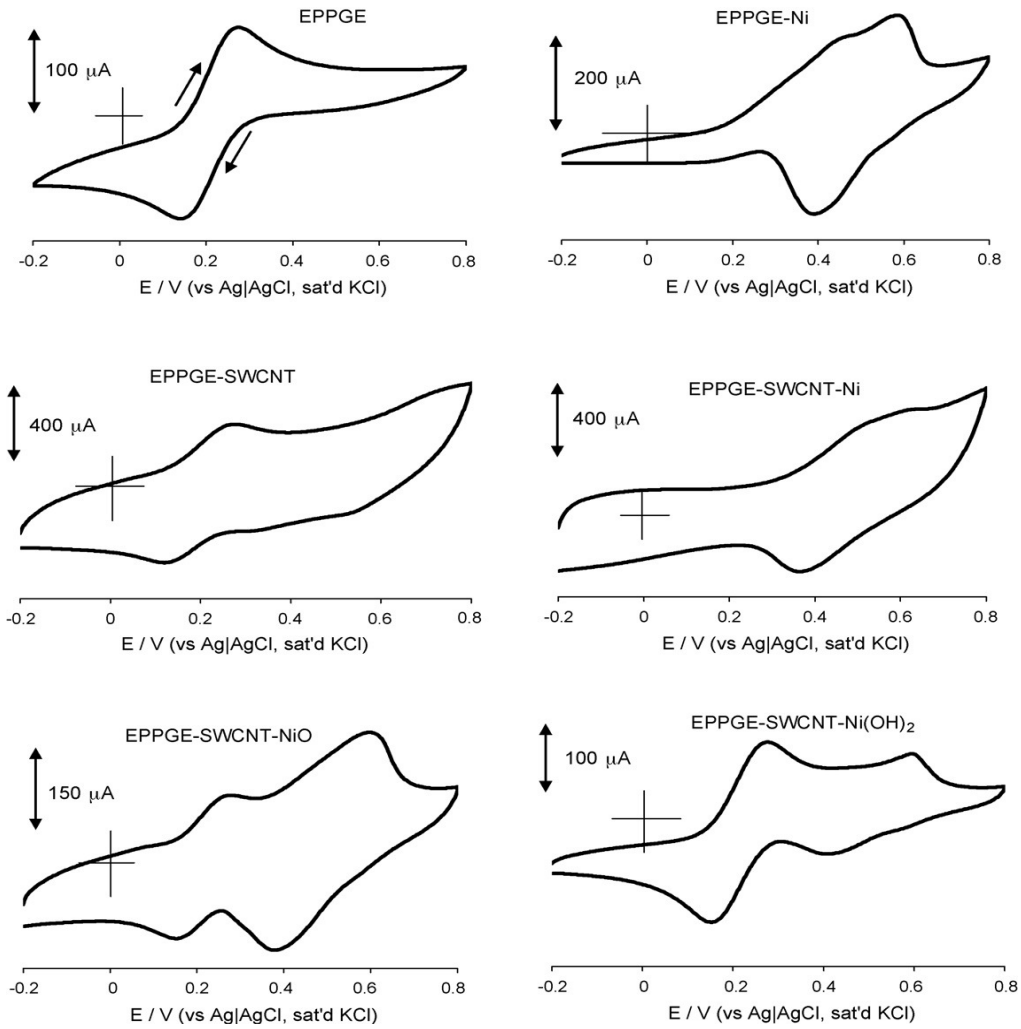

Figure 4.7: Typical examples of cyclic voltammetric evolutions of the electrodes in 5mM $[Fe(CN)_6]^{4-}$/$[Fe(CN)_6]^{3-}$ solution (PBS pH 7.0). Scan rate = 50 mVs^{-1}.

All the electrodes coated with nickel nanoparticles gave two redox processes occurring in the +0.0 to 0.4 V and +0.4 to 0.55 V regions, which was assigned to the $[Fe(CN)_6]^{4-}/[Fe(CN)_6]^{3-}$ and Ni(II)/Ni(III) redox processes, respectively. Second, all the electrodes coated with nickel nanoparticles, prior to passivation with the oxide layer, showed broad peaks with higher current response compared to others without nickel nanoparticles. These broad peaks (see for example, the EPPGE-SWCNT-Ni) were attributed to the overlap of the $[Fe(CN)_6]^{4-}/[Fe(CN)_6]^{3-}$ and Ni(II)/Ni(III) redox processes. The passivation with the oxide layer resulted in the separation of these two overlapped peaks. Upon electrochemical decoration of the EPPGE-SWCNT surface with nickel nanoparticles, an increased current response of the EPPGE-SWCNT-Ni compared to other electrodes was observed. This results suggests that the two modifiers (SWCNTs and nickel films) synergistically mediate the one-electron transport of the $Fe(CN)_6]^{4-}/[Fe(CN)_6]^{3-}$ across the EPPGE-SWCNT-Ni|solution interface.

For further insights into the electron transport properties of the electrodes, an electrochemical impedance spectroscopy (EIS) experiments at potential corresponding to the $E_{1/2}$ of the $[Fe(CN)_6]^{4-}$ $/[Fe(CN)_6]^{3}$) were carried out. Figure 4.8 shows the experimental and the fitted Nyquist plots obtained. Every attempt to fit the EIS data with the original Randles model [9] which refers to the 'true' Faradaic process (i.e., true charge transfer at the metal|electrolyte interface but not to the partial charge transfer process) proved unsuccessful. However, using the equivalent circuit models incorporating the constant phase element (CPE, Figure 4.9) yielded remarkable improvements as evident from the acceptable percentage error values in Table 4.1. Note that it is from the fitted solid lines in Figure 4.8 that the R_s (the solution/electrolyte

resistance), R_{ct} (charge transfer resistance), and Z_w (Warburg impedance) related to the semi-infinite linear diffusion were obtained.

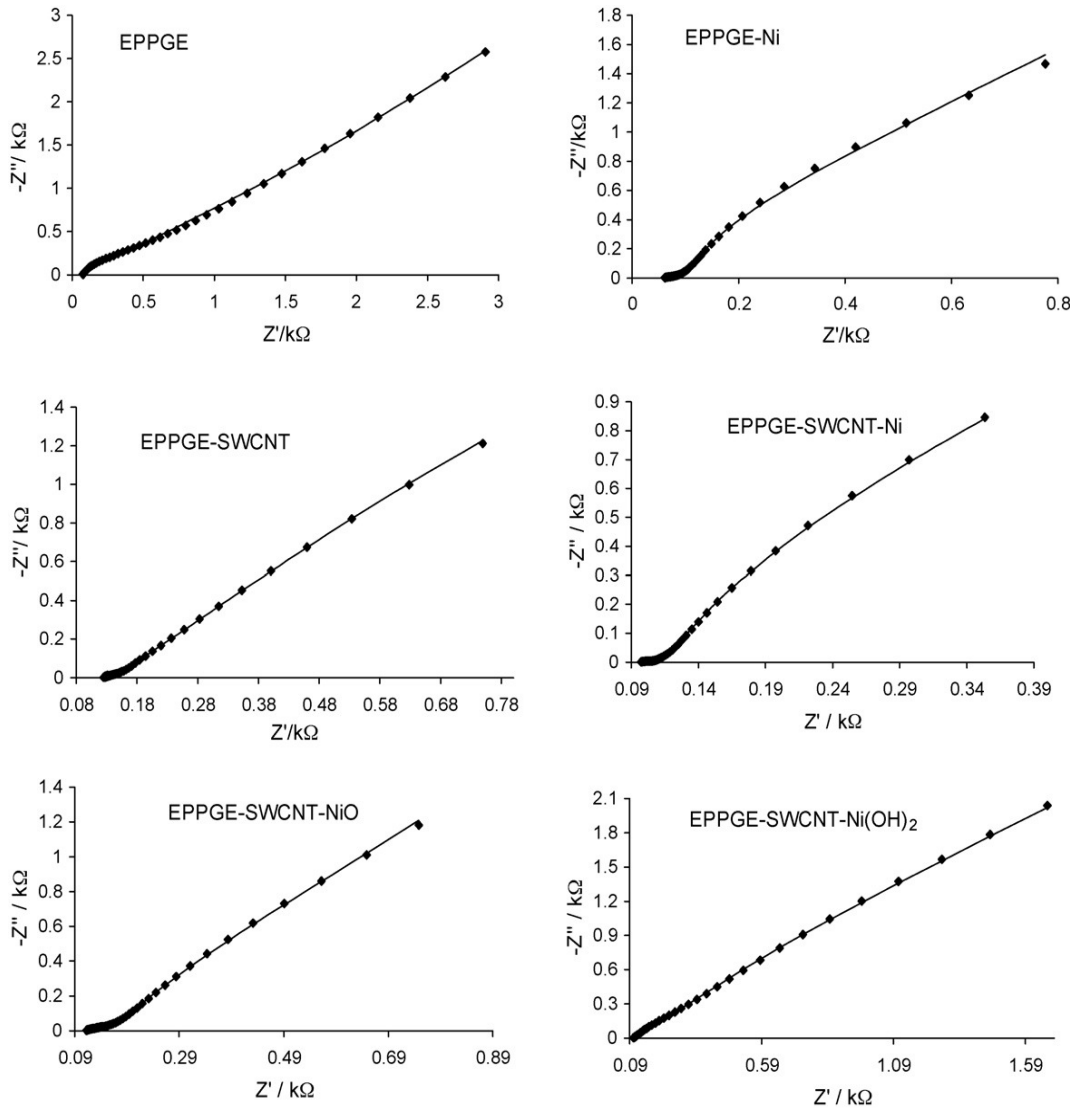

Figure 4.8: Typical Nyquist plots of the of the electrodes obtained in 5mM $[Fe(CN)_6]^{4-}/[Fe(CN)_6]^{3-}$ solution (PBS pH 7.0) at fixed potential of 0.30 V vs. Ag|AgCl sat'd KCl.

In Figure 4.9, equivalent circuit (a) was used to fit the bare EPPGE, EPPGE-SWCNT and nickel disk hydroxide electrodes, the equivalent circuit (b) was used to fit the EPPGE-Ni, EPPGE-SWCNT-Ni, EPPGE-SWCNT-NiO and EPPGE-NiO, while EPPGE-SWCNT-$Ni(OH)_2$ was best fitted with equivalent circuit (c). These results

have certain implications. First, in the absence of nickel nanoparticles, the electrodes essentially follow the Randles equivalent circuit, except that the capacitor of the electric double layer (C_{dl}) deviated from a pure capacitor because of the roughness of the electrode and so is replaced by a CPE (Figure 4.9a) [9-13]. Second, in the presence of nickel films, the structure of the electrode interface is altered leading to different models (circuits 4.9b and 4.9c). Several literature reports [9-13], associate parallel connection of R_{ct} with impedance as some electrode processes involving electrochemically adsorbed products, thus the R_{ct} here may be associated with adsorption or partial charge transfer resistance of the nickel and nickel oxide films. Also, equivalent circuits 4.9b and 4.9c exhibit good resemblance to the circuit of the so-called "electrolyte-insulator-semiconductor (EIS)" sensors [14]. An electrolyte-insulator-semiconductor device comprises a doped semiconductor acting as substrate for a thin insulating layer, normally an oxide or nitride, which can be immersed in an electrolyte containing a fixed concentration of anionic species to be measured [14]. The CPE_1 is ascribed to the energetic inhomogeneity arising from the surface roughness of the electrode ($n \approx 0.73$). The CPE_2 observed for the EPPGE-SWCNT-$Ni(OH)_2$ may be associated with the inhomogeneous semi-infinite diffusion of the probe to the electrode surface since the value of $n \approx 0.52$ indicates small deviation from the ideal semi-infinite diffusion model ($n = 0.5$) to mixed (diffusion and adsorption ($n = 1.0$) limited) kinetics. At the experimental conditions employed here, the EIS data (Table 4.1) indicate that EPPGE-SWCNT-Ni gave the least resistance to electron transfer, approximately 30 times smaller than the EPPGE-SWCNT-NiO, 25 times smaller than EPPGE-SWCNT, and between 300 and 9000 times smaller than the bare EPPGE, EPPGE-SWCNT-$Ni(OH)_2$), and nickel disk.

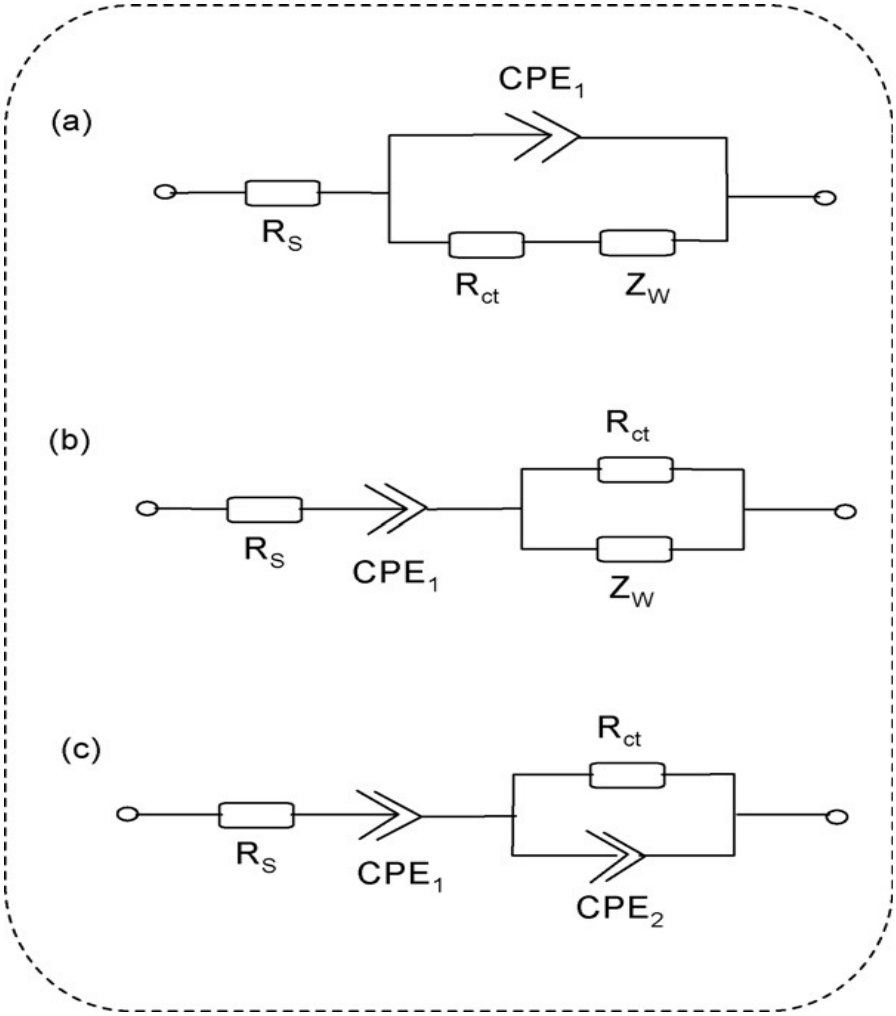

Figure 4.9: Equivalent circuit diagrams used for fitting the impedance data obtained in this work. Circuit (a) was used to fit the bare EPPGE, EPPGE-SWCNT and nickel disk hydroxide electrodes; (b) was used to fit the EPPGE-Ni, EPPGE-SWCNT-Ni, EPPGESWCNT-NiO and EPPGE-NiO; (c) was used for EPPGE-SWCNT-Ni$(OH)_2$.

It is well established that the formation of the passive oxide layer on surface-confined nickel nanoparticles impede electron transport [15]. This behaviour may be interpreted as the result of increased electrical resistance and the resistance to mass transport through the film as the film thickness increases [16]. Thus, it may be concluded here that the high current response of the EPPGE-SWCNT-Ni is the combination of two factors; the inherent faster electron transfer of the nickel nanoparticles (i.e., large surface area)

and the overlap of the $[Fe(CN)_6]^{4-}/[Fe(CN)_6]^{3-}$ and Ni(II)/Ni(III) redox processes. It is not surprising that bulk nickel metal disc electrodes, modified or unmodified, gave the least Faradaic response in this redox probe system compared to their nanoparticle-based electrodes. The n values extracted from the equivalent circuit were approximately in the 0.5 – 0.9 range, suggesting that the electrodes generally exhibit pseudocapacitive behaviour.

To obtain more useful information on the electrical properties of the films, Bode plots were compared (exemplified in Figure 4.10). From Figure 4.10a (–phase angle vs log f), the Ni disk $(OH)_2$ showed one symmetric peak, which corresponds to the relaxation process of the electrode|solution interface. The appearance of this peak at wide potential range is indicative of complex and irregular surface properties of this bulk electrode. From the other type of Bode plot (log |Z| on log f, Figure 4.10b), the electrodes yielded slopes in the –0.40 to –0.60 range, confirming the presence of a CPE. The higher phase angles of the nickel nanoparticles (–67° at 0.13 Hz for EPPGE-SWCNT-Ni and –65° at 0.2 Hz for the EPPGE-Ni) compared to their solution treated counterparts (–58° at 0.1 Hz for EPPGE-SWCNT-NiO, –46° at 0.16 Hz for the EPPGE-NiO and –51° at 0.2 Hz for EPPGE-SWCNT-$Ni(OH)_2$) may be interpreted in terms of the nickel nanoparticles exhibiting more capacitive behaviour (better structural organisation) than when treated in buffer or alkaline solutions since ideal capacitive systems should give phase angles of *ca.* –90°.

Table 4.1: Impedance data obtained for the modified electrodes in 5 mM $[Fe(CN)_6]^{4-}/[Fe(CN)_6]^{3-}$ solution (PBS pH 7.0) at 0.30 V vs. Ag|AgCl sat'd KCl. All values were obtained from the fitted impedance spectra after several iterations using the circuits. Note that the values in parentheses are errors of data fitting.

ELECTRODES	**Electrochemical Impedance Parameters**						
	R_s / Ω cm^2	**CPE_1/ mFcm^{-2}**	**n**	**10^5 Z_W/ Ω cm^2**	**R_{ct} / Ω cm^2**	**CPE_2 / mFcm^{-2}**	**10^3K^0 Cms^{-1}**
EPPGE	8.86±0.06	0.30±0.02	0.78	3.97±0.03	58.20±2.10	-	0.91
EPPGE-SWCNT	12.43±0.06	1.00±0.01	0.73	19.07±1.81	2.48±0.15	-	21.46
EPPGE-SWCNT-Ni	5.26±0.05	17.30±0.09	0.86	6.99±0.57	0.11±0.05	-	483.72
EPPGE-SWCNT-NiO	6.37±0.05	107.60±0.65	0.74	5.17±0.39	3.28±0.15	-	16.22
EPPGE-Ni	1.40±0.03	9.10±0.12	0.81	2.62±0.23	0.75±0.06	-	70.95
EPPGE-NiO	6.74±0.49	4.70±0.06	0.57	2.50±0.23	1.58±0.16	-	33.68
EPPGE-SWCNT-$Ni(OH)_2$	11.15±0.03	2.70±0.22	0.73	-	44.29±4.30	2.80±0.27	1.20
NICKEL DISK	1.82±0.10	0.10±0.01	0.64	0.04±0.01	922.35±80.25	-	0.06
NICKEL DISK$(OH)_2$	2.17±0.01	0.10±0.00	0.82	0.17±0.00	325.73±2.61	-	0.16

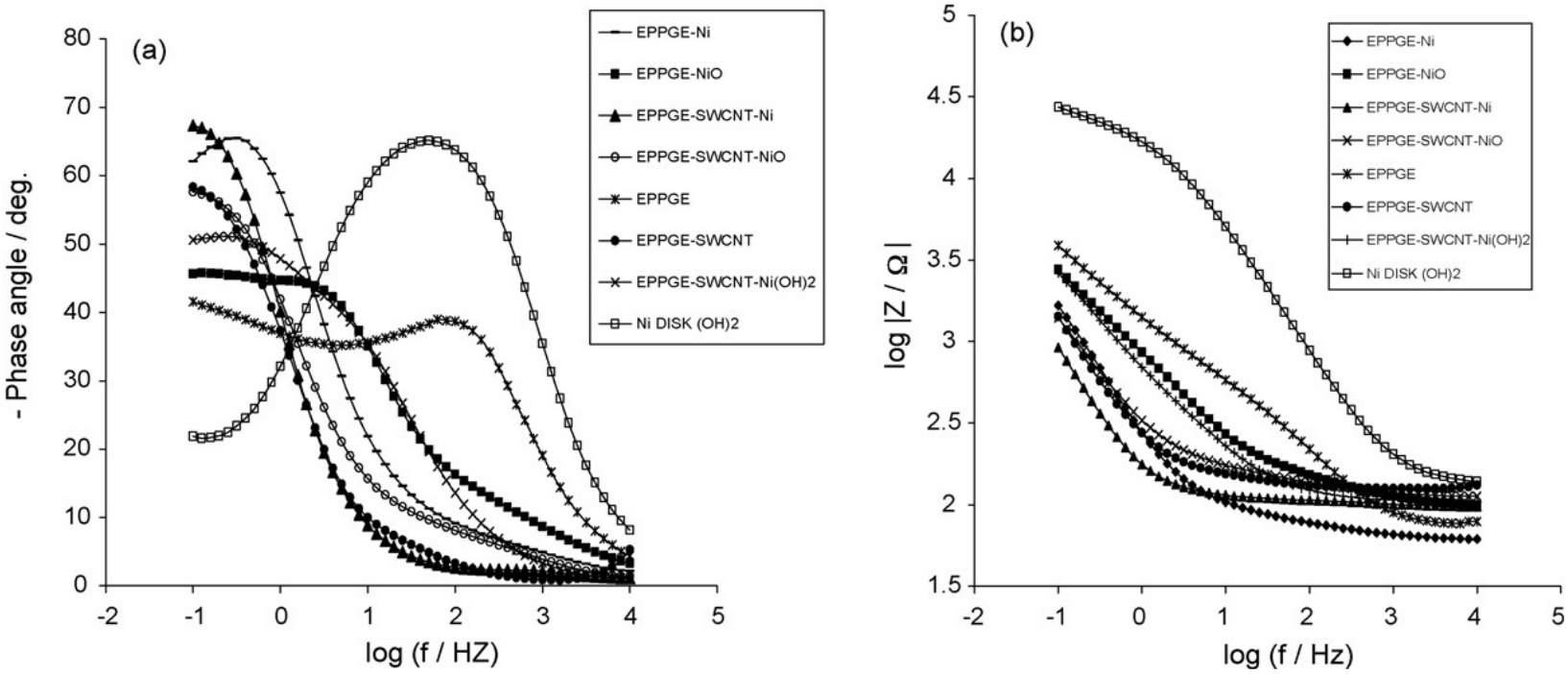

Figure 4.10: Bode plots obtained for the electrodes obtained at 0.30V vs. Ag|AgCl sat'd KCl.

4.4. Electrochemical response of the Ni-modified electrodes towards DEAET oxidation.

Figure 4.11 compares the electrocatalytic response of the various electrodes toward the oxidation of DEAET in pH 9.4 PBS, clearly showing better response of EPPGE-SWCNT-Ni (in terms of onset potential and peak current) over the other electrodes EPPGE, EPPGE-SWCNT, EPPGE-Ni, EPPGE-NiO and EPPGE-SWCNT-NiO. The EPPGE-SWCNT-Ni showed onset potential at about 0.4 V compared to others which appeared around 0.5 V. The broad voltammogram shown by the EPPGE-SWCNT-Ni may be attributed to its porous nature and the high electroactive surface area compared to other electrodes. These properties were lost on the treatment of the EPPGE-SWCNT-Ni in pH 7.0 PBS for the formation of the EPPGE-SWCNT-NiO electrode. The surface transformation between the Ni and the NiO nanoparticles modified electrodes are clearly described by their AFM and SEM images (Figure 4.2). However, background-subtracted voltammogram (not shown) clearly showed the reversible couple with formal potential ($E_{1/2}$) around 0.0 V, which was ascribed to the Ni(II)/Ni(III) redox couple that mediate this enhanced electrocatalytic activity toward DEAET. In all, the EPGGE-SWCNT-Ni gave better response towards DEAET, hence all subsequent studies were carried out with this electrode.

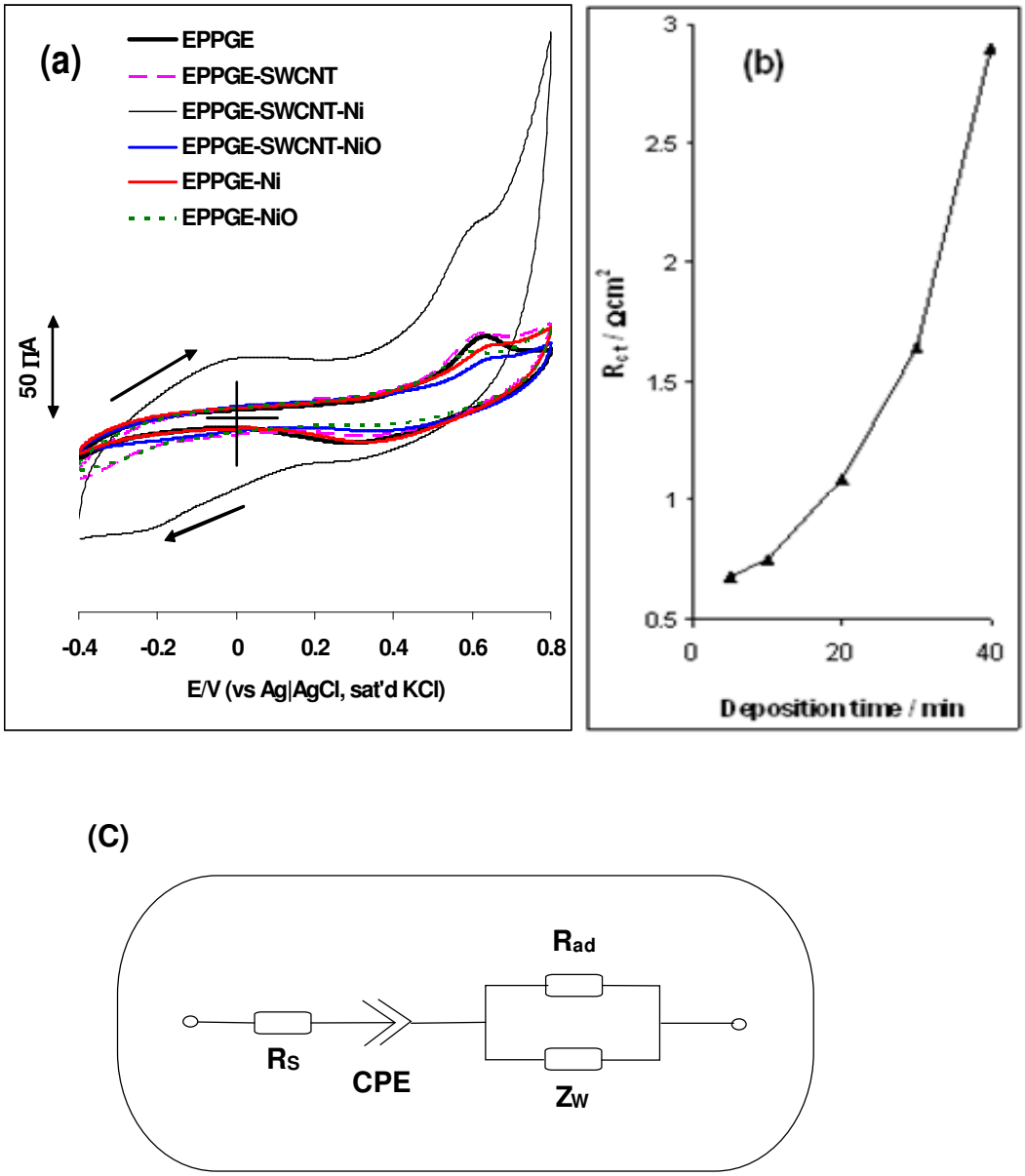

Figure 4.11: (a) Examples of comparative cyclic voltammograms recorded at the various electrodes in 0.1 M PBS (pH 9.4) containing 0.1 mM DEAET. (b) Plot of charge transfer resistance (R_{ct}) against deposition time of nickel (biased at 0.6 V vs Ag|AgCl, sat'd KCl) obtained at EPPGE-SWCNT-Ni. (c) Circuit diagram used in the fitting of impedance data in (b).

4.5 Comparative electrochemical response to DEAET at different Ni deposition time

Next, the impact of nickel deposition time (using same concentration of the nickel salt) on the current response of the DEAET at EPPGE-SWCNT-Ni was studied. Figure 4.11b shows examples of impedance spectra obtained at EPPGE-SWCNT-Ni in 0.1 M PBS (pH 9.43) containing 10^{-4} M DEAET at different electrodeposition time of the nickel nanoparticles (bias potential = 0.6 V vs Ag|AgCl, sat'd KCl). From the plot of charge transfer resistance against deposition time, it is clearly seen that the best current response was at 5 min deposition time. The same behaviour was observed with CV experiments (not shown) where 5 min deposition exhibited the best current response. The decreased current response or charge transport at > 5 min was attributed to the formation of the β-NiOH species well known to hinder the nickel reactivity [17].

The electrical circuit compatible with the impedance spectra is shown in Figure 4.11c. The R_{ct} was nicely fitted using electrical circuit wherein the R_s and Q (or CPE) are in series connected to the R_{ct} and Z_w which are in parallel, compatible with the impedance spectra (not shown) which incorporates R_s (the solution/electrolyte resistance), R_{ad} (partial charge-transfer or adsorption resistance), Z_w (Warburg impedance) related to the semiinfinite linear diffusion, and CPE (constant phase element). It is noteworthy that the equivalent electrical circuit $R_sQ(R_{ct}Z_w)$ used in fitting the impedance spectra for Figure 6.11b suggests that the oxidation of DEAET at the EPPGE-SWCNT-Ni is proceeded by a mechanism that includes adsorption. Parallel connection of R_{ad} with impedance is indicative of electrode processes involving electrochemically adsorbed products or intermediates [18].

Mechanisms that include adsorption step, in many instances, lead to passivation of the active surface of the electrode. CV experiment of the electrode at constant concentration of the DEAET showed same decrease in the peak current after the first scan, which is characteristic of electrode passivation. However, on rinsing the electrode in a buffer solution (pH 9.4) and repeating the experiment in DEAET solution, about 80% of the original current was observed suggesting partial recovery of the electrode. Similarly, after keeping the electrode for a period of four weeks and its catalysis towards DEAET oxidation was investigated, an oxidation current, very close to the same current generated four weeks earlier for the same concentration of DEAET was observed. This result suggests that the Ni nanoparticles decorated on the SWCNTs have a long-term stability that could be employed in sensing applications.

4.6 Electroanalysis of DEAET

4.6.1 Scan rate study

Cyclic voltammetry at varying scan rates (0.02 to 0.5 Vs^{-1}) of the EPPGE-SWCNT-Ni in 10^{-4} M DEAET solution showed poor linear relationship between the plot of the oxidative peak current (I_p) against the square root of scan rate ($\nu^{1/2}$) (R^2 = 0.9843) while at scan rates > 0.3 Vs^{-1}, the oxidative peak current became broad making it difficult to measure. The scan rate results show that the oxidation of DEAET species in the solution is adsorption-controlled process. For irreversible reactions [19], the peak potentials should vary with the log of the scan rates according to:

$$E_p = \frac{b}{2}\log \nu + const. \qquad (4.5)$$

All symbols retain their usual meanings. On the basis of the δEp/δlogv slopes of the plots of E_p vs log ν, the value of the Tafel slope was estimated to be *ca.* 260.0 $mVdec^{-1}$, indicating that the rate-determining step for the catalysis involves a one-electron transfer process. According to literature [20], high Tafel slopes (> 120 $mVdec^{-1}$) for a one-electron process) as obtained in this study is the consequence of strong binding of reactants or intermediates on the electrode surfaces and/or reactions occurring within a porous electrode structure. Thus, the Tafel slopes obtained in this work can be attributed to the adsorption of DEAET on the electrode.

4.6.2 Comparative Electrocatalytic Response: Adsorption Stripping Voltammetric and Chronoamperometry.

Two sensitive electrochemical methods, adsorptive stripping voltammetry and chronoamperometry, were used to investigate the impact of varying concentrations of DEAET to current response at the EPPGE-SWCNT-Ni platform. The former method was used for high concentration range (0.0, 28.6, 33.3, 37.5, 41.2 and 44.5 μM (i to vi)), Figure 4.12a) while the later technique was employed for low concentration range (0.0, 20, 40, 60, 80, 100 nM (i to vi), Figure 4.12b). To reduce the effect of adsorption during the chronoamperometric experiments, the electrode surface was conditioned between measurements by rinsing in buffer solution (pH 9.4).

The values of the limit of detection (LoD = 3.3 δ/m, where *δ* is the relative standard deviation of the intercept of the y-coordinates from the line of best fit, and *m* the slope of the same line) and limit of

quantification (LoQ = 10 δ/m) are summarized in Table 4.2. The quantification limit describes the lowest concentration of an analyte that can be quantified with acceptable precision and accuracy. When compared to the presently available literature reports on the electrocatalytic detection of DEAET (Table 4.2), it is easily observed that results obtained by these two techniques are comparable and even better than data obtained to date for the detection of DEAET.

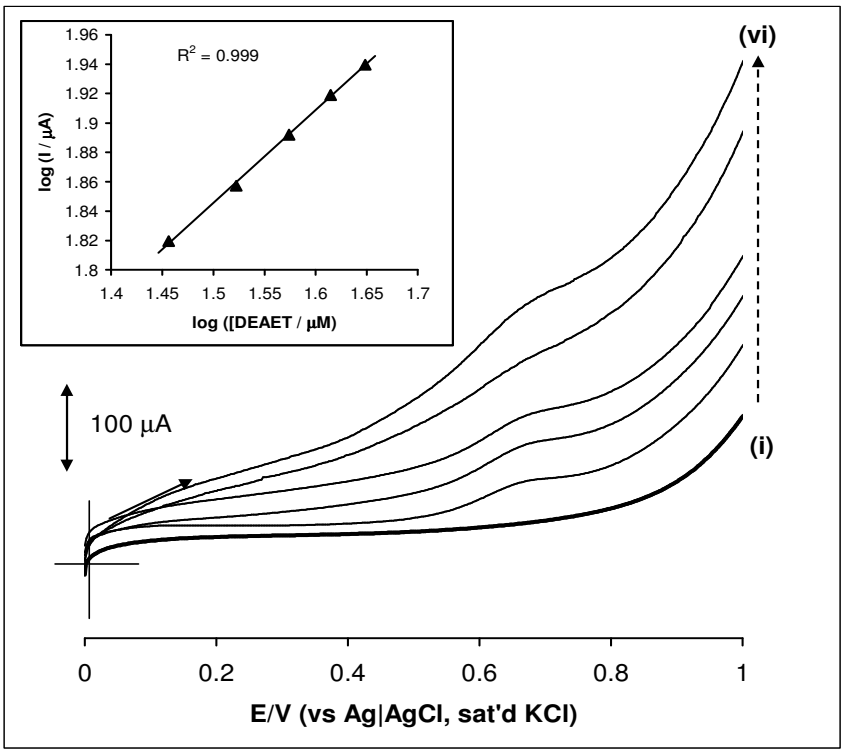

Figure 4.12: (a) Typical examples of linear sweep voltammetric evolutions of EPPGE-SWCNT-Ni in phosphate buffer solution (pH 9.4) containing different concentrations of DEAET (0.0, 28.6, 33.3, 37.5, 41.2 and 44.5 µM (i to vi)). Inset is plot of log current response (background-subtracted) vs log DEAET concentrations.

Also the electrode platform gives some notable advantages over other reports such as the avoidance of the use of enzyme [21], or cocktails of redox-active electropolymers [22], or the employment of

derivatization reactions between thiols and *o*-phthaldialdehyde [23,24]. The enhanced sensitivity obtained in this report may be ascribed to the ability of the SWCNTs to function as efficient conducting species for the catalytic nickel nanoparticles.

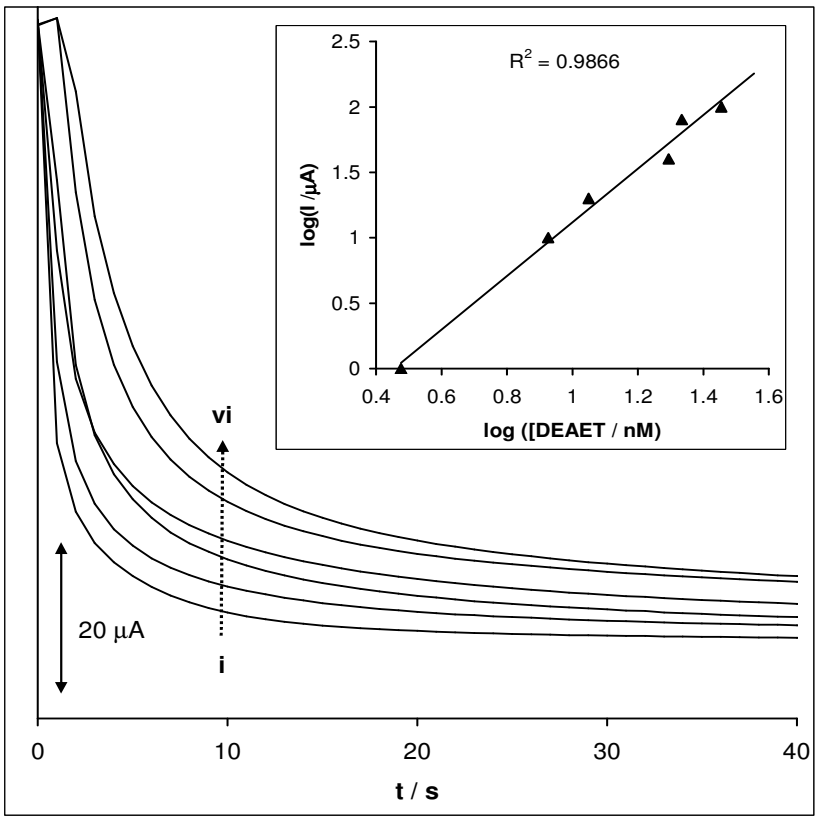

Figure 4.12: (b) Typical examples of chronoamprometric evolutions of EPPGE-SWCNT-Ni in phosphate buffer solution (pH 9.4) containing different concentrations of DEAET (0.0, 20, 40, 60, 80 100 nM (i to vi)) at fixed potential 0.6V vs Ag|AgCl, sat'd KCl. Inset is plot of log current response (background-subtracted) vs log DEAET concentrations.

Table 4.2: Comparative analytical data for the detection of DEAET at chemically modified electrodes

Electrode	**Analytical Parameter**[a]					
	Sensitivity	**LoD**	**LoQ**	ΔG^o	β	**Ref**
SPE- MWCNT-OPH	0.036 µA/mM	8.0 µM	-	-	-	21
GCE-PPy-PQQ	1.37 nA/µMcm^2	3.0 µM	-	-	-	22
BPPGE-SWCNT-CoTAPc	0.06 A/M	3.0 µM	-	-	-	25
BPPGE-Ni powder	0.023 A/M	4.0 µM	-	-	-	26
EPPGE-SWCNT-Ni[b]	1.29±0.10 A/M	2.5 ±0.23 µM	7.6±0.65 µM	–24.80 kJ mol^{-1}	2.2 x 10^4 M^{-1}	This work
EPPGE-SWCNT-Ni[c]	0.18±0.01 µA/nM	5.2±0.42 nM	15.7±1.3 nM	– 45.8 kJ mol^{-1}	10.6x10^7 M^{-1}	This work

[a]All reference electrodes were reported against Ag|AgCl wire with the exception of this present work and GCE-PPy-PQQ which were reported against Ag|AgCl (3M KCl); Screen-printed carbon electrode modified with multi-walled carbon nanotubes and organophosphorus hydrolase; Glassy carbon electrode modified with poplypyrrole and pyrroloquinoline quionone. Basal plane pyrolytic graphite electrode modified with single-walled carbon nanotube and cobalt tetraaminophthalocyanine; Basal plane pyrolytic graphite electrode modified with nickel micropowders (of size distributions in the ~17 - 60 µm range). [b]Obtained by adsorption stripping voltammetry. [c]Obtained by chronoamperometry.

Based on the results obtained here and previous reports on the mechanism of thiol electro-oxidation at modified electrodes [27], the following mechanism was proposed:

$$RSH + OH^- \rightleftharpoons RS^- + H_2O \quad (4.6)$$

$$RS^- + [SWCNT\text{-}Ni^{2+}]_{film} \rightleftharpoons [SWCNT\text{-}Ni\text{---}(SR)]^{2+}_{film} \quad (4.7)$$

$$[SWCNT\text{-}Ni\text{---}(SR)]^{2+}_{film} \longrightarrow [SWCNT\text{-}Ni^{3+}]_{film} + RS^{\bullet} + e^- \ (slow) \quad (4.8)$$

$$RS^{\bullet} + RS^{\bullet} \longrightarrow RSSR \ (fast) \quad (4.9)$$

$$[SWCNT\text{-}Ni^{3+}]_{film} + e^- \longrightarrow [SWCNT\text{-}Ni^{2+}]_{film} \quad (4.10)$$

RSH denotes the DEAET, $RS^{\bullet}$ is thiyl radical, while RSSR is the disulphide products. The thiyl ion interact with the SWCNT-confined Ni(II) film forming an adduct, i.e, the adsorption process. Equation 4.8 is assumed to be the rate-determining step which is a one-electron process. The oxidation of the Ni(II) to Ni(III) simultaneously leads to the generation of the $RS^{\bullet}$ which, in turn, undergoes fast and irreversible reaction to form the disulphide product (Equation 4.9). Ni(III) is reduced to regenerate the Ni(II) (Equation 4.10). Given the adsorption phenomenon observed so far, it seems reasonable to assume that adsorption stripping voltammetry is more conceivable than chronoamperometry. To validate this assumption, the electrochemical adsorption equilibrium constant *(β)* was established using the Langmuir Adsorption Isotherm theory [28] below:

$$\frac{[DEAET]}{\Gamma} = \frac{I}{\beta\Gamma} + \frac{[DEAET]}{\Gamma} \quad (4.11)$$

where Γ is the maximum surface coverage. Assuming that the LSV catalytic peak or chronoamperometric transient current (I_{cat}) is proportional to the surface concentration of DEAET, Equation 4.11 may be re-written as:

$$\frac{[DEAET]}{I_{cat}} = \frac{I}{\beta I_{cat}} + \frac{[DEAET]}{I_{cat}} \qquad (4.12)$$

By plotting the ratio of the DEAET concentration to the current response against the concentration of DEAET, β values were estimated from the values of the slopes and intercepts of the linear relation (R^2 = 0.9737 and 0.9887 for LSV and chronoamperometry, respectively), the electrochemical adsorption Gibbs energy change (ΔG^o) was also calculated from Equation 4.13:

$$\Delta G^o = -RT\ln\beta \qquad (4.13)$$

where R and T have their usual meanings. Table 1 presents the ΔG^o and β values obtained for the two techniques. The high negative ΔG^o values further confirm the strong adsorption of DEAET at the SWCNT-Ni film. The value of β can be used to interrogate whether the detection limit obtained in this study is realistic [29]. The β value of LSV is about three magnitudes lower than that obtained for the chronoamperometric data, meaning that LSV is more realistic than chronoamperometry.

It was envisaged that results shown in this work provide some useful insights into the electrochemical response of thiols, DEAET and related degradation products of V-type nerve agents at metal nanoparticle-decorated carbon nanotubes. The adsorptive behavior of

the SWCNT-Ni may be seen as a limitation to ultra-low detection of DEAET (and very likely other related analytes) using the chronoamperometric methodology. Importantly, this work cautions researchers who wish to use this emerging type of CNT-metal nanoparticle electrocatalytic / sensing platform to first establish the adsorption phenomenon with a view to understanding and applying the most appropriate electrochemical technique to be used for reliable analytical parameters.

References

1. M.T. Martınez, M.A. Callejas, A.M. Benito, M. Cochet, T. Seeger, A. Anson, J.Schreiber, C. Gordon, C. Marhic, O. Chauvet, J.L.G. Fierro, W.K. Maser, *Carbon* 41 (2003) 2247.

2. http://www.cem.msu.edu/<reusch/VirtualText/Spectrpy/InfraRed/infrared.htm [accessed on 9 January 2008].

3. Y.Wang, Z. Iqbal, S. Mitra, *J. Am. Chem. Soc.* 128 (2006) 95.

4. M. Pumera, *Langmuir* 23 (2007) 6453.

5. H. Luo, Z. Shi, N. Li, Z. Gu, Q. Zhuang, *Anal. Chem.* 73 (2001) 915.

6. M. Dmochowska, A. Czerwinski, *J. Solid State Electrochem.* 2 (1998) 16.

7. A. Czerwinski, M. Dmochowska, M. Grden, M. Kopczyk, G.Wojcik, G.Młynarek,J. Kołata, J.M. Skowronski, *J. Power Source* 77 (1999) 28.

8. A. Salimi, M. Roushani, S. Soltanian, R. Hallaj, *Anal. Chem.* 79 (2007) 7431.

9. I.D. Raistrick, D.R. Franceschetti, J.R. Macdonald, in: E. Barsoukov, J.R. Macdonald (Eds.), *Impedance Spectroscopy: Theory Experiment, and Applications*, second ed., Wiley, Hoboken, New Jersey, 2005, p. 27.

10. X.Wu, H. Ma, S. Chen, Z. Xu, A. Sui, *J. Electrochem. Soc.* 146 (1999) 1847.

11. G. Nurk, H. Kasuk, K. Lust, A. Janes, E. Lust, *J. Electroanal. Chem.* 553 (2003) 1.

12. C. Hu, X. Dang, S. Hu, *J. Electroanal. Chem.* 572 (2004) 161.

13. T. Thomberg, J. Nerut, E. Lust, *J. Electroanal. Chem.* 586 (2006) 237.

14. E. Bonanos, B.C.H. Steele, E.P. Butler, in: E. Barsoukov, J.R. Macdonald (Eds.), Impedance Spectroscopy: Theory

Experiment, and Applications, second ed, Wiley, Hoboken, New Jersey, 2005, p. 284.

15. J.V. Dobson, B.R. Chapman, *Electrochim. Acta* 32 (1987) 415.

16. K.I. Ozoemena, T. Nyokong, *Inorg. Chem. Commun.* 6 (2003) 1192.

17. C. Zhang, S. M. J. Park, *J. Electrochim. Soc.* 136 (1989) 3333.

18. I.D. Raistrick, D.R. Franceschetti, J.R. Macdonald, in Impedance Spectroscopy: Theory Experiment, and Applications, 2nd ed., (Eds: E. Barsoukov, J. R. Macdonald), Wiley, Hoboken, NJ 2005, ch. 2, p 27.

19. G.D. Christian Analytical Chemistry, 6th ed. John Wiley and Sons New York, 2004, p 113.

20. J.-M. Zen, A. Senthil Kumar, M.-R. Chang, *Electrochim. Acta* 45 (2000) 1691.

21. K.A. Joshi, M. Prouza, M. Kum, J. Wang, J. Tang, R. Haddon, W. Chen, A. Mulchandani, *Anal. Chem.* 8 (2006) 331.

22. O.V. Shulga, C. Palmer, *Anal. Bioanal. Chem*. 385 (2006) 1116.

23. C.L. Copper, G.E. Collins, *Electrophoresis*, 25 (2004) 897.

24. J. Wang, J. Zima, N.S. Lawrence, M.P. Chatrathi, *Anal. Chem.*, 76 (2004) 4721.

25. J. Pillay, K. I. Ozoemena, *Electrochim. Acta* 52 (2007) 3630.

26. J. Pillay, K.I. Ozoemena, *Electrochem. Commun.* 9 (2007) 1816.

27. F. Bedioui, S. Griveau, T. Nyokong, A.J. Appleby, C.A. Caro, M. Gulppi, G. Ochoa, J.H. Zagal, *Phys. Chem. Chem. Phys.* 9 (2007) 3383.

28. H.X. Lu, L. Donal, *J. Electroanal. Chem.* 484 (2000) 150.

29. W. Yang, E. Chow, G.D. Willet, D.B. Hibbert, J.J. Gooding, *Analyst* 128 (2003) 712.

CHAPTER FIVE

Electron Tranport and Electrocatalytic Properties of MWCNT/Nickel Nanocomposite: Hydrazine and Diethylaminoethanethiol as Analytical Probes*

* The publication below resulted from part of the research work presented in this chapter and it is not referenced further in this thesis:

4. **Abolanle S. Adekunle**, Kenneth I. Ozoemena, *J. Electroanal. Chem.* 645 (2010) 41-49.

5.1 Comparative TEM, XRD and EDX spectra

Figures 5.1 (a) and (b) showed the comparative transmission electron microscopy (TEM) images of the pristine and acid treated MWCNTs. The pristine MWCNTs are cylindrical, long and capped at the edges (Figure 5.1a), but on harsh treatment in the acid medium, the tubes were cut to shorter length with cut edges (Figure 5.1b) which provided the platform for modification with the acidic functional groups.

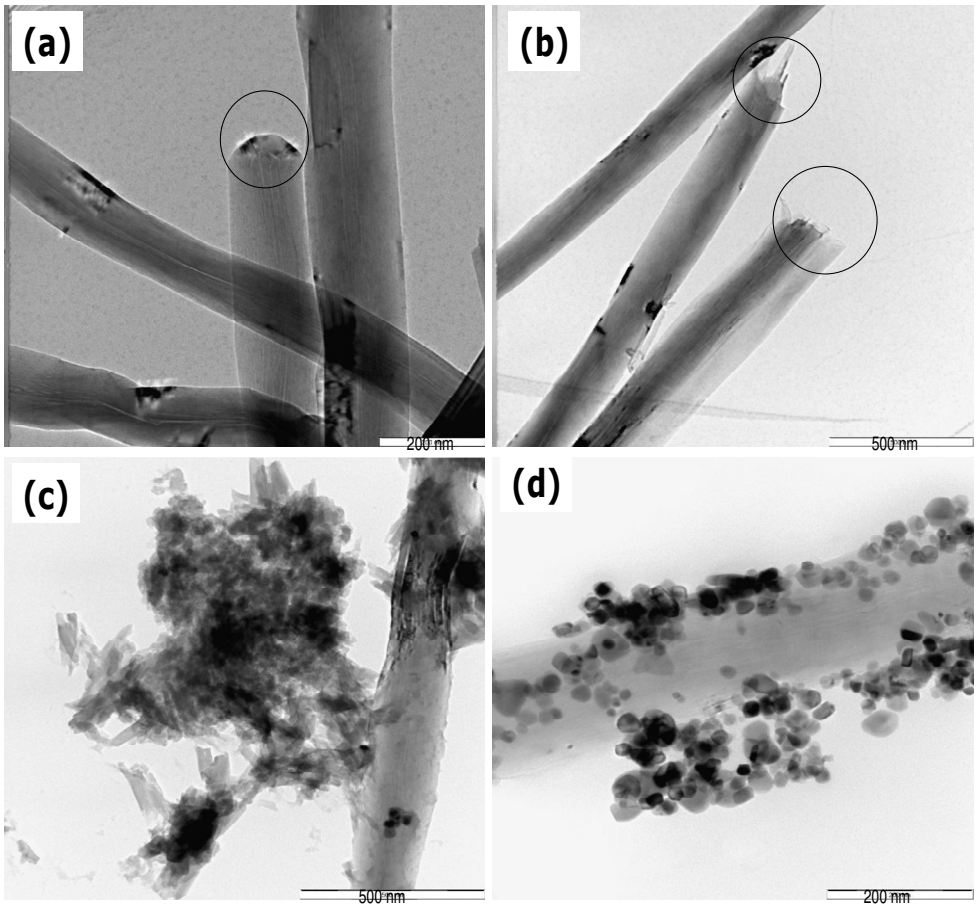

Figure 5.1: TEM images of (a) Pristine MWCNT (b) MWCNT-COOH (c) MWCNT-Ni and (d) MWCNT-NiO.

Typical TEM micrographs and size distributions for the nickel (c) and the nickel oxide (d) nanoparticles on MWCNT support are also represented in Figure 5.1 above. The Ni nanoparticles appear a little amorphous than their NiO counterparts that are very fine, crystalline mono-disperse nanoparticles. The NiO nanoparticle sizes are in the 25 – 50 nm range. The corresponding XRD spectra for the resultant particles are shown in Figure 5.2a. Three characteristic peaks for Ni (2θ = 43.4, 50.6 and 74.5), corresponding to Miller indices (111), (200) and (222) were observed [1]. The result agreed with that observed by Wu and Chen [1], which indicates that the resultant particles were pure face-centered cubic (fcc) nickel. On the other hand, it was difficult to obtain the Ni peak for the synthesised Ni nanoparticles (inset in Figure 5.2a) probably due to the amourphous nature of the particles. From Debye-Scherrer formula [2]:

$$d = \frac{K\lambda}{B\cos\theta} \tag{5.1}$$

where d is the average crystal size; K is a constant (0.89); λ is the wavelength (1.78901 nm) used; B is the full width at half maximum of the peak, θ is the Bragg's angle of the XRD peak, the crystal size of the NiO particles were estimated from the three peaks to be ~ 21.5 nm, which falls in the range shown by the TEM.

Figure 5.2b and c are the EDX profiles of the synthesised MWCNT-Ni and MWCNT-NiO, respectively. MWCNT-Ni (b) and the MWCNT-NiO (c) showed the presence of Ni peaks with very pronounced intensity corresponding to about 86% Ni implying that almost all the Ni^{2+} ions were successfully reduced to Ni nanoparticles. The occurrence of O

peak in (c) confirms the modification of the Ni to its NiO nanoparticles.

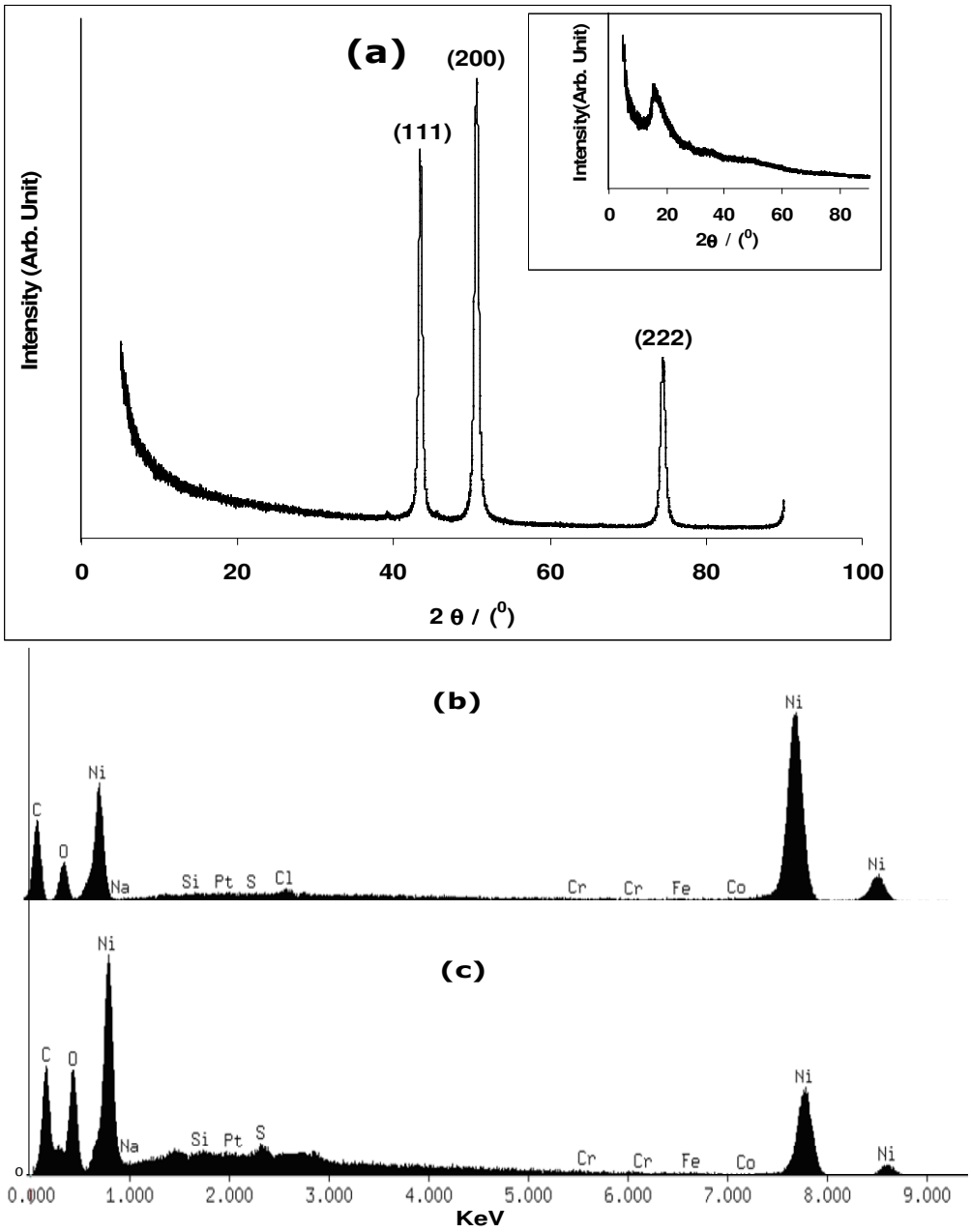

Figure 5.2: (a) XRD spectrum of NiO. Inset in (a) is the XRD spectrum of Ni. (b) and (c) represent the EDX spectra of MWCNT-Ni and MWCNT-NiO, respectively.

5.2 Comparative Electrochemical characterization

Figure 5.3 compares the cyclic voltammograms of the bare and modified EPPGEs in 0.1 M PBS (pH 7.0) (Figure 5.3a) and 5 mM $Fe(CN)_6]^{4-}/[Fe(CN)_6]^{3-}$ solution (Figure 5.3b). From Figure 5.3a, the bare EPPGE and EPPGE-MWCNT did not show any noticeable redox couple in the electrolyte employed in this work. On the contrary, all the nickel or nickel oxide based electrodes clearly showed the Ni^{2+}/Ni^{3+} redox process at formal or equilibrium potential ($E_{1/2}$) of about 0.35 V. All their peak-to-peak separation potential (ΔE_p) is ≥ 100 mV, greater than the theoretical 59.8 mV expected for a fast one-electron transport. Also, the ratios of the anodic to the cathodic peak current response (I_{pa} / I_{pc}) for these electrodes are approximately unity, indicative of reversible electrochemical process. Note that the EPPGE-MWCNT-Ni is characterised by higher current response compared to other electrodes investigated, about twice to that of the EPPGE-Ni, indicating that the enhancement of electrochemical performance arise from the synergy between the MWCNTs and the Ni nanoparticles.

The cyclic voltammetry in the solution of outer-sphere redox probe, $Fe(CN)_6]^{4-}/[Fe(CN)_6]^{3-}$, showed a pair of redox couples in the regions of 0 – 0.3 V (attributed to the $Fe(CN)_6]^{4-}/[Fe(CN)_6]^{3}$ redox process, with $E_{1/2} \approx 0.2$ V and $\Delta E_p \approx 0.17$) and in the 0.3 – 0.7 V region (attributed to the Ni^{2+}/Ni^{3+} redox process, with $E_{1/2} \approx 0.42$ V and $\Delta E_p \approx 0.12$). Like in the PBS solution, the MWCNT-Ni is associated with large current response. Note that in both electrolyte conditions, the voltammogramms of the Ni and NiO nanoparticles are slightly broad with wide ΔE_p.

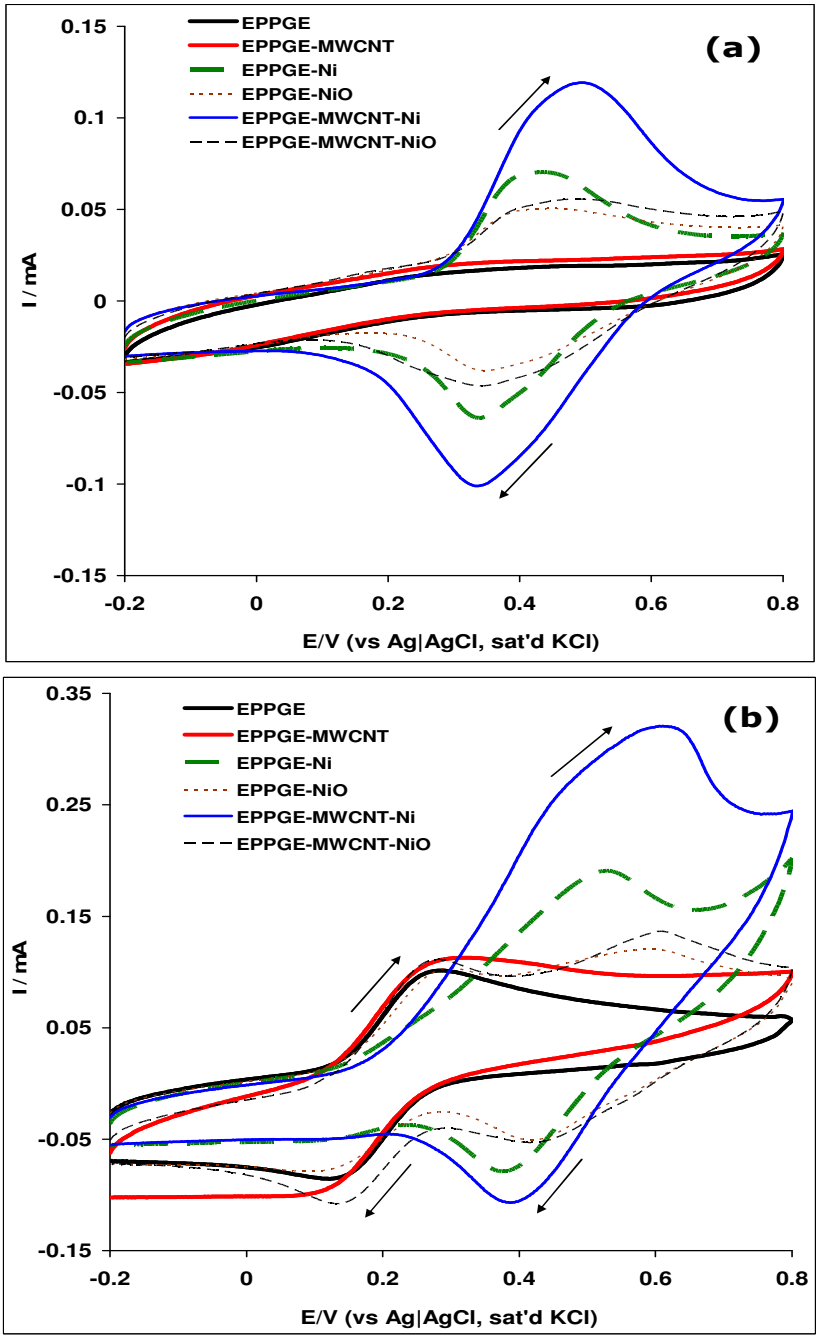

Figure 5.3: Comparative cyclic voltammetric evolutions of the electrodes in (a) 0.1 M PBS (pH 7.0), scan rate = 100 mVs^{-1}. (b) 5 mM $[Fe(CN)_6]^{4-}$ / $[Fe(CN)_6]^{3-}$ solution (in PBS pH 7.0). Scan rate = 50 mVs^{-1}.

This may be related to the different locations of these nanoparticles at the different environments of the MWCNTs leading to different formal potentials [3]. In a nutshell, these results clearly confirm the successful integration of Ni or NiO nanoparticles into the MWCNT support.

Considering that the redox process of the $Fe(CN)_6]^{4-}$ /$[Fe(CN)_6]^{3-}$ occurred at essentially the same $E_{1/2} \approx 0.2$ V and $\Delta E_p \approx 0.17$ V for all the electrodes, it becomes somewhat difficult to unequivocally establish the rate of the electron transfer for any of the electrodes. Thus, EIS was employed (at biased potential of 0.2 V) to determine the extent to which each of the electrodes permit the electron transport between the redox probe and the underlying EPPGE. Figure 5.4 shows typical Nyquist plot, satisfactorily fitted (judged by the chi-square function of $\leq 10^{-4}$, and relative % errors, corroborated by the goodness of the fitting lines, Table 5.1) using the modified Randles equivalent circuit (inset in Figure 5.4). Ideally, R_s and Z_w values should not be affected by modification of the electrode surface, but in practice slight deviations may occur [4, 5], possibly due to the resistances induced by the modifying films to the solution. The slight increase in the R_s and Z_w values for the EPPGE-MWCNT and BPPGE-MWCNT-Ni is not fully understood at this time but may be related to the interaction of the modifying films with the electrolyte.

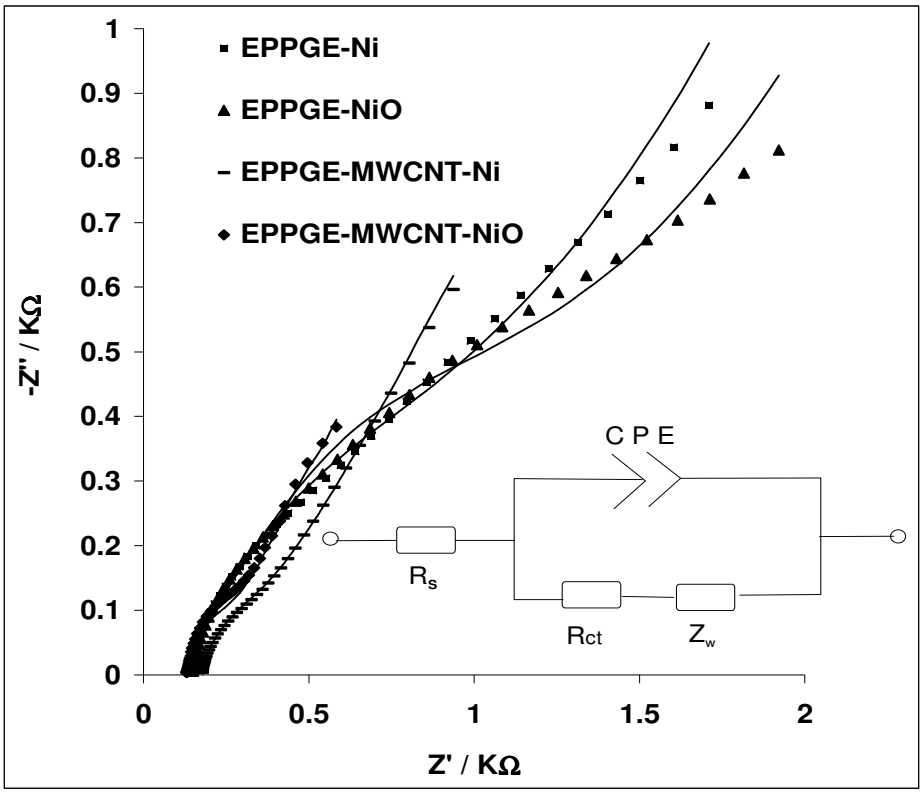

Figure 5.4: Typical Nyquist plots obtained for the electrodes in 5 mM $[Fe(CN)_6]^{4-}$ / $[Fe(CN)_6]^{3-}$ solution (PBS pH 7.0) at a fixed potential of 0.2 V (vs Ag|AgCl, sat'd KCl). Inset represents the circuit used in the fitting of the EIS data.

The values obtained from fitting the raw impedance spectra with this circuit (Table 5.1) indicates (from the values of the R_{ct}) that electron-transport is faster at the EPPGE-MWCNT-Ni and EPPGE-MWCNT-NiO electrodes compared to others. The slightly high R_{ct} of the former electrode may possibly be due to the more work done by this electrode in generating high current response compared to the latter. The n values are less than the ideal 1.0 expected from an ideal capacitive behaviour, thus suggesting pseudo-capacitive properties for these electrodes.

Table 5.1: Impedance data obtained for the bare EPPGE and the modified electrodes in 5 mM $Fe(CN)_6]^{4-}$ /$[Fe(CN)_6]^{3-}$ solution at 0.2 V (vs Ag|AgCl sat'd KCl).

Electrode	**Impedimetric Parameters**				
	R_s /Ω cm^2	CPE / μFcm^{-2}	n	R_{ct} /Ω cm^2	Z_W / mΩ cm^2
EPPGE	12.44 ±0.01	13.40 ±1.91	0.64 ±0.01	70.10 ±2.84	0.17 ±0.01
EPPGE-MWCNT	11.73 ±0.01	5.30 ±0.06	0.59 ±0.01	58.10 ±0.16	0.17 ±0.01
EPPGE-Ni	13.00 ±0.01	9.90 ±1.41	0.64 ±0.01	97.30 ±0.90	0.09 ±0.01
EPPGE-NiO	13.98 ±0.02	70.00 ±13.34	0.63 ±0.01	130.40 ±0.05	0.10 ±0.01
EPPGE-MWCNT-Ni	17.62 ±0.01	95.90 ±9.83	0.76 ±0.01	21.77 ±0.09	0.14 ±0.01
EPPGE-MWCNT-NiO	13.03 ±0.01	714.00 ±181.0	0.89 ±0.05	14.03 ±0.20	0.23 ±0.01

5.3 Comparative electrocatalytic properties: DEAET and Hydrazine as analytical probe.

Figure 5.5 presents the comparative current responses of the electrodes in 0.1 mM DEAET in PBS solution pH 9.4 (Figure 5.5a) and 1.0 mM hydrazine in 0.1 M Na_2SO_4 solution (Figure 5.5b). EPPGE-MWCNT-Ni demonstrated the best electrocatalytic properties with a less positive onset potential of about 0.2 V for DEAET (Figure 5.5a) and 0.3 V for the hydrazine (Figure 5b). Since EPPGE-MWCNT-Ni electrode gave the best result from the catalysis study, the effect of Ni nanoparticle loading on the electrocatalysis towards DEAET and hydrazine was investigated. From the cyclic voltammograms in Figure 5.6, the current responses (after background current subtraction) due to DEAET (Figure 5.6a) and hydrazine (Figure 5.6b) at different loadings of the Ni nanoparticles (2.5 to 10 mg) showed that a maximum current was reached at 7.5 mg and 2.5 mg of Ni nanoparticles for DEAET and hydrazine, respectively. The drop in current response after 7.5 mg Ni for DEAET or 2.5 mg Ni for hydrazine could be due to factors such as: (i) the transformation of the electrode surface to an insulator due to the high concentrations of the surface-confined nickel nanoparticles, which may be interpreted as a result of the increased electrical resistance and the resistance to mass transport through the film as the film thickness increases [6], and (ii) hydrazine is a strong reducing agent and can easily co-ordinate more and reduce the nickel nanoparticles as concentrations increases.

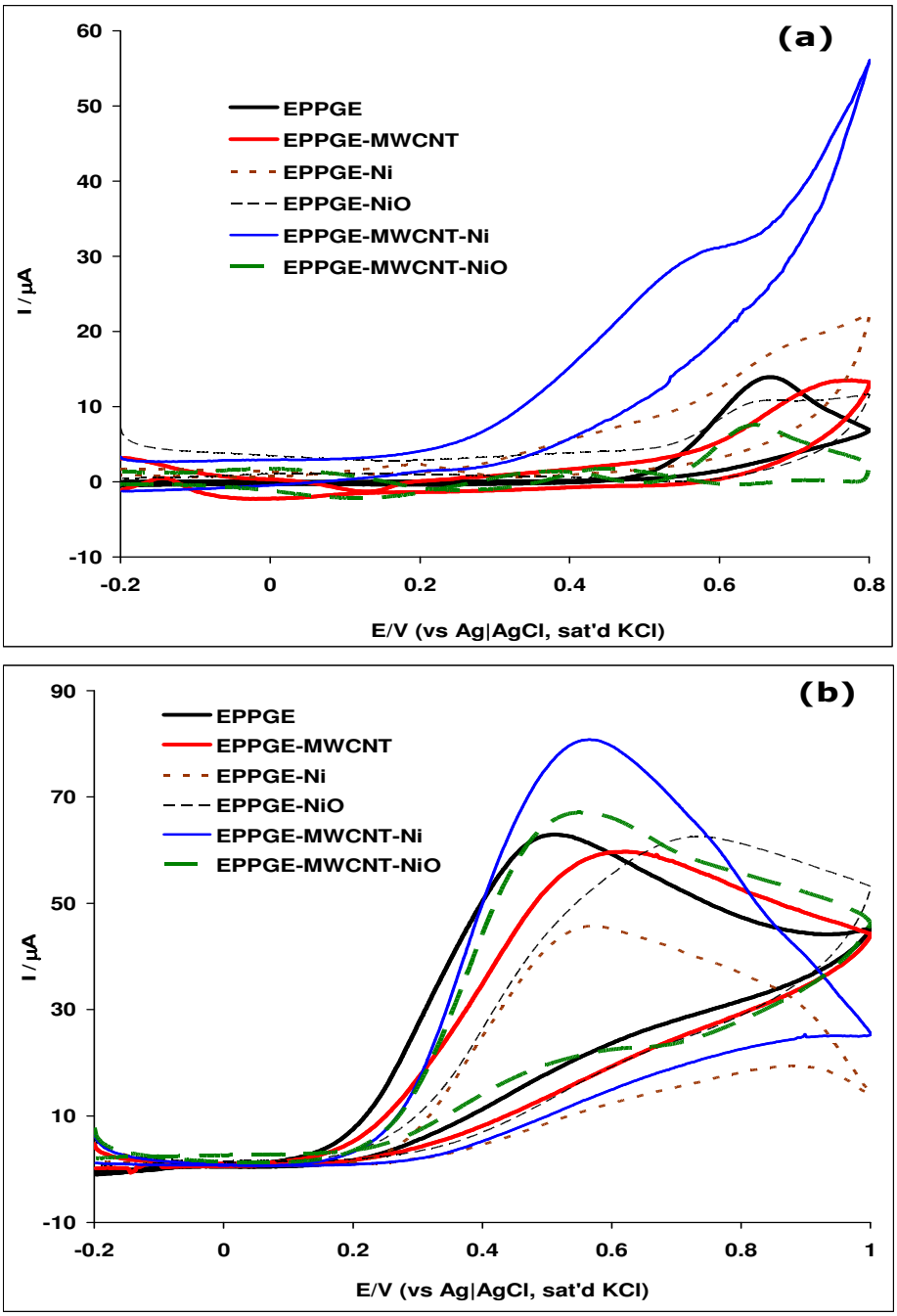

Figure 5.5: Comparative current response (after background current subtraction) of the electrodes in (a) 0.1 mM DEAET solution in pH 9.4 PBS and (b) 1.0 mM hydrazine solution in 0.1 M Na_2SO_4, scan rate = 25 mVs^{-1}.

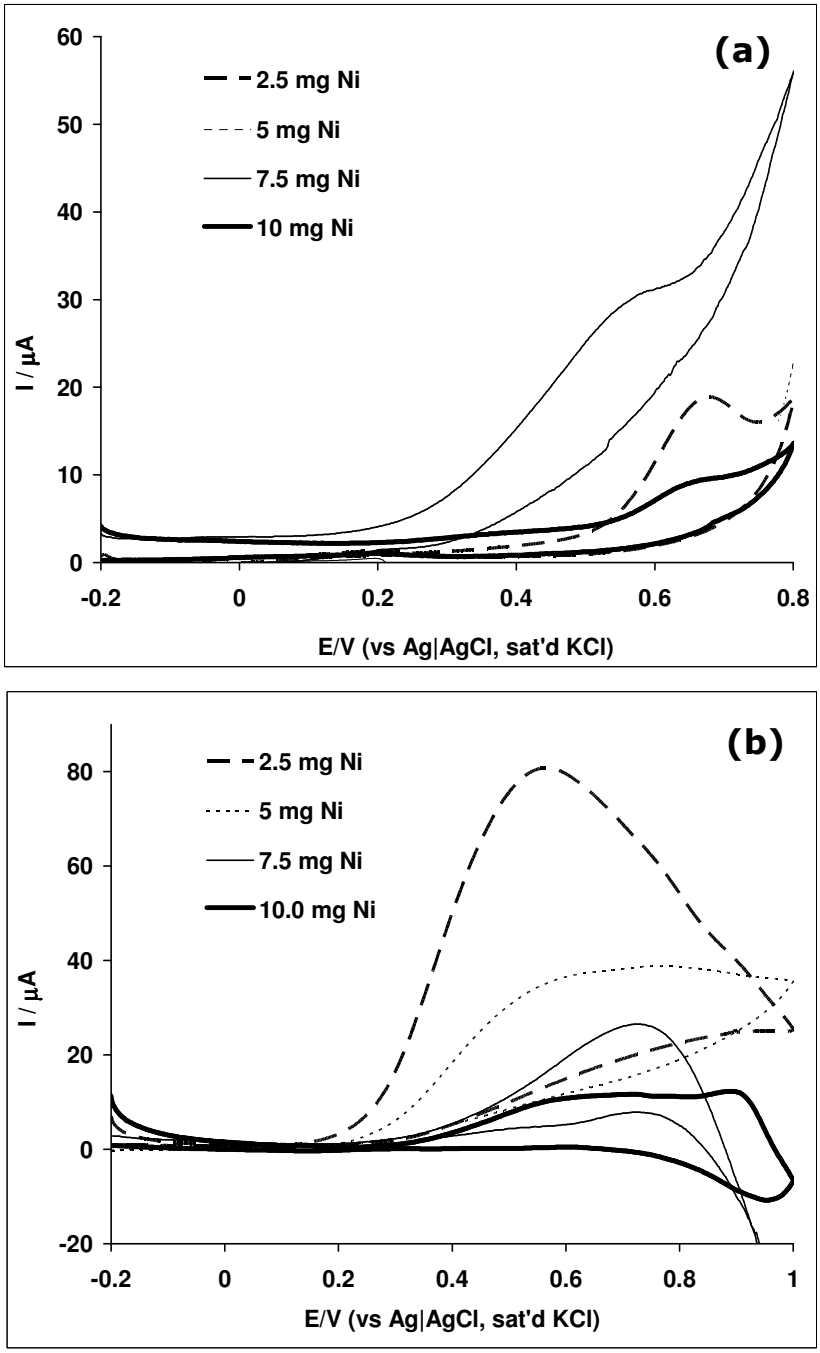

Figure 5.6 Comparative current response (after background current subtraction) for different Ni loading at the EPPGE-MWCNT-Ni electrode in (a) 0.1 mM DEAET solution in pH 9.4 PBS and (b)1.0 mM hydrazine solution in 0.1 M Na_2SO_4, scan rate = 25 mVs^{-1}.

To obtain some insights into the electrocatalytic oxidation, EIS was performed at the anodic oxidation potential, ~ 0.6 V of the analytes using the EPPGE-MWCNT-Ni electrode. Figure 5.7 shows the obtained Nyquist plot (a) and Bode plots (b) for these two analytes.

The raw impedance spectra were satisfactorily fitted with modified Randles equivalent circuit (Figure 5.7c), where L is an inductive element, R_{ad} is the resistance to adsorption, while the other elements are as already defined. R_{ad} and L are well known electrical elements associated with the adsorption of reaction intermediate(s) [7-9], clearly suggesting the involvement of the analytes intermediate products in the overall electrocatalytic oxidation process. The R_{ad} value is therefore interpreted here as the consequence of the adsorption of the intermediate(s) on the electrodes thereby creating an inductive effect on the electrode. For the DEAET, the EIS parameters are CPE (8.03 μFcm-^{2}), n (0.57), Z_w (2.60 μΩcm^2), L (0.37 mHcm^2) and R_{ad} (13.4 Ωcm^2). For the hydrazine, the parameters were CPE (1.32 μFcm-^{2}), n (0.46), Zw (2.87 μΩcm^2), L (0.23 mHcm^2) and R_{ad} (9.75 Ωcm^2). The presence of the Z_w in the circuit, coupled with the n values being close to the ideal Warburg diffusive value of 0.5, is indicative of some diffusion processes for these two analytes at this MWCNT-Ni electrode. Indeed, the occurrence of both L and Z_w (and n values) suggests both adsorption and diffusion-controlled reactions.

From the Bode plots (-phase angle vs log f), two phases' relaxation processes were observed at the low frequency (-0.6 Hz for DEAET) and high frequency (1.1 Hz for DEAET and 1.3 Hz for hydrazine) regions, an indication of a complex electrochemical process occurring at the electrode|electrolyte interface during the electrooxidation of the DEAET and hydrazine.

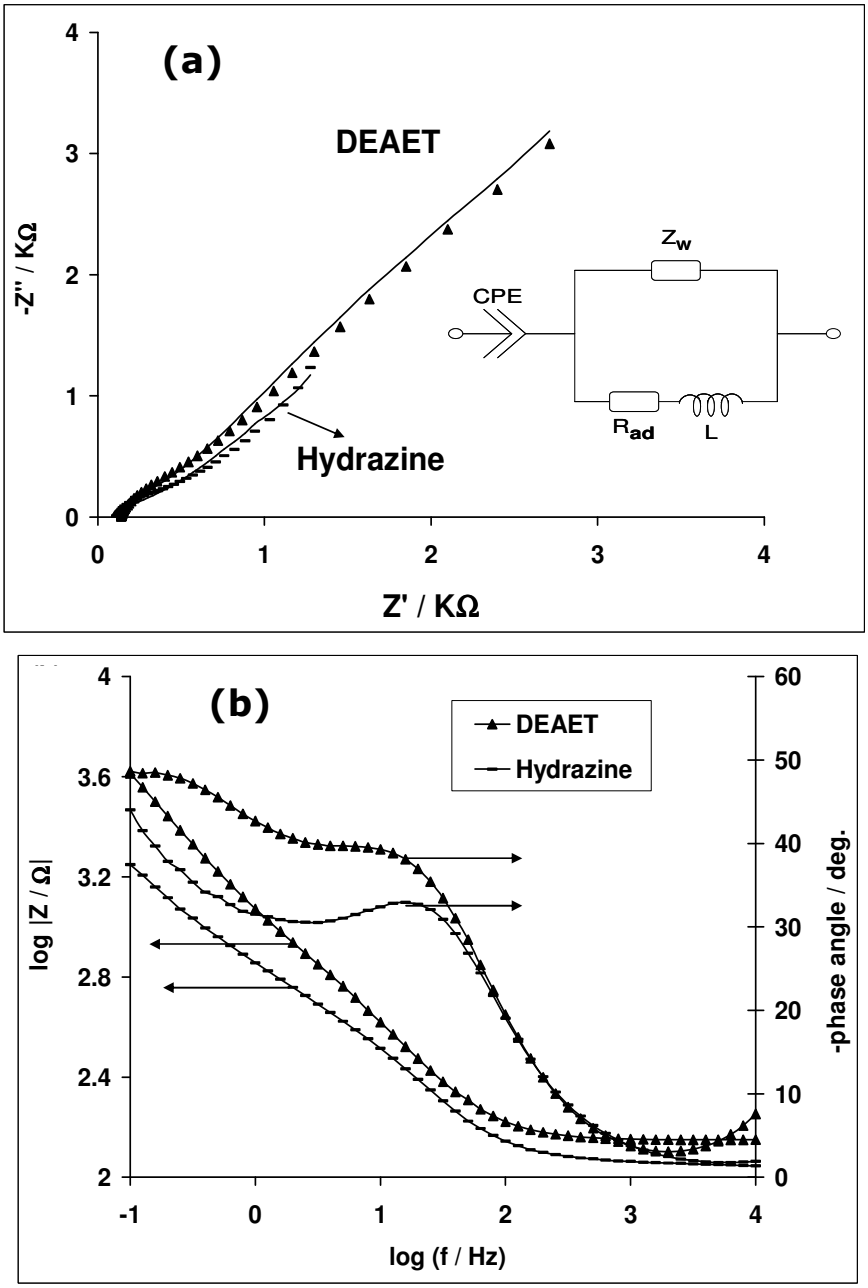

Figure 5.7: (a) Typical Nyquist plots obtained for EPPGE-MWCNT-Ni in 0.1 mM DEAET solution in PBS 9.4 and 1.0 mM hydrazine in 0.1 M Na_2SO_4 solution respectively (at fixed potential 0.6 V vs Ag|AgCl, sat'd KCl). (b) Represents the Bode plots obtained for the EPPGE-MWCNT-Ni, showing the plots of -phase angle / deg. vs log (f / Hz)) and the plot of log |Z/Ω| vs log (f/Hz) for both DEAET and hydrazine.

The complex process identified for DEAET from this study may also explain the two oxidation peaks noticed during the electroxidation of the analyte demonstrated by the voltammograms during the scan rate study discussed below. From the other Bode plots (log |Z| vs log f), the slope of the mid-frequency region (-0.54, R^2 = 0.9989) is indicative of pseudocapacitive behaviour, while the slope at the high frequency region (-0.41, R^2 = 0.9927) is indicative of strong resistance.

5.4 Effect of varying scan rates

The affect of scan rate (ν) using cyclic voltammetry at constant concentration of DEAET (0.1 mM) and hydrazine (1.0 mM) in the same electrolyte conditions as described already using the EPPGE-MWCNT-Ni was investigated. A gradual increase in current height with a slight shift in potential was observed with increase in scan rate (Figure 5.8a for DEAET and figure 5.8b for hydrazine) at scan rate ranging from 25 to 1400 mVs^{-1}. The hydrazine oxidation peak at around 0.6 V disappeared after 200 mVs^{-1}. Interestingly, the oxidation of DEAET (Figure 5.8a) is characterised by the occurrence of two oxidation peaks at about 0.6 and 1.0 V. This study represents the first time such two peaks have been observed for DEAET electro-oxidation on any electrode. DEAET, just like any other sulfhydryl analytes, contains functional groups HS and NH_2 which exist in different ionic states under different pH conditions and are thus responsible for the two anodic peaks. This interpretation is in agreement with a similar observation during the electrocatalytic detection of cysteine, a well known sulfhydryl [10].

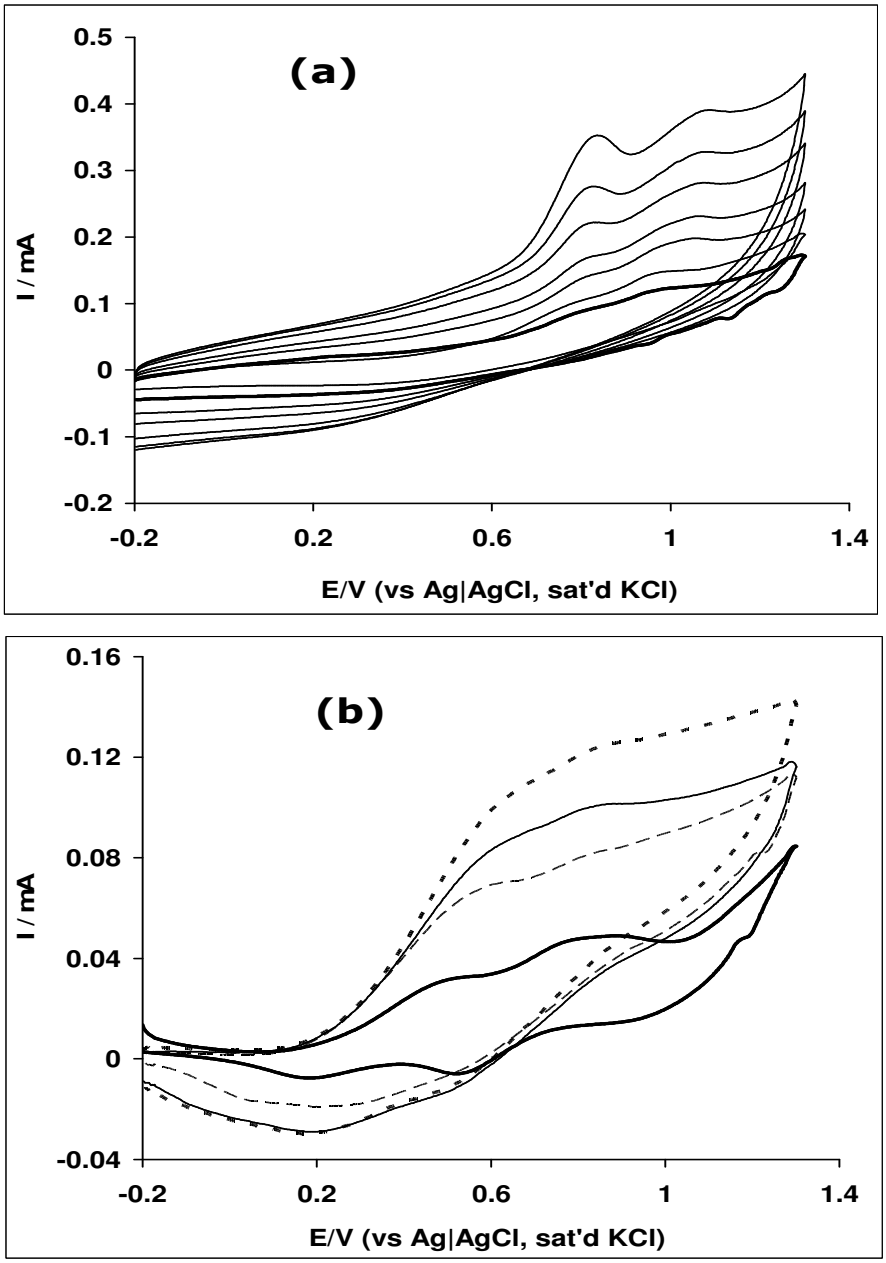

Figure 5.8: Cyclic voltammetric evolutions at the EPPGE-MWCNT-Ni for (a) 0.1 mM DEAET in 0.1 M pH 9.4 PBS (at 25, 75, 400, 600, 950, 1200 and 1400 mVs^{-1}, inner to outer), and (b) 1.0 mM Hydrazine in 0.1 M Na_2SO_4 solution after background subtraction (at 25, 75, 150 and 200 mVs^{-1}, inner to outer).

The two anodic peaks for DEAET oxidation at pH 9.4 were attributed to the oxidation of the two ionic forms of DEAET represented below:

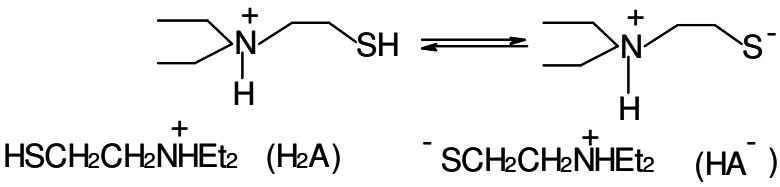

(5.2)

These two states are possible since in a less basic medium, the pKa of $HSCH_2CH_2N^+HEt_2$ is 8.3 at 25 ^{0}C [11], which is less than the pH of the medium and therefore could easily be deprotonated at pH 9.4 to give $^-SCH_2CH_2N^+HEt_2$. From the Randles-Sevčik theory for an anodic oxidation process [12], the plot of the peak current (I_p) against the square root of scan rate ($\nu^{1/2}$) gave a linear relationship (R^2 = 0.9925) for DEAET oxidation with approximately zero intercept, confirming a diffusion-controlled process. However, at higher scan rate (> 500 mVs^{-1}), plot of the peak current (I_p) against the square root of scan rate ($\nu^{1/2}$) (not shown) gave a straight line (R^2 = 0.9901) with a negative intercept suggesting that at higher scan rates the reaction is not totally diffusion-controlled. The result of the scan rate study (Figure 5.8b) for hydrazine electro-oxidation indicates adsorption of oxidation product(s) or fouling effect, evidenced by the disappearance of the hydrazine oxidation peak at around 0.5 V and that of the complex oxidation intermediate products at around 0.9 V after 200 mVs^{-1}, which may be related to the reductive activity of hydrazine solution towards nickel ions as reported by Bettahar et al. [13], thereby impeding the catalytic activities of the Ni nanoparticles. In addition, for both DEAET and hydrazine, the current function plot

showed that $I_p/\nu^{1/2}$ decreased as the scan rates increased, characteristic for coupled electrochemical and chemical reaction (EC_{cat}) mechanism.

Using Tafel equation (Equation 5.3) for a totally irreversible diffusion-controlled process [14], the linear relationship between the peaks potential E_p and the logν (not shown) confirms the chemical irreversibility of DEAET and hydrazine electrocatalytic oxidation processes.

$$E_p = \frac{b}{2}\log \nu \tag{5.3}$$

$$b = \frac{2.303RT}{\alpha n_\alpha F} \tag{5.4}$$

where R, T, α and n_α have their usual meanings. The plots of peak potential (E_p) against logarithm of scan rate (log ν) (not shown) gave a straight lines with Tafel slopes of approximately 262 and 406 mV dec^{-1} for the DEAET and hydrazine, respectively. These values are higher that the theoretical 118 mV dec^{-1} for a one-electron process involved in the rate-determining step. Such high Tafel values (leading to small α values, < 0.5) are the consequence of adsorption of reactants or intermediates on the electrode surfaces and/or reactions occurring within a porous electrode structure [15]. The Tafel slope is comparable with the values obtained using electrodeposited of Ni nanoparticles onto SWCNT.

5.6 Electroanalysis of DEAET and Hydrazine

Chronoamperometric (CA) and adsorptive linear sweep voltammetric (AdLSV) experiments were carried out for the two analytes. Figure 5.9 exemplifies typical CA (Figure 5.9a) and LSV

(Figure 5.9b) obtained for the hydrazine. The CA and LSV for the DEAET gave similar curves. The chronoamperograms were obtained by adding different aliquots of the analyte solution to their respective electrolyte solution. Each AdLSV curve was obtained after gently stirring the analyte for ~15 min in the presence of the electrode. From the CA curves, the catalytic rate constant (*k*) for each of the analyte was estimated using Equation 5.5 [12]:

$$\frac{I_{cat}}{I_L} = \pi^{1/2}(kC_o t)^{1/2} \qquad (5.5)$$

where all symbols have their usual meaning. From the plot of I_{cat}/I_L vs $t^{1/2}$ (not shown) the *k* value for the EPPGE-MWCNT-Ni in the solutions containing DEAET and hydrazine are ~ (5.9±0.50) x 10^9 and (7.7±0.66) x 10^8 $cm^3mol^{-1}s^{-1}$, respectively. The value of 5.9 x 10^9 $cm^3mol^{-1}s^{-1}$ is approximately three orders of magnitude greater than the 1123.59 $M^{-1}s^{-1}$ (i.e., 1.124 x 10^6 $cm^3mol^{-1}s^{-1}$) reported for DEAET electrocatalytic oxidation using basal pyrolytic graphite modified with SWCNT and cobalt(II)tetra-aminophthalocyanine (BPPGE-SWCNT-CoTAPc [16]). On the other hand, the 7.7 x 10^8 $cm^3mol^{-1}s^{-1}$ obtained for hydrazine is greater compared with 4.1 x 10^7 $cm^3mol^{-1}s^{-1}$ [17] reported for the analyte on gold-polypyrrole composite matrix modified glassy carbon electrode (Au/PPy/GCE), 2 x 10^7 $cm^3mol^{-1}s^{-1}$ for *o*-aminophenol modified glassy carbon electrode [18].

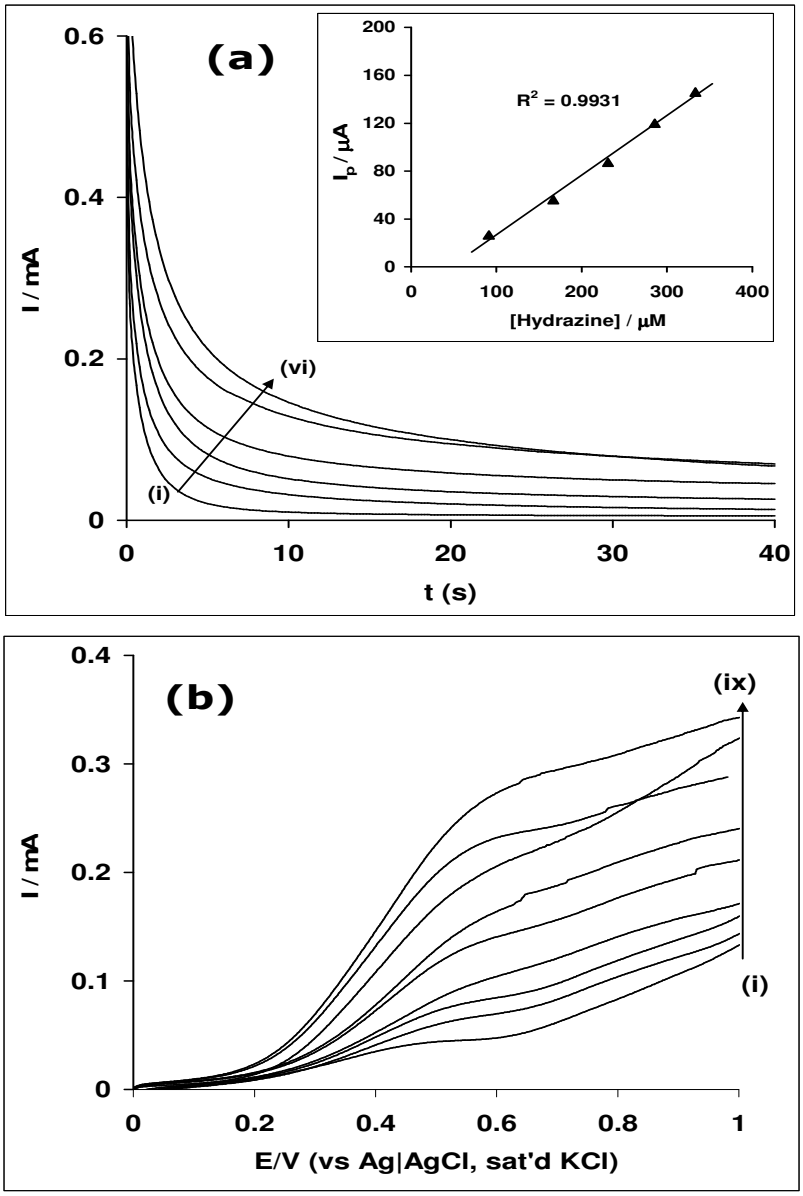

Figure 5.9: (a) Typical chronoamperograms obtained for the EPPGE-MWCNT-Ni in 0.1 M Na_2SO_4 solution containing different concentrations of hydrazine (0.0, 91, 167, 231, 286, and 333 µM, (i to vi)). Inset represents the plot of current response vs hydrazine concentration. (b) Typical linear sweep voltammograms obtained for the EPPGE-MWCNT-Ni in 0.1 M Na_2SO_4 solution containing different concentrations of hydrazine (0.0, 91, 130, 167, 231, 286, 333, 355, and 375 µM (i to ix)).

It is also greater than 6.26 x 10^6 $cm^3mol^{-1}s^{-1}$ for curcumin multi-walled nanotubes modified glassy carbon electrode [19], but about four orders of magnitude greater than reported (2.2x10^4 $cm^3mol^{-1}s^{-1}$) for electrodeposited Ni on SWCNTs. These results clearly indicate excellent catalysis for the chemically-synthesized Ni nanoparticles on MWCNTs towards these two analytes. Similarly, the plot of I_p versus [DEAET] gave the sensitivity values which are 13.6±0.33 $AM^{-1}cm^{-2}$ for DEAET and 3.33±0.13 $AM^{-1}cm^{-2}$ for hydrazine. The 3.33 $AM^{-1}cm^{-2}$ for for the electrode in hydrazine is greater compared to the 1.117 $AM^{-1}cm^{-2}$ reported for nanoporous gold particles modified platinum electrode [20]. The limit of detection was obtained using [21]:

$$LoD = 3.3\frac{\delta}{m} \tag{5.6}$$

The obtained LoDs are 0.87±0.07 and 0.29±0.02 μM for DEAET and hydrazine, respectively. The LoD value obtained in this study for DEAET is about 9 times lower than 8.0 μM obtained for screen-printed electrode modified with MWCNTs integrated with organophosphorus hydrolase [22]; ~3.5 times lower than the 3.0 μM reported at BPPGE-SWCNT-CoTAPc [16], and 3.0 μM reported for glassy carbon electrode modified with polypyrrole and pyrroloquinoline [23], ~ 4.6 times lower than 4.0 μM reported for BPPGE-Ni powder [4], and about 3 times lower than 2.5 μM for EPPGE-SWCNT-Ni (obtained by adsorption stripping voltammetry). The LoD value obtained for hydrazine (0.29 μM) is ~ 18 times lower compared to 5.3 μM detection obtained for EPPGE-SWCNT-Ni by electrodeposition. The enhanced sensitivity of the electrode used in this study and its very good limit of detection could be due to the

synergistic behaviour between the MWCNTs and the catalytic nickel nanoparticles, possibly affected by the method of electrode preparation adopted in this work. Table 5.2 compares the analytical data obtained in this work with literature [4,16,19,22,26,24-27].

Further probe into the adsorptive properties of hydrazine and DEAET was obtained from the AdLSV data. The voltammograms were analysed using the Langmuir adsorption isotherm theory [28]:

$$\frac{C}{I_{cat}} = \frac{1}{\beta I_{\max}} + \frac{C}{I_{\max}} \tag{5.7}$$

where C, I_{cat} and I_{max} are already defined (section 1.7). β is the adsorption equilibrium constant, and is related to the electrochemical Gibbs free energy change (ΔG^o) as:

$$\Delta G^o = RT \ln \beta \tag{5.8}$$

Each plot of the ratio of C/I_{cat} vs C gave straight line (not shown), suggesting an adsorption-controlled process. From the slopes and the intercepts of the curve obtained, the β value of each analyte was obtained, and then used to estimate the ΔG^o value. The ΔG^o values were −17.21 and −18.14 kJmol^{-1} for hydrazine and DEAET, respectively. There is no report to compare the ΔG^o value for hydrazine with at the moment. However, the ΔG^o obtained for DEAET in this study is lower than the value of −45.8 kJmol^{-1} on the EPPGE-SWCNT-Ni platform. The result further confirms the less adsorptive behaviour of the chemically-synthesized Ni nanoparticles on the MWCNT platform used in this study over the electrodeposited Ni nanoparticles on SWCNT platform.

Table 5.2: Comparative analytical data for the detection of DEAET and hydrazine at chemically modified electrodes.

Electrodes	**Methods**	**Analytical Parameters**			
		LCR / μM	**LoD/ μM**	***Sensitivity* /μAμM^{-1}**	**Ref**
	DEAET				
SPE- MWCNT-OPH	CA	50-250	8.0	36.0	22
GCE-PPy-PQQ	CA	5.8-100	3.0	0.00137 cm-^{2}	24
BPPGE-SWCNT-CoTAPc	CA	-	3.0	0.06	16
BPPGE-Ni powder	CA	0.01-100	4.0	0.023	4
BPPGE-MWCNT-Ni	CA	91.0-333.0	0.87±0.07	13.6±0.33cm^{-2}	This work
	Hydrazine				
Pd-BDD array Pd-Macroelectrode	LSV	6.8-102 30.6-204	1.8 2.6	0.008 0.06	26
CM-MWCNT-GCE	CA	2.0 – 44	1.4	0.0229	19
CCE-NiHCF	CV	20 - 2000	8.0	-	25
IMWCNTCPE	DPV	0.6-8.0 8.0-100.0	0.29	0.167 0.014	26
ST-NiTsPc	CA	100-600	10	–	27
BPPGE-MWCNT-Ni	CA	91.0-333.0	0.29±0.02	3.33±0.13cm^{-2}	This work

Chronoamperometry; LSV: Linear sweep voltammetry; DPV: Differential pulse voltammetry; SPE- MWCNT-OPH: Screen-printed carbon electrode modified with multi-walled carbon nanotubes and organophosphorus hydrolase; GCE-PPy-PQQ: Glassy carbon electrode modified with poplypyrrole and pyrroloquinoline quionone; BPPGE-SWCNT-CoTAPc: Basal plane pyrolytic graphite electrode modified with single-walled carbon nanotube and cobalt tetraaminophthalocyanine; BPPGE-Ni powder: Basal plane pyrolytic graphite electrode modified with nickel micropowders;Pd-BDD: palladium modified with boron-doped diamond microelectrode array; CM-MWCNT-GCE:Curcumin- multi-walled carbon nanotube modified glassy carbon electrode; CCE-NiHCF: carbon ceramic electrode (CCE) modified with nickel hexacyanoferrate; IMWCNTCCE: indenedione derivatives multi-walled carbon nanotube modified carbon ceramic electrode; ST-NiTsPc: Nickel tetrasulfonated phthalocyanine (NiTsPc) immobilized onto titanized silica gel.

Based on the report of hydrazine oxidation in aqueous medium [29], the following general mechanism for the oxidation of the analyte on the EPPGE-MWCNT-Ni electrode is suggested:

$$[\text{MWCNT-Ni}^{2+}]_{\text{film}} \longrightarrow [\text{MWCNT-Ni}^{3+}]_{\text{film(aq)}} + e^- \quad (5.9)$$

$$[\text{MWCNT-Ni}^{3+}]_{\text{film(aq)}} + N_2H_{4(aq)} \rightleftharpoons [\text{MWCNT-Ni}^{3+}\text{----}N_2H_{4(aq)}]_{\text{adduct}} \quad (5.10)$$

$$[\text{MWCNT-Ni}^{3+}\text{----}N_2H_{4(aq)}]_{\text{adduct}} \rightleftharpoons [\text{MWCNT-Ni}^{2+}]_{\text{film}} + N_2H_{3(aq)} + e^- \quad (5.11)$$

slow (rate limiting)

$$N_2H_3 + 3H_2O \longrightarrow N_2 + 3H_3O^+ + 3e^- \quad (5.12)$$

$$[\text{MWCNT-Ni}^{3+}]_{\text{film(aq)}} + e^- \longrightarrow [\text{MWCNT-Ni}^{2+}]_{\text{film}} \quad (5.13)$$

$$N_2H_4 + 4H_2O \longrightarrow N_2 + 4H_3O^+ + 4e^- \quad \text{(Overall reaction)} \quad (5.14)$$

Equation 5.9 defines the redox process of the nickel species confined in the MWCNT. The interaction of the Ni^{3+} with aqueous hydrazine results to the formation of an adduct (Equation 5.10). The adduct undergoes an internal reaction leading to the formation of hydrazine oxidation intermediate (N_2H_3) and the generation of Ni^{2+} (Equation 5.11). This also represents the rate-determining step, a one-electron process. Equation 5.12 represents the oxidation of the intermediate to give nitrogen as the final product, while Equation 5.13 represents the regeneration of the original nickel (II) catalyst. The overall electrocatalytic oxidation reaction of hydrazine (Equation 5.14) is thus a 4-electron process as also proposed by others [14, 30].

For DEAET, the mechanism follows a similar process, summarised as follows:

$$RSH + OH^- \rightleftharpoons RS^{\cdot} + H_2O \quad (5.15)$$

$$[MWCNT\text{-}Ni^{3+}]_{film(aq)} \; RS^- \rightleftharpoons [MWCNT\text{-}Ni^{3+}\text{----}(RS)]_{adduct} \quad (5.16)$$

$$[MWCNT\text{-}Ni^{3+}\text{----}(RS)]_{adduct} \rightleftharpoons [MWCNT\text{-}Ni^{2+}]_{film} \; RS^{\cdot} + e^- \quad (5.17)$$

slow (rate limiting)

$$RS^{\cdot} + RS^{\cdot} \longrightarrow RSSR \quad \text{(fast)} \quad (5.18)$$

The DEAET represented as a thiol (RSH) forms a thiyl ion (RS^-) in basic medium (Equation 5.15). The MWCNT-Ni^{2+} film interact with the thiyl ion (RS^-) in solution forming an adduct (Equation 5.16). The adduct rearranged to give the thiyl radical in a one-electron process which represent the rate-determining step (Equation 5.17). The thiyl radical ($RS^{\cdot}$) then dimerises to form the disulphide product (Equation 5.18). As in the hydrazine mechanism, Equations 5.9 and 5.13 still hold.

This study has shown that the MWCNT-Ni nanocomposite modified electrode yielded the fastest electron transport as well as the best electrocatalytic behaviour towards DEAET and hydrazine compared with other electrodes investigated or reported in the literature. This enhancement is associated with high electrical-conducting MWCNTs which form a synergistic behaviour with nickel nanoparticles. Electrocatalysis of DEAET on the EPPGE-MWCNT-Ni was predominantly diffusion-controlled, with little or no adsorption of reaction intermediates. The adsorption equilibrium constant (β) and the Gibbs free energy change due to adsorption ΔG^o for the EPPGE-MWCNT-Ni electrode in DEAET and hydrazine were estimated as 1.51×10^3 M^{-1} (-18.14 $kJmol^{-1}$) and 1.04×10^3 M^{-1} (– 17.21 $kJmol^{-1}$), respectively.

References

1. S.H. Wu, D.H. Chen, *J. Colloid Interf. Sci*. 259 (2003) 282.

2. L. Xiang, X.Y. Deng, Y. Jin, *Scripta Materialia* 47 (2002) 219.

3. D. Nkosi, J. Pillay, K. I. Ozoemena, K. Nouneh and M. Oyama, *Phys. Chem. Chem. Phys*. 12 (2010) 604.

4. J. Pillay, K.I. Ozoemena, *Electrochem. Commun.* 9 (2007) 1816.

5. L. Yang, Y. Li, *Biosens. Bioelectron*. 20 (2005) 1407.

6. K.I. Ozoemena, T. Nyokong, *Inorg. Chem. Commun.* 6 (2003) 1192.

7. J. Bisquert, H. Randriamahazaka, G. Garcia-Belmonte, *Electrochim Acta* 51(2005) 627.

8. M. Jafarian, M.G. Mahjani, H. Heli, F. Gobal, H. Khajehsharifi, M.H. Hamedi *Electrochim Acta* 48 (2003) 3423.

9. S. Majdi, A. Jabbari, H. Heli, A.A. Moosavi-Movahedi *Electrochim Acta* 52 (2007) 4622.

10. W-H Su, S-H Cheng, *Electrochem. Commun*. 10 (2008) 899-902.

11. Y.-C. Yang, L.L. Szafraniec, W.T. Beaudry, D.K. Rohrbaugh, L.R. Procell, J.B. Samuel, *J. Org. Chem.* 61 (1996) 8407.

12. A.J. Bard, L.R. Faulkner, Electrochemical Methods: Fundamentals and Applications, 2nd ed., John Wiley & Sons, Hoboken, N.J., 2001.

13. A-G Boudjahem, S. Monteverdi, M. Mercy, and M.M. Bettahar, *Langmuir* 20 (2004) 208.

14. J.A. Harison, Z.A. Khan, *J. Electroanal. Chem.* 28 (1970) 131.

15. J.N. Soderberg, A.C. Co, A.H.C Sirk, V.I. Birss, *J. Phys. Chem. B* 110 (2006) 10401.

16. J. Pillay, K.I. Ozoemena, *Electrochim. Acta* 52 (2007) 3630.
17. J. Li, X.Q. Lin, *Sens. Actuat. B: Chem.* 126 (2007) 527.

18. H. M. Nassef, A.-E. Radi, C. K. O'Sullivan, *J. Electroanal. Chem.* 592 (2006) 139.

19. L. Zheng, J.-f. Song, *Sens. Actuators B* 135 (2009) 650.

20. Q. Yi, W. Yu, J. *Electroanal. Chem.* 633 (2009) 159.

21. G. D. Christian, 2004 Analytical Chemistry, 6th ed. John Wiley and Sons New York, p 113.

22. K. A. Joshi, M. Prouza, M. Kum, J. Wang, J. Tang, R. Haddon, W. Chen, A. Mulchandani, *Anal. Chem.* 78 (2006) 331.

23. J. Wang, J. Zima, N.S. Lawrence, M.P. Chatrathi, *Anal. Chem.* 76 (2004) 4721.

24. O.V. Shulga, C. Palmer, *Anal. Bioanal. Chem*. 385 (2006) 1116.

25. A. Abbaspour, A. Khajehzadeh, A. Ghaffarinejad, *J. Electroanal. Chem.* 631 (2009) 52.

26. H.R. Zare, N. Nasirizadeh, F. Chatraei, S. Makarem, *Electrochim. Acta* 54 (2009) 2828.

27. E.F. Perez, G.-O. Neto, A.A. Tanaka, L.T. Kubota, *Electroanalysis* 10 (1998) 111.

28. H.X. Ju, L. Donal, *J. Electroanal. Chem*. 48 (2000) 150.

29. A. Abbaspour, M. Shamsipur, A. Sironeinejad, R. Kia, P.R. Raithby, *Electrochim. Acta* 54 (2009) 2916.

30. C. batchelor-McAuley, C.E. Banks, A.O. Simm, T.G.J. Jones, and R.G. Compton, *Analyst* 131 (2006) 106.

CHAPTER SIX

Probing the Electrochemical Behaviour of SWCNT-Cobalt Nanoparticles and Their Electrocatalytic Activities Towards the Detection of Nitrite in Acidic and Physiological pH Conditions*

* The following publications resulted from part of the research work presented in this chapter and are not referenced further in this thesis:

5. **Abolanle S. Adekunle**, Jeseelan Pillay, Kenneth I. Ozoemena, *Electrochim. Acta* 55 (2010) 4319-4327.
6. **Abolanle S. Adekunle**, Kenneth I. Ozoemena, *Int. J. Electrochem. Sci.* (in press).

6.1. Comparative FESEM, AFM images EDX spectra

Figure 6.1 showed the comparative scanning electron microscopy (SEM) images of the EPPGE, EPPGE-SWCNT, EPPGE-SWCNT-Co and EPPGE-SWCNT-CoO. Upon electro-deposition of Co nanoparticles, EPPGE-SWCNT-Co modified electrode was formed (Fig 6.1c). There is high dispersion of Co nanoparticles, possibly made due to the strong electrostatic interactions between the Co^{2+} ions in solution and the COO^{-} charge of the SWCNTs on the electrode surface. The Co nanoparticles form a porous and high electroactive material on the electrode surface but with several interstitial spaces or voids. Repetitive cycling (20 scans) of EPPGE-SWCNT-Co electrode in 0.1 M phosphate buffer solution, PBS (pH 7.0) gave EPPGE-SWCNT-CoO modified electrode in which the cobalt particles formed a thick amorphous film (Fig. 6.1d) with little voids. AFM topographic heights (not shown) increased from 14 nm for bare substrate to 80 nm on integrating with SWCNTs and finally to 120 nm on incorporation with cobalt or its oxides. Salimi *et al.* [1,2] employed similar method of electrode decoration with cobalt oxide nanoparticles and observed particles agglomeration with sizes ranging from 100 – 600 nm. As evident from the cross-sections (Figures 6.1g and h), the particle sizes are in the 8 – 30 nm range, suggesting some agglomeration of the nanoparticles.

Figure 6.2 is the EDX profile of the electrodes. The EPPGE electrode (a) was purely carbon (~ 100%) as would be expected for pure graphite surface. The presence of oxygen peaks in the EPPGE-SWCNT (b) is an indication of the successful modification of the SWCNT to the acid derivatives SWCNT-COOH while the sulphur peak can be attributed to the sulphuric acid used during treatment.

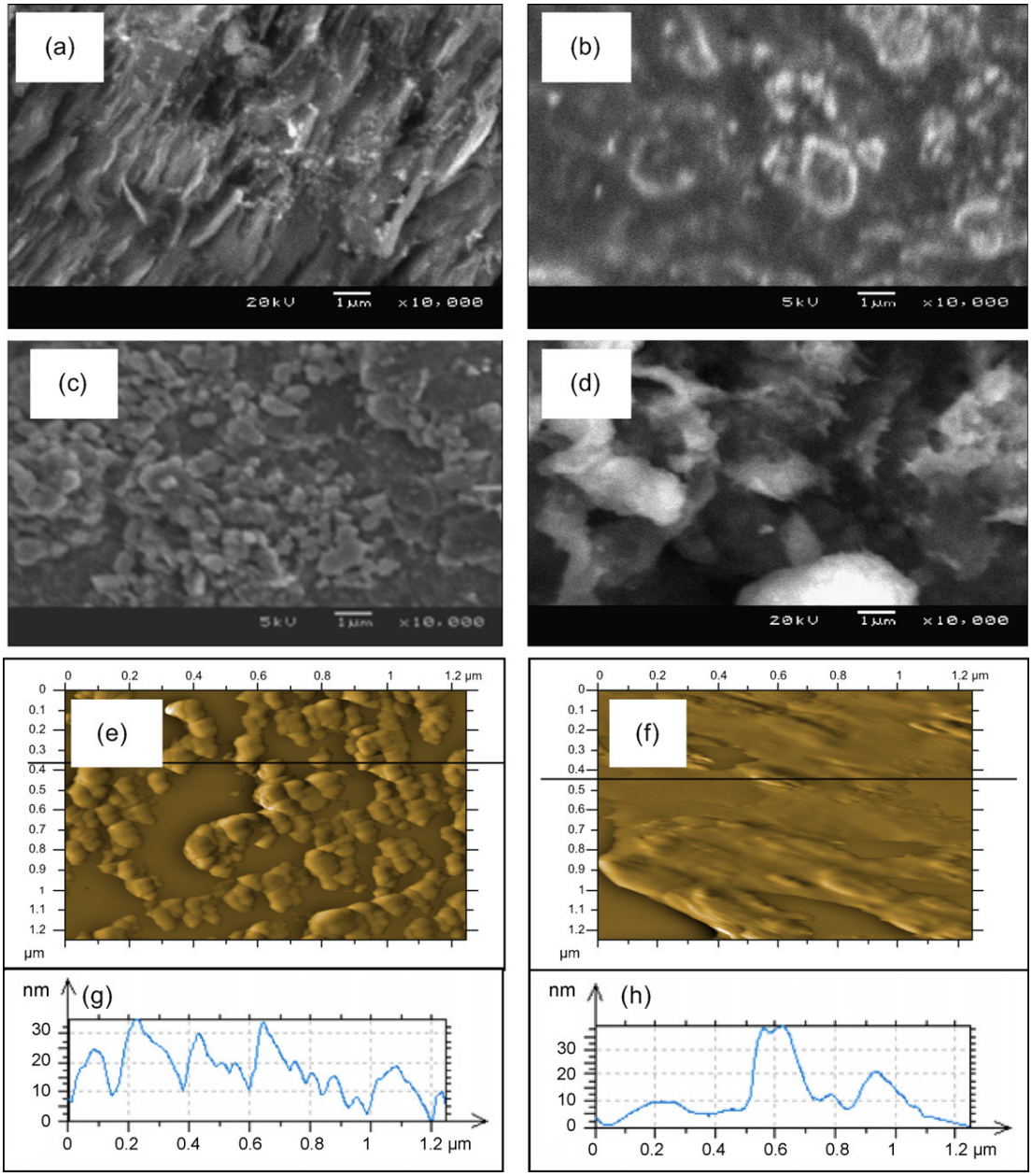

Figure 6.1: FESEM of (a) EPPGE, (b) EPPGE-SWCNT, (c) EPPGE-SWCNT-Co, (d) EPPGE-SWCNT-CoO. (e) and (f) are the AFM topography images for the EPPGE-SWCNT-Co and the EPPGE-SWCNT-CoO while (g) and (h) are their respective cross-sections.

EPPG-SWCNT-CoO (c) showed the presence of Co and oxygen peaks with very pronounced intensity implying that the electrode was successfuly modified with CoO nanoparticles. The occurrence of P and Na peaks in the EDX of EPPGE-SWCNT-CoO may be attributed to the sodium phosphate buffer solution used for the electrode treatment.

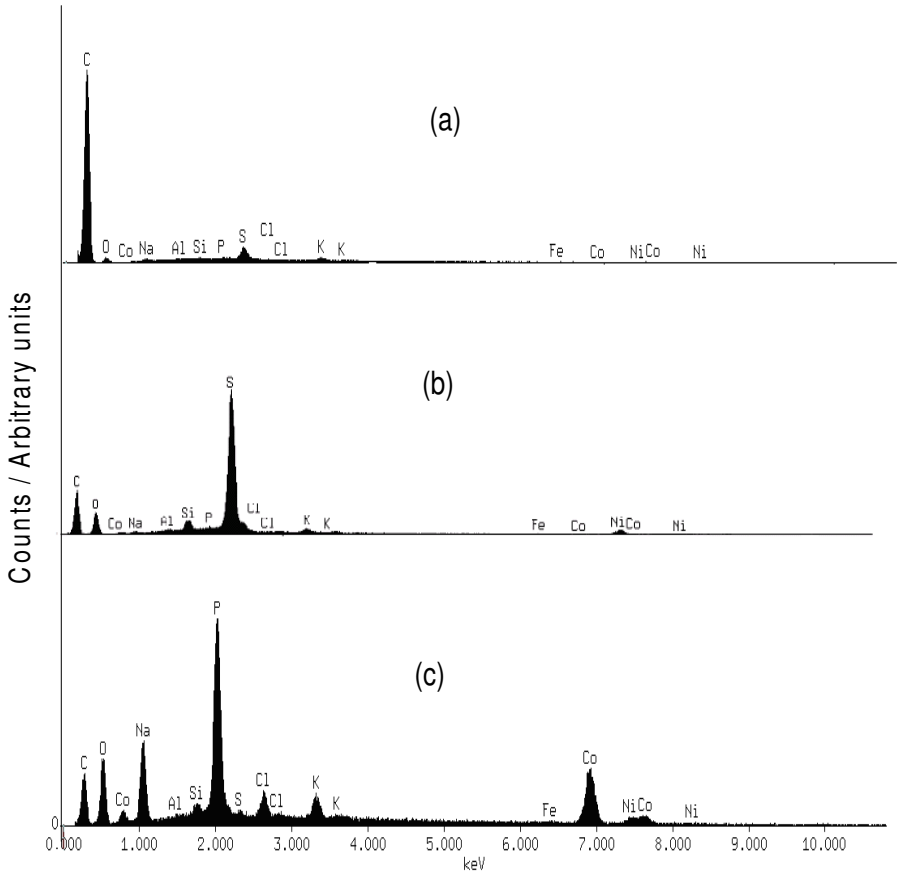

Figure 6.2: EDX spectra of (a) EPPGE (b) EPPGE-SWCNT, and (c) EPPGE-SWCNT-CoO.

6.2 Comparative Electrochemical characterization

Comparative current response (not shown) of bare-EPPGE, EPPGE-Co, EPPGE-CoO, EPPGE-SWCNT, EPPGE-SWCNT-Co and EPPG-SWCNT-CoO in PBS (pH 7.0) was investigated. From the cyclic voltammograms (not shown), the anodic peak at 0.68 V and its corresponding cathodic peak at around 0.46 V are attributed to Co(II)/Co(III) which has been reported to be at 0.7 to 0.8 V (vs SCE) [3-5] in an acidic medium. The anodic peak at 0.68 V vs Ag|AgCl, sat'd KCl (~ 0.64 V vs SCE) is close to 0.6 V vs SCE reported by Salimi et al. [2] and was attributed to the formation of Co_3O_4 through the reaction below:

$$3Co(OH)_2 + 2OH^- \longrightarrow Co_3O_4 + 4H_2O + 2e^- \qquad (6.1)$$

Another anodic peak was observed at around +1.0 V, also observed by others [2] at 0.95 V and assigned to COOH formation as a result of oxidation of $Co(OH)_2$ or the Co_3O_4 as represented by the equations below:

$$Co(OH)_2 + OH^- \longrightarrow CoOOH + H_2O + e^- \qquad (6.2)$$

$$Co_3O_4 + H_2O + OH^- \longrightarrow 3CoOOH + e^- \qquad (6.3)$$

Sunohara *et al.* [6] reported the peak at potential >1.0 V (vs Ag|AgCl) and attributed it to the Co_2O_3 / Co_3O_4 redox process. A cathodic peak was also observed at ca 0.72V and is attributed to the reduction of CoOOH to $Co(OH)_2$ or Co_3O_4. Peak at around - 0.2 V (vs Ag|AgCl, sat'd KCl) is due to Co^{2+}/Co redox process, similar to that observed by others [2] at around - 0.1 V (vs SCE) on a cobalt oxide nanoparticles modified glassy carbon electrode. The current

responses of these electrodes increase in this order: EPPGE-SWCNT-Co > EPPGE-SWCNT-CoO > EPPGE-Co > EPPGE-CoO > EPPGE-SWCNT > bare-EPPGE.

The result indicates that: (i) deposition of SWCNT on the bare–EPPGE enhances its electron transfer since SWCNTs could be acting as the conducting electrical nanowires for the flow of electrons; (ii) enhanced current response was observed when the cobalt nanoparticles were integrated with the SWCNTs, implying a positive synergistic behaviour between these two nanomaterials; and (iii) the SWCNT-Co modified electrodes gave higher current responses with decreased peak-to-peak separation potential (ΔEp = 0.23 V) compared with those without SWCNT (ΔE = 0.32 V). It is therefore reasonable to suggest that SWCNTs enhance the electrochemical response of the modified electrodes by serving as the conducting nanowires for electron transfer between the Co nanoparticles and the underlying EPPGE.

6.3 Comparative electron transport properties

The aim of this experiment was to explore the extent to which the modifiers allow the electron transport between $Fe(CN)_6]^{4-}$ / $[Fe(CN)_6]^{3-}$ redox probe and the base EPPGE. The CV experiments were performed in 5 mM $Fe(CN)_6]^{4-}$ / $[Fe(CN)_6]^{3-}$ solution (in PBS pH 7.0). The peaks in the 0 – 0.4 V region is due to the $Fe(CN)_6]^{4-}$ / $[Fe(CN)_6]^{3-}$ redox couple while the one at the 0.4 – 1.0 V region is ascribed to the Co(II)/Co(III) redox process (Figure 6.3).

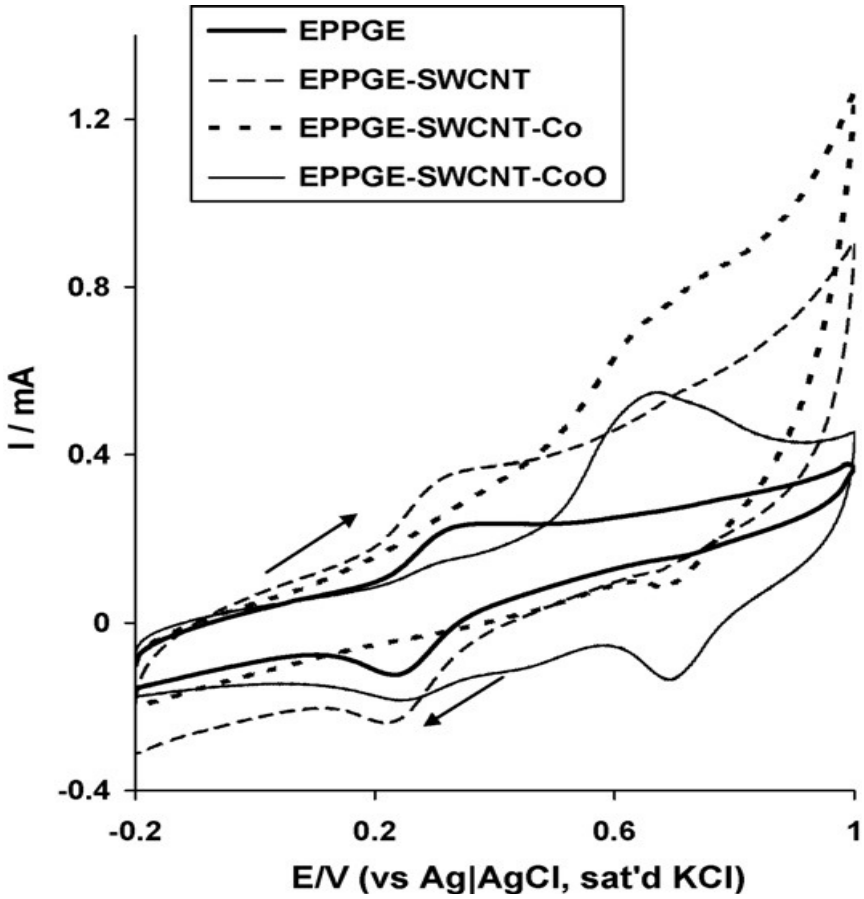

Figure 6.3: Typical examples of some cyclic voltammetric evolutions of the electrodes in 5 mM $[Fe(CN)_6]^{4-}$ / $[Fe(CN)_6]^{3-}$ solution (PBS pH 7.0). Scan rate = 50 mV/s.

For further understanding of the electronic behaviour of the SWCNT and SWCNT-Co modified electrodes (EPPGE-SWCNT, EPPGE-SWCNT-Co, EPPGE-SWCNT-CoO), EIS study in $Fe(CN)_6]^{4-}$ / $[Fe(CN)_6]^{3-}$ solution was carried out at the equilibrium potential of the redox couple ($E_{1/2}$ of 0.3 V) as seen in Figure 6.4. The impedance technique is a very sensitive technique which gives insight into the mechanism of the electron transport between the

electrode|electrolyte interface. The Nyquist plots for some of the electrodes are presented in Figure 6.4a.

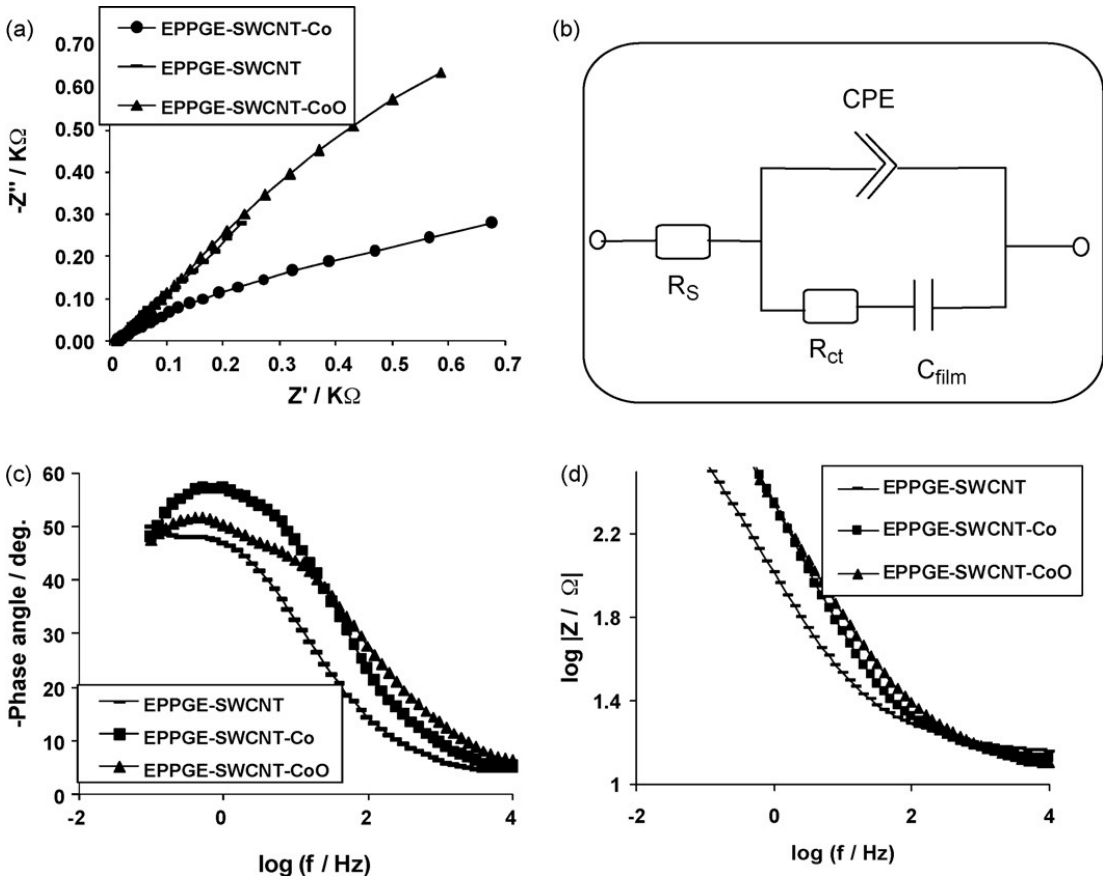

Figure 6.4: (a) Typical Nyquist plots of some of the electrodes obtained in 5 mM $[Fe(CN)_6]^{4-}$ / $[Fe(CN)_6]^{3-}$ solution (PBS pH 7.0) at fixed potential of 0.30 V vs Ag|AgCl sat'd KCl. (b) Represents the circuit used in the fitting of the EIS data. (c) and (d) are the Bode plots obtained for the electrodes, showing the plots of (-phase angle deg. vs log (f/Hz)) and log |Z / Ω| vs log (f/Hz).

The EIS data was satisfactorily fitted with the modified Dolin-Ershler equivalent circuit model (Figure 6.4b) [7], judged by the values of the pseudo χ^2 and relative % errors (Table 6.1) as well as

the goodness of fit (Figure 6.4a) wherein the true capacitance (C_{dl}) is replaced by the constant phase element (CPE). R_s, R_{ct} and C_{film} are already defined. The passive layer formed by the EPPGE-SWCNT-CoO leads to an insulated surface which could be responsible for the high R_{ct} value. It is evident from this study that the EPPGE-SWCNT-Co has the least R_{ct} value indicating faster electron transport. Circuit 6.4b description is different from the circuit used in earlier report involving SWCNT/Ni probably because of the porous nature of the EPPGE which alters its electronic properties with use [8]. The relatively low R_{ct} for the SWCNT-Co indicates faster electron transport compared to the other electrodes, possibly as a result of the porous and the high electroactive surface area of the electrode which allows for easy contact between the electrolyte and the base EPPGE. The high R_{ct} value for the SWCNT-Co_3O_4 is attributed to the formation of a thick cobalt oxide nanoparticles films which increase in thickness as the number of scans increases during modification. As has elegantly been described by the recent work of Orazem and Tribollet [9], time-constant (or frequency) dispersions leading to CPE behaviour occur as a result of distribution of time constants along either the area of the electrode surface (involving a 2-dimensional aspect of the electrode) or along the axis normal to the electrode surface (involving a 3-dimensional surface). Importantly, a 2-D distribution presents itself as an ideal RC behaviour, meaning that impedance measurements are very useful in distinguishing whether the observed global CPE behaviour is due to a 2-D distribution, from a 3-D distribution, or from a combined 2-D and 3-D distributions. It may be concluded that the observed impedimetric behaviour of the electrodes is a combination of 2-D and 3-D distributions.

Table 6.1: Impedance data obtained for the EPPGE modified electrodes in 5 mM $[Fe(CN)_6]^{4-}$ / $[Fe(CN)_6]^{3-}$ solution (PBS pH 7.0) at 0.30 V vs Ag|AgCl sat'd KCl.

Electrodes	**Impedimetric Parameters**					
	R_s / Ω cm^2	**CPE / mF**	**n**	**R_{ct} / Ω cm^2**	**C / μF**	**χ^2**
EPPGE-SWCNT	3.23 ±0.01	3.56 ±0.03	~ 0.56	12.93±0.33	135.00±12.12	2.55×10^{-3}
EPPGE-SWCNT-Co	2.93 ±0.02	1.32±0.02	~ 0.62	8.72±0.22	75.80±9.38	7.50×10^{-5}
EPPGE-SWCNT-CoO	1.24±0.01	1.56±0.01	~ 0.57	17.96±0.25	22.07±4.12	9.50×10^{-4}

From the plot of log |Z| vs log f, Figure 6.4d, the higher slope value (-0.65, R^2 = 0.9997 for EPPGE-SWCNT-Co) compared with -0.57, R^2 = 0.9991 for EPPGE-SWCNT-Co_3O_4 and -0.52, R^2 = 0.9988 for EPPGE-SWCNT suggests the more capacitive nature of EPPGE-SWCNT-Co than its oxide and the SWCNT counterparts. From the other type of Bode plot (i.e., –phase angle vs log f, (Figure 6.4c), the phase angles were 65^0 for EPPGE-SWCNT-Co compared with the EPPGE-SWCNT-CoO (51^0) and EPPGE-SWCNT (48^0), which are less than the 90° expected of an ideal capacitive behaviour confirming the presence of CPE and pseudocapacitive nature of these electrodes.

6.4 Electrocatalytic oxidation of Nitrite in neutral and acidic pH

Figure 6.5 presents the current responses of the modified electrodes in 10^{-3} M NO_2^- in PBS pH 7.4 and pH 3.0, respectively. The nitrite exists as nitrite ion (NO_2^-) in pH 7.4 PBS and at slightly acidic pH, the nitrite ion disproportionate to produce the neutral nitric oxide (NO) [10], which has a very short life time especially in an air saturated condition. Thus, the solution under the acidic pH was prepared fresh, with nitrogen purged, de-aerated phosphate buffer solution before analysis. The current response of the EPPGE-SWCNT-Co towards nitrite at pH 7.4 was approximately 3 folds higher than the other electrodes (Figure 6.5a) with slightly lower onset potentials (0.78 V). At pH 3.0 the EPPGE-SWCNT-Co exhibits faster calaysis compared to EPPGE-Co (less positive potential, ~ 100 mV lower than Co electrodes without SWCNTs), but the current response was almost the same.

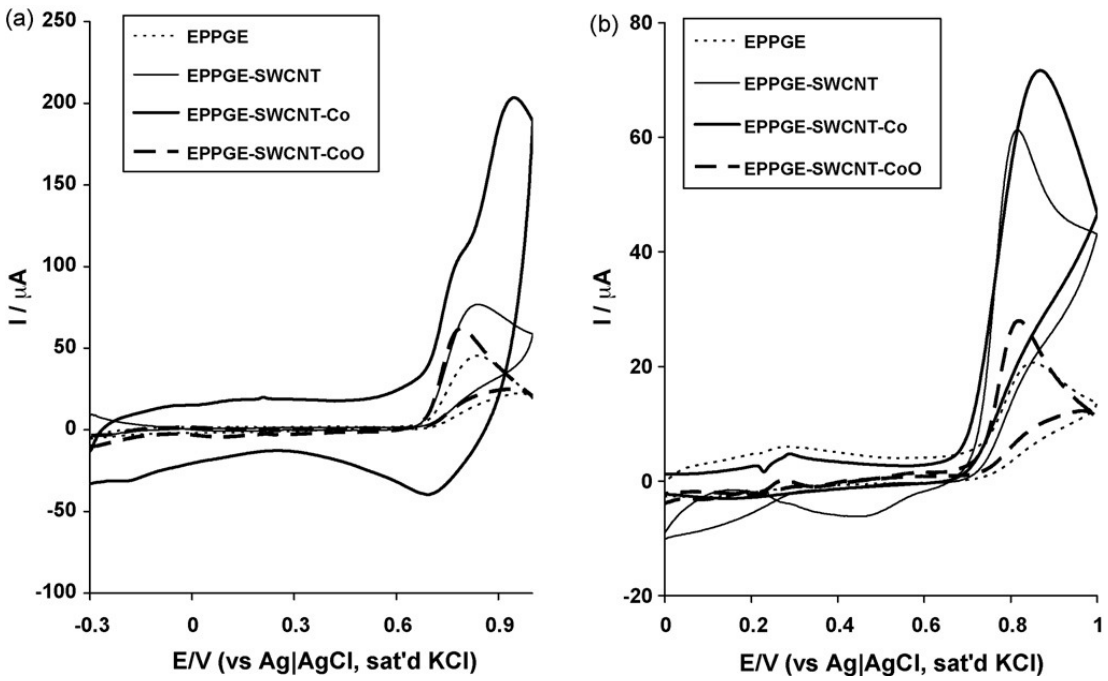

Figure 6.5: Comparative current response (after background current subtraction) of the EPPGE, EPPGE- SWCNT, EPPGE-SWCNT-Co and EPPGE-SWCNT-CoO in (a) 1 mM nitrite solution in pH 7.4 PBS and (b) 1 mM nitrite solution in pH 3.0 PBS, scan rate = 25 mV/s.

Cobalt modified electrodes have been reported to give enhanced response towards electro-oxidation of nitrite on graphite substrate [6,11,12] and on gold modified electrode [13,14]. It is evident from Figure 6.5a that the oxidation potential was lower with high current response on the EPPGE-SWCNT-Co nanoparticles modified electrode prepared by electrodeposition. The better electro-oxidation reaction of the SWCNT modified electrodes especially the EPPGE-SWCNT-Co, can be attributed to the SWCNT itself acting as an electrical conducting nanowire which enhances electron transport between the base electrode and the analyte. Since EPPGE-SWCNT-Co proved to be the best electrode towards nitrite oxidation at the pH conditions

investigated, all further studies were carried out with it, unless otherwise stated.

6.5 Electrochemical impedance studies

Figure 6.6a presents the Nyquist plots for the electrochemical impedance (EIS) data obtained at the electrodes studied during the electrocatalytic oxidation of nitrite (in pH 7.4 PBS) at a fixed potential of 0.8 V vs Ag|AgCl, sat'd KCl. The results obtained for the oxidation of the analyte at pH 3.0 PBS follow similar trend (not shown). A circuit model (Figure 6.6b) which incorporates the constant phase element (CPE) and an inductor *L,* yielded satisfactory results with acceptable values of pseudo χ^2 and % error values (Table 6.2). This suggests that there may be adsorption of the oxidation product on the electrodes. Thus, the CPE with *n* values of 0.73 and 0.87 suggest pseudocapacitive properties occuring at the electrode|solution interface. In electrocatalytic reactions, it is known that inductive behaviour takes place when the Faradaic current is governed by the occupation of an intermediate state [15-17]. This adsorption phenomenon is expected since CNT used as part of the electrode modifier, is known for adsorption properties because of their high surface area. This is the first time the adsorption associated with nitrite oxidation is proven by EIS measurement.

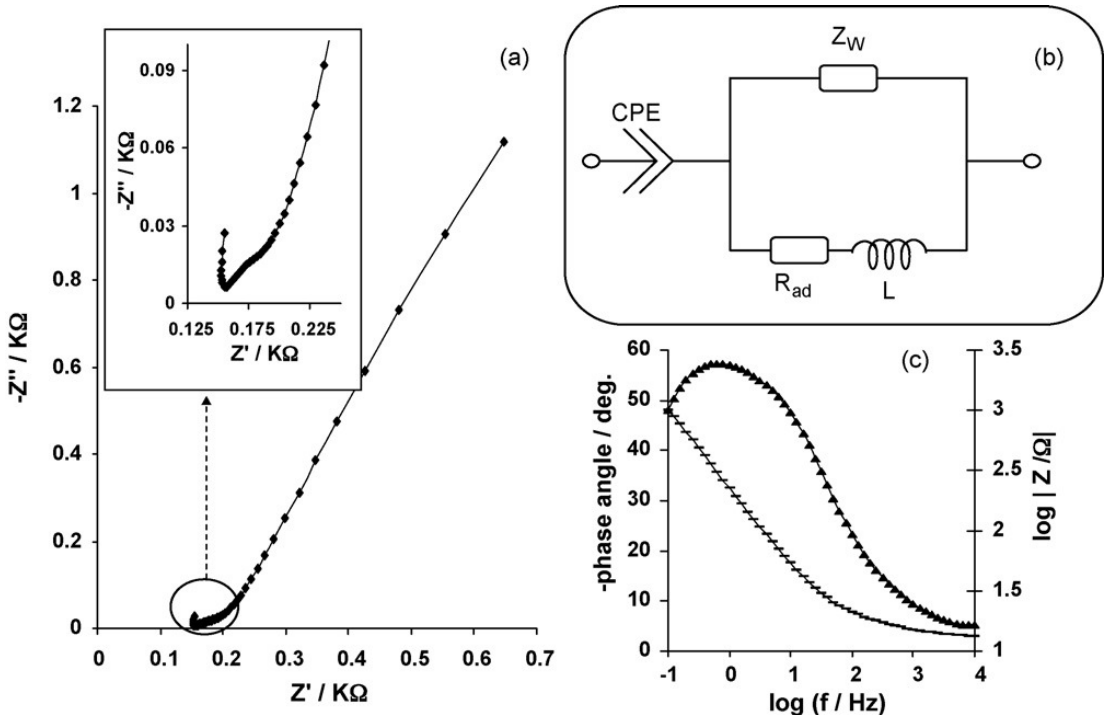

Figure 6.6: (a) Typical Nyquist plots of some electrodes in 1 mM nitrite solution (PBS pH 7.4) at fixed potential of 0.80 V vs Ag|AgCl sat'd KCl. Inset is the enlarged portion of the high frequency region (b) Represents the circuit used in the fitting of the EIS data in 6a (c) Bode plot obtained for EPPGE-SWCNT-Co showing the plot of -phase angle (deg.) vs log (f/Hz).

Table 6.2: Impedance data obtained for the modified EPPGE-SWCNT-Co electrodes in 10^{-3} M NO_2^- (in PBS pH 7.4 and 3.0) at 0.80 V vs Ag|AgCl sat'd KCl.

Electrodes	**Impedimetric Parameters**					
	CPE/ $mFcm^{-2}$	**n**	**10^6Z_w/ Ωcm^2**	**10^6L/ Hcm^2**	**R_{ad} /Ωcm^2**	**pseudo χ^2**
EPPGE-SWCNT-Co (at pH 7.4 PBS)	1.20±0.10	0.73±0.01	1.48±0.02	80. 6±1.43	38.37±0.08	1.02 x 10^{-4}
EPPGE-SWCNT-Co (at pH 3.0 PBS)	9.10±1.40	0.87±0.06	3.21±0.11	2877.93±207.50	73.36±1.26	3.49 x10^{-5}

6.6 Effect of varying scan rate

Cyclic votammetric experiments were carried out with the EPPGE-SWCNT-Co to establish the impact of scan rate (ν) at constant concentration (1 mM) of nitrite at pH 7.4 and 3.0 solutions. In cases, a shift in potential with increase in scan rate (not shown) was observed. From the Randles-Sevčik equation for an anodic oxidation process [18] (Equation 6.4):

$$I_p=3.01\times10^5 n[(1-\alpha)n_\alpha]^{1/2}AC_bD^{1/2}v^{1/2} \quad (6.4)$$

where all symbols have their usual meaning. C_b is nitrite bulk concentration (1 mM). The plot of the peak current (I_p) against the square root of scan rate ($\nu^{1/2}$) (Figure 6.7) for scan rate ranging from 25 to 200 mVs^{-1}, gave a linear relationship (R^2 = 0.9969 for nitrite oxidation at pH 7.4 with approximately zero intercept, confirming a diffusion-controlled process. However, at higher scan rate (> 200 mVs^{-1}), plot of the peak current (I_p) against the square root of scan rate ($\nu^{1/2}$) gave a straight line (R^2 = 0.996) with a negative intercept suggesting that at higher scan rates the reaction is not totally diffusion-controlled. This result supports the earlier discussed adsorption of intermediate products under the EIS study.

Using Tafel equation (Equation 6.5) for a totally irreversible-diffusion controlled process [18], the linear relationship between the peaks potential E_p and the logv (not shown) confirms the chemical irreversibility of nitrite electrocatalytic oxidation process.

$$Ep = \frac{b}{2}\log\nu + const. \quad (6.5)$$

From Equation 6.5, b = Tafel slope = 2.303RT/(1-α)nF where all symbols have their usual meaning. Assuming n = 2 for nitrite, the value of electron transfer coefficient (α) was obtained from Equation 6.5 as 0.72 for nitrite at pH 7.4.

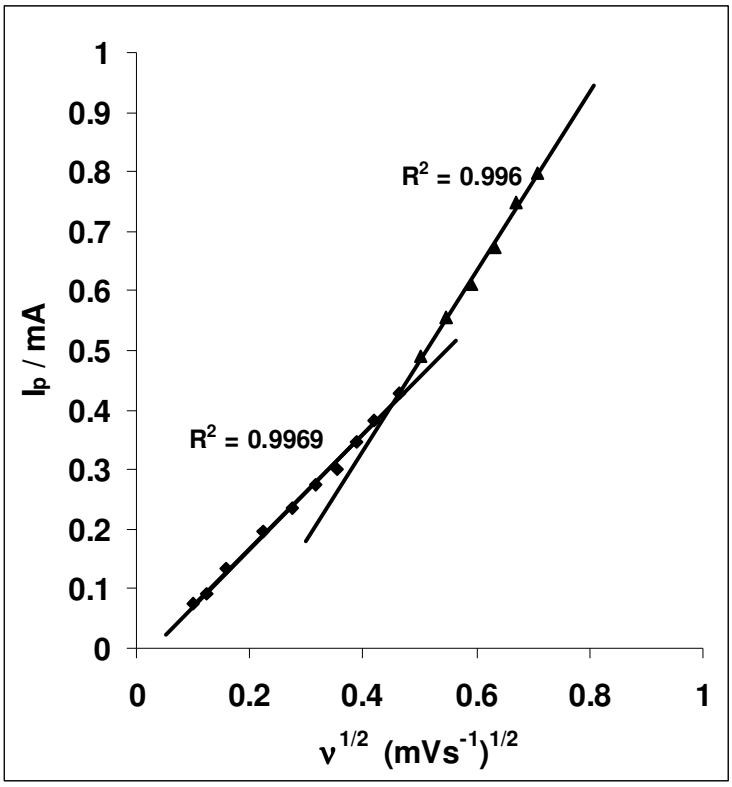

Figure 6.7: Plot of peak current (I_p) versus square root of scan rate ($v^{1/2}$) for EPPGE-SWCNT-Co in 0.1M pH 7.4 PBS containing 10^{-3} M nitrite.

Secondly, a Tafel slope of about 240 and 214 $mVDec^{-1}$ at pH 7.4 and 3.0 respectively implies a strong binding of reactants or intermediates on the electrode surface, or reactions occurring within a porous electrode structure [14]. The value agreed with 0.73 reported for cobalt phthalocyanide modified electrode for the oxidation of nitrite [13]. The minimum α value should be 0.5 for all

standard reaction mechanism [19]. α values at approximately 0.5 indicate that there is an equal probability that the reaction activated transition state can form either products or reactants [14]. Thus, α value larger than this indicates a more favoured reaction mechanism [19], which may explain why the electrocatalytic oxidation of nitrite to its oxidation product was more favoured on the EPPGE-SWCNT-Co electrode compared with the bare EPPGE.

6.7 Electroanalysis of nitrite at neutral and acidic pH

Chronoamperometric experiment was carried out by setting the peak potential at which the analyte was best catalysed. The chronoamperogram (Figure 6.8) was obtained by adding different aliquots of the nitrite solution. Using Equation 6.6 [2]:

$$\frac{I_{cat}}{I_L} = \pi^{1/2}\left(kC_o t\right)^{1/2} \tag{6.6}$$

where all symbols have their usual meaning. From the plot of I_{cat}/I_l vs $t^{1/2}$ (not shown) the catalytic rate constant *K* for EPPGE-SWCNT-Co in pH 7.4 and 3.0 PBS containing 10^{-3}M NO_2^- are (0.32±0.03) and (0.34±0.05) x 10^5 cm^3 $mol^{-1}s^{-1}$ respectively. The results are approximately same as the 2.75 x 10^3 M^{-1} s^{-1} (or 2.75 x 10^6 cm^3 mol^{-1} s^{-1}) reported by Reza *et. al.*, 2006 [20] for the electrocatalytic reduction of nitrite on carbon paste electrode modified with ferricyanide but lower than 7 x 10^5 M^{-1} s^{-1} (or 7 x 10^8 cm^3 mol^{-1} s^{-1}) reported by Natalia et. al., 2005 [21] for catalytic oxidation of nitric oxide and nitrite by water-soluble manganese (III) meso-tetrakis(*N*-methylpyridinium-4-yl) porphyrin (Mn(III)(4-TMPyP) on indium-tin oxide (ITO) electrode in pH 7.4 phosphate buffer solutions. The

difference in the magnitude of *K* could be due to the different electrode modifier and their interaction with the nitrite molecules.

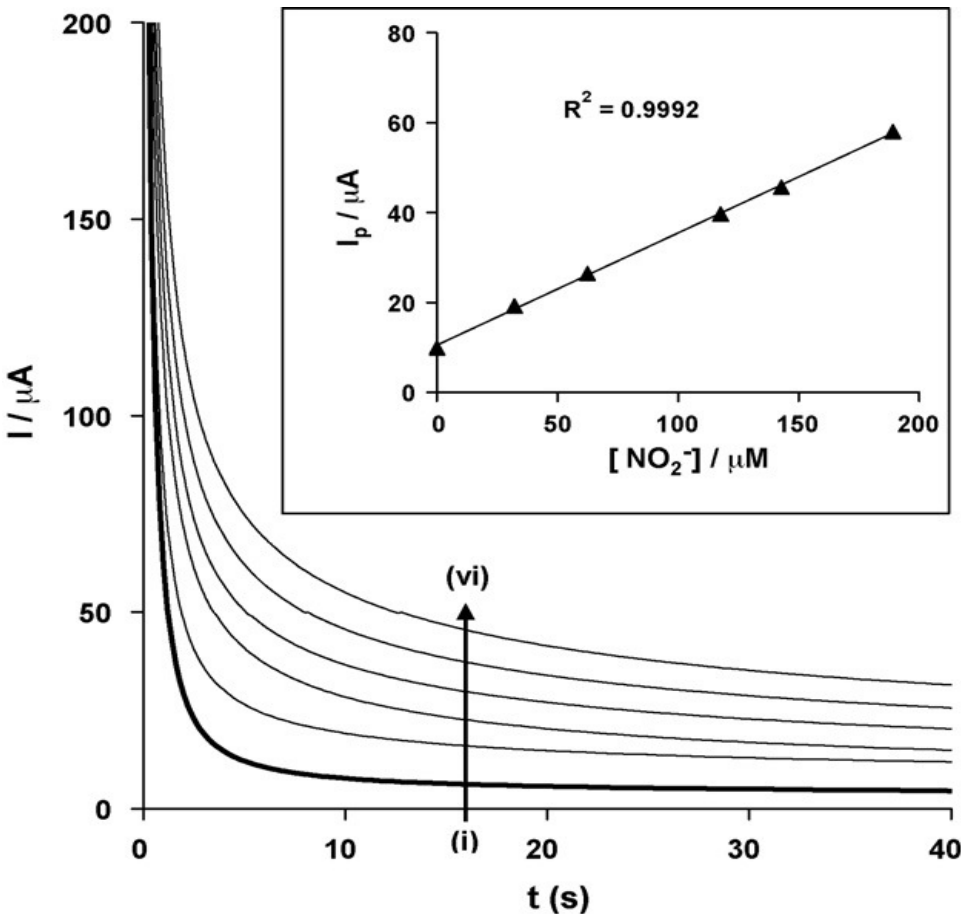

Figure 6.8: Typical examples of chronoamperogram obtained for EPPGE-SWCNT-Co in phosphate buffer solution (pH 7.4) containing different concentrations of nitrite (0.0, 32.3, 62.5, 118.0, 143.0, and 189.0 μM (i to vi)). Inset is typical plot of current response vs nitrite concentration.

Similarly, the plot of I_p versus [NO_2^-] gave the sensitivity values which are (0.250 ± 0.001) μA/μM NO_2^- at pH 7.4 and (0.032 ± 0.001) μA/μM for NO at pH 3.0. The limits of detection (LoD = 3.3 δ/m) are 5.61±0.48 and 8.03±0.68 μM for nitrite and nitric oxide

respectively. The result is in the same μM detection range reported for nitrite and nitric oxide on electropolymerizable iron (III) and cobalt (II) complexes on glassy carbon electrode [22] or indium (III) hexacyanoferate (III) (InHCF) on glassy carbon electrode [23]. Presently, no literature on the electrooxidation of nitrite using this type of electrode has been reported. The sensitivity obtained in this study could be due to the ability of SWCNTs to function as efficient conducting species for the catalytic cobalt nanoparticles. From Langmuir adsorption isotherm theory (Equation 6.7) [24], the plot of the ratio of concentration [nitrite] and the catalytic current I_{cat} ([nitrite] / I_{cat}) against concentration [nitrite] (not shown) gave a straight line which can be interpreted as an adsorption controlled electrochemical process.

$$\frac{[\text{Nitrite}]}{I_{cat}} = \frac{1}{\beta I_{max}} + \frac{[\text{Nitrite}]}{I_{max}} \qquad (6.7)$$

The adsorption equilibrium constant for the EPPGE-SWCNT-Co was estimated as β (9.94 ± 0.05) x 10^3 M^{-1} and (4.80 ± 0.02) x 10^3 M^{-1} for NO_2^- and NO. Thus, the Gibbs free energy change due to adsorption was estimated as -22.81 and -21.00 $kJmol^{-1}$ using Equation 6.8.

$$\Delta G^o = -RT\ln\beta. \qquad (6.8)$$

From the scan rate study and other studies, adsorption of the analyte on the electrode was evident. Further probe into the adsorptive properties of nitrite was carried out using the adsorption

stripping voltammetry. The linear sweep voltammetric evolutions (not shown) of EPPGE-SWCNT-Co in PBS containing different aliquots of nitrite was obtained. Plot of I_p vs $[NO_2^-]$ gave LoD values of 8.4±0.71 and 11.6±0.99 μM for nitrite at pH 7.4 and 3.0. Using Equations 6.7 and 6.8 above, the adsorption equilibrium constant β was estimated as (13.02 ± 0.03) x 10^3 M^{-1} and (56.7 ± 0.01) x 10^3 M^{-1} for nitrite at pH 7.4 and 3.0. Thus, the Gibbs energy change due to the adsorption was estimated as -6.36 and -10.00 $kJmol^{-1}$ for pH 7.4 and 3.0, respectively.

From the result, adsorption of NO_2^- and NO on the electrode followed about the same kinetics based on the insignificant difference in their standard free energy of adsorption (ΔG^o). This is not unexpected since the tendency for the two analytes to interchange is very high, and they both give nitrate (NO_3^-) as their final oxidation product. The adsorption stripping voltammetry technique seems to be more viable for nitrite analysis on the electrode system since the high negative ΔG^o further confirms the strong adsorption of nitrite. From the above discussion, and based on the previous reports on the mechanism of NO_3^- electro-oxidation at modified electrodes [25], it is assumed that the electrocatalytic response of NO_3^- at EPPGE-SWCNT-Co in aqueous solutions follows a similar mechanism:

$$[\text{SWCNT-Co}]_{film} + H_2O \longrightarrow [\text{SWCNT-Co}^{2+}]_{film\ (aq)} + e^- \quad (6.9)$$

$$[\text{SWCNT-Co}^{2+}]_{film} + NO_2^- \rightleftharpoons [\text{SWCNT-Co}^{2+}\text{---}(NO_2^-)]_{adduct} \quad (6.10)$$

$$[\text{SWCNT-Co}^{2+}\text{---}(NO_2^-)]_{adduct} \rightleftharpoons [\text{SWCNT-Co}^{3+}]_{film} + NO_2 + e^- \ (\text{slow}) \quad (6.11)$$

$$2NO_2 + H_2O \rightleftharpoons 2H^+ + NO_3^- + NO_2^- \quad (6.12)$$

$$NO_2^- + H_2O \longrightarrow 2H^+ + NO_3^- + 2e^- \quad (6.13)$$

$$[\text{SWCNT-Co}^{3+}]_{film} + e^- \longrightarrow [\text{SWCNT-Co}^{2+}]_{film} \quad (6.14)$$

The nitrite ion interact with the SWCNT-confined Co(II) film forming an adduct (Equation 6.10). This step represents the adsorption process. Equation 6.11 is assumed to be the rate-determining step which is a one-electron process. The oxidation of the Co(II) to Co(III) simultaneously leads to the generation of the nitrogen dioxide. The formation of the NO_2 (Equation 6.11) is followed by its disproportionation to give nitrite and nitrate (Equations 6.12 and 6.13). Co(III) is reduced to regenerate the Co(II) (Equation 14).

In a related study, the surface electrochemistry of synthesised Co and Co_3O_4 nanoparticles as well as their electrocatalytic detection ability towards nitrite on EPPGE platform was explored. Surprisingly most work focus more on electrocatalysis of the metal nanoparticles other than their electron transport behaviour that form the basis for electrocatalysis. The prime motivating factor for carrying out this study is the ability to produce nano-scaled cobalt and cobalt oxides in high commercial quantity compared to the commercially unvailable quantity from the electrodeposition method. Figures 6.9a and b showed the comparative transmission electron microscopy (TEM) images of Co (a) and the Co_3O_4 nanoparticles while (b) while Figure 6.9c and d are their corresponding FESEM images. The Co nanoparticles form amorphous nanoparticles or nanowires (Figures 6.9a and 6.9c). On the other hand, Co_3O_4 nanoparticles appeared crystalline (Figure 6.9b). The crystals aggregated and form a web-like structure (Figure 6.9d). From the TEM result, the size of most of the particles is in 20 to 50 nm for Co and 10 to 30 nm for the Co_3O_4.

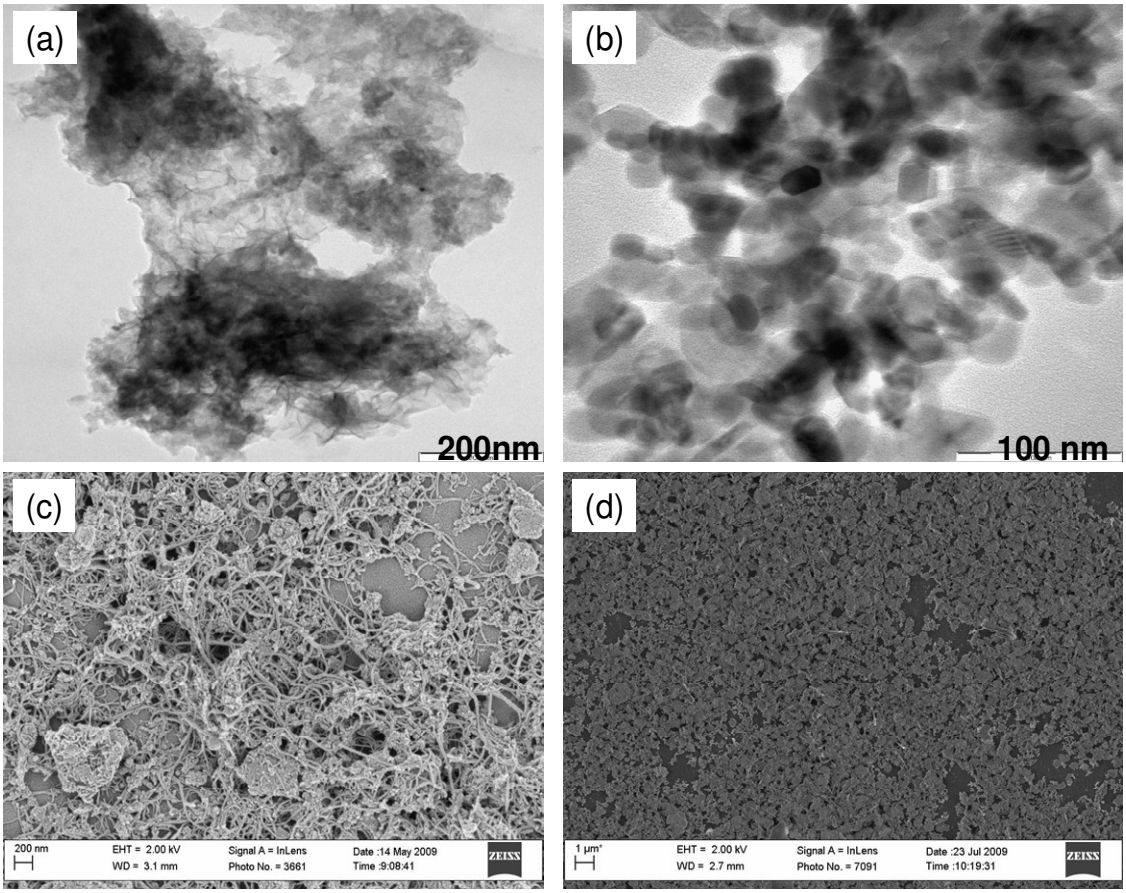

Figure 6.9: TEM images of (a) Co and (b) Co_3O_4 nanoparticles. Figures 6.9c and d are the FESEM micrographs of Co and Co_3O_4 nanoparticles, respectively.

The XRD spectra for the nanosized particles are shown in Figure 6.10. The nanoscaled Co (Figure 6.10a) is characterised by XRD peaks at 2θ of 47.9°, 59.8° and 79.6° which could be assigned to (111), (200) and (222) of a cubic structures Co nanoparticles [26,27]. The Co_3O_4 nanaoparticles (Figure 6.10b) show characteristic peaks at 2θ of 22.1, 36.5, 43.1, 45.1, 52.5, 57.7, 65.7, 70.2 and 77.5 due to the indices of (111), (220), (311), (222), (400), (331), (422), (511) and (440) corresponding to Cubic Fd-3m Co_3O_4 crystal

lattice [27,28]. From Debye-Scherrer equation [29,30], average crystalite size of 22.8 nm was obtained which is in consistent with the TEM result.

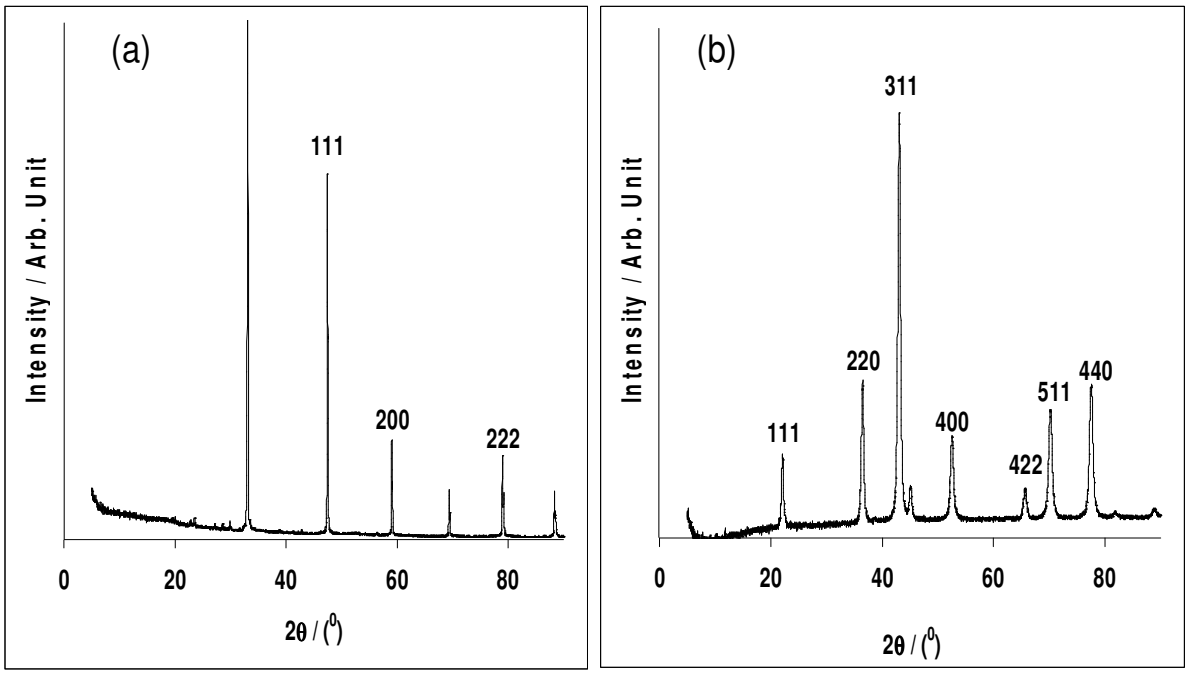

Figure 6.10: XRD spectra of Co (a) and Co_3O_4 (b) nanoparticles.

Figure 6.11 compares the current response of the bare and the modified electrodes in (a) 0.1 M PBS (pH 7.0) and (b) 5 mM $Fe(CN)_6]^{4-}/[Fe(CN)_6]^{3-}$ solution. In Figure 6.11a, the electrode based on the Co nanoparticles showed broad anodic peak at *ca* 0.6 V, presumable due to the formation of Co_3O_4 through the reaction represented in Equation 6.1 above.

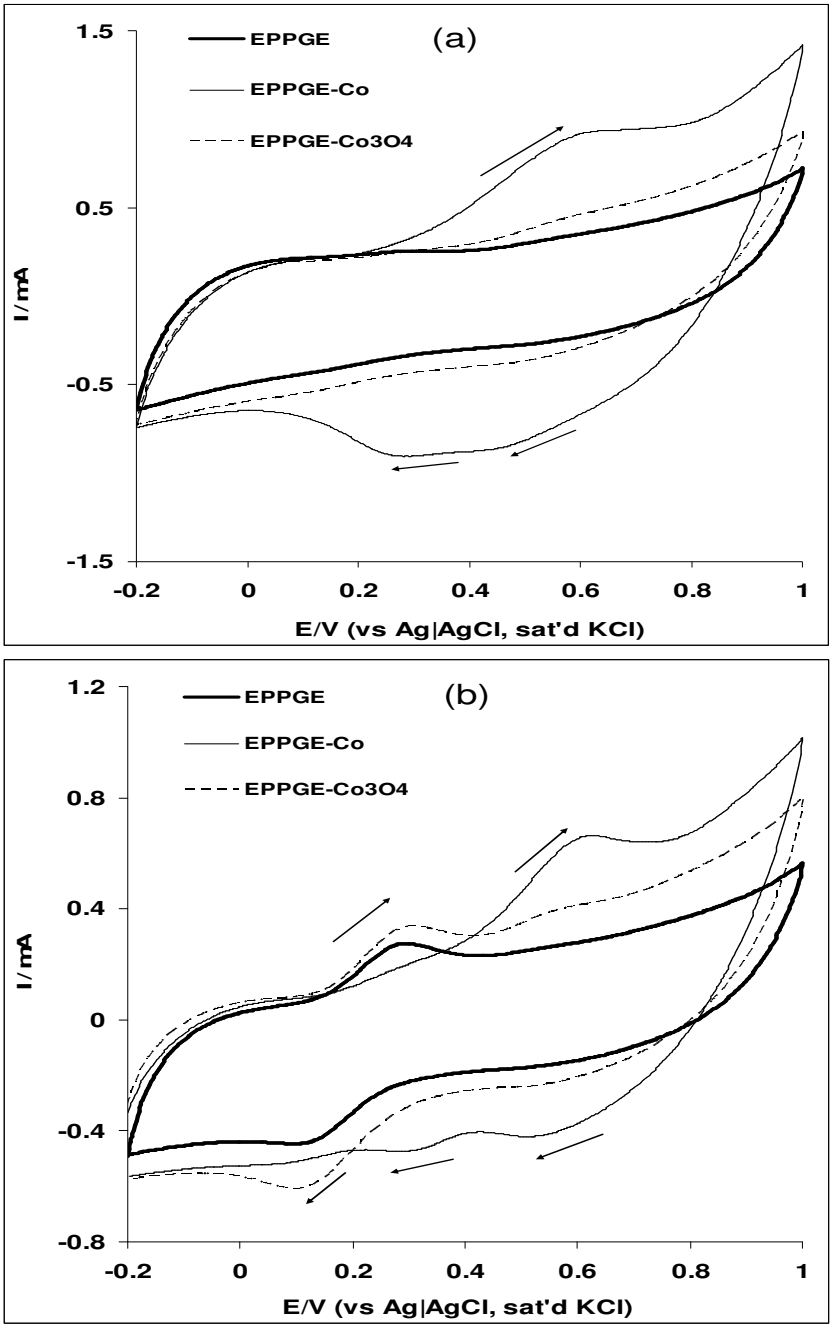

Figure 6.11: Comparative cyclic voltammetric evolutions of the EPPGE, EPPGE-Co and EPPGE-Co_3O_4 electrodes in (a) 0.1 M PBS (scan rate = 100 mVs^{-1}), and (b) 5 mM $[Fe(CN)_6]^{4-}/[Fe(CN)_6]^{3-}$ solution in pH 7.0 PBS (scan rate = 50 mVs^{-1}).

The broadness of the peak may be due to the formation of other oxidation products (Equation 6.2). The cathodic peaks observed at ca 0.52 and 0.22 V are attributed to the reduction of CoOOH to $Co(OH)_2$ or Co_3O_4. Interestingly, the electrodes based on the Co_3O_4 nanoparticles did not show recognisable redox process as the Co nanoparticles in the neutral pH conditions used.

Next, the extent to which these electrodes mediate the electron transport of the redox probe, $Fe(CN)_6]^{4-}/[Fe(CN)_6]^{3-}$, to and from the underlying electrodes was questioned. Two redox couples are noticed for the electrodes in $Fe(CN)_6]^{4-}/[Fe(CN)_6]^{3-}$ solution (Figure 6.11b); the redox couples in the 0 – 0.3 V region being attributed to the $Fe(CN)_6]^{4-}/[Fe(CN)_6]^{3-}$ redox process, while the redox couples in the 0.3 – 0.7 V region correspond to cobalt processes. Electrochemical impedance spectroscopy (EIS) experiment was carried at fixed potential of 0.2 V (the equilibrium potential, $E_{1/2}$, of the $[Fe(CN)_6]^{4-}/[Fe(CN)_6]^{3-}$ couple). The Nyquist plot obtained (Figure 6.12) was satisfactorily fitted using the modified Randles electrical equivalent circuit model shown in the inset. The R_{ct} values follow the trend: EPPGE-Co (0.36 Ωcm^2) < EPPGE-Co_3O_4 (0.60 Ωcm^2) << bare-EPPGE (1.23 Ωcm^2) (Table 6.3). The modified electrodes showed lower R_{ct} values compared to the bare EPPGE, indicating that the nanoparticle catalysts enhance electron transfer of the redox probe compared to the unmodified EPPGE.

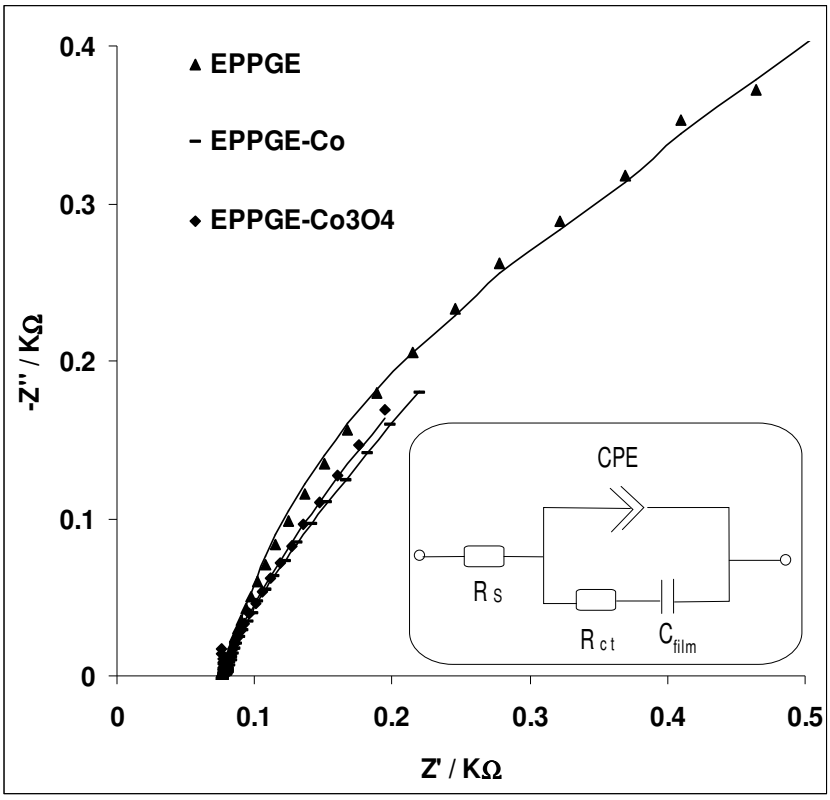

Figure 6.12: Typical Nyquist plots obtained for the electrodes in 5 mM $[Fe(CN)_6]^{4-}$ / $[Fe(CN)_6]^{3-}$ solution at a fixed potential of 0.2 V (vs Ag|AgCl, sat'd KCl). Inset in Figure 6.12 is the circuit used in the fitting of the EIS data.

Table 6.3: Impedance data obtained for EPPGE, EPPGE-Co and EPPGE-Co_3O_4 electrodes in 5 mM $Fe(CN)_6]^{4-}/[Fe(CN)_6]^{3-}$ solution at 0.2 V (vs Ag|AgCl sat'd KCl).

Electrodes	**Impedimetric Parameters**				
	R_s/ Ωcm^2	**CPE/ μFcm^{-2}**	**N**	**R_{ct}/ Ωcm^2**	**C_{film}/ $mFcm^{-2}$**
EPPGE	7.02±0.01	0.82±0.35	0.40±0.01	1.23±0.02	3.09±0.11
EPPGE-Co	7.80±0.01	216.40±25.47	0.50±0.01	0.36±0.01	13.02±0.34
EPPGE-Co_3O_4	7.57±0.01	381.3±13.01	0.52±0.05	0.60±0.04	15.98±3.77

At 2.5 mg/mL Co loading, the current responses in NO_2^- follow the order: bare EPPGE (43.7 μA) > EPPGE-CoO (21.0 μA) > EPPGE-Co (18.0 μA) (Figure 6.13). The result agreed with the recent report by Compton group [31] in terms of onset potential of catalysis and the peak potential for nitrite oxidation on bare glassy carbon electrode. However, at 7.5 mg/mL Co and Co_3O_4 loading, EPPGE-Co gave the highest current response (83.0 μA) with lower onset potential (0.3 V) of catalysis which is ~ 380 mV lower than *ca* 0.67 V recorded for the other electrodes (Figure 6.13). At this loading, its current response was ~ 2 times the bare EPPGE and 2.5 times EPPGE-CoO. Thus, contribution of modified electrode to reducing nitrite overpotential on bare electrode, and in enhancing its oxidation current are a possibility, which may depend on the method of modification, the nature of the electrocatalyst and amount used in modifying the electrode.

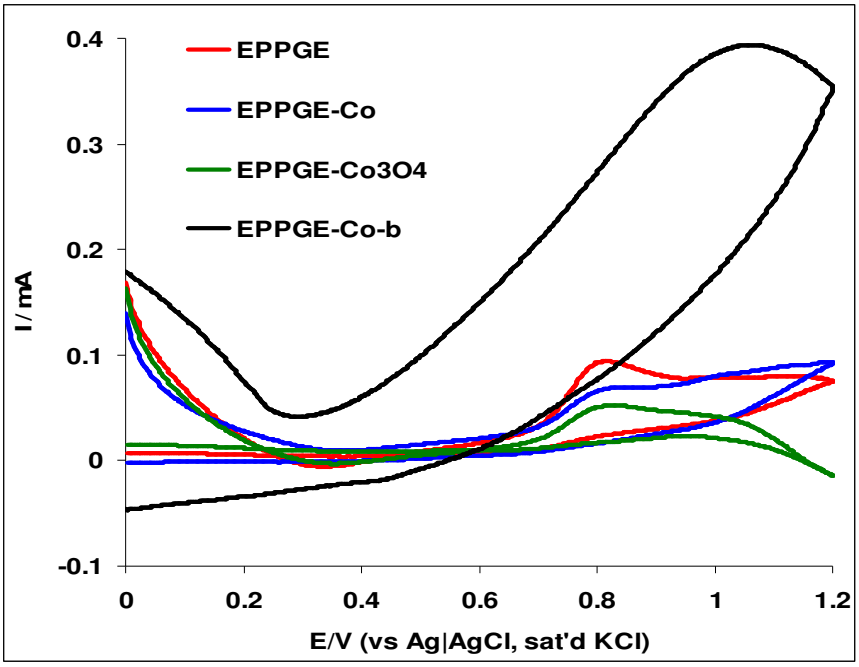

Figure 6.13: Comparative current response of (a) EPPGE, EPPGE-Co and EPPGE-Co_3O_4 (after background current subtraction) in pH 7.4 PBS containing 1.0 mM NO_2^- solution (scan rate = 25 mVs^{-1}). EPPGE-Co-b represents 7.5 mg/mL Co loading in pH 7.4 PBS containing 1.0 mM NO_2^- solution.

The results here also show enhanced electrochemical performance compared to several reports, including the earlier work above incorporating carbon nanotubes in terms of onset potentials and current response. Surprisingly, attempts to use CNTs as supports for these synthesised Co and Co_3O_4 nanoparticles did not improve the electrochemistry of nitrite, a further advantage of these metal nanoparticles over their electrodeposited counterparts that require CNTs. Since EPPGE-Co electrode proved to be better towards nitrite oxidation, all further studies were carried out with it, unless otherwise stated.

The catalytic behaviour of the electrodes towards nitrite oxidation was also investigated using EIS. The Nyquist plots obtained for the electrodes during nitrite oxidation at pH 7.4 (at fixed potential of 0.8 V vs Ag|AgCl, sat'd KCl) is presented in Figure 6.14. A modified Randles circuit model already discussed above (inset in Figure 6.12) satisfactorily fitted the data from nitrite oxidation (Table 6.4). The C_{film} is replaced by C_{ads} which is attributed to the high capacitive nature of the synthesised Co and Co_3O_4 nanoparticles or adsorption of NO_2^- intermediate product on the electrode. The low R_{ct} of the EPPGE-Co (0.31 Ωcm^2) compared with the bare EPPGE (0.36 Ωcm^2) and EPPGE-Co_3O_4 (0.46 Ωcm^2) also explain the good electron transport and catalysis witness at the electrode.

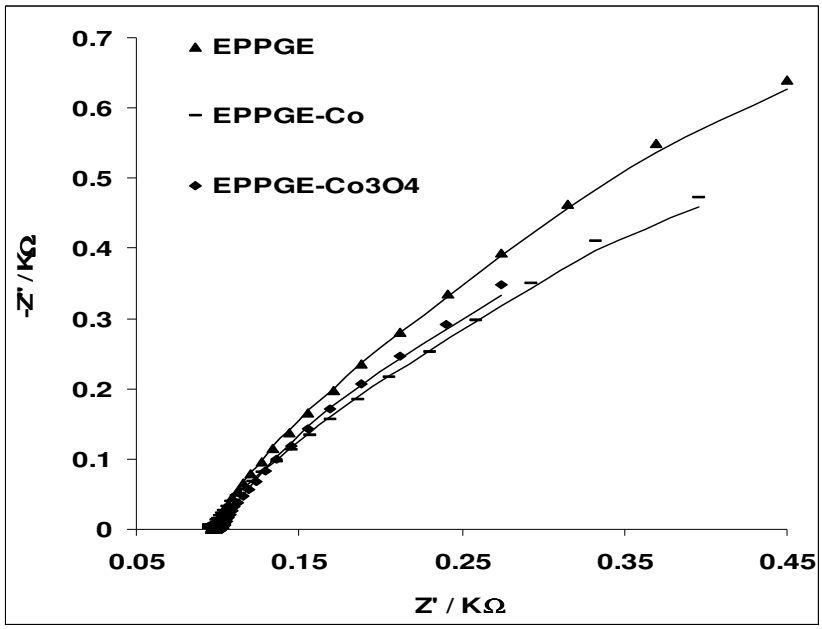

Figure 6.14: Typical Nyquist plots obtained for EPPGE, EPPGE-Co and EPPGE-Co_3O_4 in 1.0 mM NO_2^- solution at a fixed potential of 0.8 V (vs Ag|AgCl, sat'd KCl).

Table 6.4: Impedance data obtained for some of the electrodes in 1.0 mM NO_2^- (in PBS pH 7.4 at 0.80 V vs Ag|AgCl sat'd KCl.

Electrodes	**Impedimetric Parameters**				
	R_s/Ωcm^2	**CPE/μFcm^{-2}**	**N**	**R_{ct}/Ωcm^2**	**C_{ads}/mFcm^{-2}**
EPPGE	9.48±0.01	133.8±35.39	0.59±0.01	0.36±0.01	6.98±0.30
EPPGE-Co	9.31±0.01	170.6±48.80	0.57±0.01	0.31±0.01	6.83±0.43
EPPGE-Co_3O_4	10.00±0.01	160.4±42.17	0.55±0.02	0.46±0.01	17.07±0.87

Cyclic voltammograms showing the current responses in NO_2^- with increasing scan rates were also studied (25 – 500 mVs^{-1}). A shift in potential with increase in scan rate was observed. The plot of the peak current (I_p) against the square root of scan rate ($\nu^{1/2}$) gave a linear relationship (R^2 = 0.9915) with a positive intercept, suggesting a diffusion-controlled process. There was a linear relationship between the peak potential E_p and the logν (not shown), which confirms the chemical irreversibility of nitrite electrocatalytic oxidation process. The value of the Tafel slope is somewhat huge (540.8 mV dec^{-1}) compared to the normal reported values for various analytes including nitrite on SWCNT-Co modified electrode. As earlier mentioned, high Tafel values generally indicate binding of the analyte or its intermediates on the electrode surface, or reactions occurring within a porous electrode structure [14,32]. From the above discussion, the electrocatalytic response of NO_2^- at EPPGE-Co followed the same mechanism as proposed in Equations 6.9 to 6.14 above.

Next, the effect of current response on varying concentrations of nitrite using chronamperometric technique (Figure 6.15) was studied. Plot of current response versus nitrite concentration (inset in Figure 6.15) gave a linear relationship (Y = (1.32±0.01)X + 16.82±0.29 (R^2 = 0.9996)) and sensitivity of 1.32±0.01 μA μM^{-1}. The limit of detection (LoD = 3.3 δ/m) was calculated as 0.73±0.06 μM. The 0.73 μM detection limit obtained is about 8 times lower than reported for the SWCNT-Co modified electrode reported. Nitrite at neutral pH has been detected at 4.0 μM using thionin/multiwalled carbon nanotubes/glassy carbon modified electrode [33] and myoglobin/ZnO/graphite modified electrode [34], 1.2 μM on haemoglobin/colloidal gold

nanoparticles/TiO_2-sol gel film/GCE modified electrode [35]. From the plot of I_{cat}/I_l vs $t^{1/2}$ (not shown) the catalytic rate constant for nitrite was obtained as (2.32±0.20) x 10^6 cm^3 $mol^{-1}s^{-1}$. This result is close to the 6.03 x 10^6 $M^{-1}s^{-1}$ reported for the electrocatalytic reduction of nitrite at Vanadium–Schiff base complex/MWCNTs modified GC electrode [36].

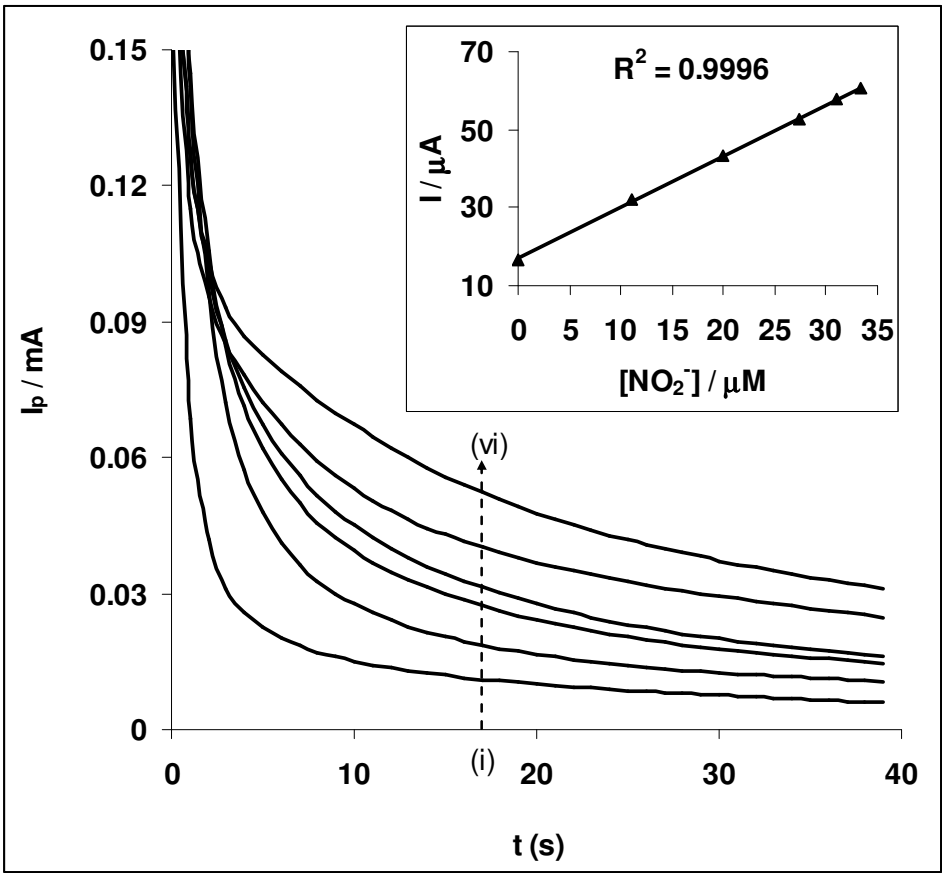

Figure 6.15: Typical chronoamperogram of EPPGE-Co in (a) 0.1 M PBS pH 7.4 containing different concentration of NO_2^- (0.0, 11.1, 20.0, 27.3, 31.0 and 33.3 µM (i to vi)). Inset is the plot of peak current (I_p) versus NO_2^- concentrations.

This study showed that the Co nanoparticle modified electrodes exhibited faster electron transfer behaviour in $[Fe(CN)_6]^{3-/4-}$ redox probe than their corresponding nano-oxides. The high charge transfer resistance of the cobalt oxide modified electrodes have been attributed to surface passivation and low surface active materials. EPPGE-SWCNT-Co has the fastest electron transport, aided by the electrical conducting single-walled carbon nanotubes which form a synergistic effect with the cobalt nanoparticles. In the contrary, attempts to use CNTs as supports for synthesised Co and Co_3O_4 nanoparticles did not improve the electrochemistry of nitrite, a further advantage of these metal nanoparticles over their electrodeposited counterparts that require CNTs. The detection and the electro-catalytic oxidation of nitrite were successful on all the electrodes studied. In both electrodeposition and synthesis experiment, EPPGE-SWCNT-Co or EPPGE-Co gave the highest current response, and at lower potential compared with other electrodes investigated. The electrocatalytic-oxidation of nitrite on the electrode followed adsorption-controlled electrochemical process with complex impedance behaviour. There is no significant difference in the standard free energy change (ΔG^0) due to adsorption, suggesting that the adsorption of NO_2^- and NO on the EPPGE-SWCNT-Co followed about the same mechanism. The study showed that, using this kind of electrode system for sensing and analytical application requires a special caution since the adsorptive nature of the electrode may have an effect on its sensing properties towards the analyte.

References

1. A. Salimi , H. Mamkhezri, R. Hallaj , S. Soltanian, *Sens. Actuators B* 129 (2008) 246.

2. A. Salimi, R. Hallaj, S. Soltanian, H. Mamkhezri, *Anal. Chim. Acta* 594 (2007) 24.

3. J. Zagal, M. Paez, A.A. Tanaka and J.R. dos Santos Jr, C.A. Linkous, *J. Electroanal Chem.* 339 (1992) 13.

4. S. Zecevic, B. Simic-Glavaski, E. Yeager, A.B.P. Lever and P.C. Minor, *J. Electroanal. Chem.* 196 (1985) 339.

5. A.B.P. Lever, S. Liccocia, K. Magnell, P.C. Minor and B.S. Ramaswamy, *Am. Chem. Sot. Symp.Ser.* 201 (1982) 237.

6. S. Sunohara, K. Nishimura, K. Yahikozawa, M. Ueno, *J. Electroanal. Chem.* 354 (1993) 161.

7. H. Kasurk, G. Nurk, E. Lust, *J. Electroanal. Chem.* 613 (2008) 80.

8. W. Lajnef, J.-M. Vinassa, S. Azzopardi, O. Briat, E. Woirgard, C. Zardini, J.L. Aucouturier, *PESC* 04 1 (2004) 131.

9. M.E. Orazem, B. Tribollet, *Electrochemical Impedance Spectroscopy*, John Wiley & Sons Inc, Hoboken, NJ., 2008, Chapter 13.

10. C. Yang, Q. Lu, S. Hu, *Electroanalysis* 18 (2006) 2188.

11. M. Thamae, T. Nyokong, *J. Electroanal. Chem.* 470 (1999) 126.

12. P. Tau, T. Nyokong, *Electrochim. Acta* 52 (2007) 4547.

13. F. Matemadombo, T. Nyokong, *Electrochim. Acta* 52 (2007) 6856.

14. B.O. Agboola, T Nyokong, *Anal. Chim. Acta* 587 (2007)116.

15. J. Bisquert, H. Randriamahazaka, G.Garcia-Belmonte, *Electrochim. Acta* 51 (2005) 627.

16. M. Jafarian, M. G. Mahjani, H. Heli, F. Gobal, H. Khajehsharifi, M. H. Hamedi, Electro*chim. Acta* 48 (2003) 3423.

17. S. Majdi, A. Jabbari, H. Heli, A. A. Moosavi-Movahedi, *Electrochim. Acta* 52 (2007) 4622.

18. A.J. Bard, L.R. Faulkner, Electrochemical Methods: *Fundamentals and Applications*, 2nd ed., John Wiley & Sons, Hoboken, NJ., 2001.

19. J.N. Soderberg, A.C. Co, A.H. C. Sirk, V.I. Birss, *J. Phys. Chem. B* 110 (2006) 10401.

20. R. Ojani, J-B, Raoof, E. Zarei, *Electrochim. Acta* 52 (2006) 753.

21. N.S. Trofimova, A.Y. Safronov, O. Ikeda, *Electrochim. Acta* 50 (2005) 4637.

22. K.I. Ozoemena, Z. Zhao, T. Nyokong, *Inorg. Chem. Commun.* 9 (2006) 223.

23. E. Casero, J. Losada, F. Pariente, E. Lorenzo, *Talanta* 61 (2003) 61.

24. H.X. Ju, L. Donal, *J. Electroanal. Chem.* 484 (2000) 150.

25. F. Armijo, M.C. Goya, M. Reina, M.J. Canales, M.C. Arevalo, M.J. Aguire, *J. Mol. Cat. A*: 268 (2007) 148.

26. H. Shao, Y. Huang, H. Lee, Y.J. Suh, C.O. Kim, *Current Applied Physics* 6S1 (2006) e195.

27. M. Salavati-Niasari, Z. Fereshteh, F. Davar, *Polyhedron* 28 (2009) 1065.

28. M. Salavati-Niasari, F. Davar, M. Mazaheri, M. Shaterian *J. Magnetism Magnetic Materials* 320 (2008) 575.

29. Y-K. Sun, M. Ma, Y. Zhang, N. Gu, Coll. Surf. A: *Physicochem. Eng. Aspects* 245 (2004) 15.

30. R.M. Cornell, U. Schertmann, Iron Oxides in the laboratory: Preparation and Characterization, VCH, Weinheim (1991).

31. B.R. Kozub, N.V. Rees, R.G. Compton, *Sens. Actuat. B* 143 (2010) 539.

32. J.N. Soderberg, A.C. Co, A.H.C. Sirk, V.I. Birss, *J. Phys. Chem. B* 110 (2006) 10401.

33. A. Salimi, A. Noorbakhash, F.S. Karonian, *Int. J. Electrochem. Sci.* 1 (2006) 435.

34. G. Zhao, J.J. Xu, H.Y. Chen, *Anal. Biochem.* 350 (2006) 145.

35. W. Yang, Y. Bai, Y. Li, C. Sun, *Anal. Bioanal. Chem.* 382 (2005) 44.

36. A. Salimi, H. Mamkhezri, S. Mohebbi, *Electrochem. Commun.* 8 (2006) 688.

CHAPTER SEVEN

Electrocatalytic Detection of Dopamine at Single-Walled Carbon Nanotubes-Iron (iii) Oxide Nanoparticles Platform*

* The following publications resulted from part of the research work presented in this chapter and are not referenced further in this thesis:

7. **Abolanle S. Adekunle**, Bolade O. Agboola, Jeseelan. Pillay, Kenneth I. Ozoemena, *Sens. Actuator: Chemical B*, 148 (2010) 93-102.
8. **Abolanle S. Adekunle**, Kenneth I. Ozoemena, *Int. J. Electrochem. Sci.* (in press).

7.1. Characterisation with FESEM, AFM, EDX and XPS

FESEM images of typical modification steps are summarised in scheme 7.1. There is a clear evidence of edge-plane sites uniformly distributed on the bare-EPPGE. The electrode is covered with SWCNT after modification with the acid-treated SWCNT on the bare EPPGE (EPPGE-SWCNT).

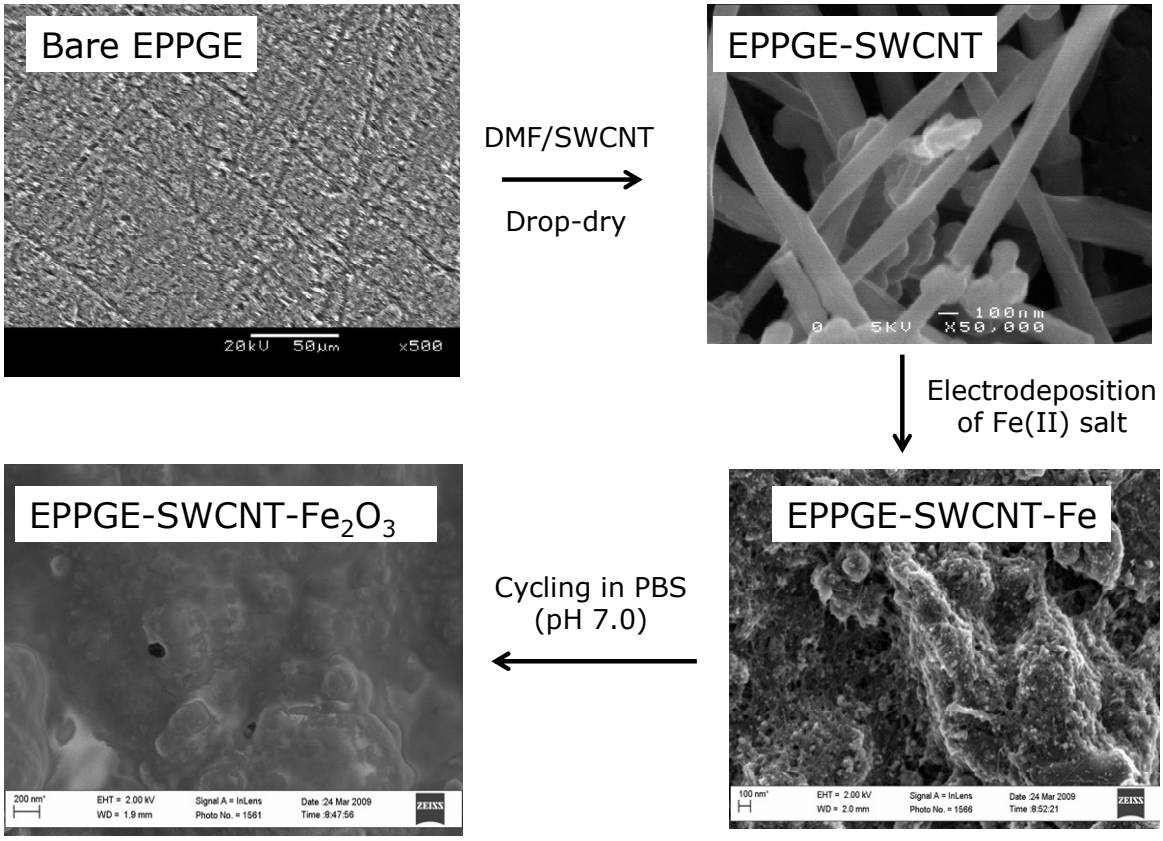

Scheme 7.1: Schematic of electrode modification process.

The ease of dispersion of the SWCNT suspension on the EPPGE bare electrode may be attributed to the strong π-π interaction between EPPGE and SWCNT. Electro-deposition of Fe particles on the EPPGE-SWCNT gave EPPGE-SWCNT-Fe. There is high dispersion of a

network of Fe nanoparticles that completely cover the SWCNT layer. This could be made possible because of the strong electrostatic interactions between the Fe^{2+} ions in solution and the COO^- of SWCNT on the electrode. After treating EPPGE-SWCNT-Fe electrode in aqueous PBS, pH 7.0, an EPPGE-SWCNT-Fe_2O_3 electrode was obtained. There is a clear transformation of the iron nanoparticles to iron oxides, mainly Fe_2O_3 as proved by XPS.

The AFM topography images (Figure 7.1) show similar surface morphology, which can be explained in the same manner as that given for the SEM images. It is much easier to view the particle distribution on the bare glassy carbon plate, SWCNT, SWCNT-Fe and SWCNT/Fe_2O_3 in nano sizes from the AFM images. From the cross section profile of the different modified electrodes (Figure 7.1), it could be observed that while the surface thickness of the bare plate are between 6–7 nm, the SWCNT paste are in the magnitude of 25 nm while the Fe and Fe_2O_3 particles are in the order of about 30 nm, indicating successful deposition and growth of nanoparticles on the electrode.

The EDX profile (Figure 7.2) gives insights into the elemental compositions of the modified electrodes. Bare EPPGE (a) predominantly showed carbon (~ 100%) which is an indication of a clean, unmodified electrode. The acid-treated SWCNT (b) confirmed presence of sulfur peak and oxo-functionality (presence of oxygen peak), attributed to the treatment of the SWCNT with sulfuric acid solution and its subsequent washing with copious amount of water. The metal impurities especially nickel is characteristic of Aldrich SWCNT used in this study and cannot be completely removed during acid treatment.

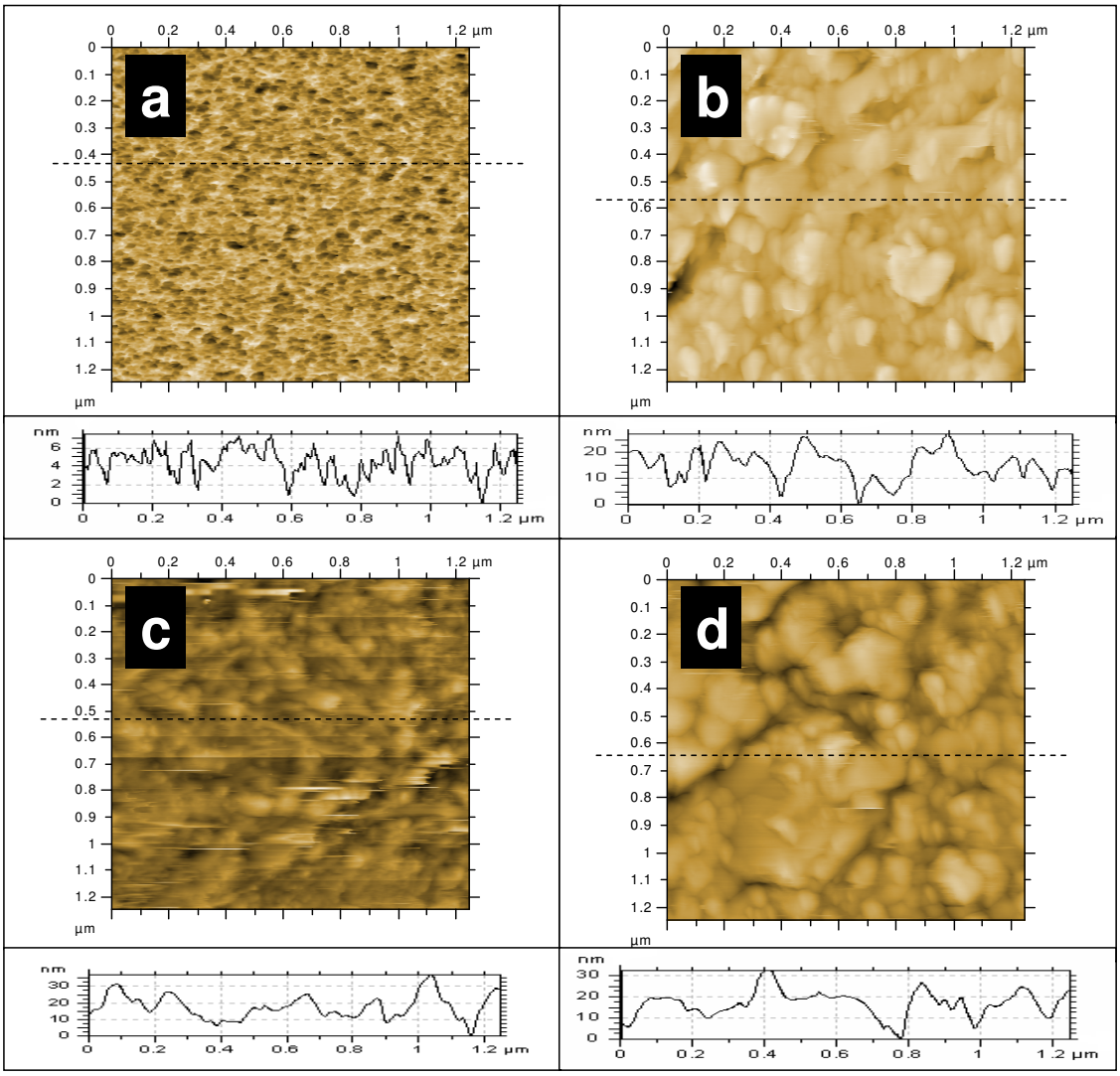

Figure 7.1: Typical AFM images of (a) bare glassy carbon (GC) plate, (b) GC-SWCNT, (c) SWCNT-SWCNT-Fe and (d) GCE-SWCNT-Fe_2O_3.

EDX profile of c and d shows the presence of iron peaks which is a proof for the successful modification of EPPGE-SWCNT-Fe (c) and EPPGE-SWCNT-Fe_2O_3 (d) with iron nanoparticles. The P and Na peaks in the EDX of EPPGE-SWCNT-Fe_2O_3 arise from the sodium phosphate

salt used for the electrolyte while the enhanced oxygen peak confirms the modification of the electrode to its oxide form.

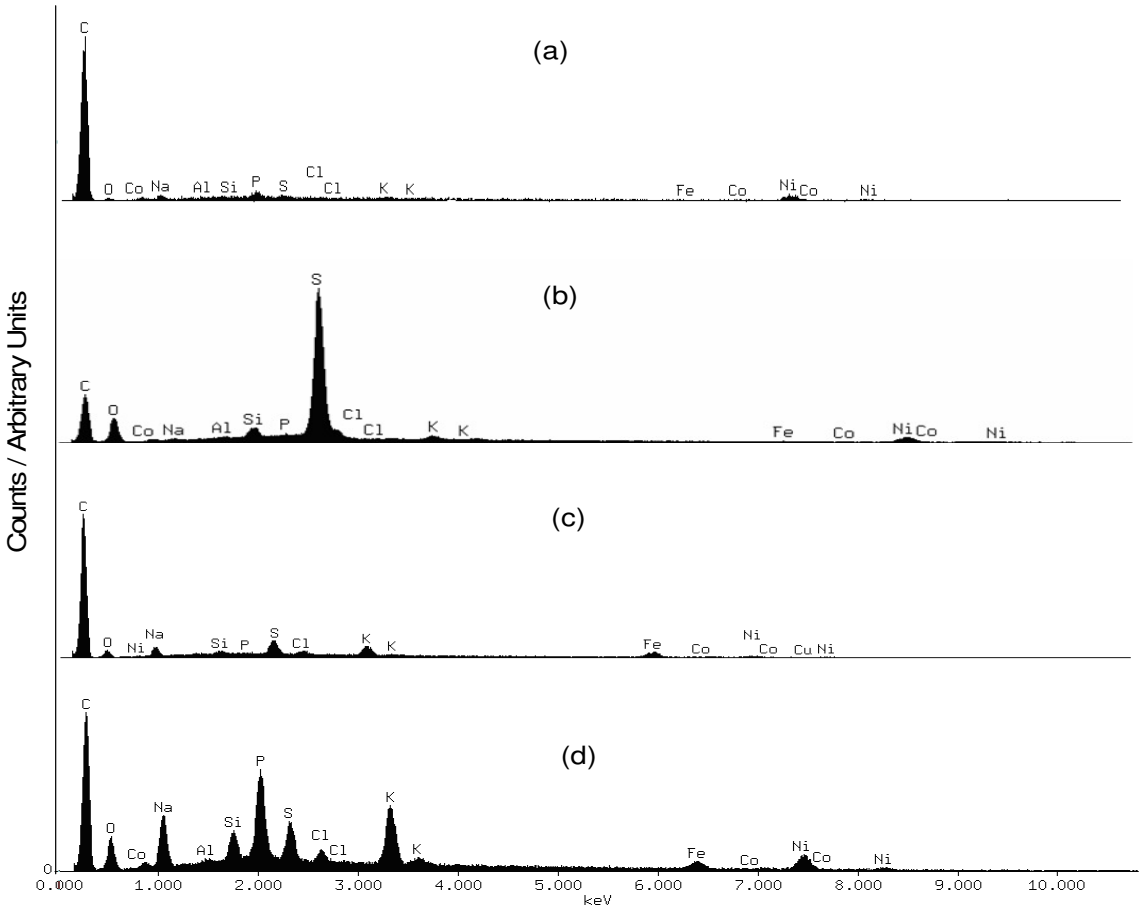

Figure 7.2: Typical EDX profile of the (a) bare EPPGE, (b) EPPGE-SWCNT, (c) EPPGE-SWCNT-Fe and (d) EPPGE-SWCNT-Fe_2O_3.

Figure 7.3 presents the XPS results of the EPPGE-SWCNT-Fe_2O_3 modified electrode in 0.1 M pH 7.0 PBS. XPS data analysis was aimed at determining quantitatively the relative amounts of the two chemical species of Fe, which are Fe^{2+} and Fe^{3+} in the recorded spectrum. The Fe $2p_{3/2}$ peak at 713.6 eV (enlarged in the inset, Figure 7.3) agreed with literature value of 711.0 eV which indicates the presence of Fe_2O_3 species [1,2]. The weak peak at 727.2 eV

corresponding to Fe $2p_{1/2}$, agreed closely with 724.6 eV reported in literature [2], associated with Fe_3O_4 species. The sharp nature of the O1s peak (532 eV) also suggests that the oxygen is in one oxidation state. The O1s peak is very close to the 530 eV reported to be the lattice oxygen of Fe_2O_3 and Fe_3O_4 [2,3]. The dominant oxide of Fe on modified electrode from this result can be taken as Fe_2O_3 since species of Fe_3O_4 are not apparent. The Na and the P peaks in Figure 7.3 can be attributed to the Na and P of the PBS used during electrode modification while the C peak can be attributed to the carbon of the SWCNT and the base EPPGE electrode.

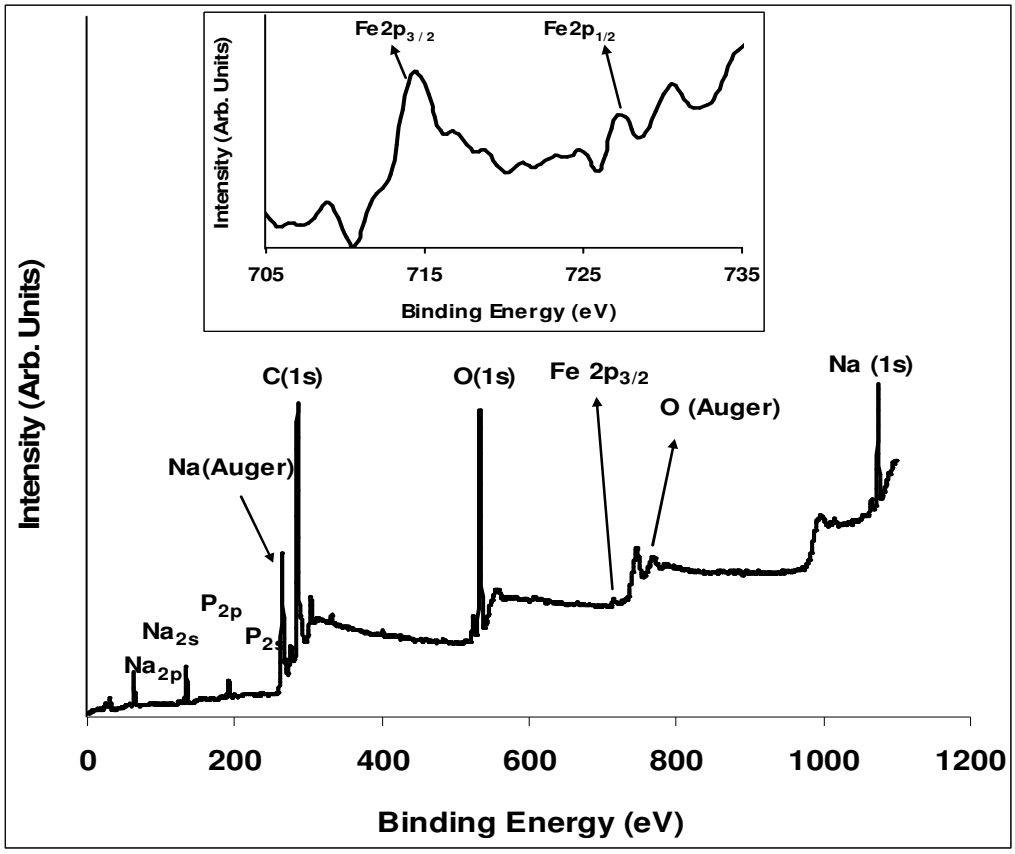

Figure 7.3: Typical XPS of EPPGE-SWCNT-Fe_2O_3 modified electrode. Inset shows the enlarged portion showing the peak corresponding to the Fe $2p_{3/2}$ and Fe $2p_{1/2}$ bands.

7.2. Electrocatalytic detection of dopamine: Voltammetric and Impedimetric properties

Figure 7.4 compares the cyclic voltammograms, original (a) and background-subtracted (b) of bare EPPGE (i), EPPGE-SWCNT (ii), EPPGE-SWCNT-Fe (iii), and EPPGE-SWCNT-Fe_2O_3 (iv) in 0.1 M PBS (pH 7.0) containing 2 x 10^{-4} M dopamine (DA). As easily seen from the original voltammograms, the electrodes containing SWCNT are associated with large background (capacitive) current responses, characteristic of acid-treated SWCNT [4]. DA redox couple at $E_{1/2}$ of *ca* 0.2 V is due to Dopamine / Quinone redox process. The current response of each electrode after the subtraction of the buffer current follow this trend: EPPGE-SWCNT-Fe_2O_3 (~ 50.45 μA) > EPPGE-SWCNT (~ 23.24 μA) and EPPGE-SWCNT-Fe (~ 22.80 μA), bare EPPGE (~ 6.62 μA), indicating the enhanced response of the EPPGE-SWCNT-Fe_2O_3 compared to other electrodes.

Next, the electron transfer properties of the four electrodes towards the voltammetric detection of dopamine using the EIS strategy were investgated. EIS is a powerful non-destructive and very informative technique for probing molecules at surfaces. It provides vital information about the charge transfer phenomenon across the electrode|electrolyte interface [5-7]. Figure 7.5a shows the impedance spectra (Nyquist plots) obtained for the electrodes, EPPGE (i), EPPEGE-SWCNT (ii), EPPGE-SWCNT-Fe (iii) and EPPGE-SWCNT-Fe_2O_3 (iv) in 2 x 10^{-4} M DA solution performed at a fixed potential (0.2 V vs. Ag|AgCl sat'd KCl) and frequencies between 10 kHz and 0.1 Hz. The choice of the fixed potential was based on the formal potential, $E_{1/2}$, of the DA which is the sum of the values of the anodic and the cathodic peak potential divided by two (i.e., $(E_{pa}+E_{pc})/2$). The experimental data were successfully fitted with the

Randles circuit model (Figure 7.5b) where the element R_s, R_{ct}, C_{dl} and Z_w are already defined. The parameters were fitted with satisfactory results (Table 7.1).

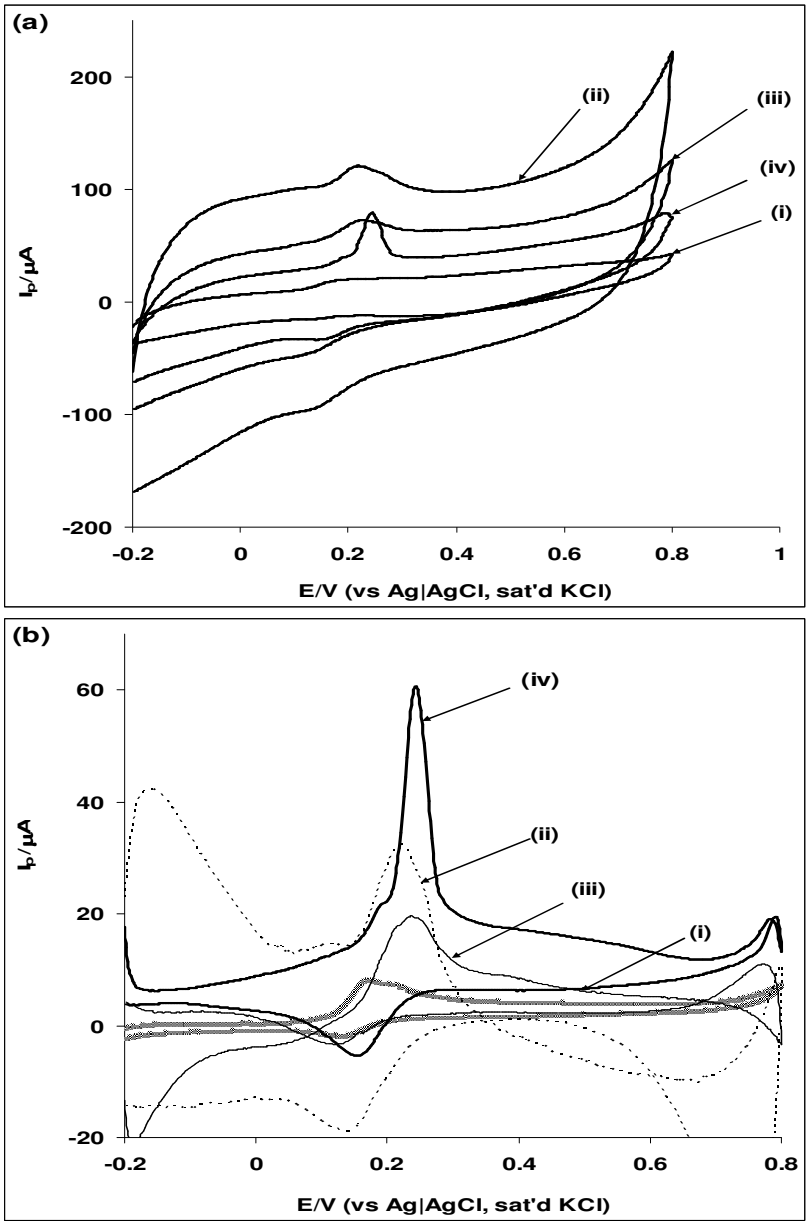

Figure 7.4: Typical cyclic voltammograms, original (a) and background- subtracted (b) of bare EPPGE (i), EPPGE-SWCNT (ii), EPPGE-SWCNT-Fe (iii), and EPPGE-SWCNT-Fe_2O_3 (iv) in 0.1 M PBS (pH 7.0) containing 2 x 10^{-4} M DA (Scan rate = 25 mV s^{-1}).

EPPGE-SWCNT-Fe_2O_3 has the lowest R_{ct} value (1.29 Ωcm^2) compared with the bare EPPGE (16.20 Ωcm^2), EPPGE-SWCNT (1.68 Ωcm^2) and the EPPGE-SWCNT-Fe (1.92 Ωcm^2) electrodes. Note that the C_{dl} is treated here as a constant phase element, CPE (a real application situation) rather than the ideal double layer capacitance [8, 9].

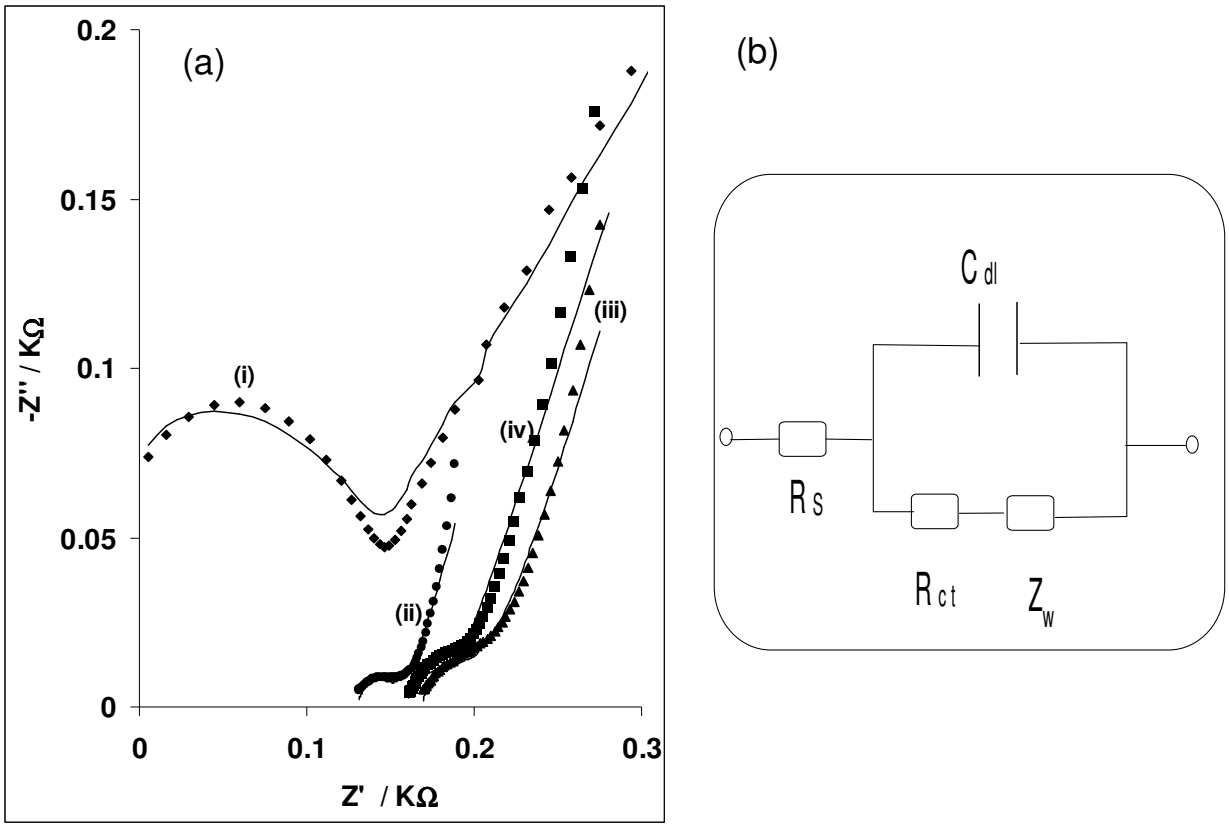

Figure 7.5: (a) Typical Nyquist plot of the bare EPPGE (i), EPPGE-SWCNT (ii), EPPGE-SWCNT-Fe (iii), and EPPGE-SWCNT-Fe_2O_3 (iv) obtained in 0.1 M PBS containing 2 x 10^{-4} M DA (biased at 0.2 V), between 10 KHz and 0.1 Hz, and (b) Equivalent circuit model used in fitting the spectra obtained in Figure 7.5 (a).

Table 7.1: Impedance data obtained for the electrodes in 2 x 10^{-4} M DA solution in pH 7.0 PBS (at 0.2 V vs Ag|AgCl sat'd KCl).

Electrodes	Electrochemical impedance spectroscopy data				
	$R_s/\Omega\ cm^2$	$C_{dl}/\mu Fcm^{-2}$	$R_{ct}/\Omega cm^2$	$Z_W/\Omega\ cm^2$	k_s/cms^{-1}
EPPGE	-4.34±0.04	1.42±0.06	16.20±0.03	30.54±0.04	0.02±0.03
EPPGE-SWCNT	13.13±0.01	76.30±14.93	1.68±0.02	522.00±1.72	0.20±0.02
BPPGE-SWCNT-Fe	16.94±0.02	80.7±18.75	1.92±0.02	255.00±0.71	0.17±0.02
BPPGE-SWCNT-Fe_2O_3	15.88±0.04	53.3±11.56	1.29±0.04	193.80±0.72	0.26±0.04

The electron transfer rate constants (k_s) may be obtained from the R_{ct} values from the derived Equations (7.1-7.3) [10, 11].

$$R_{ct} = \frac{RT}{nFi_o} \tag{7.1}$$

$$i_o = nFAk_s C_O^{\infty} C_R^{\infty} \tag{7.2}$$

Combining Equations 7.1 and 7.2, taking the activity coefficients (∞) equal to unity, and assuming the bulk concentrations of the oxidized and reduced species to be equal ($C_O^{\infty} = C_R^{\infty} = C$) such that the equilibrium potential ($E_{1/2}$) equals the formal redox potential ($E_{O/R}^{\phi}$), then the k_s becomes:

$$k_s = \frac{RT}{n^2 F^2 A R_{ct} C} \tag{7.3}$$

where n = 2, *A* is the area of the electrode, C is the concentrations of (mol cm^{-3}) of dopamine, R, T and F have their usual meanings. The k_s value decreases as follows: EPPGE-SWCNT-Fe_2O_3 (~ 0.26 cms^{-1}) > EPPGE-SWCNT (~ 0.20 cms^{-1}) > EPPGE-SWCNT-Fe (~ 0.17 cms^{-1})> bare EPPGE (~ 0.02 cms^{-1}). The high k_s value of the EPPGE-SWCNT-Fe_2O_3 indicates faster electron transfer response towards the electrocatalysis of DA. Both CV and EIS data prove that the EPPGE-SWCNT-Fe_2O_3 hybrid exhibit better response towards the electrochemistry of DA compared to the other electrodes studied in this work. CNTs are known to enhance electrocatalytic response [12, 13]. Thus, these results could be associated with a combination of factors, such as the synergistic behaviour between the high electron-

conducting CNTs and the affinity between Fe^{3+} and DA [14], the ease of diffusion of the DA through the porous-like SWCNT-Fe_2O_3 film to the catalytic sites of the electrode, the larger available surface area of the modified electrode due to the nanometric dimension of the nanotubes and, finally the strong combination tendency of SWCNT-Fe_2O_3 to DA by electrostatic interaction. The last point can be substantiated by looking at the ionic form of DA in PBS. DA is positively charged at pH under 7.4 or in neutral environment [15]. This is due to the protonation of the nitrogen atom on the molecule. Hence, while the EPPGE-SWCNT-Fe electrodes will attract DA with weaker force as a result of repulsion between like charges, it becomes easier for DA to be attracted towards the EPPGE-SWCNT-Fe_2O_3 film because of the electron-rich oxygen atom. This phenomenon may explain why the detection and catalysis of DA was much favoured at the EPPGE-SWCNT-Fe_2O_3 compared to other electrodes. Aside the fact that Fe is in its most stable oxidation state of +3 (Fe^{3+}) in the electrolyte, which makes it a strong catalyst and oxidant, it has also been reported that Fe^{3+} is chelated by the dihydroxy catechol group of dopamine, catechol, 5, 6-dihydroxyindole etc [14]. A report demonstrated that 7(2-aminoethyl)-3,4-dihydro-5-hydroxy-2H-1,4-benzothiazine-3 carboxylic acid (DHBT-1), containing –OH phenolic and >NH in six ring, had an ability of binding Fe^{3+} like 5, 6-dihydroxyindole [16]. It can therefore be concluded from these previous reports that the EPPGE-SWCNT-Fe_2O_3 modified electrode could be the best electrode towards DA oxidation based on the ability of Fe^{3+} to bind and form chelate with DA [14] and its oxidation intermediates. All other studies carried out in this work, unless otherwise stated, were focused on EPPGE-SWCNT-Fe_2O_3 electrode.

7.3. Effect of varying potential scan rates

Effect of potential scan rate (ν) was investigated by carrying out cyclic voltammetry experiment at constant concentration ($2x10^{-4}$ M) of the DA in 0.1 M PBS using the EPPGE-SWCNT-Fe_2O_3 electrode (Figure 7.6a). At a potential scan rate of 25 mVs^{-1}, a pair of well defined redox peaks, equilibrium potential ($E_{1/2}$) of 165 mV, a ratio of anodic to cathodic peak current (I_{pa} / I_{pc}) approximately 1.3 (slightly higher than the unit value expected for an ideal voltammetric reversibility), and a peak-to-peak separation (ΔE_p) of ~70 mV (slightly higher than the 59.8 mV value expected for a one-electron reversible process) was observed. The CV data indicate a quasi-reversible electro-oxidation of DA. The ΔE_p increases at higher potential scan rates. This slight deviation from ideality may be due to chemical interaction between DA and the film. It was observed that DA anodic and cathodic peaks increase simultaneously with increase in scan rates (scan rates ranged from 25–1000 mVs^{-1}). As in Figure 7.4, the anodic current is more pronounced than the reduction current, suggesting that the potential sweep favours electro oxidation of DA. This observed non-symmetrical forward and reverse peaks of DA in 0.1 M PBS (pH 7.0) should perhaps not be surprising as other workers [17] have also observed the same and ascribed it to the working pH conditions. At pH 5, the peaks are symmetrical but with increase in pH, the cathodic (reverse) peak significantly decreased. The plots of peak current, I_p for both anodic and cathodic versus square root of scan rate ($\nu^{1/2}$) (Figure 7.6b) were linear (R^2 = 0.9956 and 0.9939), signifying a diffusion-controlled redox process [18-21].

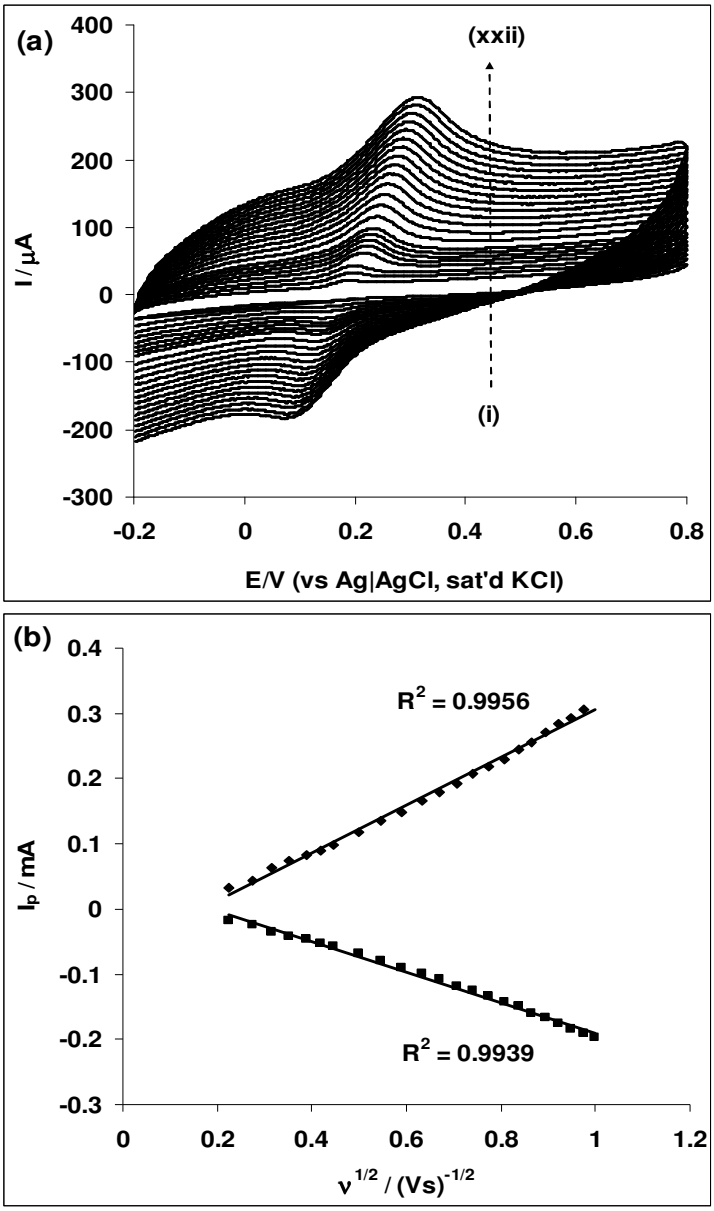

Figure 7.6: (a) Cyclic voltammetric evolutions of EPPGE-SWCNT-Fe_2O_3 obtained in 0.1 M PBS containing 2 x 10^{-4} M DA at scan rates 25 to 1000 mV s^{-1} (inner to outer). (b) Plot of I_p vs. $\nu^{1/2}$ for both anodic and cathodic process.

7.4. Analytical Application

Concentration study was carried out by investigating the response of EPPGE-SWCNT-Fe_2O_3 electrode to the different concentrations of DA (Figure 7.7) using square wave voltammetry (SWV). At DA concentration greater than 32 μM, the current response did not increase any further, a phenomenon usually attributed to the saturation of the catalytic sites.

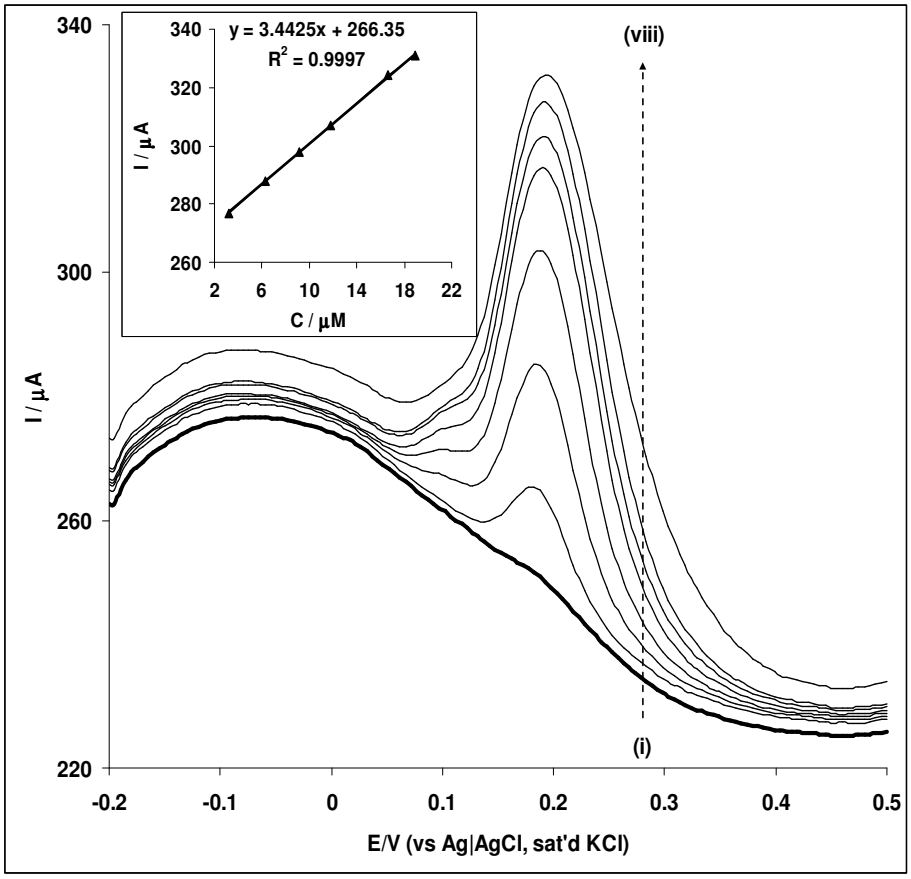

Figure 7.7: Square wave voltammetric evolutions of the EPPGE-SWCNT-Fe_2O_3 in 0.1 M PBS solution containing different concentrations of DA (i–viii represent 0.00, 3.23, 6.25, 9.09, 11.76, 14.30, 18.92, and 31.82 μM, respectively). Inset is the plot of current vs. concentration of DA.

From the plot of current response against concentration (inset in Figure 7.7), a linear relationship (Equation 7.4) was obtained for concentration range of 0.0 to 31.8 μM.

$$I_p / \mu A = (3.44 \pm 0.03)\ [DA] / \mu M + (266.35 \pm 0.38) \qquad (7.4)$$

The sensitivity was calculated as 3.44±0.03 μA μM^{-1} (R^2 = 0.9997), while the limit of detection (LoD = 3.3 s/m [22]) was (3.6±0.3)x10^{-7} M. The limit of detection of the electrode was much lower, and at about the same magnitude with values reported in literature (Table 7.2) for some modified electrode towards DA electrocatalysis and detection [18,23,24-27]. Dopamine is present at a micromolar concentration level in biological fluids [28] thus the 3.6 x 10^{-7} M detection limit of EPPGE-SWCNT-Fe_2O_3 suggest that SWCNT/Fe_2O_3 hybrid material might be suitable for the modification of ultramicroelectrodes for in-vivo detection of dopamine.

The stability of the electrode was first interrogated by continuous scanning in a 2x10^{-4} M DA at 25 mVs^{-1}. A decrease in peak currents (>50%) was usually observed after the first scan, which is a typical behaviour for a poisoned electrode. However, on rinsing the electrode in a fresh PBS (pH 7.0) solution, the electrode surface was renewed and more than 95% of the initial catalytic current was obtained, indicating the electrochemical stability and reusability of the electrode after analysis. Also, using SWV technique, the same result as in Figure 7.7 was obtained. The electrode can be used for the analysis of DA after storage in a refrigerator for up to two weeks without a significant change in its response.

Table 7.2: Voltammetric response for dopamine using various modified electrodes.

Electrode	Electrolyte	Method	LCR range/μM	LoD/ μM	Ref.
EPPGE-SWCNT-Fe_2O_3	0.1 M PBS (pH 7.0)	SWV	3.2 – 31.8	0.36	This work
GCE-Poly-EBT	0.05 M PBS (pH 4.0)	DPV	0.1 – 200.0	0.02	16
CPE-Cobalt salophen	0.1 M ACS (pH 5.0)	DPV	1.0 – 100.0	0.50	20
GCE-CNT-IL gel	0.1 M PBS (pH 7.08)	DPV	1.0 – 100.0	0.10	23
GCE-polycresol red	0.1 M PBS (pH 5.0)	LSV	10.0 – 100.0	1.50	21
GCE-PEDOT-PANS	ACS (pH 5.0)	LSV	2.0 – 8.0	0.50	22
Au-Penicillamine SAM	0.1 M PBS (pH 6.8)	–	20.0 – 800.0	4.0	24

EBT: erichrome black T; CPE: carbon paste electrode; GCE: Glassy carbon electrode; CNT: Carbon nanotubes; IL: Ionic liquid; PEDOT: Poly(3,4-ethylenedioxythiophene-co-(5-amino-2-naphthalenesulfonic acid)); PANS: Poly 5-amino-2-naphthalenesulfonic acid; SAM: Self-assembled monolayer; PBS: Phosphate buffer solution; ACS: Acetate buffer solution; LCR: Linear concentration range; LoD: Limit of detection; SWV: Square wave voltammetry; DPV: Differential pulse voltammetry; LSV: Linear sweep voltammetry

Chronoamperometric study was carried out by setting the operating condition at a potential of 0.2 V. The catalytic rate constant (k) for the oxidation of DA at the EPPGE-SWCNT-Fe_2O_3 electrode was estimated from already known relationship [29,30]. From the plots of I_{cat}/I_{buff} vs. $t^{1/2}$ at different DA concentrations (not shown), and the plot of the slopes vs. square root of the DA concentrations (not shown), k value was estimated to be 8.7±0.74 x 10^5 cm^3 mol^{-1} s^{-1} for EPPGE-SWCNT-Fe_2O_3. The k value obtained in this study is *ca* 3 times higher than the 3.1 x 10^2 M^{-1} s^{-1} (3.1 x 10^5 cm^3 mol^{-1} s^{-1}) reported for DA oxidation at aluminium electrode modified with nickel pentacyanonitrosylferrate films [31], approximately 2 times higher than 4.67 x 10^2 M^{-1} s^{-1} (4.67 x 10^5 cm^3 mol^{-1} s^{-1}) reported at palladium hexacyanoferrate film, electroless plated electrode [32] and a magnitude less compared with 8.813 x 10^3 M^{-1} s^{-1} (8.813 x 10^6 cm^3 mol^{-1} s^{-1}) reported for the analyte oxidation on a modified carbon nanotube paste electrode [33]. The difference in the k value is due to the different electrode modifier. The diffusion coefficient (D) of DA at this electrode was estimated from the Cottrell Equation (7.5) below [10]:

$$I = \frac{nFAD^{1/2}C}{\pi^{1/2}t^{1/2}} \qquad (7.5)$$

where C is the bulk concentration (mol cm^{-3}), A is the area of the electrode in cm^2 and assuming n ≈ 2 [18,34,], from the experimental plots of I versus $t^{-1/2}$ at different concentrations (not shown), the diffusion coefficient D of DA was calculated as (3.5±0.27) x 10^{-5} cm^2s^{-1} for the EPPGE-SWCNT-Fe_2O_3, which closely agree with the 6.5

x 10^{-5} cm^2s^{-1} reported for *poly* (malachite green) film-coated glassy carbon electrode [21] but about a magnitude higher than 4.15 x 10^{-6} cm^2 s^{-1} reported for DA on penicillamine self-assembled gold electrode [27].

7.5. Interference study

Typical square wave voltammetric responses of AA in the absence (i) and presence of DA (ii – iv) at the EPPGE-SWCNT-Fe_2O_3 platform are shown in Figure 7.8. Curve (i) represents 1 mM AA alone, and mixture of (ii) 33.3 μM DA and 0.83 mM AA, (iii) 46.2 μM DA and 0.77 mM AA, and (iv) 88.9 μM DA and 0.56 mM AA in PBS pH 7.0. Attempts to obtain much lower concentration of the DA was not successful probably due to the base line drifts of the SWV. In the absence of DA, AA signal appeared close to zero volt. On addition of DA, there was a clear separation of signal with DA located at around 0.2 V. The height and amplitude of the peak corresponding to DA also increase proportionally with the DA concentration. It is interesting to observe that good signal of the DA at 33 μM could be obtained in the presence of 1 mM AA. In fact, in all the concentrations of the DA studied there was no detectable interference of the AA, the signal of the AA was about 200 mV away from that of the DA.

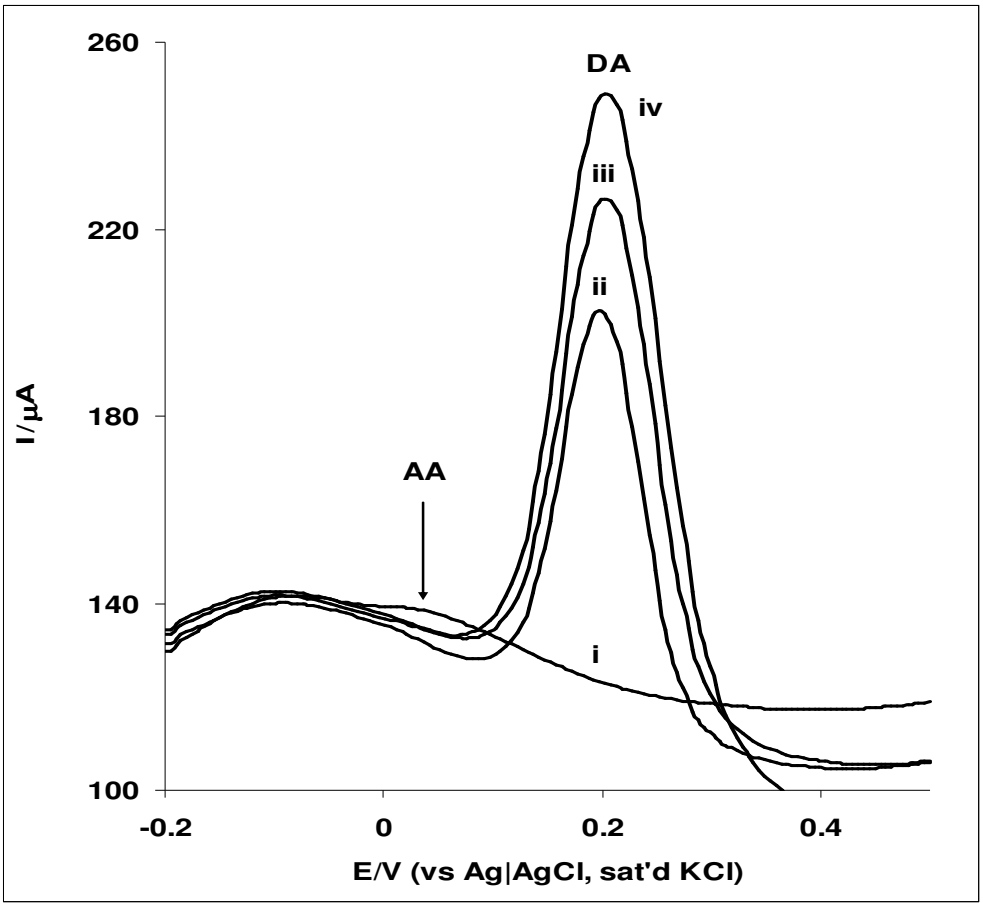

Figure 7.8: Typical square wave voltammograms responses of EPPGE-SWCNT-Fe_2O_3 in (i) 1 mM AA alone, and mixture of (ii) 33.3 µM DA /0.83 mM AA, (iii) 46.2 µM DA / 0.77 mM AA, and (iv) 88.9 µM DA / 0.56 mM AA in PBS pH 7.0.

7.6. Real sample analysis: Dopamine drug

To evaluate the potential applicability of the EPPGE-SWCNT-Fe_2O_3 electrode, a square wave voltammetric assay of dopamine present in a dopamine hydrochloride injection, with dopamine content of 200 mg / 5 mL (i.e., 40 mg mL^{-1}) was carried out. The concentration found in each dopamine drug (Table 7.3) is approximately within the labelled amount (n = 5) at 95% confidence limit. The result clearly indicates that dopamine can be reliably assayed from its drug, thus demonstrating the suitability of the proposed EPPGE-SWCNT-Fe_2O_3 electrode as a sensor.

Table 7.3: Determination of dopamine content in dopamine hydrochloride injections (40 mg mL^{-1}), n =5 (at 95% confidence limit).

Sample	Concentration found/mg mL^{-1}	Recovery/%
1	41.7 ± 2.73	104.3 ± 6.70
2	40.4 ± 0.63	101.0 ± 1.02
3	39.8 ± 0.77	99.4 ± 1.92
4	41.1 ± 0.48	102.7 ± 1.19

In a similar study, the voltammetric detection of dopamine using easily prepared nano-scaled iron oxide (Fe_2O_3) catalyst supported on multi-walled carbon nanotubes (MWCNT) modified pyrolytic graphite electrode was carried out. Some of the motivating factors for embarking on this particular study include (i) the ability to produce nano-scaled iron oxides in high commercial quantity compared to the very low and commercially unviable amount

inherent with the electrodeposition method, (ii) low or non-passivation of the electrode modified with laboratory-synthesised Fe_2O_3 nanoparticles compared with their electrodeposited counterparts, and (iii) commercial availability of MWCNTs over the SWCNTs in terms of cost implication

Figure 7.9 is the typical TEM micrograph for the MWCNT-Fe (a) and the MWCNT-Fe_2O_3 (b). Their corresponding HRSEM images are represented in Figure 7.9c and d respectively. All the micrographs showed very high dispersion of Fe and Fe_2O_3 nanoparticles along the MWCNTs which is made possible because of the strong electrostatic interactions between the Fe^{2+} or Fe^{2+} ions in solution and the COO^- charge of the MWCNTs. From the TEM and using the UTHSCSA Image Tool for windows version 3.0, for the image calibration, a representative single particle size is around 20-50 nm for Fe and 5-13 nm for Fe_2O_3 which agreed closely with 60-70 nm reported for Fe [35], and 8.6 nm for γ-Fe_2O_3 nanoparticles [36].

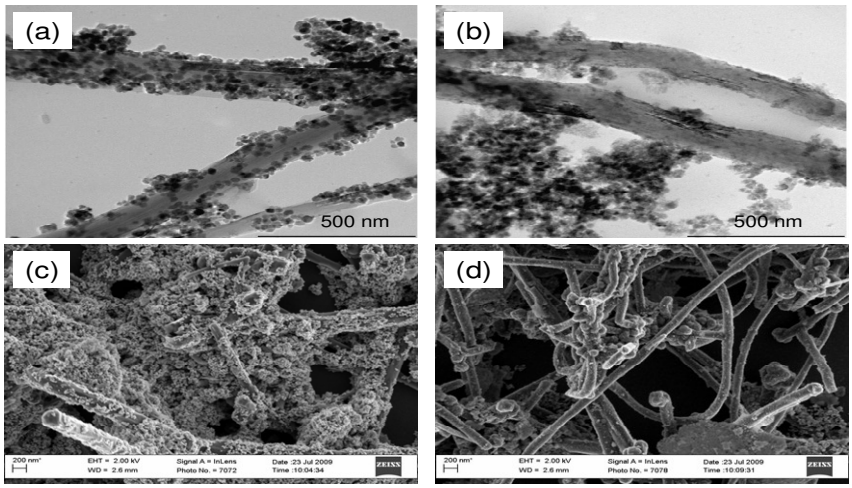

Figure 7.9: TEM images of (a) MWCNT-Fe (b) MWCNT-Fe_2O_3. (c) and (d) HRSEM picture of MWCNT-Fe and MWCNT-Fe_2O_3 respectively.

The XRD spectra for the nanosized particles are shown in Figure 7.10. Characteristic peaks at 2θ of 21.3, 35.2, 41.5, 50.6, 62.6, 67.4 and 74.3, which are indexed as (111), (220), (311), (400), (422), (511) and (440) were observed. The result agreed with that observed by others [36,37] indicating that the resultant particles were cubic spinel structure for γ-Fe_2O_3. From Debye-Scherrer equation [36], the crystal size of the Fe_2O_3 particles were estimated from the peaks to be ~ 10.3 nm, which falls in the range shown by the TEM. Inset in Figure 7.10 is the XRD spectrum of the Fe nanoparticles. Apparent peaks at 2θ of 41.8 and 35.4 indicate the presence of both zero-valent iron (Fe) and iron oxide (FeO) [35]. Traces of FeO particles not completely reduced to Fe were also confirmed by the presence of trace oxygen peak in the EDX profile (see Figure 7.11a).

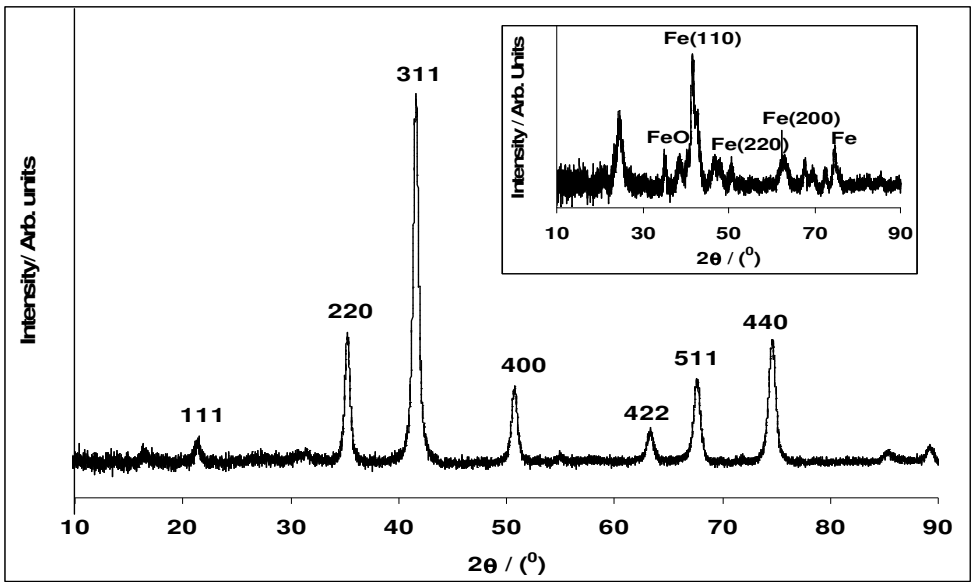

Figure 7.10: XRD spectrum of Fe_2O_3 nanoparticles. Inset is the XRD spectrum of Fe nanoparticles.

Figure 7.11 shows the EDX profile of the synthesised MWCNT-Fe (a) and MWCNT-Fe_2O_3 (b). The carbon peak in both is attributed to the carbon of the MWCNT or the base carbon coating for enhancing the conductivity of the material. The presence of Fe peaks in both (a) and (b) compared with other elements also confirm the successful modification of the MWCNTs with Fe or Fe_2O_3 nanoparticles. Presence of O peak in (b) is linked to traces of unreduced iron oxide and the oxo-functionalities of the functionalised MWCNTs. The sulphur peak can be attributed to the sulphuric acid used during MWCNT treatment.

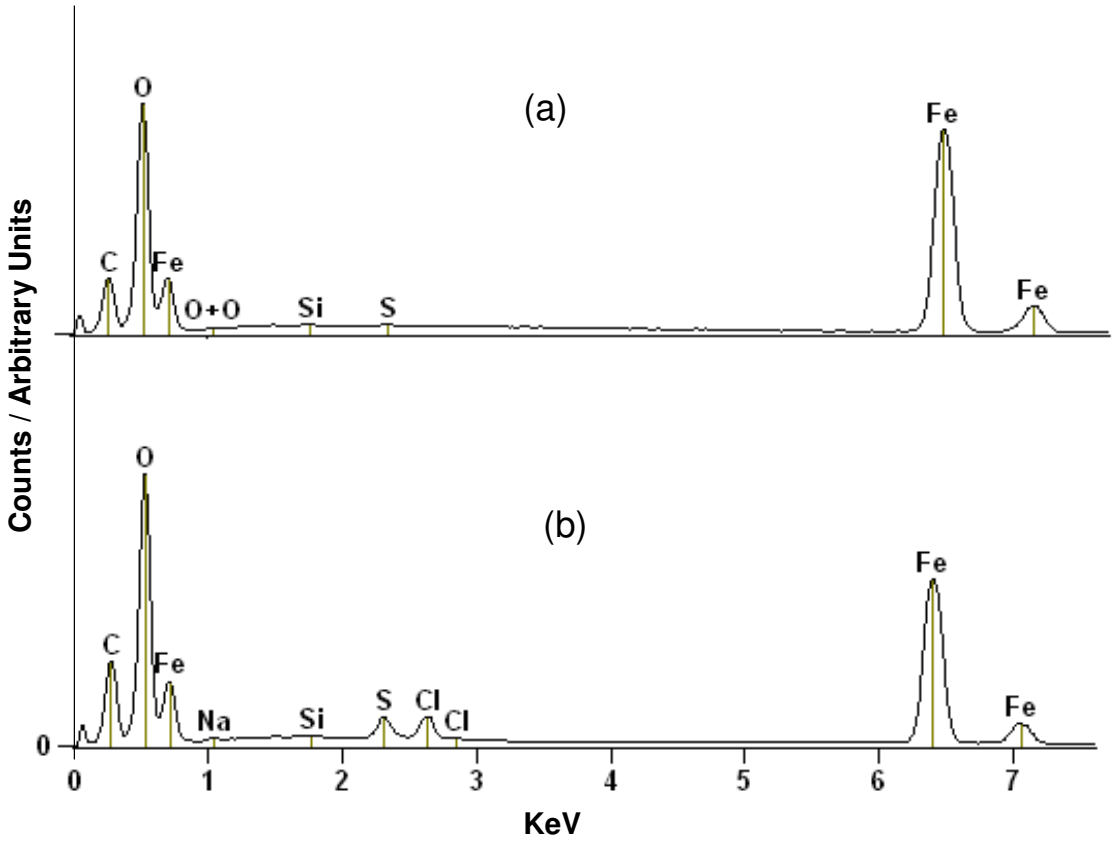

Figure 7.11: EDX profiles of MWCNT-Fe and MWCNT-Fe_2O_3 respectively.

Figure 7.12(a) is the comparative cyclic voltammograms of the electodes in 5 mM $Fe(CN)_6]^{4-}/[Fe(CN)_6]^{3-}$ solution. The redox couple in the 0.0 – 0.4 V regions (II) is due to the $Fe(CN)_6]^{4-}/[Fe(CN)_6]^{3-}$ redox process. This couple is absent in 0.1 M PBS (pH 7) alone (b). The broad redox process in the -0.2 – 0.2 V region (I) is ascribed to the Fe^{3+}/Fe^{2+} of the iron or iron oxide, presumably the γ-Fe_2O_3 / Fe_3O_4. The poorly defined redox couples in the 0.5 – 0.7 V (III) is presumably due to the redox process involving the α-phase (i.e., α-Fe_2O_3 / FeOOH).

Further study to understand the electronic transport properties of the modified electrodes was carried out using electrochemical impedance spectroscopic (EIS) technique (biased at 0.2 V, the equilibrium potential, $E_{1/2}$, of the $[Fe(CN)_6]^{4-}/[Fe(CN)_6]^{3-}$ couple). The Nyquist plot obtained (Figure 7.13a) was satisfactorily fitted using the electrical equivalent circuit model shown in Figure 7.13b. The circuit elements are already defined. From the R_{ct} value (Table 7.4), the electron-transport is faster at the EPPGE-MWCNT-Fe and EPPGE-MWCNT-Fe_2O_3 electrodes (R_{ct} ~ 20.0 Ωcm^2) compared to others. The n values close to the ideal Warburg diffusive value of 0.5, is indicative of some diffusion process at the electrode.

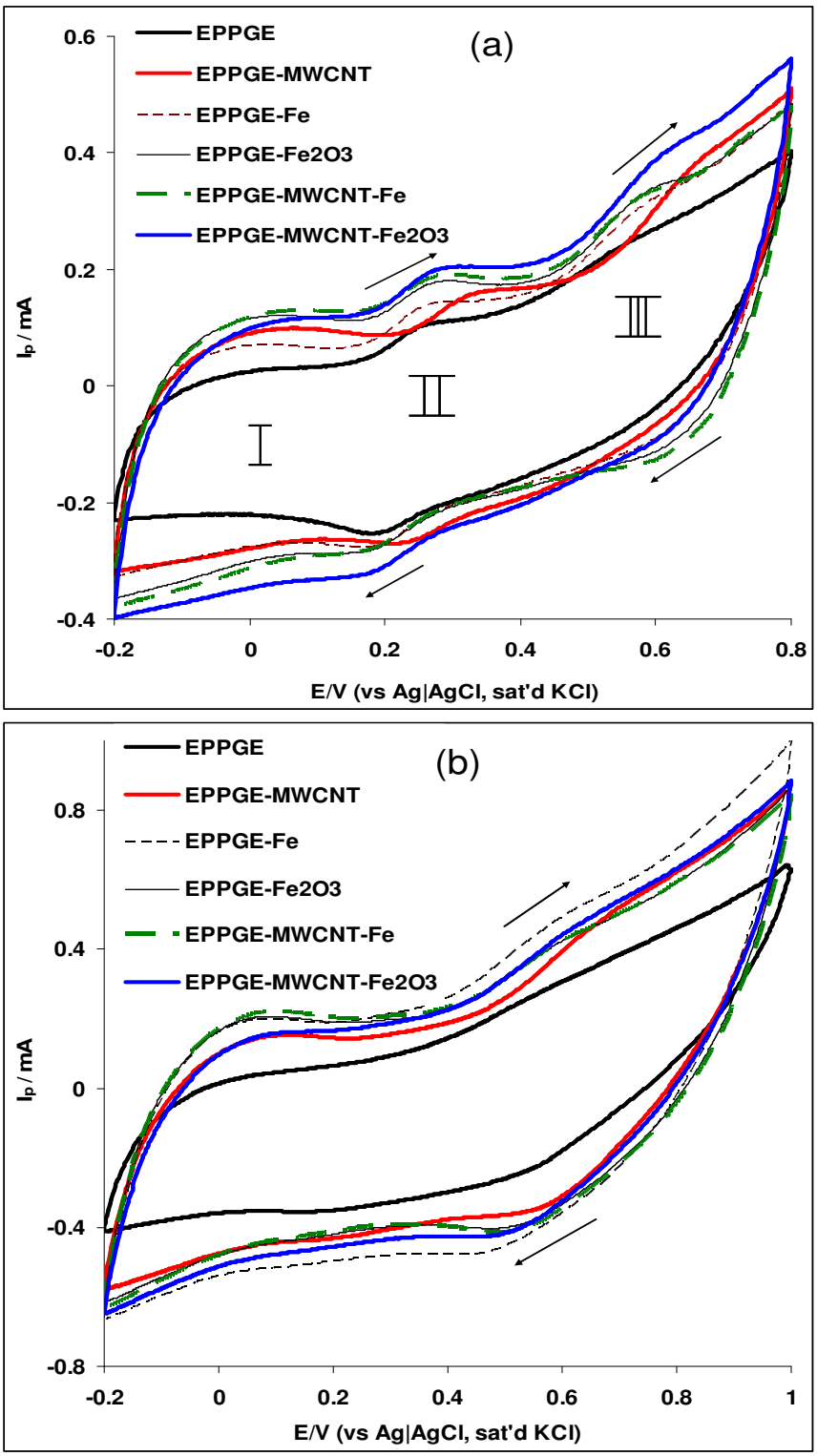

Figure 7.12: Comparative cyclic voltammetric evolutions of the bare and Fe/Fe_2O_3 modified electrodes in (a) 5 mM $[Fe(CN)_6]^{4-}/[Fe(CN)_6]^{3-}$ in pH 7.0 PBS and (b) 0.1 M pH 7.0 PBS (scan rate = 50 mVs^{-1}).

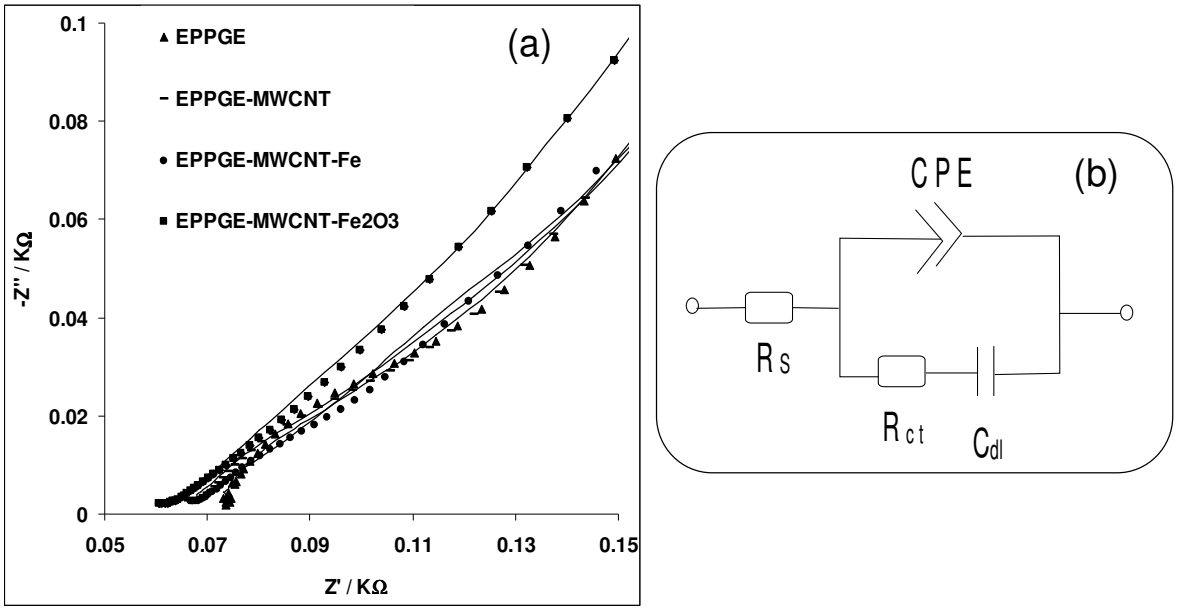

Figure 7.13: (a) Typical Nyquist plots obtained for some of the MWCNT modified electrodes in 5 mM $[Fe(CN)_6]^{4-}$ / $[Fe(CN)_6]^{3-}$ solution at a fixed potential of 0.2 V (vs Ag|AgCl, sat'd KCl). (b) is the circuit used in the fitting of the EIS data in (a).

Table 7.4: Impedance data obtained for the bare and the MWCNT modified EPPGE electrodes in 5 mM $Fe(CN)_6]^{4-}/[Fe(CN)_6]^{3-}$ solution at 0.2 V (vs Ag|AgCl sat'd KCl).

Electrodes	**Impedimetric parameters**				
	R/Ωcm^2	**Q/μFcm^{-2}**	**N**	**R/Ωcm^2**	**C_{dl}/mFcm^{-2}**
EPPGE	6.96±0.01	14.0±1.24	0.51±0.01	35.00±0.19	1.28±0.06
EPPGE-MWCNT	6.46±0.01	11.3±1.16	0.49±0.01	35.30±0.20	1.72±0.08
EPPGE-Fe	3.14±0.01	10.8±1.01	0.47±0.01	24.15±0.13	3.10±0.15
EPPGE-Fe_2O_3	3.29±0.01	161.8±19.61	0.55±0.01	27.10±0.69	1.15±0.22
EPPGE-MWCNT-Fe	3.33±0.01	38.0±4.74	0.49±0.01	20.2±0.18	3.94±0.30
EPPGE-MWCNT-Fe_2O_3	3.08±0.01	91.8±8.18	0.52±0.01	19.75±2.05	2.78±0.23

Figure 7.14 is the comparative cyclic voltammograms of the electrodes in 0.1 M PBS containing $2x10^{-4}$ M dopamine (DA). DA catalysis was studied at different loading (2.5 – 10 mg mL^{-1}) of Fe and Fe_2O_3 nanoparticles or their nanocomposite with MWCNT on the electrode. Since Fe, Fe_2O_3 and the MWCNTs are characterised with background (or capacitive) current, the current due to dopamine electro-oxidation (*ca* 0.2 V) on the electrodes was obtained after the background subtraction. Interestingly, when compared with all known literature reports on dopamine oxidation at modified electrodes, this result represents the first time that two pairs of redox couples are observed for dopamine. From the preceding discussion, the first DA redox couple (Dopamine / Quinone) at $E_{1/2}$ of 0.16 V is the usual mediated by the Fe^{3+}/Fe^{2+} (i.e., the γ-Fe_2O_3 / Fe_3O_4). The second redox couple at $E_{1/2}$ of 0.40 V is the same Dopamine / Quinone, which is now presumably mediated by the α-phase (i.e., α-Fe_2O_3 / FeOOH). The highest DA signal was obtained at 5.0 $mgmL^{-1}$ loading of the nanocomposite on the electrode and the trend in current response follows as: MWCNT-Fe_2O_3 >> MWCNT-Fe > MWCNT > EPPGE ≈ Fe_2O_3 > Fe. The current response at the MWCNT-Fe_2O_3 electrode is about two times higher than that at the bare electrode as well as the electrodes based on MWCNT or Fe nanoparticles alone. The DA oxidation current decreased with increasing loading (7.5 to 10 $mgmL^{-1}$) of the nanocomposite suggesting electrode layer passivation. The enhanced DA response at EPPGE-MWCNT-Fe_2O_3 may be ascribed to either (1) facile interaction of MWCNTs and Fe_2O_3, or (2) the ease of diffusion of DA through the MWCNT-Fe_2O_3 film to the electrode surface, or (3) the ability of the iron (III) to forms a chelate with the dihydroxy catechol group of dopamine, catechol, 5, 6-dihydroxyindole [38], or all of them. The

DA current response at the MWCNT-Fe_2O_3 films modified electrode is also higher compared with 50.45 μA reported for the SWCNT-Fe_2O_3 electrode prepared by electrodeposition method. The result therefore suggest that the synthetic method adopted in this study could be a better approach for electrode modification with the nanocomposite materials in large quantity, and at lesser cost for commercial application in sensor and other electrochemical devices. Therefore, all other studies carried out in this work, unless otherwise stated, were carried out using EPPGE-MWCNT-Fe_2O_3 electrode.

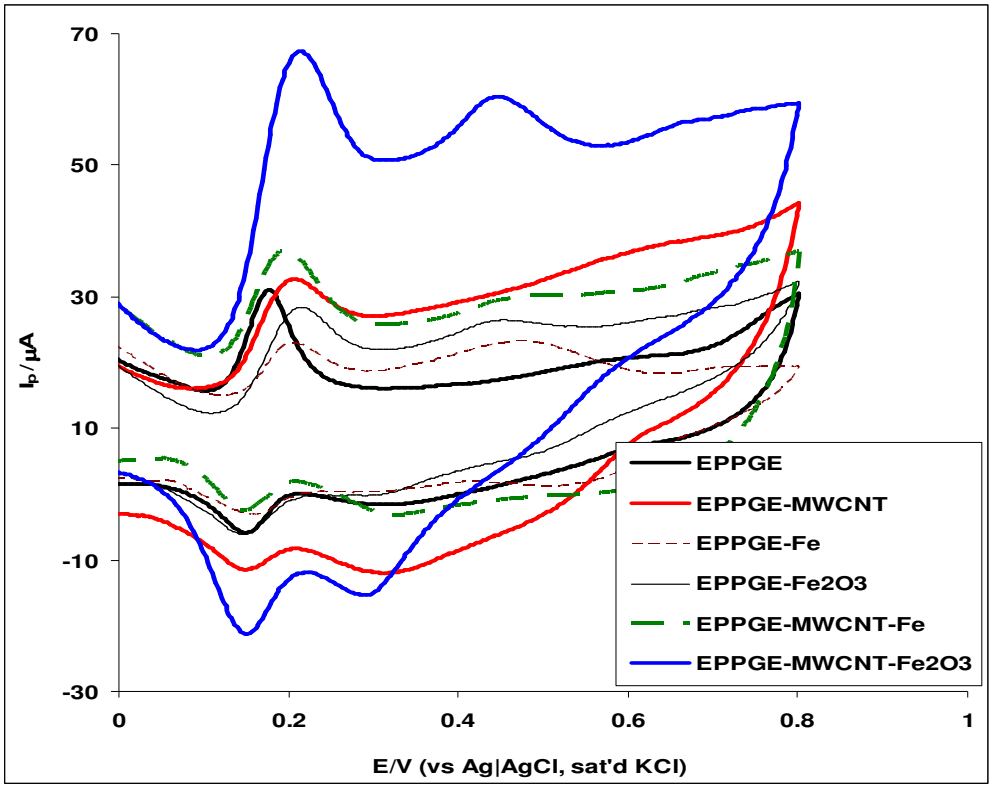

Figure 7.14: Comparative current response (after background current subtraction) of the electrodes: (i) EPPGE, (ii) EPPGE-MWCNT, (iii) EPPGE-Fe, (iv) EPPGE-Fe_2O_3, (v) EPPGE-MWCNT-Fe, and (vi) EPPGE-MWCNT-Fe_2O_3 in $2x10^{-4}$ M DA solution in pH 7.0 PBS (scan rate = 25 mVs^{-1}).

Effect of scan rate (ν) was investigated by carrying out cyclic voltammetry experiment at constant concentration (2 x 10^{-4} M) of DA in 0.1 M PBS using the EPPGE-MWCNT-Fe_2O_3 electrode (Figure 7.15). It was observed that DA anodic and cathodic peaks increase simultaneously with increase in scan rates (25–1000 mV s^{-1}). A pair of well defined symmetrical redox peaks (I_{pa} /I_{pc} ~ 1.0), were observed even at high scan rates. However, plots of the anodic (I_{pa}) against the square root of scan rate ($\nu^{1/2}$) (not shown) for the scan rate range studied gave a linear relationship with scan rates (R^2 = 0.9932), suggesting a diffusion-controlled redox process.

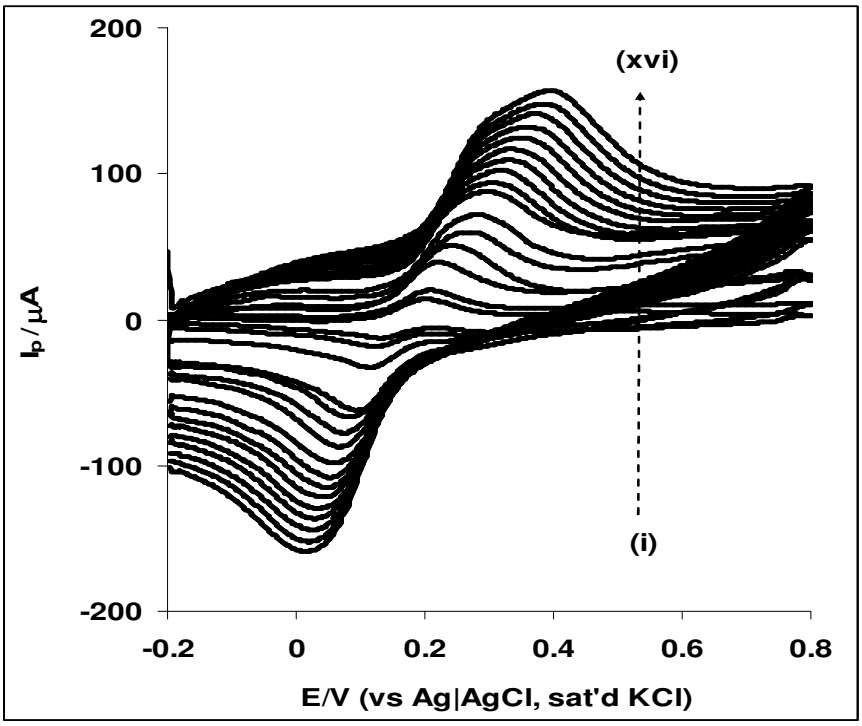

Figure 7.15: Cyclic voltammetric evolutions of EPPGE-MWCNT-Fe_2O_3 obtained in 0.1 M PBS containing 2 x 10^{-4} M DA (scan rate range 25 – 1000 mVs^{-1}; inner to outer).

Electro-oxidation of DA at the electrodes was investigated using EIS at a fixed potential (0.2 V vs. Ag|AgCl, sat'd KCl) and frequency range of 10 kHz to 10 mHz. Figure 7.16 represents the Nyquist plots obtained for some of the electrodes. Inset is the modified Randles circuit model used in the fitting of the experimental data. The circuit elements are already defined. The R_{ct} value (31.6 Ωcm^2) for EPPGE-MWCNT-Fe_2O_3 is relatively low compared with the 33.4 Ωcm^2 for bare EPPGE and 38.9 Ωcm^2 for EPPGE-MWCNT (Table 7.5). The results demonstrated the role of the MWCNT in forming a synergy with the Fe_2O_3 nanoparticles in improving the catalysis and electron transport of the MWCNT-Fe_2O_3 electrode towards DA oxidation. Presently, there is very little information on DA electrochemical impedance study. The information using a fibre (SiC-C) electrode for DA sensing [34] indicated that the electrode showed a capacitive behaviour which, according to the authors, is highly desirable for chemical and electrochemical stability of the electrodes.

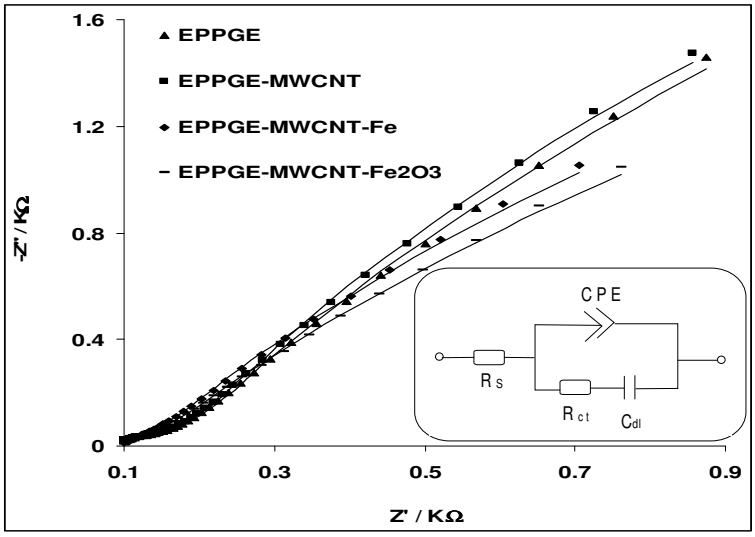

Figure 7.16: Typical Nyquist plots obtained for some of the MWCNT modified electrodes in 2 x 10^{-4} M DA solution at a fixed potential of 0.2 V. Inset is the Randles circuit model used in fitting the data.

Table 7.5: Impedance data obtained for the bare and the modified EPPGE electrodes in 2 x 10^{-4} M DA in pH 7.0 PBS at 0.2 V (vs Ag|AgCl sat'd KCl).

Electrodes	**Impedimetric parameters**				
	$R_s/\Omega cm^2$	**$Q/\mu Fcm^{-2}$**	**N**	**$R_{ct}/\Omega cm^2$**	**$C/mFcm^{-2}$**
EPPGE	8.32±0.01	24.19±2.15	0.57±0.01	33.40±0.13	2.20±0.05
EPPGE-MWCNT	8.30±0.01	25.06±2.09	0.58±0.01	38.90±0.16	2.19±0.08
EPPGE-Fe	8.71±0.01	12.39±1.27	0.53±0.01	40.30±0.17	2.40±0.09
EPPGE-Fe_2O_3	8.71±0.01	96.23±4.86	0.61±0.01	57.50±0.36	1.40±0.07
EPPGE-MWCNT-Fe	8.77±0.01	133.50±12.88	0.62±0.01	30.85±0.31	1.67±0.12
EPPGE-MWCNT-Fe_2O_3	8.42±0.01	83.06±4.86	0.59±0.01	31.60±0.21	1.46±0.07

The stability of the electrode was studied by continuous scanning in 2×10^{-4} M DA at 25 mVs^{-1}. About 40% current decrease was observed after the first scan which could be due to the adsorbed species on the electrode. However, on rinsing the electrode in a fresh PBS (pH 7.0) solution, the electrode surface became renewed and a current increase (> 90%) of the initial catalytic current was obtained. The result therefore suggests that the electrode is electrochemically stable and can be reused after an experiment. The electrode also demonstrated an insignificant change to DA current response during DA analysis after storage in a refrigerator for up to two weeks.

Concentration study was carried out by investigating the response of EPPGE-MWCNT-Fe_2O_3 electrode to the different concentrations of DA (Figure 7.17) using square wave voltammetry (SWV) experiments at a fixed potential of 0.20 V. From the plot of current response against concentration (not shown), a linear relationship was obtained for concentration range of 6.3 to 25.0 μM. The sensitivity was calculated as 0.026±0.002 $\mu A\mu M^{-1}$, while the limit of detection (LoD = 3.3 s/m) was (3.3±0.28) x 10^{-7} M. The limit of detection obtained in this study agreed closely with the 0.36 μM reported for EPPGE-SWCNT-Fe_2O_3 using same technique but much lower, or at about the same magnitude with values reported in literature for DA electro-oxidation [24,26,29,39-43]. The catalytic rate constant (*k*) for the oxidation of DA at the EPPGE-SWCNT-Fe_2O_3 electrode was estimated using chronoamperomatric technique and a known relationship [29,30,44]. From the slope of the plots of I_{cat}/I_{buff} vs. $t^{1/2}$ at different DA concentrations (not shown), the *k* value was estimated as (16.4±1.48) x 10^5 $cm^3mol^{-1}s^{-1}$.

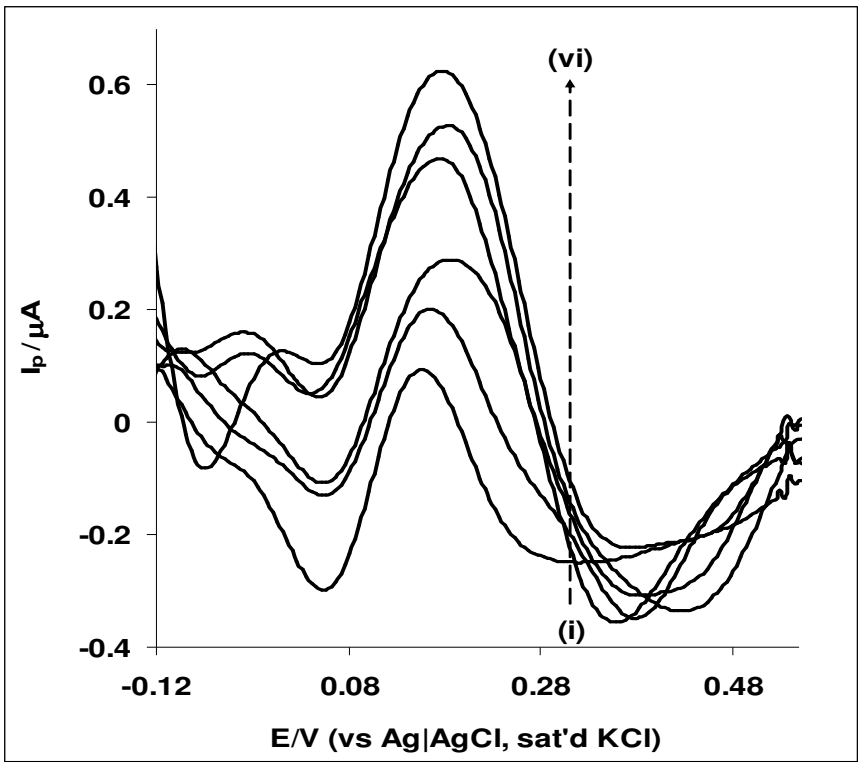

Figure 7.17: Square wave voltammetric evolutions of the EPPGE-MWCNT-Fe_2O_3 in 0.1 M PBS pH 7.0 containing different concentration of DA (6.25, 11.8, 14.7, 21.1, 23.1 and 27.0 µM).

The *k* value is greater compared with 4.67 x 10^5 cm^3 $mol^{-1}s^{-1}$ reported for DA on aluminium electrode modified with palladium hexacyanoferate (PdHCF) films [32] and 3.1 x 10^5 $cm^3mol^{-1}s^{-1}$ on aluminium electrode modified with nickel pentacyanonitrosylferrate (NiPCNF) film [33]. The diffusion coefficient *D* for DA at the electrode was estimated from Equation 7.5 above. The diffusion coefficient *D* for DA was calculated as (8.4±0.67) x 10^{-5} cm^2s^{-1}. The *D* value is a magnitude higher than the 2.5 x 10^{-6} cm^2s^{-1} reported for DA on aluminium electrode modified with palladium hexacyanoferate (PdHCF) films [32], and 3.4 x 10^{-6} cm^2s^{-1} for DA on aluminium electrode modified with nickel pentacyanonitrosylferrate (NiPCNF)

film [33]. The difference in *K* and *D* reported for the electrodes is due to their different surface electroactive materials.

Figure 7.18 shows the square wave voltammetric responses of AA in the absence (1 mM AA alone) (i), and mixture of (ii) 4.76 μM DA and 0.95 mM AA, (iii) 9.09 μM DA and 0.91 mM AA, (iv) 13.04 μM DA and 0.87 mM AA, (v) 20.0 μM DA and 0.8 mM AA, (vi) 25.93 μM DA and 0.74 mM AA and (vii) 28.57 μM DA and 0.71 mM AA in PBS pH 7.0 at the EPPGE-MWCNT-Fe_2O_3 electrode. In the presence of DA, AA signal was seen at about 0.18 V and DA at around 0.37 V on the electrode, which is contrary to AA and DA position observed at *ca* 0.1 and 0.2 V respectively on EPPGE-SWCNT-Fe_2O_3 electrode made by electrodeposition. Cao et al. [45] also observed AA and DA signal at 0.14 and 0.43 V respectively on CPB/chitosan composite films modified glassy carbon electrode. In this study, the potential difference of 190 mV between the two analytes is large enough for the determination of one in the presence of the other. However, the electrode appeared weak towards AA detection thus enhancing a negative shift (about 170 mV) in DA signal, with increasing DA current as DA concentration increases (ii-vii) while AA peaks disappeared completely. The implication of this result is that, there is no possible fouling effect due to AA oxidation intermediates, and the EPPGE-MWCNT-Fe_2O_3 electrode attracted DA strongly leading to enhanced catalysis and fast electron transport towards DA oxidation.

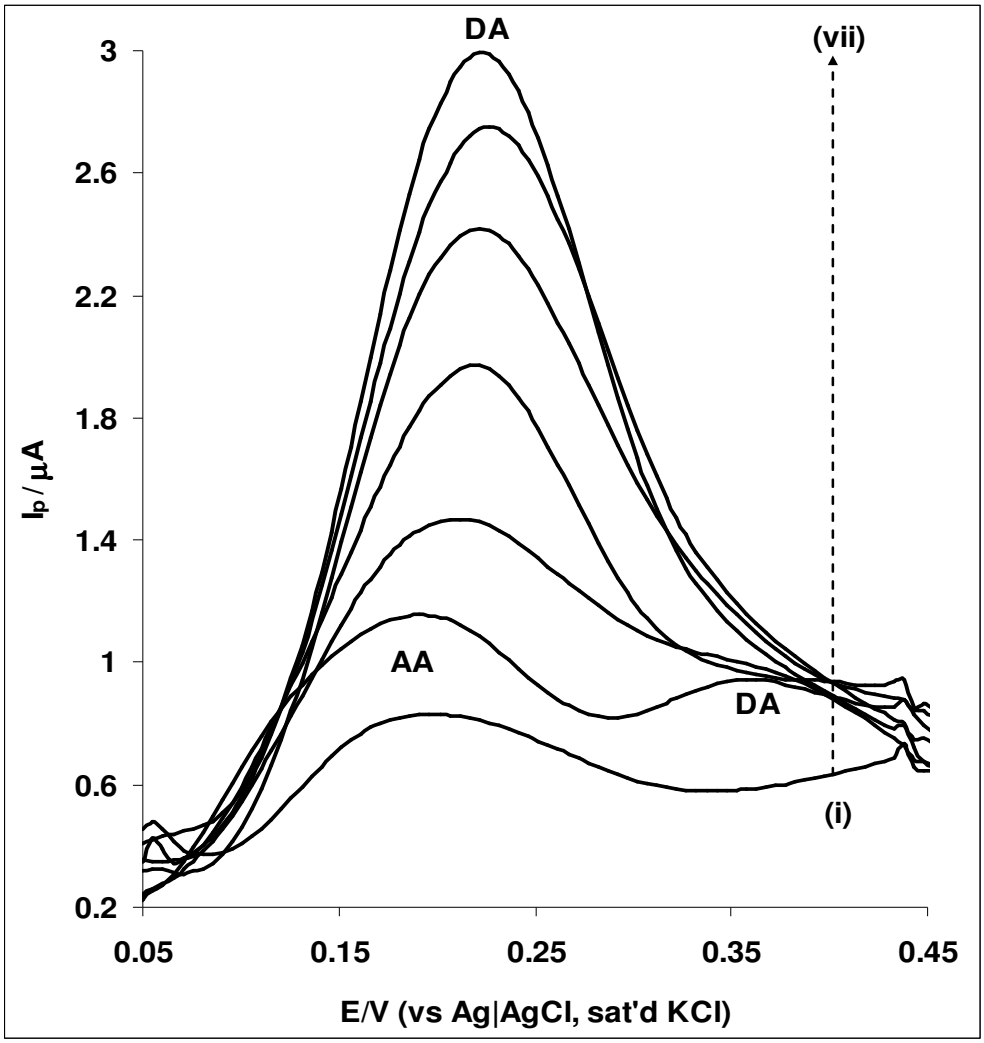

Figure 7.18: Typical square wave voltammograms responses of EPPGE-MWCNT-Fe_2O_3 in (i) 1 mM AA alone, and mixture of (ii) 4.76 µM DA and 0.95 mM AA, (iii) 9.09 µM DA and 0.91 mM AA, (iv) 13.04 µM DA and 0.87 mM AA, (v) 20.0 µM DA and 0.8 mM AA, (vi) 25.93 µM DA and 0.74 mM AA, and (vii) 28.57 µM DA and 0.71 mM AA in PBS pH 7.0.

The potential applicability of the EPPGE-MWCNT-Fe_2O_3 electrode was tested with a square wave voltammetric assay of dopamine present in a dopamine hydrochloride injection (dopamine content of 200 mg / 5 mL or 40 mg / mL). The concentration found in each dopamine drug (Table 7.6) agreed closely with the labelled amount, with average recovery (n=5) of 100.6±2.37% at 95%

confidence limit. The result proves the suitability of the EPPGE-MWCNT-Fe_2O_3 electrode for DA detection in biological samples.

Table 7.6: Determination of dopamine content in dopamine hydrochloride injections (40 mg mL^{-1}), n =5 (at 95% confidence limit) using EPPGE-MWCNT-Fe_2O_3 electrode.

Sample	Concentration found/mg mL^{-1}	Recovery/%
1	40.6 ± 0.52	101.5 ± 1.30
3	39.9 ± 1.01	99.8 ± 2.53
4	39.5± 0.96	98.7 ± 2.38
2	40.9 ± 1.24	102.2 ± 3.09

This study describes the efficient electrocatalytic detection of DA using electrodeposited Fe_2O_3 nanoparticle catalyst supported on a SWCNT-modified edge-plane pyrolytic graphite electrode (EPPGE) platform (EPPGE-SWCNT-Fe_2O_3). The SWCNT-Fe_2O_3 nanoparticles enhanced the electrocatalytic response towards the detection of DA, in terms of peak current compared to other electrodes investigated. Electron transfer properties and electrocatalytic behaviour towards the detection of dopamine using iron oxide nanoparticle (γ-Fe_2O_3) catalysts supported on MWCNTs was also carried out. It was shown that these synthesized γ-Fe_2O_3 nanoparticles exhibit comparable electrocatalytic behaviour with their electrodeposited forms, but uniquely different in terms of the electrochemical properties. From EIS, the pseudo-capacitive nature of the modified EPPGE electrodes is a function of their electrochemical stability towards DA. Analysis of DA at both the EPPGE-SWCNT-Fe_2O_3 and the EPPGE-MWCNT-Fe_2O_3

electrodes showed that DA oxidation proceeded through diffusion and surface controlled electrochemical process. The limit of detection, catalytic rate constant of the electrodes, and the diffusion coefficient of DA agreed favourably with values reported earlier in literature. The modified SWCNT-Fe_2O_3 /MWCNT-Fe_2O_3 electrodes clearly separated DA signal from the interfering effect of AA even at AA concentration which is 50-100 folds that of DA. The electrode had also proven to be a potential sensor for dopamine detection in real drug analysis.

References

1. N. S. McIntyre, M. G. Cook, *Anal. Chem.* 47 (1975) 2208.

2. Sunohara, K. Nishimura, K. Yahikozawa, M. Ueno, M. Enyo, Y. Takasu, *J. Electroanal. Chem.* 354 (1993) 161.

3. M. Aronniemi, J. Sainio, J. Lahtinen, *Appl. Surf. Sci.* 253 (2007) 9476.
4. H. Luo, Z. Shi, N. Li, Z. Gu, Q. Zhuang, *Anal. Chem.* 73 (2001) 915.

5. I.D. Raistrick, D.R. Franceschetti, J.R. Macdonald, In: *Impedance Spectroscopy: Theory Experiment, and Applications*, 2nd ed, E. Barsoukov and J.R. Macdonald (eds.), Wiley, Hoboken, New Jersey, 2005, Chap. 2, pp.27-128.

6. X. Wu, H. Ma, S. Chen, Z. Xu, A. Sui*, J. Electrochem. Soc.* 146 (1999)1847.

7. G. Nurk, H. Kasuk, K. Lust, A.E. Janes, *J. Electroanal. Chem.* 553 (2003) 1.
8. M.E. Orazem, B. Tribollet, *Electrochemical Impedance Spectroscopy*, John Wiley & Sons Inc, Hoboken, NJ., 2008, (ch. 13).

9. A.T. Chidembo, K.I. Ozoemena, B.O. Agboola, V. Gupta, G.G. Wildgoose, R.G. Compton, *Energy Environ. Sci.* 3 (2010) 228.

10. A.J. Bard, L.R. Faulkner, *Electrochemical. Methods: Fundamentals and Applications*, 2nd Ed, John Wiley & Sons, 2001, Hoboken NJ.
11. H.H. Girault, *Analytical and Physical Electrochemistry*, EPFL Press, Lausanne, Switzerland, 2004, (ch. 7).

12. K.I. Ozoemena, D. Nkosi, J. Pillay, *Electrochim. Acta* 53 (2008) 2844.

13. H. R. Zare, N. Nasirizadeh, F. Chatraei, S. Makarem, *Electrochim. Acta* 54 (2009) 2828.
14. L.K. Charkoudian, K.J. Franz, *Inorg. Biochem.* 45 (2006) 3657.

15. M.J. Giz, B. Duong, N.J. Tao, *J. Electroanal. Chem.* 465 (1999) 72.
16. J. Wang, Y. Wang, H. Lv, F. Hui, Y. Ma, S. Lu, Q. Sha, E. Wang, *J. of Electroanal. Chem.* 594 (2006) 59.

17. S. Shahrokhian, S. Bozorgzadeh, *Electrochim. Acta* 51 (2006) 4271.
18. S. Majdi, A. Jabbari, H. Heli, A.A. Moosavi-Movahedi, *Electrochim. Acta* 52 (2007) 4622.

19. H. Yao, Y. Sun, X. Lin, Y. Tang, L. Huang, *Electrochim. Acta* 52 (2007) 6165.
20. S. Jo, H. Jeong, S.R. Bae, S. Jeon, *Microchem. Journ.* 88 (2008) 1.

21. X. Wang, N. Yang, Q. Wan, X. Wang, *Sens. Actuators B Chem.* 128 (2007) 83.

22. G. D. Christian, *Analytical Chemistry*, 6th ed. John Wiley and Sons New York, 2004, p 113.
23. Y. F Zhao, Y. Q. Gao, D. P. Zhan, H. Liu, Q. Zhao, Y. Kou, Y. H. Shao, M. X. Li, Q. K.; Zhuang, Z. W. Zhu, *Talanta* 66 (2005) 51.

24. S. Shahrokhian, H. R. Zare-Mehrjardi, *Sens. Actuators B Chem.* 121 (2007) 530.

25. W. Chen, X. Lin, L. Huang, H. Luo, *Microchim. Acta* 151 (2005) 101.
26. A. Balamurugan, S. Chen, *Anal. Chim. Acta* 596 (2007) 92.

27. Q. Wang, D. Dong, N. Li, *Bioelectrochem.* 54 (2001) 169.

28. T. Selvaraju, R. Ramaraj, *J. Electroanal. Chem.* 585 (2005) 290.

29. M. H. Pournaghi-Azar, R. Sabzi, *J. Electroanal. Chem.* 543 (2003) 115.
30. K. M. Manesh, P. Santosh, A. I. Gopalan, K. P. Lee, Enhanced *Electroanalysis* 18 (2006) 894.

31. H. Razmi, M. Agazadeh, B. Habibi-A, *J. Electroanal. Chem.* 547 (2003) 25.

32. H. Razimi, A. Azadbakht, *Electrochim. Acta* 50 (2005) 2193.

33. M. Mazloum-Ardakani, H. Beitollahi, B. Ganjipour, H. Naeimi, M. Nejati, *Bioelectrochem.* 75 (2009) 1.

34. S. Singh, R. C. Buchanan, SiC-C fiber electrode for biological sensing, *Mat. Sc. Engnr. C.* 27 (2007) 551.

35. Y-P. Sun, X-q. Li, J. Cao, W-x. Zang, H. P. Wang, *Advances in Colloid and Interface Science* 120 (2006) 47.

36. Y-K. Sun, M. Ma, Y. Zhang, N. Gu, *Colloids and Surfaces A: Physicochem.Eng.Aspects* 245 (2004) 15.

37. G. Carja, Y. Kameshima, K. Okada, *Microporous and Mesoporous Materials* 115 (2008) 541.

38. K.L. Double, L. Zecca, P. Costi, M. Mauer, C. Griesinger, S. Ito, D. Ben-shachar, G. Bringmann, R.G. Fariello, P. Riederer, M. Gerlach, *J. Neurochem*. 75 (2000) 2583.

39. B.N. Chandrashekar1, B.E. Kumara Swamy, M. Pandurangachar, S.S Shankar1, O. Gilbert1, J.G. Manjunatha, B.S., Sherigara, *Int. J. Electrochem. Sci.* 5 (2010) 578.

40. S.S Shankar, B.E.K. Swamy, M. Pandurangachar, U. Chandra1, B.N. Chandrashekar, J.G. Manjunatha, B.S. Sherigara, *Int. J. Electrochem. Sci.* 5 (2010) 944.

41. G. Alarco´n-Angeles, B. Pe´rez-Lo´pez, M. Palomar-Pardave, M.T. Ramı´rez-Silva, S. Alegret, A. Merkoci, *Carbon* 46 (2008) 898.

42. M. Pandurangachar1, B.E.K. Swamy, B.N. Chandrashekar, O. Gilbert, S. Reddy, B.S. Sherigara, *Int. J. Electrochem. Sci.* 5 (2010) 1187.

43. M.T. Shreenivas1, B.E.K. Swamy, U. Chandra, S.S. Shankar, J.G. Manjunatha, B.S. Sherigara, *Int. J. Electrochem. Sci.* 5 (2010) 774.

44. Z. Galus, Fundamentals of Electrochemical Analysis, Ellis Horwood Press, New York, 1976, p. 313, Ch. 10.

45. X. Cao, L. Luo, Y. Ding, X. Zou, R. Bian, *Sens. Actuat. B Chem.* 129 (2008) 941.

CHAPTER EIGHT

Electrocatalytic Properties of Prussian Blue Nanoparticles Supported on Poly(m-Aminobenzenesulfonic Acid) – Funtionalized Single-Walled Carbon Nanotubes Towards the Detection of Dopamine*

* The publication below resulted from part of the research work presented in this chapter and it is not referenced further in this thesis:

9. **Abolanle S. Adekunle**, Jeseelan Pillay, Kenneth I. Ozoemena, (Submitted)

8.1 Comparative TEM and AFM images and UV-vis spectra

Figure 8.1 showed the transmission electron (TEM) micrographs and size distributions for the PB (a) and the SWCNT-PB (b) nanocomposite material. The PB nanoparticles appear a little amorphous and distribute uniformly across the SWCNT-PABS due to the strong electrostatic interaction between the functionalised SWCNT-PABS and the PB nanoparticles. There is an electrostatic interaction between the hydrophilic ends (SO_3^{2-}) of the SWCNT-PABS and the Fe^{3+} cations from $FeCl_3$ which eventually leads to the permeation and adsorption of the Fe^{3+} ions into the interlayer of the SWCNT-PABS. XPS study had also shown that Fe^{3+} was successfully adsorbed on the surface of MWCNTs [1] The adsorbed Fe^{3+} reacts with the $[Fe(CN)_6]^{4-}$ anion from $K_4[Fe(CN)_6]$ forming non-stoichiometric deposits of $Fe_x[Fe(CN)_6]_y$ on the interlayer of the SWCNT-PABS. Since the precipitation is non-stoichiometric, there are more active sites of C=N groups with which more Fe^{3+} ions can react for further PB deposition from several deposition cycles. For the GC-PB, the mechanism may be described as a physical adsorption of the Fe^{3+} on the electrode which later react with the Fe^{2+} from $[Fe(CN)_6]^{4-}$ to form PB nanoparticles. The PB nanoparticle sizes are in the 50 – 500 nm range. The particle sizes are much lower as obtained from the AFM analysis.

The AFM results (Figure 8.1c and 8.1d) clearly showed the successful deposition of PB nano particles on the GC plate. The topographic image of the GC-SWCNT-PB gave a particle size dimension in the nano range of about 90 nm (Figure 8.1c) while the cross-sectional size diameter is in the range of 11-18 nm compared with the bare-GC and the GC-SWCNT-PABS (not shown) with particle size diameters of about 2 and 10 nm respectively, indicating

successful deposition of PB nanoparticles. GC plate was used as substitute for EPPGE in obtaining this result since it fits conveniently into the equipment.

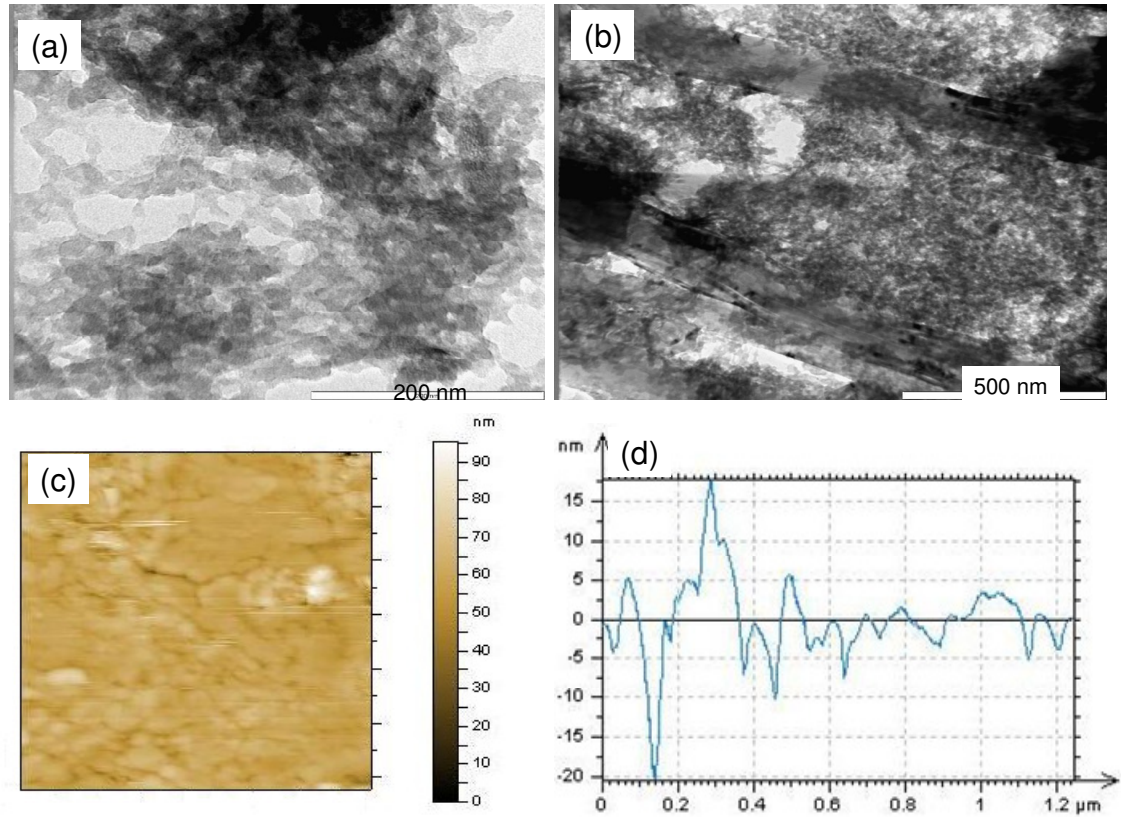

Figure 8.1: Typical TEM images of (a) PB and (b) SWCNT-PB nanoparticles. (c) and (d) are the AFM topography image and the cross section of the SWCNT-PB showing the particle size distribution in nano dimensions.

8.1.1. UV-vis-absorption spectroscopy characterization of the SWCNT-PABS, PB and the SWCNT-PB nanoparticles.

UV-vis absorption spectroscopy experiment was performed to further prove the deposition of PB on the SWCNT-PABS. The thin solid PB film deposited on the electrode was washed with distilled water and made into solution for UV-vis analysis. Figure 8.2

compares the UV-vis spectra of the PB, SWCNT-PABS and the SWCNT-PB film formed on the electrode after deposition. The SWCNT-PABS have a characteristic absorption band at about 243 nm which is lower than the 260 nm reported by Wang et al. [2] and described previously by authors as the characteristic of the adsorption of the assembled CNTs [3]. The difference can be attributed to the smooth and the pure nature of the SWCNT-PABS, with the absence of other light absorbing groups that may lead to an increase absorption band. The PB have a characteristic absorption band at around 667 nm, corresponding to the mixed-valence charge-transfer absorbance of the [Fe(II)-C-N-Fe(III)] complex. This result agreed with literature values [1,2]. The absorption bands at 243 nm for the SWCNT-PABS disappeared after the deposition of PB nanoparticles on the SWCNT-PABS to give SWCNT-PB nanoparticles indicating successful transformation of the SWCNT-PABS to SWCNT-PB.

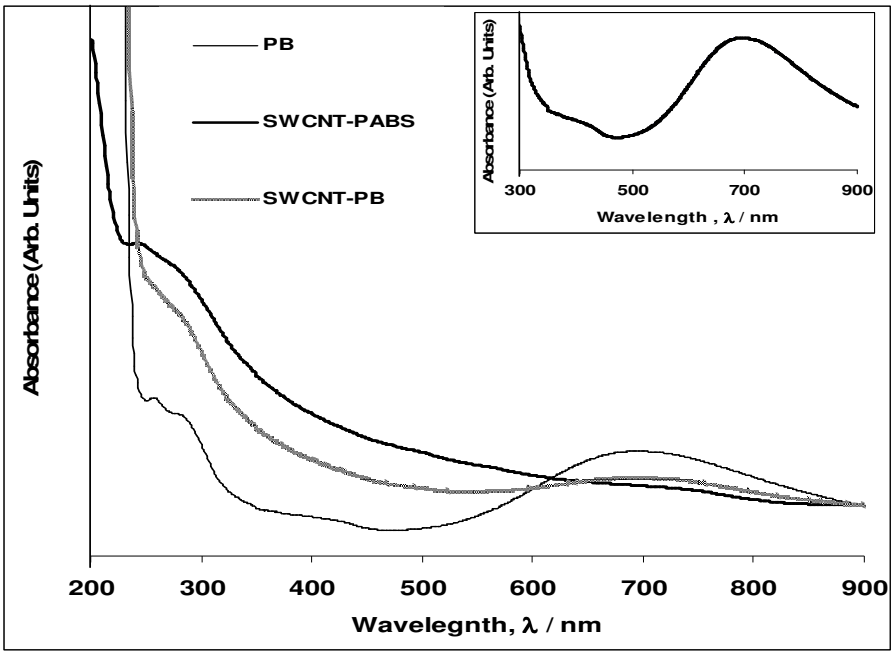

Figure 8.2: UV/VIS spectra of Prussian blue (PB), SWCNT-PABS and SWCNT-PB.

8.2. Cyclic voltammetric characterisation of the electrodes.

Figure 8.3a represents the cyclic voltammograms obtained for the EPPGE (i), EPPGE-SWCNTPABS (ii), and EPPGE-SWCNTPABS-PB (iii) in pH 7.0 PBS containing 0.1 M KCl (scan rate: 25 mVs^{-1}). The broad redox couple at around 0.5 – 0.8 V prominent at the bare EPPGE and SWCNTPABS is related to the redox processes arising from the oxo-containing species existing at the edge plane sites of these species. Unlike the bare EPPGE and EPPGE-SWCNTPABS, the EPPGE-SWCNTPABS-PB showed well defined redox peaks: anodic peak at 0.25 V due to PB, reduction peak at 0.1 V due to the Prussian white (PW), and a very weak anodic peak at ~0.9 V due to the Prussian yellow (PY) [4]. These signature peaks confirm the successful integration of the PB onto the SWCNTPABS structure. These characteristic peaks of the PB were best observed when higher concentration of the PB (i.e., EPPGE-SWCNTPABS-3PB) is integrated onto the SWCNTPABS (see Figure 8.3b). As evident in Figure 8.3b, the EPPGE-SWCNT-3PB film showed little or no drop in current density when the electrode was subjected to continuous cycling (50 scans) in the electrolyte, which is a clear indication of excellent electrochemical stability. In addition, the broad peak at around 0.5-0.8 V (of the oxo-containing species) disappeared, suggesting the replacement or covering of these oxo-species with the PB nanoparticles. The different redox processes observed at the PB modified electrodes can be summarised by the Equations (8.1 and 8.2) below [4]:

$$KFe(III)[Fe(II)(CN)_6] - e^- - K^+ \longrightarrow Fe(III)[Fe(III)(CN)_6] \quad (8.1)$$

PB PY

$$KFe(III)[Fe(II)(CN)_6] + e^- + K^+ \longrightarrow K_2Fe(II)[Fe(II)(CN)_6] \quad (8.2)$$

PB PW)

The surface coverage of the electroactive PB films (Γ_{PB}) on the EPPGE-SWCNT-3PB electrode was estimated using Equation 8.3 below:[5]

$$\Gamma_{PB} = \frac{Q}{nFA} \quad (8.3)$$

where *Q* is the quantity of charge obtained by integration of the area under the anodic PB peak, *n* is number of electron transfer during the process, *F* is the Faraday constant, and *A* is the geometric area of the working electrode. The Γ_{PB} is approximately 4.8 x 10^{-8} mol cm^{-2}.

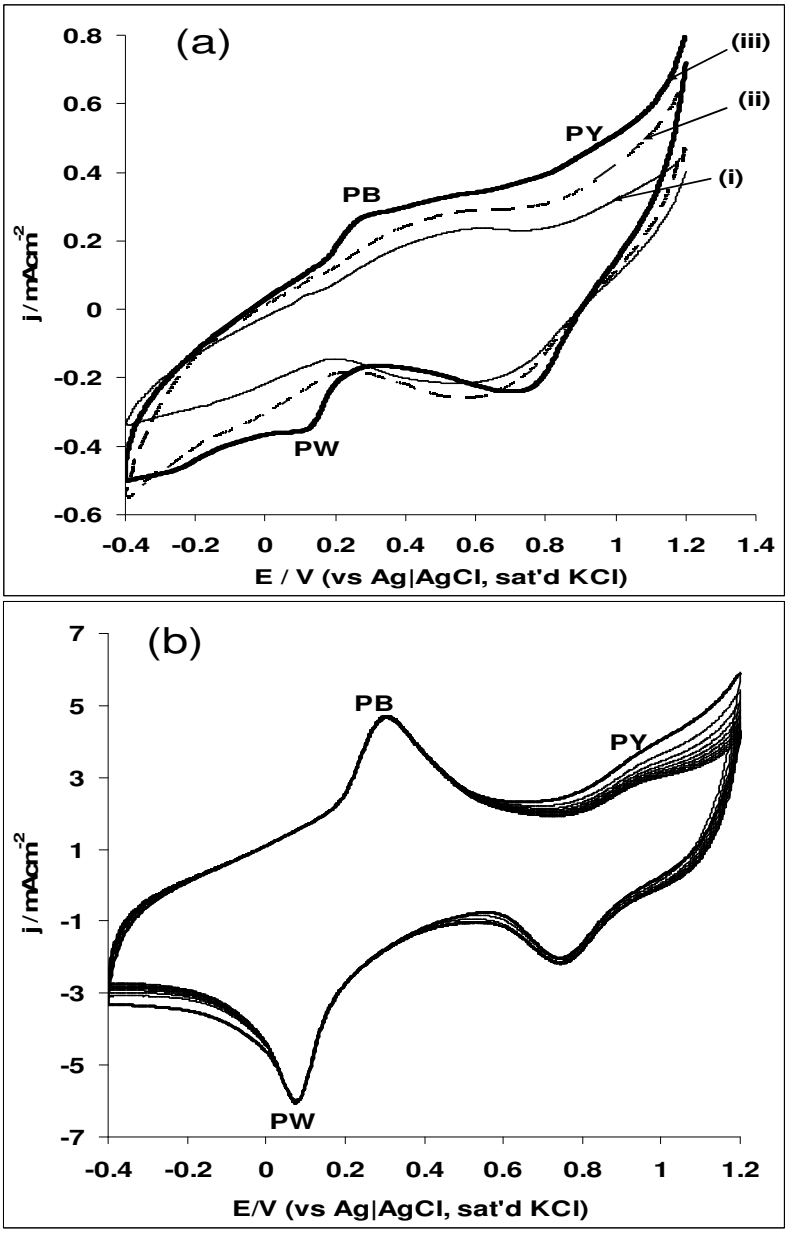

Figure 8.3: Typical cyclic voltammograms of (a) EPPGE (i), EPPGE-SWCNT-PABS (ii) and EPPGE-SWCNT-PB (iii) in 0.1 M KCl electrolyte (scan rate: 25 mVs^{-1}). (b) is the cyclic voltammogram showing the electrochemical stability of EPPGE–SWCNT-3PB modified electrode (50 cycles) in pH 7.0 PBS containing 0.1 M KCl electrolytes (scan rate: 100 mVs^{-1}).

8.3. Electrocatalytic oxidation of dopamine

Figure 8.4a compares the cyclic voltammograms (after background current subtraction) of the electrodes in pH 7.0 PBS containing $2x10^{-4}$ M dopamine. The current density follows the order: EPPGE-SWCNTPABS-PB (~ 617.0 μAcm^{-2}) > EPPGE-SWCNTPABS (~ 301.0 μAcm^{-2}) > bare-EPPGE (~ 124.0 μAcm^{-2}) > EPPGE-PB (~ 140.0 μAcm^{-2}). In addition, DA catalysis was much favoured at EPPGE-SWCNTPABS-PB in terms of low onset (~0.04 V) as well as anodic peak potential (E_{pa} ≈ 0.279 V) compared to other electrodes that show higher values. Similar experiment was performed using CTAB/SWCNTPABS-PB electrodes where CTAB acts as PB stabilizer on the electrode. Contrary to expectation, the CTAB modified electrodes gave poor DA response compared with electrode without CTAB. EPPGE-SWCNTPABS-PB was identified as the best electrode for DA oxidation in this study, thus all subsequent studies were carried out with this electrode unless otherwise stated.

Next, the impact of different PB layers/concentrations as well as the concentrations of the $FeCl_3$ and $K_4[Fe(CN)_6]$ in the deposition solution on the electro-oxidation of DA (Figure 8.4b) was investigated. Three concentrations of $FeCl_3$ and $K_4[Fe(CN)_6]$ solutions (10^{-4}, 10^{-3} and 10^{-2} M) were used. Using the 10^{-4} M deposition solution, it was observed that as the PB layers increase the current response of the DA oxidation follow increases: 295.0 μAcm^{-2} (SWCNTPABS-3PB) > 257.0 μA (SWCNTPABS-2PB) > 146.0 μAcm^{-2} (SWCNTPABS-PB) (Figure 7.5b). Interestingly, using the different deposition solutions (10^{-4}, 10^{-3} and 10^{-2} M) to obtain the SWCNTPABS-3PB, the current rersponse for the DA remained essentially the same (295.0 μAcm^{-2}). This result suggests that at high concentration, the PB nanoparticles may form an insulating

layer thereby lowering DA catalysis. Han et al. [1] also observed similar situation and concluded that the low concentration of the deposition solution of PB would be preferred. Thus, it seems very reasonable and economical using low concentration (10^{-4} M) of $FeCl_3$ and $K_4[Fe(CN)_6]$ for the electrode modification with PB nanoparticles.

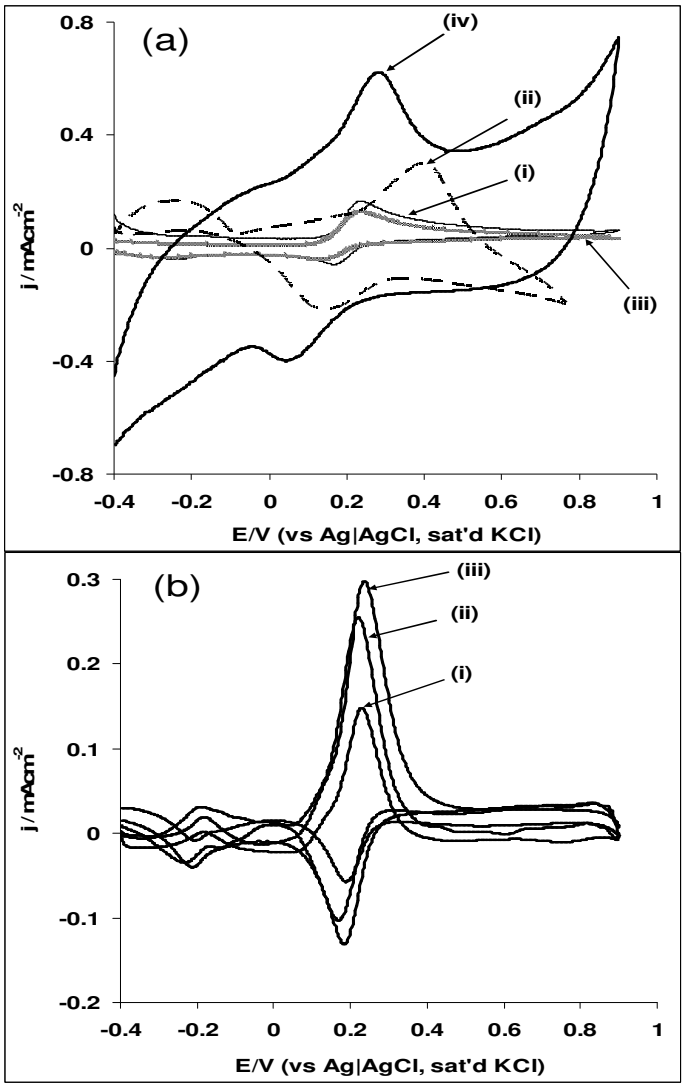

Figure 8.4: Cyclic voltammograms showing the current responses (background subtracted) of (a) (i) bare EPPGE, (ii) EPPGE-SWCNT-PABS, (iii) EPPGE-PB and (iv) EPPGE-SWCNT-PB in 0.1 M pH 7.0 PBS containing 2 x10^{-4} M DA (scan rate: 25 mVs^{-1}). (b) (i) EPPGE-SWCNT-PB, (ii) EPPGE-SWCNT-2PB and (iii) EPPGE-SWCNT-3PB in 0.1 M pH 7.0 PBS containing 2 x10^{-4} M DA (scan rate: 25 mVs^{-1}).

To examine the electron transfer behaviour of the three electrodes towards the oxidation of DA, electrochemical impedance spectroscopy (EIS) experiment was conducted in 2 x 10^{-4} M DA solution at the EPPEGE-SWCNTPABS-PB, EPPGE-SWCNTPABS-2PB and EPPGE-SWCNTPABS-3PB at a fixed potential of 0.2 V vs Ag|AgCl, sat'd KCl (Figure 8.5a). Figure 8.5a presents the Nyquist plots obtained and the circuit (inset) used to fit the spectra. The data obtained from the fittings are presented in Table 8.1, clearly showing satisfactory fitting as judged by the low chi-square function (χ^2) and relative errors. From Table 8.1, EPPGE-SWCNT-3PB electrode has the fastest electron transport. The R_{ct} values followed the order: EPPGE-SWCNTPABS-3PB (3.95 Ωcm^2) < EPPGE-SWCNTPABS-2PB (5.01 Ωcm^2) < EPPGE-SWCNTPABS-PB (5.33 Ωcm^2), indicating faster electron transfer towards DA electrocatalysis at the EPPGE-SWCNTPABS-3PB.

Bode plot of –phase angle vs. log (f/Hz) obtained for the different PB layers (Figure 8.5b) gave phase angles less than -90° expected for an ideal capacitive behaviour. Also, the *n* values obtained (Table 8.1) are < 1.0, indicating the pseudocapacitive nature of the electrodes at every PB layer. Presently, there is little information on the electrochemical impedance study on DA oxidation.

Table 8.1: Impedance data obtained for the EPPGE-SWCNT-PB modified electrodes (at different deposition cycles) in 0.1M pH 7.0 PBS containing 2 x 10^{-4} M DA ($E_{1/2}$ = 0.2 V vs Ag|AgCl sat'd KCl).

EPPGE modifier	**Electrochemical Impedance Parameters**					
	R_s /Ωcm^2	**10^3 CPE/Fcm^{-2}**	**N**	**R_{ct} /Ωcm^2**	**10^3 Z_W/Ωcm^2**	**10^4 χ^2**
SWCNTPABS-PB	21.87±0.01	7.70±0.02	0.86±0.01	5.33±0.02	0.18±0.01	0.20
SWCNTPABS-2PB	19.66±0.01	7.10±0.04	0.87±0.01	5.01±0.04	0.15±0.01	2.37
SWCNTPABS-3PB	18.31±0.01	7.20±0.03	0.87±0.01	3.95±0.02	0.14±0.01	1.05

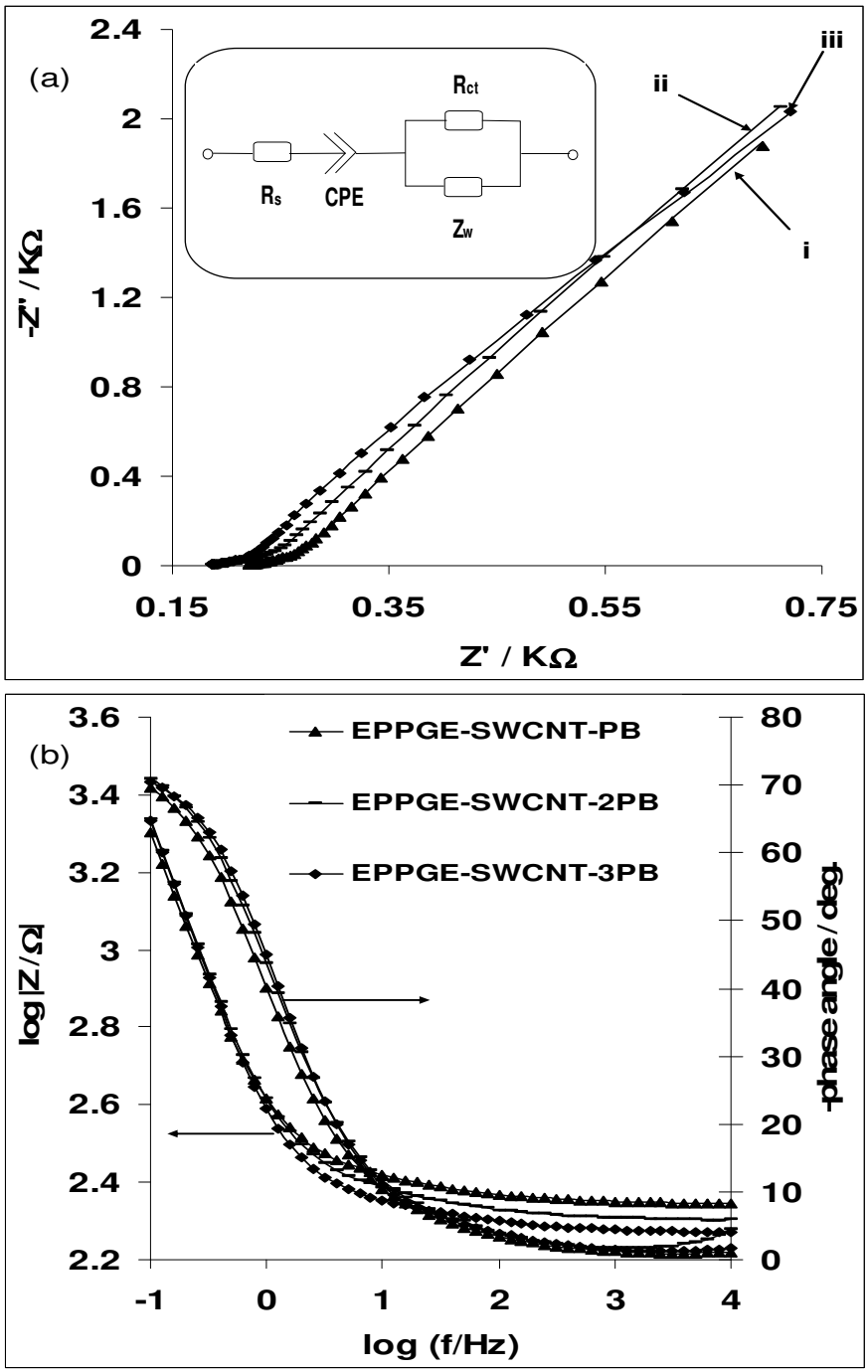

Figure 8.5: (a) Typical Nyquist plots obtained for (i) EPPGE-SWCNT-PB, (ii) EPPGE-SWCNT-2PB and (iii) EPPGE-SWCNT-3PB in 0.1 M pH 7.0 PBS containing 2 x10^{-4} M DA. (b) is the Bodes plot of –phase angle versus logf, and log |Z/Ω| versus logf for the electrodes in (a) above.

8.4. Effect of varying scan rate

The effect of scan rate (25 to 1000 mVs^{-1}) on the electrode kinetics during dopamine oxidation was investigated using the best electrode, EPPGE-SWCNTPABS-3PB. A pair of well-defined redox peaks, with equal peak current heights at all scan rates, was observed (Figure 8.6a). The peak-to-peak separation (ΔE_p) increase from 76 mV at 25 mVs^{-1} to 654 mV at 1000 mVs^{-1}. Deviation of ΔE_p from the ideal 59.8 mV value expected for a one-electron reversible process is indicative of weak electron transfer as the scan rate is increased. The plot of the anodic (I_{pa}) peak current against square root of scan rate ($\nu^{1/2}$) is linear (Figure 8.6b), indicative of diffusion-controlled reaction.

Further, the catalytic reaction kinetic using the RDE technique was explored. Figure 8.6c represents the RDE voltammograms obtained at different rotating speed (ω) for 2 x 10^{-4} M DA electro-oxidation in PBS pH 7.0 using at the EPPGE-SWCNT-3PB. Figure 8.6d is the plot of I_{lim}^{-1} versus $\omega^{-1/2}$ employing the Koutecky-Levich equation below:

$$\frac{1}{i_{\lim}} = \frac{1}{i_k} + \frac{1}{i_{lev}} = \frac{1}{(nFAk_{ch}\Gamma C)} + \frac{1}{(0.620nFAcD^{2/3}\gamma^{-1/6}\omega^{1/2})} \qquad (8.4)$$

where i_{lim}, i_k, i_{lev} are the measured current, kinetic and diffusion-limited currents, respectively, n is the number of electrons transferred which is 2 for DA electrooxidation, k_{ch} is the catalytic rate constant ($mol^{-1}cm^3\ s^{-1}$), F is the Faraday constant (96485 C mol^{-1}), A is the electrode surface area (0.196 cm^2), ω is the rotating speed (rpm), Γ ($molcm^{-2}$) is the redox active species (4.78 x 10^{-8} mol cm^{-2}) concentration on electrode surface, c is the bulk concentration of DA

(2×10^{-7} molcm^{-3}), *D* is the diffusion coefficient (cm^{2}s^{-1}) of DA and γ is the kinematic viscosity of the solution.

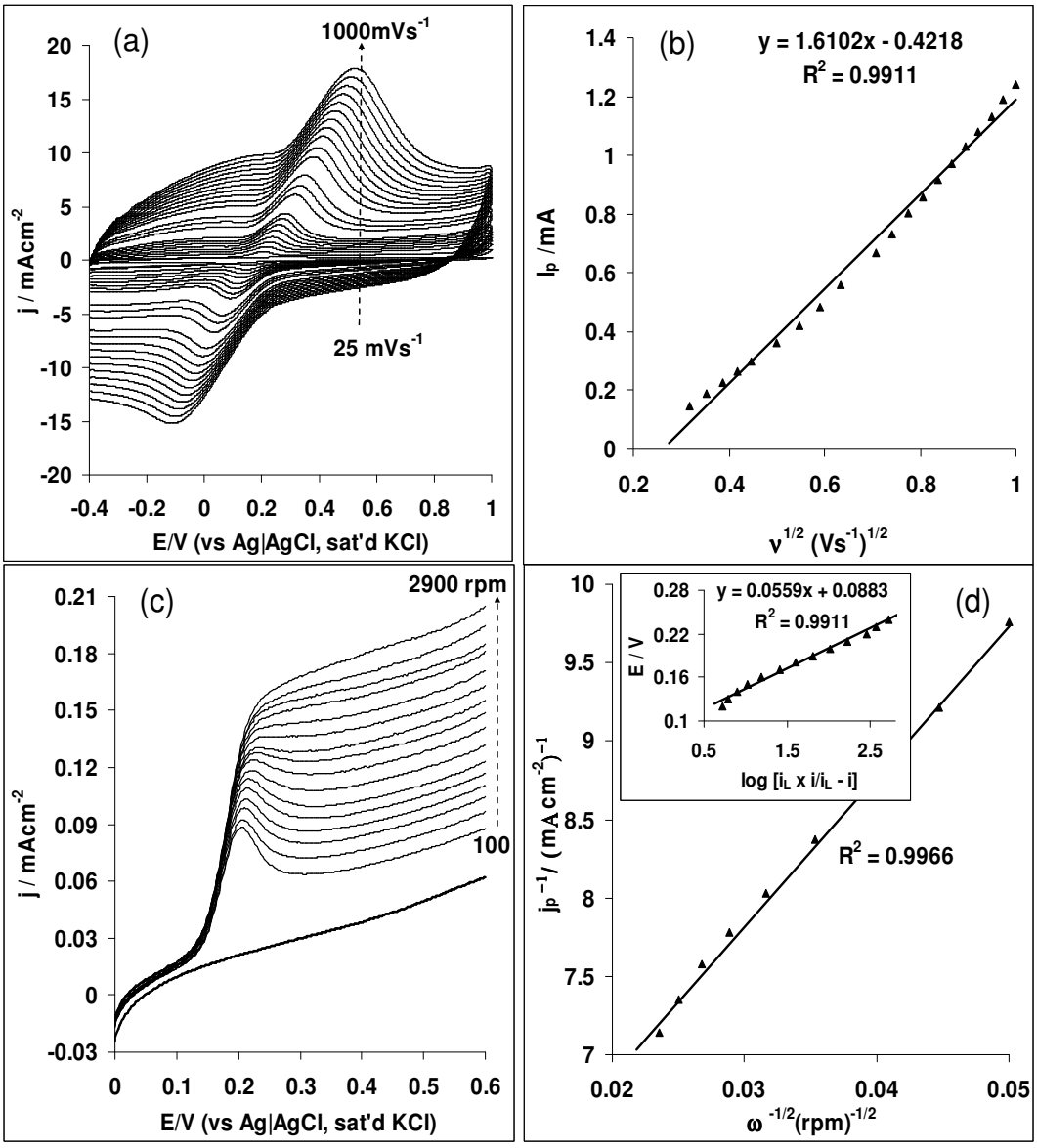

Figure 8.6: (a) Cyclic voltammogram showing the current response of EPPGE-SWCNT-3PB electrodes in 0.1 M PBS solution containing 2×10^{-4} M DA, (b) plot of I_p vs $\nu^{1/2}$ (c) a RDE voltammograms obtained for the EPPGE-SWCNT-3PB in 0.1 M PBS solution containing 2×10^{-4} M DA, (d) is the plot of I_p^{-1} vs. $\omega^{-1/2}$. Inset in (d) is the plot of E/V versus log [i x i_L/i_L – i].

The plot is linear with positive intercept, indicating that the electrode reactions are controlled by both kinetics at the electrode surface and the mass transport of DA species. The k_{ch} value obtained from the intercepts of the regression lines was found to be (1.69±0.13)x 10^5 $mol^{-1}cm^3s^{-1}$ (1.69 x 10^2 M^{-1} s^{-1}) which agreed closely with the range of 3.3 x 10^2 to 2.9 x 10^2 M^{-1} s^{-1} for the DA concentration range (5 - 7.5 mM), reported for aluminium electrode modified with nickel pentacyanonitrosylferrate films (NiPCNF/Al) [6]. The difference in the k_{ch} value is due to the catalytic interaction of DA with the different electrode modifier. Correcting the polarization curve for diffusion effects for first order reaction, the Tafel equation may be simplified as Equation 8.5: [7-9].

$$E_{app} = E_{eq} + b \log I_K \tag{8.5}$$

$$I_K = \frac{(i_L . i)}{(i_L - i)} \tag{8.6}$$

$$b = \frac{2.303RT}{\alpha n_\alpha F} \tag{8.7}$$

where E_{app} is the applied potential, E_{eq} is the equilibrium potential, I_k is the kinetic current, i_L is the limiting current (plateau in RDE voltammogram), i is the measured current at a given potential, R, T and F have their usual meaning, αn is the kinetic parameters for the electrode process. At 2500 rpm, the plot of E_{app} versus log I_k (inset in Figure 8.6d) gave Tafel slope of ~ 56 $mVdec^{-1}$ was obtained. The value is closer to the 60 $mVdec^{-1}$ for a fast, one-electron transfer process, followed by a chemical step. An α value close to 1.0 suggest high probability of product formation, meaning an enhanced electrocatalysis [10]. Based on the results, the following reaction

mechanism may be proposed for the electrocatalytic oxidation of DA at the EPPGE-SWCNTPABS-3PB:

$$\text{SWCNT-PABS/Fe}^{3+}\text{/Fe}^{2+} \longrightarrow \text{SWCNT-PABS/Fe}^{3+}\text{/Fe}^{3+} \quad (8.8)$$

$$\text{SWCNT-PABS/Fe}^{3+}\text{/Fe}^{3+} + \text{DA}^{+} \longrightarrow \text{SWCNT-PABS/Fe}^{3+}\text{/Fe}^{3+}\text{-------}\ \text{DA}^{+} \quad (8.9)$$

$$\text{SWCNT-PABS/Fe}^{3+}\text{/Fe}^{3+}\text{--------}\ \text{DA}^{+} \longrightarrow \text{SWCNT-PABS/Fe}^{3+}\text{/Fe}^{2+} + \text{QDA}^{+} \quad (8.10)$$

Slow (rate determining step)

$$\text{SWCNT-PABS/Fe}^{3+}\text{/Fe}^{3+} + e^{-} \longrightarrow \text{SWCNT-PABS/Fe}^{3+}\text{/Fe}^{2+} \quad (8.11)$$

At pH 7, DA (p*Ka* 8.9) exists as a cation with a positively charged amino group [11]. Equation 8.8 represents the catalyst redox pre-equilibrium reaction which shows the electrochemically driven oxidation of the Fe ions in SWCNT-PAB-SO_3^{2-}/$Fe^{3+/}Fe^{2+}$ to SWCNT-PAB-SO_3^{2-}/$Fe^{3+/}Fe^{3+}$. Thereafter, the oxidized catalyst form an adduct with DA. This represents the rate (slow) determining step (rds) (Equation 8.9). Finally, chemical redox process involving oxidation of DA to Dopamine-O-quinone (QDA^{+}) through a two-electron oxidation process occurs (Equation 8.10) and simultaneously, reduction of the oxidized catalyst to the original form takes place. The catalyst is regenerated by the reduction process as represented in Equation 8.11.

8.5. Electroanalysis using square wave voltammetry (SWV), chronoamperometric (CA) and Linear Sweep Voltammetry (LSV).

Concentration study was carried out using different techniques at a fixed potential of 0.20 V exemplified with square wave voltammograms (Figure 8.7a) and the linear sweep voltammogram

(Figure 8.7b). From the plots of current response against concentration, linear relationships (Equations 8.12-8.14) were obtained as:

CA: I_p/μA =(0.16±0.01)[DA]/μM + (3.20±0.01) (R^2 = 0.9999) (8.12)

SWV: I_p/μA =(0.48±0.04)[DA]/μM + (207.25±0.14) (R^2 =0.9996) (8.13)

LSV: I_p/μA = (0.65±0.07) [DA] / μM + (27.78±0.39) (R^2 = 0.9993) (8.14)

The limit of detection (LoD = 3.3 s/m [12]) for the different techniques employed in this study and the linear concentration range are presented in Table 8.2. The analytical values obtained compared favourably and even better than other values reported earlier in the literature for some modified electrodes towards DA detection [13-19]. The re-usability and stability of the EPPGE-SWCNTPABS-3PB were also examined. First, the electrode was repeatedly cycled (50 runs) in pH 7.0 PBS containing 2 x 10^{-4} M DA (not shown). The current decreased from the first scan until about the 30th scan where it then stabilised. However, upon rinsing the electrode in a fresh electrolyte solution and the analysis repeated, about 85% of the initial current height of the DA was obtained, meaning the electrode can be reused after analysis. Similarly, after storage for two weeks in a refrigerator, no significant change in DA current was observed which indicates the electrode stability towards the analyte.

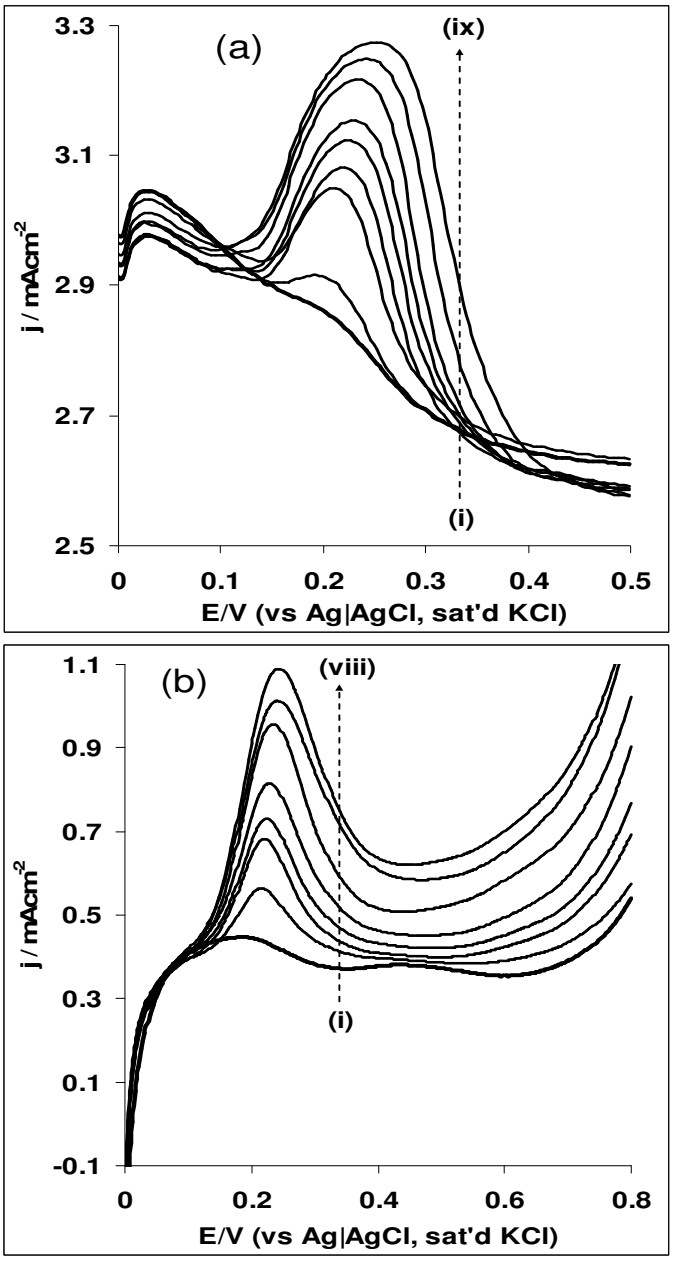

Figure 8.7: (a) Square wave voltammograms evolution of the EPPGE-SWCNT-3PB in 0.1 M PBS solution containing different concentrations of DA (0.0, 6.5, 12.5, 18.2, 23.5, 28.6, 33.3, 42.1 and 50.0 μM (inner to outer; i – ix). (b) Linear sweep voltammogram responses of the EPPGE-SWCNT-3PB in 0.1 M PBS solution containing different concentrations of DA (0.00, 18.2, 28.6, 37.8, 50, 60.5, 66.7, 72.3 μM (inner to outer; i – viii).

Table 8.2: Voltammetric response for dopamine using various modified electrodes.

Electrode	Electrolyte	Method	LCR range (μM)	LoD (μM)	References
EPPGE-SWCNTPABS-3PB	PBS (pH 7.0)	CA	2.4 – 23.1	0.21±0.02	This work
EPPGE-SWCNTPABS-3PB	PBS (pH 7.0)	SWV	6.5 – 50.0	0.92±0.07	This work
EPPGE-SWCNTPABS-3PB	PBS (pH 7.0)	LSV	3.2 – 31.8	1.98±0.16	This work
EPPGE-SWCNT-Fe_2O_3	PBS (pH 7.0)	SWV	0.0 – 31.8	0.36	13
CNT/graphite electrode	PBS (pH 5.0)	DPV	0.5 – 10.0	0.10	14
SDS/MWNTs	PBS (pH 7.4)	DPV	20 – 200.0	3.75	15
CPE-Cobalt salophen	ACS (pH 5.0)	DPV	1.0 – 100.0	0.50	16
PVA modified GCE	PBS (pH 7.0)	DPV	2.0 – 70.0	1.40	17
GCE-PEDOT-PANS	ACS (pH 5.0)	LSV	2.0 – 8.0	0.50	18
GCE/MWCNT-βCD	PBS (pH 7.4)	CR	10.0 – 80.0	6.7	19

SDS: Sodium dodecyl sulfate; **PVA:** Poly(vinyl alcohol); **GCE:** Glassy carbon electrode; **CNT:** Carbon nanotubes; **βCD:** β-cyclodextrin; **CA:** Chronoamperometric; **SWV:** Square wave voltammetry; **DPV:** Differential pulse voltammetry; **LSV:** Linear sweep voltammetry; **PEDOT:**Poly (3,4-ethylenedioxythiophene-co-(5-amino-2-naphthalenesulfonic acid)); **PANS:** Poly 5-amino-2-naphthalenesulfonic acid; **SAM:** Self-assembled monolayer; **PBS:** Phosphate buffer solution; **ACS:** Acetate buffer solution; **LCR:** Linear concentration range; **LoD:** Limit of detection.

8.6. Detection of DA in the presence of AA: Interference study

Figure 8.8 is the cyclic voltammetric responses of EPPGE-SWCNT-3PB electrode in (i) 0.1 M pH 7.0 PBS, (ii) 10 mM AA alone, and mixture of (iii) 9.1 μM DA and 9.1 mM AA, (iv) 16.7 μM DA and 8.3 mM AA, (v) 23.1 μM DA and 7.7 mM AA, (vi) 28.6 μM DA and 7.1 mM AA, (vii) 33.3 μM DA and 6.7 mM AA and (viii) 41.2 μM DA and 5.9 mM AA in PBS pH 7.0. The AA signal which was initially observed at around 0.0 V in the absence of DA remains same after the addition of DA, while the DA signal occurred at around 0.2 V. The results showed that for all the concentrations of the DA studied there was no detectable interference of the AA. Infact, it is interesting to know that DA could be simultaneously detected even at high AA concentration (9.1 mM), which is 1000 times that of DA (9.1 μM), and a potential separation of about 200 mV. The height and amplitude of the peak corresponding to DA also increase proportionally with the DA concentration. On the other hand, at the bare EPPGE (not shown) the AA peaks completely interfere and suppressed the DA signal at around 0.2 V. Indeed, this result is unique when compared to a recent work with Fe_2O_3 nanoparticle that did not allow for the simultaneous detection of DA and AA [13].

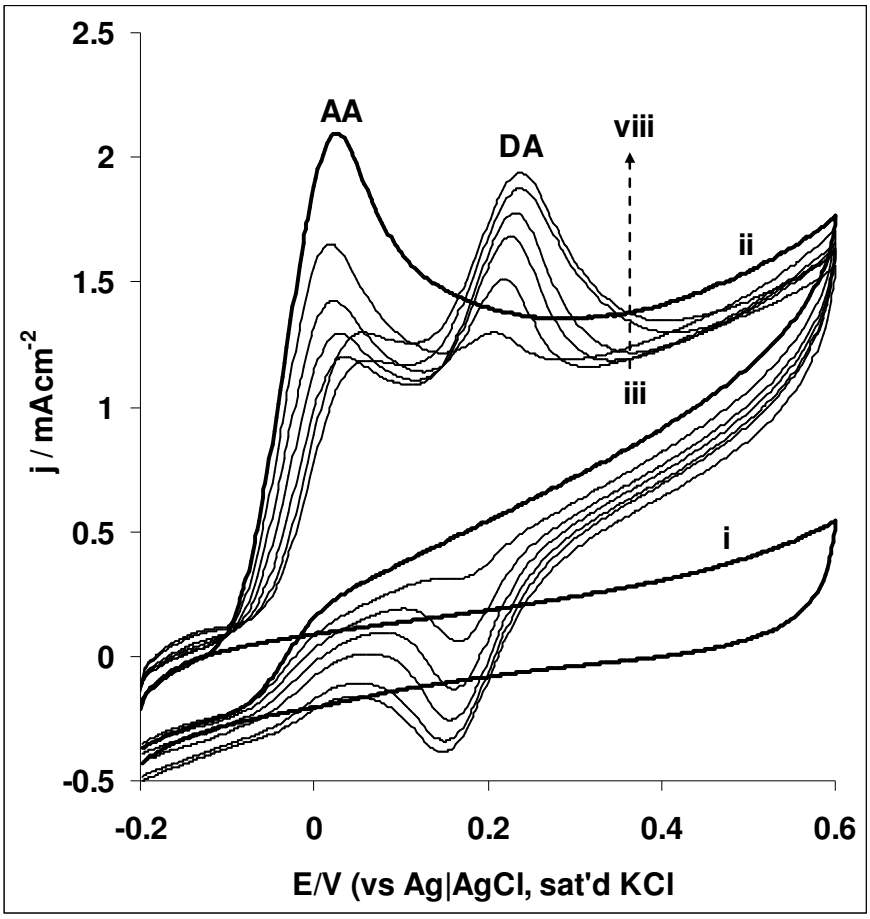

Figure 8.8: Typical square wave voltammograms responses of EPPGE-SWCNT-3PB in (i) 0.1 M pH 7.0 PBS, (ii) 10 mM AA alone, and mixture of (iii) 9.1 μM DA / 9.1 mM AA, (iv) 16.7 μM DA / 8.3 mM AA, (v) 23.1 μM DA / 7.7 mM AA, (vi) 28.6 μM DA/7.1 mM AA, (vii) 33.3 μM DA/6.7 mM AA and (viii) 41.2 μM DA/5.9 mM AA in PBS pH 7.0.

8.7. Real sample analysis: Dopamine drug

To evaluate the potential applicability of the EPPGE-SWCNT-3PB electrode, a square wave voltammetric assay of dopamine present in a dopamine hydrochloride injection, with dopamine content of 200 mg / 5 mL (i.e., 40 mg mL^{-1}) was carried out. The

concentration found in each dopamine drug (Table 8.3) is approximately within the labelled amount, with average recovery (n=5) of 101.60±2.79% at 95% confidence limit. The result further confirms the suitability and reliability of the EPPGE-SWCNT-3PB electrode as a potential sensor for the analysis of neurotransmitter such as DA.

Table 8.3: Determination of dopamine content in dopamine hydrochloride injections (40 mg mL^{-1}), n =5 (at 95% confidence limit) using EPPGE-SWCNT-3PB modified electrode.

Sample	Concentration found/mg mL^{-1}	Recovery/%
1	40.6 ± 0.52	101.5 ± 1.30
3	39.9 ± 1.01	99.8 ± 2.53
4	39.5± 0.96	98.7 ± 2.38
2	40.9 ± 1.24	102.2 ± 3.09

Investigation of the electron transfer behaviour and the catalysis of EPPGE modified with and without SWCNT-PABS/PB nanoparticles towards DA oxidation were carried out. Catalysis of DA was more favoured on the EPPGE-SWCNT-PB in terms of current response and onset potential for catalysis compared with other electrodes investigated. DA response increases with increasing PB layer on the electrode making EPPGE-SWCNT-3PB the best electrode. EPPGE-SWCNT-3PB electrode has the fastest electron transport and lowest R_{ct} towards DA electrocatalysis. The electrode would conveniently detect DA in the presence of AA (1000 times higher) with a wide potential separation of about 200 mV. The electrode is electrochemically stable, re-usable and can be used for the analysis of DA in real drug samples with satisfactory accuracy and reproducibility.

References

1 S. Han, Y. Chen, R. Pang, P. Wan, M. Fan, *Ind. Eng. Chem. Res.* 46 (2007) 6847.

2 L. Wang, S. Guo, X. Hu, S. Dong, *Colld. Surf. A: Physicochem. Eng. Aspects* 317 (2008) 394.

3 Z. Xu, N. Gao, H. Chen, S. Dong, *Langmuir* 21 (2005) 10808.

4 A. Ernst, O. Makowski, B. Kowalewska, K. Miecznikowski, P.J. Kulesza, *Bioelectrochem.* 71 (2007) 23.

5 J. Wang, *Analytical Electrochemistry*, VCH Publisher Inc., New York, 1994, Chapt. 6, p. 171.

6 H. Razmi, M. Agazadeh, B. Habibi-A, *J. Electroanal. Chem.* 547 (2003) 25.

7 A.J. Bard, L.R. Faulkner, *Electrochemical methods-fundamentals and applications*, Wiley, New York 1980.

8 N. Kobayashi, Y. Nishiyama, *J. Phys. Chem.* 89 (1985) 1167.

9 N. Sehlotho, T. Nyokong, *J. Electroanal. Chem.* 595 (2006) 161.

10 J.N. Soderberg, A.C. Co, A.H.C. Sirk, V.I. Birss, *J. Phys. Chem. B.* 110 (2006) 10401.

11 M.J. Giz, B. Duong, N.J. Tao, *J. Electroanal. Chem.* 465 (1999) 72.

12 G.D. Christian, *Analytical Chemistry*, 6th ed. John Wiley and Sons New York, 2004, p113.

13 A.S. Adekunle, B.O. Agboola, J. Pillay, K.I. Ozoemena, *Sens. Actuat. B* 148 (2010) 93.

14 Z. Wang, J. Liu, Q. Liang, Y. Wang, G. Luo, *Analyst* 127 (2002) 653.

15 D. Zheng, J. Ye, W. Zhang, *Electroanalysis* 20 (2008) 1811.

16 S. Shahrokhian, H.R. Zare-Mehrjardi, *Sens. Actuators B Chem.* 121 (2007) 530.

17 Y. Li, X. Lin, *Sens. Actuators B Chem.* 115 (2006) 134.

18 A. Balamurugan, S. Chen, *Bioelectrochem.* 54 (2001) 169.

19 G. Alarco´n-Angeles, B. Pe´rez-Lo´pez, M. Palomar-Pardave, M.T. Ramı´rez-Silva, S. Alegret and A. Merkoci, *Carbon* 46 (2008) 898.

CHAPTER NINE

Electrocatalytic Oxidation of Diethylaminoethanethiol, Hydrazine and Nitrite at Single-Walled Carbon Nanotubes Modified with Prussian Blue Nanoparticles*

* The publication below resulted from part of the research work presented in this chapter and it is not referenced further in this thesis:

10. **Abolanle S. Adekunle**, Kenneth I. Ozoemena, *Electroanalysis* DOI:10.1002/élan.201000289 (in press).

9.1 Microscopic and spectroscopic characterisation

Figure 9.1 presents the TEM images of PB nanparticles (Figure 9.1a) and SWCNT-PB nanocomposite (Figure 9.1b). From the TEM pictures, the PB particles appeared porous, amorphous, evenly distributed along the nanotubes and are in the size distribution of 5 – 15 nm.

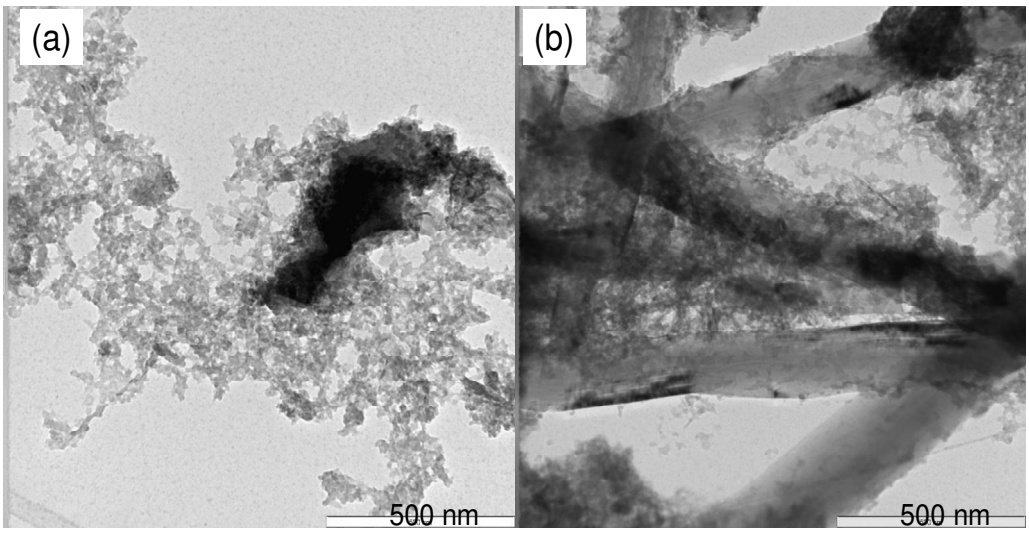

Figure 9.1: TEM of (a) Prussian blue (PB) nanoparticles (b) SWCNT-PB nanocomposite.

The PB particle distribution on the walls of the CNT could be due to both electronic (Covalent bonding) and ionic interaction between the phenyl ring, NH_2 or the SO_3^{2-} groups of the SWCNT-PABS and the PB ($Fe_4(III)[Fe(II)(CN)_6]_3$) nanoparticles. Figure 9.2 is the FTIR of (i) SWCNT-PABS and (ii) SWCNT-PB. The band at around 1026 cm^{-1} could be due to S=O stretching modes of the sulfonic acid group ($-SO_3^{2-}$) of the SWCNT-PABS. The strong band at 1380 cm^{-1} which appeared sharper in (ii) could be due to the N=O of NO_2 formed from the oxidation of NH_2 of the SWCNT-PABS. The band at around 1620

cm^{-1} common to (i) and (ii) is due to the vibration mode of C=C bonds. The bands at 2194, 2082 and 1936 cm^{-1}, found in (ii) but absent in (i) confirms the presence of C=N bond formed by the interaction of PB nanoparticles with the SWCNT-PABS. The band at 2915 and 2847 cm^{-1} common to both spectra can be attributed to C-H stretching bond of the sp^3 hybridised carbon of the SWCNT-PABS. The intense band at 3419 cm^{-1}, common to both spectra is ascribed to the N-H and/or O-H group of adsorbed moisture during sample preparations and was more in (ii) due to its broad band.

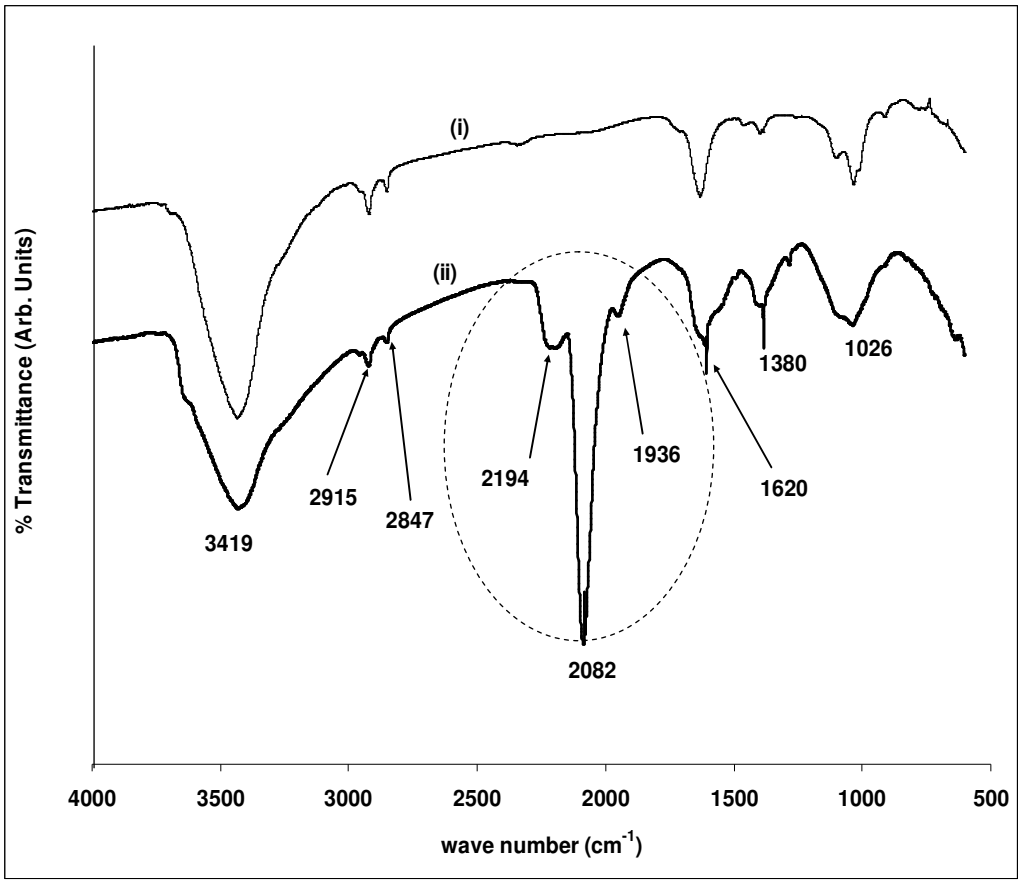

Figure 9.2: FTIR spectra of (i) SWCNT-PABS and (ii) SWCNT-PB nanocomposite.

XPS result (Figure 9.3) shows the two oxidized forms of iron, Fe^{2+} and Fe^{3+}. This is in agreement with the molecular structure of PB ($Fe_4(III)[Fe(II)(CN)_6]_3$) where the Fe occurs in two oxidation states. Inset in Figure 9.3 is the XPS indicating clearly the Fe peaks, and the dominance of Fe^{3+} peak over Fe^{2+} peak. The binding energies for the peaks at 712.5 and 726.0 eV are characteristic doublet from Fe $2p_{3/2}$ and Fe $2p_{1/2}$ [1] and agreed closely with literature values of 711.0 and 724.6 eV associated with the presence of Fe_2O_3 and Fe_3O_4 species respectively [2]. The nitrogen (N) and the carbon (C) peaks of the SWCNT-PABS and PB nanoparticles were seen at 401 and 285.5 eV respectively.

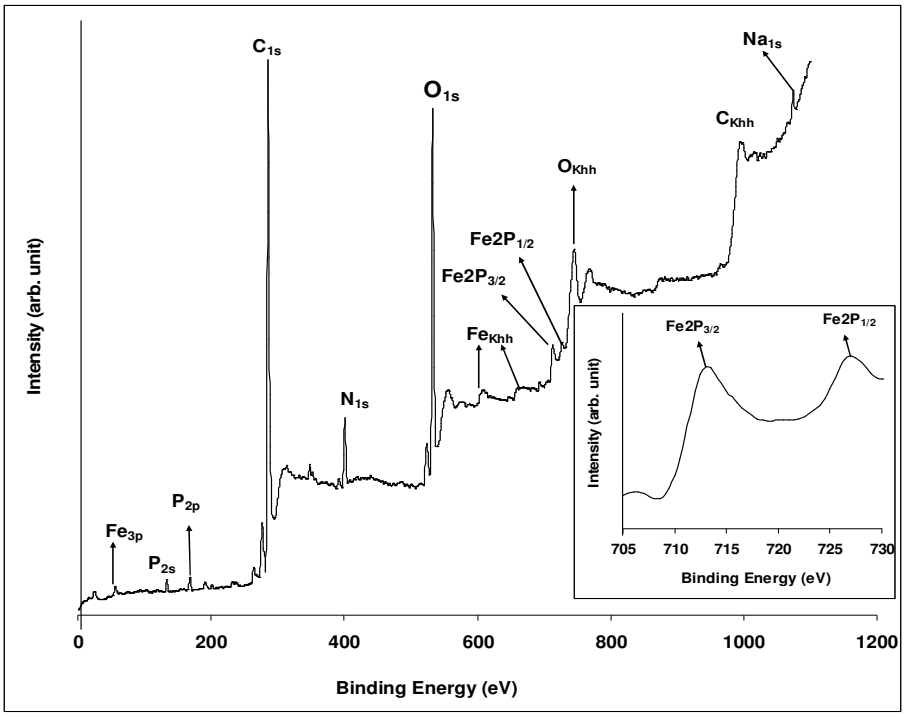

Figure 9.3: XPS spectrum of SWCNT-PB showing the presence of Fe^{2+} and Fe^{3+} ions the PB nanoparticles. Inset is the XPS spectrum indicating clearly the Fe peaks and the dominance of Fe^{3+} peak over Fe^{2+} peak.

Figure 9.4a and 9.4b showed the EDX spectrum of the SWCNT-PABS the SWCNT-PB nanocomposite of bare glassy carbon (GC) plate. GC plate was used as supporting electrode for obtaining the pictures since it is the next available platform (in place of EPPGE) to fit into the equipment. As expected, the EDX of the SWCNT-PABS was predominantly dominated by carbon peaks. The carbon peak was also prominent on the EDX of the SWCNT-PB. The N peak overlaps with the C peak but the elemental results indicates its occurrence in reasonable amount (13%), while the Fe peak was associated with the Fe^{2+} and the Fe^{3+} of the PB nanoparticles thus implying successful transformation of the SWCNT-PABS to SWCNT-PB. The potassium (K) peak is expected from the PB nanoparticles.

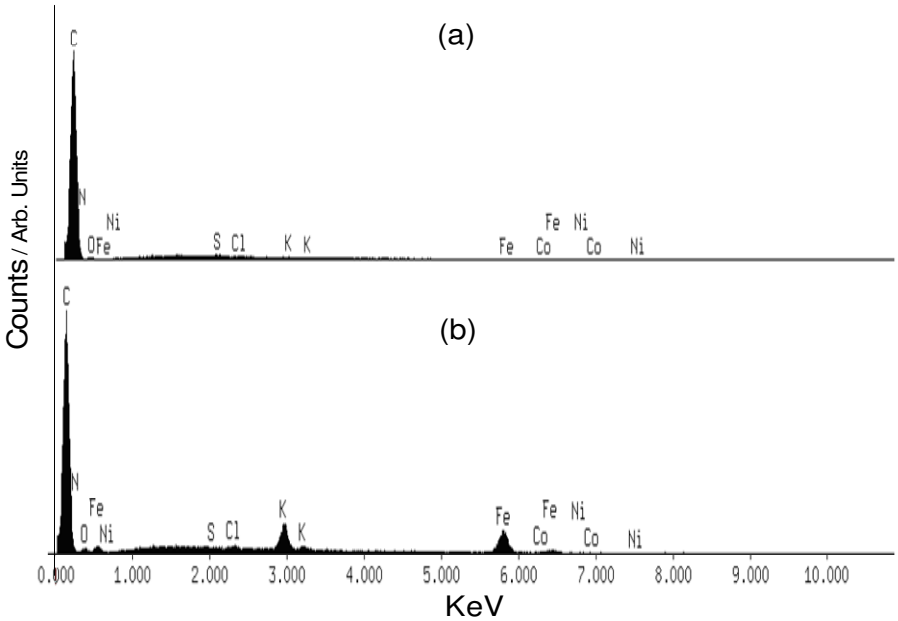

Figure 9.4: EDX spectra of (a) SWCNT-PABS and (b) SWCNT-PB nanocomposites.

9.2 Electrochemical characterization

Figure 9.5 compares the cyclic voltammograms of the bare EPPGE, EPPGE-SWCNT-PABS, EPPGE-PB and EPPGE-SWCNT-PB in PBS (pH 7.0) containing 0.1 M KCl. The CVs gave several properties already described under section 8.2. The signature peaks (PB/PW) were enhanced by the presence of the SWCNT, indicating the enhanced electron-conducting impact of the SWCNTs as redox mediator. The Prussian yellow (PY) is ill-defined at ~ 0.8 V (see Figure 9.5b). These peaks are consistent with literature [3,4]. Note from Figure 9.5b that the SWCNT-PB film showed little change (13% current decrease) when the electrode was subjected to continuous cycling in the electrolyte, a clear indication of excellent electrochemical stability (*ca* 90%). The surface concentration of the PB nanoparticles on the EPPGE-SWCNT-PB platform (Γ_{PB} / mol cm^{-2}) was estimated using a known relationship [5]. The value of the Γ_{PB} was estimated as ~ 4.8 x 10^{-8} mol cm^{-2}. The value is a magnitude higher than 4-5 x 10^{-9} mol cm^{-2} of PB films on glassy carbon (GC) electrode [6] for electrocatalytic reduction of H_2O_2, and agrees favourably with the 1.1 to 2.2 x 10^{-8} mol cm^{-2} of PB concentration on GC for electrocatalytic reduction of molecular oxygen [7].

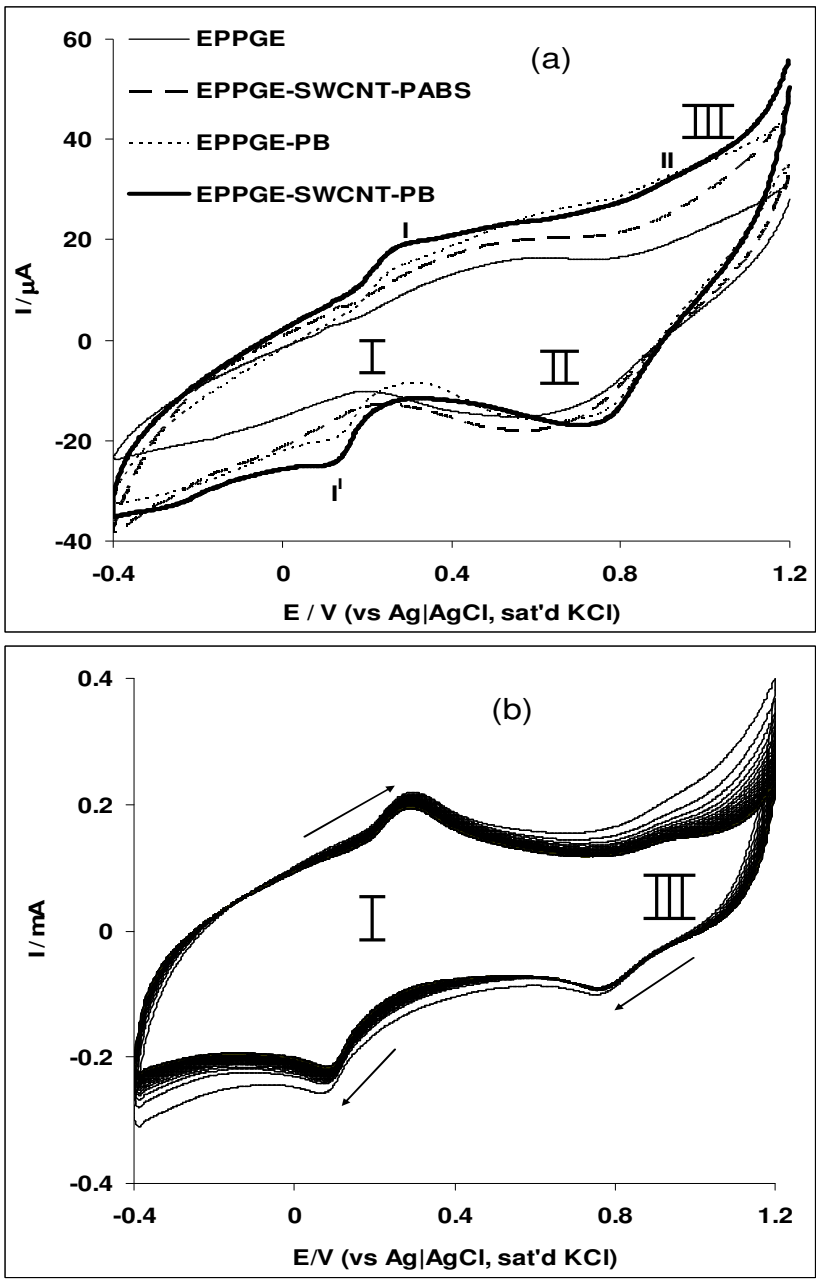

Figure 9.5: (a) Cyclic voltammograms showing the current responses of the electrodes modified with and without 10^{-4} M PB Prussian blue in 0.1 M KCl within the potential range of -0.4 to 1.2 V. Scan rate: 25 mVs^{-1}. (b) Current response of the EPPGE-SWCNT-PB electrode (30 scans) in (a) 0.1 M KCl electrolyte.

9.3 Electrocatalytic oxidation properties

Figure 9.6 presents the comparative background-subtracted voltammetric responses of the four electrodes in the solutions of (a) 0.1 mM DEAET (pH 9.4 PBS), (b) 1 mM hydrazine (0.1 M Na_2SO_4), (c) 10^{-3} M NO_2^- at pH 7.4 PBS and (d) 10^{-3} M NO at pH 3.0 PBS (Scan rate: 25 mVs^{-1}).

Electrocatalytic oxidation of DEAET was carried out in pH 9.4 PBS since previous studies had shown that DEAET gave best response under alkaline pH conditions [8,9]. The voltammetric data, in terms of current response (I_p) and peak potential (E_p) are summarised in Table 9.1. In all cases, the EPPGE-SWCNT-PB gave the best electrochemical response, thus all further studies were concentrated on this electrode.

The stability of the EPPGE-SWCNT-PB electrode towards the detection of these analytes was studied by repetitively cycling the solution of the analyte (30 scans, CV not shown). A decrease in peak current was observed after the first scan, which is typical of a poisoned electrode. However, upon rinsing the electrode in a fresh electrolyte, the electrode surface was renewed with about 84% of the initial catalytic current obtained, suggesting satisfactory electrochemical stability and reusability of the electrode after analysis. The electrode can be used for the analysis of DEAET, hydrazine and nitrite after storage in a refrigerator for up to two weeks without a significant change in its response.

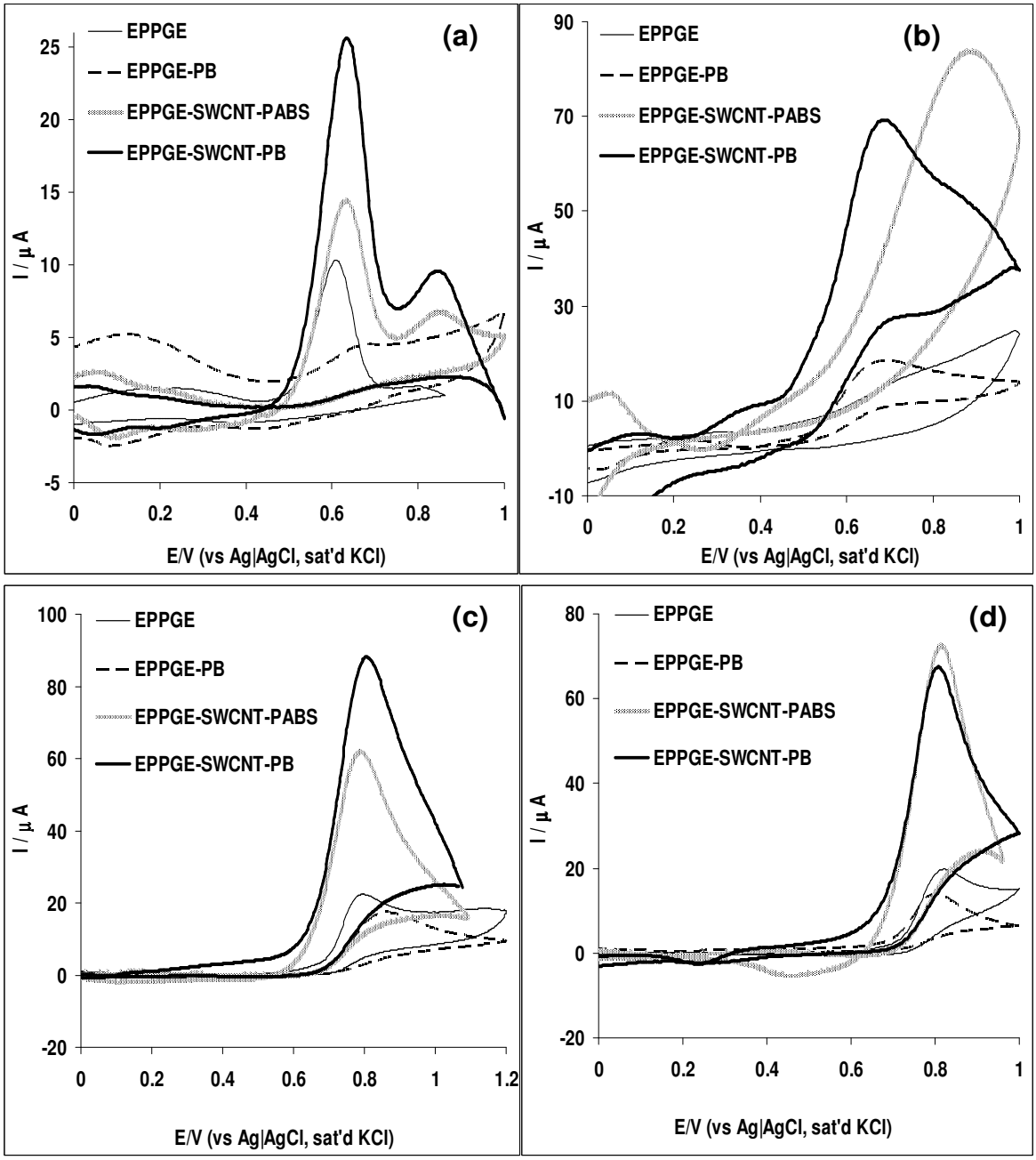

Figure 9.6: Comparative current response (after background current subtraction) of the modified electrodes in (a) 10^{-4} M DEAET in pH 9.4 PBS and (b) 0.1 M Na_2SO_4 solution containing 10^{-3} M hydrazine, (c) 10^{-3} M NO_2^- at pH 7.4 and (d) 10^{-3} M NO at pH 3.0 PBS (Scan rate: 25 mVs^{-1}).

Table 9.1: Electrocatalytic and electroanalytical parameters of the EPPGE-SWCNT-PB towards the detection of DEAET, hydrazine and nitrite. The values in parentheses are values obtained from the linear sweep voltammetry.

Analyte	Electrocatalytic and electroanalytical parameters							
	Electrolyte	E_p/V	Sensitivity/ $\mu A(\mu M)^{-1}$	LCR/μM	LoD/μM	Tafel slope/ $mVdec^{-1}$	$10^{-6}k_{cat}$/ $cm^3mol^{-1}s^{-1}$	ΔG^o/ $kJmol^{-1}$
DEAET	1 M PBS, pH 9.4	0.63	3.05±0.04	28.6 – 37.5	1.43±0.04	273	3.71±0.35	-22.64
Hydrazine	1 M Na_2SO_4	0.68	0.15±0.01	47.6 – 286.0	6.60±0.02	411	7.56±0.68	-25.40
Nitrite	1 M PBS (pH 3.0)	0.80	0.02±0.00	62.5-302.0	6.6±0.50	492	0.64±0.06	-29.53
Nitrite	1 M PBS (pH 7.4)	0.82	0.25±0.03	32.3-286.0	5.4±0.03	279	4.37±0.03	-20.76

The electrocatalytic behaviour of the EPPGE-SWCNT-PB towards the analytes was further interrogated using the impedimetric technique; each study being performed at the peak potential for which the analyte was catalysed. The Nyquist plots obtained from the fitting of the EIS spectra are presented in Figure 9.7a and the data obtained are presented in Table 9.2. Figure 9.7b represents the electrical equivalent circuit used in the fitting. The circuit elements are already defined.

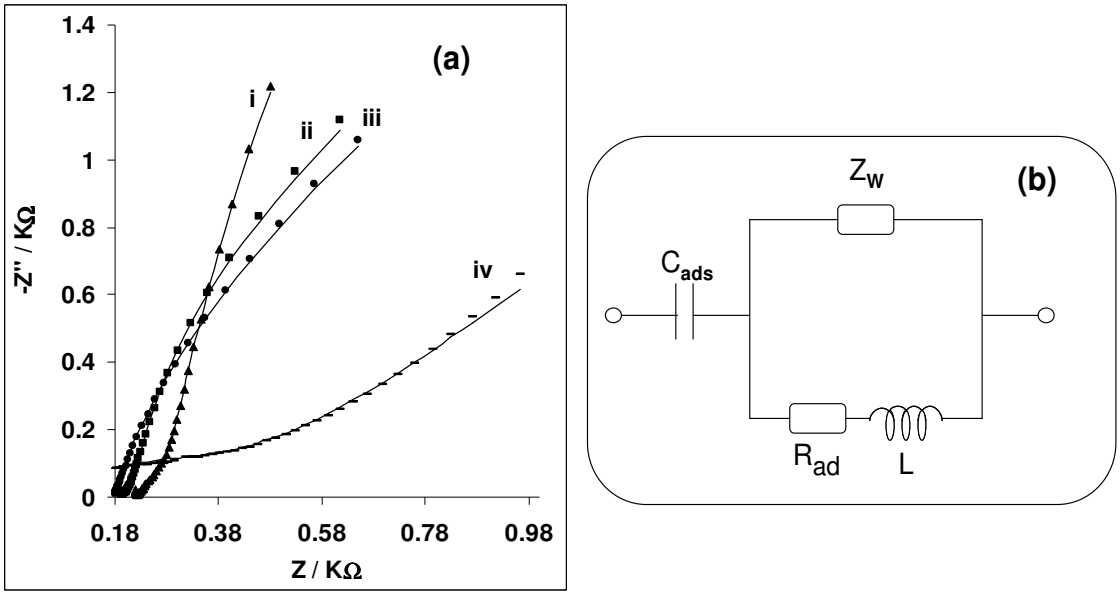

Figure 9.7: (a) Nyquist plots for the EPPGE-SWCNT-PB electrode in (i) 0.1 M pH 9.4 PBS containing 10^{-4} M DEAET, (ii) 0.1 M pH 3.0 PBS containing 10^{-3} M NO, (iii) 0.1 M pH 7.4 PBS containing 10^{-3} M NO_2-, (iv) 0.1 M Na_2SO_4 solution containing 10^{-3} M hydrazine. (b) is the circuit diagram used in the fitting of the impedance data in (a).

The presence of the inductor parameter suggests some adsorption of the reaction intermediate(s) in the overall electrocatalytic processes of these analytes [10,11]. The most

important parameter in Table 9.2 is the R_{ads}, which gave smaller value for the DEAET (20.95 Ωcm^2), an indication that the partial charge transport is faster for the DEAET than for the hydrazine, in the experimental conditions employed. This study has also used EIS measurement to prove adsorption associated with catalysis of the analyte on the PB film which is lack from the other literature reports.

The effect of scan rate (ν) on the electrocatalytic oxidation of the analytes were investigated, exemplified in Figure 8.8 with (a) DEAET. Generally, the oxidation peak potential shifted positively with increasing scan rates for all the analyte studied. The plots of $\log I_p$ vs $\log\nu$ (Figure 9.8b) are linear with slopes values slightly greater than the 0.5 expected fro an ideal diffusion-controlled process, suggesting some involvement of adsorption process [12,13]. Also, the current function plots (I_p/ν vs. ν) obtained for the analytes (Figure 9.8c) gave the characteristic curves confirming the interplay of coupled electrochemical-chemical (EC_{cat}) reactions process at the electrode.

Using the scan rate data and employing the Tafel equation [14], the linear relationships (the peak potential E_p and the $log\upsilon$ (not shown)) confirm the chemical irreversibility of the electrocatalytic oxidation processes of these analytes. The Tafel slopes were 273 mV dec^{-1} (DEAET), 411 mV dec^{-1} (hydrazine), 279 and 492 for nitrite at pH 7.4 and 3.0 respectively. These values are higher than the theoretical 118 mV dec^{-1} for a one-electron process involved in the rate-determining step. Such high Tafel values (leading to small α values, < 0.5) are ascribed to the adsorption of reactants or intermediates on the electrode surfaces and/or reactions occurring within a porous electrode structure [15].

Table 9.2: Impedance data at EPPGE-SWCNT-PB modified electrodes in 10^{-4} M DEAET (in PBS 9.4, at 0.60 V) and 10^{-3} M hydrazine in 0.1 M Na_2SO_4 solution at 0.68 V

Analyte	Electrochemical impedimetric parameters				
	Electrolyte	C_{ads}/μFcm^{-2}	Z_W/μΩcm^2	R_{ads}/ Ωcm^2	L/mHcm^2
DEAET	1 M PBS, pH 9.4	727.0±28.43	1.58±0.02	20.95 ±0.06	0.33 ±0.01
Hydrazine	1 M Na_2SO_4	3040.0±321.94	4.34±0.04	37.20 ±0.14	0.78 ±0.05

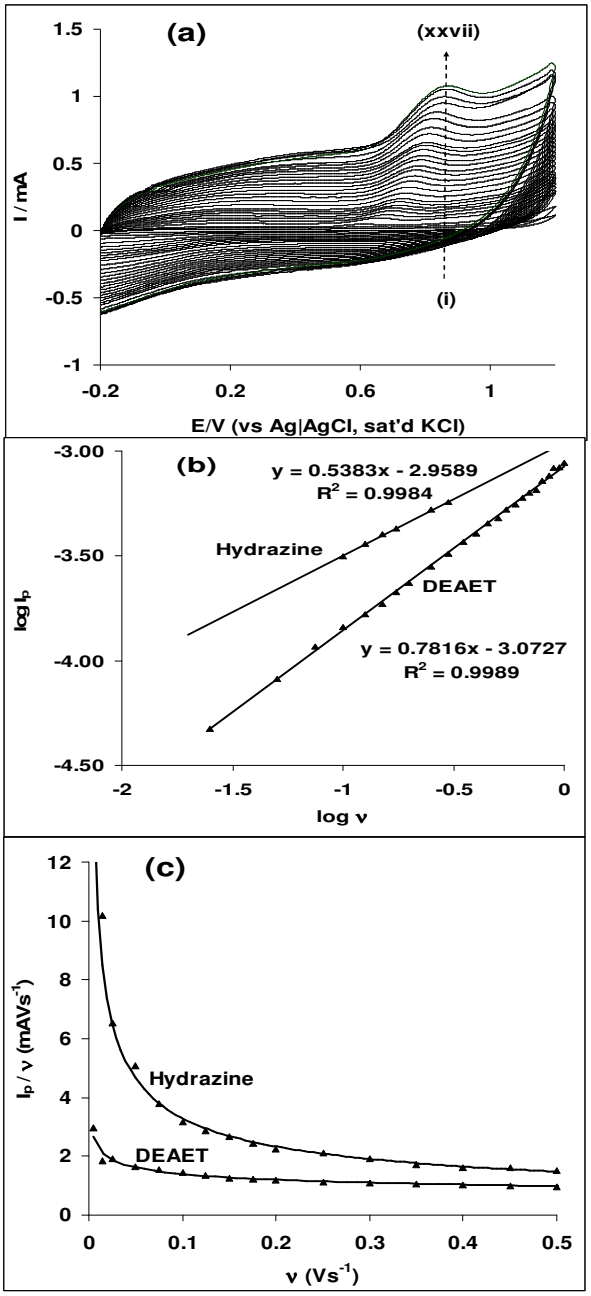

Figure 9.8: Current response of the EPPGE-SWCNT-PB electrode in (a) 0.1 M pH 9.4 PBS containing 10^{-4} M DEAET (scan rates between 25 and 1200 mVs^{-1}, from inner to outer). (b) Plots of E_p vs logν for (I) DEAET and (II) Hydrazine. (c) Current function plots (I_p/ν vs ν).

The catalytic rate constants (k_{cat}) were estimated using chronamperometric technique (at fixed potential of 0.6 V vs Ag|AgCl, sat'd KCl), employing the previous equation 6.6 [16, 17], where I_{cat} and I_{buff} are the currents in the presence and absence of the analyte, C is the bulk concentration and t is the time. From the plots of I_{cat}/I_{buff} vs $t^{1/2}$ at different concentrations of the analytes (exemplified in Figure 9.9a with hydrazine), and a plot of the slopes vs. concentrations of the analytes, the k_{cat} for EPPGE-SWCNT-PB in the analytes were obtained (see Table 9.1). The k_{cat} value of 3.71 x 10^6 $cm^3mol^{-1}s^{-1}$ obtained for DEAET in this study is about 3 times higher than the 1123.59 $M^{-1}s^{-1}$ (i.e., ~ 1.12 x 10^6 $cm^3mol^{-1}s^{-1}$) reported for the SWCNT/cobalt(II)tetraaminophthalocyanine films in DEAET [18]. The k_{cat} value obtained for hydrazine (7.56 x 10^6 $cm^3mol^{-1}s^{-1}$) is about two magnitudes higher than the ~ 2 x10^4 $cm^3mol^{-1}s^{-1}$ for the SWCNT-Ni and SWCNT-Fe films. The difference in the magnitude of k_{cat} could be due to the different electrode modifiers, the different experimental conditions and their degree of interaction with the analytes. Since the CV results suggested some degree of adsorption of these analytes onto the SWCNT-PB films, the adsorptive or stripping linear sweep voltammetry (AdsLSV) technique was employed to analyse the analyte and the Langmuir adsorption theory was used to obtain insights into their degree of adsorption. Each linear sweep voltammogram (LSV) was obtained after gently stirring the analyte for ~15 min in the presence of the electrode. Figure 9.10 is a typical linear sweep voltammetric evolution obtained at different concentrations of the DEAET, hydrazine and nitrite.

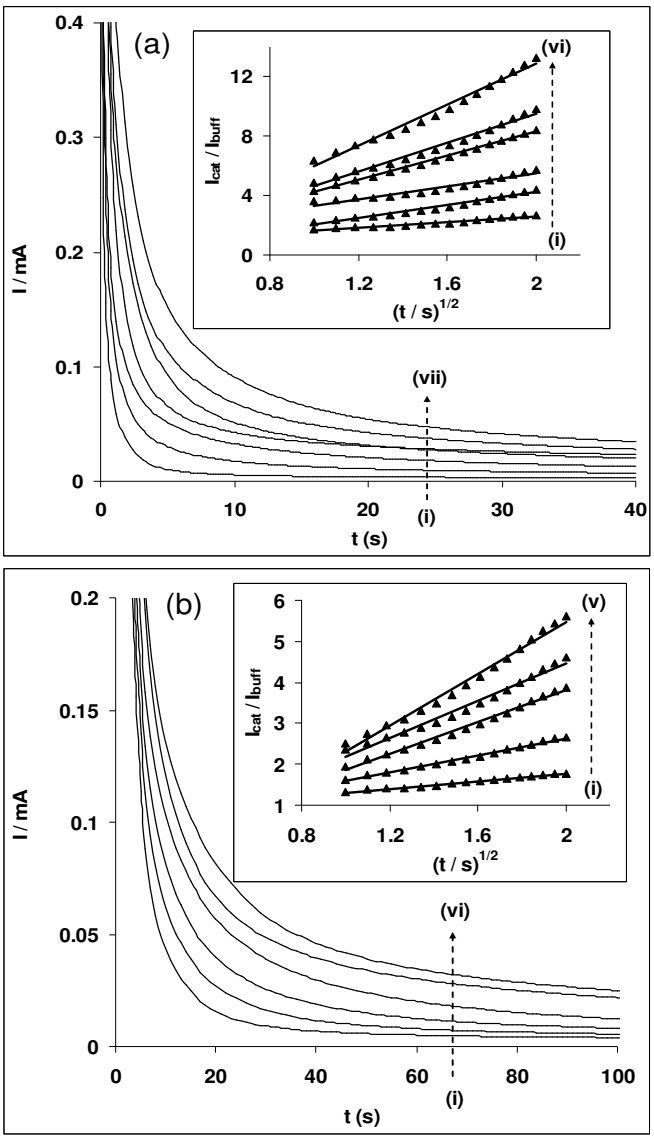

Figure 9.9: Typical chronoamperogram of EPPGE-SWCNT-PB in (a) 0.1 M Na_2SO_4 solution containing different concentrations of hydrazine (0.0, 47.6, 90.9, 130.0, 167.0, 231.0, and 286.0 μM (i to vii)). Inset represents the plots of I_{cat} / I_{buff} vs $t^{1/2}$ obtained from the chronoamperometric evolutions (i-vi correspond to 47.6, 90.9, 130.0, 167.0, 231.0 and 286.0 μM, respectively). (b) pH 9.4 PBS containing different concentrations of DEAET (0.0, 16.7, 23.1, 28.6, 31.0 and 33.3 μM (i to vi)). Inset represents the plots of I_{cat} / I_{buff} vs $t^{1/2}$ obtained from the chronoamperometric evolutions (i-v correspond to 16.7, 23.1, 28.6, 31.0 and 33.3 μM respectively).

The linear sweep voltammograms were analysed using the Langmuir adsorption isotherm theory [19]. From the theory, each plot of the ratio of C/I_{cat} vs C gave straight line (not shown), suggesting an adsorption-controlled process. From the slope and the intercept of the curve obtained, the β value of each analyte was obtained, and then used to estimate the ΔG^o value (Table 9.1). The ΔG^o values are -22.64 kJmol^{-1} (DEAET) and -25.40 kJmol^{-1} (hydrazine) which are in the same fashion as the Tafel slope, suggesting the adsorption behaviour for the different analytes at different experimental/electrolyte conditions.

9.4 Concentration studies and proposed mechanism

Concentration studies were carried out by investigating the response of EPPGE-SWCNT-PB to the different concentrations of the analytes using data from AdsLSV (Figure 9.10). The analytical data, sensitivity, linear range and limit of detection (LoD) obtained from LSV data are summarised in Table 9.1. AdsLSV is the preferred technique in this study due to its reliability over the chronoamperometry. The LoD was calculated based on the relationship ($LoD = 3.3\delta/s$ [20]). The detection limits recorded in this work for these analytes are in the same order and lower than several of those reported in the literature. For example, hydrazine has been detected at 8 μM reported on CCE/NiHCF [21], and at 5.3 μM using SWCNT-Ni nanocomposite. The 1.4 μM obtained for DEAET is lower or comparable with some literature reports [18,22,23].

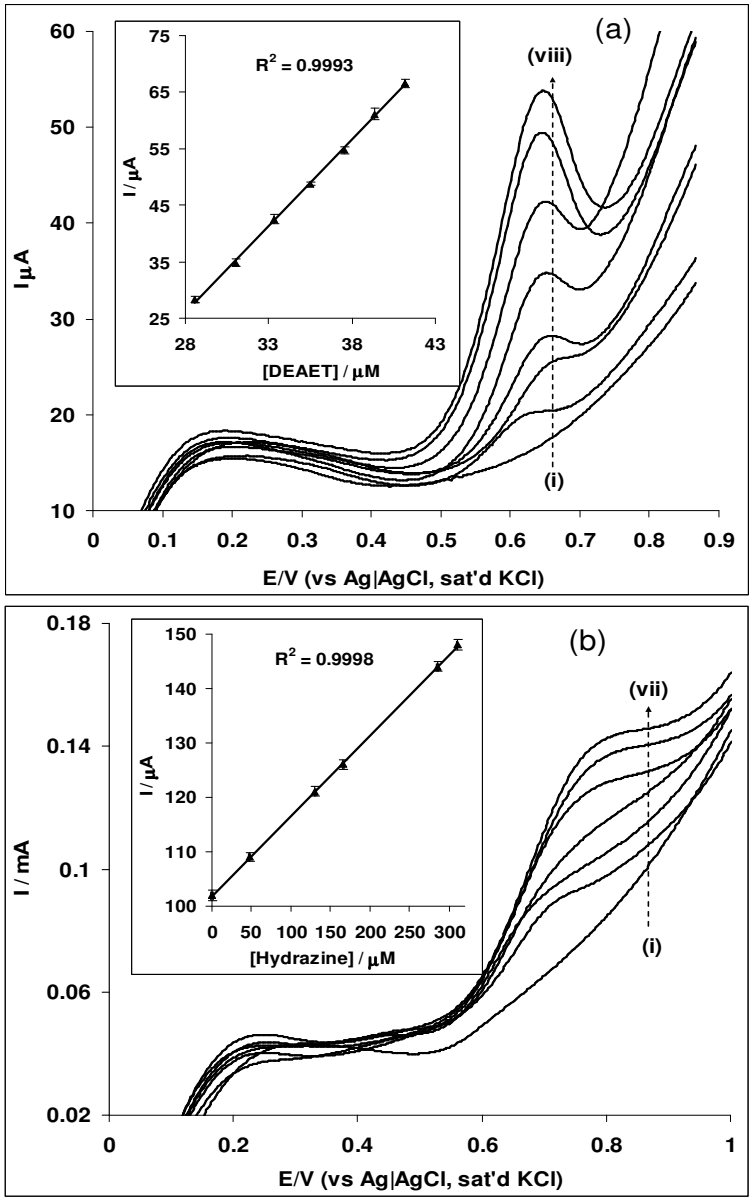

Figure 9.10: Typical linear sweep voltammograms of EPPGE-SWCNT-PB in (a) 0.1 M pH 9.4 PBS containing different concentrations of DEAET (0.0, 20.0, 28.6, 31.0, 33.3, 35.5, 37.5 and 41.2 µM (i) – (viii)). Inset in (a) represents the plot of peak current vs DEAET concentrations. (b) 0.1 M Na_2SO_4 solution containing different concentrations of hydrazine (0.0, 47.6, 90.9, 130.0, 167.0, 200 and 231 mM (i to vii)). Inset in (b) is the plot of peak current vs hydrazine concentrations.

From the results and discussion so far, it may be concluded that the electrocatalytic mechanism is mediated by the PB, summarised as follows:

$$(\text{SWCNT-PB})_{\text{film}} + A_R \longrightarrow (\text{SWCNT-PB....}A_R)_{\text{adduct}} \quad (9.1)$$

$$(\text{SWCNT-PB....}A_R)_{\text{adduct}} \longrightarrow (\text{SWCNT-PY})_{\text{film}} + A_{Ox} + e^- \quad (9.2)$$

(Rate-determining step)

$$A_{Ox} \longrightarrow \text{Oxidation products} \quad (9.3)$$

$$(\text{SWCNT-PY})_{\text{film}} + ne^- \longrightarrow (\text{SWCNT-PB})_{\text{film}} \quad (9.4)$$

(Regeneration step)

The A_R and A_{OX} represent the reduced and oxidized forms of the analytes, respectively. In general, the mechanism is proposed to involve an initial co-ordination of the reduced form of the analyte with the SWCNT-PB to form an adduct (Equation 9.1). Equation 9.2 is related to the rate-determining step (rds) as discussed in Tafel slope, which involves the oxidation of the PB to its PY form, and the generation of oxidized products such as the thiyl radical ($RS^{\cdot}$) for the DEAET, N_2H_3 for the hydrazine and nitrogen (iv) oxide (NO_2) for nitrite. Other oxidized products (Equation 9.3) include the disulphide products (RSSR) for the DEAET, nitrogen for the hydrazine and nitrate for nitrite. Equation 9.4 represents the subsequent regeneration of the PB catalyst via PY/PW.

In this study, electron-transport and electrocatalytic efficiency of SWCNT/PB nanohybrids towards the oxidation of environmental molecules (DEAET, hydrazine and nitrite) in aqueous media were investigated. The results clearly show that SWCNT/PB nanohybrids represent important electrocatalytic platforms for the sensitive detection of DEAET, hydrazine and nitrite.

References

1. C. C. Rajeev, K-W Jun, C. V. Rode, *Polyhedron* 27 (2008) 933.

2. M. Oku, K. Hirokawa, S. Ikeda, *J. Electron Spectrosc. Relat. Phenom.* 7 (1975) 465.

3. Y-L Hu, J-H Yuan, W. Chen, K. Wang, X-H Xia, *Electrochem. Commun.* 7 (2005) 1252.

4. A. Ernst, O. Makowski, B. Kowalewska, K. Miecznikowski, P. J. Kulesza, *Bioelectrochem.* 71 (2007) 23.

5. J. Wang, *Analytical Electrochemistry*, VCH Publisher Inc., New York, 1994, Chapt. 6, p. 171.

6. A.A. Karyakin, E.E. Karyakina, L. Gorton, *Talanta* (1996) 1597.

7. K. Itaya, N. Shoji, I. Uchida, *J. Am. Chem. Soc.* (1984) 106.

8. N.S. NcIntyre, M.G. Cook, *Anal. Chem.* 47 (1975) 2208.

9. S. Sunohara, K. Nishimura, K. Yahikozawa, M. Ueno, *J. Electroanal. Chem.* 161 (1993) 354.

10. J. Bisquert, H. Randriamahazaka, G. Garcia-Belmonte, *Electrochim. Acta* 51 (2005) 627.

11. M. Jafarian, M. G. Mahjani, H. Heli, F. Gobal, H. Khajehsharifi, M.H. Hamedi, *Electrochim. Acta* 48 (2003) 3423.

12. Y. Shih, J.-M. Zen, A.S. Kumar, P-Y. Chen, *Talanta* 62 (2004) 912.

13. J.-M. Zen, A.S. Kumar, J.-C. Chen, *Anal. Chem.* 73 (2001) 1169.

14. J.A. Harrison, Z.A. Khan, *J. Electroanal. Chem.* 28 (1970) 131.

15. J.N. Soderberg, A.C. Co, A.H.C. Sirk, V.I. Birss, *J. Phys. Chem. B.* 110 (2006) 10401.

16. K.M. Manesh, P. Santosh, A.I. Gopalan, K.P. Lee *Electroanalysis* 18 (2006) 894.

17. Z. Galus, Fundamentals of Electrochemical Analysis, Ellis Horwood Press, New York, 1976, p. 313, Ch. 10.

18. J. Pillay, K.I. Ozoemena, *Electrochim. Acta* 52 (2007) 3630.

19. H.X. Ju, L. Donal, *J. Electroanal. Chem.* 484 (2000) 150.

20. G.D. Christian, *Analytical Chemistry*, 6th ed., John Wiley and Sons, New York, 2004, p. 113.

21. K.C. Pan, C.S. Chuang, S.H. Cheng, Y.O. Su, *J. Electroanal. Chem.* 50 (2001) 160.

22. J. Pillay, K.I. Ozoemena, *Electrochem. Commun.* 9 (2007) 1816.

23. J. Wang, J. Zima, N.S. Lawrence, M.P. Chatrathi, *Anal. Chem*. 76 (2004) 4721.

CHAPTER TEN

Supercapacitive Behaviour of Single-Walled/Multi-Walled Carbon Nanotubes-Metal (Ni, Fe, Co) Oxide Nanocomposites in Acidic and Neutral pH Conditions*

* The publication below resulted from part of the research work presented in this chapter and it is not referenced further in this thesis:

11. **Abolanle S. Adekunle**, Kenneth I. Ozoemena, *Electroanalysis* (Submitted).
12. **Abolanle S. Adekunle**, Kenneth I. Ozoemena, *J. Power Sources* (Submitted).

10.1 Comparative EDX, XPS and FESEM

Figure 10.1 is the EDX profile of the electrodes. The presence of Ni, Co and Fe peaks in (a), (b) and (c) showed that the electrodes were successfully modified with the respective metal nanoparticles while the occurrence of oxygen peaks with very pronounced intensity implies that the electrodes were successfully transformed to their oxide derivatives. The presence of Ni peak on the EDX of Fe is attributed to Ni impurities from the Fe salts and / or SWCNTs since the EDX of the SWCNTs (not shown) indicated presence of Ni impurities. The occurrence of P and Na peaks in the EDX profiles may be attributed to the sodium phosphate buffer solution used for the electrode preparation.

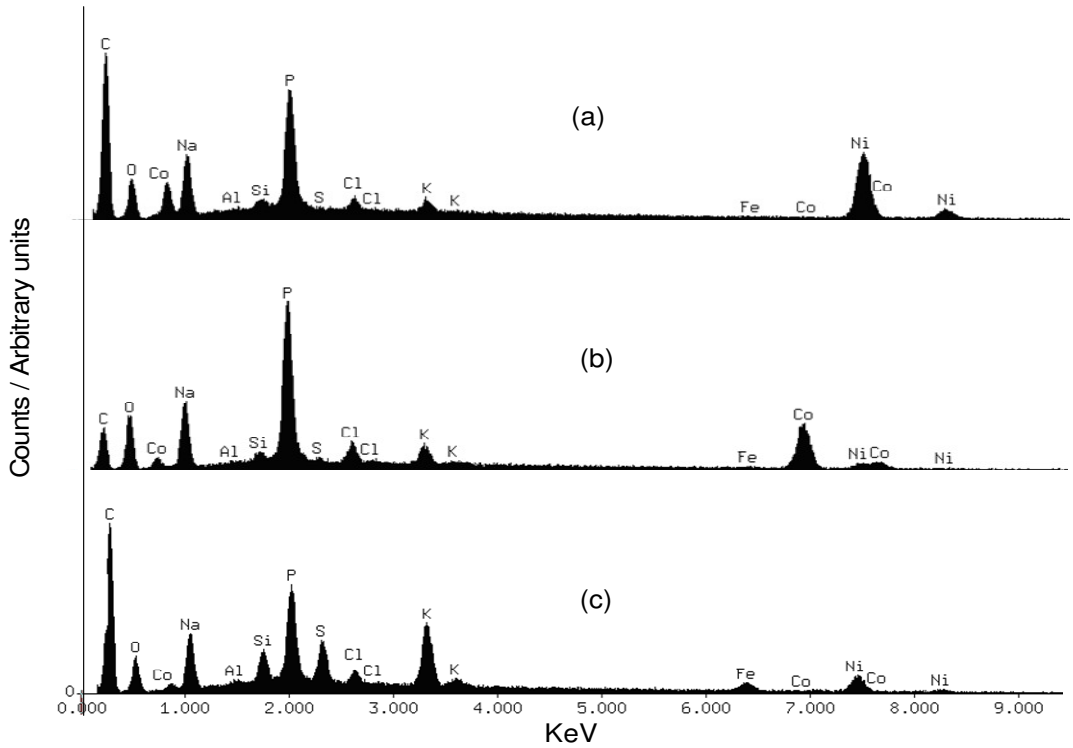

Figure 10.1: EDX spectra of (a) SWCNT-NiO, (b) SWCNT-Co_3O_4 and (c) SWCNT-Fe_2O_3

The XPS data (Figure 10.2) confirmed qualitatively the nature of the species or the oxidation state of the metal nanoparticles in their oxide forms. For example, Ni $2p_{3/2}$ peak at 858.5 eV (Figure 10.2a) is closer to 854.0 eV considered to be NiO [1], which is supported again by the Ni $2p_{1/2}$ peak at 876.0 eV, very close to 873.3 eV observed by Sunohara et al [2]. The Co oxide specimen had $2p_{3/2}$ and $2p_{1/2}$ peaks of Co at 783.0 and 795.7 eV (Figure 10.2b) which is in close agreement with reported values, corresponding to Co_3O_4 [1,3]. The $2p_{3/2}$ and $2p_{1/2}$ peaks at 712.6 and 726.8 eV for Fe oxide modified electrode (Figure 10.2c) agreed with literature value of 710.7 and 724.3 eV which indicates the presence of Fe_2O_3 species [4]. The O1s peak at 532 eV is very close to 530 eV reported to be the lattice oxygen of Fe_2O_3 and Fe_3O_4 [2]. However, the dominant oxide of Fe on the electrode from this result was taken as Fe_2O_3 since species of Fe_3O_4 are not apparent. The Na and the P peaks in Figure 10.2 are attributed to the Na and P of the PBS used during electrode modification while the C peak can be attributed to the carbon of the SWCNTs and the base BPPGE electrode. Hence, the oxides of Fe and Co from this study are taken to be Fe_2O_3 and Co_3O_4 respectively. The metal oxide nanoparticles are porous and somewhat aggregated (Figure 9.3), due possibly to the strong electrostatic interactions between the metal ions and the COO^- charge of the acid-treated SWCNTs. From the SEM image, the average particle size distributions are 20 -50 nm for NiO, 30 – 90 nm for Co_3O_4, and 120 – 200 nm for Fe_2O_3 nanoparticles. Salimi *et al* [5], employed similar method of electrode decoration with cobalt oxide nanoparticles and observed particles agglomeration with sizes ranging from 100 – 600 nm.

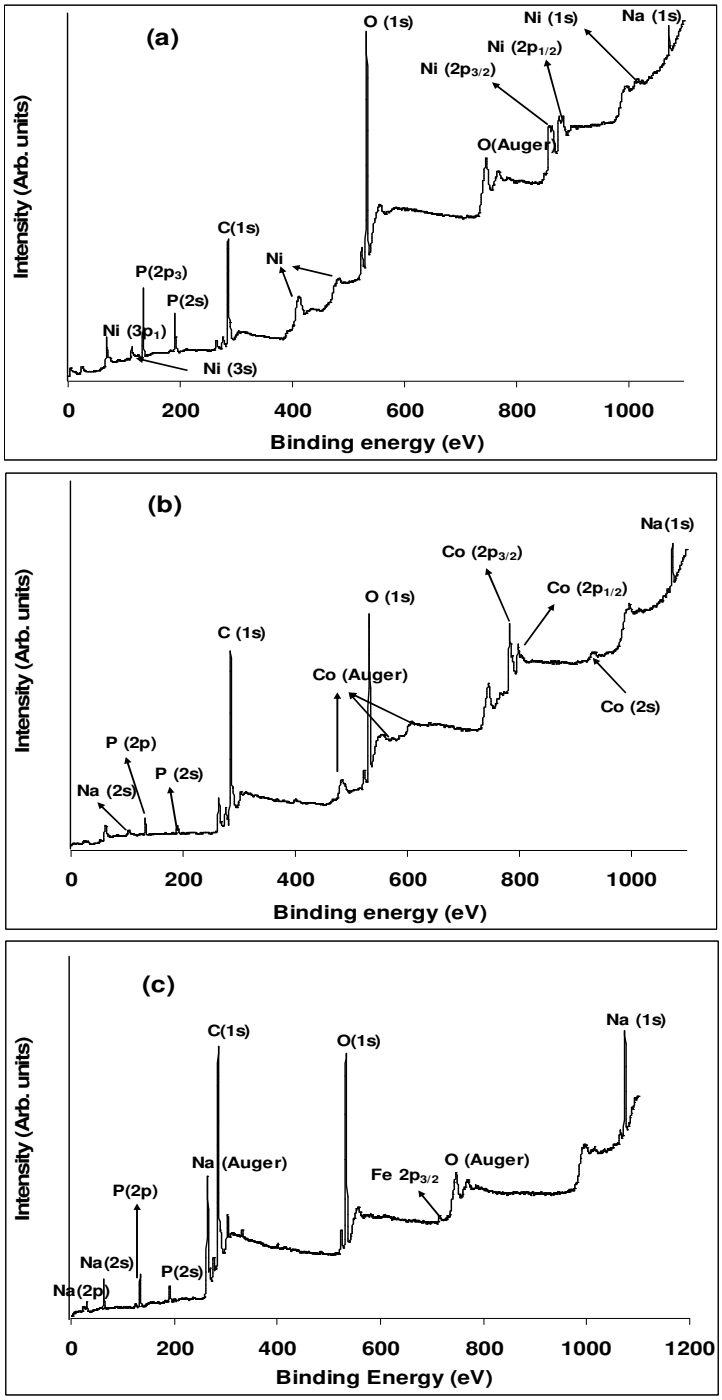

Figure 10.2: XPS spectra of (a) SWCNT-NiO, (b) SWCNT-Co_3O_4 and (c) SWCNT-Fe_2O_3.

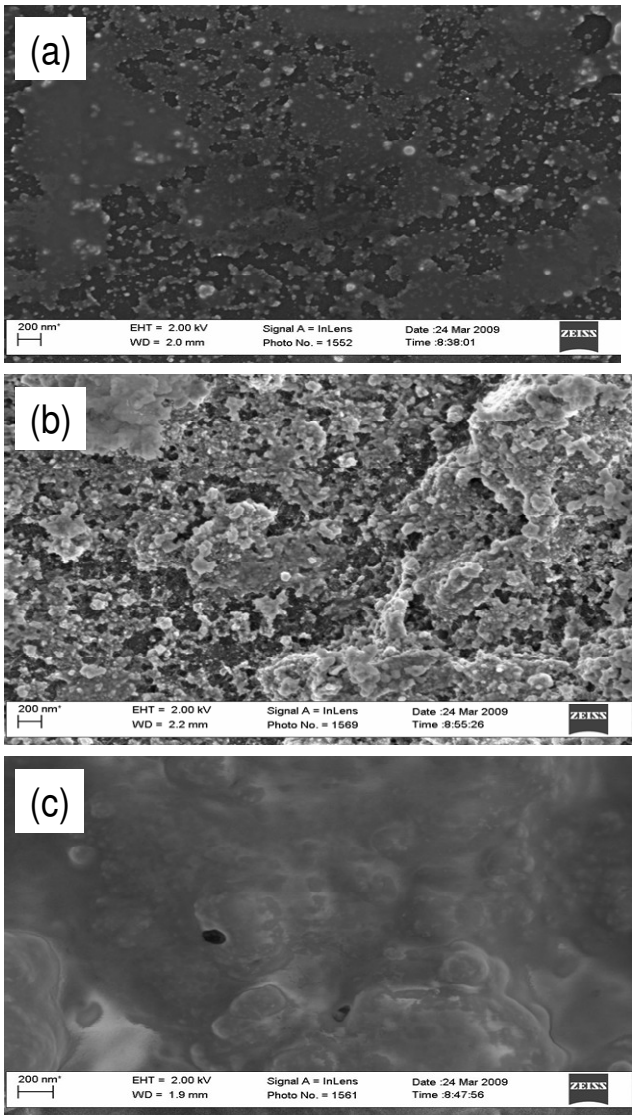

Figure 10.3: FESEM images of (a) SWCNT-NiO (b) SWCNT-Co_3O_4 and (c) SWCNT-Fe_2O_3.

10.2 Comparative cyclic voltammetric experiments

Figure 10.4 presents the comparative CVs of the electrodes in 1 M Na_2SO_4 and 1 M H_2SO_4 solution respectively at a scan rate of 25 mVs^{-1}. The CV indicates several important differences between the composite nanoparticles modified electrodes and the bare BPPGE. First, the SWCNTs exhibit redox couple at $E_{1/2} \approx 0.22$ V and weak oxidation peak at about 0.4 V which may be attributed to the redox processes arising mainly from the oxo-groups at the basal plane sites of the SWCNTs [6]. Second, unlike the voltammograms of the electrodes based on the FeO and CoO nanoparticles, the NiO-based electrodes exhibit huge capacitive current response with irreversible peak around 0.65 V due to the Ni(II)/Ni(III) redox process. The lack of perfect rectangular shape for the curves is attributed to the combination of double layer and pseudo-capacitances contributing to the total capacitance [7]. Third, the capacitive behaviour of the three BPPGE-SWCNT-MO are more pronounced in H_2SO_4 than in Na_2SO_4 electrolyte as can be observed from the charge-discharge study (discussed later).

The ability of the films to store charges may be obtained from the film capacitance (C_{film} / Fcm^{-2}) estimated using the simple expression [8,9]:

$$C_{film}\ (F\ cm^{-2}) = \frac{I_{ch}}{\nu A} \qquad (10.1)$$

where I_{ch} is the average current, ν the scan rate and A the area (cm^2) of the electrode. The equivalent SC values in Fg^{-1} are also estimated and reported (Table 10.1).

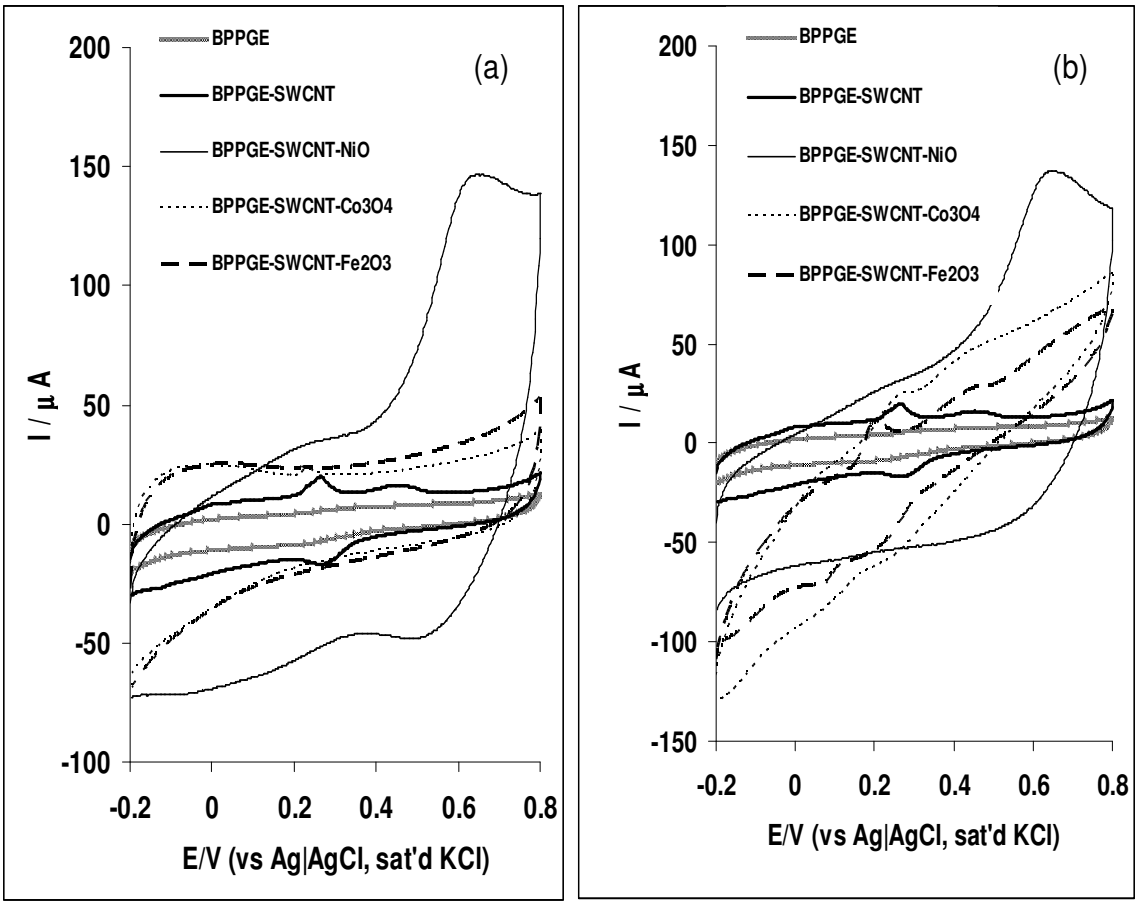

Figure 10.4: Comparative CVs showing the capacitive behaviour of: BPPGE, BPPGE-SWCNT, BPPGE-SWCNT-NiO, BPPGE-SWCNT-Co_3O_4 and BPPGE-SWCNT-Fe_2O_3 in (a) 1 M Na_2SO_4 and (b) 1 M H_2SO_4 aqueous electrolytes. Scan rate = 25 mVs^{-1}.

10.3 Comparative galvanostatic charge / discharge experiments

The ability of the films to store and deliver charges was interrogated using the galvanostatic charge-discharge strategy, the most reliable and accurate method for evaluating the supercapacitive properties of electrodes. Figure 10.5 shows the comparative current charge/discharge curves of the three BPPGE-SWCNT-MO electrodes

conducted in 1 M aqueous Na_2SO_4 and H_2SO_4 solutions at a current density of 0.1 Acm^{-2}, and potential range of - 0.2 to 0.8 V. The specific capacitance (SC) was obtained from Equations 10.2 and 10.3 [10]:

$$SC\ (Fcm^{-2}) = \frac{I \times \Delta t}{\Delta E \times A} \qquad (10.2)$$

$$SC\ (F\ g^{-1}) = \frac{I \times \Delta t}{\Delta E \times m} \qquad (10.3)$$

where I is the discharge current in ampere, Δt is the discharge time in second, ΔE is the discharge voltage in volt, A and m are the area and the mass of the electrode active material in cm^2 and g respectively. A is obtained from the peak corresponding to the respective metal oxide in ferri cyanide redox probe while the active mass m was obtained using the Sartorius CP225D micro-balance with an accuracy of 0.01 mg. The magnitude of SC obtained for the electrodes in 1 M Na_2SO_4 solution is in the order of BPPGE-SWCNT-NiO (140.0 $mFcm^{-2}$) > BPPGE-SWCNT-Co_3O_4 (79.8 $mFcm^{-2}$) > BPPGE-SWCNT-Fe_2O_3 (64.4 $mFcm^{-2}$). The SC values were higher (at the same current density) for the electrodes in H_2SO_4: BPPGE-SWCNT-NiO (186.0 $mFcm^{-2}$) > BPPGE-SWCNT-Co_3O_4 (117.8 $mFcm^{-2}$) > BPPGE-SWCNT-Fe_2O_3 (84.8 $mFcm^{-2}$). The magnitude of SC (Fg^{-1}) obtained for the electrodes in 1 M Na_2SO_4 solution is in the order of BPPGE-SWCNT-NiO (708 Fg^{-1}) > BPPGE-SWCNT-Co_3O_4 (399.0 Fg^{-1}) > BPPGE-SWCNT-Fe_2O_3 (322 Fg^{-1}). The SC values were higher (at the same current density) for the electrodes in H_2SO_4: BPPGE-SWCNT-NiO (928 Fg^{-1}) > BPPGE-SWCNT-Co_3O_4 (589 Fg^{-1}) > BPPGE-SWCNT-Fe_2O_3 (424 Fg^{-1}).

Table 10.1: Supercapacitive properties of the MO nanoparticles integrated with SWCNTs determined using cyclic voltammetry and galvanostatic discharge methods.

Electrode Modifier/Electrolyte	**Supercapacitive parameters**					
	Cyclic voltammetry (25 mVs^{-1})		**Galvanostatic discharge method (0.1 mA cm^{-2})**			
	SC (F g^{-1})	**SC (mF cm^{-2})**	**SC (F g^{-1})**	**SC (mF cm^{-2})**	**SP (W kg^{-1})**	**SE (KW kg^{-1})**
SWCNT-NiO/ 1 M H_2SO_4	178.0±12.5	35.6±2.5	927.6±65.0	186.0±13.0	330.0±23.1	330.0±19.8
SWCNT-Co_3O_4 / 1 M H_2SO_4	82.5±5.8	16.5±1.2	588.5±41.2	117.8±8.3	440.0±30.8	440.0±27.1
SWCNT-Fe_2O_3 / 1 M H_2SO_4	79.0±5.5	15.8±1.1	424.0±29.7	84.8±5.9	490.0±34.3	490.0±29.3
SWCNT / 1 M H_2SO_4	33.0±2.3	6.6±0.5	-	-	-	-
SWCNT-NiO/ 1 M Na_2SO_4	198.0±13.9	39.6±2.8	707.7±49.5	140.0±9.8	374.0±26.2	374.0±26.2
SWCNT-Co_3O_4 / 1 M Na_2SO_4	36.0±2.5	7.2±0.5	399.0±28.0	79.8±5.6	450.0±32.2	450.0±21.4
SWCNT-Fe_2O_3 / 1 M Na_2SO_4	40.0±2.8	8.0±0.6	321.7±22.5	64.4±4.5	500.0±35.0	442.5±21.5
SWCNT / 1 M Na_2SO_4	36.0±2.0	7.2±0.3	-	-	-	-

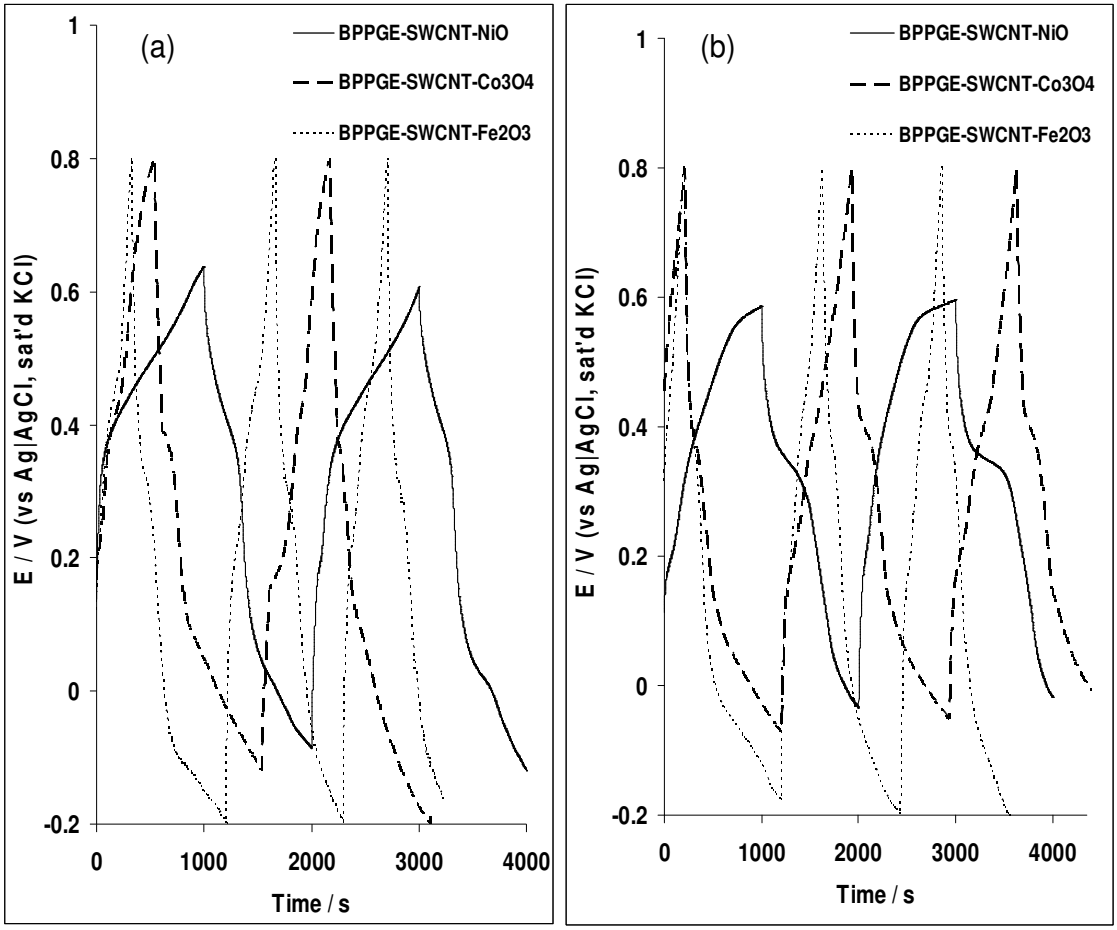

Figure 10.5: Typical examples of comparative galvanostatic charge discharge plot of the metal oxide SWCNTs/nanocomposite modified electrodes at an applied current density of 0.1 $mAcm^{-2}$ in (a) 1 M Na_2SO_4 and (b) 1 M H_2SO_4 aqueous electrolyte.

The values reported in this work are comparable or even higher than those reported in the literature using the same conditions (electrolytes and 3-electrode systems). For example, the values of 186 and 140 $mFcm^{-2}$ obtained for the BPPGE-SWCNT-NiO in 1 M H_2SO_4 and 1 M Na_2SO_4 respectively are greater than 96 and ~ 30 μFcm^{-2} reported for Fe_3O_4 nanofilm electrodeposited on gold

electrode in neutral environment [11], 27 $mFcm^{-2}$ reported for micro-polypyrrole (ppy) films doped with $ClO4^-$ (PPY_{ClO4}), prepared on Ni layers modified three-dimentional (3D) structures [12], 6.6 μFcm^{-2} obtained for carbon/zinc-aluminium (C-Zn_2Al) double layer hydroxide nanocomposite in 1 M H_2SO_4 [13], the 42 and 135.5 μFcm^{-2} reported for carbon/nickel-aluminium (C-Ni_2Al) layer double hydroxide (LDH) nanocomposite in 0.5 M Na_2SO_4 and 1 M $NaNO_3$ electrolyte respectively [14], or the value of 1117 μFcm^{-2} reported for the nitrogen-enriched carbon electrode described as 'extra-ordinary capacitor [15]. However, the result obtained in this study compares favourably with the recent report of 186 $mFcm^{-2}$ for nickel (II) octa [(3,5-bicarboxylate)-phenoxy] pthalocyanine integrated with functionalised single-walled carbon nanotubes (SWCNT-phenylamine) [16] and 112 $mFcm^{-2}$ for MWCNT-polyNiTAPc [17]. Also, these results are higher or comparable to literature values of 777 Fg^{-1} for MWCNT-polyNiTAPc in 1 M H_2SO_4 [17], 400 Fg^{-1} for polypyrrole [18,19], and a value of 616 Fg^{-1} for 3-methylthiophene using galvanostatic method [20]. The higher SC values obtained in this electrolyte may be attributed to its strong ionic nature, with greater diffusion, adsorption and storage capacity along the pores of the nanocomposites. One of the main reasons for the higher value obtained in this study may possibly be due to the stringent conditions adopted in functionalising the SWCNTs with carboxylic, phenolic and ketonic groups which make them more able to enhance ion mobility and storage, and also undergo both non-Faradaic (capacitive) and Faradaic (pseudocapacitive) reactions.

The specific power density (SP) and specific energy (SE) were easily estimated from the discharge process using Equations 10.4 and 10.5 [10,17,21]:

$$SP\ (Wkg^{-1}) = \frac{I \times \Delta E}{m} \quad (10.4)$$

$$SE\ (WhKg^{-1}) = \frac{I \times t \times \Delta E}{m} \quad (10.5)$$

where ΔE represents the potential range; other units retain their usual meaning. The SP and SE values are summarized in Table 10.1. The energy deliverable efficiency (η / %) of the best electrode film (BPPGE-SWCNT-NiO) was obtained from Equation 10.6 [21].

$$\eta\ (\%) = \frac{t_d}{t_c} \times 100 \quad (10.6)$$

where t_d and t_c are discharge time and charging time, respectively. The energy deliverable efficiency for BPPGE-SWCNT-NiO is 99.9±9.0% and 99.9±9.4% in H_2SO_4 and Na_2SO_4, respectively. Since BPPGE-SWCNT-NiO electrode gave the highest capacitance, stability study of the electrode in Na_2SO_4 and H_2SO_4 was carried out at current density of 2 $mAcm^{-2}$ (Figure 10.6). Inset in Figure 10.6 represents some typical repetitive charge-discharge cycling for 1000 cycles, lasting about 3 days. The Figure clearly showed that the electrode is able to charge and discharge continuously without any significant loss in capacitance. Compared with the performance of the electrode in Na_2SO_4 (not shown), a better stability was observed in this electrolyte, showing about 5% loss of its initial specific capacitance after 100 cycle life in H_2SO_4, while an insignificant drop (about 0.1%) in SC value was noticed for the last 900 cycles. This indicates high stability characteristics of the SWCNT-NiO nanocomposites. Factors such as ionic strength, diffusion of ions and a favourable interaction between the ions and the nanoparticles

pores for complete ion insertion reaction may be some of the reasons for the observed phenomenon.

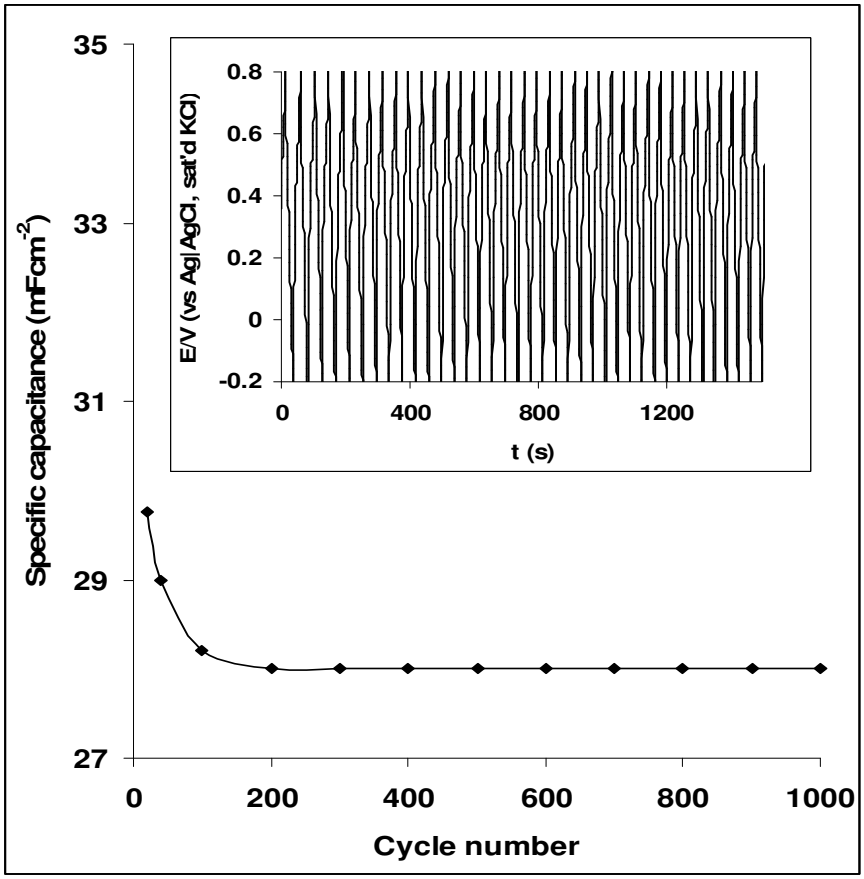

Figure 10.6: shows the effect of cycle number (1000) or cycle life on stability of BPPGE-SWCNT-NiO electrode in 1 M H_2SO_4 aqueous electrolytes. Inset is the typical examples of some of the charge-discharge curve (1000 cycles) for the BPPGE-SWCNT-NiO electrode in 1 M H_2SO_4 aqueous electrolytes.

10.4 Electrochemical impedance studies

Figure 10.7a and b presents the Nyquist plots obtained at a bias potential of 0.3 V for the three SWCNT-MO nanocomposites in 1 M Na_2SO_4 and H_2SO_4, respectively. The 0.3 V potential was chosen for

this experiment as the maximum capacitance was obtained at this potential.

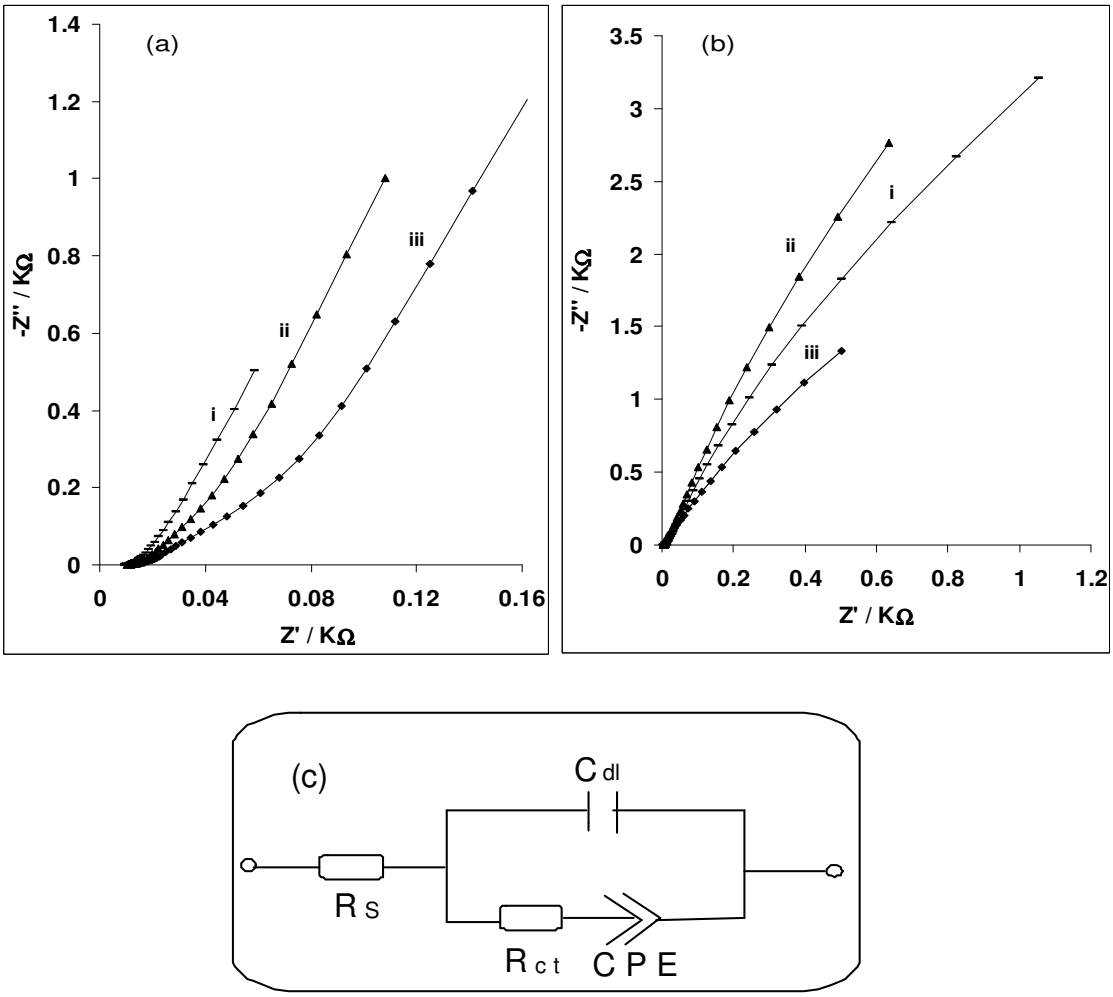

Figure 10.7: Typical Nyquist plots of (i) BPPGE-SWCNT-Fe_2O_3, (ii) BPPGE-SWCNT-NiO and (iii) BPPGE-SWCNT-Co_3O_4 electrodes in (a) 1 M Na_2SO_4 and (b) 1 M H_2SO_4 aqueous solutions at a fixed potential of 0.30 V vs Ag|AgCl sat'd KCl.

The low-frequency differential capacitance (C_d) for each of the electrodes can be obtained from the slope ($1/2\pi C_d$) of the plot of the

imaginary component of the impedance versus the reciprocal of the frequency (i.e., -*Z*″ vs 1/*f*). The values of the SC for the three BPPGE-SWCNT-MO in 1 M Na_2SO_4 and H_2SO_4 were much smaller than values obtained using the galvanostatic discharge method. For example, the BPPGE-SWCNT-NiO gave approximately 7.7 and 4.7 $mFcm^{-2}$ in 1 M H_2SO_4 and Na_2SO_4, respectively. This discrepancy should perhaps not be surprising as other workers have observed similar behaviour, mainly for conducting polymers [22-31]. These workers have attributed the discrepancy to several factors such as the involvement of some physical and chemical heterogeneities [22], deeply trapped counter ions which remain immobile during impedance experiment [24], slow conformational changes occurring in the polymer network [26,27], or redox-switching hysteresis associated with conducting polymers [29]. Interestingly, SWCNTs have also been regarded as the ultimate polymeric material [31]. The impedance data were satisfactorily fitted, judged mainly by the values of the pseudo-χ^2 ($\leq 10^{-4}$) and relative % errors (Table 10.1), with the modified Randles electrical equivalent circuit model (Figure 10.7c).

Two important findings can be made from the impedance data. First, the R_{ct} values obtained for the electrodes in 1 M H_2SO_4 electrolyte are in the order: BPPGE-SWCNT-Co_3O_4 (0.18 Ωcm^2) < BPPGE-SWCNT-NiO (0.47 Ωcm^2) < BPPGE-SWCNT-Fe_2O_3 (0.99 Ωcm^2), indicating faster charge transport in the CoO and NiO based nanocomposites than the FeO-based electrode. Similar behaviour was observed in 1 M Na_2SO_4 (Table 10.1).

Table 10.2: Impedance data obtained for MO nanocomposite modified electrodes in 1 M H_2SO_4 and 1 M Na_2SO_4 electrolytes at a fixed potential of 0.30 V vs Ag|AgCl sat'd KCl.

Electrode	**Impedimetric parameters**					
	R_s (Ω cm	C_{dl} (μFcm^{-2})	R_{ct} (Ω cm^2)	CPE(μFcm^{-2})	*n*	*f°* *(Hz)*
	1 M H_2SO_4					
BPPGE-SWCNT-NiO	0.46±0.01	69.70±4.3	0.47±0.0	1321.0±48.88	0.85±0.01	398.0
BPPGE-SWCNT-Co_3O_4	0.44±0.01	116.3±12.30	0.18±0.0	9334.0±14.00	0.80±0.01	199.5
BPPGE-SWCNT-Fe_2O_3	0.47±0.01	66.0±2.14	0.99±0.0	750.0±26.78	0.83±0.01	63.1
	1 M Na_2SO_4					
BPPGE-SWCNT-NiO	1.10±0.01	200.20±16.14	0.62±0.01	5963.0±231.36	0.89±0.01	199.5
BPPGE-SWCNT-Co_3O_4	1.13±0.01	107.50±8.99	0.83±0.01	3552.0±175.4	0.85±0.01	158.5
BPPGE-SWCNT-Fe_2O_3	0.98±0.01	702.0(6.57)	0.58±0.01	12070.0±511.1	0.90±0.01	125.9

The *n* values in the range 0.83 – 0.9 (Table 10.1) describe the porous nature of the electrodes, significant for the facile diffusion of ions to and from the electrode|solution interface.

Second, the transition point between the high frequency and low frequency component, referred to as the "knee" or "onset" frequency (f_o) describes the maximum frequency at which the capacity behaviour is dominant, and is a measure of the power capability of a supercapacitor; the higher the f_o the more rapidly the supercapacitor can be charged or the higher the power density that can be achieved from the supercapacitor [30,32]. As summarized in Table 10.1, the values of the f_o for the BPPGE-SWCNT-NiO are approximately 398 and 200 Hz in H_2SO_4 and Na_2SO_4, respectively. These values are greater than other electrodes, and again corroborate the high SC values of the electrode in H_2SO_4 solution. This means that the response time of the BPPGE-SWCNT-NiO (i.e., reciprocal of the f_o) is about 2.5 ms, suggesting that most of its stored energy is still accessible at frequencies as high as 398 Hz. Considering that even the most commercially available supercapacitors, including those specifically designed for higher power applications, operate at frequencies less than 1 Hz [33], the response time of this electrode is quite significant.

Since NiO nanocomposite modified electrode has the best SC from the three electrode system results above, the supercapacitive behaviour of chemically synthesised NiO integrated with MWCNT was investgated using two-electrode system in a coin cell type capacitor (already discussed in Chapter 2) for its potential commercial application. Figure 10.8 presents the cyclic voltammograms obtained for the symmetry (a) and (b); and the asymmetry (c) and (d) MWCNT-NiO based supercapacitor in 1 M H_2SO_4 and 1 M Na_2SO_4

aqueous electrolyte respectively at scan rate 5, 25, 50, 100, 200, 300, 400 and 500 mVs^{-1} (i-viii, inner to outer).

For the symmetric based electrode, there is a redox peaks at E_a ~ 0.80 V and E_c ~ 0.40 V due to the Ni(II)/Ni(III) redox process (Figure 10.8a). The ratio of the anodic and the cathodic current (I_{pa}/I_{pc}) is 1.0, which implies a favoured reversible or charge/discharge process of the supercapacitor material. On the other hand, in H_2SO_4, the asymmetry base supercapacitor showed an anodic peak at a lower potential (E_a ~ 0.57) and a weak cathodic peak at *ca* 0.50 V (Figure 10.8c). However as scan rate increases, the cathodic peak disappears while the anodic peak shift with increasing scan rate indicating a high capacitive behaviour. As scan rate increases, a large current separation with mirror images are observed at higher scan rate for both the symmetry and asymmetry supercapacitors. The CVs tend to be rectangular in H_2SO_4 than in Na_2SO_4. The specific capacitance (SC) was estimated from the cyclic voltammograms using Equation 10.1 above.

The capacitance values decreases with increasing scan rate (Table 10.3) with the highest values of 80 and 194 $mFcm^{-2}$ (obtained for the symmetry); and 950 and 220 $mFcm^{-2}$ obtained for the asymmetry supercapacitor in 1 M H_2SO_4 and 1 M Na_2SO_4 respectively (scan rate, 5 mVs^{-1}). The specific capacitance per mass of one cell electrode was calculated according to Equation 10.7 [34]:

$$\text{SC (F/g)} = 2\frac{C}{m} \qquad (10.7)$$

where C is the experimental measured capacitance of the supercapacitor, m is the mass of one composite electrode. The specific capacitance in F/g is represented in parenthesis in Table 10.3.

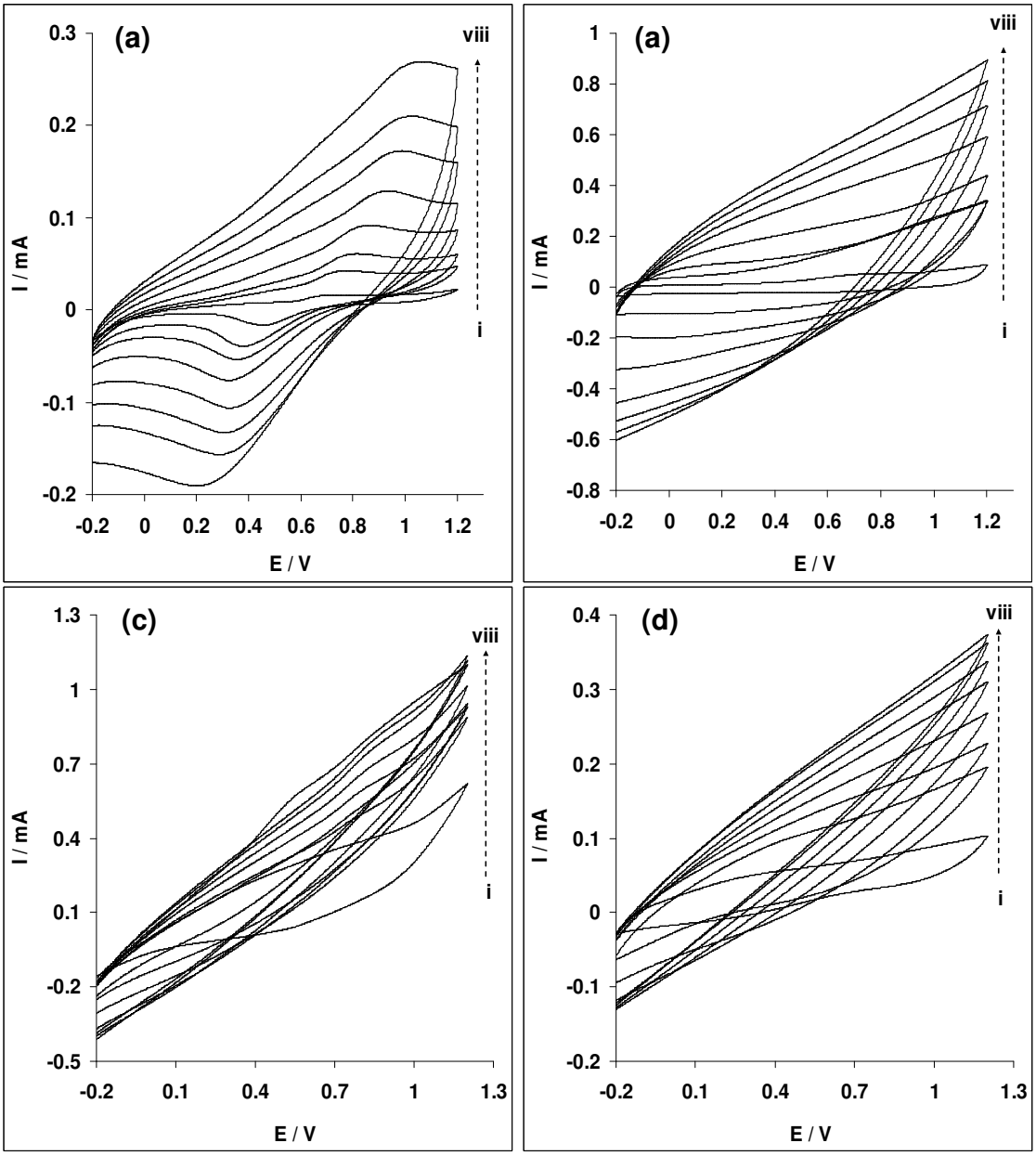

Figure 10.8: Cyclic voltammograms obtained for the symmetry (a) and (b); and the asymmetry (c) and (d) MWCNT-NiO baased supercapacitor (two–electrode cell) in 1 M H_2SO_4 and 1 M Na_2SO_4 aqueous electrolyte respectively at scan rate 5, 25, 50, 100, 200, 300, 400 and 500 mVs^{-1} (i-viii, inner to outer); mass of each electrode, 1.4 mg.

From Table 10.3, this result agreed with other reports where it was established that the asymmetry assembly gave higher specific capacitance values than the symmetry counterpart [34-38]. The results followed the same trend with those obtained by Ganesh et al. [35] but the highest value of 960 $mFcm^{-2}$ obtained at 5 mVs^{-1} is quite higher than the 83 $mFcm^{-2}$ obtained (at the same scan rate) for asymmetric supercapacitor cell assembly based on NiO in 6 M KOH [35]. The difference can be attributed to the different methods of obtaining the supercapacitor material and the well conducting and the mesoporous nature of MWCNT in enhancing charge flow in the nanocomposite used in this study. The equivalent specific capacitance value of 54.3 F/g at 5 mVs^{-1} is also greater compared with 34 and 27.67 F/g obtained at 2 and 5 mVs^{-1} respectively for an asymmetric NiO supercapacitor cell assembly in 6 M KOH electrolyte [35].

To further examine the detailed electrical properties or capacitive behaviour of the MWCNT-MO electrodes in the electrolytes, electrochemical impedance spectroscopy (EIS) experiment was conducted at $E_{1/2}$ of 0.55 V vs Ag|AgCl, sat'd KCl. Figure 10.9a presents the Nyquist plots obtained for the symmetry and the asymmetry assembly in both electrolytes. The Nyquist plots showed a good capacitor-like behaviour with a small diffusion limitation. Figures 10.9b – 10.9d are the equivalent electrical circuits' diagrams for fitting of the impedance data. The data obtained from the fittings are presented in Table 10.4, clearly showing satisfactory fitting as judged by the low relative errors.

Table 10.3: Specific capacitance ($mFcm^{-2}$) for the symmetric and asymmetric MWCNT-NiO based supercapacitor (two-electrode cell) in 1 M H_2SO_4 and 1 M Na_2SO_4 aqueous electrolyte respectively. Values in parenthesis are the specific capacitance in Fg^{-1}.

Scan rate (mVs^{-1})	**Specific capacitance ($mFcm^{-2}$)**		**Specific capacitance ($mFcm^{-2}$)**	
	MWCNT-NiO|H_2SO_4|NiO-MWCNT	**MWCNT-NiO|H_2SO_4|MWCNT**	**MWCNT-NiO|Na_2SO_4|NiO-MWCNT**	**MWCNT-NiO|Na_2SO_4|MWCNT**
5	80.0 (4.6 Fg^{-1})	950.0 (54.3 Fg^{-1})	194.0 (11.1 Fg^{-1})	220.0 (12.6 Fg^{-1})
25	40.0 (3.2)	450.0 (25.7)	152.0 (8.7)	92.0 (5.3)
50	27.5 (2.2)	160.0 (9.1)	110.0 (6.3)	47.5 (2.7)
100	21.2 (1.2)	65.0 (3.7)	62.5 (3.6)	30.0 (1.7)
200	15.0 (0.9)	41.6 (2.4)	47.5 (2.7)	16.3 (0.93)
300	12.5 (0.72)	29.6 (1.7)	34.2 (2.0)	11.7 (0.7)
400	11.9 (0.68)	24.6 (1.4)	30.6 (1.8)	10.0 (0.6)
500	12.0 (0.68)	21.4 (1.2)	28.0 (1.6)	7.0 (0.4)

Circuit 10.9b fitted impedance data obtained for the symmetry assembly in both 1 M H_2SO_4 and 1 M Na_2SO_4, while circuit 10.9c fitted the impedance data for the asymmetry assembly in 1 M H_2SO_4. Circuit 10.9d fitted the impedance data for the asymmetry assembly in 1 M Na_2SO_4. From Table 10.4, the assymetry supercapacitor, MWCNT-NiO|H_2SO_4|MWCNT has the lowest R_{ct} values (32.1 Ω or 1.28 Ωcm^{-2}) in 1 M H_2SO4. The result indicates faster charge transport of the supercapacitor, which also could be responsible for its high SC values. A phase angle of 31° and 21° are obtained for the symmtery (MWCNT-NiO|H_2SO_4|MWCNT-NiO) and asymmetry (MWCNT-NiO|H_2SO_4|MWCNT) supercapacitors respectively, indicating a pseudocapacitive behaviour. On the other hand, a phase angle of 11° and 52° are obtained for the symmtery (MWCNT-NiO|Na_2SO_4|MWCNT-NiO) and asymmetry (MWCNT-NiO|Na_2SO_4|MWCNT) supercapacitors respectively. A phase angle of 90° is expected for pure and ideal capacitive behaviour. The low-frequency differential capacitance (C_d) for the symmetric and the asymmetric electrodes in 1 M Na_2SO_4 and H_2SO_4 were much smaller than values obtained using the galvanostatic discharge method. The symmtery (MWCNT-NiO|H_2SO_4|MWCNT-NiO) gave approximately 3.58 and 2.58 $mFcm^{-2}$ in 1 M H_2SO_4 and Na_2SO_4 while the asymmetry (MWCNT-NiO|H_2SO_4|MWCNT) gave values of 3.08 and 2.17 $mFcm^{-2}$ in 1 M H_2SO_4 and Na_2SO_4 respectively. The discrepancy in the values has been discussed above.

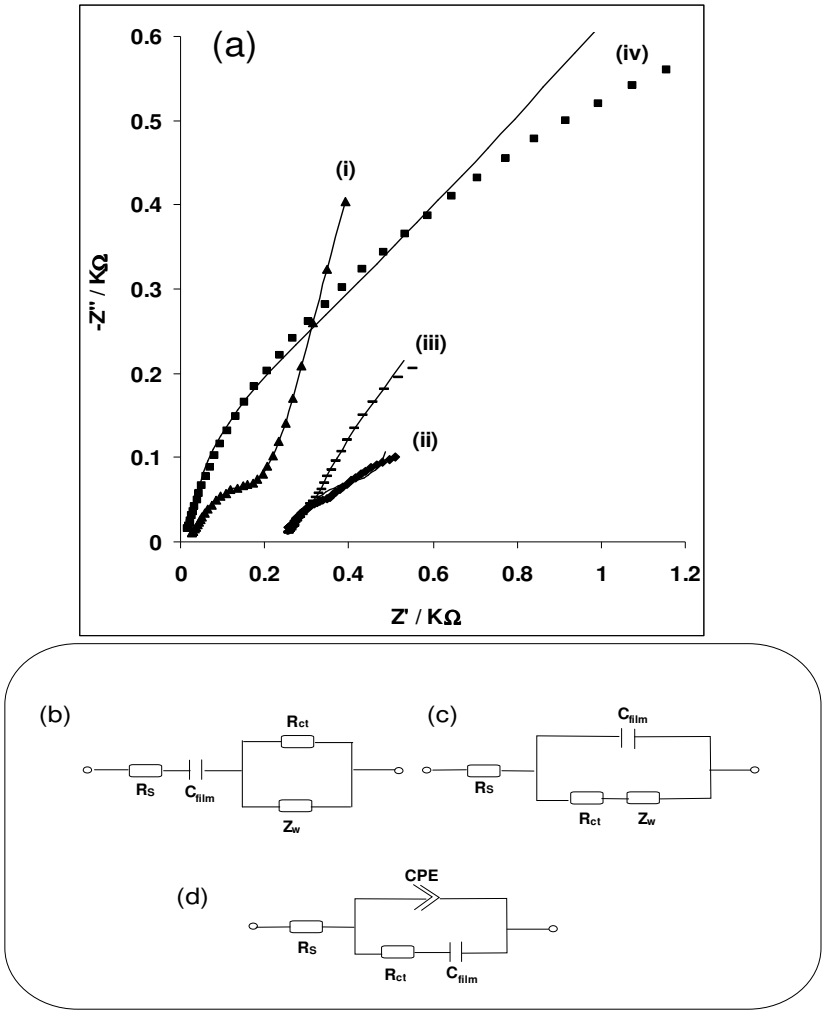

Figure 10.9: (a) Typical Nyquist plots obtained for symmetry: (i) MWCNT-NiO|H_2SO_4|MWCNT-NiO, (ii) MWCNT-NiO|Na_2SO_4|MWCNT-NiO;andthe asymmetry:(iii)MWCNT-NiO|H_2SO_4|MWCNT,(iv)MWCNT-NiO|Na_2SO_4|MWCNT supercapacitors at a fixed potential of 0.55 V vs Ag|AgCl sat'd KCl. Figures 5b-d are the circuit used for fitting the impedance data in (a). Circuit 10.9b fitted impedance data obtained for the symmetry assembly in both 1 M H_2SO_4 and 1 M Na_2SO_4, while circuit 10.9c fitted the impedance data for the asymmetry assembly in 1 M H_2SO_4. Circuit 10.9d fitted the impedance data for the asymmetry assembly in 1 M Na_2SO_4.

Table 10.4: Impedance data obtained for the symmetry and asymmetry MWCNT-NiO nanocomposite based supercapacitor (two-electrode cell) in 1.0 M H_2SO_4 and 1.0 M Na_2SO_4 electrolytes at a fixed potential of 0.55 V vs Ag|AgCl sat'd KCl.

Electrode	**Impedimetric parameters**					
	R_s (Ω cm^2)	**C_{dl} (μFcm^{-2})**	**R_{ct} (Ω cm^2)**	**CPE (μFcm^{-2})**	**n**	**Z_w (mΩ cm^2)**
MWCNT-NiO|H_2SO_4|MWCNT-NiO	2.15±0.03	1330.30±121.99	52.05±0.64	-	-	11.6±0.1
MWCNT-NiO|Na_2SO_4|MWCNT-NiO	24.73±0.02	1100.00±156.00	30.94±0.10	-	-	8.9±0.1
MWCNT-NiO|H_2SO_4|MWCNT	25.69±0.02	4.90±0.78	1.28±0.01	-	-	23.8±0.1
MWCNT-NiO|Na_2SO_4|MWCNT	-2.39±0.04	0.70±0.04	9.42±0.12	1308.0±84.1	0.33±0.01	-

The comparative current charge/discharge experiment of the supercapacitor cell assembly in (a) 1 M H_2SO_4 and (b) 1 M Na_2SO_4 electrolyte solutions at current density of 0.25 mA cm^{-2} was studied at potential range of - 0.2 to 0.8 V to observe the pseudocapacitance arising from the redox reaction at this voltage range. Figure 10.10 (symmetry) and Figure 10.11 (asymmetry) represent the charge/discharge curve obtained. It was observed that the charging-discharging time are almost the same. The specific capacitance of the supercapacitor (SC) was calculated using the Equation 10.3 above. The calculated SC is 277.8 $mAcm^{-2}$ (or 7.8 F/g) and 255.0 $mAcm^{-2}$ (or 7.2 F/g) for the symmetry supercapacitor in 1 M H_2SO_4 and 1 M Na_2SO_4 respectively. The values are higher, 925.9 $mAcm^{-2}$ (53.9 F/g) and 568.2 $mAcm^{-2}$ (15.9 F/g) for the asymmetry assembly in 1 M H_2SO_4 and 1 M Na_2SO_4 respectively. The SC values obtained from the charge-discharge experiment are slightly higher especially for the symmetry supercapacitor compared with those obtained from the CV experiment but there is a good correlation between the CV and galvanostatic measurements for the asymmetry cell. The SC value (53.9 F/g) recorded for the asymmetry MWCNT-NiO|H_2SO_4|MWCNT supercapacitor in H_2SO_4 is higher compared with 37 and 40 F/g reported for the symmetry (NiO|KOH|NiO) and the asymmetry (NiO|KOH|activated carbon) supercapacitors respectively using same technique [35]. Aside the fact that the high capacitance of the MWCNT-NiO has been related to the possible consequence of its high surface area and quality pore networks, the higher SC values in H_2SO_4 observed in this study can also be attributed to the strong ionic nature of the H_2SO_4 electrolyte among other factors already mentioned above.

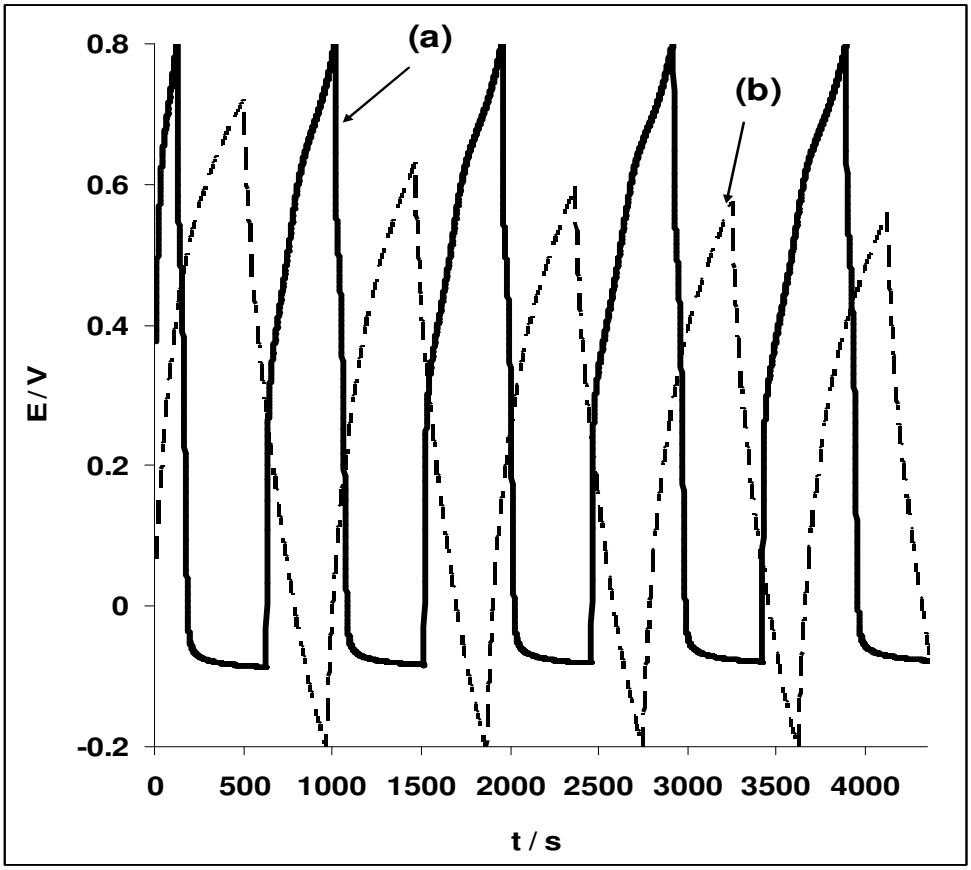

Figure 10.10: Typical examples of galvanostatic charge discharge profile of the symmetry MWCNT-NiO based supercapacitor (two-electrode cell) in (a) 1 M H_2SO_4 and (b) 1 M Na_2SO_4 aqueous electrolytes, at an applied current density of 0.25 $mAcm^{-2}$.

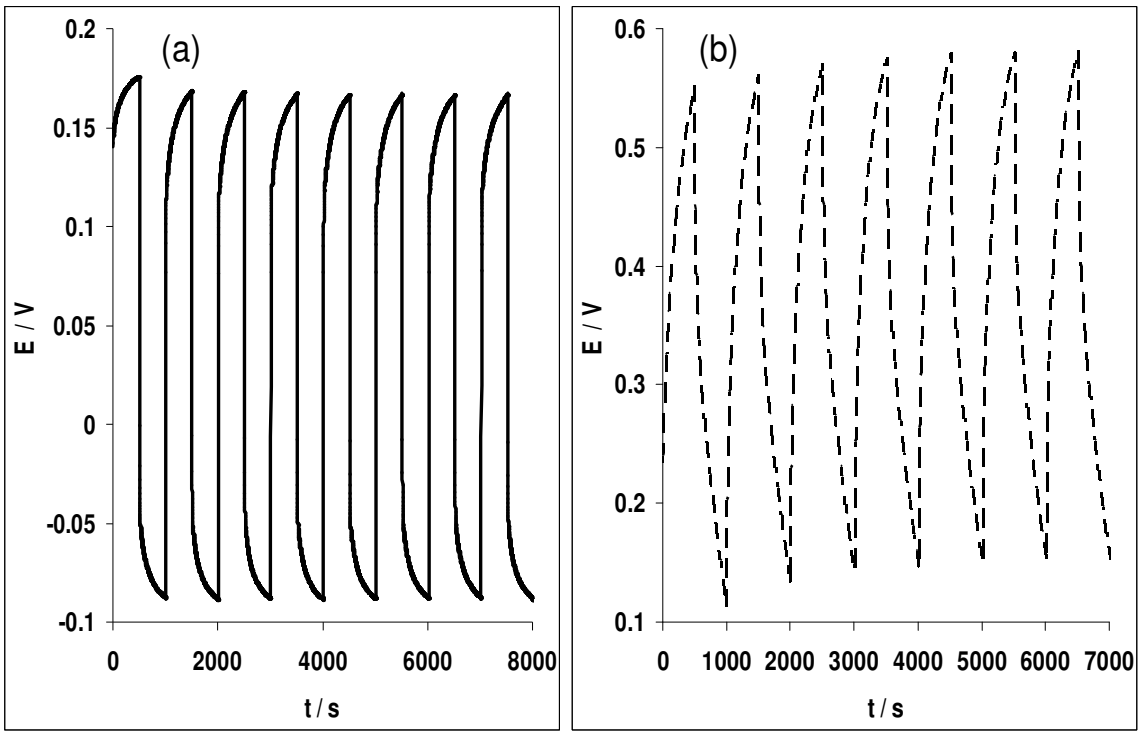

Figure 10.11: Typical examples of galvanostatic charge discharge profile of the asymmetry MWCNT-NiO bases supercapacitor (two-electrode cell) in (a) 1 M H_2SO_4 and (b) 1 M Na_2SO_4 aqueous electrolytes, at an applied current density of 0.25 $mAcm^{-2}$.

Since the asymmetry MWCNT-NiO|H_2SO_4|MWCNT cell gave the highest capacitance, its SP, SE and the energy deliverable efficiency (η / %) are estimated as 3.8 Wkg^{-1} and 1.9 $KWhKg^{-1}$ and 101.0±8.1% respectively using Equations 10.4, 10.5 and 10.6. The stability of the cell at a current density of 2.5 $mAcm^{-2}$ was also investigated. A typical repetitive charge-discharge cycling for 1000 cycles, lasting about 24 h is shown in Figure 10.12. The electrode is able to charge and discharge continuously without any significant loss (< 5 %) SC value was noticed for the last 900 cycles. The electrode stability was attributed to the contribution of the chemical stability of MWCNT in the nanocomposite.

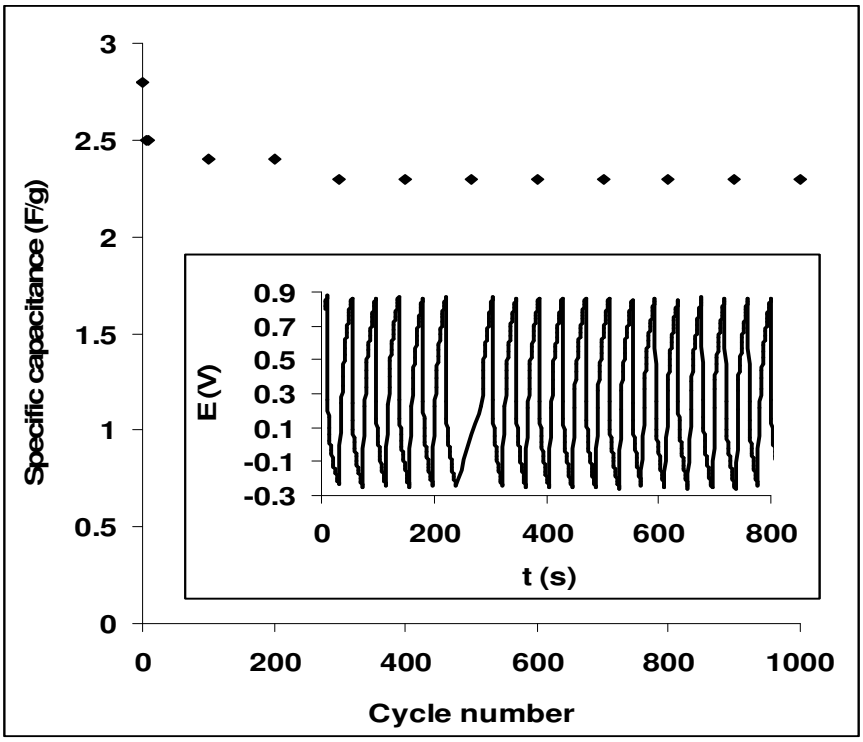

Figure 10.12: Cyclic life (1000 cycles) of the asymmetry MWCNT-NiO |H_2SO_4|MWCNT supercapacitor showing the stability in 1 M H_2SO_4 aqueous electrolytes. Inset is the section of the charge-discharge curves obtained for the electrodes at applied current density of 2.5 $mAcm^2$.

This study showed that SWCNT-NiO nanocomposite modified electrode exhibits remarkable supercapacitive behaviour in neutral and acidic media compared to SWCNT-Fe_2O_3 and SWCNT-Co_3O_4 counterparts. Interestingly, the capacitive behaviour of the SWCNT-NiO was more enhanced in a H_2SO_4 solution than the Na_2SO_4 electrolyte. Asymmetry assembly of MWCNT-NiO|H_2SO_4|MWCNT gave the highest specific capacitance value compared with the symmetric conterpart. Both the SWCNT-NiO electrode and the MWCNT-NiO|H_2SO_4|MWCNT supercapacitor maintained good stability with less than 5% loss of their specific capacitance after 1000 cycles.

References

1. N.S. NcIntyre, M.G. Cook, *Anal. Chem.* 47 (1975) 2208.

2. S. Sunohara, K. Nishimura, K. Yahikozawa, M. Ueno, *J. Electroanal. Chem.* 161 (1993) 354.

3. J-K. Chang, M-T. Lee, C-H. Huang, W-T. Tsai, *Mater. Chem. Phys.* 108 (2008) 124.

4. R.C. Chikate, K-W. Jun, C.V. Rode, *Polyhedron* 27 (2008) 933.

5. A. Salimi, H. Mamkhezri, R. Hallaj, S. Soltanian, *Sens. Actuators B* 129 (2008) 246.

6. H-S. Choo, T. Kinumoto, M. Nose, K. Miyazaki, T. Abe, Z. Ogumi, *J. Power sources* 185 (2008) 740.

7. A.L.M. Reddy, S. Ramaprabhu, *J. Phys. Chem. C* 111 (2007) 7727.

8. M. S. Wu, H-H Hsieh, *Electrochim. Acta* 53 (2008) 3427.

9. J. Pillay, K. I. Ozoemena, *Chem. Phys. Lett.* 441 (2007) 72.

10. T. Shinomiya, V. Gupta, N. Miura, *Electrochim. Acta* 51 (2006) 4412.

11. S.Y. Wang, K.C. HO, S.L. Kuo, N.L. Wu, *J. Electrochem. Soc.* 153 (2006) A75.

12. W. Sun, X. Chen, *J. Power Sources* 193 (2009) 924.

13. F. Leroux, E. Raymundo-Pinero, J-M. Nedelec, F. Beguin, *J. mater. Chem.* 16 (2006) 2074.

14. T. Stimpfling, F. Leroux, *Chem. Mater.* 22 (2010) 974.

15. D. Hulicova-Jurcakova, M. Kodama, S. Shiraishi, H. Hatori, Z.H. Zhu, G.Q. Lu, *Adv. Funct. Mater.* 19 (2009) 1.

16. B.O. Agboola, K.I. Ozoemena, *J. Power Sources* 195 (2010) 3841.

17. A.T. Chidembo, K.I. Ozoemena, B.O. Agboola, V. Gupta, G.G. Wildgoose, R.G. Compton, *Energy Environ. Sci.* 3 (2010) 228.
18. E. Frackowiak, K. Jurewicz, S. Delpeux, F. Beguin., *J. Power Sources* 97 (2001) 822.

19. R.K. Sharma, A.C. Rastogi, S.B. Desu, *Electrochem. Commun.* 10 (2008) 268.

20. C.P. Fonseca, J.E. Benedetti, S. Neves, *J. Power Sources* 158 (2006) 789.

21. S. G. Kandalkar, J. I. Gunjakar, C. D. Lokhande, *Appl. Surf. Sci.,* 254 (2008) 5540.

22. B.J. Feldman, P. Burgmayer, R.W. Murray, *J. Am. Chem. Soc.* 107 (1985) 872.

23. N. Mermilliod, J. Tanguy, F. Petior, *J. Electrochem. Soc.* 133 (1986) 1073.

24. J. Tanguy, N. Mermilliuod, M. Hoclet, *J. Electrochem. Soc.* 134 (1987) 795.

25. T. Tanguy, M. Slama, M. Hoclet, J.L. Baudin, *Synth. Met.* 28 (1989) 145.

26. M. Kalaji, L.M. Peter, *J. Chem. Soc. Faraday Trans.* 87 (1991) 853.

27. X. Ren, P.G. Pickup, *J. Electroanal. Chem.* 372 (1994) 289.

28. T.C. Girija, M.V. Sangaranarayanan, *J. Appl. Electrochem.* 36 (2006) 531.

29. G. Xu, W. Wang, X. Qu, Y. Yin, L. Chu, B. He, H. Wu, J. Fang, Y. Bao, L. Liang, *Eur. Polym. J.* doi :10.1016/j.europolymj.2009.05.016.

30. C. Du, N. Pan, *J. Power Sources* 160 (2006) 1487.

31. M.J. Green, N. Behabtu, M. Pasquali, W.W. Adams, *Polymer* 2009.(doi:10.1016/j.polymer.2009.07.044).

32. C-W. Huang, Y-T. Wu, C-C. Hu, Y-Y. Li, *J. Power Sources* 172 (2007) 460.

33. Miller JR, Proceedings of the Electrochemical Society Meeting, Chicago, October, 1995, 246.

34. V. Khomenko, E. Frackowiak, F. Beguin, *Electrochim. Acta* 50 (2005) 2499.

35. V. Ganesh, S. Pitchumani, V. Lakshminarayanan, *J. Power Sources* 158 (2006) 1523.

36. H.-Q. Wang, Z.-S. Li, Y.-G. Huang, Q.-Y. Li, X.-Y. Wang, *J. mater. Chem.*, 2010|DOI:10.1039/c000339e.

37. Q. Wang, Z. Wen, J. Li, *Adv. Funct. Mater.* 16 (2006) 2141.

38. Q.T. Qu, Y. Shi, S. Tian, Y.H. Chen, Y.P. Wu, R. Holze, J. *Power Sources* 194 (2009) 1222.

CONCLUSIONS

AND

RECOMMENDATIONS

CONCLUSIONS

This thesis describes the electron transport and electrocatalytic properties of both electrodeposited and the chemically-synthesized metal and metal oxides MO (where M = Ni, Co, Fe) nanoparticles supported on single-walled carbon nanotubes (SWCNT) or multi-walled carbon nanotubes (MWCNT) platforms towards the electrocatalytic oxidation of important molecules such as hydrazine, diethylaminoethanethiol (DEAET), nitrite and dopamine. It has been shown that edge plane pyrolytic graphite electrodes modified with funtionalised CNTs electro-decorated with metal and metal oxide nanoparticles exhibit enhanced electrochemical response towards electro-oxidation of these analytes in aqueous buffered solution at different pH conditions where the analytes ionise maximally. The flowing results should be emphasised:

(i) SWCNT-Ni and the SWCNT-Fe modified electrodes demonstrated comparable electrochemical response towards hydrazine oxidation.

(ii) Electrochemical impedance spectroscopy study indicated that hydrazine oxidation on SWCNT-metal hybrids are rather complicated and follow electrical equivalent circuit model typical of adsorption-controlled charge transfer kinetics with some resemblance to the behaviour of electrolyte-insulator-semiconductor sensors.

(iii) This thesis provide some insights into the electrooxidative mechanism of hydrazine at carbon electrodes modified with single-walled carbon nanotubes decorated with metal and metal oxide films.

(iv) The SWCNT-Ni modified electrode showed enhanced current response towards detection of DEAET compared with other

SWCNT-M or SWCNT-MO nanocomposite modified electrodes.

(v) DEAET was detected at nano molar concentration, but the adsorptive behavior of the SWCNT-Ni may be seen as a limitation to its ultra-low detection (and very likely other related analytes) using the chronoamperometric methodology.

(vi) Synthesised M and MO nanoparticles on MWCNT platform offered less adsorptive behaviour towards hydrazine and DEAET electrooxidation compared with their counterpart electrodeposited nanocomposite on SWCNT platform.

(vii) The ability to synthesised nano-scaled metal and metal oxide nanoparticles in high commercial quantity compared to the very low and commercially unavailable nano material by electrodeposition method is one of the factors explored in this study.

(viii) MWCNT-Ni nanocomposite modified electrode yielded the fastest electron transport as well as the best electrocatalytic behaviour towards DEAET and hydrazine compared with other electrodes investigated or reported in the literature.

(ix) The enhancement is associated with high electrical-conducting MWCNTs which form a synergistic behaviour with the nickel nanoparticles.

(x) Electrocatalytic oxidation of nitrite was favoured on Co nanoparticles modified electrode.

(xi) The detection and the electro-catalytic oxidation of nitrite were successful on all the Co modified electrodes investigated.

(xii) EPPGE-SWCNT-Co electrode made by electrodeposition has the fastest electron transport towards nitrite compared with other Co modified electrodes.

(xiii) Attempts to use CNTs as supports for synthesised Co and Co_3O_4 nanoparticles did not improve the electrochemistry of nitrite, a further advantage of the synthesis method over the electrodeposited counterparts that require CNTs.

(xiv) The electrocatalytic-oxidation of nitrite on the electrodes followed adsorption-controlled electrochemical process with complex impedance behaviour.

(xv) Electrocatalytic detection of DA was best at electrode modified by both electrodeposited and synthesised Fe_2O_3 nanoparticle catalyst supported on CNT platform.

(xvi) From EIS, the pseudo-capacitive nature of the Fe_2O_3 modified electrodes is a function of their electrochemical stability towards DA.

(xvii) Analysis of DA at these electrodes showed that DA oxidation proceeded through diffusion and surface controlled electrochemical process.

(xviii) The limit of detection (LoD), catalytic rate constant (k) of the electrodes, and the diffusion coefficient (D) of DA agreed favourably with values reported earlier in literature.

(xix) The CNT-Fe_2O_3 modified electrodes clearly separated DA signal from the interfering effect of AA even at AA concentration of 50-100 folds that of DA.

(xx) The electrodes have also proven to be a potential sensor for dopamine detection in real sample analysis.

(xxi) Electrocatalytic oxidation of the four analytes (DEAET, hydrazine, nitrite and dopamine) was successful on EPPGE-

SWCNT-PB modified electrode in terms of current response and on-set potential for catalysis compared with the bare EPPGE.

(xxii) The analytes oxidation current response increases with increasing PB layer on the electrode making EPPGE-SWCNT-3PB the best electrode. This electrode has the fastest electron transport and lowest R_{ct} towards the analytes electrocatalysis.

(xxiii) DA oxidation on the EPPGE-SWCNT-3PB proceeds via diffusion-controlled process while DEAET, hydrazine and nitrite oxidation was affected by some degree of adsorption of the reaction intermediates as indicated by their Tafel slopes and the standard free energy change due to adsorption.

(xxiv) The sensitivities, linear concentration ranges, and detection limits of these analytes on the EPPGE-SWCNT-3PB electrode agreed favourably and even better than values reported in the literature.

(xxv) The EPPGE-SWCNT-3PB electrode detects DA even at AA concentration which is 1000 times that of DA, with a wide potential separation of about 200 mV.

(xxvi) The electrode is electrochemically stable, re-usable and can be used for the analysis of DA in real drug samples with satisfactory accuracy and reproducibility.

(xxvii) The CNT-MO nanocomposite modified electrodes were screened for their supercapacitive properties.

(xxviii) SWCNT-NiO nanocomposite modified electrode exhibits remarkable supercapacitive behaviour in neutral and acidic

media compared to SWCNT-Fe_2O_3 and SWCNT-Co_3O_4 counterparts.

(xxix) The capacitive behaviour of the SWCNT-NiO was more enhanced in a H_2SO_4 solution than the Na_2SO_4 electrolyte, possibly due to the high conductivity of the former.

(xxx) EIS study indicated that the electrolyte ions could penetrate more easily into the pores of the BPPGE-SWCNT-NiO electrode at a reasonable frequency range.

(xxxi) SWCNT-NiO electrode maintained good stability with only about 5% loss of its specific capacitance after 1000 cycle life.

RECOMMENDATIONS

(1) This work recommends and cautions researchers who wish to use this emerging type of CNT-metal nanoparticle electrocatalytic / sensing platform to first establish the adsorption phenomenon with a view to understanding and applying the most appropriate electrochemical technique to be used for reliable analytical parameters.

(2) The adsorption phenomenon should be subject of future concern more importantly, in reducing the effect on the limit of detection of the fabricated sensors.

(3) Large scale fabrication of the sensors for industrial application in food, agriculture, pharmaceuticals, military, and forensic use should be maximised.

(4) The CNT-MO nanocomposite materials have also demonstrated some potential that needs to be further explored for future application in energy generating and storing devices such as batteries and suoercapacitors.

APPENDIX A

List of publications in peer-reviewed journals from this thesis

1. **Abolanle S. Adekunle**, Bolade O. Agboola, Jeseelan. Pillay, Kenneth I. Ozoemena, Electrocatalytic detection of dopamine at single-walled carbon nanotubes-iron (III) oxide nanoparticles platform, *Sens. Actuator: Chemical B* 148 (2010) 93-102.

2. **Abolanle S. Adekunle**, Jeseelan Pillay, Kenneth I. Ozoemena, Probing the electrochemical behaviour of SWCNT-Cobalt nanoparticles and their electrocatalytic activities towards the detection of nitrite at acidic and physiological pH conditions, *Electrochim. Acta* 55 (2010) 4319-4327.

3. **Abolanle S. Adekunle**, Kenneth I. Ozoemena, Electrocatalytic Oxidation of hydrazine and diethylaminoethanethiol at Single-walled carbon nanotubes / Prussian Blue Nanoparticles Modified Electrode, *Electroanalysis* 22 (2010), 2519-2528

4. **Abolanle S. Adekunle**, Kenneth I. Ozoemena, Electron transport and electrocatalytic properties of MWCNT/nickel nanocomposites: Hydrazine and Diethylaminoethanethiol as analytical probes, *J. Electroanal.l Chem.* 645 (2010) 41-49.

5. **Abolanle S. Adekunle**, Kenneth I. Ozoemena, Comparative surface electrochemistry of Co and Co_3O_4 nanoparticles: Nitrite as an analytical probe, *Int. J. Electrochem.* 5 (2010) 1972-1983.

6. **Abolanle S. Adekunle**, Kenneth I. Ozoemena, Voltammetric and impedimetric properties of nano-scaled γ-Fe_2O_3 catalysts supported on multi-walled carbon nanotubes: catalytic detection of dopamine, *Int. J. Electrochem. Sci.* 5 (2010) 1726-1742.

7. **Adekunle A. S.**, Pillay J., Ozoemena K. I., Electrocatalytic detection of V-type nerve agent on SWCNT/Ni modified electrode: Adsorption controlled process, *Electroanalysis*, 20 (2008) 2587-2591.

8. **Abolanle S. Adekunle**, Kenneth I. Ozoemena, Electron transfer behaviour of single-walled carbon nanotubes electro-decorated with nickel and nickel oxide layers. *Electrochim. Acta* 53 (2008) 5774-5782.

9. **Abolanle S. Adekunle**, Kenneth I. Ozoemena, Insights into the electro-oxidation of hydrazine at single-walled carbon-nanotube-modified edge-plane pyrolytic graphite electrodes electro-decorated with metal and metal oxide film, *J. Solid State Electrochem*. 12 (2008) 1325–1336.

10. **Abolanle S. Adekunle**, Jeseelan Pillay, Kenneth I. Ozoemena, Electrocatalytic properties of prussian blue nanoparticles supported on poly(m-aminobenzenesulfonic acid) – functionalized single-walled carbon nanotubes toward the detection of dopamine, (Submitted).

11. **Abolanle S. Adekunle,** Kenneth I. Ozoemena, Electrosynthesised metal (Ni, Fe, Co) oxide films on single-walled carbon nanotube platforms and their supercapacitance in acidic and neutral pH media, *Electroanalysis* (In-press).

12. **Abolanle S. Adekunle**, Kenneth I. Ozoemena, MWCNTs/Metal (Ni, Fe, Co) oxide nanocomposites as potential material for supercapacitors application in acidic and neutral media, *J. Power Sources* (Submitted).

APPENDIX B

List of conference Presentations from this thesis.

1. "Synthesis, characterization and the Electrocatalytic Properties of Prussian blue/Single-walled Carbon Nanotubes Composites" Adekunle A. Saheed, Abdullahi M. Farah and Kenneth I. Ozoemena, NanoAfrica 2009 International Conference on NanoScience and Nanotechnology, CSIR International Convention Centre Pretoria,South Africa, February 1-4, 2009 (**ORAL PRESENTATION BY A.S. ADEKUNLE**).

2. "Metal-Decorated Single Walled Carbon Nanotubes in Elctrocatalysis" A.S. Adekunle and K.I. Ozoemena, International (SA-UK research Network)Workshop on Electrochemistry for Nanotechnology, CSIR Intrnational Convention Centre, Pretoria, South Africa, April 9-10, 2008 (**ORAL PRESENTATION BY A.S. ADEKUNLE**).

3. "Electron Transport and Electrocatalytic Properties of Nickel Nanoparticle-Electrodecorated Single-Walled Carbon nanotubes" Adekunle Abolanle S. and Kenneth I Ozoemena, 1st International Symposium on Electrochemistry ElectrochemSA, University of Western cape, Belville, Cape Town, South Africa, July 9-11, 2008 (**POSTER PRESENTATION BY A.S. ADEKUNLE**).

4. "Electrodecorated Single-Walled Carbon Nanotubes Metal Nanoparticles Composite in Electrocatalysis" Adekunle Abolanle S. and Kenneth I. Ozoemena, 1st Annual DST/MINTEK Nanotechnology Innovation Centre Sensor Workshop, Rhodes University, Grahamstown,South Africa, September 11-12, 2008 (**ORAL PRESENTATION BY A.S. ADEKUNLE**).

5. "Synthesis and Electrocatalysis of Metal Nanoparticles-Decorated Carbon Nanotubes" Adekunle Abolanle S and Kenneth I. Ozoemena, 39th National Convention of the South Africa Chemical Institute (SACI), Stellenbotch University, South Africa, 30 Nov. – 5 Dec. 2008 (**ORAL PRESENTATION BY A.S. ADEKUNLE**).

6. "Electrocatalytic Oxidation of Chemical Warfare Agents at Edge Plane Pyrolytic Graphite Electrodes Decorated with Single-walled Carbon Nanotubes and Nickel Nanoparticles" Abolanle S. Adekunle and Kenneth I. Ozoemena, The South African Chemical Institute Young Spectroscopists' Symposium, Film Auditorium, University of South Africa, Pretoria, South Africa 10 October, 2007 (**ORAL PRESENTATION BY A.S. ADEKUNLE**).

7. "Nano-Architectures and Nanoparticles Incorporating Carbon Nanotubes and Fullerenes: New Hybrids with Excellent Electron Transports " Kenneth I. Ozoemena, and Duduzile Nkosi, Jeseelan Pillay, Abolanle S Adekunle, Alfred Mocheko, Solomon Mamuru, Bolade Agboola. SACI, INORG 007, Langebaan, Cape Town, July 8-12, 2007.